

THESIS

THE MAGMATIC-HYDROTHERMAL FLUID HISTORY OF THE HARRISON PASS PLUTON,
RUBY MOUNTAINS, NV: IMPLICATIONS FOR THE RUBY MOUNTAIN-EAST HUMBOLDT
RANGE METAMORPHIC CORE COMPLEX AND CARLIN-TYPE AU DEPOSITS

Submitted by

Christopher Harry Gates

Department of Geosciences

In partial fulfillment of the requirements

For the Degree of Master of Science

Colorado State University

Fort Collins, Colorado

Summer 2016

Masters Committee:

Advisor: John Ridley

Sally Sutton

Steven Strauss

Copyright by Christopher Harry Gates 2016

All Rights Reserved

ABSTRACT

THE MAGMATIC-HYDROTHERMAL FLUID HISTORY OF THE HARRISON PASS PLUTON, RUBY MOUNTAINS, NV: IMPLICATIONS FOR THE RUBY MOUNTAIN-EAST HUMBOLDT RANGE METAMORPHIC CORE COMPLEX AND CARLIN-TYPE AU DEPOSITS

Intrusion of the ~36 Ma, calc-alkaline, granodiorite-monzogranite Harrison Pass Pluton (HPP) occurred as magmatic fronts migrated southwest across the Great Basin during the Eocene. The HPP was locally intruded into the Ruby Mountains-East Humboldt Range (RMEHR), a classic Cordilleran metamorphic core complex that would undergo rapid tectonic exhumation during the late Cenozoic. Although the emplacement depth of the HPP provides an estimate for the magnitude and timing of subsequent uplift, disagreement exists between published mineral thermobarometry data and stratigraphic reconstructions. Synchronous with emplacement of the HPP was a regional hydrothermal fluid event responsible for deposition of >200 Moz of Au in sediment-hosted Carlin-type deposits (CTD's) along four linear trends. Magmatic, meteoric, and metamorphic models have been invoked to explain the origin of fluids and Au for CTD's, but few studies have directly examined the fluids generated by a potential source intrusion such as the HPP. Investigation of the magmatic-hydrothermal fluid history of the HPP, particularly the pressure-temperature conditions of fluid entrapment and fluid geochemistry, is an effective means of testing and improving existing models for the development of the RMEHR metamorphic core complex and for the origin of CTD's.

Field and petrographic observations of pegmatites, aplites, miarolitic cavities, quartz veins, and multiple types of hydrothermal alteration, coupled with data from fluid inclusion microthermometry, LA-ICP-MS fluid inclusion geochemistry, and oxygen stable isotopes from magmatic and hydrothermal quartz, demonstrate that two-stage intrusive assembly was paralleled by a two-stage magmatic-hydrothermal fluid system. Early stage fluid activity was dominated by two aqueous, low salinity (~ 3 wt % eq. NaCl), B-Na-K-Rb-Sr-Cs-bearing, ore metal-poor fluids. These fluids were entrapped at ~ 600 - 700°C and ~ 2400 - 7600 bar in pegmatites, miarolitic cavities, and quartz veins within early stage units, as well as in quartz and calcite veins in base-metal skarns along the pluton margin and in the contact metamorphic aureole. Late stage fluid activity was dominated by one aquo-carbonic, low salinity (~ 3 wt % eq. NaCl), B-Na-K-Rb-Sr-Cs-bearing, ore metal-poor fluid. This fluid was entrapped at 570 - 680°C and ~ 4800 - 7200 bar in pegmatites, aplites, and quartz veins, and did not migrate out of late-stage intrusive units. Magmatic $\delta^{18}\text{O}$ values for quartz demonstrate that this magmatic-hydrothermal fluid system evolved without significant dilution from meteoric inputs until the late influx of post-intrusion hydrothermal fluids, interpreted to be of mixed magmatic-meteoric origin. These fluids were aqueous, low-temperature (320 - 410°C), low salinity (<4 wt % eq. NaCl), and were entrapped at <2400 bar in fault-hosted microcrystalline quartz veins.

The entrapment conditions for early stage magmatic-hydrothermal fluids determined from fluid inclusion microthermometry data indicate that the HPP was emplaced at depths of 9 - 18 km in the Ruby Mountains-East Humboldt Range. Brittle-ductile deformation of the HPP on the regionally-exposed Ruby Mountain Shear Zone indicate that at least 9 km of vertical exhumation has occurred since the intrusion of the

HPP. Such emplacement depth estimates are consistent with published mineral thermobarometry from the HPP and from nearby metamorphic rocks. It is interpreted that the disparity between these estimates and the relatively shallow minimum emplacement depths of 4-6 km suggested by stratigraphic reconstructions is supportive of the existence of poorly preserved Mesozoic thrust sheets that augmented the thickness of the overlying rock package during the Eocene.

Although a well-accepted model for the origin of fluids and Au for CTD's remains outstanding, the model of Muntean et al. (2011) argues for the separation of a low-salinity, vapor-rich, Au-partitioning fluid from a high-salinity, base metal-partitioning fluid in mid-crustal magma chambers as a critical process in the evolution of CTD ore fluids. Although HPP emplacement depths and the existence of a robust magmatic-hydrothermal fluid system are broadly supportive of this model, no evidence of a high-salinity fluid was observed. Low concentrations of base metals (Cu, Pb) and CTD pathfinder elements (As, Tl) relative to whole-rock values are not consistent with the efficient fluid partitioning of metals invoked by Muntean et al. (2011). Also, low concentrations of CTD pathfinder elements relative to published values for CTD ore fluids indicate that the HPP was not Au-enriched. However, similar salinities and $\delta^{18}\text{O}$ values suggest that HPP fluids may represent the minor magmatic component of ore fluids detected at some CTD's, but other fluid inputs and an external Au source would be required to produce these ore fluids. Thus, it is suggested that the magmatic-hydrothermal fluid history of the HPP is more consistent with a dominantly amagmatic fluid model for the origin of CTD's.

ACKNOWLEDGEMENTS

Funding for this thesis was provided by a Graduate Student Fellowship from the Society of Economic Geologists, and by the Steininger Fellowship and McCallum Scholarship from Colorado State University.

I would like to thank my advisor, Dr. John Ridley, for his extensive instruction, constant availability, and tireless editing. I am also appreciative of the guidance from the other members of my thesis committee, Dr. Sally Sutton and Dr. Steven Strauss.

Erin Marsh and Alan Koenig of the USGS are due recognition for their guidance in the use of the LA-ICP-MS at the Crustal Geophysics and Geochemistry Science Center and for assisting with data treatment and interpretation.

The geologists of the Barrick Gold Exploration group, particularly Dr. Jeremy Vaughan, were helpful in supplying field equipment, teaching me about Carlin-type deposits, and providing thoughtful critiques to my interpretations.

Friendships with my fellow graduate students in the Geosciences department, especially in Room 319, were indispensable to the writing of this thesis. Adrian, Kate, Russell, Tucker, Zander, and Katharine – thank you for the engaging discussions and the many fun times.

Most importantly, I want to thank my wife, Michelle, for her help as my field assistant, and for her constant love and support throughout this endeavor.

DEDICATION

This thesis is dedicated to my wife.

Michelle, you have been a part of this from the very beginning.

I can't imagine doing any of it without you.

TABLE OF CONTENTS

ABSTRACT..... ii
ACKNOWLEDGMENTS..... v
DEDICATIONvi
TABLE OF CONTENTS.....vii
LIST OF TABLES.....xi
LIST OF FIGURES.....xii
DEFINITION OF TERMS AND ABBREVIATIONS..... xiv
CHAPTER 1: PROJECT OVERVIEW 1
 1.1 RATIONALE FOR STUDY..... 1
 1.2 CONCEPTUAL BACKGROUND..... 2
 1.2.1 GRANITIC INTRUSIONS 2
 1.2.2 MAGMATIC-HYDROTHERMAL FLUIDS..... 4
 1.2.3 GRANITOID INTRUSIONS AND ORE DEPOSITS 8
 1.3 GEOLOGIC BACKGROUND 9
 1.3.1 GEOLOGIC HISTORY OF THE GREAT BASIN 9
 1.3.2 METAMORPHIC CORE COMPLEXES 14
 1.3.2.1 CHARACTERISTICS 14
 1.3.2.2 STRUCTURAL DEVELOPMENT 15
 1.3.2.3 EXHUMATION DYNAMICS 16
 1.3.2.4 RELATIONSHIP WITH PLUTONISM..... 18
 1.3.3 CARLIN-TYPE AU DEPOSITS..... 19
 1.3.3.1 CHARACTERISTICS 19
 1.3.3.2 ORE FLUIDS 21
 1.3.3.3 THEORIES FOR FLUID ORIGIN..... 22
 1.4 THESIS GOALS 24
 1.5 THESIS ORGANIZATION 25
 1.6 SUMMARY 26
 1.7 REFERENCES 27

CHAPTER 2: THE HARRISON PASS PLUTON AND EVIDENCE FOR FLUID
EXSOLUTION AND MIGRATION DURING EMPLACEMENT AND
COOLING..... 42
 2.1 INTRODUCTION..... 42
 2.2 GEOLOGIC FRAMEWORK AND STRUCTURAL REVIEW 43
 2.2.1 THE RUBY MOUNTAINS-EAST HUMBOLDT RANGE..... 44
 2.2.2 THE HARRISON PASS PLUTON..... 48
 2.2.3 CONTACT METAMORPHIC AUREOLE..... 51
 2.3 FIELD AND ANALYTICAL TECHNIQUES 53
 2.3.1 FIELD MAPPING AND SAMPLING..... 53
 2.3.2 PETROGRAPHIC INVESTIGATION 54
 2.4 FIELD GEOLOGY OF THE HARRISON PASS PLUTON..... 55
 2.4.1 HARRISON PASS..... 55

2.4.2 DESCRIPTIONS OF INTRUSIVE PHASES.....	56
2.4.2.1 EARLY STAGE.....	56
2.4.2.2 LATE STAGE.....	58
2.5 EVIDENCE OF HYDROTHERMAL ACTIVITY IN THE HPP.....	59
2.5.1 QUARTZ-FELDSPAR PEGMATITES.....	60
2.5.2 MUSCOVITE-QUARTZ-FELDSPAR PEGMATITES.....	61
2.5.3 APLITE VEINS AND DIKES.....	62
2.5.4 MIAROLITIC CAVITIES.....	63
2.5.5 QUARTZ VEINS.....	64
2.5.6 ALTERATION TYPES.....	69
2.5.6.1 SKARN.....	70
2.5.6.2 POTASSIC.....	71
2.5.6.3 PHYLIC.....	72
2.5.6.4 CHLORITE-SERICITE.....	73
2.5.6.5 SILICIFICATION.....	74
2.6 DISCUSSION.....	75
2.6.1 FLUID ACTIVITY IN EARLY STAGE GRANITIC UNITS.....	76
2.6.1.1 ORTHOMAGMATIC FEATURE TYPES.....	76
2.6.1.2 HYDROTHERMAL FEATURE TYPES.....	77
2.6.2 FLUID ACTIVITY IN LATE STAGE GRANITIC UNITS.....	82
2.6.2.1 ORTHOMAGMATIC FEATURE TYPES.....	82
2.6.2.2 HYDROTHERMAL FEATURE TYPES.....	84
2.7 SUMMARY.....	86
2.8 REFERENCES.....	100

CHAPTER 3: THE MAGMATIC-HYDROTHERMAL FLUIDS OF THE HARRISON
PLUTON: IMPLICATIONS FOR THE RMEHR METAMORPHIC CORE
COMPLEX AND CARLIN-TYPE AU DEPOSITS.....

.....	105
3.1 INTRODUCTION.....	105
3.2 GEOLOGIC SETTING.....	107
3.2.1 GEOLOGIC HISTORY OF THE HARRISON PASS PLUTON.....	107
3.2.2 MAGMATISM AND CARLIN-TYPE AU DEPOSITS.....	111
3.3 EVIDENCE OF MAGMATIC-HYDROTHERMAL FLUID ACTIVITY.....	112
3.3.1 FLUID ACTIVITY WITHIN THE HPP.....	112
3.3.1.1 PEGMATITES.....	113
3.3.1.2 APLITES.....	114
3.3.1.3 MIAROLITIC CAVITIES.....	114
3.3.1.4 HYDROTHERMAL VEINS.....	115
3.3.1.5 HYDROTHERMAL ALTERATION.....	116
3.3.2 FLUID ACTIVITY WITHIN THE CONTACT METAMORPHIC AUREOLE.....	117
3.3.2.1 HYDROTHERMAL VEINS.....	118
3.3.2.2 HYDROTHERMAL ALTERATION.....	119
3.4 RESULTS.....	119
3.4.1 FLUID INCLUSION PETROGRAPHIC OBSERVATIONS.....	119
3.4.2 FLUID INCLUSION MICROTHERMOMETRY DATA.....	124
3.4.2.1 ASSEMBLAGE COMPOSITIONAL TYPES.....	126

3.4.2.2	ISOCHORE DATA.....	128
3.4.2.3	FEATURE TYPES	130
3.4.2.4	SPATIAL AND TEMPORAL TRENDS IN MICROTHERMOMETRY DATA.....	137
3.4.3	MULTI-ELEMENT GEOCHEMISTRY.....	144
3.4.3.1	FIRST PASS RESULTS.....	145
3.4.3.2	MULTI-ELEMENT DATA	147
3.4.3.3	BACKGROUND QUARTZ COMPOSITIONS.....	152
3.4.3.4	SPATIAL AND TEMPORAL COMPOSITIONAL TRENDS.....	153
3.4.4	STABLE ISOTOPE RESULTS.....	155
3.5	DISCUSSION.....	157
3.5.1	OVERALL CHARACTERISTICS OF MAGMATIC-HYDROTHERMAL FLUIDS	157
3.5.2	CLASSIFICATION OF MAGMATIC-HYDROTHERMAL FLUIDS	158
3.5.2.1	A1 AQUEOUS FLUID TYPE	159
3.5.2.2	A2 AQUEOUS FLUID TYPE	159
3.5.2.3	A3 AQUEOUS FLUID TYPE	161
3.5.2.4	BC AQUO-CARBONIC FLUID TYPE	162
3.5.3	REVIEW OF FEATURE TYPE DISTRIBUTION	164
3.5.4	SPATIAL AND CATEGORICAL VARIATION IN FLUID TYPES.....	165
3.5.4.1	AQUEOUS FLUID TYPES.....	166
3.5.4.2	AQUO-CARBONIC FLUID TYPE	167
3.5.5	DISCUSSION OF FLUID TYPES	168
3.5.5.1	MICROTHERMOMETRY	168
3.5.5.2	CONDITIONS OF ENTRAPMENT	169
3.5.5.3	MULTI-ELEMENT GEOCHEMISTRY	170
3.5.5.4	DISTRIBUTION.....	171
3.5.6	INTEGRATION WITH EXTERNAL DATA	172
3.5.6.1	FLUID INCLUSION DATA.....	172
3.5.6.2	MULTI-ELEMENT GEOCHEMISTRY	175
3.5.6.3	STABLE ISOTOPE DATA.....	178
3.6	FLUID HISTORY	181
3.6.1	EARLY STAGE	182
3.6.2	LATE STAGE	184
3.6.3	POST-INTRUSION	185
3.7	IMPLICATIONS FOR RMEHR METAMORPHIC CORE COMPLEX DEVELOPMENT ...	187
3.7.1	REVIEW OF HPP EMPLACEMENT DEPTH	188
3.7.2	NEW HPP EMPLACEMENT DEPTH ESTIMATES	189
3.7.3	REVIEW OF RMEHR METAMORPHIC CORE COMPLEX DEVELOPMENT	191
3.7.4	THE HPP AND RMEHR METAMORPHIC CORE COMPLEX DEVELOPMENT	192
3.8	IMPLICATIONS FOR CARLIN-TYPE AU DEPOSITS	195
3.8.1	REVIEW OF CTD'S.....	195
3.8.2	COMPARISON BETWEEN THE HPP AND CARLIN-TYPE ORE FLUIDS	198
3.8.3	MAGMATIC-HYDROTHERMAL PHASE SEPARATION MODEL.....	201
3.8.4	THE HPP AND THE MAGMATIC-HYDROTHERMAL PHASE SEPARATION MODEL	202
3.8.5	PROPOSED FLUID MODELS.....	205

3.9 SUMMARY	208
3.10 REFERENCES.....	245
CHAPTER 4: CONCLUSIONS.....	255
4.1 SIGNIFICANT RESEARCH FINDINGS	255
4.2 APPLICATIONS OF RESEARCH FINDINGS.....	257
4.3 FUTURE RESEARCH DIRECTIONS	258
4.4 REFERENCES	261
APPENDICES.....	263
APPENDIX A: METHODS.....	264
A.1 FLUID INCLUSION PETROGRAPHY AND MICROTHERMOMETRY METHOD.....	264
A.1.1 FLUID INCLUSION PETROGRAPHY AND SAMPLE PREPARATION	264
A.1.2 FLUID INCLUSION MICROTHERMOMETRY ANALYTICAL PROCEDURE.....	265
A.1.3 CALCULATION AND MODELING OF FLUID PROPERTIES	267
A.2 LA-ICP-MS METHODS	268
A.2.1 LA-ICP-MS ANALYTICAL PROCEDURE	268
A.2.2 LA-ICP-MS DATA REDUCTION PROCEDURE	269
A.3 STABLE ISOTOPE METHODS.....	271
A.4 REFERENCES.....	274
APPENDIX B: FIELD SAMPLE DATA.....	276
APPENDIX C: STEREOSETS	330
APPENDIX D: PETROGRAPHIC DESCRIPTIONS.....	336
APPENDIX E: FLUID INCLUSION PETROGRAPHY AND MICROTHERMOMETRY DATA.....	351
E.1 FLUID INCLUSION PETROGRAPHY DATA	351
E.2 ANNOTATED FLUID INCLUSION THIN SECTION MOSAICS.....	369
E.3 FLUID INCLUSION MICROTHERMOMETRY DATA.....	392
E.3.1 RAW MICROTHERMOMETRY DATA	392
E.3.2 STATISTICAL COMPILATION OF MICROTHERMOMETRY DATA FOR PRIMARY FLUID INCLUSIONS BY SAMPLE.....	400
E.3.3 STATISTICAL COMPILATION OF MICROTHERMOMETRY DATA FOR PRIMARY FLUID INCLUSIONS BY FEATURE TYPE.....	408
E.3.4 STATISTICAL COMPILATION OF MICROTHERMOMETRY DATA FOR PRIMARY FLUID INCLUSIONS BY INTRUSIVE UNIT	413
E.3.5 STATISTICAL COMPILATION OF MICROTHERMOMETRY DATA FOR PRIMARY FLUID INCLUSIONS BY FLUID INCLUSION COMPOSITIONAL TYPE.....	418
E.4 ISOCHORE CALCULATION DATA.....	423
APPENDIX F: LA-ICP-MS DATA	492
F.1 ANNOTATED LA-ICP-MS FLUID INCLUSION SAMPLE PHOTOMICROGRAPHS..	492
F.2 LA-ICP-MS DATA.....	501
F.2.1 RAW LA-ICP-MS DATA FOR SELECT INCLUSIONS.....	501
F.2.2 RAW LA-ICP-MS DATA FOR HOST QUARTZ OF SELECT INCLUSIONS.....	507
F.3 FIRST PASS DATA.....	510

LIST OF TABLES

TABLE 2.1 - Basic descriptions of orthomagmatic, hydrothermal, and post-intrusion hydrothermal feature types observed in the HPP	89
TABLE 2.2 - Basic descriptions of hydrothermal alteration types observed in and around the HPP	90
TABLE 3.1 - Sample locations, descriptions, and analytical designations	211
TABLE 3.2 - Tabulated mean fluid inclusion microthermometry data for all fluid inclusion compositional types, feature types, and intrusive units.....	214
TABLE 3.3 - Descriptions of LA-ICP-MS fluid inclusion assemblages.....	215
TABLE 3.4 - Na, K, Rb, Cs concentrations from LA-ICP-MS with calculated K:Na, Na:Cs, K:Cs, and Rb:Cs molar element ratios from selected inclusions.....	216
TABLE 3.5 - Descriptions and calibrated $\delta^{18}\text{O}$ values for stable isotope samples.....	217
TABLE 3.6 - Comparison of selected mean fluid inclusion molar element ratios with the corresponding whole-rock data of Barnes et al. (2001).....	218
TABLE A.1 - Fluid inclusion microthermometry procedure.....	266

LIST OF FIGURES

FIGURE 2.1 - Simplified geologic map of the southern North American Cordillera. Areas of magmatic and tectonic significance are identified. Adapted from Konstantinou et al. (2012).....	91
FIGURE 2.2 - Generalized geologic map of the RMEHR metamorphic core complex.....	92
FIGURE 2.3 - Geologic map of the HPP showing intrusive units and delineating the contact metamorphic aureole. Adapted from Burton (1997)	93
FIGURE 2.4 - Cross sectional schematic of the intrusive units of the HPP. Modified after Barnes et al. (2001)	94
FIGURE 2.5 - Representative photographs of major and minor HPP intrusive units	95
FIGURE 2.6 - Geographic distribution of samples collected in this study	96
FIGURE 2.7 - Representative photographs and photomicrographs of orthomagmatic, hydrothermal, and post-intrusion hydrothermal feature types related to fluid activity.....	97
FIGURE 2.8 - Representative photographs and photomicrographs of the five types of hydrothermal alteration observed within and around the HPP.....	99
FIGURE 3.1 - Regional geological map after Henry & Ressel (2006). The HPP, RMEHR, and major trends of CTD's are identified	219
FIGURE 3.2 - Geologic map and schematic cross-section of the HPP showing constituent intrusive units (modified after Barnes et al. (2001))	220
FIGURE 3.3 - Detailed geologic map of the RMEHR metamorphic core complex. The HPP is intruded into the transition zone between the infrastructural core of high-grade metamorphic/igneous rocks and the suprastructure of low-grade and unmetamorphosed sedimentary rocks. Adapted from Snoke & Lush (1984).....	221
FIGURE 3.4 - Map showing the regional distribution of Carlin-Type Au Deposits in the Great Basin in relationship to the HPP. Also shown are other features relevant to the formation of these deposits, including the southward migration Cenozoic silicic magmatic fronts, the Roberts Mountain lithotectonic domain, and the western margin of the North American craton. Adapted from Muntean et al. (2011) and Vaughan (2013).....	222
FIGURE 3.5 - Map of the HPP showing the locations of microthermometry samples. Adapted from Burton (1997)	223
FIGURE 3.6 - Representative photomicrographs of major deformation microstructures in microthermometry samples.....	224
FIGURE 3.7 Representative photomicrographs of fluid inclusion petrographic groups....	224
FIGURE 3.8 - Representative photomicrographs of fluid inclusion compositional types...	224
FIGURE 3.9 - Histogram of Th_{tot} values for fluid inclusion compositional types	225
FIGURE 3.10 - Isochore plots subdivided by fluid inclusion compositional type.....	225
FIGURE 3.11 - Compiled fluid entrapment conditions by fluid inclusion compositional type and by select feature types.....	227
FIGURE 3.12 - Select Th_{tot} (°C) vs. Salinity (wt % eq. NaCl) scatter plots demonstrating spatial and temporal trends in microthermometry data.....	228

FIGURE 3.13 - Isochore plots subdivided by feature type	229
FIGURE 3.14 - Maps illustrating spatial variation in select microthermometry data throughout the HPP	230
FIGURE 3.15 - Compiled isochore plots and entrapment conditions for the three major categories of feature type	231
FIGURE 3.16 - Histograms of Pt values subdivided by intrusive stage and by orthomagmatic and hydrothermal feature types	233
FIGURE 3.17 - Compiled isochore plots and entrapment conditions for the stages of intrusive activity with interpreted Pt ranges	234
FIGURE 3.18 - LA-ICP-MS multi-element data for selected fluid inclusions, organized by fluid inclusion compositional type	235
FIGURE 3.19 - LA-ICP-MS multi-element data for host quartz crystals, organized by fluid inclusion compositional type	236
FIGURE 3.20 - LA-ICP-MS multi-element data for selected fluid inclusions, organized by feature type	237
FIGURE 3.21 - LA-ICP-MS multi-element data for selected fluid inclusions, organized by intrusive unit	238
FIGURE 3.22 - Compiled isochore plots and estimated entrapment conditions for the fluid types observed in the HPP	239
FIGURE 3.23 - Graphical comparison between multi-element compositions of fluid inclusions (this study) and host intrusive units (Barnes et al., 2001)	240
FIGURE 3.24 - Schematic cross section of the HPP illustrating exsolution, migration, and entrapment of early stage magmatic-hydrothermal fluids during the early stage of intrusive assembly	241
FIGURE 3.25 - Schematic cross section of the HPP illustrating exsolution, migration and entrapment of late stage magmatic-hydrothermal fluids during the late stage of intrusive assembly	242
FIGURE 3.26 - Schematic cross section of the HPP illustrating the late influx and entrapment of post-intrusion hydrothermal fluids	243
FIGURE 3.27 - Schematic WNW-ESE cross-section of the HPP and stratigraphic/structural framework showing emplacement depths determined in this study	244
FIGURE C.1.1 - Compiled stereonet of orientations for all feature types in the HPP	330
FIGURE C.2.1 - Stereonet for all feature types in the early stage Ttc granodiorite	330
FIGURE C.2.2 - Stereonet for all feature types in the early stage Tcc monzogranite	331
FIGURE C.2.3 - Stereonet for all feature types in the late stage Tmg biotite and two-mica monzogranite sheets and dikes	331
FIGURE C.2.4 - Stereonet for all feature types in the late stage Tgm two-mica monzogranite	332
FIGURE C.3.1 - Stereonet for all QF Pegmatites	332
FIGURE C.3.2 - Stereonet for all MQF Pegmatites	333
FIGURE C.3.3 - Stereonet for all Aplites	333
FIGURE C.3.4 - Stereonet for all Type (I) Quartz Veins	334
FIGURE C.3.5 - Stereonet for all Type (III) Quartz Veins	334
FIGURE C.3.6 - Stereonet for all Type (IV) Microcrystalline Quartz Veins	335
FIGURE C.3.7 - Stereonet for all Type (V) Microcrystalline Quartz Veins	335

DEFINITION OF TERMS AND ABBREVIATIONS

ASI - Alumina Saturation Index

C-S - Chlorite-Sericite

CTD - Carlin-Type Deposit

$\delta^{18}\text{O}$ - Measure of the ratio between the stable isotopes oxygen-18 and oxygen-16.

ϵ_{Nd} - Measure of the ratio between the isotopes 143-Neodymium and 144-Neodymium relative to the Chondritic Uniform Reservoir evolution line.

FIA - Fluid Inclusion Assemblage

FI/WR - Element concentration ratios determined by dividing values from LA-ICP-MS analysis of fluid inclusions in orthomagmatic and hydrothermal features in the HPP (this study), by values from whole-rock geochemical analysis of intrusive rocks in the HPP (Barnes et al. 2001).

HPP - Harrison Pass Pluton

LA-ICP-MS - Laser Ablation Inductively Coupled Mass Spectrometry

LANF - Low-Angle Normal Fault

MCC - Metamorphic Core Complex

MQF Peg - Muscovite-Quartz-Feldspar pegmatite

MVP - Magmatic Volatile Phase

Opm - Ordovician Pogonip group

Pt - Fluid entrapment pressure

QF Peg - Quartz-Feldspar pegmatite

QSP - Quartz-Sericite-Pyrite, or phyllic, hydrothermal alteration

REE - Rare Earth Element

RMEHR - Ruby Mountains-East Humboldt Range

RMSZ - Ruby Mountain Detachment/Shear Zone

RVFZ - Ruby Valley Fault Zone

SAFZ - San Andreas Fault Zone

SCLM - Sub-Continental Lithospheric Mantle

SHRIMP - Sensitive High Resolution Ion Microprobe

T_{A} - Ambient temperature

Tcc - Early stage Corral Creek monzogranite unit

T_{eutectic} - Temperature at which "first melting" of H_2O is observed during heating from -100°C .

Tgm - Late stage Green Mountain two-mica monzogranite

T_{HCO_2} - Temperature at which CO_2 homogenizes with H_2O in fluid inclusions of the $\text{H}_2\text{O-CO}_2\text{-NaCl-(KCl)}$ system.

T_{Htot} - Temperature at which all constituent phases of a fluid inclusion homogenize

Tmg - Late stage biotite and two-mica monzogranite sheets and dikes

$T_{\text{mclathrate}}$ - Temperature at which melting is observed for clathrate, (a metastable form of CO_2 hydrate).

T_{mCO_2} - Temperature at which melting is observed for CO_2 .

$T_{m_{ice}}$ - Temperature at which “final melting” of H_2O is observed during heating from $-100^{\circ}C$.

Trd - Early stage porphyritic rhyodacite and equigranular leucogranite roof dikes

Tt - Fluid entrapment temperature

Ttc - Early stage Toyn Creek granodiorite

UST - Unidirectional Solidification Textures

WFZ - Wells Fault Zone

CHAPTER 1: PROJECT OVERVIEW

1.1 RATIONALE FOR STUDY

This study reconstructs the magmatic-hydrothermal fluid history of the Harrison Pass Pluton, which informs and contributes to future research into the structural and metallogenic history of the Great Basin. The origins of two striking geologic phenomena in northeastern Nevada – metamorphic core complexes and Carlin-type gold mineralization – are still unclear, despite decades of scientific inquiry. Current understandings of metamorphic petrology and core complex development require burial of upper crustal material to lower crustal or mantle depths and subsequent tectonic exhumation and uplift to thousands of meters above sea level (e.g. Hodges et al., 1992; McGrew et al., 2000). The pressure and temperature regime at the time of hydrothermal activity within the HPP, in conjunction with existing estimates of emplacement depth for the HPP (Snoke & Sullivan, 1977; Burton, 1997; Howard, 2003; Colgan, 2010), provides a new line of inquiry into the burial and exhumation history of the Ruby Mountain-East Humboldt Range core complex. Furthermore, as exploration for Carlin-type gold deposits has spread to China, Macedonia, and the Yukon, understanding the relationship between deep basement structures, regional back arc-style magmatism, and gold mineralization has become a key component for future exploration. While the chemistry of the ore-forming fluids has been characterized at several deposits (Hofstra & Cline, 2000; Cail & Cline, 2005), several explanations exist for the origin and history of these fluids (meteoric: Ilchik & Barton, 1997; Emsbo et al., 2006; metamorphic: Arehart, 1996; Hofstra & Cline, 2000; magmatic:

Ressel & Henry, 2006; Muntean et al., 2011; Lubben et al., 2012). By defining select physicochemical parameters of the fluids preserved within the HPP, this study will further define the role of magmatic exsolution in the evolution of fluids in the crust at the time of gold mineralization along the Carlin Trend.

1.2 CONCEPTUAL BACKGROUND

1.2.1 GRANITIC INTRUSIONS

Crystallized and eroded intrusive bodies of subvolcanic granitic magma have been observed and studied around the world for over a century. They are the fundamental input to the development of the continental crust and are directly or indirectly associated with the formation of many different types of economic mineral deposits (reviewed by Cox & Singer, 1986). These bodies range in size from meters to hundreds of kilometers and may exhibit a broad spectrum of shapes beyond the classic diapiric inverse teardrop, including concordant and discordant tabular sheet and pencil-shaped columns. However, the term “pluton” is typically reserved for single or multi-phase intrusions that exhibit the classic morphology and a “unity of structure” (Pitcher et al., 1985). Traditional IUGS field and petrographic classification of granitic rocks, which are composed of medium to coarse-grained felsic minerals and few mafic minerals, is based on the modal abundances of the three dominant mineral species: quartz, plagioclase feldspar, and alkali feldspar (Streckeisen, 1967). Many additional classification schemes (genetic and non-genetic) have been proposed since (see Frost et al., 2001).

Despite their centrality to the development of the continental crust, the origin and evolution of granitic magmas is a complex and incompletely understood process (see Frost et al., 2001; Glazner et al., 2004). They are believed to be the products of magmas formed by differentiation of more mafic parent melts (Bateman & Chappell, 1979), anatexis or partial melting of surrounding rock (Harker, 1904; White & Chappell, 1977) or magma mixing (Reid et al., 1983). These processes can form granitic rocks from evolved mantle melts, oceanic crust, continental material, or any combination of the three (Frost et al., 2001). Primary magma generating processes have often been inferred from classification of intrusions by certain geochemical and mineralogical parameters and the tectonic setting of emplacement (White & Chappell, 1974; Loiselle & Wones, 1979; White & Chappell, 1983; Kilpatrick & Ellis, 1992).

There lacks a single thermodynamically feasible, observationally supported model for the mechanism and timescale of plutonic emplacement. The traditional pluton emplacement model of relatively rapid ($<10^5$ yrs), density-driven, diapiric bulk magma ascent by stoping and ductile wallrock deformation is supported by field evidence such as entrained wall rock xenoliths and doming of overlying rock units, petrographic homogeneity of plutonic bodies, thermal modeling, and large-volume ignimbrite eruptions recorded in the rock record (Miller et al., 1988; Weinberg & Podladchikov, 1994; Schwerdtner, 1995). However, this has been challenged by a model of incremental growth by magma sourced along deeply rooted dike-like conduits over millions of years (Clemens & Mawer, 1992; Petford, 1996; Mahan et al., 2003; Glazner et al., 2004). This model is supported by the lack of field evidence for volumetrically significant stoping, field observations of sheeted segregations, chemical zonation within visually homogeneous

granites, and calculations of magma ascent velocities (e.g. Wiebe & Collins, 1988; Clemens & Mawer, 1992; Petford, 1996; Coleman et al., 2004; Glazner et al., 2004).

Plutons may be emplaced into crustal rocks at a wide range of depths, from epizonal (<300 °C, low hydrostatic stress, high shear stress; generally <8 km), to mesozonal (300–500 °C, moderate hydrostatic stress, moderate shear stress; generally 8–12 km), to katazonal (500–700°C, high hydrostatic stress, low shear stress; generally >12 km) depths (Buddington, 1959). The thermal conditions of emplacement exert primary controls on magmatic textures and the temperature contrast between the intrusion and the surrounding rock. This contrast drives heat and mass transfer out of, into, or around the intrusion, which is accomplished by either thermal conduction or advective fluid flow, which is the theoretical basis of all intrusion-related hydrothermal systems (Hickey et al., 2014). However, it has been argued that the requisite thermal conditions for the formation of mineralizing hydrothermal systems restricts the depth of their parent intrusions to <10 km depth (e.g. Barnes, 1997; Uchida, 2007). Manifestations of mass and heat transfer processes include, but are not limited to, partial melting (migmatites), contact metamorphic aureoles, and hydrothermal veining, metasomatism, alteration, greisenization, and mineralization up to kilometers away from plutonic margins (Norton & Knight, 1977; Beane & Tittley, 1981; Candela, 1997; Audètat et al., 1998, 2000; Machek et al., 2013).

1.2.2 MAGMATIC-HYDROTHERMAL FLUIDS

The emplacement of granitic melts into the crust is often accompanied by saturation and exsolution, or chemical separation, of a magmatic volatile phase(s) (MVP) from the crystallizing magma (Candela, 1997). In addition to contributing to the crustal fluid budget,

magmatic intrusions also act as thermal engines driving regional fluid convection and migration (Cathles, 1990). These fluids are responsible for forming granitic intrusion-related deposits of Au, Cu, Mo, Sn, W, Ag, Pb, Zn and associated hydrothermal alteration (e.g. Burnham, 1997; Kesler, 1994). Volatile molecules, such as H₂O, CO₂, NH₃, S, Cl, F and other species, are concentrated at the magma source by processes such as fractional crystallization, magma mixing, and assimilation of country rock (Whitney, 1988; Wallace, 2005; Annen et al., 2006). During the magmatic-hydrothermal transition, chemical components, including economic metals, are partitioned into the melt, crystalline, or volatile phase. The presence of these species may dramatically affect the chemistry of the crystallizing melt and the ability for the fluids to harvest metal ions from the melt (Rasmussen & Mortensen, 2013).

Although the physical mechanics of volatile exsolution and migration are not fully understood, textural evidence from high-level granitic intrusions provides clues into these dynamic processes. Exsolution occurs in granites when they become saturated with respect to volatile components. The formation of vapor and/or brine bubbles in the melt, or boiling, signals this transition (Webster, 1997). In addition to the concentration and composition of the fluids, other factors such as the temperature of the magma and the pressure of emplacement govern the timing of fluid exsolution and the partitioning behavior of metals (Candela, 1996; 1997). Boiling may be caused by decompression associated with magmatic ascent or unroofing (first boiling) or by crystallization of non-volatile-bearing phases above the solidus of the melt (second boiling) (Whitney, 1988; Burnham, 1997; Candela, 1997). Thus, magma that is slowed in its crustal ascent by far-field stresses or increased viscosity due to crystallization may remain in the subvolcanic environment and exsolve the fluids

(Candela & Blevin, 1995a). While this remains fundamentally true for composite, episodically emplaced intrusions, the rate of magma input and local strain variation will also govern the fluid exsolution process (Hanson & Glazner, 1995).

It is proposed that the buoyant bubbles of exsolved volatile phase, which are represented texturally as miarolitic cavities, begin to coalesce as they rise to apical regions of the magma chamber, either by buoyancy or advection along interconnected channels and scavenge metal cations from the surrounding melt during the ascent (Candela, 1991; Shinohara & Kazahaya, 1995; Christiansen & Keith, 1996). In the event of two exsolved volatile phases, (i.e. a vapor and a brine), density-driven separation and stratification will occur, concentrating the low-density vapor phase near the roof of the intrusion and relegating the high-density brine below (Candela, 1997). The vapor-rich fluids in these cases may eventually exceed the confining pressure of the surrounding country rock and be expelled along brittle fractures, effectively equilibrating high internal pressures. The discharged fluids create hydrothermal veins, breccias, and alteration zones within and beyond the intrusion or passively migrate through preexisting permeability networks. Brines also play an important role in metal partitioning (by concentrating base metals) and the physiochemical evolution of the magmatic-hydrothermal system (by late catastrophic expulsion or reequilibration with the melt phase) (Burnham, 1985; Rye, 1993; Candela, 1997).

The magmatic volatile phase (MVP) (or “fluids”) demonstrate high fluidity and buoyancy, as well as an affinity for ore-forming metals. Although H₂O and CO₂ dominate fluids in terms of mass, other species, particularly compounds of S and Cl, are vital in forming neutral to negatively-charged ligands that complex metal cations, particularly gold,

which strongly partitions into the MVP instead of the brine phase (Jugo et al., 1999; Williams-Jones & Heinrich, 2005; Simon et al., 2005, 2007). Experimental partition coefficients for gold and copper during volatile exsolution (800°C, 120–140 MPa) favor the fluid phase to varying degrees (Jugo, 1997; Muntean et al., 2011). Early MVP saturation relative to crystallization and the availability of volatiles in an H₂O-rich volatile phase are important controls on the extraction, enrichment, and transport of economic metals from and within granitic intrusions (Candela & Holland, 1986; Seward & Barnes, 1997; Audétat & Pettke, 2003). However, Audétat et al. (2008) argued convincingly that “mineralization potential” is fundamentally controlled by the absolute concentration of metals in an intrusion (determined by the conditions and processes of magma generation) rather than by efficient complexing and partitioning of metals into the MVP or a spatially restricted mechanism for ore precipitation.

Although textural variation within an isolated pluton or a suite of intrusions is typical, there is a broad, poorly constrained group of primary magmatic textures that have been invoked as evidence of volatile saturation and exsolution by first or second boiling. These include skeletal and dendritic quartz crystals, quartz “eye” phenocrysts, micrographic quartz-feldspar intergrowth, pegmatite, aplite, and layered aplite/pegmatite zones, unidirectional solidification textures (UST), and miarolitic cavities (both interconnected and isolated) (Candela, 1991, 1997; Candela & Blevin, 1995; Burnham, 1997). Unfortunately, these textures (including oft-cited pegmatites) can also form in volatile-undersaturated conditions by undercooling crystal kinetics driven by large temperature contrasts (London, 1992). Miarolitic cavities, (preserved crystal-lined vapor bubbles) and UST’s are one of the few undisputed indications of fluid exsolution in plutonic

rocks, but may be conspicuously absent in intrusions suspected of fluid exsolution (London, 1986; Lowenstern, 1994; Candela, 1997). Due to the processes of vapor ascent, decompression, and bubble coalescence, zones of miarolitic cavities and UST's are often observed near the roof zone of fluid-bearing intrusions (Shannon et al., 1982; Candela, 1991).

1.2.3 GRANITOID INTRUSIONS AND ORE DEPOSITS

Granitoid-related hydrothermal mineralizing systems consist of economic concentrations of elements that have been directly tied to the exsolution and egress of fluids from intrusions of silicic composition. Such deposits and their parent intrusions can be found at collisional plate margins, orogenic belts, and extensional back-arc settings as isolated or clustered occurrences. Source magmas demonstrate a broad range of possible bulk compositions (including silica and alkali contents) and chemical parameters (redox state, oxygen, sulfur, and water fugacity, and aluminum saturation) that often correlate with specific metallogenic styles (Candela, 1989; Audétat et al., 2008; Hedenquist & Lowenstern, 1994). Visually, they can be aplitic, equigranular, or porphyritic/megacrystic, and typically contain textures indicative of volatile exsolution. They are emplaced at <10 km depth, and are often hosted in reduced and reactive carbonate host rocks (Ishihara, 1981; Blevin, 2005).

Granitoid-related hydrothermal ore deposits demonstrate strong or immediate spatial relationships to intrusive centers, predictable and observable alteration and/or metal zonation, contemporaneous or overlapping radiometric age dates with igneous crystallization, and microthermometric, isotopic, and textural evidence of relatively high-temperature fluid activity (Blevin, 2005; Hedenquist & Lowenstern, 1994). Focusing

structures and efficient chemical mechanisms for stripping metals from ore fluids are required for their formation in hydrothermal systems (Hedenquist & Lowenstern, 1994). The deposit types unequivocally included in this category are listed here with increasing distance to their source granite: pegmatite Li-REE, porphyry Au-Cu-Mo-W-Sn, endo- and exoskarn and carbonate replacement Sn-W-Zn-Cu-Au, distal-disseminated Au-Ag, and high-temperature, vein-hosted Au-Ag-Cu deposits (Lowell & Guilbert, 1970; Sillitoe & Bonham, 1990; Meinert, 1992; Candela, 1997; Partington & Williams, 2000; Lang & Baker, 2001; Tkachev, 2011). However, other deposit types, such as epithermal Au-Cu, Proterozoic iron oxide Cu-Au (IOCG), and Carlin-type Au deposits (CTD) are suggested to be magmatic-hydrothermal in nature, but have unclear and complex relationships with intrusive activity (Sillitoe & Hedenquist, 2003; Johnston & Ressel, 2004; Ressel & Henry, 2006; Lubben et al., 2012). The ambiguity or lack of one or more of the aforementioned characteristics of granitoid-related deposits have led to alternative models being proposed for the genesis of these deposits.

1.3 GEOLOGIC BACKGROUND

1.3.1 GEOLOGIC HISTORY OF THE GREAT BASIN

The Great Basin, as part of the Basin and Range province and the larger tectonic environment of the North American Cordillera, has experienced multiple cycles of compressional, extensional, and transform stress regimes and associated deformation, magmatism, and erosion over the last 600 million years (Parsons, 1995; Dickinson, 2006, Wallace & John, 1998; Jones, et al., 1992). Compressional events are primarily identified in

the rock record by thin-skinned allochthonous thrust sheets driven eastward by plate-scale forces. Extension is characterized by composite overprinting of periods of localized and distributed deformation. Evidence of both, preserved as metamorphic core complexes (MCC's) and block faulting systems, respectively, are both well preserved in the regional geology (see Thorman, 1991). Magmatism and the formation of economic ore deposits also punctuate the history of the Great Basin and have often accompanied shifts in the dominant stress regime (Ressel & Henry, 2006) To provide a general overview, the most significant episodes of crustal evolution within the complex history of this region are described below.

Archean rocks of the Wyoming Province, and the Proterozoic Mojave Province and Yavapai-Mazatzal crustal terrains make up the composition of the basement rocks beneath the present-day Great Basin, traversed by the Archean-Proterozoic suture zone (Karlstrom & Houston, 1984). Compositional differences between the ancient crustal fragments and the structures created along their margins are theorized to be the deep-seated focusing conduits responsible for later Carlin-type gold deposits (see Muntean et al., 2011). Following the breakup of Rodinia at ~750 Ma, the western edge of Laurentia became a passive continental margin. From the Neoproterozoic to the Devonian age, shelf-slope sediments were deposited along the western margin of the North American Cordillera due to post-rifting subsidence (Poole et al., 1993; Snoke, 2005). These units formed the Cordilleran miogeocline, an enormous prism of clastic and carbonate sedimentary strata up to 3000 m thick (Dietz & Holden, 1966).

From the Paleozoic to the middle Mesozoic, the tectonic evolution of the Great Basin was defined by periods of thin-skinned compression and deformation. Subduction of the Farallon plate beneath the western margin of North America drove crustal thickening by

30–50% and plutonism in a 200 km-wide zone known as the Cordilleran fold and thrust belt (Armstrong, 1968). First, the Devonian-Mississippian Antler Orogeny (380–360 Ma) was characterized by 70 km of eastward obduction of oceanic sedimentary and volcanic sequences onto the pre-Cordilleran continental margin forming the Roberts Mountain allochthon (Speed & Sleep, 1984; Dickinson, 2006; diPietro, 2012). The Permo-Triassic Sonoma Orogeny (280–200 Mya) emplaced the Golconda Allochthon 60–80 km ESE, partially overriding the subjacent Roberts Mountain Allochthon. During the middle Mesozoic, multiple compressional accretionary events occurred along the western margin of the North American Cordillera, resulting in the stacking of multiple thin-skinned thrust nappes on top of the Paleozoic allochthons. These events were bracketed by the Mid-Jurassic Nevadan orogeny, (coeval with the emplacement of the Sierra Nevada Batholith), and the Cretaceous Sevier orogeny (Oldow, 1983; Thorman, 1991; Dickinson, 2006).

The Sevier Orogeny (140–50 Ma) was the most recent major compressive tectonic event in the history of the Great Basin (DeCelles et al., 1995). The low-angle subduction of the oceanic Farallon plate is often credited as a common cause for both the Sevier Orogeny and the temporally overlapping Laramide Orogeny to the east during the Cretaceous. Thin-skinned thrusting of the miogeoclinal sedimentary prism from the passive western margin of the Cordillera onto the adjacent platform sedimentary sequences to the east formed a 160 km-wide deformational belt (Armstrong, 1968). These thrust sheets, with thicknesses of >12 km, overrode and augmented the thickness of the continental crust that was already loaded from previous periods of contraction and thrusting (Camilleri & Chamberlain, 1997; Hildebrand, 2013). High-grade crustal material exposed in core complexes throughout the

Cordillera record the peak regional metamorphic conditions caused by burial during this compressive event.

A major transition from a contractional to an extensional regional stress regime occurred in the Cenozoic due to a change in plate kinematics. The steepening and subsequent delamination of the subducting Farallon slab, coupled with asthenospheric upwelling, reduced intraplate stress and caused the gravitational collapse and cryptic, large-scale extension of the overthickened crustal “welt” (50–60 km thick) that formed in the hinterland of the Sevier thrust belt starting at ~50 Ma (Coney & Harms, 1984; Humphreys, 1995). NE-SW oriented rifting was largely accommodated by discrete zones of large-magnitude extension, where deeply rooted, low-angle normal faults (LANF) exposed domes of mid-crustal crystalline rocks known as metamorphic core complexes (MCC’s) (Crittenden, 1980). Controversy has surrounded the driving force behind extension, the magnitude and mechanism for burial and uplift, and the mode of slip for detachment faults (Lister & Davis, 1989). However, the hyperextensional denudation of metamorphic core complexes is hypothesized as the dominant expression of regional extension during the tectonic development of Eocene Great Basin (Lister et al., 1986; McGrew et al, 2000; Colgan et al, 2010).

The widespread calc-alkaline magmatism that occurred inboard of the major Cordilleran volcanic arc during Eocene extension also occurred following the delamination, flexure, and/or “drip” of the subducting Farallon slab from the North American plate (Armstrong, 1969; Christensen & Yeats, 1992; Humphreys, 1995; Humphreys et al., 2003). Intra- or underplating of upwelling asthenospheric mafic magmas with the hydrated and metasomatized subcontinental lithospheric mantle (SCLM) resulted in partial melting of

the crustal material and long-lived (50–25Ma) profuse magmatism that swept southwest across the Great Basin (Dickinson & Snyder, 1979; Johnson, 1991; Christiansen & Yeats, 1992; Humphreys, 1995). Systematic compositional trends of these intrusive rocks indicate that magma was generated from fractionated mantle melts in the western Great Basin and from partial melts of Precambrian basement in the eastern Great Basin (Farmer & DePaolo, 1986). This high thermal energy flux produced an intense period of hydrothermal activity that is temporally and spatially associated with the formation of multiple types of base and precious metal deposits, most notably the unique, sediment-hosted Carlin-type Au deposits of northeastern Nevada (Ressel & Henry, 2006; Muntean et al., 2011).

The classic Basin and Range structural architecture of the Great Basin began to form in the Miocene as the mode of extension transitioned from detachment to block faulting and continues to the present. However, thermochronology studies indicate that episodes of rapid crustal exhumation and detachment faulting persisted through the mid-Miocene (10 Ma) (Colgan et al., 2006, 2010). At 17.5 Ma, rheological stiffening of the lower crust facilitated the transfer of stress from the dextral strike-slip San Andreas Fault Zone (SAFZ) to the Great Basin via the Walker Lane transition zone (Harry et al., 1993; Dilles & Gans, 1995). Voluminous basaltic magmatism also accompanied this change in stress regime and continued until 10 Ma (Wallace & John, 1998). Heterogeneous en echelon normal fault blocks in the upper 5–15 km of the crust, spaced 25–35 km apart, accommodated extension (Zoback et al., 1981; Jones et al., 1992). These fault mosaics display high angle dips at the surface, but rotate to gentler angles at depth. A mean crustal thickness of ~30 km, as measured by Thatcher et al. (1999), is significantly thinner than other mountainous regions within the Cordillera, which indicates significant extension.

1.3.2 METAMORPHIC CORE COMPLEXES

Metamorphic core complexes (MCC's) in the North American Cordillera were first identified as such by Misch (1960) and Armstrong & Hanson (1966), who perceived a discontinuous "core" orogenic belt of high-grade metamorphic structural domes in the hinterland of west-dipping shallow thrust sheets. MCC's can be identified as topographically prominent footwall units of mid-crustal igneous and metamorphic rocks unroofed by low-angle, normal-sense, brittle-ductile detachment faults with upper crustal rock in the hanging wall (Armstrong, 1972; Crittenden, 1980; Coney, 1980; Wernicke, 1995). There are three major MCC's in the Great Basin, the Snake Range, Albion-Raft River-Grouse Creek, and the Ruby Mountain-East Humboldt Range (RMEHR), which hosts the Harrison Pass pluton (Sullivan & Snoke, 2007). However, similar features have been exposed elsewhere the North American Cordillera, forming a discontinuous belt that extends from Canada to Mexico, as well as in mature orogenic belts around the world (Crittenden, 1980). These extensive tracts of well-exposed, hyper-extended rock provide geoscientists with unique opportunities to study the dynamics of crustal-scale tectonic processes associated with post-orogenic intracontinental spreading.

1.3.2.1 CHARACTERISTICS

MCC's juxtapose downthrown hanging wall blocks of unmetamorphosed rocks with uplifted footwalls of schists and gneisses of metamorphic grades reaching upper amphibolite facies (Crittenden, 1980). The domed or anticlinal footwall or infrastructure of metamorphic core complexes is largely composed of metasedimentary units with metamorphic grades reaching upper amphibolite intermixed with, or distinct from, unmetamorphosed to gneissic/migmatized intrusive rocks (often two-mica granites)

(Armstrong, 1982). Original sedimentary bedding may still be visible within the infrastructure, but is commonly folded or obscured by these intrusions, which may locally occupy 90% or more of the total rock volume (Howard, 2011). It has been suggested that anatexis of the pre-extensional overthickened crust is the primary source of intrusive granitoids that are characteristic of many MCC's (Armstrong, 1983; Barnes et al., 2001). The detachment surfaces bounding the infrastructure are laterally extensive low-angle detachment faults responsible for huge lateral displacement and removal of 5-15 km of the overlying crustal section (Axen, 2004). These structures are characterized by a carapace (up to 1 km thick) of brittle-ductile, chlorite-silicic cataclasites, breccias, and mylonites (Davis & Coney, 1979; Davis, 1983; Haines & van der Pluijm, 2010). The suprastructure of an MCC is generally composed of unmetamorphosed, highly fractured, and brittlely deformed upper-crustal material. While core complexes share these first-order characteristics, differing extensional rates and durations in each have resulted in different flavors of deformation and metamorphism (Rey et al., 2009).

1.3.2.2 STRUCTURAL DEVELOPMENT

Due to a common history of transitional compressional-to-extensional tectonics, metamorphic core complex development in extended orogenic belts around the world is attributed to a similar sequence of structural events (e.g. Dewey, 1988). Km-scale, thin-skinned thrust nappe stacking during orogenic events structurally buried upper crustal rocks to mid-crustal depths inboard of primary volcanic arcs (Hodges et al., 1992; McGrew et al., 2000; Gans & Wong, 2014). Thermobarometry of minerals in high-grade metamorphic assemblages and associated igneous rocks coupled with thermodynamic modeling provides the strongest support for this burial depth, which assumes lithostatic

conditions were equivalent to metamorphic pressure estimates (Jolivet et al., 2003, 2010). However, extreme variation in metamorphic grade within and adjacent to many core complexes challenges simple conceptualizations of burial and prograde metamorphism (Wright & Snoke, 1993). Furthermore, studies performing retrodeformation and untilting of preserved extensional structures dispute the thickness of the overlying rock package often invoked for core complexes burial (e.g. Colgan et al., 2010).

The post-compressional collapse of back-arc, overthickened continental highlands was predominantly accommodated by km-scale, low-angle detachment faults with complex, brittle-ductile deformational histories that bound metamorphic core complexes and accommodate tens of kilometers of lateral transport (Lister & Davis, 1989; McGrew & Snee, 1994; McGrew et al., 2000; Colgan et al., 2010). Partial melting of overthickened crustal roots is a potential cause for the viscosity contrast-driven decoupling of the brittle upper crust from the ductile lower crust and the localization of strain required for discrete detachment faulting (Bendick & Baldwin, 2009; Rey et al., 2009; Hallett & Spear, 2015). Localized strain may have been focused by rheological or density anomalies (such as preexisting normal faults or thrust nappes) on or near the brittle-ductile transition (Patel et al., 1993; Rey et al., 2009; Huet et al., 2011) but has also been successfully modeled without any such features (Regenauer-Lieb et al., 2006). Following initiation of slip along these detachment faults, the heterogeneously deforming lithosphere experienced episodic spurts of collapse and extension over tens of millions of years (Colgan et al., 2010).

1.3.2.3 EXHUMATION DYNAMICS

The central unresolved problems of detachment faults are the disputed mechanical favorability of low-angle normal faults and the nature of their enigmatic brittle-ductile

deformational histories. Three models have traditionally explained the dynamics of low-angle detachment faulting: the brittle-ductile exhumation model, the low-angle shear zone model, and the rolling hinge model (see Cooper et al., 2010). The brittle-ductile exhumation model proposed by McKenzie (1978), argues for symmetric, distributed block faulting along a basal detachment zone that represents the brittle-ductile transition. The low-angle shear zone model describes these structures as being mosaics of superposed normal fault blocks that lie on a deeply rooted basal “décollement” (Wernicke, 1981; Davis et al., 1986; John & Foster, 1993). The rolling hinge model proposes that detachments form from upward flexure of the ductile lower crust, exposing alternating non-rotated mylonite zones of high and low-angle attitudes. The asymmetrical transition (hinge) between these zones behaves like a ripple through which the rotating lower crust flows and over which the brittle upper crust breaks into rotated, domino-style fault blocks (Buck, 1988; Wernicke & Axen, 1988; Axen & Bartley, 1997). Post- or syn-extensional rotation of detachment faults has also been proposed as a potential explanation for their characteristically shallow dip (Thomson & Ring, 2006; Huet et al., 2011).

These models have been applied and tested in numerous field and laboratory settings using techniques such as mapping deformation style and metamorphic grade around detachment faults and mylonitic shear zones (e.g. Snoke, 1980; MacCready et al., 1997; Granillo & Calmus, 2003; Jolivet et al., 2010), seismic reflectance surveys of synextensional, fault-bounded basins (e.g. Allmendinger et al., 1987; Satarugsa & Johnson, 2000, 2005), reconstructing hanging wall stratigraphy and orientations (e.g. Bartley & Wernicke, 1984; Pape, 2010; Colgan et al., 2010), and characterizing footwall exhumation histories with thermobarometry, thermochronology, and/or geochronology (e.g. Hurlow et

al., 1991; Lewis et al., 1999; Lee, 1995; Cooper et al., 2010; Singleton et al., 2014). These studies have carefully described the characteristics of low-angle normal faulting in the rock record and have constrained the timing, mode, and magnitude of slip on these structures around the world. However, there is little consensus between different experimental and observational models at individual core complexes or in comparative studies. This uncertainty is compounded by the unique structural characteristics of individual core complexes and their associated detachment faults.

1.3.2.4 RELATIONSHIP WITH PLUTONISM

Many authors have explored the close spatial and temporal relationship between tectonic exhumation of metamorphic core complexes and intrusive activity (Crittenden, 1980; Coney and Harms, 1984; Axen et al., 1993; Vanderhaeghe et al., 1999). Although it remains controversial, some studies have argued for magmatism as a trigger and amplifier of large-scale extension, uplift, and MCC formation through buoyancy contributions (Lister & Baldwin, 1993; Foster et al., 2001). Post-orogenic extensional relaxation of crustal highlands is often accompanied by upwelling and partial melting of the asthenosphere and partial melting of the crust, resulting in voluminous magmatism (Lipman et al., 1971, 1972; Wernicke, 1992; Dickinson, 2002). Discrete granitic intrusions were often focused into the relatively depressurized dilational weaknesses represented by the high-grade cores of MCC's. These synkinematic plutons record the thermodynamic conditions of their emplacement within developing host core complexes and present a laboratory for studying the tectonomagmatic factors and processes involved in the origin, evolution, and exhumation of these hyperextended terranes (e.g. Howard, 2003; Denele et al., 2011; Charles et al., 2011; Erkul & Erkul, 2012)

1.3.3 CARLIN-TYPE AU DEPOSITS

Carlin-Type Au deposits (CTD's) are sediment-hosted, epigenetic, Au-only deposits originally recognized and defined in the Basin and Range tectonic province of the western United States. Since being recognized as a distinct class of deposits in the 1960s with the discovery and exploitation of the type deposit near Carlin, NV, more than one hundred similar CTD's have been discovered in the region (Hofstra & Cline, 2000). Boasting historic production and reserves in excess of 6,000 tons Au, these deposits constitute the second largest concentration of Au in the world and are responsible for making the United States a global leader in Au production (Cline et al., 2005). While several localities outside the Great Basin, (i.e. China, the Yukon, and eastern Europe) host similar, "Carlin-like" deposits, none has demonstrated the same deep-seated tectonic associations or the endowment of Au as northeastern Nevada (see Fuxin & Jing, 2003; Arehart et al., 2013; Kochneva et al., 2006). However, despite their economic significance and growing global potential, a single, well-accepted model for CTD formation in northeast Nevada has not been developed (Muntean et al., 2011).

1.3.3.1 CHARACTERISTICS

The vast majority of CTD's are concentrated on or near five linear populations, or "trends" that are responsible for the world-class Au endowment in northeastern Nevada: Carlin, Battle Mountain-Eureka, Getchell, Jerritt Canyon, and Alligator Ridge. The two most prolific trends (Carlin and Battle Mountain-Eureka) obliquely intersect the northeast-striking Basin and Range normal faults and have been shown to exist above reactivated Precambrian basement rift structures (Marshak et al., 2000; Grauch et al., 2003).

Crosscutting mineralization relationships, Rb-Sr dating of ore-stage minerals, and deposit

and district-scale fission track dating at many CTD's has been successful in demonstrating that shallow (0.5-2.2 km) mineralization occurred from 42–36 Ma along all major trends (Chakurian et al., 2003; Arehart et al., 2003; Hickey et al., 2003; Ressel & Henry, 2006). While the individual deposits vary with respect to ore body geometry, grade, alteration zones, and precise stratigraphic associations, CTD's can be identified by several common characteristics. Mineralization is hosted in Silurian to Devonian-age, laminated to wispy-bedded, impure continental slope and shelf edge carbonate lithologies within unmetamorphosed sedimentary sequences and within Eocene lamprophyre dikes and other intrusive rocks. Au is present as a trace component in highly disseminated arsenian pyrite/marcasite with spatially variable compositions indicating fluid chemistry evolution during the genesis of an ore zone (Bakken & Einaudi, 1986; Hofstra & Cline, 2000; Barker et al., 2009).

Carlin-type ore bodies demonstrate varying degrees of stratigraphic and structural control. Deposits within a single mining district (such as the northern Carlin Trend) may be laterally extensive within host units, strongly fault-bounded, hosted in dissolution breccias, and/or associated with intrusive igneous stocks (see review by Hofstra & Cline, 2000). Ore grade is rarely correlated with any particular alteration type, although zones of carbonate dissolution, silicification, dolomitization, and clay alteration are typically present (Kuehn, 1989; Bakken, 1990; Hofstra et al., 1991; Cail & Cline, 2001; Lubben, 2004; Yigit et al., 2006). Consistent element patterns associated with alteration and mineralization are the enrichment of Au, As, Hg, S, Sb, Tl, and Te, the depletion of Ca, Mn, Mg, Sr, and Sc and the immobility of Al, Ti, P, and Si (slightly depleted) (Cail & Cline, 2001; Emsbo et al., 2003). However, these authors also identified a suite of elements that behave erratically in these

systems (As, Fe, Cs, Si, S, W, Cu, and Mo). The overall geological and geochemical ambiguity of CTD's has presented significant challenges in developing a cohesive and well-accepted model for their formation.

1.3.3.2 ORE FLUIDS

A comprehensive understanding of the origin and evolution of the main ore-stage, gold-bearing hydrothermal fluids responsible for Carlin-type mineralization in the Great Basin remains elusive. Currently, there are arguments for CTD's as distal expressions of (1) fluid exsolution from epizonal plutons (e.g. Ressel & Henry, 2006), (2) gold-scavenging convecting groundwater (e.g. Emsbo et al., 2006), or (3) deeply-sourced orogenic metamorphic-magmatic fluids (e.g. Seedorf, 1991; Hofstra & Cline, 2000). Fluid inclusion studies and thermal modeling of Carlin-type deposits have constrained ore fluid temperatures to 180–240 °C, salinities to 2–4 wt % NaCl eq., and CO₂, H₂S, and CH₄ concentrations to <2–4 mol%, 10⁻¹–10⁻² mol, and <0.4 mol%, respectively (Lamb, 1995; Hofstra & Cline, 2000; Cline & Hofstra, 2000; Lubben, 2004; Lubben et al., 2012). The temperature-dependant dissociation of carbonic acid (H₂CO₃), led to increased acidity with cooling (pH = 3.0–3.5), likely creating porosity by dissolution in reactive carbonate horizons (Cline et al., 2005). Several studies have discounted theories of fluid boiling and/or immiscibility as mechanisms for Au precipitation, favoring sulfidation of Fe-bearing host rocks and/or pyrite surface reactions instead (e.g. Hofstra et al., 1991; Kesler et al., 2003). Characteristically high S:Cl ratios in ore fluids resulted in depressed base metal solubility, and bisulfide complexing and transport of Au (Hofstra, 1994; Emsbo et al, 2003). However, these data do not provide compelling support for any particular fluid model, and have been interpreted differently by many workers at many deposits.

1.3.3.3 THEORIES FOR FLUID ORIGIN

Magmatic Fluid Model

The southwest sweep of intermediate, calc-alkaline, intrusive magmatism across the Great Basin during the Eocene was synchronous with the formation of numerous types of ore deposits across the region (Henry & Ressel, 2000b; Howard, 2003; Ressel & Henry, 2006). Dating of Carlin-type mineralization reveals a southward-younging pattern consistent with this migration of magmatic activity (Henry & Ressel, 2000; Ressel & Henry, 2006; Muntean et al., 2011). It has been proposed that fluid exsolution and egress from source plutons and the subsequent partitioning of Au into a low density vapor phase occurred at greater depths (~10 km) than in classic porphyry systems (~4 km), obscuring expected metal zonation patterns at depth (Muntean et al., 2011). Ubiquitous and intimate spatial and temporal associations between igneous rocks and CTD's at shallow depths are supported by aeromagnetic imagery revealing batholithic intrusions beneath deposits along the Carlin Trend (Bettles, 2002; Johnston & Ressel, 2004). Isotopic evidence from ore-stage minerals in the Getchell district and at the Deep Star deposit indicate a magmatic component in the exchanged oxygen isotope depleted ore-stage fluids (Cline et al., 1997, 2003; Heitt et al., 2003).

Metamorphic Fluid Model

This group of models invokes the voluminous discharge of volatile-bearing fluids generated from dehydration reactions during deep prograde metamorphism of sedimentary rocks. Intrusive magmatism provided the thermal energy for metamorphism and also drove extensional fault-focused upward flow of hydrothermal fluids, which harvested Au from the preexisting crustal endowment and mixed with shallow, low-

temperature basinal brines (Seedorff, 1991; Arehart, 1996; Cline et al., 2005). Proponents of this model cite similarities with the tectonic settings (deep-seated suture zones), fluid chemistry (low salinity, high sulfur), and metallurgy (high Au:Ag, low base metals) of orogenic Au deposits (Groves et al., 1998). In addition, this theory has many basic similarities with the meteoric fluid source model, particularly the source of heat, gold, and sulfur.

Meteoric Fluid Model

Although there are several variants, the most popular amagmatic fluid source model fundamentally argues for extension-driven convection of ore-scavenging groundwater through long-lived, superimposed, gold-rich hydrothermal systems. Crustal thinning and/or calc-alkaline plutonism during the Eocene elevated the paleo-geotherm, resulting in the migration of relatively low-temperature, basinal fluids through preexisting Au anomalies, (possibly extinct sedimentary exhalative settings or organic-rich shales) (Emsbo, 2003; Long et al., 2012). Reactivated Devonian normal faults reflecting basement architecture focused ore fluids upward and into contact with permeable, Fe-rich carbonate host units during Eocene basin inversion (Emsbo, 2006). This model is supported by the relatively thin crust and the presence of active geothermal systems throughout Nevada (Emsbo et al., 2003). δD_{H_2O} data from clay alteration reveal an exchanged meteoric signature, and $\delta^{34}S$ studies indicate that sulfur was leached from Paleozoic strata (Hofstra et al., 1999; Hofstra & Cline, 2000; Vikre, 2000; Emsbo, 2003). Proponents of this model also cite the lack of direct links between intrusions and mineralization commonly observed with other granitoid-related deposit types (Emsbo, 2006).

1.4 THESIS GOALS

The purpose of this research is to characterize the fluid history of a multiphase silicic intrusive body emplaced into an exhumed metamorphic terrane at a time of elevated crustal heat and fluid fluxes associated with the formation of massive Au deposits. The two fundamental investigative prongs of this study of the Harrison Pass Pluton (HPP) are to examine (1) the thermodynamic conditions of emplacement and (2) the chemistry of the fluids originating from this magmatic body. Four main objectives are proposed here to accomplish these tasks.

- A. Identify, describe, and classify the evidence of magmatic-hydrothermal fluid activity in the HPP, (miarolitic cavities, vein types, and alteration styles).
- B. Constrain the thermodynamic parameters of primary fluids exsolved by the HPP during cooling, (temperature, pressure, and volume/density), and provide constraints on the conditions of emplacement prior to tectonic exhumation.
- C. Determine the chemical compositions of primary fluids exsolved by the HPP during cooling, (major and trace element chemistry).
- D. Compare and contrast the physical and chemical fingerprint of HPP fluids with existing characterizations of ore fluids from Carlin-type deposits.

1.5 THESIS ORGANIZATION

Chapter 1 of this manuscript provides a comprehensive introduction to the project, including the motivation for conducting it and the central questions addressed therein. Also incorporated into this chapter is an overview of the tectonic, structural, and metallogenic history of the Great Basin and a summary of the debates surrounding the origins of metamorphic core complexes and Carlin-type Au deposits and the unanswered questions relevant to this project.

Chapter 2 introduces the HPP, its geologic setting, and the field and petrographic methods employed to characterize the evidence of fluid activity. Field descriptions of the host intrusive units and hydrothermal features are followed by detailed hand sample and petrographic characterizations of such features, which include vein types and subtypes, miarolitic cavities, and alteration styles. A brief discussion of the hydrothermal activity in the HPP is also included.

Chapter 3 presents an investigation of the fluids exsolved by the HPP during crystallization using fluid inclusion petrography, microthermometry, and LA-ICP-MS, numerical modeling of fluid properties, and oxygen stable isotope analysis of quartz. The physical and geochemical data generated by these analyses are described, discussed, and applied to research questions regarding the conditions of emplacement for the HPP and the role of magmatic fluids in the formation of CTD's. This chapter will be submitted as an independent manuscript to *The American Mineralogist* for publication in the special collection "From Magmas to Ore Deposits." This purpose is reflected in the repetition of certain subjects addressed in other chapters.

Chapter 4 includes a summary of the most significant results of this study, describes potential applications for these results, and suggestions for avenues of future research on the topics addressed in this manuscript.

1.6 SUMMARY

The relationship between plutonism, localized extension, and Au mineralizing hydrothermal systems represents a complex interplay of tectonic setting, stress distribution, and fluid dynamics. Despite decades of study, this component of the geologic history of the Great Basin remains fraught with questions. This study is devoted to addressing two fundamental questions: what does one granitic intrusion record about the structural history of a major Cordilleran metamorphic core complex, and what was the contribution of this intrusion to the crustal fluid budget at the time of intense hydrothermal activity in the northeastern Great Basin? Granitic intrusions are central components to core complex development and are spatially and temporally associated with the world-class Au endowment of northeastern Nevada's Carlin-type deposits. This study demonstrates that the chemistry and thermodynamic parameters of fluids exsolved from such an intrusion, the Harrison Pass Pluton, can provide insight into these outstanding problems.

1.7 REFERENCES

- Allmendinger, R. W., Hauge, T. A., Hauser, E. C., Potter, C. J., Klemperer, S. L., Nelson, K. D., & Oliver, J. (1987). Overview of the COCORP 40 N transect, western United States: The fabric of an orogenic belt. *Geological Society of America Bulletin*, 98(3), 308–319.
- Anderson, E.M. (1951), *The dynamics of faulting*. 2nd ed. Edinburgh: Oliver & Boyd.
- Annen, C., Blundy, J. D., & Sparks, R. S. J. (2006). The genesis of intermediate and silicic magmas in deep crustal hot zones. *Journal of Petrology*, 47(3), 505–539.
- Arehart, G.B. (1996), Characteristic and origin of sediment-hosted disseminated Au deposits: A review. *Ore Geology Reviews*, 11, 383–403.
- Arehart, G. B., Chakurian, A. M., Tretbar, D. R., Christensen, J. N., McInnes, B. A., & Donelick, R. A. (2003). Evaluation of Radioisotope Dating of Carlin-Type Deposits in the Great Basin, Western North America, and Implications for Deposit Genesis. *Economic Geology*, 98(2), 235–248.
- Arehart, G. B., Ressel, M., Carne, R., & Muntean, J. (2013). A comparison of Carlin-type deposits in Nevada and Yukon. *Tectonics, Metallogeny, and Discovery: The North American Cordillera and Similar Accretionary Settings*, M. Colpron, T. Bissig, BG Rusk, and JFH Thompson (eds.), Society of Economic Geologists, Inc., Special Publication, 17, 389–401.
- Armstrong, R. L., & Hansen, E. (1966). Cordilleran infrastructure in the eastern Great Basin. *American Journal of Science*, 264(2), 112-127.
- Armstrong, R. L. (1968). Sevier orogenic belt in Nevada and Utah. *Geological Society of America Bulletin*, 79(4), 429–458.
- Armstrong, R. L., Ekren, E. B., McKee, E. H., & Noble, D. C. (1969). Space-time relations of Cenozoic silicic volcanism in the Great Basin of the western United States. *American Journal of Science*, 267(4), 478–490.
- Armstrong, R. L. (1972), Low-angle (denudation faults), hinterland of the Sevier orogenic belt, eastern Nevada and western Utah. *Geological Society of America Bulletin*, 83, 1729–1754.
- Armstrong, R. L. (1982). Cordilleran metamorphic core complexes-from Arizona to southern Canada. *Annual review of earth and planetary sciences*, 10, 129.
- Audétat, A., Günther, D., & Heinrich, C. A. (1998). Formation of a magmatic-hydrothermal ore deposit: Insights with LA-ICP-MS analysis of fluid inclusions. *Science*, 279(5359), 2091–2094.

Audétat, A., Günther, D., & Heinrich, C. A. (2000). Magmatic-hydrothermal evolution in a fractionating granite: A microchemical study of the Sn-W-F-mineralized Mole Granite (Australia). *Geochimica Et Cosmochimica Acta*, 64(19), 3373–3394.

Audétat, A., & Pettke, T. (2003). The magmatic-hydrothermal evolution of two barren granites: a melt and fluid inclusion study of the Rito del Medio and Canada Pinabete plutons in northern New Mexico (USA). *Geochimica et Cosmochimica Acta*, 67(1), 97–121.

Audétat, A., Pettke, T., Heinrich, C. A., & Bodnar, R. J. (2008). Special Paper: The Composition of Magmatic-Hydrothermal Fluids in Barren and Mineralized Intrusions. *Economic Geology*, 103(5), 877–908. <http://doi.org/10.2113/gsecongeo.103.5.877>

Axen, G. J., Taylor, W. J., & Bartley, J. M. (1993). Space-time patterns and tectonic controls of Tertiary extension and magmatism in the Great Basin of the western United States. *Geological Society of America Bulletin*, 105(1), 56–76.

Axen, G. J., & Hartley, J. M. (1997). Field tests of rolling hinges: Existence, mechanical types, and implications for extensional tectonics. *Journal of Geophysical Research: Solid Earth* (1978–2012), 102(B9), 20515–20537.

Axen, G. J. (2004). Mechanics of low-angle normal faults. In Buck, W. R., & Karner, G. D. (2004). *Rheology and deformation of the lithosphere at continental margins*. 46–91. New York: Columbia University Press.

Bakken, B. M. (1990). Au mineralization, wall-rock alteration, and the geochemical evolution of the hydrothermal system in the main orebody, Carlin Mine, Nevada. PhD Dissertation: Stanford University, Stanford, CA.

Bakken, B. M., & Einaudi, M. T. (1986). Spatial and temporal relations between wall rock alteration and gold mineralization, main pit, Carlin gold mine, Nevada, USA. In *Gold*, 86, 388–403.

Barnes, H. L. (1997). *Geochemistry of hydrothermal ore deposits* (Vol. 1). John Wiley & Sons.

Barnes, C. G., Burton, B. R., Burling, T. C., Wright, J. E., & Karlsson, H. R. (2001). Petrology and Geochemistry of the Late Eocene Harrison Pass Pluton, Ruby Mountains Core Complex, Northeastern Nevada, 42(5), 901–929.

Bartley, J. M., & Wernicke, B. P. (1984). The Snake Range décollement interpreted as a major extensional shear zone. *Tectonics*, 3(6), 647–657.

Barker, S. L., Hickey, K. A., Cline, J. S., Dipple, G. M., Kilburn, M. R., Vaughan, J. R., & Longo, A. A. (2009). Uncloaking invisible gold: use of nanoSIMS to evaluate gold, trace elements, and sulfur isotopes in pyrite from Carlin-type Au deposits. *Economic Geology*, 104(7), 897–904.

Bateman, P. C., & Chappell, B. W. (1979). Crystallization, fractionation, and solidification of the Tuolumne intrusive series, Yosemite National Park, California. *Geological Society of America Bulletin*, 90(5), 465–482.

- Beane, R. E., & Titley, S. R. (1981). Porphyry copper deposits. Part II. Hydrothermal alteration and mineralization. *Economic Geology 75th Anniversary Volume*, 235–269.
- Bendick, R., & Baldwin, J. (2009). Dynamic models for metamorphic core complex formation and scaling: The role of unchanneled collapse of thickened continental crust. *Tectonophysics*, 477(1–2), 93–101.
- Bettles, K. (2002). Exploration and geology, 1962 to 2002, at the Goldstrike Property, Carlin Trend, Nevada. *Integrated Methods for Discovery: Global Exploration in the Twenty-First Century*, Society of Economic Geologists Special Publication, 9, 275–298.
- Buddington, A. F. (1959). Granite emplacement with special reference to North America. *Geological Society of America Bulletin*, 70, 671.
- Buck, W. R. (1988). Flexural rotation of normal faults. *Tectonics*, 7(5), 959–973.
- Burnham, C. W. (1985). Energy release in subvolcanic environments; implications for breccia formation. *Economic Geology*, 80(6), 1515–1522.
- Burnham CW (1997). Magmas and hydrothermal fluids. In: Barnes HL (ed) *Geochemistry of hydrothermal ore deposits*, 3 ed. New York: Wiley.
- Burton, B. R. (1997). Structural geology and emplacement history of the Harrison Pass pluton, central Ruby Mountains, Nevada. PhD Dissertation: University of Wyoming, Laramie, WY.
- Cail, T. L., & Cline, J. S. (2001). Alteration Associated with Au Deposition at the Getchell Carlin-Type Au Deposit, North-Central Nevada. *Economic Geology*, 96(6), 1343–1359.
- Camilleri, P. A., & Chamberlain, K. R. (1997). Mesozoic tectonics and metamorphism in the Pequop Mountains and Wood Hills region, northeast Nevada: Implications for the architecture and evolution of the Sevier orogen. *Geological Society of America Bulletin*, 109(1), 74–94.
- Candela, P. A., & Holland, H. D. (1986). A mass transfer model for copper and molybdenum in magmatic hydrothermal systems; the origin of porphyry-type ore deposits. *Economic Geology*, 81(1), 1–19.
- Candela, P. A. (1989). Felsic magmas, volatiles, and metallogensis. *Reviews in Economic Geology*, 4, 223–233.
- Candela, P. A. (1991). Physics of aqueous phase evolution in plutonic environments. *American Mineralogist*; (United States), 76.
- Candela, P. A., & Blevin, P. L. (1995). Do some miarolitic granites preserve evidence of magmatic volatile phase permeability? *Economic Geology*, 90(8), 2310–2316.
- Candela, P. A. (1997). A Review of Shallow, Ore-related Granites: Textures, Volatiles, and Ore Metals. *Journal of Petrology*, 38(12), 1619–1633.

- Cathles, L. M. (1990). Scales and effects of fluid flow in the upper crust. *Science*, 248(4953), 323–329.
- Charles, N., Gumiaux, C., Augier, R., Chen, Y., Zhu, R., & Lin, W. (2011). Metamorphic Core Complexes vs. synkinematic plutons in continental extension setting: Insights from key structures (Shandong Province, eastern China). *Journal of Asian Earth Sciences*, 40(1), 261–278.
- Chakurian, A. M., Arehart, G. B., Donelick, R. A., Zhang, X., & Reiners, P. W. (2003). Timing Constraints of Au Mineralization along the Carlin Trend Utilizing Apatite Fission-Track, $^{40}\text{Ar}/^{39}\text{Ar}$, and Apatite (U-Th)/He Methods. *Economic Geology*, 98(6), 1159–1171.
- Christiansen, R. L., and Yeats, R. L. (1992) Post-Laramide geology of the U.S. Cordilleran region, in Burchfiel, B. C., Lipman, P. W., and Zoback, M. L., eds., *The Cordilleran Orogen: Conterminous U.S.: Boulder, CO, Geological Society of America, Geology of North America, G-3*, 261–406.
- Christiansen, E. H., & Keith, J. D. (1996). Trace element systematics in silicic magmas: a metallogenic perspective. Trace element geochemistry of volcanic rocks: applications for massive sulphide exploration. Edited by DA Wyman. Geological Association of Canada, Short Course Notes, 12, 115–151.
- Clemens, J. D., & Mawer, C. K. (1992). Granitic magma transport by fracture propagation. *Tectonophysics*, 204(3), 339–360.
- Cline, J. S., Hofstra, A., Landis, G., & Rye, R. O. (1997). Ore fluids at the Getchell, Carlin-type Au deposit, north-central Nevada. *Society of Economic Geologists Field Trip Guidebook*, 28, 155–166.
- Cline, J. S., & Hofstra, A. A. (2000). Ore-fluid evolution at the Getchell Carlin-type Au deposit, Nevada, USA. *European Journal of Mineralogy*, 12(1), 195–212.
- Cline, J. S., Stuart, F. M., Hofstra, A. H., Premo, W., Riciputi, L., Tosdal, R. M., & Tretbar, D. R. (2003). Multiple sources of ore-fluid components at the Getchell Carlin-type Au deposit, Nevada, USA. *Mineral exploration and sustainable development*. Millpress, Rotterdam, 965–968.
- Cline, J. S., Hofstra, A. H., Muntean, J. L., Tosdal, R. M., & Hickey, K. A. (2005). Carlin-Type Au Deposits in Nevada: Critical Geologic Characteristics and Viable Models. *Economic Geology*, 100th Anniversary Volume, 451–484.
- Colgan, J. P., Dumitru, T. A., McWilliams, M., & Miller, E. L. (2006). Timing of Cenozoic volcanism and Basin and Range extension in northwestern Nevada: New constraints from the northern Pine Forest Range. *Geological Society of America Bulletin*, 118(1–2), 126–139.
- Colgan, J. P., Howard, K. A., Fleck, R. J., & Wooden, J. L. (2010). Rapid middle Miocene extension and unroofing of the southern Ruby Mountains, Nevada. *Tectonics*, 29(6).

- Coney, P. J. (1980). Cordilleran metamorphic core complexes: An overview. *Geological Society of America Memoirs*, 153, 7–31.
- Coney, P. J., & Harms, T. A. (1984). Cordilleran metamorphic core complexes: Cenozoic extensional relics of Mesozoic compression. *Geology*, 12(9), 550–554.
- Cooper, F. J., Platt, J. P., Anczkiewicz, R., & Whitehouse, M. J. (2010). Footwall dip of a core complex detachment fault: thermobarometric constraints from the northern Snake Range (Basin and Range, USA). *Journal of Metamorphic Geology*, 28(9), 997–1020.
- Crittenden, M. D., Coney, P. J., Davis, G. H., & Davis, G. H. (Eds.). (1980). Cordilleran metamorphic core complexes (Vol. 153). Geological Society of America.
- Davis, G. H., & Coney, P. J. (1979). Geologic development of the Cordilleran metamorphic core complexes. *Geology*, 7(3), 120–124.
- Davis, G. H. (1983). Shear-zone model for the origin of metamorphic core complexes. *Geology*, 11(6), 342–347.
- Davis, G. A., Lister, G. S., & Reynolds, S. J. (1986). Structural evolution of the Whipple and South Mountains shear zones, southwestern United States. *Geology*, 14(1), 7–10.
- DeCelles, P. G., Lawton, T. F., & Mitra, G. (1995). Thrust timing, growth of structural culminations, and synorogenic sedimentation in the type Sevier orogenic belt, western United States. *Geology*, 23(8), 699–702.
- Dewey, J. F. (1988). Extensional collapse of orogens. *Tectonics*, 7(6), 1123–1139.
- Dickinson, W. R., & Snyder, W. S. (1978). Plate tectonics of the Laramide orogeny. *Geological Society of America Memoirs*, 151, 355–366.
- Dickinson, W.R. (2002). The Basin and Range Province as a composite extensional domain. *International Geology Review*, 44, 1–38.
- Dickinson, W.R. (2006). Geotectonic Evolution of the Great Basin. *Geosphere*, 2, 353–368.
- Dietz, R.S. & Holden, J.C. (1966). Miogeoclines (Miogeosynclines) in Space and Time, *Journal of Geology*, 74, 5, 566–583.
- Dilles, J.H. & Gans, P.B. (1995). The chronology of Cenozoic volcanism and deformation in the Yerington area, western Basin and Range and Walker Lane. *GSA Bulletin*, 107, 474–486.
- diPietro, J.A. (2013). *Landscape Evolution in the United States: an Introduction to the Geography, Geology, and Natural History*. Waltham, MA: Elsevier.
- Denele, Y., Lecomte, E., Jolivet, L., Lacombe, O., Labrousse, L., Huet, B., & Le Pourhiet, L. (2011). Granite intrusion in a metamorphic core complex: the example of the Mykonos laccolith (Cyclades, Greece). *Tectonophysics*, 501(1), 52–70.

- Emsbo, P., Hofstra, A.H., Lauha, E.A., Griffin, G.L., Hutchinson, R.W. (2003). Origin of High-Grade Au Ore, Source of Fluid Components, and Genesis of the Meikle and Neighboring Carlin-Type Deposits, Northern Carlin Trend, Nevada. *Economic Geology*, 98, 1069–1105.
- Emsbo, P., Groves, D.I., Hofstra, A.H. (2006). The giant Carlin Au province: a protracted interplay of orogenic, basinal, and hydrothermal processes above a lithospheric boundary. *Mineralium Deposita*, 41, 517–525.
- Erkül, S. T., & Erkül, F. (2012). Magma interaction processes in syn-extensional granitoids: The Tertiary Menderes Metamorphic Core Complex, western Turkey. *Lithos*, 142–143(C), 16–33.
- Farmer, G. L., & DePaolo, D. J. (2014). Origin of Mesozoic and Tertiary Granite in the Western United States and Implications for Pre-Mesozoic Crustal Structure. *Journal of Geophysical Research*, 1–23.
- Foster, D. A., Schafer, C., Fanning, C. M., & Hyndman, D. W. (2001). Relationships between crustal partial melting, plutonism, orogeny, and exhumation: Idaho–Bitterroot batholith. *Tectonophysics*, 342(3), 313–350.
- Frost, B. R., Barnes, C. G., Collins, W. J., Arculus, R. J., Ellis, D. J., & Frost, C. D. (2001). A geochemical classification for granitic rocks. *Journal of petrology*, 42(11), 2033–2048.
- Fuxin, Z., & Jing, Z. (2003). Geological-geochemical characteristics of Carlin- and Carlin-like-type Au deposits in South Qinling mountains. *Chinese Journal of Geochemistry*, 22(1), 11–22.
- Gans, P. B., & Wong, M. (2014). Late Cretaceous Localized Crustal Thickening as a Primary Control on the 3-D Architecture and Exhumation Histories of Cordilleran Metamorphic Core Complexes. In *AGU Fall Meeting Abstracts*, 1, 4698.
- Glazner, A. F., Bartley, J. M., Coleman, D. S., Gray, W., & Taylor, R. Z. (2004). Are plutons assembled over millions of years by amalgamation from small magma chambers? *GSA Today*, 14(4), 4–8.
- Granillo, R. V., & Calmus, T. (2003). Mazatan metamorphic core complex (Sonora, Mexico): structures along the detachment fault and its exhumation evolution. *Journal of South American Earth Sciences*, 16(4), 193–204.
- Grauch, V. J. S., Rodriguez, B. D., & Wooden, J. L. (2003). Geophysical and isotopic constraints on crustal structure related to mineral trends in north-central Nevada and implications for tectonic history. *Economic Geology*, 98(2), 269–286.
- Groves, D. I., Goldfarb, R. J., Gebre-Mariam, M., Hagemann, S. G., & Robert, F. (1998). Orogenic Au deposits: a proposed classification in the context of their crustal distribution and relationship to other Au deposit types. *Ore Geology Reviews*, 13(1–5), 7–27.

- Haines, S. H., & van der Pluijm, B. A. (2010). Dating the detachment fault system of the Ruby Mountains, Nevada: Significance for the kinematics of low. *Tectonics*, 29, 1–20.
- Hallett, B. W., & Spear, F. S. (2015). Monazite, zircon, and garnet growth in migmatitic pelites as a record of metamorphism and partial melting in the East Humboldt Range, Nevada. *American Mineralogist*, 100(4), 951–972.
- Hanson, R. B., & Glazner, A. F. (1995). Thermal requirements for extensional emplacement of granitoids. *Geology*, 23(3), 213–216.
- Harker, A., & Clough, C. T. (1904). *The Tertiary igneous rocks of Skye*. Glasgow: HM Stationery Office.
- Harry, D.L., Sawyer, D.S., and Leeman, W.F. (1993). The mechanics of continental extension in western North America: Implications for the magmatic and structural evolution of the Great Basin: *Earth and Planetary Science Letters*, 117, 59–71.
- Hedenquist, J. W., & Lowenstern, J. B. (1994). The role of magmas in the formation of hydrothermal ore deposits. *Nature*, 370(6490), 519–527.
- Heitt, D. G., Dunbar, W. W., Thompson, T. B., & Jackson, R. G. (2003). Geology and geochemistry of the Deep Star Au deposit, Carlin trend, Nevada. *Economic Geology*, 98(6), 1107–1135.
- Henry, C. D., & Ressel, M. W. (2000). Interrelation of Eocene magmatism, extension, and Carlin-type Au deposits in northeastern Nevada. *Great Basin and Sierra Nevada: Boulder, Colorado, Geological Society of America Field Guide*, 2, 165–187.
- Hickey, K. A. (2003). Restoration of the Eocene landscape in the Carlin-Jerritt Canyon mining district: constraining depth of mineralization for Carlin-type Au-Deposits using low-temperature apatite thermochronology. In 2003 Seattle Annual Meeting.
- Hickey, K. A., Barker, S. L. L., Dipple, G. M., Arehart, G. B., & Donelick, R. A. (2014). The Brevity of Hydrothermal Fluid Flow Revealed by Thermal Halos around Giant Au Deposits: Implications for Carlin-Type Au Systems. *Economic Geology*, 109, 1451–1497.
- Hildebrand, R. S. (2013). *Mesozoic Assembly of the North American Cordillera (Vol. 495)*. Geological society of America.
- Hodges, K. V., & Walker, J. D. (1992). Extension in the Cretaceous Sevier orogen, North American Cordillera. *Geological Society of America Bulletin*, 104(5), 560–569.
- Hofstra, A. H., Leventhal, J. S., Northrop, H. R., Landis, G. P., Rye, R. O., Birak, D. J., & Dahl, A. R. (1991). Genesis of sediment-hosted disseminated-gold deposits by fluid mixing and sulfidization: Chemical-reaction-path modeling of ore-depositional processes documented in the Jerritt Canyon district, Nevada. *Geology*, 19(1), 36–40.

- Hofstra, A. H. (1994). Geology and genesis of the Carlin-type Au deposits in the Jerritt Canyon district, Nevada: Unpublished PhD (Doctoral dissertation, dissertation, Boulder, University of Colorado).
- Hofstra, A.H., Snee, L.W., Rye, R.O., Folger, H.W. (1999). Age constraints on Jerritt Canyon and other Carlin-type Au deposits in the western United States: relationship to mid-Tertiary extension and magmatism. *Economic Geology*, 94, 769–802.
- Hofstra, A. H., & Cline, J. S. (2000). Characteristics and models for Carlin-type Au deposits. *Reviews in Economic Geology*, 13, 163–220.
- Howard, K. A. (2003). Crustal Structure in the Elko-Carlin Region, Nevada, during Eocene Au Mineralization: Ruby-East Humboldt Metamorphic Core Complex as a Guide to the Deep Crust. *Economic Geology*, 98, 249–268.
- Howard, K. A., Wooden, J. L., Barnes, C. G., Premo, W. R., Snoke, A. W., & Lee, S. Y. (2011). Episodic growth of a Late Cretaceous and Paleogene intrusive complex of pegmatitic leucogranite, Ruby Mountains core complex, Nevada, USA. *Geosphere*, 7(5), 1220–31.
- Huet, B., Le Pourhiet, L., Labrousse, L., Burov, E. B., & Jolivet, L. (2011). Formation of metamorphic core complex in inherited wedges: A thermomechanical modelling study. *Earth and Planetary Science Letters*, 309(3–4), 249–257.
- Humphreys, E. D. (1995). Post-Laramide removal of the Farallon slab, western United States. *Geology*, 23(11), 987–4.
- Humphreys, E., Hessler, E., Dueker, K., Farmer, G. L., Erslev, E., & Atwater, T. (2003). How Laramide-age hydration of North American lithosphere by the Farallon slab controlled subsequent activity in the western United States. *International Geology Review*, 45(7), 575–595.
- Hurlow, H. A., Snoke, A. W., & Hodges, K. V. (1991). Temperature and pressure of mylonitization in a Tertiary extensional shear zone, Ruby Mountains-East Humboldt Range, Nevada: Tectonic implications. *Geology*, 19, 82–86.
- Ilchik, R. P., & Barton, M. D. (1997). An Amagmatic Origin of Carlin-Type Au Deposits. *Economic Geology*, 92, 269–288.
- Ishihara, S. (1981). The granitoid series and mineralization. *Econ. Geol. 75th Anniv. Vol.*, 458–484.
- John, B. E., & Foster, D. A. (1993). Structural and thermal constraints on the initiation angle of detachment faulting in the southern Basin and Range: The Chemehuevi Mountains case study. *Geological Society of America Bulletin*, 105(8), 1091–1108.
- Johnson, C. M. (1991). Large-scale crust formation and lithosphere modification beneath Middle to Late Cenozoic calderas and volcanic fields, western North America. *Journal of Geophysical Research: Solid Earth* (1978–2012), 96(B8), 13485–13507.

- Johnston, M. K., & Ressel, M. W. (2004). Controversies on the origin of world-class Au deposits, Pt. I: Carlin-type Au deposits in Nevada, II. Carlin-type and distal disseminated Au-Ag deposits: Related distal expressions of Eocene intrusive centers in north-central Nevada: Society of Economic Geologists Newsletter, 59, 12–14.
- Jolivet, L., Faccenna, C., Goffé, B., Burov, E., & Agard, P. (2003). Subduction tectonics and exhumation of high-pressure metamorphic rocks in the Mediterranean orogens. *American Journal of Science*, 303(5), 353–409.
- Jolivet, L., Lecomte, E., Huet, B., Denèle, Y., Lacombe, O., Labrousse, L., et al. (2010). The North Cycladic Detachment System. *Earth and Planetary Science Letters*, 289(1–2), 87–104.
- Jones, C.H., Wernicke, B.P., Farmer, G.L., Walker, J.D., Coleman, D.S., Mckenna, L.W., Perry, F.V. (1992). Variations across and along a major continental rift: An interdisciplinary study of the Basin and Range Province, western USA. *Tectonophysics*, 213, 57–96.
- Jugo, P. J., Candela, P. A., & Piccoli, P. M. (1999). Magmatic sulfides and Au: Cu ratios in porphyry deposits: an experimental study of copper and Au partitioning at 850 C, 100 MPa in a haplogranitic melt–pyrrhotite–intermediate solid solution–gold metal assemblage, at gas saturation. *Lithos*, 46(3), 573–589.
- Karlstrom, K. E., & Houston, R. S. (1984). The Cheyenne belt: Analysis of a Proterozoic suture in southern Wyoming. *Precambrian Research*, 25(4), 415–446.
- Kesler, S. E. (1994). *Mineral resources, economics, and the environment*. Prentice Hall.
- Kesler, S. E., Fortuna, J., Ye, Z., Alt, J. C., Core, D. P., Zohar, P., et al. (2003). Evaluation of the Role of Sulfidation in Deposition of Gold, Screamer Section of the Betze-Post Carlin-Type Deposit, Nevada. *Economic Geology*, 98, 1137–1157.
- Kilpatrick, J. A., & Ellis, D. J. (1992). C-type magmas: igneous charnockites and their extrusive equivalents. *Geological Society of America Special Papers*, 272, 155–164.
- Kistler, R. W., Ghent, E. D., & O'neil, J. R. (1981). Petrogenesis of garnet two-mica granites in the Ruby Mountains, Nevada. *Journal of Geophysical Research: Solid Earth (1978–2012)*, 86(B11), 10591–10606.
- Kochneva, N. T., Volkov, A. V., Serafimovski, T., Tasev, G., & Tomson, I. N. (2006). Tectonic position of the Alshar Au-As-Sb-Tl deposit, Macedonia. *Doklady Earth Sciences*, 407(1), 175–178.
- Kuehn, C. A. (1989). *Studies of disseminated Au deposits near Carlin, Nevada: Evidence for a deep geologic setting of ore formation*. PhD Dissertation: Pennsylvania State University, Middletown, PA.
- Lamb, J. B. (1995). *A petrographic and fluid inclusion study of the Purple Vein and Post-Betze orebodies, Carlin, Nevada*. M.S. Thesis: University of Nevada, Las Vegas, NV.

- Lang, J., & Baker, T. (2001). Intrusion-related Au systems: the present level of understanding. *Mineralium Deposita*, 36(6), 477–489.
- Dixon, T. H., Robaudo, S., Lee, J., & Reheis, M. C. (1995). Constraints on present-day Basin and Range deformation from space geodesy. *Tectonics*, 14(4), 755–772.
- Lewis, C. J., Wernicke, B. P., Selverstone, J., & Bartley, J. M. (1999). Deep burial of the footwall of the northern Snake Range décollement, Nevada. *Geological Society of America Bulletin*, 111(1), 39–51.
- Lipman, P. W., Prostka, H. J., & Christiansen, R. L. (1971). Evolving subduction zones in the western United States, as interpreted from igneous rocks. *Science*, 174(4011), 821–825.
- Lipman, P. W., Prostka, H. J., & Christiansen, R. L. (1972). Cenozoic volcanism and plate-tectonic evolution of the western United States. I. Early and Middle Cenozoic. *Philosophical Transactions of the Royal Society of London A: Mathematical, Physical and Engineering Sciences*, 271(1213), 217–248.
- Lister, G. S., & Baldwin, S. L. (1993). Plutonism and the origin of metamorphic core complexes. *Geology*, 21(7), 607–610.
- Lister, G. S., & Davis, G. A. (1989). The origin of metamorphic core complexes and detachment faults formed during Tertiary continental extension in the northern Colorado River region, USA. *Journal of Structural Geology*, 11(1), 65–94.
- Lister, G.S., Etheridge, M.A., Symonds, P.A. (1986). Detachment faulting and the evolution of passive continental margins. *Geology*, 14, 246–250.
- Loiselle, M. C., & Wones, D. R. (1979). Characteristics and origin of anorogenic granites. In *Geological Society of America Abstracts with Programs*, 11(7), 468.
- London, D. (1986). Formation of tourmaline-rich gem pockets in miarolitic pegmatites. *American Mineralogist*, 71(3–4), 396–405.
- London, D. (1992). The application of experimental petrology to the genesis and crystallization of granitic pegmatites. *The Canadian Mineralogist*, 30(3), 499–540.
- Long, S.P. (2012). Magnitudes and spatial patterns of erosional exhumation in the Sevier hinterland, eastern Nevada and western Utah, USA: Insights from a Paleogene paleogeologic map. *Geosphere*, 8, 881–901.
- Lowell, J. D., & Guilbert, J. M. (1970). Lateral and vertical alteration-mineralization zoning in porphyry ore deposits. *Economic Geology*, 65(4), 373–408.
- Lowenstern, J. B. (1994). Dissolved volatile concentrations in an ore-forming magma. *Geology*, 22(10), 893–896.

- Lubben, J. D. (2004). Silicification Across the Betze-Post Carlin-type Au Deposit: Clues to Ore Fluid Properties and Sources, Northern Carlin Trend, Nevada. PhD dissertation: University of Nevada, Las Vegas.
- Lubben, J. D., Cline, J. S., & Barker, S. L. L. (2012). Ore Fluid Properties and Sources from Quartz-Associated Au at the Betze-Post Carlin-Type Au Deposit, Nevada, United States. *Economic Geology*, 107, 1351–1383.
- MacCready, T., Snoke, A. W., Wright, J. E., & Howard, K. A. (1997). Mid-crustal flow during Tertiary extension in the Ruby Mountains core complex, Nevada. *Geological Society of America Bulletin*, 109(12), 1576–1594.
- Machek, M., Roxerová, Z., Janoušek, V., Staněk, M., Petrovský, E., & René, M. (2013). Petrophysical and geochemical constraints on alteration processes in granites. *Studia Geophysica Et Geodaetica*, 57(4), 710–740.
- Mahan, K. H., Bartley, J. M., Coleman, D. S., Glazner, A. F., & Carl, B. S. (2003). Sheeted intrusion of the synkinematic McDoogie pluton, Sierra Nevada, California. *Geological Society of America Bulletin*, 115(12), 1570–1582.
- Marshak, S., Karlstrom, K. & Timmons, J. M. (2000). Inversion of Proterozoic extensional faults: An explanation for the pattern of Laramide and Ancestral Rockies intracratonic deformation, United States. *Geology*, 28, 735–738.
- McGrew, A. J., & Snee, L. W. (1994). $^{40}\text{Ar}/^{39}\text{Ar}$ thermochronologic constraints on the tectonothermal evolution of the Northern East Humboldt range metamorphic core complex, Nevada. *Tectonophysics*, 238(1), 425–450.
- McGrew, A. J., Peters, M. T., & Wright, J. E. (2000). Thermobarometric constraints on the tectonothermal evolution of the East Humboldt Range metamorphic core complex, Nevada. *Geological Society of America Bulletin*, 112(1), 45–60.
- McKenzie, D. (1978). Some remarks on the development of sedimentary basins. *Earth and Planetary science letters*, 40(1), 25–32.
- Meinert, L. D. (1992). Skarns and skarn deposits. *Geoscience Canada*, 19(4).
- Miller, C. F., Watson, E. B., & Harrison, T. M. (1988). Perspectives on the source, segregation and transport of granitoid magmas. *Transactions of the Royal Society of Edinburgh: Earth Sciences*, 79(2–3), 135–156.
- Misch, P. (1960). Regional structural reconnaissance in central-northeast Nevada and some adjacent areas: Observations and interpretations.
- Muntean, J.L., Cline, J.S., Simon, A.C., Longo, A.A. (2011). Magmatic-hydrothermal origin of Nevada's Carlin-type Au deposits. *Nature Geoscience*, 4, 122–127.

Norton, D., & Knight, J. (1977). Transport phenomena in hydrothermal systems: cooling plutons. *American Journal of Science*, 277.

Oldow, J. S. (1983). Tectonic implications of a late Mesozoic fold and thrust belt in northwestern Nevada. *Geology*, 11(9), 542–546.

Pape, J. R. (2010). Reconstructions of Cenozoic Extensional Faulting Within the Southern Ruby Mountains Metamorphic Core Complex and Adjacent Areas, Northeastern Nevada. M.S. Thesis: University of Arizona, Tucson, AZ.

Parsons, T. (1995). The Basin and Range Province, in *Continental Rifts: Evolution, Structure, Tectonics*. ed. K. H. Olsen, Elsevier, Amsterdam, 277–324.

Partington, G. A., & Williams, P. J. (2000). Proterozoic lode Au and (iron)–copper–gold deposits: a comparison of Australian and global examples. *Reviews in Economic Geology*, 13, 69–101.

Petford, N. (1996). Dykes or diapirs?. *Geological Society of America Special Papers*, 315, 105–114.

Pitcher, W. S., Atherton, M. P., Cobbing, E. J., & Beckinsale, R. D. (1985). Magmatism at a plate edge: the Peruvian Andes. Blackie.

Poole, F.G., Stewart, J.H., Palmer, A.R., Sandberg, C.A., Madrid, R.J., Ross, R.J., Hintze, L.F., Miller, M.M., & Wrucke, C.T. (1993). Latest Precambrian to latest Devonian time: Development of a continental margin: In Burchfiel, B.C., Lipman, P.W., and Zoback, M.L., eds., *The Cordilleran Orogen: Conterminous U.S.: Boulder, Geological Society of America, The Geology of North America*, G-3, 9–56.

Rasmussen, K. L., & Mortensen, J. K. (2013). Magmatic petrogenesis and the evolution of (F:Cl:OH) fluid composition in barren and tungsten skarn-associated plutons using apatite and biotite compositions: Case studies from the northern Canadian Cordillera. *Ore Geology Reviews*, 50(C), 118–142.

Regenauer-Lieb, K., Weinberg, R. F., & Rosenbaum, G. (2006). The effect of energy feedbacks on continental strength. *Nature*, 442(7098), 67–70.

Reid, J. B., Evans, O. C., & Fates, D. G. (1983). Magma mixing in granitic rocks of the central Sierra Nevada, California. *Earth and Planetary Science Letters*, 66, 243–261.

Ressel, M. W., & Henry, C. D. (2006). Igneous Geology of the Carlin Trend, Nevada: Development of the Eocene Plutonic Complex and Significance for Carlin-Type Au Deposits. *Economic Geology*, 101, 347–383.

Rey, P. F., Teyssier, C., & Whitney, D. L. (2009). Extension rates, crustal melting, and core complex dynamics. *Geology*, 37(5), 391–394.

Rye, R. O. (1993). The evolution of magmatic fluids in the epithermal environment; the stable isotope perspective. *Economic Geology*, 88(3), 733–752.

Satarugsa, P., & Johnson, R. A. (2000). Cenozoic tectonic evolution of the Ruby Mountains metamorphic core complex and adjacent valleys, northeastern Nevada. *Rocky Mountain Geology*, 35(2), 205–230.

Schwerdtner, W. M. (1995). Local displacement of diapir contacts and its importance to pluton emplacement study. *Journal of Structural Geology*, 17(6), 907–910.

Seedorff, E. (1991). Magmatism, extension, and ore deposits of Eocene to Holocene age in the Great Basin—Mutual effects and preliminary proposed genetic relationships. *Geology and ore deposits of the Great Basin*, 1, 133–178.

Seward, T. M., & Barnes, H. L. (1997). Metal transport by hydrothermal ore fluids. *Geochemistry of hydrothermal ore deposits*, 3, 435–486.

Shannon, J. R., Walker, B. M., Carten, R. B., & Geraghty, E. P. (1982). Unidirectional solidification textures and their significance in determining relative ages of intrusions at the Henderson Mine, Colorado. *Geology*, 10(6), 293–297.

Cox, D. P., & Singer, D. A. (1986). *Mineral deposit models*, 1693. Washington, DC, USA: US Government Printing Office.

Sillitoe, R. H., & Bonham, H. F., Jr. (1990). Sediment-hosted Au deposits: Distal products of magmatic-hydrothermal systems. *Geology*, 18(2), 157–166.

Sillitoe, R. H., & Hedenquist, J. W. (2003). Linkages between volcanotectonic settings, ore-fluid compositions, and epithermal precious metal deposits. *Special Publication-Society of Economic Geologists*, 10, 315–343.

Simon, A. C., Frank, M. R., Pettke, T., Candela, P. A., Piccoli, P. M., & Heinrich, C. A. (2005). Au partitioning in melt-vapor-brine systems. *Geochimica et Cosmochimica Acta*, 69(13), 3321–3335.

Simon, A. C., Pettke, T., Candela, P. A., Piccoli, P. M., & Heinrich, C. A. (2007). The partitioning behavior of As and Au in S-free and S-bearing magmatic assemblages. *Geochimica et Cosmochimica Acta*, 71(7), 1764–1782.

Singleton, J. S., Stockli, D. F., Gans, P. B., & Prior, M. G. (2014). Timing, rate, and magnitude of slip on the Buckskin-Rawhide detachment fault, west central Arizona. *Tectonics*, 33(8), 1596–1615.

Snoke, A. W. (2005). Southern Cordillera, in Selley, R. C., Cocks, L.R.M., & Plimer, I. R., eds., *Encyclopedia of Geology*, 4, 48–61.

Sullivan, W. A., & Snoke, A. W. (2007). Comparative anatomy of core-complex development in the northeastern Great Basin, USA. *Rocky Mountain Geology*, 42(1), 1–29.

Speed, R.C., & Sleep, N.H. (1982). Antler orogeny and foreland basin: A model. *Geological Society of America Bulletin*, 93, 815–828.

- Streckeisen, A. L. (1967). Classification and nomenclature of igneous rocks. (Final report of an inquiry.) *Neues Jahrbuch für Mineralogie, Abhandlungen*, 107, 144–240.
- Sullivan, W. A., & Snoke, A. W. (2007). Comparative anatomy of core-complex development in the northeastern Great Basin, USA. *Rocky Mountain Geology*, 42(1), 1–29.
- Shinohara, H., Kazahaya, K., & Lowenstern, J. B. (1995). Volatile transport in a convecting magma column: Implications for porphyry Mo mineralization. *Geology*, 23(12), 1091–1094.
- Tkachev, A. V. (2011). Evolution of metallogeny of granitic pegmatites associated with orogens throughout geological time. *Geological Society of London, Special Publications*, 350(1), 7–23.
- Thatcher, W., Foulger, G. R., Julian, B. R., Svarc, J., Quilty, E., & Bawden, G. W. (1999). Present-day deformation across the Basin and Range province, western United States. *Science*, 283(5408), 1714–1718.
- Thomson, S. N., & Ring, U. (2006). Thermochronologic evaluation of postcollision extension in the Anatolide orogen, western Turkey. *Tectonics*, 25(3).
- Thorman, C. H., Ketner, K. B., Brooks, W. E., Snee, L. W., & Zimmerman, R. A. (1991). Late Mesozoic-Cenozoic tectonics in northeastern Nevada. In *Geology and ore deposits of the Great Basin: Symposium Proceedings*, Geological Society of Nevada, Reno, Nevada, 1, 25–45.
- Uchida, E., Endo, S., & Makino, M. (2007). Relationship between solidification depth of granitic rocks and formation of hydrothermal ore deposits. *Resource Geology*, 57(1), 47–56.
- Thorman, C. H., Ketner, K. B., Brooks, W. E., Snee, L. W., & Zimmermann, R. A. (n.d.). *Mesozoic–Cenozoic Tectonics in Northeastern Nevada*, 25–46.
- Vikre, P. G. (2000). Subjacent crustal sources of sulfur and lead in eastern Great Basin metal deposits. *Geological Society of America Bulletin*, 112(5), 764–782.
- Wallace, A.R., and John, D.A. (1998). New studies of Tertiary volcanic rocks and mineral deposits, northern Nevada rift, in Tosdal, R.M., ed., *Contributions to the Au metallogeny of northern Nevada: U.S. Geological Survey Open-File Report*, 98–338, 264–278.
- Webster, J. D. (1997). Exsolution of magmatic volatile phases from Cl-enriched mineralizing granitic magmas and implications for ore metal transport. *Geochimica et Cosmochimica Acta*, 61(5), 1017–1029.
- Wiebe, R. A., & Collins, W. J. (1998). Depositional features and stratigraphic sections in granitic plutons: implications for the emplacement and crystallization of granitic magma. *Journal of Structural Geology*, 20(9), 1273–1289.
- Weinberg, R. F., & Podladchikov, Y. (1994). Diapiric ascent of magmas through power law crust and mantle. *Journal of Geophysical Research*, 99(B5), 9543–9560.

- Wernicke, B. (1981). Low-Angle Normal Faults in the Basin and Range Province: Nappe Tectonics in an Extending Orogen. *Nature*, 291, 645–648.
- Wernicke, B., & Axen, G. J. (1988). On the role of isostasy in the evolution of normal fault systems. *Geology*, 16(9), 848–851.
- Wernicke, B. (1992). Cenozoic extensional tectonics of the US Cordillera. *The Geology of North America*, 3, 553–581.
- Wernicke, B. (1995). Low-angle normal faults and seismicity. A review. *Journal of Geophysical Research*, 100, 20159–20174.
- Chappell, B., & White, A. (1974). Two contrasting granite types. *Pacific geology*, 8(2), 173–174.
- Wallace, P. J. (2005). Volatiles in subduction zone magmas: concentrations and fluxes based on melt inclusion and volcanic gas data. *Journal of Volcanology and Geothermal Research*, 140(1), 217–240.
- White, A. J., & Chappell, B. W. (1977). Ultrametamorphism and granitoid genesis. *Tectonophysics*, 43(1), 7–22.
- White, A. J. R., & Chappell, B. W. (1983). Granitoid types and their distribution in the Lachlan Fold Belt, southeastern Australia. *Geological Society of America Memoirs*, 159, 21–34.
- Whitney, J. A. (1988). The origin of granite: the role and source of water in the evolution of granitic magmas. *Geological Society of America Bulletin*, 100(12), 1886–1897.
- Williams-Jones, A. E., & Heinrich, C. A. (2005). 100th Anniversary special paper: vapor transport of metals and the formation of magmatic-hydrothermal ore deposits. *Economic Geology*, 100(7), 1287–1312.
- Wright, J. E., & Snoke, A. W. (1993). Tertiary magmatism and mylonitization in the Ruby-East Humboldt metamorphic core complex, northeastern Nevada: U-Pb geochronology and Sr, Nd, and Pb isotope geochemistry. *Geological Society of America Bulletin*, 105(7), 935–952.
- Yigit, O., Hofstra, A. H., Hitzman, M. W., & Nelson, E. P. (2006). Geology and geochemistry of jasperoids from the Au Bar district, Nevada. *Mineralium Deposita*, 41(6), 527–547.
- Zoback, M. L., Anderson, R. E., & Thompson, G. A. (1981). Cainozoic Evolution of the State of Stress and Style of Tectonism of the Basin and Range Province of the Western United States. *Philosophical Transactions of the Royal Society a: Mathematical, Physical and Engineering Sciences*, 300(1454), 407–434.

CHAPTER 2: THE HARRISON PASS PLUTON AND EVIDENCE FOR FLUID EXSOLUTION AND MIGRATION DURING EMPLACEMENT AND COOLING

2.1 INTRODUCTION

Describing the effects of hydrothermal systems in granitic rocks provides critical insights into the fundamental link between intrusive magmatism and crustal fluid flow. Fluid and heat generated by hydrous silicate melts are responsible for and associated with hydrothermal ore deposits of myriad mineralization styles, metal species, grade, and scale (Holland, 1972; Burnham, 1979; Lowenstern, 1991; Heinrich et al., 1992; Hedenquist & Lowenstern, 1994; Shinohara, 1994). Previous field-based investigations of the transition from magma emplacement to sub and super-solidus hydrothermal circulation in mineralizing and barren intrusions have sought to define the geologic features formed by these systems and to constrain the compositions of the constituent fluids (e.g. Candela & Blevin, 1995; Dunbar et al., 1996; Candela, 1997; Audétat et al., 1998; 2000; 2008; Audétat & Pettke, 2003). These studies relied upon meticulous mapping and description of the spatial distribution and timing relationships of subsolidus igneous and hydrothermal features preserved in their study areas. Effective integration of field observations with quantitative geochemical analyses permits a detailed reconstruction of the magmatic-hydrothermal progression that reflects key spatial and temporal heterogeneities present in an intrusion.

This chapter presents detailed field and petrographic descriptions of the evidence of primary, intrusion-driven hydrothermal activity in the Harrison Pass Pluton (HPP).

Pegmatites, aplites, miarolitic cavities, and hydrothermal veins and alteration were mapped, sampled, and described for this study. The physical characteristics (i.e. relative volume, mineral assemblage, deformational features), geographic locations, and associations of these orthomagmatic and hydrothermal features permit a tentative reconstruction of their sequential progression in space and time. Fundamentally, all observations indicate that the magmatic-hydrothermal transition of the HPP was complex, multi-stage, and spatially variable. The two-stage assembly of the intrusion broadly controlled the behavior and evolution of the hydrothermal system. The early stage was characterized by relatively high temperatures, voluminous volatile exsolution, extensive fluid migration, and metal deposition in reactive wallrock units. The late stage hydrothermal system was less substantial, possibly due to magmatic volatile retention coupled with lower metal concentrations.

2.2 GEOLOGIC FRAMEWORK AND STRUCTURAL OVERVIEW

The field area for this study is located in the northeast quadrant of the Great Basin, a region of internal drainage bounded by Utah's Wasatch Mountains to the east and the Sierra Nevada Mountains of California to the west, and defined by the distinctive repeating "Basin and Range" topography (Gilbert, 1928). Since the Precambrian, the Great Basin has experienced numerous compressional episodes (characterized by thin-skinned deformation and crustal overthickening), and at least two periods of extension (characterized by magmatic activity and either localized detachment faulting or distributed fault-block extension) (see Dickinson, 2002; 2006) for detailed review of Great Basin

tectonics). The region is a composite medley of overprinted and dismembered geologic features and systems within the greater context of the evolving North American Cordillera (Figure 2.1). This section provides comprehensive descriptions of the Ruby Mountains-East Humboldt Range metamorphic core complex and the Harrison Pass Pluton and presents a detailed review of their positions within this geologic framework.

2.2.1 THE RUBY MOUNTAINS-EAST HUMBOLDT RANGE

Along with the Snake Range and the Albion-Raft River-Grouse Creek Mountains (ARG), the Ruby Mountains-East Humboldt Range (RMEHR) is a classic example of a Cordilleran metamorphic core complex exposed in the hinterland of the thin-skinned deformation belt formed during the Cretaceous Sevier Orogeny (Sullivan & Snoke, 2007). Many workers have investigated the tectonic, structural, magmatic, and thermochronological evolution of the RMEHR over several decades (e.g. Sharp, 1942; Armstrong, 1982; Snoke & Lush, 1984; Dallmeyer et al., 1986; Lush et al., 1988; Snoke & Miller, 1988; Snoke et al., 1990b; Hodges et al., 1992; Hudec, 1992; Camilleri & Chamberlain, 1997; McGrew et al., 2000; Satarugsa & Johnson, 2005). Fundamentally, the RMEHR is a fault-bounded dome of intrusions and high-grade metamorphic rocks exhumed by a large-scale extensional structure (Howard, 1980; Snoke, 1980) (See Figure 2.2). The geologic architecture of the RMEHR is divided into the *infrastructure* (core of migmatitic, polydeformed greenschist to upper amphibolite facies metamorphic and plutonic rocks), the *suprastructure* (adjacent zone of weakly metamorphosed to unmetamorphosed Paleozoic strata with Tertiary igneous and sedimentary rocks), and the intervening *transition zone* (mostly metamorphosed Paleozoic sedimentary rocks and Mesozoic and Cenozoic intrusive rocks) (Howard, 1980; Snoke, 1980; Wright & Snoke, 1993).

Mesozoic formation of the high-grade metamorphic infrastructure of the RMEHR was initiated by the tectonic burial of Proterozoic and Paleozoic miogeoclinal rocks to midcrustal depths (13–30 km) (Coney & Harms, 1984; Hodges et al., 1992; Snoke, 1992; Camilleri & Chamberlain, 1997; Howard, 2003; Decelles, 2004). Burial was accompanied by voluminous plutonism and prograde metamorphism ranging from upper amphibolite facies in the northern Ruby Mountains and adjoining East Humboldt Range to lower greenschist facies in the southern Ruby Mountains. This transition in metamorphic grade has been interpreted as evidence of increasingly deeper burial depths from south to north along the range (Snoke & Lush, 1984; Snoke et al., 1990b; Hudec, 1990, 1992). The clockwise prograde pressure-temperature-time evolution of the RMEHR peaked in the East Humboldt Range during the late Cretaceous (max. pressure \cong 9 kbar; max. temperature \cong 800°C) and was associated with intense ductile deformation (including recumbent fold-nappe emplacement), migmatization, and voluminous intrusive peraluminous granitic magmatism (Howard, 1980; Snoke, 1980; Armstrong, 1982; Snoke & Lush, 1984; Dallmeyer et al., 1986; Lush et al., 1988; Snoke & Miller, 1988; Snoke et al., 1990b; Hodges et al., 1992; Hudec, 1992; Camilleri & Chamberlain, 1997; McGrew et al., 2000; Satarugsa & Johnson, 2005; Sullivan & Snoke, 2007).

Post-orogenic extensional collapse of the overthickened crustal highland in the Sevier hinterland during the early Cenozoic resulted in exhumation of the RMEHR, which was achieved by brittle-ductile detachment faulting and closely followed by the intrusion of the granitic Harrison Pass Pluton (HPP). The western flank of the RMEHR is demarcated by the Ruby Mountain Detachment/Shear Zone (RMSZ), a semi-planar zone of deformation striking NNE and dipping \sim 20°W, with a top-to-the-northwest sense of shear (Snoke &

Lush, 1984). The RMSZ is interpreted to be a brittle-ductile, normal-sense detachment surface that was superimposed on an earlier midcrustal shear zone (Snoke & Lush, 1984; Mueller & Snoke, 1993; Wright & Snoke, 1993). $^{40}\text{Ar}/^{39}\text{Ar}$ biotite and hornblende geochronology coupled with zircon and apatite fission track data from mylonitic biotite monzogranite in the shear zone indicate that extension occurred from approximately 45–23 Ma, (Dallmeyer et al., 1986; Dokka et al., 1986). However, Colgan et al. (2010) and Haines & van der Pluijm (2010) argued for late, rapid slip on the RMSZ that began at 16–17 Ma with the initiation of the San Andreas transform fault and ceased no later than 10–12 Ma. This was largely based on reinterpretation of K-Ar and Ar-Ar ages from the western margin of the HPP as indicators of exhumation-driven cooling and supported by dates from fault-derived fill in the footwall valley, (which does not show evidence of pre-Miocene slip), and apatite fission-track ages, (which record rapid cooling in the late Miocene) (Colgan et al., 2010).

Various methods have been employed to estimate the magnitude of lateral displacement between the footwall and hanging wall of the RMSZ (reviewed by Howard, 2003). Calculations of the width of the exhumed metamorphic terrane (without accounting for the effects of later Basin and Range faulting), place the displaced part of the RMEHR ~50 km to the northwest beneath the Piñon and Adobe ranges and adjacent to the gold deposits of the Carlin Trend during the Eocene (Jansma & Speed, 1990; Newman & Witter, 1992; Camilleri & Chamberlain, 1997; Ketner, 1998). The 65–70 km of Cenozoic displacement on the E–W dextral Wells Fault Zone (WFZ), (which bounds the RMEHR extensional terrane to the north), has also been interpreted as a measure of total slip on the RMSZ (Thorman and Brooks, 1988; Brooks et al., 1995; Camilleri and Chamberlain, 1997;

Mueller et al., 1999). Other studies have generated far more modest estimates of 18 km and 4–8 km, using westward-younging K-Ar and apatite fission track cooling ages, respectively, which may record progressive unroofing (Kistler et al., 1981; Reese, 1986; McGrew & Snee, 1994).

Evidence of slip on the RMSZ is pervasive in a 10–1000 m thick, 100 km long swathe of mylonitic and brecciated silicic rocks along the western margin of the HPP and most of the RMEHR (Snoko, 1980; Lister & Snoko, 1984; Snoko et al., 1990; Burton, 1997; Colgan et al., 2010). Several enigmatic juxtaposed blocks of strata remain on this surface, notably at Cedar Mountain at the western margin of the HPP, which has been interpreted as a Paleozoic thrust block (Willden et al., 1967; Willden and Kistler, 1969; 1979), a Paleozoic klippen (Armstrong, 1972; Reese, 1986; Hudec, 1990; Burton, 1997), and as a megabreccia block superimposed on the RMSZ during late Miocene slip, (Colgan et al., 2010). Regardless, this feature illustrates the low-angle unroofing of the RMEHR and the HPP during slip along the RMSZ (Burton, 1997; Howard, 2003, Colgan et al., 2010; Howard et al., 2011). Although the deformational fabrics vary along the strike of this fault, both brittle and ductile deformation features have been observed in the HPP. NNW-striking cataclasite units have also been mapped as younger, crosscutting zones characterized by hydrothermal quartz and breccia clasts (Burton, 1997). Burton (1997) also observed several mildly deformed monzogranite dikes cutting the mylonites and silicic breccias of the RMSZ near the southwestern corner of the HPP, possibly indicating that intrusive activity persisted during and/or after the episode of extension on the RMSZ. However, their relationship with the early and late stage intrusive units remains unclear.

The NE-striking, high-angle, Basin and Range normal faults that define the modern physiography of the Great Basin were formed during most recent phase of regional tectonism. One of these structures, the Ruby Valley Fault Zone (RVFZ), exposed the impressive eastern flank of the RMEHR (striking N–NW, dipping 35–70° E) (Dohrenwend et al., 1991). A similar structure has been interpreted to either crosscut or sole into the RMSZ on the western margin of the range (Mueller & Snoke, 1993a; Howard, 2003; Colgan et al., 2010). Observations at the HPP, including observed roof dike geometries, wallrock bedding orientations, and west-younging apatite and zircon fission-track dates it is interpreted that eastward tilting of the southern RMEHR by ~30° occurred during this time, and subsequent relative uplift exposed a 5 km oblique structural section through the HPP (Kistler et al., 1981; Burton, 1997).

2.2.2 THE HARRISON PASS PLUTON

The Harrison Pass Pluton (HPP) is a high-K, calc-alkaline, multi-phase granitic intrusion that was emplaced into the transition zone of the RMEHR at ~36 Ma (Snoke, 1980; Burton, 1997; Barnes et al., 2001) (Figure 2.3). South-southwest migrating magmatic activity in the Great Basin during this time has been attributed to the delamination of the subducting Farallon plate beneath North America and subsequent interaction between the upwelling asthenosphere and the lower crust (see Section 1.3.1) (Snoke, 1980; Christiansen & Yeats, 1992; Humphreys, 1995; Dickinson, 2006). On most published geologic maps, including the USGS Jiggs quadrangle by Willden & Kistler (1969) and the regional map of the Ruby Mountains by Howard et al. (1979), the intrusive phases of the HPP are described as undifferentiated granodiorite and monzogranite. However, several workers have identified spatial variations based on mineralogy, textures, spatial

distribution, crosscutting relationships, and geochemical compositional trends, (see field and petrographic descriptions in section 2.4) (Wright & Snoke, 1984; Kistler et al., 1981; Burling, 1996; Burton, 1997; Barnes et al., 2001). Barnes et al. (2001) provided a detailed geochemical and petrographic characterization of the HPP and convincingly argued for two-stage assembly by an early and a late stage magmatic pulse (each containing three constituent units) (idealized intrusive relationships illustrated in Figure 2.4).

Compositionally, the early stage intrusive suite is broadly granodioritic, represented by the Toyn Creek (Ttc) unit, and accompanied by a significant comagmatic monzogranitic phase, represented by the Corral Creek (Tcc) unit, with sparse rhyodacite porphyry and equigranular granite-granodiorite roof dikes (see Figure 2.4) (Barnes et al., 2001). This suite is mildly peraluminous ($ASI = 0.99-1.07$) and characterized by relatively flat chondrite-normalized rare-earth element patterns and isotopic variation indicating a heterogeneous source region (Barnes et al., 2001). Isotopic signatures of the early stage magmatic suite are varied, with no clear distinction between units ($\epsilon_{Nd} = -10--18$; $^{87}Sr/^{86}Sr = 0.7096-0.7142$; $\delta^{18}O = 9.7-11.1$) (Barnes et al., 2001). Due to the generally linear compositional trends between the constituent units, it is interpreted that early stage magmas were generated by a single event in which end member tonalite and monzogranite magma became mixed (Barnes, 2001). Stoping, diking, folding, and internal deformation of adjacent wallrock units accommodated emplacement of early stage intrusive units (Burton, 1997).

Dominantly monzogranitic in composition, the late stage magmatic suite includes the sheeted biotite and two-mica monzogranite intrusions (Tmg), the Green Mountain (Tmg) two-mica monzogranite, and rare intermediate to mafic dikes (Barnes et al., 2001).

This suite is mildly to strongly peraluminous ($ASI = 1.01\text{--}1.3$) and characterized by diverse elemental abundances and deep negative Eu anomalies (Barnes et al., 2001). Isotopically, late stage magmas are similar to early stage magmas, with the notable exception of the volumetrically significant Tgm, which has relatively low ϵ_{Nd} (mean = -21.3) and high initial $^{87}Sr/^{86}Sr$ (~ 0.725) and was interpreted to be the final major intrusive phase in the HPP (Barnes et al., 2001). These late stage melts were generated by low-volume partial melting of the middle or lower crust during ascent of the HPP thermal anomaly (Barnes et al., 2001). Late stage units were emplaced as sheeted dikes and sills (Tmg) or as homogeneous masses (Tgm) by brittle and ductile deformation of their early stage magmatic hosts (Burton, 1997).

Radiometric dating of the HPP indicate that intrusion occurred during the southward migration of a regional magmatic arc in the Great Basin from 43–20 Ma. The 36 Ma age yielded by the U-Pb zircon geochronology conducted by Wright & Snoke (1993) does not indicate a sequential emplacement history. However, the two-stage assembly proposed by Barnes et al. (2001) is supported by recent SHRIMP U-Pb dates of zircons from the three major intrusive phases of the HPP acquired by Colgan et al. (2010). Sample ages ranged from 38.1 ± 0.4 Ma to 36.3 ± 0.4 Ma and were broadly consistent with relative ages determined by field relationships, but indicate that there may have been temporal overlap between the early and late stage magmatic pulses (Colgan et al., 2010; Burton, 1997). Howard et al. (2011) sampled granitic suites from elsewhere in the RMEHR that are petrographically similar to those observed in the HPP, but appear to have been incrementally emplaced from the Late Cretaceous through the Paleogene, with at least one

suite coeval with the HPP. However, the relationship between intrusive bodies within the Ruby Mountains remains unclear.

The depth of emplacement of the HPP has been quantitatively estimated by reconstructing the overlying stratigraphy (Burton, 1997; Colgan et al., 2010), and by thermobarometric analysis on the equilibrium igneous mineral assemblage (Burton, 1997; Barnes et al., 2001). The Al-in-hornblende thermobarometer used by Burton (1997) produced emplacement pressures of $4.5\text{--}5.5\pm 0.6$ kbar, which correspond to depths of $12.1\text{--}14.8\pm 1.6$ km, (using open-hole geophysical well log density estimates from adjacent sedimentary basins). Similar analyses using different calibrations by Barnes et al. (2001) yielded pressures of 4.6–6.9 kbar and 3.3–4.0 kbar for early and late stage intrusive suites, respectively. This disparity was interpreted as evidence for partial crystallization of early stage magmas under higher pressure, possibly deeper, conditions. However, reassemblies of the overlying stratigraphy by Burton (1997), and Colgan et al. (2010) indicate somewhat shallower depth of emplacement for the exposed plutonic section (4–12 km).

2.2.3 CONTACT METAMORPHIC AUREOLE

The HPP is intruded into a >8 km homoclinal sequence of variably metamorphosed Neoproterozoic to Paleozoic miogeoclinal strata that comprise much of the RMEHR transition zone. High-temperature, low-pressure metamorphism of these units was synchronous with crystallization of the Jurassic pegmatitic granite that abuts the HPP to the north. Metamorphic grade increases from sub-greenschist to amphibolite facies over ~10 km with proximity to this intrusion (Kistler et al., 1981; Hudec & Wright, 1990; Hudec, 1992). The relationship of the contact between the HPP and these units is highly discordant along the southern margin, but gradually shifts to concordant at the eastern roof zone of

the intrusion. The HPP is also responsible for a contact metamorphic thermal aureole that extends 0.5–1.5 km from the HPP contact and is characterized by andalusite growth and static recrystallization of carbonate and calc-silicate wallrock units (Burton, 1997; Musekamp, 2012). However, the thermal effects of the HPP are largely obscured along the northern and northeastern contact due to earlier high metamorphic grades. The relatively limited extent of the aureole and the presence of miarolitic cavities in the plutonic roof zone provide further indication for the emplacement of the HPP at 3–4 kbar (Barnes et al., 2001).

A fluid inclusion and stable isotope investigation of the hydrothermal activity in the contact metamorphic aureole of the HPP was conducted by Musekamp (2012). This study emphasized examination of quartz and calcite veins and skarn deposits on and up to 2 km away from the pluton-wallrock interface. Pre-intrusion fluids, preserved in calcite veins in unaltered wallrock units, were characterized by relatively low temperatures (195–340°C) and salinities (~1 wt % eq. NaCl) and typical limestone $\delta^{18}\text{O}$ and $\delta^{13}\text{C}$ values (~27‰ and ~2.5‰, respectively). Musekamp (2012) interpreted that one major phase of high temperature fluid (~450–650°C) migrated from the HPP into wallrock units, resulting in quartz veins, hydrothermal alteration, and skarn mineralization. This fluid phase was characterized by moderate CO_2 concentrations (mol% CO_2 : <2), low salinity (~3 wt % eq. NaCl), and near-magmatic isotope $\delta^{18}\text{O}$ and $\delta^{13}\text{C}$ values (~13‰ and ~0.25‰, respectively). Subsequent dilution by lower temperature (200–480°C), very low salinity (~1 wt % eq. NaCl) meteoric fluids was also documented in the HPP and the contact metamorphic aureole, and is dominantly expressed by large, microcrystalline quartz-hosting fault veins.

2.3 FIELD AND ANALYTICAL TECHNIQUES

2.3.1 FIELD MAPPING AND SAMPLING

The author and his field assistant completed three weeks of fieldwork during the 2014 summer in order to investigate field relationships and collect samples and structural measurements. To properly represent the different igneous and hydrothermal features of the constituent intrusive phases, sampling was conducted on three traverses across the HPP. In Traverse 1, samples were largely collected from the Tcc, beginning at the southern contact of the pluton and progressing due north to the Harrison Pass parking lot in the Ttc unit. Traverse 2 was a W–E transect across the entire pluton, sampling the Tmg and Ttc units. Traverse 3, also a W–E transect, was conducted approximately 1.5 km to the north of Traverse 2 in order to sample the Tgm in addition to the Tmg and Ttc. Two additional field visits were conducted to investigate areas of interest along the plutonic margin, particularly areas of historic mineral exploration and mining. Many outcrops were accessible by a network of unmarked 4WD roads that generally follow the linear E–W drainage on either side of the pass itself, but hiking was often required to reach more rugged localities.

In total, 239 samples were collected and localities and contexts described during the field component of this study. It should be noted that this sample population is a nearly exhaustive representation of the orthomagmatic-hydrothermal feature types related to fluid saturation, exsolution, migration, and expulsion encountered during the three traverses of the HPP. Samples include intrusive rocks, pegmatites, aplites, miarolitic cavities, crystalline and microcrystalline quartz veins, and hydrothermal alteration zones,

and a small number of samples from contact skarns and metasedimentary rocks in the contact metamorphic aureole surrounding the pluton. Each sample was geo-located using a Garmin eTrex 10 handheld GPS unit, photographed in situ, and described in a field notebook. Field descriptions include lithology, mineralogy, dimensions, crystal size, relationships to other features and units, alteration type, (if applicable), and structural measurements, (typically of vein orientations or mineral lineations). Sample descriptions, transcribed from the author's field notes, can be found in Appendix B.

2.3.2 PETROGRAPHIC INVESTIGATION

For the petrographic component of this study, samples were observed in transmitted light on a Leica DM2500 petrographic microscope. Annotated photomicrographs were taken using the attached Camex petrographic camera. The following samples were selected for further study from the 239 collected in the field:

1. 16 samples were selected for a petrographic study of the intrusive phases of the HPP, (in addition to 15 samples that were examined only as polished slabs). Standard $\sim 30\ \mu\text{m}$ thin sections were manufactured by Paula Leek Petrographics for these samples. This sample suite contains unaltered granitic rocks (including aplites) from the four major plutonic phases of the HPP, as well as several samples from the volumetrically minor sub-units (i.e. rhyodacite and equigranular roof dikes, mafic dikes, etc).
2. 14 samples were selected for a petrographic overview of the orthomagmatic-hydrothermal feature types and alteration styles present in the HPP. The mineral assemblages, textures, paragenetic relationships, and microstructures were described. Again, standard $\sim 30\ \mu\text{m}$ thin sections were

manufactured by Paula Leek Petrographics. Detailed petrographic descriptions can be found in Appendix D.

3. 43 samples were selected for the fluid inclusion analysis component of this study. Six ~120 μm double-polished thin sections were manufactured by Paula Leek Petrographics, and an additional 41 thin sections were manufactured by Mann Petrographics, with two duplicates. Of these samples, 2 are from granitic rocks, 12 are from pegmatites, 4 are from aplites, 1 is from a miarolitic cavity, 14 are from quartz veins, 4 are from the contact metamorphic aureole, (quartz veins in skarn/carbonate replacement deposits and metasedimentary rocks), and 6 are from microcrystalline quartz veins. For this chapter, the mineral assemblages, textures, paragenetic relationships, and microstructures of these samples are described.

2.4 FIELD GEOLOGY OF THE HARRISON PASS PLUTON

2.4.1 HARRISON PASS

The Harrison Pass Pluton (HPP) outcrops in a roughly 110 km^2 , half-circular area in the south-central Ruby Mountains within Humboldt National Forest and the Ruby Mountains Wilderness Area, approximately 50 km southeast of Elko, NV. At an average elevation of ≈ 2255 m, the HPP forms a relative topographic low in the backbone of the Ruby Mountains between Green Mountain (3255 m) to the north and Pearl Peak (3306 m) to the south. East–west trending drainage valleys on either side of the divide at Harrison Pass have eroded several kilometers-long, near-continuous ridges while numerous isolated

granite tors and large crag complexes provide excellent exposure of all intrusive phases of the HPP. However, several areas of glacial and fluvial cover, particularly in the northern portion of the HPP, obscure outcrops and phase contacts. Sampling areas were accessed by hiking from either the main Harrison Pass Road, (NF-113/NF-357), or from the many high-clearance, 4WD Forest Service roads that traverse the area.

2.4.2 DESCRIPTION OF INTRUSIVE UNITS

The following descriptions are based on the field observations made in this study as well as those by Burling (1996); Burton (1997), Barnes et al. (2001), Deans (2010), and Musekamp 2012) and follow the lithologic nomenclature and geochemical subdivisions used by Barnes et al. (2001). Representative photographs of each intrusive phase can be found in Figure 2.5. See Appendix B for field descriptions of the samples of intrusive rocks collected in this study.

2.4.2.1 EARLY STAGE

The early stage suite of intrusive rocks occupies the eastern half of the exposed tilted pluton and is inextricably enmeshed with late stage units in the western half. This suite is texturally coarse-grained to megacrystic/porphyritic and is broadly granodioritic in composition, but contains mappable monzogranite subunits and includes equigranular granitic and porphyritic dacite roof dikes. The contact between the early stage units and surrounding Proterozoic metasedimentary sequences is generally sharp, but varies irregularly between concordant and discordant (Barnes et al., 2001; Musekamp, 2012).

The oldest unit of the early stage suite (and the entire HPP) is the Toyn Creek granodiorite (Ttc), which varies in composition from granodiorite to biotite-hornblende tonalite. Snoke & Lush (1984) originally believed that this unit comprised most of the

eastern half of the exposed section of the HPP, but it has since been reduced to the northeastern quadrant and as an dismembered host of voluminous late stage intrusive units in the western half. Texturally, this unit is medium to coarse-grained to megacrystic (which is diagnostic of this unit) with generally anhedral to subhedral quartz and subhedral-euhedral alkali feldspar crystals. Magmatic foliation of megacrystic alkali feldspar phenocrysts (1–4 cm; present in localized segregations, diagnostic of this unit), biotite and hornblende has been observed (Burton, 1997; Barnes, 2001). Also, 10–30 cm-sized, elliptical melanocratic microdioritic enclaves oriented parallel to magmatic foliation are observed in isolated areas up to 10s of meters across where they may comprise up to 5% of the total rock volume (Burton, 1997).

The Corral Creek monzogranite (Tcc) is identified as a member of the early stage igneous suite, but may be up to a million years younger than the Ttc granodiorite and coeval with emplacement of late stage magmas according to recently published U-Pb zircon age dates (Colgan et al., 2010). It outcrops as impressive crags and tors throughout the southeastern quarter of the pluton, (facilitating detailed study), and may extend westward to the contact with the RMSZ, (Barnes et al., 2001). This unit is difficult to distinguish from the Ttc in the field due to similarities in grain size, crystal textures, and mineral abundances. Once thought to be a relatively minor magmatic body within the granodiorite suite the Tcc is now recognized as far more volumetrically significant (Burton, 1997; Barnes et al., 2001). Evidence of hydrothermal fluid exsolution movement is most common in this unit, with the majority of miarolitic cavities and mineralized skarn deposits hosted within and along this unit, respectively. Mafic enclaves are far less common than in the Ttc.

Porphyritic rhyodacite and equigranular leucogranitic dikes (Trd) (1–5 m wide) radiate up 10s of meters away from the equigranular, compositionally heterogeneous granites at the roof zone of the HPP into the metamorphosed Ordovician Pogonip (Opm) carbonates. The genetic relationship between these dike sets and the granites at the highest structural levels within the HPP is unclear, but dike locations and geometries indicate that they originate from both the Ttc and Tcc units (Barnes et al., 2001).

2.4.2.2 LATE STAGE

The late stage suite is structurally lower than the early phases, and is largely restricted to the western half of the HPP. It is characterized by voluminous monzogranite sheets and dikes and a homogeneous two-mica monzogranite mass that intrude the Ttc granodiorite. The contact between these units and the surrounding Paleozoic sedimentary sequences, where present, is sharp and largely discordant (Burton, 1997; Barnes et al., 2001; Musekamp, 2012).

A volumetrically major biotite and two-mica monzogranitic swarm of dikes and sills (Tmg) outcrops throughout the western half of the HPP. Within this zone, the Ttc granodiorite host rock is increasingly obscured by these features from west to east (moving structurally upward). However, the Tmg is absent from the eastern half of the HPP. Sheets display a consistent NE strike and a relatively shallow dip (~30°) to the SE and often alternate with layers of composite pegmatitic monzogranite. Dikes (15–45 cm) are variably oriented, generally striking N–S with subvertical dips to the west, and often identified by QF Pegmatite cores (Burton, 1997).

In this study, three examples of meter-scale, fine-grained melanocratic microdiorite to biotite tonalite bodies were observed and sampled in the areas of voluminous aplite

sheets and dikes along high ridges in the central-west parts of the HPP. One of these bodies, as well as an additional locality near the head of Longhair Smith Canyon, was recognized by Burton (1997). These irregular bodies have complex, variably sharp contacts with the surrounding granodiorite and leucogranites with some evidence of melting and mingling. Leucogranitic xenoliths and injection veins from the surrounding rock were observed at two of these bodies. While a common geometry for these mafic bodies is not readily apparent, they were interpreted as dismembered dikes or sills by Burton (1997). However, one example observed in this field study displayed a locally continuous (10 m) tabular geometry and steep dip.

While the enmeshed aplites and monzogranites make up the volumetric bulk of the late stage magmas, the chemically distinct and homogeneous Green Mountain Creek two-mica monzogranite (Tgm) is the youngest, largest, and most continuous late stage subunit. This unit forms an irregular N-S oriented, oblong body in the NW quadrant of the HPP. Texturally, the Tgm is uniformly medium to coarse-grained hypidiomorphic granular and is most easily recognized in the field by the presence of muscovite and pervasive jarositic surface weathering (Barnes, 2001). It is not intruded by the other late stage dikes and sheets. Both subvertical and subhorizontal exfoliation joint patterns are observed in this unit.

2.5 EVIDENCE OF HYDROTHERMAL FLUID ACTIVITY IN THE HPP

Indications of fluid saturation, exsolution, migration, disequilibrium, and expulsion in the HPP are widespread and varied in nature and scale. The following section includes

classification, geographic distribution, and summarized descriptions for the 224 samples of feature types related to orthomagmatic-hydrothermal fluid activity. Figure 2.6 illustrates the locations and identities of these samples in the HPP. Feature type taxonomy is constructed from observed mineralogy and primary field expression(s) and/or setting(s). Geographic distributions and spatial associations are based on field observations and sample maps. Geologic descriptions are derived from field data, petrographic observations, and previous characterizations (Willden & Kistler, 1969; Burton, 1997; Musekamp, 2012). Representative photographs and photomicrographs for each feature type are included in Figure 2.7. Brief descriptions of these feature types, their relationships with hydrothermal alteration, and their abundance and distribution throughout the HPP are included in Table 2.1. Spatial associations and taxonomic or geologic similarities between feature types are strictly observational and do not necessarily imply a genetic link.

2.5.1 QUARTZ-FELDSPAR PEGMATITES

The most ubiquitous feature type in the HPP (excluding the quartz vein family) is the Quartz-Feldspar Pegmatite (QF Pegmatite) feature type. The 46 samples of this feature type collected in this study originate from all major intrusive units. However, they are concentrated in the late stage Tmg monzogranite as either diffuse groups of crystal zones distributed across 10s of meters or within stacks of layered aplite/pegmatite zones. They are only rarely observed in the late stage Tgm two-mica granite unit. Occurrences of these veins in the structurally higher intrusive units (Ttc and Tcc) become increasingly rare in proximity to the plutonic margin. However, several QF Pegmatite veins have been observed near miarolitic cavities or within 100 m of the adjacent metasedimentary units (often with orientations orthogonal to the contact). QF Pegmatite veins are not typically associated

with any style of alteration, but have been observed near the only outcrop of potassic alteration sampled in this study.

QF Pegmatites have, on average, greater volumes than Type (I) and (II) Quartz Veins or other pegmatites, (width: 2–55 cm, mean = 8 cm) and are usually exposed over 10s of meters. While highly irregular geometries (i.e. angular crystal protrusions into wallrock) and inconsistent thicknesses are most common, some are planar with sharp margins. Very large (2–20 cm) subhedral-anhedral glassy grey quartz is intergrown with or included in euhedral-subhedral matte white orthoclase crystals in approximately equal abundances. It is common for the feldspar crystals to form zones along crystal zone selvages, particularly in more planar veins. In thin section, quartz from deformed samples may display evidence of shearing and recrystallization, such as ribbon textures, sutured crystal boundaries, and undulose extinction. Minor and trace minerals such as titanite and apatite are uncommon in this feature type.

2.5.2 MUSCOVITE-QUARTZ-FELDSPAR PEGMATITES

Muscovite-Quartz-Feldspar Pegmatites (MQF Pegmatites) are one of the least common feature types observed in the HPP. Only nine examples were collected in this study due to being located almost exclusively within, on, or proximal to the late stage Tgm in the NW quadrant of the HPP. They are texturally similar to other pegmatites, (coarse, subhedral crystals with irregular to planar margins and discontinuous exposures), with moderate thicknesses (5–20 cm) and little to no evidence of post-emplacement deformation. However these features contain abundant coarse (1–3 cm) books and/or splays of muscovite along margins and intergrown with quartz and alkali feldspar. At least two examples of this feature type also contain very coarse (~1 cm) euhedral-subhedral Fe-

Mg garnets. Two samples contain moderately thick (<5 cm) crystalline quartz zones. In thin section quartz crystals also exhibit easily identifiable fluid inclusion growth zones.

Alteration associated with these feature types, (characterized by minor bleaching and silicification) is minor to nonexistent.

2.5.3 APLITE VEINS AND DIKES

Aplite veins and dikes are primarily restricted to several geographic clusters, but have been observed in all granitic units and still comprise one of the most common vein types in the HPP. Of all the samples collected in this study, 57 samples are texturally homogeneous Aplites, 11 are Layered Aplite/Pegmatite zones, and 4 contain discrete quartz or quartz-feldspar cores. E-W striking, steeply dipping pure aplite veins and dikes are concentrated in southeastern quadrant of the HPP near the roof zone of the relatively vein-poor Tcc (see Appendix C for stereonet). NE-SW striking, shallowly dipping (<30°) aplites intrude and are enmeshed with the Tmg unit at lower structural levels (see Appendix C for compiled stereonet). Composite layering of alternating aplite and pegmatite zones is also common only in the structurally lower zones of the Tmg, and become increasingly rare at higher structural levels. Aplites are identified by their light color and generally linear geometry in outcrop, and may range in thickness from 4 cm to >50 cm. Many aplites display evidence of post or syn-emplacement deformation, including jogs, offset, and minor folding. They possess a ubiquitous mineral assemblage of quartz + alkali feldspar (oligoclase>microcline) ± muscovite ± biotite ± magnetite ± garnet.

Texturally homogenous Aplites have a typical anatomy of thin (<1–3 cm) zones of pure crystalline quartz with isolated splays of small biotite crystals and very small miarolitic cavities (1–3 mm) flanking coarse zones (1–8 cm) of equigranular quartz + alkali

feldspar. These crystal size in these zones becomes increasingly large with growing proximity to the core of very fine-grained quartz + alkali feldspar with small (1–2 mm) biotite phenocrysts. Aplites cored by quartz, or quartz-feldspar zones retain the same mineral zonation, but also possess central zones of either biotite or hypidiomorphic equigranular quartz ± feldspar (alkali feldspar included in plagioclase). Layered Aplite/Pegmatite zones are characterized by alternating zones (typically 5–15 cm thick) of fine-grained aplitic material and pegmatitic quartz and feldspar crystals, (similar in textures to the QF Pegmatites described in Section 2.5.3). Garnet has been observed in coarse and fine-grained zones, but is often concentrated with biotite-rich swathes in the intervening transitions (Burling, 1996). There is no evidence of hydrothermal alteration associated with aplite veins and dikes.

2.5.4 MIAROLITIC CAVITIES

Miarolitic cavities are sparse and volumetrically minor features in the HPP. In this study, eight examples of large miarolitic cavities were observed, and Musekamp (2012) recognized four additional examples. With the exception of one outcrop, which contained numerous examples, most miarolitic cavities are observed as solitary, isolated features. They are commonly spatially associated with, but distinct from, Type (I) and (III) Quartz Veins and QF Pegmatites. Miarolitic cavities are primarily observed in the Tcc monzogranite within 1 km of the roof zone and less commonly in the Ttc granodiorite. However, they have also been infrequently recognized in cupolas at the roof zone of the Ttc granodiorite and very rarely at deeper structural levels in the Tmg monzogranite. Of the four miarolitic cavities observed by Musekamp (2012), two were within the HPP (one in

the Ttc granodiorite, and one in the Tmg monzogranite) and two were in detached granitic bodies away from the southern contact of the main intrusion.

Miarolitic cavities are generally circular with aspect ratios of 1:2 to 1:4. While the maximum diameter varies from 2–30 cm, the average diameter is ~8 cm. However, one aforementioned locality exhibits abundant isolated and interconnected miarolitic cavities with linkages up to 20 cm long. Euhedrally-terminated or massive clear, milky, or smoky quartz crystals are observed in all samples, with a size range of <0.5–5 cm. Visual estimates of open space volume in miarolitic cavities range from 0.25 cm³ to 5 cm³ and positively correlate to the diameter of these features. Subordinate alkali feldspar and muscovite are present with quartz in many samples. Jarosite and hematite staining derived from the oxidation of small (<1 mm), disseminated pyrite and anhedral magnetite crystals around the rim of the miarolitic cavities was observed in this study and by Musekamp (2012). In thin section, miarolitic quartz is coarse, equigranular, euhedral-subhedral with growth zones indicating inward-directed growth. Where they occur, interconnected miarolitic cavities also host large (1–6 cm), heavily metasomatized and oxidized, pelitic enclaves composed of biotite + muscovite + quartz + pyrite.

2.5.5 QUARTZ VEINS

Quartz veins represent one of the most common and diverse vein types in this study area, (comprising 75 of the 224 samples related to magmatic-hydrothermal activity collected in this study). Quartz veins are significant to this study in part because of their viability for fluid inclusion studies, but also because of field associations with alteration zones and previously identified relationships between mineralization and quartz veins in intrusive settings (e.g. Landtwing et al., 2010). The most basic distinction between veins

(crystalline or microcrystalline) can be further subdivided into five Types: Type (I) minor crystalline Quartz Veins, Type (III) pegmatitic crystalline Quartz Veins, Type (II) (skarn) and (wallrock) Quartz Veins, Type (IV) minor Microcrystalline Quartz Veins, and Type (V) major Microcrystalline Quartz Veins. These types vary widely in geographic affinity, volume, internal structure, deformation, and associated wallrock alteration type and intensity.

Type (I) Quartz Veins are a widespread, but relatively uncommon vein type in the HPP. In this study, the 18 examples of this vein type were observed in all four major granitic units, but did demonstrate spatial association with skarn deposits and with a broad zone at the structural core of the exposed plutonic section near the Ttc–Tmg contact. Musekamp (2012) observed several of these veins within the HPP, on the contact, and in detached granitic bodies in the contact metamorphic aureole. As their name implies, these veins are volumetrically minor, generally 1–5 cm thick, and typically outcrop over distances of <1–6 m. They are mineralogically and texturally homogeneous, white to translucent, and composed of pure subhedral quartz (<2–18 mm) with crystal boundaries observable in hand sample. However, crystal growth directions are heterogeneous and do not appear to be inwardly directed. Although vein–wallrock contacts are invariably sharp and planar, associated wallrock alteration ranges from nonexistent to pervasive but narrow. Occasional wallrock modification in granodiorite is characterized by the replacement of biotite from the host granodiorite or monzogranite with coarse, shreddy muscovite and minor subhedral pyrite within a 1–2 cm-wide selvage zone. In one case, titanite overgrowths on amorphous magnetite crystals are present as sparse crystal aggregates (1 mm) replacing secondary mica crystals on the vein-wallrock interface. Small

euohedral magnetite crystals (~0.25 mm) have also been observed in association with this secondary muscovite but have been heavily oxidized, contributing to zones of intense hematite staining. While evidence for post-emplacement deformation is rare, there is at least one example of a folded quartz vein.

Type (II) (skarn) and (wallrock) Quartz Veins are exclusively located in skarns, hosting polymetallic mineralization, or crosscutting contact metamorphosed metasedimentary rocks at the plutonic margin, particularly along the roof zone, southern contact, and in roof pendants. 10 samples were collected from four mineralized contact skarns and three samples were collected from metasedimentary units. These veins are texturally similar to Type (I) Quartz Veins, but may be planar or irregular and discontinuous, and may also be either single-phase (glassy quartz) or two-phase (milky quartz zones encasing a glassy quartz core). Veins range in thickness from 0.5 to >150 cm. Quartz crystals are typically coarse, anhedral-subhedral, and variably deformed (i.e. undulose extinction, multiple fractures, brecciation). Post-emplacement deformation can also be inferred from irregular, sometimes anastomosing, vein geometries. Musekamp (2012) identified a predictable assemblage of vein alteration minerals in skarn rocks but did not note the multiphase anatomy of some veins. This assemblage includes euohedral tremolite needles (<560 μm) replacing diopside and calcite and chlorite partially to completely replacing biotite along immediate vein margins. One major skarn quartz vein also displayed pervasive internal jarosite staining. Quartz veins in unmineralized, skarn-free metasedimentary wallrock have sharp margins and no visible associated alteration.

Type (III) Quartz Veins are mostly restricted to the north-central area of the HPP near the boundary between the Ttc granodiorite and Tmg monzogranite (similar to Type

(I) Quartz Veins), but have been observed in all other granitic units as well. Of the 18 samples recognized to belong to this type, three can be described as “pods” due to their non-linear outcrop geometry. While thicknesses vary (5–35 cm) they are characterized by variable continuity, (sometimes pinching and swelling with amplitudes of up to 10 cm and frequencies of <0.5 m) and typical exposures of no more than 3 m along strike. Maximum diameters range from 9–150 cm. They are composed of dull white, subhedral quartz crystals with strong textural similarities to QF Pegmatites, such as irregular and jagged vein–wallrock interfaces and large subhedral crystal agglomerates. In some samples, vein quartz is highly brecciated with microcrystalline quartz infill. The extent of associated wallrock modification is usually restricted (<0.5 m) and characterized by moderate to strong hematite–jarosite staining and texture-destructive silicification,. However, these veins are often hosted in highly weathered granite, making it difficult to determine the effects of vein-sourced alteration fluids.

Type (IV) Microcrystalline Quartz Veins are not widespread in the HPP, but instead have a strong spatial affinity for the internal contacts between constituent granitic phases, and often intersect or join with Type (V) Microcrystalline Quartz Veins. The 18 examples of this type sampled in this study are volumetrically minor (0.5–5 cm wide) and usually only visible in outcrop for <1–3 m. However, several outcrops proximal to Type (V) Microcrystalline Quartz Vein systems along the southern plutonic margin in the Tcc monzogranite and Tmg monzogranite units were heavily and chaotically veined, with veins comprising approximately 15% of the outcrop over distances of 3–7 m. The internal structure of Type (IV) Microcrystalline Quartz Veins ranges from simple, sharp (curvi-)planar wallrock contacts to complex, multi-cored, anastomosing zones with sparse breccia

clasts of crystalline quartz (<1–7 mm). Some Type (IV) Microcrystalline Quartz Veins also contain cores of crystalline quartz (4–9 mm) with envelopes of alternating microcrystalline quartz and pyrite-rich zones that contain crystalline quartz breccia clasts (100–500 µm). Others have multiple elongate vuggy cavities (1–8 cm wide) lined with cockade, comb, or colloform, euhedrally-terminated quartz crystals (<1 cm) with envelopes of microcrystalline quartz and abundant, small (100 µm) euhedral pyrite cubes. There is strong evidence of multi-stage growth including zones of dense, chaotic, crosscutting veins, orthogonal injection veinlets within vein zone, and micro-breccia textures. Alteration in and on these vein zones is characterized by strong silicification (recognized by exceptional hardness and smoothness of outcrop and destruction of primary granitic textures) up to 1 m away from the vein, occasional chlorite-sericite alteration accompanied by euhedral titanite crystals (~1 mm), and occasional strong, localized sulfate/jarosite staining. Type (IV) Microcrystalline Quartz Veins associated with Type (V) Microcrystalline Quartz Vein systems are invariably accompanied by pervasive chlorite-sericite alteration.

In this study, Type (V) Microcrystalline Quartz Veins were sampled at 13 locations throughout the HPP. Although they indiscriminately crosscut both early and late granitic units, (as well as the plutonic margin and surrounding metasedimentary units), they demonstrate a slight preference for upper structural levels. Willden and Kistler (1969), Hudec (1990), Lapointe (1991), and Musekamp (2012) recognized these veins in the metasedimentary wall rocks south of the HPP. Within the pluton, Burton (1997) recognized approximately 12 steeply dipping, large-scale, hydrothermal quartz-hosting lineaments in addition to the 19 mapped by Willden and Kistler (1969). Typically, Type (V) Microcrystalline Quartz Veins are composed of massive microcrystalline quartz and exhibit

little to no internal structure. However, some also contain complex vuggy zones with cockade and comb quartz textures similar to those observed in Type (IV) Microcrystalline Quartz Veins. Although they are often closely spatially associated, Type (V) Microcrystalline Quartz Veins are distinguished from Type (IV) Microcrystalline Quartz Veins by their volume (25–300 cm thick). These veins outcrop as moderately to steeply dipping, NE to NW-striking ridges and lineaments that are resistant to erosion and weathering and are visible for 10s to 1000s of meters along strike with no evidence of offset or post-emplacement deformation. At least one of these major veins appears to be concave-east and roughly parallel to the roof zone. Wallrock displays silicification and extreme chlorite-sericite alteration (recognized by green/grey color and oxidized biotite crystals in outcrop). The chlorite-sericite alteration is strongest in association with a Type (V) Microcrystalline Quartz Vein on the ridge north of Toyn Creek (this study; Burton, 1997). Alteration haloes around Type (V) Microcrystalline Quartz Veins may be as wide as 10 meters.

2.5.6 ALTERATION TYPES

Hydrothermal alteration, the mineralogical and textural modification of rock by migrating fluids in thermal and chemical disequilibrium with their surroundings, results in the addition, removal, and/or redistribution of mobile elements. Recognizing, describing, and mapping alteration types in an extinct hydrothermal system is the initial step in defining fluid compositions, relative volumes, and pathways of migration, which can ultimately identify potential fluid sources and constrain the evolution of the system. Four types of alteration have been identified within the granitic rocks of the HPP: potassic, phyllic, chlorite-sericite, and silicification. Additionally, skarn alteration has been observed

in carbonate rocks along the pluton contact (particularly at the roof zone). This alteration type has been studied by by Musekamp (2012) and is briefly described in Section 3.3.2.2. Representative photographs and photomicrographs of these five major alteration types are included in Figure 2.8. Descriptions of these alteration types, relationships with feature types, and their abundance and distribution throughout the HPP are included in Table 2.2. The following descriptions apply to both isolated zones of alteration and from altered wallrock in association with specific vein systems, unless specifically noted otherwise.

2.5.6.1 SKARN

Skarn (and carbonate replacement) wallrock alteration and mineralization is relatively uncommon (observed at 5 localities), but easily recognized at the HPP. It is present as irregular meter-scale tactite bodies along the contact between the HPP and Opm carbonate units and roof pendants. Skarn and carbonate replacement deposits along this contact were historically mined for a diverse suite of elements, (including W, Cu, Ag, Mo, Sn, Ca, Be, Bi, and Cd) (Klepper et al, 1944; Tingley, 1981a). The largest deposits in this district were exploited at the Star Mine (W) on the roof zone contact of the Tcc. Skarn alteration is typically associated with fractures, Type (II) (skarn) Quartz Veins and/or Type B calcite veins, and may be interlayered with less altered metacarbonate wall rock. Although the contacts with unaltered metasedimentary rocks may be gradational and ambiguous, this type of alteration demonstrates relatively sharp contacts with granitic rocks. Iron oxide gossans were rarely observed with skarn alteration.

In the field, this alteration style is characterized by partial to complete replacement of the carbonate host rock. Altered rocks appear dark green/black, but may also have distinct segregations of specific minerals such as hydrogrossular, diopside, and quartz.

Skarn mineral assemblages vary by locality, but generally consist of diopside + calcite (+ epidote) (+ hydrogrossular) + tremolite + quartz + sericite + biotite/chlorite (\pm plagioclase) \pm magnetite \pm pyrite, (minerals in parentheses are major components in some, but not all skarn outcrops). Ore minerals observed are chalcopyrite, galena, scheelite, and heubnerite (this study), and sphalerite (Musekamp, 2012). In thin section, many skarns are dominated by fine to coarse-grained (<200–700 μm), equant, blocky diopside crystals. Multi-stage reaction fronts (characterized by zones of mineral growth) between quartz veins and skarn minerals are evidence for dynamic fluid flow.

2.5.6.2 POTASSIC

Potassic alteration is the least common and most difficult to identify of any of the alteration styles in the HPP. Altered rocks are limited to discrete zones in or proximal to cupolas and porphyritic dikes at the roof zone of the HPP or in detached granitic masses within the metasedimentary country rocks intruded by the HPP. The only potassically-altered locality observed in this study was in the early stage Ttc granodiorite. Musekamp (2012) also observed potassic alteration in an isolated leucogranite body intruded into Cambrian limestone 1.5 km south of the plutonic contact. Where present, potassic alteration may be either independent of any vein systems or closely associated with Type (I) Quartz Veins. However, potassic alteration does not overprint and is not overprinted by any other alteration style. In these settings, potassically altered zones have sharp contacts with surrounding unaltered rocks.

This type of alteration is relatively weak compared to the other three discussed; altered rocks appears darker and slightly reddish-grey compared to their unaltered equivalents due to the oxidation of secondary biotite. A characteristic alteration mineral

assemblage of biotite + alkali feldspar + sericite ± titanite is added to the granitic host rock. According to Musekamp (2012), in thin section, small (<250–500 µm) secondary biotite crystals are observed to be densely scattered throughout altered rock as individual grains or as aggregate replacing plagioclase and quartz. Alkali feldspar is present as fine to coarse (0.2–2 mm), anhedral-subhedral, granular crystals.

2.5.6.3 PHYLLIC

Phyllic, or quartz-sericite-pyrite (QSP), alteration is a less common style of hydrothermal alteration in the HPP. In the sample suite collected in this study, 15 samples were recognized to host phyllic wallrock alteration. It is observed as large (>2 m) zones variably associated with Type (IV) and Type (V) Microcrystalline Quartz Vein systems, and uncommonly near crystalline quartz veins (Types (I) & (III)). In the cases where silicification overprints phyllic alteration, (which occurs less frequently than for C-S alteration), crystal textures are obscured and the altered host rock is extremely resistant. This type of alteration was first recognized in the HPP by Musekamp (2012) as massive, pervasive zones of alteration within granite on and near the plutonic margin and in disconnected granite bodies in metasedimentary wallrocks. Phyllic alteration also demonstrates a distal but consistent association with mineralized contact skarns along the plutonic contact.

In the field, phyllically altered rock is crystalline, dark grey/green with localized jarosite staining caused by abundant oxidized cubic pyrite crystals. The diagnostic alteration mineral assemblage for these rocks is quartz + chlorite + sericite + pyrite ± magnetite ± titanite. In thin section, secondary quartz is coarse-grained (>1 mm) to cryptocrystalline (<200 µm) and allotriomorphic to hypidiomorphic granular and forms

either as crystalline veinlets and breccia matrix or as fine-grained aggregates. Sericite forms larger (~300 µm) isolated plates or patchy or massive crystal agglomerates in fractures or in reacted primary quartz, feldspar, or biotite crystals. Euhedral pyrite cubes between 50 and 150 µm are concentrated in microcrystalline quartz zones along vein selvages in Type (IV) Microcrystalline Quartz Veins and finely disseminated throughout altered granitic wallrock. Some pyrite twinning was observed in this study and by Musekamp (2012). The presence of pyrite and prevalence of coarse-grained chlorite (>1 mm) distinguishes this style of alteration from chlorite-sericite alteration.

2.5.6.4 CHLORITE-SERICITE

Although significantly less abundant than silicification, chlorite-sericite (C-S) alteration is the second most common alteration style observed in the HPP. In this study, 23 samples containing C-S alteration were collected. C-S alteration is expressed as intense and pervasive zones on and near microcrystalline quartz-hosting structures (Types (IV) and (V) veins) and less frequently near minor crystalline quartz veins (Type (I) Quartz Veins). Silicification almost always overprints this type of alteration, as evidenced by introduction of quartz along microfractures that deform and crosscut chlorite crystals. However, at least one area of pervasive C-S alteration has largely escaped such modification and preserves many original alteration textures. This alteration style is restricted to a zone within 1.5 km of the roof zone and margins of the HPP, is absent within the core of the intrusion. Expressions of C-S alteration are also more frequent and intense in the early stage Ttc than other intrusive units.

First observed by Burton (1997), C-S alteration is found in zones up to 5 m away from vein-wallrock interfaces as massive replacement and is identified in the field by a

distinct green color, partial to complete destruction of biotite (as evidenced by iron oxidation halos around remnant crystals), and sugary aggregates of white mica after alkali feldspar. In thin section, this style of alteration is characterized by the addition of quartz + chlorite + sericite to the original igneous mineral assemblage. Quartz forms undeformed, anhedral blebs between euhedral plagioclase and alkali feldspar crystals, which are often partially replaced by sericite. Biotite is partially or completely replaced by blue/grey chlorite and fine-grained white mica forms isolated or massive clusters in plagioclase and alkali feldspar. Although similar to phyllic alteration, C-S alteration contains more abundant fine-grained chlorite (<250 μm) and lacks pyrite and other sulfur-bearing phases.

2.5.6.5 SILICIFICATION

Silicification, or silicic alteration, is the most common type of alteration in the HPP. Of the 224 samples collected, 59 exhibited varying degrees of silicification. This type of alteration is almost always proximal to at least one vein system and has been observed in all major intrusive units of the HPP, with no preference for any structural level. Microcrystalline Quartz Veins (Types (IV) & (V)) are most closely associated with pervasive silicification zones, which can extend up to 10 m away from the nearest veins. However, other vein types have been recognized with silicified wall rock. Silicification often overprints other alteration styles in the HPP, particularly chlorite-sericite alteration, but it noticeably absent at or near contact skarns.

Silicification is present as pervasive wallrock alteration that is partially or completely destructive of igneous textures in outcrop, resulting in host granites that appear bleached, granular to smooth, and aplitic to aphanitic. Altered rock is also extremely durable and resistant to weathering and is typically stained with iron from oxidized magnetite or pyrite

grains. In thin section, micro/cryptocrystalline quartz is precipitated as thin veinlets in microfracture networks and as microbreccia matrices, and by replacement of primary minerals, particularly biotite.

2.6 DISCUSSION

Initiation of hydrothermal systems by the heat and fluid inputs of hypabyssal intrusions has been well documented (e.g. Hedenquist & Lowenstern, 1994; Audétat et al., 2008). Characteristics of these hydrothermal systems reflect the magma chemistry, emplacement style, and thermodynamic conditions of their parent melt(s). The geochemical relationships between the distinct intrusive units in the HPP have been well documented by Barnes et al. (2001) who demonstrated that magmas were emplaced in two compositionally heterogeneous pulses characterized by voluminous magma mixing (early stage) and low-volume partial melts (late stage). The age relations between these events are understood from field observations of late stage units intruding early stage units (Burton, 1997). Dating of early and late stage units by Wright & Snoko (1993) clearly indicate a ~36 Ma crystallization, but did not reveal a statistically significant age gap between magma pulses. However, recently published U-Pb zircon dates by Colgan et al. (2010) support temporally overlapping two-stage assembly from ~38–36 Ma, as evidenced by nearly identical ages of the early stage Tcc and the late stage Tmg.

The super and sub-solidus hydrothermal systems preserved in the HPP reflect its relatively swift but fundamentally incremental assembly. The evidence of final orthomagmatic crystallization, magmatic fluid saturation and exsolution, and subsequent

hydrothermal activity are significantly different in the early stage units compared to the late stage units. While the likelihood of interaction between early and late stage hydrothermal systems exists, field and petrographic observations suggest that this did not significantly alter the degree and style of activity. Thus, this section separately presents these three categories of observed features (orthomagmatic, primary magmatic-hydrothermal, and hydrothermal features) for early and late stage units. There are also important differences in these features between and within the constituent intrusive units of the early and late stage groups. Key aspects of the degree, style, and relative timing of events in the magmatic-hydrothermal evolution of the HPP are here interpreted from the field relationships and petrographic observations made in this study.

2.6.1 FLUID ACTIVITY IN EARLY STAGE INTRUSIVE UNITS

2.6.1.1 ORTHOMAGMATIC FEATURE TYPES

Emplacement of numerous fine-grained aplites served as an igneous prologue for the early stage hydrothermal system(s) that developed in the HPP. Where they are concentrated in the Tcc, aplite veins and dikes represent volumetrically significant remnants of the final silicate melt phase of their host granitic unit that were focused into discrete fractures. Although the relationship between magmatic fluids and aplite formation in the absence of associated pegmatites is unclear, it has been proposed that aplites crystallize rapidly after volatile saturation and escape (Jahns & Tuttle, 1963). Alternatively, Candela (1997) argued that aplites and pegmatites represent end members of the internal vs. external nucleation spectrum, respectively, and that increased undercooling favors aplite formation. Regardless, the dense clustering of texturally homogeneous aplites in the Tcc relative to the Ttc indicates that crystallization of the Tcc may have been accompanied

by a major volatile exsolution event, while the limited number of aplites in the Ttc may have released volatiles periodically or in lower volumes. The E–W strike and near vertical dip of many aplites in the SE corner of the Tcc indicate that the principal stress axis was oriented vertically (likely due to lithostatic pressure) at the conclusion of the early stage of igneous crystallization (Anderson, 1951). However, the lack of observed relationships between aplites and unequivocally hydrothermal features makes it difficult to characterize the relationship between them.

The relative deficiency of pegmatite zones relative to aplite veins in the Ttc and Tcc provides further insight into the sequence of events that characterize the magmatic-hydrothermal transition of the HPP. Pegmatites form by the crystallization of a volatile-saturated interstitial silicic melt or by the interaction of melt and coexisting fluids (Jahns & Burnham, 1963; Jahns & Tuttle, 1963). Most pegmatites in the Ttc and Tcc are discrete, irregularly planar features (rather than pods or masses) that crystallized slowly compared to the bulk of surrounding magmas in syn-emplacement fracture or dilatant zones. Spatially, there exists an inverse correlation between aplites and pegmatites in Ttc and Tcc, which further supports the interpretation that large-scale volatile discharge preceded aplite formation. Pegmatite zones at deeper structural levels in the Ttc may either represent a localized ponding of early stage melt that was largely unaffected by fluid activity at the roof zone, or may be related to the intrusion and crystallization of the late stage Tmg unit and associated pegmatites.

2.6.1.2 HYDROTHERMAL FEATURE TYPES

The magmatic-hydrothermal transition of plutonic bodies is often accompanied by volatile saturation and exsolution, which has been identified as a prerequisite for the

formation of many types of granite-related ore deposits (Audéat et al., 2008). Although this transition can be inferred by the presence of abundant aplite veins and dikes, miarolitic cavities have been demonstrated to be one of the few observable features directly formed by the exsolution and coalescence of the magmatic fluids during igneous crystallization (Candela, 1997). Thus, their distribution, spacing, internal characteristics (i.e. volume, interconnectedness, mineralogy), and relationships with veins and alteration zones provide insights into the final stages of igneous crystallization and the earliest episode of fluid activity within the Harrison Pass pluton.

The clustering of miarolitic cavities in the apical and marginal regions of the HPP is consistent with previous observations and theoretical models, which propose that as fluids exsolve and coalesce, the density contrast with the surrounding crystal and melt phases drives upward migration of vapor bubbles (Candela, 1997). Since nearly all observed miarolitic cavities were observed within 1 km of the plutonic contact, it is interpreted that the bulk of the exsolved fluids either had reached or was generated at this structural level at the time of final crystallization of the Ttc and Tcc. Furthermore, six of the ten miarolitic cavities observed within the main plutonic body are located within the Tcc, which despite occupying only ~12% of the total surface area of the HPP, is adjacent to the vast majority of mineralized and unmineralized skarns and carbonate replacement deposits on the HPP contact. This association indicates that the metal-bearing fluids ascended to and were concentrated predominantly in the apical and marginal regions of the Tcc before being expelled into reactive carbonate units in the country rock.

Heavily oxidized, sulfur-rich, micaceous fragments (2–7 cm) hosted within interconnected miarolitic cavities are interpreted to be xenoliths plucked from unknown

pelitic wallrock units during magma ascent. Interaction with the surrounding magma may have caused these fragments to release fluids by several well-documented dehydration reactions involved in metamorphism and anatexis (Thompson, 1979, 1982; Spear et al., 1991). The presence of numerous nearby miarolitic cavities suggests that dehydration fluids may have acted as nucleation or scavenging centers for rising exsolved fluids. Partially digested wallrock xenoliths were proposed by Kontak et al. (2002) as potentially significant volatile sources for granitic intrusions. It is unclear if the larger metasedimentary enclaves of the carbonate Pogonip group (Opm) mapped in the Tcc by Willden & Kistler (1979) contributed volumetrically significant fluids to the crystallizing magma by this process. The degree of metasomatism is considerably greater in the miarolitic cavity-hosted schistose xenoliths, which are nearly completely replaced by mica, than in the Pogonip enclaves, which have been recrystallized to marble along their margins and variably host skarn mineralization (Burton, 1997). One possible hypothesis for the relationship between the Tcc and these two groups of xenoliths is that the smaller, oxidized fragments were included earlier and from greater depths, while the large-scale metasedimentary enclaves were a late addition to the cooler, subsolidus monzogranite near its current structural position.

The hydrothermal vein systems observed in the Harrison Pass pluton represent the final phase of syn and post-crystallization fluid activity. Type (I) and (III) Quartz Veins are relatively rare in early stage intrusive units. They are tightly clustered within ~500 m of the pluton margin in the Tcc, and are consistently associated with skarn deposits. In the Ttc, they are found at deeper structural levels and often exhibit a distinctive muscovitic selvage. Lewis (1990, 2001) identified quartz veining with associated secondary muscovite

and minor pyrite as quartz-muscovite alteration in Au-mineralized Cretaceous granodiorite in southern Idaho. Isotopically, these veins indicate a magmatic fluid origin (muscovite $\delta^{18}\text{O} = 7.7\text{--}8.0\text{‰}$; quartz $\delta^{18}\text{O} = 11.6\text{‰}$; $\Delta_{\text{musc-qtz}} = 3.9\text{‰}$). Altering fluids preferentially removed Na and Fe, and added Ca and K. Similar veins in the HPP may have been formed by a high-temperature, chemically unexchanged end member of the fluids responsible for other quartz veins in the Ttc and Ttc. Thus, Types (I) and (III) quartz veins likely represent the non-mineralizing equivalents of Type (II) Quartz Veins that crystallized from primary magmatic fluids generated by fluid exsolution. These fluids migrated along synplutonic fractures before crystallizing due to a decline in SiO_2 solubility due to cooling or depressurization.

Quartz veins observed in metasomatic skarn deposits, hosting polymetallic mineralization, and crosscutting unmineralized (meta-)sedimentary wallrock are interpreted to be part of the final stage of the primary magmatic-hydrothermal system in the HPP. Veining and mineralization by the infiltration of magmatic-hydrothermal fluids into carbonate host rocks has been well-documented model for skarn formation (e.g. Meinert, 1992). Type (II) (skarn) Quartz Vein thicknesses range from minor (<2 cm) to volumetrically significant (2 m). Mineralizing veins at the Star mine (W) and in Pb-Zn-Ag-Cu-W workings and prospects along the southern pluton contact are among the largest of this type. The range of vein sizes, metal suites, and the variety of vein quartz habits and morphologies within and between individual skarn localities suggest that unique and spatially restricted fluid injection sequences were responsible for mineralization. However, common features between skarn quartz veins are strong spatial associations with the Tcc,

relatively high-temperature mineral haloes (hydrogrossular, diopside, tremolite, quartz, calcite), and a positive correlation between vein size and the scale of mineralization.

Pervasive alteration of granitic rocks by magmatic-hydrothermal fluids is largely constrained to early stage units. Potassic alteration is exceedingly rare and represents a minor high-temperature phase that modified roof dikes and other apical granitic rocks by the addition of secondary potassium-bearing minerals. This event did not play a significant role in the overall magmatic-hydrothermal evolution of the HPP, but does provide a useful upper bound on the temperature range associated with hydrothermal activity. Conversely, phyllic alteration is relatively common and exhibits a similar association with skarn mineralization as Type (I) and (III) Quartz Veins. It was also observed by Musekamp (2012) to be present in metasedimentary wallrocks adjacent to skarn deposits. Phyllic alteration is interpreted to be a product of a high-temperature, moderately acidic, iron and sulfide-bearing fluids that accompanied ore fluids responsible for skarn mineralization. Pirajno (2009) describes the effects of this alteration by the addition of potassium, sulfur, and hydrogen ions and confirms its association with greisenization (not observed in the HPP), vein formation, and other styles of metal deposition.

The Type (V) Microcrystalline Quartz Veins observed in the early stage intrusive units of the HPP have been interpreted as major, low-temperature hydrothermal fluid conduits that exploited brittle fractures late in the emplacement history of the HPP (Burton, 1997). They are closely associated with many Type (IV) Microcrystalline Quartz Veins and zones of pervasive silicification and/or C-S alteration. Although both types of wallrock modification are associated with Type (V) Microcrystalline Quartz Veins, crosscutting relationships indicate that chlorite-sericite alteration preceded silicification.

C-S alteration is interpreted to be a moderately low-temperature product of an early post-crystallization episode of fluid flow and infiltration along brittle structures that added Fe and Mg (Parry & Downey, 1982). Pollard et al. (1991) observed similar alteration textures in the Sn-REE mineralized Bushveld granites and determined a fluid temperature of 260–320°C. Silicification associated with Type (V) Microcrystalline Quartz Veins is interpreted to be the lowest-temperature hydrothermal feature in the HPP and is characterized by the late precipitation of silica in pore space created by the dissolution of primary magmatic minerals, and by brittle injection into irregular, web-like fracture patterns, and occasionally micro-breccias.

2.6.2 FLUID ACTIVITY IN LATE STAGE INTRUSIVE UNITS

2.6.2.1 ORTHOMAGMATIC FEATURE TYPES

There are three types of texturally distinct orthomagmatic features associated with volatile saturation in the Tmg and Tgm: QF Pegmatites, aplites, and Layered Aplite/Pegmatites. All three are present in the sheeted intrusions of the Tmg, while only QF Pegmatite zones are found in the chemically distinct Tgm. Multi-element characterizations by Barnes et al. (2001) and observed mineralogical differences between pegmatites in the Tmg and Tgm units indicate an overall lack of interaction between these magmas. In the Tmg, field relationships indicate that contemporaneous crystallization of Layered Aplite/Pegmatites and pegmatite zones was followed by the late injection of aplite veins and dikes. Layered Aplite/Pegmatite zones and texturally homogeneous Aplites are conspicuously absent from the Tgm monzogranite.

In the HPP, subhorizontal, Layered Aplite/Pegmatite zones are unique to the core of the Tmg and represent a different style of fluid saturation and exsolution than observed in

early stage granitic units. Stereonets illustrating the orientations of these features can be found in Appendix C. Several workers have reviewed and proposed mechanisms of formation for composite pegmatite-aplite zones (Candela, 1997; Kontak et al., 2002; London, 2005). Kontak et al. (2002) interpreted similar flat-lying sheets of layered aplites and pegmatites at Peggys Cove in Nova Scotia, Canada to have formed by the infilling of dilatant fissures in the host granite by a late, interstitial melt. Fundamentally, the pegmatite zones form by the crystallization of a volatile-saturated melt and the aplite zones form when volatiles have been expelled from the system (Jahns & Tuttle, 1963). However, there have been several chemical and kinetic models for the alternating textures in these zones, most convincingly that fluctuations of internal fluid pressure (P_{H_2O}) resulted in systematic oscillations in the composition of the quartz-feldspar cotectic (London, 2005). The repeated layering of these zones in the HPP indicates that this process was simultaneously active in multiple zones. The formation of subhorizontal dilatent zones required high fluid pressures and/or a significant component of vertical extension, possibly from the unroofing of the HPP.

Discrete QF Pegmatite zones with no associated aplites are also common throughout the Tmg. Many cluster near the structural apex of this unit and extend into the adjacent Ttc. Further complicating this unclear structural setting, they bear many textural similarities to pegmatites in the Ttc and Tcc, such as crystal size and mineralogical abundances. However, the greater volumes of pegmatite zones in the Tmg relative to those in early stage units, coupled with a structural position above the texturally Layered Aplite/Pegmatite zones and the lack of miarolitic cavities, indicate that the “roof” of the late stage magmatic system

differed from its early stage counterpart. Rather than hosting ascending exsolved fluids, the highest levels of the Tmg hosted a migrating volatile-saturated melt.

Examples of texturally homogeneous aplites in the Tmg are very similar in appearance to aplites hosted in the Ttc and Tcc (i.e. typical mineralogy and textures in sharply-bounded planar structures). These features also represent the rapid, structurally focused crystallization of the terminal melt phase of a granitic intrusion after the removal of dissolved volatile components. Regardless of their position in late stage units, texturally homogeneous aplites crosscut all other igneous structures, indicating that they represent the final episode of magmatic crystallization. However, they are far less common in the late stage units than in the early stage units, but, where present, possess somewhat greater volumes. The high ratio of pegmatite zones to texturally homogeneous aplites in the Tmg is interpreted as evidence that the rate of fluid saturation in the remaining melt stalled during pegmatite crystallization and did not reach large-scale volatile exsolution and subsequent aplite crystallization.

The Tgm has been described as a texturally homogeneous, chemically distinct body that intruded into a structurally weakened zone in the deeper levels of the HPP. While the Tgm does not contain many hydrothermal features and is not associated with any peripheral ore deposits, it is the only intrusive unit to host MQF Pegmatites. The presence of muscovite in these pegmatites indicates the unique chemistry of the fluids and their source melt. Aluminum saturation in the parent magma is responsible for the presence of muscovite in these veins and in the surrounding igneous rocks and has been attributed to a sedimentary crustal component introduced to the magma by partial melting (Barnes et al., 2001). However, the relatively low volume of this intrusive unit, its deep structural setting

in the HPP, the sharp contact between it and the surrounding Tmg, and the overall lack of other vein types and alteration indicate that the Tgm did not contribute large volumes of fluids to the late stage hydrothermal system of the HPP.

2.6.2.2 HYDROTHERMAL FEATURE TYPES

The late stage units of the HPP contain relatively few indications of magmatic fluid saturation and exsolution. Only one miarolitic cavity was observed within the mapped area of the Tmg, but is located in a host block of older, dismembered Ttc, and thus can be considered an early stage feature. The absence of observed miarolitic cavities in late stage units may be due to lower initial volatile concentrations, volatile sequestration in the abundant pegmatites, (which is supported by theoretical models of pegmatite formation), or near-complete and passive egress of fluids from the late stage magmas.

Hydrothermal veins in the late stage units are more common in the Tmg than the Tgm. However, the largest concentration of Type (I) and (III) Quartz Veins in the HPP was observed in the northern half of the Tmg near its poorly defined contact with the Tgm. It is possible that these veins were formed by exsolved fluids escaping from the Tgm, or by fluids in the Tmg mobilized by the Tgm thermal system. Type (I) Quartz Veins are also common at the apical regions of the Tmg west of the contact with the Ttc. Veins interpreted to be late stage features crosscut both monzogranite and granodiorite, which is present as the dismembered early stage host of the late stage intrusive units. These features crystallized from exsolved metal-poor fluids that escaped incorporation into pegmatite. The only known evidence of metal deposition associated with late stage hydrothermal activity is a Type (II) (skarn) Quartz Vein-hosting Pb-Zn skarn on the southern contact of the Tmg sampled by Musekamp (2012). The overall lack of ore occurrences adjacent to the

late stage further supports the characterization of this system as being dominated by melt and crystal-phase volatile retention and low metal concentrations.

Type (V) Microcrystalline Quartz Veins are present throughout the Tmg and Tgm. Like those found in early stage units, these structures are interpreted as late-forming fluid conduits that exploited brittle faults that crosscut all preexisting magmatic and hydrothermal features. They are responsible for many Type (IV) Microcrystalline Quartz Veins, as well as large zones of silicification and C-S alteration. However, there are fewer of these veins in the Tmg and Tgm than in the Ttc and Tcc, indicating that veining was promoted at shallower structural levels where confining pressure was relatively low. Isolated Type (IV) Microcrystalline Quartz Veins likely represent the far-field migration of the same fluids responsible for Type (V) Microcrystalline Quartz Veins.

2.7 SUMMARY

The Harrison Pass Pluton is a composite, calc-alkaline granitic body that intruded into a metamorphic terrane undergoing core complex development at the time of regional Carlin-type gold mineralization. While previous studies have investigated the igneous geochemistry of this intrusion or the external meteoric-hydrothermal system, this study explores the transition from orthomagmatic crystallization and fluid saturation and exsolution to fluid migration, expulsion, and mineralization. This chapter has described field and petrographic observations of this transition and presents a preliminary characterization of the primary hydrothermal systems of the HPP. The two-stage assembly of the HPP exerts a first-order control on its magmatic-hydrothermal evolution. The early

and late stage magmatic suites provided the heat and fluid responsible for most of the hydrothermal activity during intrusion and crystallization. Early stage intrusive melts exsolved metal-bearing fluids that migrated into surrounding metasedimentary rocks, while volatiles in late stage units were only present in low concentrations and/or retained the melt and crystal phases.

The magmatic-hydrothermal system preserved in the early stage units of the HPP was characterized by fluid saturation, moderate degrees of exsolution, upward migration, expulsion, and skarn mineralization. Profuse aplite emplacement and scattered miarolitic cavities in the Tcc and dispersed crystalline quartz veins throughout both early stage units illustrate the transition from voluminous fracture-focused melt generation to fluid exsolution and extensive migration. Skarn and carbonate replacement/quartz vein deposits are also exclusively located on the margins of the Tcc, suggesting that the bulk of the metals sourced by the HPP originated from this intrusive unit as opposed to the Ttc. Hydrothermal fluids related to metal deposition in skarns and carbonate replacement deposits might also have been responsible for the phyllic alteration of granitic rocks associated with or adjacent to these deposits. Potassic alteration remains a minor component to the early stage hydrothermal history of the HPP and was intimately related to the emplacement of high-temperature subvolcanic, silicic dikes and apophyses from the plutonic margin.

The magmatic-hydrothermal system preserved in the late stage intrusive units of the HPP was characterized by saturation and retention of volatiles in localized melts, minor fluid exsolution, and low metal concentrations. Abundant aplite dikes, pegmatite zones, and composite Layered Aplite/Pegmatite zones in the volumetrically significant monzogranitic sheeted intrusions denote the introduction of volatile-rich magmas that maintained those

volatile concentrations throughout protracted crystallization. The distinct mineralogy of pegmatite zones in the two-mica Tgm reflects a transition to a peraluminous magma composition from the earlier intrusive units. The lack of miarolitic cavities in late stage units and hydrothermal ore deposits on their margins further supports the interpretation that volatiles remained predominantly partitioned in a relatively metal-poor melt or resulting crystal phases. Fluids that did exsolve from the magma were in equilibrium with the surrounding rocks, and formed pure quartz veins without any significant or pervasive wallrock alteration.

Post-intrusion hydrothermal activity was defined by the voluminous influx of relatively low-temperature, moderately acidic, silica-rich fluids responsible for silicification and chlorite-sericite alteration. This fluid event overprints many igneous and hydrothermal features, particularly near the roof zone of the HPP, and may obscure important elements of the primary fluid history of the intrusion.

TABLE 2.1 – Basic descriptions of the orthomagmatic, hydrothermal, and post-intrusion hydrothermal feature types observed in the HPP.

Feature Type	Minerals	Typical Thickness (cm)	Associated Alteration	Key Characteristics	Abundance and Geographic Distribution
QF Pegmatite	Quartz, Feldspar	2 - 55		Large, subhedral crystals with irregular margins. No associated alteration, but often associated with aplites.	Common; observed in all intrusive units, but more abundant in late stage units.
MQF Pegmatite	Muscovite, Quartz, Feldspar, (Garnet)	5 - 20		Similar to QF Pegmatites, but contain splays and books of muscovite.	Rare; restricted to Tgm
Aplite (Homogenous)	Feldspar, Quartz, (Biotite, Muscovite, Magnetite, Garnet)	<2 - 11		Fine-grained, texturally homogenous, sugrosic veins and dikes with sharp, planar margins.	Very common; observed in all intrusive units, but clustered in Tcc and Tmg.
Aplite (Q & QF-cored)	Feldspar, Quartz, (Biotite, Muscovite, Magnetite, Garnet)	10 - 13		Similar to homogeneous aplites, but contain a relatively thin core of crystalline quartz \pm feldspar.	Very rare
Aplite (Layered QF Pegmatite)	Feldspar, Quartz, (Biotite, Muscovite, Magnetite, Garnet)	Each Layer: 5 - 15		Generally shallowly dipping, alternating zones of aplitic and pegmatitic material.	Common; restricted to Tmg
Miarolitic Cavity	Quartz, Feldspar, Muscovite, (Pyrite, Magnetite)	Diameter: 2 - 30		Spherical or oblate void or filled crystal zone with inward-directed, euhedrally terminated quartz crystals.	Rare; restricted to Tcc
Type (I) Quartz Vein	Quartz (Muscovite, Pyrite)	1 - 5		Thin veins of crystalline quartz. Occasionally with muscovite-pyrite selvage zones.	Common; observed in all intrusive units.
Type (II) (skarn) Quartz Vein	Quartz	<1 - 5 (much larger at mined deposits)	Skarn	Crystalline quartz veins invariably associated with skarn alteration and mineralization on pluton margin.	Uncommon; only observed in skarn deposits on pluton margin.
Type (II) (wallrock) Quartz Vein	Quartz	<1 - 5		Massive, often discontinuous, milky quartz veins with no associated alteration in metasedimentary units	Common; observed throughout contact metamorphic aureole by Musekamp (2012).
Type (III) Quartz Vein	Quartz	5 - 35	Silicification	Thick veins of crystalline quartz. Often associated with jarosite staining. High fluid inclusion density.	Uncommon; somewhat restricted to Ttc and Tmg.
Type (IV) Microcrystalline Quartz Vein	Microcrystalline Quartz	0.5 - 5	Silicification, Chlorite-Sericite, Phyllic	Thin, milky white microcrystalline quartz veins often near to Type (V) Microcrystalline Quartz Veins. Surrounding rock often appears green from alteration.	Uncommon; observed in contact metamorphic aureole and all intrusive units.
Type (V) Microcrystalline Quartz Vein	Microcrystalline Quartz	25 - 300	Silicification, Chlorite-Sericite, Phyllic	Very large, massive, white microcrystalline quartz structures. Often more resistant to weathering than surrounding rock. Surrounding rock often appears green from alteration.	Uncommon; observed in contact metamorphic aureole and all intrusive units.

TABLE 2.2 – Basic descriptions of the hydrothermal alteration types observed in and around the HPP.

Alteration Type	Minerals	Outcrop Geometry	Associated Feature Types	Key Characteristics	Abundance and Geographic Distribution
Skarn	Diopside, Calcite, (Hydrogrossular, Epidote), Tremolite, Quartz, Sericite, Biotite, Chlorite, (Plagioclase), Magnetite, Pyrite, (Chalcopyrite, Galena, Heubnerite, Scheelite, Sphalerite)	Irregular bodies, vein envelopes, and mantos ranging in size from 1-100m	Type (II) (skarn) Quartz Veins	Complete replacement of carbonate host rock by skarn mineral assemblage. Altered rocks may appear green/black or have distinct diopside and hydrogrossular segregations.	Uncommon; Observed in Opm impure limestone units on pluton margin and in roof pendants. Largest deposits were mined along roof zone
Potassic	Biotite, K-Feldspar, Sericite, (Titanite)	Isolated pods (<4m)		Red/grey color in outcrop, ubiquitous secondary biotite needles.	Very rare; Observed in granitic cupolas and dikes along the HPP roof zone
Phyllic	Quartz, Sericite, Pyrite, Chlorite, (Magnetite, Titanite)	Irregular zones and pods (1-5m)	Type (IV) and (V) Microcrystalline Quartz Veins	Green/grey in outcrop, coarse chlorite and ubiquitous small pyrite cubes. Nearly total removal of biotite and feldspar.	Rare; Observed along southern pluton margin and in contact metamorphic aureole
Chlorite-Sericite	Chlorite, Sericite	Narrow (1-5 m) envelopes around microcrystalline quartz veins that extend 10s of meters along strike	Type (IV) and (V) Microcrystalline Quartz Veins	Altered rocks appear green and may be friable. Biotites are replaced by chlorite and may have iron oxide haloes. Some secondary pore space may be visible.	Uncommon; More abundant in early stage units
Silicification	Microcrystalline Quartz	Large, irregular zones (<10 m) around veins that extend 10s of meters along strike	Type (III) Quartz Veins, Type (IV) and (V) Microcrystalline Quartz Veins	Altered rocks are resistant to weathering, and typically exhibit dense microfracture patterns. Igneous textures are obscured, rock appears bleached and granular.	Common; Observed in all intrusive units

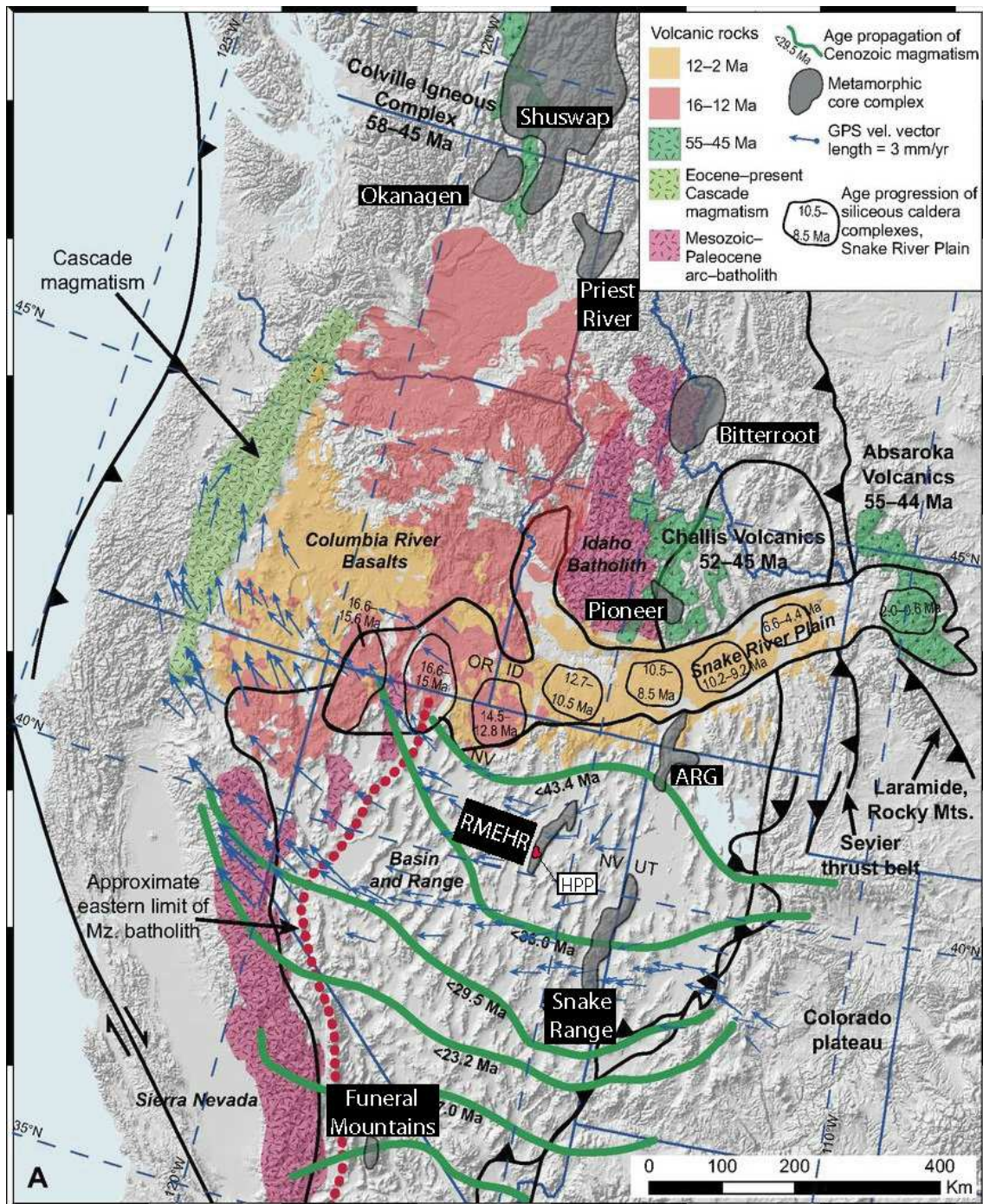


FIGURE 2.1 – Simplified geologic map of the southern North American Cordillera. Areas of magmatic and tectonic significance are identified, including, but not limited to, the Sierra Nevada Batholith, Cascade Arc, Columbia River Basalts, Idaho Batholith, path of the Yellowstone hotspot, and Basin and Range province. Additionally, metamorphic core complexes are delineated in grey and labeled accordingly. RMEHR = *Ruby Mountain-East Humboldt Range*, ARG = *Albion-Raft River-Grouse Creek*. Adapted from Konstantinou et al., 2012.

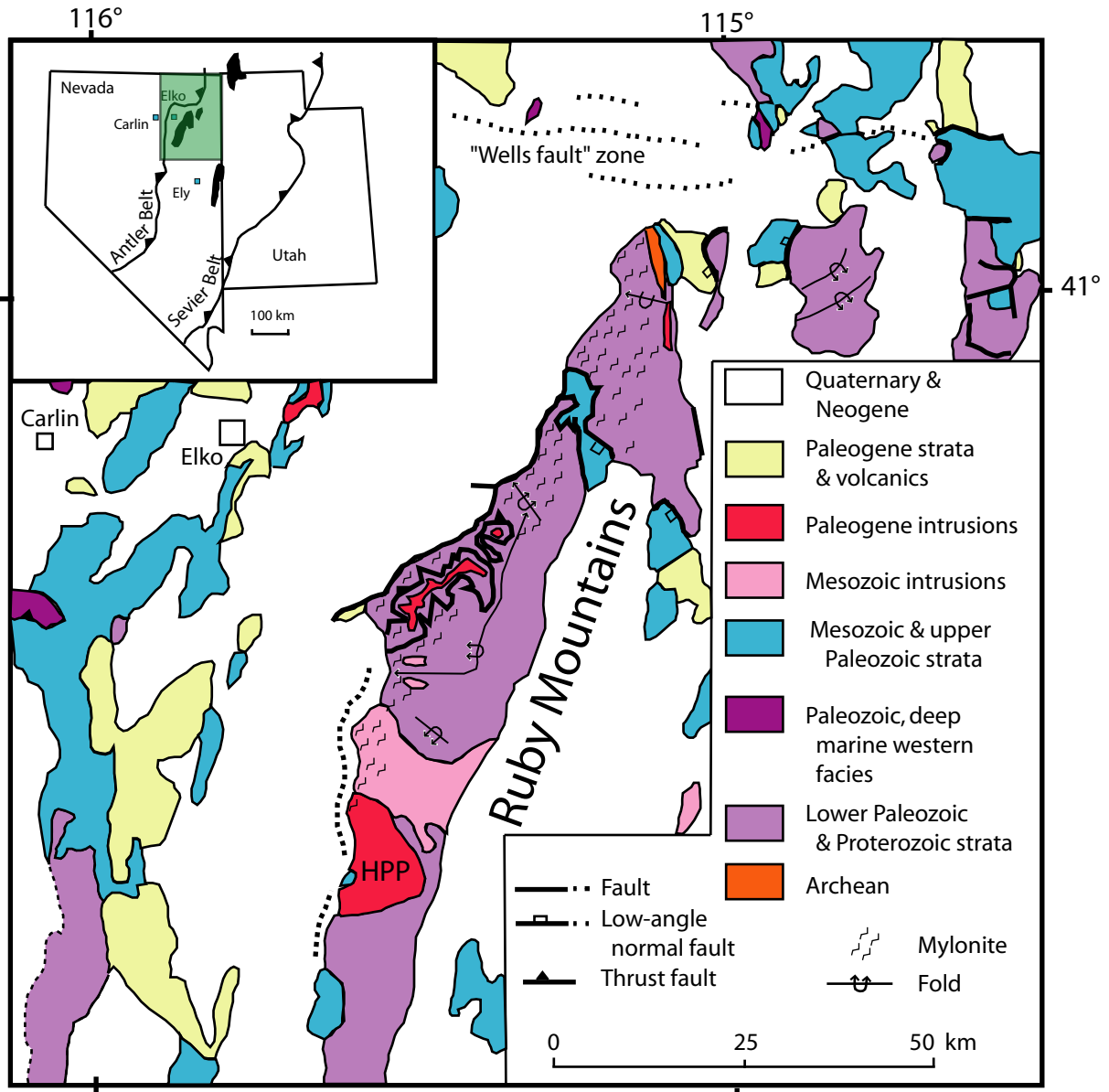


FIGURE 2.2 – Generalized geologic map of the RMEHR metamorphic core complex. Adapted from Howard (2003).

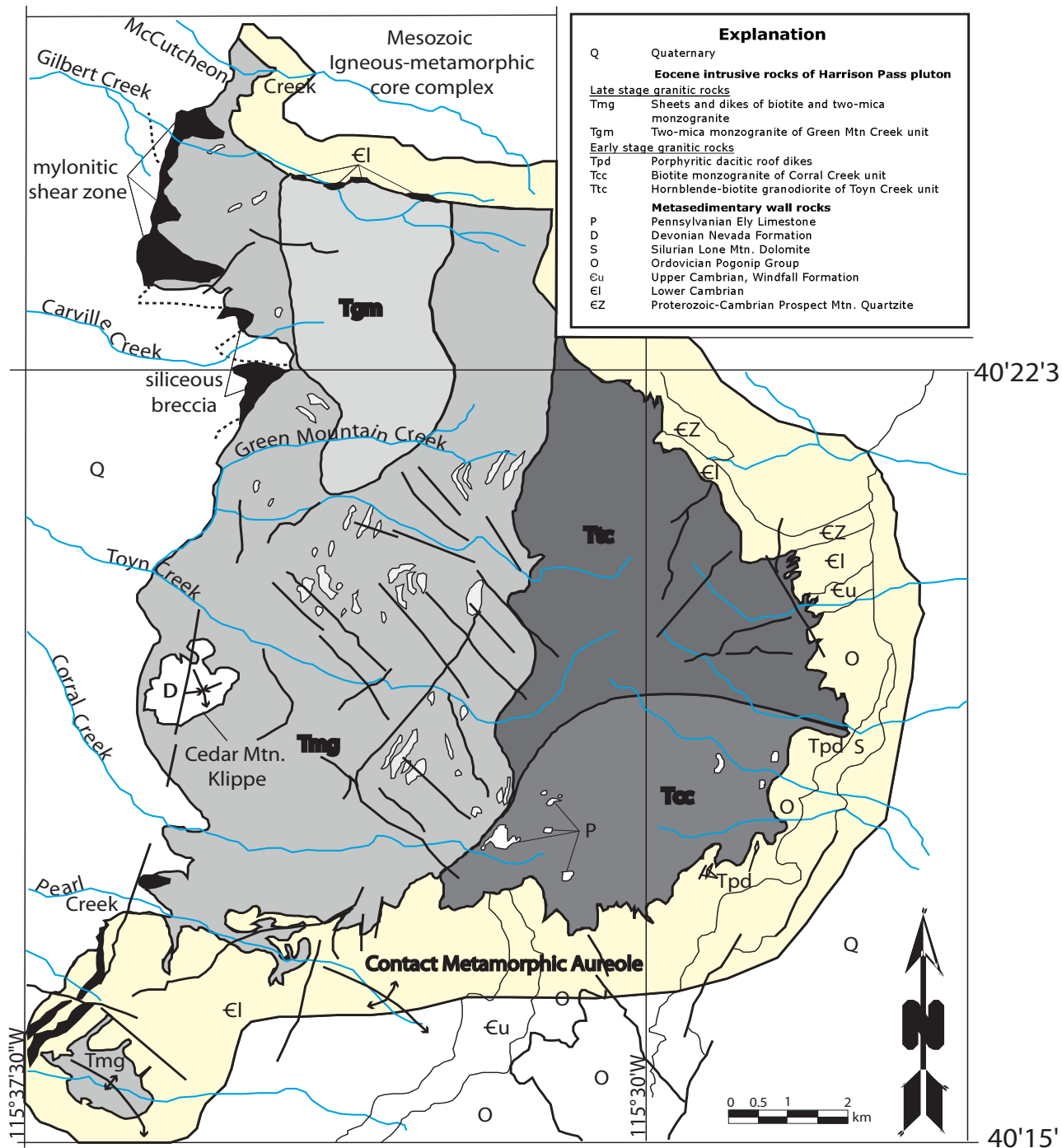


FIGURE 2.3 – Geologic map of the HPP showing intrusive units and delineating the contact metamorphic aureole. Adapted from Burton (1997).

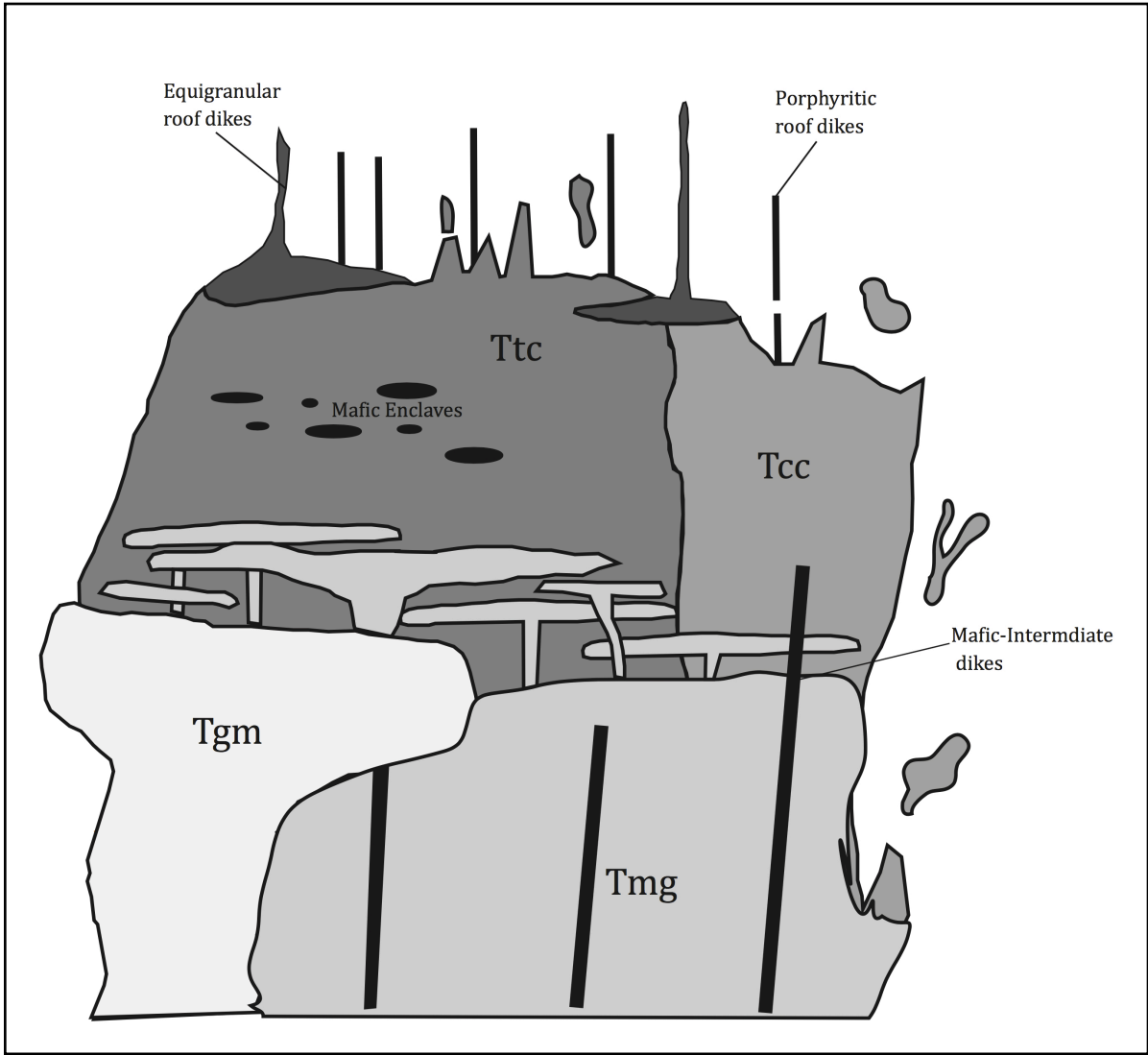


FIGURE 2.4 – Cross sectional schematic of the intrusive units of the HPP. Adapted from Barnes et al. (2001). Late stage sheets and dikes of Tmg monzogranite can be seen intruding into early stage units above the main body of Tmg.

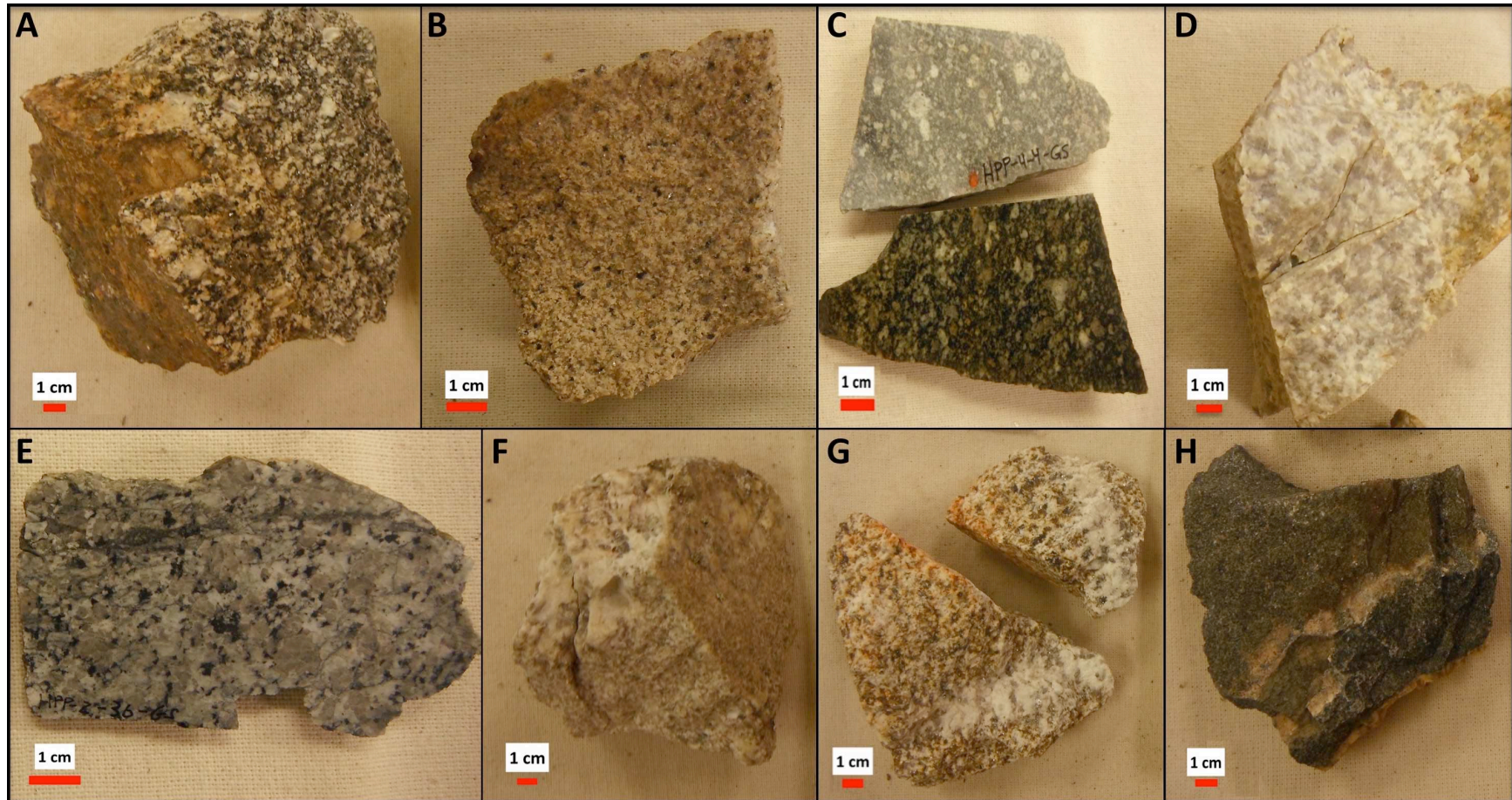


FIGURE 2.5 – Representative photographs of major and minor HPP intrusive units. A: early stage Ttc granodiorite. B: early stage Tcc monzogranite. C: porphyritic rhyodacite (from roof dike). D: Equigranular leucogranite (from roof dike). E: late stage Tmg biotite monzogranite. F: late stage Tmg two-mica monzogranite. G: late stage Tgm two-mica monzogranite. H: microdiorite (from mafic-intermediate dike).

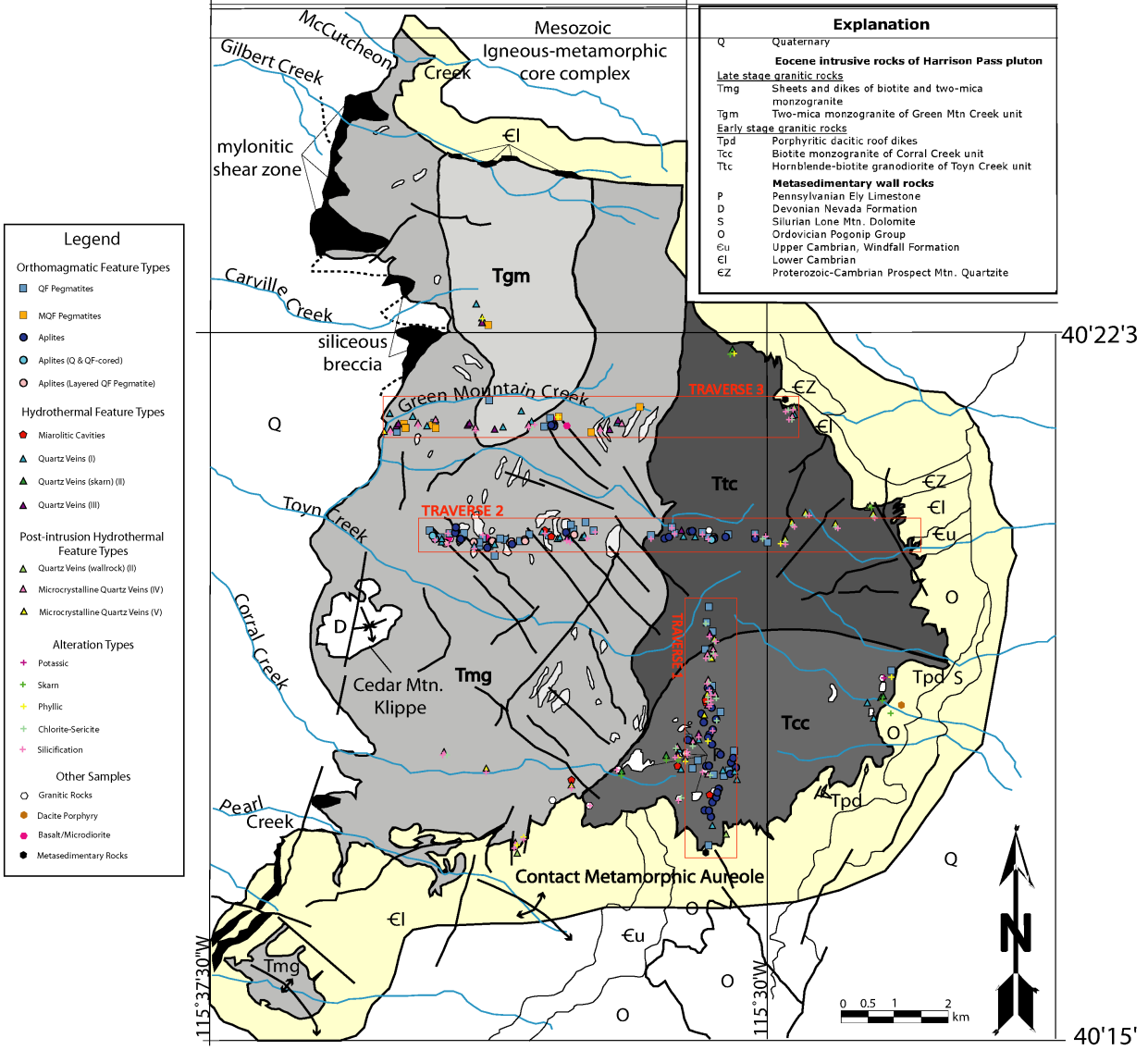





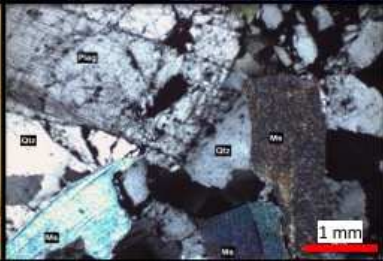





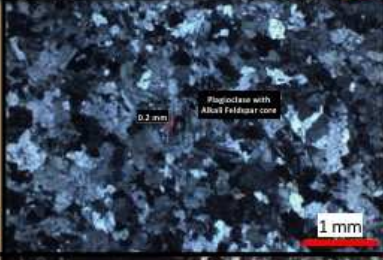





FIGURE 2.6 – Geographic distribution of samples collected in this study. Predefined sampling traverses are outlined and labeled in red. Map adapted from Burton (1997).

A	Outcrop	Hand Sample	Thin Section
QF Pegmatites			
MQF Pegmatites			
Aplites			
Aplites (Q & QF-cored)			
Aplites (Layered QF Pegmatites)			

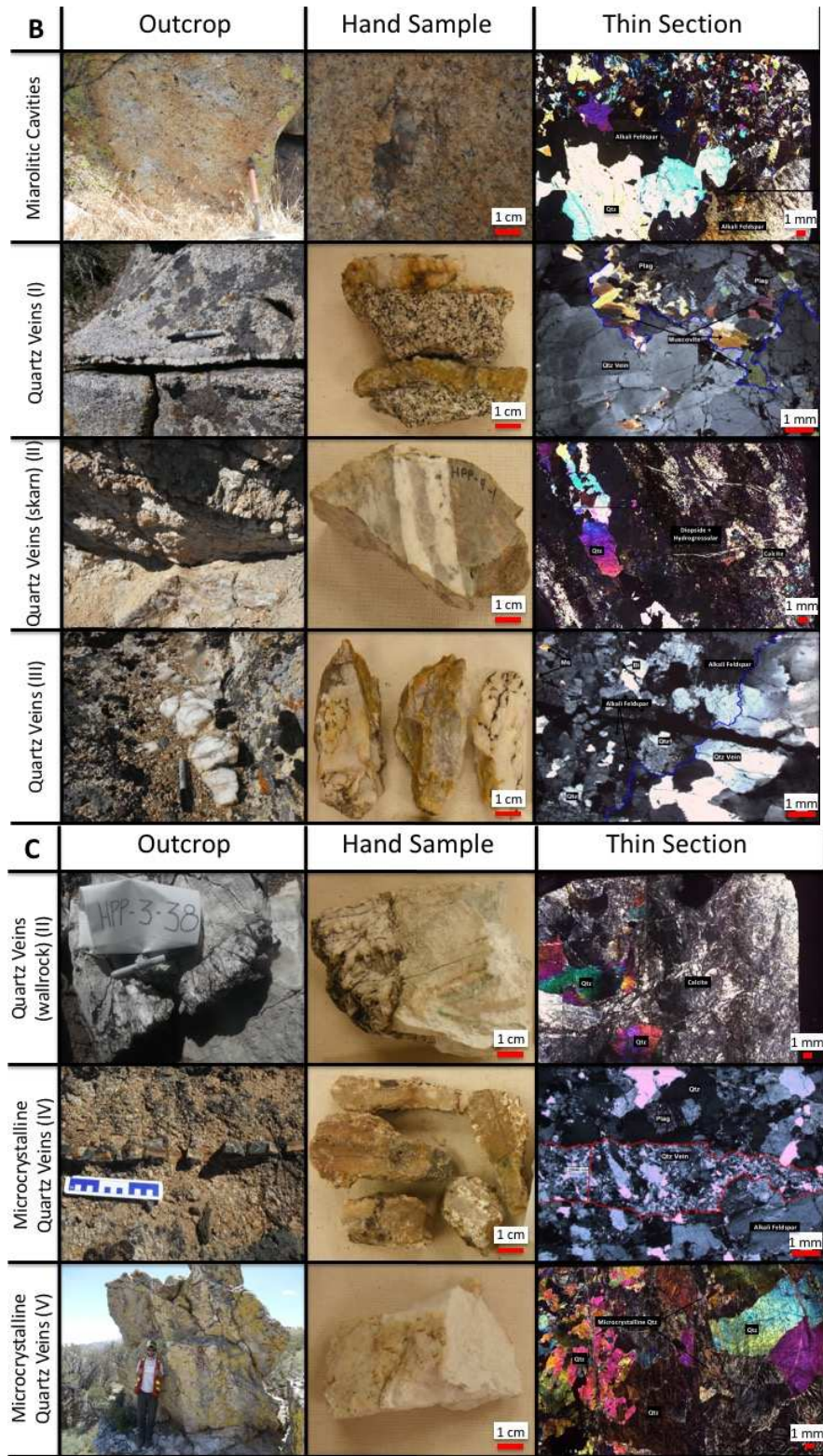


FIGURE 2.7 – Representative photographs and photomicrographs of (A) orthomagmatic, (B) hydrothermal, and (C) post-intrusion hydrothermal feature types related to fluid activity.

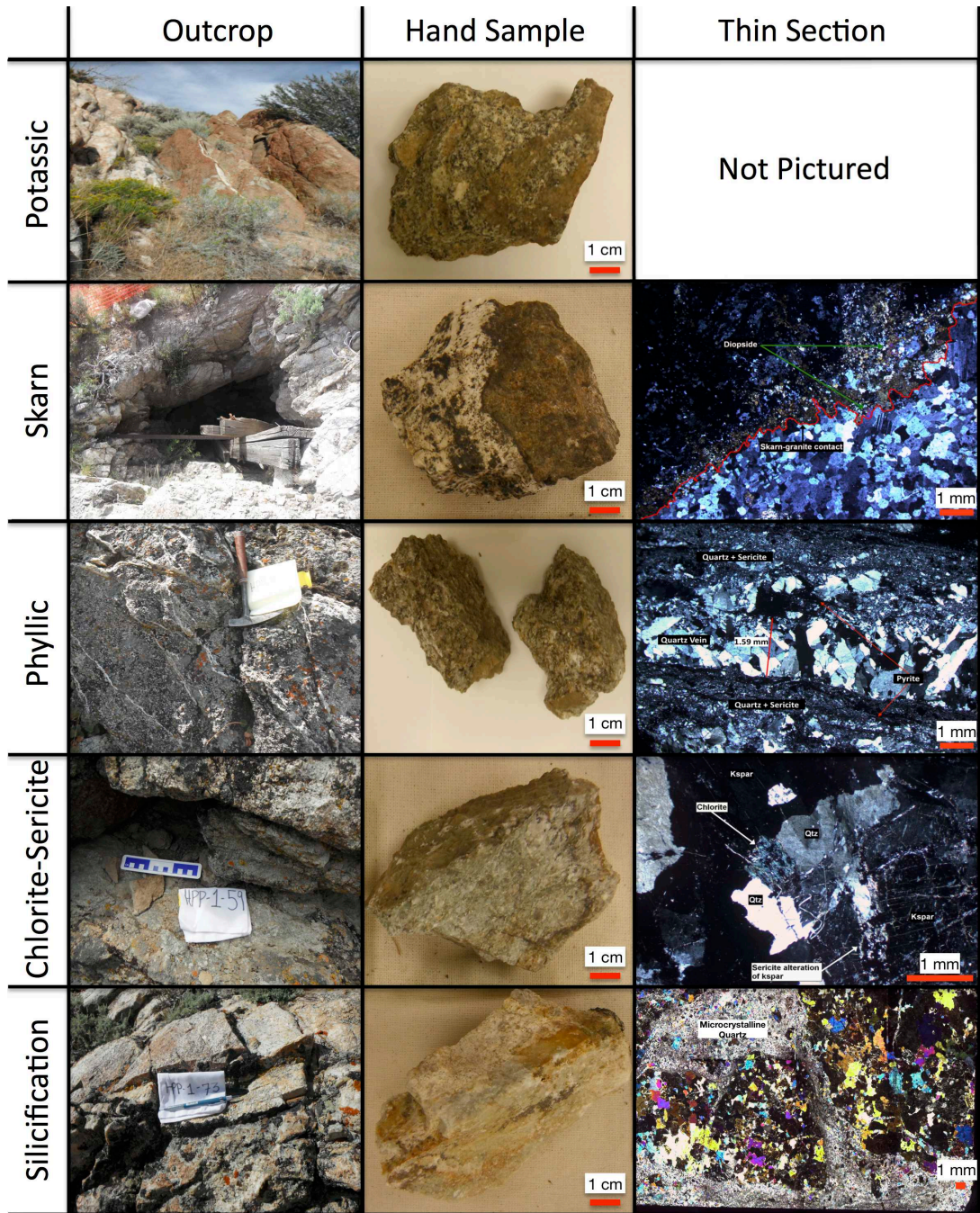


FIGURE 2.8 – Representative photographs and photomicrographs of the five types of hydrothermal alteration observed within and around the HPP.

2.8 REFERENCES

- Anderson, E. M. (1951). *The dynamics of faulting and dyke formation with applications to Britain*. London: Hafner Pub. Co.
- Armstrong, R. L. (1972). Low-angle (denudation) faults, hinterland of the Sevier orogenic belt, eastern Nevada and western Utah. *Geological Society of America Bulletin*, 83(6), 1729–1754.
- Audétat, A., Günther, D., & Heinrich, C. A. (1998). Formation of a magmatic-hydrothermal ore deposit: Insights with LA-ICP-MS analysis of fluid inclusions. *Science*, 279(5359), 2091–2094.
- Audétat, A., Günther, D., & Heinrich, C. A. (2000). Causes for large-scale metal zonation around mineralized plutons: fluid inclusion LA-ICP-MS evidence from the Mole Granite, Australia. *Economic Geology*, 95(8), 1563–1581.
- Audétat, A., & Pettke, T. (2003). The magmatic-hydrothermal evolution of two barren granites: a melt and fluid inclusion study of the Rito del Medio and Canada Pinabete plutons in northern New Mexico (USA). *Geochimica et Cosmochimica Acta*, 67(1), 97–121.
- Audétat, A., Pettke, T., Heinrich, C. A., & Bodnar, R. J. (2008). Special paper: the composition of magmatic-hydrothermal fluids in barren and mineralized intrusions. *Economic Geology*, 103(5), 877–908.
- Barnes, C. G., Burton, B. R., Burling, T. C., Wright, J. E., & Karlsson, H. R. (2001). Petrology and geochemistry of the late Eocene Harrison Pass pluton, Ruby Mountains core complex, northeastern Nevada. *Journal of Petrology*, 42(5), 901–929.
- Burnham, C. W. (1979). Magmas and hydrothermal fluids. *Geochemistry of Hydrothermal Ore Deposits*. (Barnes, H.L., ed.), 71–136.
- Burton, B. R. (1997). Structural geology and emplacement history of the Harrison Pass pluton, central Ruby Mountains, Nevada. PhD Dissertation: University of Wyoming, Laramie, WY.
- Candela, P. A., & Blevin, P. L. (1995). Do some miarolitic granites preserve evidence of magmatic volatile phase permeability?. *Economic Geology*, 90(8), 2310–2316.
- Candela, P. A. (1997). A review of shallow, ore-related granites: textures, volatiles, and ore metals. *Journal of petrology*, 38(12), 1619–1633.
- Colgan, J. P., Howard, K. A., Fleck, R. J., & Wooden, J. L. (2010). Rapid middle Miocene extension and unroofing of the southern Ruby Mountains, Nevada. *Tectonics*, 29(6).

- Dallmeyer, R. D., Snoke, A. W., & McKee, E. H. (1986). The Mesozoic-Cenozoic tectonothermal evolution of the Ruby Mountains, East Humboldt Range, Nevada: A Cordilleran Metamorphic Core Complex. *Tectonics*, 5(6), 931–954.
- Dickinson, W. R. (2002). The Basin and Range Province as a composite extensional domain. *International Geology Review*, 44(1), 1–38.
- Dickinson, W. R. (2006). Geotectonic evolution of the Great Basin. *Geosphere*, 2(7), 353–368.
- Dokka, R. K., Mahaffie, M. J., & Snoke, A. W. (1986). Thermochronologic evidence of major tectonic denudation associated with detachment faulting, Northern Ruby Mountains-East Humboldt Range, Nevada. *Tectonics*, 5(7), 995–1006.
- Dunbar, N. W., Campbell, A. R., & Candela, P. A. (1996). Physical, chemical, and mineralogical evidence for magmatic fluid migration within the Capitan pluton, southeastern New Mexico. *Geological Society of America Bulletin*, 108(3), 318–333.
- Gilbert, G. K. (1928). *Studies of basin-range structure (Vol. 153)*. US Government Printing Office.
- Hedenquist, J. W., & Lowenstern, J. B. (1994). The role of magmas in the formation of hydrothermal ore deposits. *Nature*, 370(6490), 519–527.
- Heinrich, C. A., Ryan, C. G., Mernagh, T. P., & Eadington, P. J. (1992). Segregation of ore metals between magmatic brine and vapor; a fluid inclusion study using PIXE microanalysis. *Economic Geology*, 87(6), 1566–1583.
- Holland, H. D. (1972). Granites, solutions, and base metal deposits. *Economic Geology*, 67(3), 281–301.
- Howard, K. A. (2003). Crustal structure in the Elko-Carlin region, Nevada, during Eocene gold mineralization: Ruby-East Humboldt metamorphic core complex as a guide to the deep crust. *Economic Geology*, 98(2), 249–268.
- Howard, K. A., Wooden, J. L., Barnes, C. G., Premo, W. R., Snoke, A. W., & Lee, S. Y. (2011). Episodic growth of a Late Cretaceous and Paleogene intrusive complex of pegmatitic leucogranite, Ruby Mountains core complex, Nevada, USA. *Geosphere*, 7(5), 1220–1248.
- Hudec, M. R. (1990). The structural and thermal evolution of the central Ruby Mountains, Elko County, Nevada. PhD Dissertation: University of Wyoming, Laramie, WY.
- Jahns, R. H., & Burnham, C. W. (1969). Experimental studies of pegmatite genesis: A model for the derivation and crystallization of granitic pegmatites. *Economic Geology*, 64(8), 843–864.
- Jahns, R. H., & Tuttle, O. F. (1963). Layered pegmatite-aplite intrusives. *Mineralogical Society of America Special Paper*, 1, 78–92.

Jansma, P. E., & Speed, R. C. (1990). Omissional faulting during Mesozoic regional contraction at Carlin Canyon, Nevada. *Geological Society of America Bulletin*, 102(4), 417–427.

Jones, C. H., Wernicke, B. P., Farmer, G. L., Walker, J. D., Coleman, D. S., McKenna, L. W., & Perry, F. V. (1992). Variations across and along a major continental rift: An interdisciplinary study of the Basin and Range Province, western USA. *Tectonophysics*, 213(1), 57–96.

Ketner, K. B. (1998). The nature and timing of tectonism in the western facies terrane of Nevada and California; an outline of evidence and interpretations derived from geologic maps of key areas (No. 1592). USGPO: US Dept. of the Interior, US Geological Survey; For sale by US Geological Survey, Information Services.

Kistler, R. W., Ghent, E. D., & O'Neil, J. R. (1981). Petrogenesis of garnet two-mica granites in the Ruby Mountains, Nevada. *Journal of Geophysical Research: Solid Earth* (1978–2012), 86(B11), 10591–10606.

Konstantinou, A., Strickland, A., Miller, E. L., & Wooden, J. P. (2012). Multistage Cenozoic extension of the Albion–Raft River–Grouse Creek metamorphic core complex: Geochronologic and stratigraphic constraints. *Geosphere*, GES00778–1.

Kontak, D. J., Dostal, J., Kyser, T. K., & Archibald, D. A. (2002). A petrological, geochemical, isotopic, and fluid-inclusion study of the 370 Ma pegmatite-aplite sheets, Peggys Cove, Nova Scotia, Canada. *The Canadian Mineralogist*, 40(5), 1249–1286.

Landtwing, M. R., Furrer, C., Redmond, P. B., Pettke, T., Guillong, M., & Heinrich, C. A. (2010). The Bingham Canyon porphyry Cu-Mo-Au deposit. III. Zoned copper-gold ore deposition by magmatic vapor expansion. *Economic Geology*, 105(1), 91–118.

Lapointe, D. D., Tingley, J. V., & Jones, R. B. (1991). Mineral resources of Elko County, Nevada (No. 106). Reno: University of Nevada, Reno, MacKay School of Mines.

Lewis, R. S. (1990). Geology, geochemistry and mineral potential of Cretaceous and Tertiary plutons in the eastern part of the Soldier Mountains, Idaho. PhD Dissertation: Oregon State University, Corvallis, OR.

Lewis, R. S. (2001). Alteration and mineralization in the eastern part of the Soldier Mountains, Camas County, Idaho. US Department of the Interior, US Geological Survey.

Lowenstern, J. B., Mahood, G. A., Rivers, M. L., & Sutton, S. R. (1991). Evidence for extreme partitioning of copper into a magmatic vapor phase. *Science*, 252(5011), 1405–1409.

Mueller, K. J., & Snoke, A. W. (1993). Progressive overprinting of normal fault systems and their role in Tertiary exhumation of the East Humboldt-Wood Hills Metamorphic Complex northeast Nevada. *Tectonics*, 12(2), 361–371.

- Musekamp, C. O. J. (2012). Field, fluid inclusion and isotope chemistry evidence of fluids circulating around the Harrison Pass pluton during intrusion: A fluid model for Carlin-type deposits. MSc. thesis, 189 p: Colorado State University, Fort Collins, CO.
- Parry, W. T., & Downey, L. M. (1982). Geochemistry of hydrothermal chlorite replacing igneous biotite. *Clays Clay Miner*, 30(2), 81–90.
- Pirajno F. (2009). Hydrothermal processes and mineral systems. Springer, Berlin, 1250 pp.
- Pollard, P. J., Taylor, R. G., Taylor, R. P., & Groves, D. I. (1991). Petrographic and geochemical evolution of pervasively altered Bushveld granites at the Zaaiploats tin mine. *Economic Geology*, 86(7), 1401–1433.
- Reese, N. M. (1986). Cenozoic tectonic history of the Ruby Mountains and adjacent areas, northeastern Nevada: constraints from radiometric dating and seismic reflection profiles. M.S. thesis, 87 p: Southern Methodist Univ., Dallas, TX.
- Shinohara, H. (1994). Exsolution of immiscible vapor and liquid phases from a crystallizing silicate melt: implications for chlorine and metal transport. *Geochimica et Cosmochimica Acta*, 58(23), 5215–5221.
- Snoke, A. W. (1980). Transition from infrastructure to suprastructure in the northern Ruby Mountains, Nevada. *Geological Society of America Memoirs*, 153, 287–334.
- Snoke, A. W., & Lush, A. P. (1984). Polyphase Mesozoic-Cenozoic deformational history of the northern Ruby Mountains-East Humboldt Range, Nevada. In *Western Geological Excursions*, prepared for the 1984 Annual Meetings of the Geological Society of America and affiliated societies at Reno, 232–260.
- Spear, F. S., Kohn, M. J., & Cheney, J. T. (1999). P–T paths from anatectic pelites. *Contributions to Mineralogy and Petrology*, 134(1), 17–32.
- Thompson, A. B., & Tracy, R. J. (1979). Model systems for anatexis of pelitic rocks. *Contributions to Mineralogy and Petrology*, 70(4), 429–438.
- Thompson, A. B. (1982). Dehydration melting of pelitic rocks and the generation of H₂O-undersaturated granitic liquids. *American Journal of Science*, 282(10), 1567–1595.
- Willden, R., & Kistler, R. W. (1969). Geologic map of the Jiggs quadrangle. Elko County, Nevada: US Geological Survey Map GQ-859, scale, 1:62,500, 1.
- Willden, R., Thomas, H. H., & Stern, T. W. (1967). Oligocene or younger thrust faulting in the Ruby Mountains, northeastern Nevada. *Geological Society of America Bulletin*, 78(11), 1345–1358.
- Willden, R., & Kistler, R. W. (1979). Precambrian and Paleozoic stratigraphy in central Ruby Mountains, Elko County, Nevada. In *Basin and Range Symposium and Great Basin Field Conference: Denver*, Rocky Mountain Association of Geologists, 221–243.

Wright, J. E., & Snoke, A. W. (1993). Tertiary magmatism and mylonitization in the Ruby-East Humboldt metamorphic core complex, northeastern Nevada: U-Pb geochronology and Sr, Nd, and Pb isotope geochemistry. *Geological Society of America Bulletin*, 105(7), 935–952.

Zoback, M. L., Anderson, R. E., & Thompson, G. A. (1981). Cainozoic evolution of the state of stress and style of tectonism of the Basin and Range province of the western United States. *Philosophical Transactions of the Royal Society of London A: Mathematical, Physical and Engineering Sciences*, 300(1454), 407–434.

CHAPTER 3: THE MAGMATIC-HYDROTHERMAL FLUIDS OF THE HARRISON PASS PLUTON: IMPLICATIONS FOR THE RMEHR METAMORPHIC CORE COMPLEX AND CARLIN-TYPE AU DEPOSITS

3.1 INTRODUCTION

Emplacement of hydrous silicic magmas into the earth's crust is a routine geologic process (Pitcher, 1979; Wickham, 1987; Petford et al., 2000). Fluids produced by these intrusions represent a minor but important component of the crustal fluid budget, and have been linked to the formation of several different types of ore deposits (Cathles, 1981; Hedenquist & Lowenstern, 1994). While the fossil hydrothermal systems directly responsible for the formation of the world-class Carlin-type Au deposits in the Great Basin are frequently described as being distal expressions of intrusive magmatism (e.g. Sillitoe & Bonham, 1990; Henry & Boden, 1998; Ressel & Henry, 2006; Muntean et al., 2011), few studies have investigated the fluid activity at potential source intrusions. Furthermore, entrapped fluids of magmatic origin often record the prevailing pressure-temperature regime during crystallization of source magmas, providing insight into the structural position and style of post-intrusion cooling. To address these questions, this study has reconstructed the magmatic-hydrothermal fluid history of the late Eocene Harrison Pass Pluton (HPP), a composite granitic intrusion in the Ruby Mountains-East Humboldt Range (RMEHR) metamorphic core complex. This fluid history provides new, independent estimates of the emplacement depth of the HPP prior to the onset of major tectonic

exhumation of the RMEHR, while also assessing possible genetic links with the broadly contemporaneous regional fluid event responsible for Carlin-type Au deposition.

The Harrison Pass Pluton (HPP) is a composite, calc-alkaline, high-K, granodiorite-monzogranite intrusion that outcrops over an area of 150 km² in the central-southern RMEHR metamorphic core complex in the northeastern Great Basin tectonic province (Burton, 1997; Barnes et al., 2001). Eastward tilting of this fault-bounded horst block exposes a structural cross section of the HPP and a contact metamorphic aureole within the surrounding Paleozoic strata. Field observations and sampling determined the spatial distribution and relationships between the types of evidence related to fluid activity in the HPP (see Section 2.3 for description of field study). In this study, ten different “feature types” related to fluid saturation, exsolution, migration, expulsion, and entrapment were recognized, described, and sampled within the HPP. Feature types include pegmatites, aplites, miarolitic cavities, and a several styles of crystalline and microcrystalline quartz veins. Additionally, four types of hydrothermal alteration were recognized.

Fluid inclusions entrapped in quartz from orthomagmatic and hydrothermal feature types preserved small volumes of the fluids circulating within the HPP during emplacement and crystallization. Oxygen stable isotope analysis of host quartz crystals were conducted to constrain the source of these fluids, and demonstrate the degree of infiltration of cooler, external fluids. Determination of the major constituent phases and entrapment conditions of fluids was accomplished by meticulous petrography and microthermometry of fluid inclusions. LA-ICP-MS microanalysis of fluid inclusions produced a characterization of the multi-element geochemistry of these fluids. These results were integrated with published datasets, including whole-rock geochemical data from the HPP, and fluid inclusion and

stable isotope data from the contact metamorphic aureole, to facilitate detailed reconstruction of the multi-stage fluid history of the HPP. The pressure regime invoked by this fluid history was used to estimate the emplacement depth of the HPP and was compared to existing models of Mesozoic-Cenozoic crustal development of the RMEHR. Finally, possible genetic relationships between the HPP and CTD's were considered in light of the geochemical compositions of the fluids entrapped within the HPP.

3.2 GEOLOGIC SETTING

3.2.1 GEOLOGIC HISTORY OF THE HARRISON PASS PLUTON

The ~36 Ma HPP was emplaced during a period of regional extension, Au mineralization, and voluminous back arc-style magmatic activity in the Great Basin, (Figure 3.1) (Armstrong et al., 1969; Christiansen & Lipman, 1972; Gans et al., 1989; Wright & Snoke, 1993). Driven by delamination of the subducting Farallon plate and subsequent asthenospheric upwelling, semi-latitudinal magmatic fronts migrated south-southwest across the Great Basin from 43–20 Ma where they were characterized by high K, calc-alkaline ignimbrite eruptions and shallowly emplaced intrusions (Christiansen & Yeats, 1992; Humphreys, 1995; Henry & Ressel, 2000a; Dickinson, 2006; Ressel & Henry, 2006). However, the HPP is the only exposed example of an Eocene intrusive body of near-batholith proportions that is coeval with and within the crustal domain of the widespread hydrothermal activity responsible for CTD's. Genetic relationships with locally exposed volcanic and volcanoclastic units proposed by Howard (2003) remain unconfirmed, and

Barnes et al. (2001) argued that this was unlikely due to the disparity between relative mafic inputs.

Assembly of the HPP was accomplished by two compositionally heterogeneous pulses of magma originating from a magma chamber in the underlying Mojave basement province (Barnes et al., 2001). The spatial relationships of these two pulses are illustrated in Figure 3.2. The first pulse, generated by a tonalite-monzogranite hybridization, was broadly granodioritic with a significant and temporally distinct comagmatic monzogranite unit (Barnes, 2001; Colgan et al., 2010). Early stage units are dominantly hypidiomorphic granular with alkali feldspar megacrysts and localized swarms of mafic enclaves, (although roof dikes may be equigranular or porphyritic). Stoping, diking, folding, and internal deformation of adjacent wallrock units accommodated emplacement of early stage intrusive units. The second pulse, dominantly generated by low-volume crustal anatexis, was monzogranitic with a peraluminous, geochemically anomalous constituent phase (Barnes et al., 2001). Late stage units may be either texturally heterogeneous with extreme grain-size variation, or almost completely homogeneous. Late stage units were emplaced as sheeted dikes and sills or as homogeneous masses by brittle and ductile deformation of their early stage magmatic hosts (Burton, 1997). The northern and southern margins of the HPP are strongly discordant with surrounding rocks, while the roof zone is variably concordant, with the exception of relatively low-volume roof dikes.

The HPP was emplaced into the RMEHR, a well-exposed example of a classic Cordilleran metamorphic core complex in the hinterland of the Sevier fold-thrust belt (Figure 3.3) (see Dallmeyer et al. (1986) for overview of the RMEHR, see Armstrong (1982); Coney & Harms (1984) for review of metamorphic core complexes). The RMEHR

records a history of Mesozoic compressional deformation, burial to midcrustal depths (13–30 km), and metamorphism followed by multiple phases of Cenozoic tectonic exhumation and uplift (Howard, 1980; Snoke, 1980; Armstrong, 1982; Snoke & Lush, 1984; Dallmeyer et al., 1986; Lush et al., 1988; Snoke & Miller, 1988; Snoke et al., 1990b; Hodges et al., 1992; Hudec, 1992; Camilleri & Chamberlain, 1997; McGrew et al., 2000; Satarugsa & Johnson, 2005). The HPP occupies the gradational transition from the infrastructural core of high-grade metamorphic and igneous rocks to the low-grade to unmetamorphosed suprastructure of homoclinal Paleozoic strata (Hudec, 1990; Burton, 1997). Jurassic pegmatitic granite abutting the HPP to the north was synchronous with the north-to-south low pressure, high temperature metamorphic gradient in the Paleozoic suprastructural stratigraphic section (Kistler et al., 1981; Hudec & Wright, 1990; Hudec, 1992). A thermal aureole extends 0.5–1.5 km from the eastern and southern margins of the HPP and is characterized by andalusite growth and static recrystallization of carbonate and calc-silicate wallrock units (Burton, 1997; Musekamp, 2012).

Eastward tilting of the RMEHR horst block has exposed a 5 km structural section of the HPP. Estimates of the depth of emplacement have been proposed on the basis of field and petrographic observations, equilibrium igneous mineral assemblage compositions and structural and stratigraphic reconstructions of the RMEHR. The presence of miarolitic cavities near the roof zone and andalusite in the contact metamorphic aureole suggests roof-zone emplacement pressures of 3–4 kbar (Barnes et al., 2001). Al-in-hornblende thermobarometry by Burton (1997) yielded emplacement pressures of $4.5\text{--}5.5\pm 0.6$ kbar, corresponding to depths of $12.1\text{--}14.8\pm 1.6$ km. However, analytical uncertainty and textural evidence of partial post-crystallization reequilibration have cast some doubt on this

interpretation. Reconstructions of the overlying rock package by Burton (1997) constrained intrusion depths to 6–13 km, while Colgan et al. (2010) produced a slightly lower range of 4–12 km. However, uncertainty is also inherent in these calculations due to the possibility of stratigraphic duplication by orogenic events, ambiguity in the position of the Eocene land surface, and the degree of preceding erosion.

The Ruby Mountain Detachment/Shear Zone (RMSZ) is a major west-northwest rooted, brittle-ductile deformation zone that defines the western flank of the RMEHR and cuts the HPP with present-day dips of 10–19° (Snoke, 1980; Lister & Snoke, 1984; Hurlow et al., 1991; Colgan et al., 2010). It is interpreted to be a major, normal-sense, low-angle, brittle-ductile detachment fault superimposed on an earlier midcrustal shear zone (Snoke & Lush, 1984; Mueller & Snoke, 1993; Wright & Snoke, 1993). Normal-sense slip on the RMSZ may have lasted from ~45–17 Ma, (although Colgan et al. (2010) and Haines & van der Pluijm (2010) argued for episodic brittle extension until 11 Ma) (Dallmeyer et al., 1986; Dokka et al., 1986; McGrew & Snee, 1994; McGrew et al., 2000; Wells et al., 2000; Wells, 2001). Estimates of 50 km of WNW lateral extension on the RMSZ place the rocks exposed in the Ruby Mountains beneath the Piñon and Adobe ranges and near the Carlin Trend Au deposits (Jansma & Speed, 1992; Howard, 1992; Newman & Witter, 1992; Howard, 2003). Brittle-ductile deformation delineates the western margin of the HPP and some gently deformed igneous dikes have been observed to intrude across this fault surface (Hudec, 1990; Burton, 1997; Colgan et al., 2010). Eastward tilting of the range by 30° postdates the HPP, but may have accompanied slip on the RMSZ (Kistler et al., 1981; Blackwell et al., 1985; Reese, 1986; Hudec, 1990; McGrew & Snee, 1994; Burton, 1997; Howard, 2003; Colgan et al., 2010). Post-detachment structural modification of the RMEHR is defined by

Miocene-recent slip on the high-angle, east-dipping, normal-sense RVFZ on the eastern margin of the range (Dohrenwend et al., 1996)

3.2.2 MAGMATISM AND CARLIN-TYPE AU DEPOSITS

Eocene intrusive magmatism in the Great Basin is spatially and temporally associated with world-class Carlin-type Au mineralization (Christiansen & Yeats, 1992; Hofstra et al., 1999; Howard, 2003; Henry & Ressel, 2000b; Ressel & Henry, 2006). CTD's are disseminated, epigenetic deposits dominantly hosted in Silurian-Devonian slope-facies silty carbonate units and concentrated along four regional lineaments (Figure 3.4) (see Hofstra & Cline, 2000; Cline et al., 2005 for review). Ore zones are characterized by decarbonatization, silicification, clay alteration, enrichment in certain trace elements, and fine-grained arsenian pyrite-hosted gold (Bakken & Einaudi, 1986; Simon et al., 1999; Hofstra & Cline, 2000; Lubben, 2004; Cline et al., 2005; Reich et al., 2005). Over brief intervals (<15–45 ka) between 42–30 Ma, ore-forming hydrothermal systems exploited preexisting high-angle zones of permeability and passively expelled fluids into reactive host rock units (Radtke et al., 1980; Hofstra et al., 1999, 2005; Hofstra & Cline, 2000; Ressel et al., 2000; Teal, 2002; Arehart et al., 2003; Chakurian et al., 2003; Yigit et al., 2003; Hickey et al., 2014a). In addition to being closely associated with Jurassic and Cretaceous igneous suites, many deposits are partially hosted by, adjacent to, or geophysically imaged above broadly synchronous Eocene igneous intrusions (Henry & Boden, 1998; Ressel et al., 2000; Bettles, 2002; Emsbo et al., 2003; Johnston & Ressel, 2004; Ressel & Henry, 2006).

Numerous geochemical characterizations of ore fluids in CTD's indicate or are permissive of a primitive magmatic fluid component. Although there is some heterogeneity between deposits, petrographic, lithochemical, fluid inclusion and stable isotope studies

of ore-stage minerals indicate a highly exchanged, mixed magmatic-meteoric origin for gold-bearing fluids (e.g. Cline et al., 2005). These reduced, mildly acidic aqueous fluids were entrapped at a temperature range of 180–240°C, and were characterized by low salinities (2–5 wt % NaCl), and low concentrations of CO₂ (<4 mol%), CH₄ (<0.4 mol. %), and H₂S (10⁻¹–10⁻² mol) (Lamb, 1995; Hofstra & Cline, 2000; Cline et al., 2005; Lubben et al., 2012). Hydrogen and oxygen stable isotope data indicate that magmatic ore fluids were progressively diluted by unevolved meteoric fluids over the lifespan of the hydrothermal system, while sulfur stable isotopes are permissive of either a sedimentary or magmatic sulfur source (Cline et al., 1997; 2003; 2005; Heitt et al., 2003; Lubben, 2004; Hofstra et al., 2005; Lubben et al., 2012).

3.3 EVIDENCE OF MAGMATIC-HYDROTHERMAL FLUID ACTIVITY

The HPP and surrounding wallrock units exhibit evidence of the progression from subsolidus magma to fluid saturation and exsolution to super and subsolidus hydrothermal activity. Features indicative of these stages within early and late stage intrusive units of the HPP are described here. Field descriptions of individual samples can be found in Appendix B; detailed petrographic descriptions can be found in Appendix D. The evidence of fluid activity in external wallrock units was investigated by Musekamp (2012) and is briefly summarized.

3.3.1 FLUID ACTIVITY WITHIN THE HPP

Detailed field study yielded a comprehensive characterization of the features associated with magmatic-hydrothermal transition of the HPP. Relevant field observations

made by previous studies are also included (i.e. Burton, 1997; Musekamp, 2012). Four types of orthomagmatic features (i.e. pegmatites and aplites), miarolitic cavities, five types of hydrothermal quartz veins, and five styles of hydrothermal alteration were recognized and sampled. Representative photographs and photomicrographs of feature types and hydrothermal alteration are included in Figures 2.7 and 2.8, respectively. Many exhibit close spatial relationships with other features, or are concentrated in specific intrusive units or near the roof zone of the intrusion.

3.3.1.1 PEGMATITES

Pegmatites are the crystallized equivalents of a fluid-saturated melt phase formed near the end of supersolidus intrusive activity, and thus represent one of the earliest observed indicators of fluid activity in the HPP (London, 2005). Two major types of pegmatites were documented in the HPP, and a third, less common, variety (Layered Aplite-pegmatite zones) is described below in Section 3.3.1.2.

Quartz-Feldspar Pegmatites – Coarse-grained (1–8 cm) crystalline zones containing only euhedral alkali feldspar and subhedral-anhedral quartz. These features can be found throughout the HPP, but are most common in late stage units. They may be planar or broadly anastomosing with inconsistent thicknesses.

Muscovite-Quartz-Feldspar Pegmatites – Coarse-grained (1–8 cm) crystalline zones containing alkali feldspar, quartz, muscovite ± garnet. These features are largely restricted to within and around the Tgm. They are similar in geometry to QF Pegmatites. However, abundant splays and books of muscovite are distinctive to this vein type. Rare euhedral Fe-Mg garnets (1–2 cm) also observed.

3.3.1.2 APLITES

Aplite veins and dikes are considered to form by the relatively rapid crystallization of a fluid-depleted, terminal melt phase along synplutonic fractures and dilatent zones. Aplite formation may occur in response to volatile exsolution from the melt (Candela, 1997; Kontak et al., 2002). Like pegmatites, aplites represent an early, orthomagmatic indicator of fluid activity.

Aplites (Texturally Homogeneous) – Fine-grained (1–3 mm), sucrosic, planar intrusions with characteristic quartz+alkali feldspar±muscovite±biotite±magnetite±garnet mineralogy. Although these features are present throughout most of the HPP, they are clustered in the Tcc, (where they exhibit subvertical dips), and in the Tmg, (where they exhibit moderate eastward dips).

Layered Aplite/Pegmatites – Subhorizontal, alternating zones (5–15 cm) of fine-grained (1–3 mm), sucrosic quartzofeldspathic rock and quartz-feldspar pegmatite (>2 cm). These features are also composed of characteristic quartz+alkali feldspar±muscovite±biotite±magnetite±garnet assemblage and are restricted to the structurally lower regions of the Tmg. Where present, garnet is restricted to pegmatite zones and biotite-rich transitions between zones.

3.3.1.3 MIAROLITIC CAVITIES

Miarolitic cavities are unequivocal evidence of magmatic fluid saturation and exsolution in igneous intrusions and most closely define the magmatic-hydrothermal transition (Candela, 1997). They are ellipsoidal to spherical cavities that are recognized by partial or complete filling by inward-directed euhedral crystals. These features are typically small (cross sectional area = <80 cm²) and dominated by euhedrally-terminated

(smoky) quartz (<1–4 cm) with minor alkali feldspar and muscovite. Most miarolitic cavities in the HPP are exposed within 1 km of the roof zone contact in the Tcc, and are typically individual, isolated features. However, one outcrop in the Tcc containing numerous interconnected miarolitic cavities was observed.

3.3.1.4 HYDROTHERMAL VEINS

Hydrothermal quartz veins crystallize from migrating aqueous fluids in brittle fractures in super and subsolidus magmatic systems (Jamtveit & Yardley, 1997). These veins were observed throughout the HPP, and have been subdivided based on crystallinity and volume. The two general categories are Quartz Veins (Types (I), (II), and (III)) and Microcrystalline Quartz Veins (Types (IV) and (V)).

Quartz Veins – Includes Type (I) minor (<1–5 cm) and Type (III) intermediate (5–35 cm), pure, translucent crystalline quartz veins with subhedral crystals and sharp boundaries hosted throughout the HPP. Crystal growth is perpendicular to vein margins. Weathering of disseminated sulfides and restricted vein selvages (2–5 cm) of coarse muscovite are observed in the wallrock of some samples, however no style of hydrothermal alteration is consistently associated with these veins. An additional type of crystalline quartz veins is recognized for those hosted in skarn/carbonate replacement deposits and other wallrock units (Type II). These veins vary greatly in thickness (0.5 to >150 cm), typically contain coarse subhedral-anhedral quartz, and often exhibit evidence of post-emplacement deformation.

Microcrystalline Quartz Veins – Includes pure, largely micro- to cryptocrystalline quartz veins ranging in thickness from 1–5 cm (Type (IV)), and 5–400 cm (Type (V)) hosted throughout the HPP. Quartz habit varies from massive and homogeneous to

complex, vuggy, sulfide-bearing, multi-zoned systems. Large Type (V)

Microcrystalline Quartz Veins (200–400 cm) dip steeply, crosscut all igneous and hydrothermal features, and may be traceable for 100s of meters along strike. Type

(V) Microcrystalline Quartz Veins are often associated with Type (IV)

Microcrystalline Quartz Veins, and zones of silicification and chlorite-sericite alteration. Type (IV) Microcrystalline Quartz Veins are observed as isolated features as well as in densely and chaotically veined outcrops in chlorite-sericite or phyllic-altered outcrops near Type (V) Microcrystalline Quartz Veins.

3.3.1.5 HYDROTHERMAL ALTERATION

Hydrothermal alteration results from disequilibrium between migrating hydrothermal fluids and surrounding rock, and is characterized by mineral replacement and growth. The following are field descriptions derived from field observations of several alteration zones and types within the HPP that have been recognized by this study and previous workers (Burton, 1997; Musekamp, 2012).

Potassic – Observed rarely in small (<4 m) pods in the pluton roof zone and in rhyodacite porphyry and granitic roof dikes. This alteration type is relatively mild and difficult to identify in the field, but is characterized by the locally pervasive addition of secondary biotite, K-feldspar, and sericite. Altered rock appears reddish grey with ubiquitous biotite needles (1–3 mm).

Phyllic – Observed primarily in the Tcc as discontinuous, localized zones (1–5 m wide) occasionally associated with Type (IV) and Type (V) Microcrystalline Quartz Veins, but also observed without nearby veins. Altered rock appears grey-green and is more easily weathered than its unaltered equivalent. This pegmatite type is

characterized by partial to complete replacement of feldspars and biotite by fine-grained white mica and coarse chlorite, respectively, and the addition of quartz and euhedral pyrite cubes (<1.5 mm). Phyllic alteration can be distinguished from chlorite-sericite alteration by the presence of pyrite and the larger grain size and lower abundance of chlorite.

Chlorite-Sericite – Typically restricted to localized zones (<5 m wide) consistently associated with Types (IV) and (V) quartz veins. Altered rock appears green to white with some crystal textures obscured and may be cohesive and hard or friable and powdery with varying degrees of silicification. Fine-grained aggregates of chlorite and sericite pervasively replace biotite and feldspars, respectively. Some secondary pore space from crystal dissolution is observed.

Silicification – Observed commonly in large, pervasive zones (<10 m wide) around Types (IV) and (V) microcrystalline quartz veins. Altered granites are resistant to weathering, appear bleached, and exhibit dense (cm-scale) microfracture patterns in which microcrystalline quartz has precipitated. This pegmatite type often overprints chlorite-sericite alteration.

3.3.2 FLUID ACTIVITY WITHIN THE CONTACT METAMORPHIC AUREOLE

Musekamp (2012) completed a detailed field and geochemical characterization of the fluid activity within contact metamorphic aureole surrounding the HPP. The following descriptions and subdivisions summarize the field observations made in that study and include relevant additions from this study. Observable features indicating the migration of fluids through the country rock, both on and away from the HPP contact, have been classified and subdivided based on mineralogy and locality type, which refers to the spatial

relationship with the HPP contact (on or away). The two main vein types of quartz veins (two locality types) and calcite veins (three locality types), and skarn/carbonate replacement alteration.

3.3.2.1 HYDROTHERMAL VEINS

Crystalline Quartz Veins – Quartz veins on and away from the HPP contact (equivalent to Type (II) (skarn) and (wallrock) Quartz Veins) are generally thin, (mm to <5 cm, with a maximum of <20 cm), with sharp contacts, and geometries varying from parallel to sheeted to branching. Quartz cement in fractured and brecciated limestone and granodiorite has also been observed near the HPP contact. Observed veins are thinner, less common, and are preferentially bedding-parallel with increasing distance from the HPP. Quartz veins have no consistent relationship with alteration zones.

Calcite Veins – Calcite veins on the HPP contact have been subdivided into Type A and Type B veins, while calcite veins away from the HPP contact have only been classified as being distal equivalents of Type A veins (Musekamp, 2012). Type A veins contain medium to coarse-grained calcite and are generally thinner than the quartz veins (mm to cm), with sharp contacts and no associated alteration. Type B veins have variable thicknesses, (mm to 50 cm), and are invariably located within skarn and carbonate replacement zones along the pluton margin and within roof pendants. Type B veins crosscut Type A veins, but have a mutually crosscutting relationship with quartz veins on the HPP contact. This vein type typically contains coarse calcite, quartz, and may locally host pockets of Pb, Zn, and Fe sulfides.

3.3.2.2 HYDROTHERMAL ALTERATION

Skarn/Carbonate Replacement – This type of wallrock alteration is present as irregular meter-scale bodies along the contact between the HPP and surrounding metacarbonate units and roof pendants. Skarn and carbonate replacement deposits along this contact were historically mined for a diverse suite of elements, (including W, Cu, Ag, Mo, Sn, Ca, Be, Bi, and Cd) (Klepper et al, 1944; Tingley, 1981a). The largest deposits in this district were exploited at the Star Mine (W) on the roof zone contact of the Tcc. Skarn alteration is typically associated with fractures and quartz or Type B calcite veins, and may be interlayered with less altered metacarbonate wall rock. In the field, this pegmatite type is characterized by partial to complete replacement of the carbonate host rock. Skarn mineral abundances vary by locality, but the typical mineralogy is diopside + calcite (+ epidote) (+ hydrogrossular) + tremolite + quartz + sericite + biotite/chlorite (\pm plagioclase) \pm magnetite \pm pyrite, (minerals in parentheses are major components in some, but not all skarn outcrops). Ore minerals observed are chalcopyrite, galena, scheelite, and heubnerite (this study), and sphalerite (Musekamp, 2012).

3.4 RESULTS

3.4.1 FLUID INCLUSION PETROGRAPHIC OBSERVATIONS

In this study, 43 quartz-bearing samples were prepared as double-polished (120 μm) thin sections (with three duplicates) for fluid inclusion petrography and microthermometry. The procedure for fluid inclusion petrography and sample preparation

can be found in Appendix A.1.1. Ten of these samples were also selected for stable isotope analysis (see Section 3.4.4). The diversity of orthomagmatic and hydrothermal features in the HPP is reflected in this sample set; samples represent the range of observed orthomagmatic and hydrothermal features in all early and late stage intrusive units. Of the 43 samples, 2 are from granitic rocks, 10 are from QF Pegmatites, 2 are from MQF Pegmatites, 4 are from Aplites, 1 is from a Mirolitic Cavity, 18 are from crystalline quartz veins (8 Type (I) Quartz Veins, 4 Type (II) (skarn) and (wallrock) Quartz Veins, 6 Type (III) Quartz Veins), and 6 are microcrystalline quartz veins (five Type (IV) Microcrystalline Quartz Veins, one Type (V) Microcrystalline Quartz Vein), (see Table 3.1). Petrographic descriptions of these igneous and hydrothermal features and petrographic as well as assessment of 124 fluid inclusion assemblages and their host crystals were recorded to aid in the interpretation of fluid inclusion composition, type, and timing, and to document any evidence of pre or post-entrapment deformation that may affect microthermometric and multi-element data. Detailed sample and fluid inclusion assemblage descriptions can be found in Appendix E.1. Annotated photo mosaics of microthermometry thin section samples (showing the locations of selected fluid inclusion assemblages) can be found in Appendix E.2. The geographic locations of these samples within the HPP are shown in Figure 3.5.

In this study, host minerals for fluid inclusions are strictly crystalline quartz crystals of igneous and hydrothermal origin. In igneous features, host quartz ranges from euhedral to subhedral in pegmatites (reflecting externally nucleated crystal growth), to anhedral in aplites, (reflecting internally nucleated crystal growth). In pegmatites, crystal morphology and inclusion relationships indicate a paragenetic sequence of initial muscovite growth (where present), followed by alkali feldspar growth, with contemporaneous and/or

subsequent quartz crystallization. In miarolitic cavities, quartz crystals are characteristically euhedral and directed towards the center of the cavity, which is indicative of externally nucleated crystal growth into open space. Type (I), (II) (skarn) and (wallrock), and (III) Quartz Veins exhibit anhedral-subhedral crystal morphology, with only local evidence for inward growth from vein walls. Microcrystalline material in Types (IV) and (V) quartz veins does not host primary fluid inclusions. Fluid inclusions observed in these veins are hosted in anhedral crystalline quartz clasts entrained in microcrystalline material, in fractured crystalline quartz with microcrystalline veinlets, or in discrete crystalline zones surrounded by microcrystalline quartz.

Recognition of the microstructural evidence of deformation of fluid inclusion-hosting quartz in many samples is important for assessing the quality of resulting microthermometric data. The most common microstructures observed in these samples are small, inclusion-free neoblasts along grain contacts, sutured or recrystallized grain contacts, and undulose extinction. Representative photomicrographs are included in Figure 3.6. Where present, these microstructures record high strain events that may have decrepitated or re-equilibrated primary fluid inclusions in affected grains. Primary fluid inclusions are rare in samples exhibiting strong, pervasive deformation (i.e. “ribbon” textures in quartz veins). In samples where evidence of deformation is minor, primary fluid inclusion assemblages were selected from largely unstrained areas, (often within the cores of deformed crystals). However, all microthermometric and multi-element geochemical data derived from deformed samples should be interpreted with caution.

Fluid inclusions were observed and classified according to the criteria of Roedder (1984). In this study, 69 primary fluid inclusion assemblages (representing a total

population of 294 individual fluid inclusions) were described at ambient conditions (~25 °C) and selected for microthermometry. Primary assemblages were observed in three petrographic groupings: (1) diffuse, relatively isolated 3-dimensional clusters, (2) planes within growth zones, and (3) isolated single inclusions. Representative photomicrographs are included in Figure 3.7. Group (1) primary assemblages are the most common, and have been observed in all igneous and hydrothermal features. These assemblages are spatially restricted (size and spacing), may be concentrated near the center of the host crystal, and typically consist of 2–8 individual inclusions. Group (2) assemblages are also common; these assemblages are recognized as diffuse, parallel planes (<30–50 μm wide) that terminate well within the host crystal. These assemblages may be parallel to the crystal boundaries and/or clearly outline the crystal shape during an earlier growth stage. Inclusions are closely spaced (10–20 μm apart) and are often aligned within these zones. Group (3) assemblages are uncommon, and are composed of single, usually ovoid/tabular, relatively large (15–30 μm) inclusions that are isolated from other assemblages and often located near the core of the host crystal.

Based on petrographic observations of internal phase relations and ratios and microthermometry, three compositional types of the 69 primary fluid inclusion assemblages have been recognized in these samples. Salient features of these three types are listed in Table 3.2 and described in more detail here. Representative photomicrographs of these types are included in Figure 3.8. Type (A) inclusions (comprising 35 primary assemblages), are relatively small (<5–20 μm), and contain only two phases (liquid and vapor) with a consistent degree of filling ($f_v = (L+V)/V$) of 0.93–0.97. Rarely, Type (A) inclusions contain three phases (crystalline solid, and liquid and vapor). Daughter solids

are small (<1% of inclusion volume), cubic, and interpreted to be accidental inclusions of NaCl or KCl. Type (B) inclusions are present in 21 assemblages and are relatively large (10–30 μm) and contain three phases (wetting liquid, non-wetting liquid, and vapor) with a heterogeneous f_v ranging from 0.85–0.95 (of which 0.02–0.06 is occupied by the non-wetting liquid). Type (C) inclusions are present in 13 assemblages, and typically appear to only contain two phases at ambient conditions, but on slight cooling reveal a third, non-wetting liquid. This type of inclusion is usually impossible to distinguish from Type (A) inclusions, except by microthermometry.

Pseudosecondary fluid inclusion assemblages are relatively uncommon in these samples; only 5 assemblages of this type were observed. These inclusions (identified as Group (4) assemblages) are observed on diffuse (30–50 μm) planes that terminate at or within the host quartz crystal, but crosscut primary growth zones. It is interpreted that they were trapped along fracture planes during stages of crystal growth. Internal phase relations and ratios indicate that one of these assemblages can be classified as Type (A), three as Type (B), and one as Type (C).

Secondary fluid inclusions, (those interpreted as likely trapped in post-crystallization crosscutting fracture planes) are more common than primary fluid inclusions in all igneous and hydrothermal samples, particularly in QF Pegmatite and Type (I), (II), and (III) Quartz Veins. Secondary fluid inclusions are observed exclusively along narrow planes (10–20 μm) that crosscut crystal boundaries, primary assemblages, and occasionally other secondary assemblages. However, only 52 of these assemblages were petrographically described. Microthermometry of these assemblages (identified as Group (5) assemblages) can provide information about the nature and conditions of the fluids

migrating through the HPP after cessation of primary igneous and hydrothermal activity. However, they are beyond the scope of this study and are only briefly described here. These inclusions are typically small (2–10 μm), two-phase (liquid and vapor), exhibit a high f_v (0.96–0.99), and bear the most similarity to Type (A) primary inclusions. However, five examples of three-phase secondary inclusions have been observed in crystalline and microcrystalline quartz veins, and bear the most similarity to Type (B) primary inclusions.

Several correlations between sample type, petrographic setting, assemblage type, inclusion size, and internal phase ratios amongst primary fluid inclusions have been observed and documented in this study. First, the highest concentrations of primary fluid inclusion assemblages of any grouping are found in Type (I) and Type (III) Quartz Veins. However, growth zone assemblages (Group 2) are more common in quartz from (M)QF Pegmatite zones. Second, as a percentage of all primary assemblages described for each vein type, CO_2 -bearing assemblages were most common in aplites (100% of samples); Type (I) Quartz Veins (76.5% of samples), and QF Pegmatites (50% of samples). Third, as noted earlier, there is a crude positive correlation between the relative volume of CO_2 and the size of the inclusion.

3.4.2 FLUID INCLUSION MICROTHERMOMETRY DATA

Microthermometry of fluid inclusions was conducted on 74 primary and pseudosecondary assemblages, (a total of 294 individual inclusions) from 33 samples to determine the thermodynamic parameters of igneous and hydrothermal fluid activity in the HPP. Analyses were performed on a Linkam THMS 600 stage attached to an Olympus BX-51 petrographic microscope. In addition to routine petrographic observations, the temperatures at which select phase changes occur were recorded during heating of

primary and pseudosecondary fluid inclusion assemblages from -100 °C to 350 °C (detailed methodology included in Appendix A.1.2). Measurements include the melting, eutectic, and homogenization points in the H₂O-(CO₂)-NaCl-(KCl) system in these assemblages. Raw and statistical presentation of measurements from all selected samples can be found in Appendix E.3. Densities, compositions, and isochores for all were calculated using the FLUIDS software packages (programs BULK and ISOC) developed by Bakker (2003) (see Appendix A.1.3 for detailed methodology).

Fluid inclusion microthermometry provides data about the thermodynamic conditions of fluid entrapment and some useful information about the chemical composition of fluids (i.e. major constituent phases, salinities). Tabulated fluid inclusion microthermometry data by fluid inclusion assemblage type are presented in Table 3.2. However, there are several key assumptions, limitations, and constraints on the data presented in this section that are either inherent to the methodology or a product of the experimental design. First, fluid inclusion microthermometry is dependent on the observations of often subtle phase changes. Thus, anomalous values may be the result of human error. In this study, a limited number of samples were collected from the field, and fewer still were selected for microthermometry. As a result, some areas of the HPP (i.e. the T_{tc} and the T_{gm}) and some feature types (i.e. granitic rocks, aplites, miarolitic cavities and Type (II) (wallrock) Quartz Veins) are incompletely or minimally represented in the data. Caution should be exercised in extrapolating regional patterns from microthermometry data derived from a small sample set. Population sizes for inclusions and assemblages within samples and feature types are included in all relevant tables. Furthermore, not all phase changes were observed within each assemblage, resulting in incomplete

characterizations. Caution should also be exercised comparison or interpretation of data in these cases.

3.4.2.1 FLUID INCLUSION ASSEMBLAGE COMPOSITIONAL TYPES

Raw microthermometry data for fluid inclusion assemblage compositional types can be found in Appendix E.3.5. Type (A) inclusions are the most common type of primary fluid inclusions observed in samples in the HPP and contain two phases (L+V) at ambient conditions. These inclusions are interpreted to be aqueous in composition. Mean values for microthermometry measurements are as follows: T_{eutectic} : -25 °C; T_{mice} : -1.6 °C; T_{tot} : ~230 °C. Mean salinity is 2.7 wt % eq. NaCl, with a range of 0–7 wt % eq. NaCl. Mean density is 0.8 g/cm³ with a range of 0.67–0.92 wt % eq. NaCl. Based on observed internal phase relations (including the rare occurrence of small, crystalline solids) and the range of observed eutectic points during heating, these inclusions are interpreted to belong to the H₂O-NaCl-KCl chemical system. Two populations of Type (A) inclusions are apparent from homogenization temperatures; the first consists of inclusions with T_{tot} values of >250 °C, and the second consists of inclusions with T_{tot} values of 180–250 °C (see Figure 3.9). Several categories of microthermometry measurements are similar for these two populations, but mean T_{tot} values for the first and second populations are ~280 °C and ~210 °C, respectively, demonstrating a clear division between them. Also, mean salinity for the second population is lower (2.5 wt % eq. NaCl) than the first population (3.2 wt % eq. NaCl), and mean density is higher for the second population (0.89 g/cm³) than the first population (0.79 g/cm³), (both with significant overlap in ranges).

Type (B) inclusions are the second most common type of primary fluid inclusions observed, and contain three phases (L1+L2+V) at ambient conditions. These inclusions are

interpreted to be aquo-carbonic in composition. For all microthermometry data, temperatures of homogenization of CO₂ (Th_{CO2}) are subdivided based on the state of the homogenized carbonic phase (i.e. vapor (v) or liquid (l)). Mean values for select microthermometric measurements are as follows: T_{mCO2}: -57.1 °C; T_{eutectic}: -24.6 °C; T_{mclathrate}: 7.7 °C; Th_{CO2}: 29.6°C (v), 28.8 (l); Th_{tot}: 293.3 °C. Concentrations of CO₂ range from 3.1 to 10.5 mol% with an average of 6.4 mol%. Mean salinity is 3.8 wt % eq. NaCl, with a range of 1.7–8.0 wt % eq. NaCl. Mean density is 0.9 g/cm³ with a range of 0.72–1.07 g/cm³. These inclusions are interpreted to belong to the H₂O-CO₂-NaCl-KCl system due to the characteristic depression of the eutectic melting point and the observed behavior of a second, non-wetting liquid phase. The means of the unimodal, normal populations of Th_{tot} and salinity for Type (B) inclusions are approximately the same as the first population of Type (A) inclusions. However, density values are higher for Type (B) inclusions than for Type (A) inclusions, with significant overlap in ranges.

Type (C) primary inclusions are the least common type of primary fluid inclusions observed, and appear to contain only two phases (L+V) at ambient conditions. These inclusions are also interpreted to be aquo-carbonic in composition. Mean values for select microthermometric measurements are as follows: T_{mCO2}: -56.9 °C; T_{eutectic}: -26.1 °C; T_{mclathrate}: 8.2 °C; Th_{CO2}: 31.0°C (v), Th_{tot}: 251.0 °C. Mean salinity is 3.4 wt % eq. NaCl, with a range of 1.1–8.1 wt % eq. NaCl. Mean density is 0.90 g/cm³ with a range of 0.68–0.98 wt % eq. NaCl. These inclusions are also interpreted to belong to the H₂O-CO₂-NaCl-(KCl) system, but typically lack a aquo-carbonic phase that is visible at ambient conditions. However, observations of CO₂ freezing and clathrate melting (7–10 °C) indicate a measurable quantity of CO₂ (mean: 1.9 mol%) (Schmidt & Bodnar, 2000). While several key similarities

exist between Type (C) and Type (B) inclusions (i.e. salinity and density), melting points for CO₂ are lower for Type (C) inclusions, whereas the eutectic points are higher. Although Th_{tot} values are slightly bimodal for these inclusions (populations at ~290 °C and ~230 °C), there exists a close correlation between the first (higher) population and the distribution of Th_{tot} values for Type (B) inclusions (see Figure 3.9).

3.4.2.2 ISOCHORE DATA

A total of 73 isochores were calculated for fluid inclusion assemblages representing most feature types using the ISOC program in the FLUIDS software suite developed by Bakker (2003). A detailed description of the numerical parameters used can be found in Appendix A.1.3, and raw isochore calculation data can be found in Appendix E.4. Isochore data was plotted separately in Excel by compositional assemblage type (Figure 3.10). Isochores for aqueous fluid inclusions are represented by solid lines, while aquo-carbonic inclusions are represented by dashed lines. Linear trendlines are estimates of mean isochores and are derived from the mean slope and y-intercept values of the plotted isochores. Also included are boxes (in black) representing a range of possible pressures and temperatures of entrapment bounded by a $\pm 50^\circ\text{C}$ error around the experimentally determined wet granite solidus curve (in red) and by the 10th and 90th percentiles within each population of isochores. The assumption that all fluids were entrapped within this temperature range follows previous studies of fluid activity in magmatic-hydrothermal systems (Candela, 1997; Audètat et al., 2003; 2008) and is supported by the relative similarity in isochore slope between different assemblage and feature types. Boxes are not included where populations are of insufficient size to generate these percentiles. Certain isochores are designated as outliers based on the distribution of Th_{tot} values, salinities, and

densities. These isochores are denoted by a series of circles and are not included in trendline calculations or Pt estimations. A summarized graphical representation of entrapment conditions for the three fluid inclusion compositional types is presented in Figure 3.11.

A population of 34 isochores of Type (A) inclusions demonstrates a normal distribution of slopes from 7.08 to 18.28 bar/°C, with a mean of 13.14 and no outliers (Figure 3.10a). Due to the unimodal population of isochore slopes, regardless of variation in Th_{tot} values, it is unlikely that these inclusions were entrapped at significantly disparate thermodynamic conditions. Assuming that fluids were entrapped within ~50°C above or below the approximate wet granite solidus temperature for both orthomagmatic and hydrothermal feature types, this range of proposed entrapment temperatures (Tt) is ~590–720°C for Type (A) inclusions indicates a possible Pt range of ~2800–7200 bar. Not only is there little variation in isochore systematics amongst Type (A) inclusions, there are only minor differences between them and Type (B) and Type (C) inclusions. Some type (A) inclusions may have been entrapped at lower pressures than Type (B) and (C) aquo-carbonic inclusions.

Ignoring one outlier, a population of 21 isochores of Type (B) inclusions demonstrates a generally normal distribution of slopes from 7.24 to 17.23 bar/°C with a mean of 12.39 (Figure 3.10b). Similar to Type (A) inclusions, Type (B) inclusions do not demonstrate any statistically significant groupings based on isochore slope. The range of proposed Tt temperatures is ~600–720°C for Type (B) inclusions. Thus, possible Pt values for this inclusion type range from ~3600–7600 bar. Although Th_{tot} values are generally

higher for aqueous inclusions than for aquo-carbonic inclusions, isochore slopes are nearly identical between assemblage types.

Due to the compositional similarity to Type B assemblages, isochores for Type C inclusions were also constructed based on an “any gas mixture + NaCl” system and utilizing the equation of state of Bowers & Helgeson (1983) and Bakker (1999) (Figure 3.10c). Ignoring two outliers, a population of 9 isochores of Type (C) inclusions demonstrates a narrow distribution of slopes from 11.87 to 15.26 bar/°C with a mean of 13.35. Type (C) inclusions also do not demonstrate any statistically significant groupings based on isochore slope. The range of proposed Tt temperatures is ~600–690°C for Type (C) inclusions. Thus, possible Pt values for this inclusion type range from ~4800–6600 bar. The relatively tight cluster of isochore slope values for Type (C) inclusions falls near the center of the distribution for Type (B) isochores, and may provide a tighter constraint on the pressure and temperature conditions at which the majority of aquo-carbonic inclusions were entrapped.

3.4.2.3 FEATURE TYPES

The sample population represents all 12 major types of orthomagmatic and hydrothermal features related to fluid saturation, exsolution, and migration in the HPP. This section provides a detailed comparison of microthermometric measurements (i.e. T_{mCO_2} , $T_{eutectic}$, T_{mice} , $T_{mclathrate}$, T_{hCO_2} , T_{htot}), calculated values (i.e. salinity, CO₂, density), and isochore results (i.e. isochore slope, and Tt and Pt) between these feature types. Compiled microthermometric data by feature type are recorded in Table 3.2, (raw data in Appendix E.3.3). Figure 3.12 contains scatter plots illustrating trends in microthermometry data between feature types. Isochore plots organized by feature type are presented in

Figure 3.13. Summarized entrapment conditions for feature types with sufficient data are presented in Figure 3.11.

Granitic Rocks – The population of five fluid inclusions assemblages analyzed by microthermometry from two unique samples of granitic matrix quartz includes both Type (A) and Type (B) inclusions. Interpretation of data from granite samples may be confounded by the fact that one sample contained exclusively Type (A) aqueous inclusions while the other contained Type (B) aquo-carbonic inclusions. Mean T_{eutectic} and T_{mice} values are similar to mean values for all Type (A) inclusions in the HPP, while mean T_{htot} values are significantly lower, and mean salinity and density values are higher. For Type (B) and (C) inclusions, mean T_{mCO_2} and T_{hCO_2} (l) (only homogenization of CO_2 to liquid was observed), T_{htot} , salinity, density, and CO_2 values are higher than the corresponding mean values for these data for all Type (B) and (C) inclusions. However, mean T_{eutectic} and $T_{\text{mclathrate}}$ values for these inclusions are lower than mean values for all aquo-carbonic inclusions in the HPP. Ignoring one outlier, the isochores for all fluid inclusion assemblages from granite samples are relatively steep (mean slope = 13.33 bar/°C), with calculated Pt values of ~4600–6400 bar.

(M)QF Pegmatites – The population of sixteen assemblages from the eight pegmatite samples (seven QF and one MQF) contains all three compositional types of inclusions. Although both assemblages from MQF Pegmatites contained measurable CO_2 concentrations, the relatively small population size may not necessarily be representative of all MQF pegmatite veins. For Type (A) inclusions from pegmatites, mean T_{eutectic} , T_{mice} , and salinity values are slightly lower, whereas T_{htot} , and density values are both higher than mean values for all aquo-carbonic inclusions. For Type (B) and (C) aquo-carbonic

inclusions, mean T_{mCO_2} , $T_{mclathrate}$, salinity, density, and CO_2 values are very similar to mean values for all aquo-carbonic inclusions. Mean $T_{eutectic}$ values are higher. The mean Th_{CO_2} (v) value for pegmatites are lower than mean values for all aquo-carbonic inclusions (only homogenization to the vapor phase was observed). Isochores for pegmatite assemblages exhibit a normal distribution, intermediate slopes (QF Pegmatite mean slope = 12.33 bar/°C; MQF Pegmatite mean slope = 13.13 bar/°C), and calculated overall Pt values of ~3000–7200 bar.

Aplites – The five fluid inclusions assemblages analyzed by microthermometry from matrix quartz in the three samples of different types of aplites (i.e. texturally homogeneous, QF-cored, layered QF Pegmatite) consisted of aquo-carbonic inclusions (Type (B) and Type (C)). Depending on the type of aplite, mean T_{mCO_2} , salinity, density, and CO_2 values may be above or below the corresponding mean values for these measurements. Mean $T_{eutectic}$ and $T_{mclathrate}$ values are generally higher. The mean Th_{CO_2} (v) value recorded is lower than the mean value, but is calculated from only two disparate measurements (only homogenization to the vapor phase was observed). Mean Th_{tot} values for the different types of aplites display a wide scatter. Pure and QF-cored aplites demonstrate significantly higher Th_{tot} values (<290°C) than the Layered Aplites/QF Pegmatites (~191°C). The two non-outlier isochores that could be calculated for aplites (from a QF-cored Aplite) are significantly shallower than isochores from all other feature types (mean slope = 8.22 bar/°C), indicating significantly lower densities and higher minimum Tt and Pt values (~2800–4400 bar).

Miarolitic Cavities – Two Type (A) and one Type (C) assemblages were recognized in the one analyzed sample from a miarolitic cavity. Type (B) inclusions are absent, indicating

relatively low CO₂ concentrations in this sample. Caution should be exercised in interpretation of these data due to the small sample size. However, since miarolitic cavities represent the conceptual (and possibly the chronological) bridge between orthomagmatic and hydrothermal fluid activity, appropriate comparison with other feature types is important for characterizing the overall evolution of the system. For Type (A) inclusions in this sample, mean T_{eutectic}, T_{ice} values are slightly to moderately lower than corresponding mean values for all Type (A) inclusions, while Th_{tot}, salinity, and density values are higher than corresponding mean values for all Type (A) inclusions. Compared to mean values for all aquo-carbonic inclusions, mean T_{mCO2} values for this sample are higher, mean T_{eutectic}, T_{mclathrate}, Th_{tot}, salinity, and CO₂ values are lower, and the mean density value is approximately the same. Th_{tot} values for all inclusions in this sample are lower than Type (I) and (II) (skarn) Quartz Veins, within the scatter of pegmatite samples, and higher than Type (II) (wallrock) Quartz Veins and Type (IV) Microcrystalline Quartz Veins. The mean isochore slope value for this sample is 12.15 bar/°C, which is very similar to QF Pegmatites and Type (I) and Type (II) (skarn) Quartz Veins. The calculated range of Pt values is ~4000–6400 bar.

Type (I) Quartz Veins – Although both were observed, Type (A) aqueous inclusions heavily outnumber the Type (B) and Type (C) aquo-carbonic inclusions in the 17 assemblages from the seven samples of Type (I) Quartz Veins. For Type (A) aqueous inclusions in these veins, T_{ice}, and density values exhibited lower mean values than the mean values of these measurements in all Type (A) inclusions in the HPP. This is consistent with Th_{tot} and salinity values being higher than mean values for these measurements in all Type (A) inclusions. T_{eutectic} values are very similar to mean values for all Type (A) inclusions. Salinity

values exhibit a wide scatter. For Type (B) and (C) aquo-carbonic inclusions, mean $T_{m_{CO_2}}$, $T_{eutectic}$, $T_{m_{clathrate}}$, Th_{CO_2} (v), salinity, and density values are all very similar to mean values for all aquo-carbonic inclusions. The mean Th_{CO_2} (l) value for this feature type is lower than the mean value for all aquo-carbonic inclusions. Only Th_{tot} and CO_2 values are significantly higher than mean values for all aquo-carbonic inclusions. Th_{tot} values for all inclusion compositional types for this vein type are among the highest for any feature type. The isochores for this feature type demonstrate a normal distribution, intermediate slopes (mean slope = 11.87 bar/°C), and produce the widest range of calculated Pt values (~3000–7600 bar).

Type (II) (skarn) Quartz Veins – Similar to Type (1) quartz veins, the six fluid inclusion assemblages in the three samples of Type (II) Quartz Veins in skarn deposits are dominated by Type (A) aqueous inclusions. For Type (A) inclusions, $T_{eutectic}$, $T_{m_{ice}}$, Th_{tot} values are higher than the mean values for these data for all Type (A) inclusions. Also, the mean salinity value is lower, and the mean density value is approximately the same as the corresponding mean values for these data for all Type (A) inclusions. $T_{eutectic}$, $T_{m_{ice}}$, and CO_2 values for Type (C) aquo-carbonic inclusions are lower than mean values for this type of inclusions. Mean Th_{tot} , salinity, and density values are higher than mean values for all aquo-carbonic inclusions. Isochores for this feature type are few, but demonstrate a generally normal distribution with two outliers. These isochores also have shallow slopes similar to miarolitic cavities and Type (I) Quartz Veins (mean slope = 11.34 bar/°C), but produce a relatively low range of calculated Pt values (~3400–5400 bar). It should be noted that the granite solidus may not be a useful estimate of temperatures of entrapment (T_t), due to a large range of documented temperatures for other skarn deposits (e.g. Meinert, 1992).

However, the similarity in slope and intercept values to isochores for other hydrothermal features and the clearly magmatic oxygen isotope value for one Type (II) (skarn) Quartz Vein provide support for its use.

Type (III) Quartz Veins – The population of 13 assemblages from four samples of Type (III) Quartz Veins contains both Type (A) aqueous and Type (B) aquo-carbonic inclusions, although aqueous inclusions are significantly more abundant. For Type (A) inclusions, $T_{m_{ice}}$ values are slightly lower and hence salinity is higher than mean values for all inclusions of this type. Mean $T_{eutectic}$ values are very similar to mean values for all Type (A) inclusions, while mean $T_{h_{tot}}$ and density values are higher than mean values for Type (A) inclusions. In Type (B) and (C) aquo-carbonic inclusions, $T_{eutectic}$ values are lower than mean values for all aquo-carbonic inclusions. Mean values for $T_{m_{CO_2}}$, $T_{m_{clathrate}}$, salinity, and density are very similar to mean values for all aquo-carbonic inclusions. Mean values for $T_{h_{CO_2}}$ (v & l) and CO_2 are higher than mean values for all aquo-carbonic inclusions in the HPP. Mean $T_{h_{tot}}$ values for aquo-carbonic inclusions in Type (III) Quartz Veins are also higher than mean values for all aquo-carbonic inclusions, and significantly higher than Type (A) inclusions in these samples. Isochores for Type (III) Quartz Veins demonstrate a normal distribution and similar slopes (mean slope = 13.09 bar/°C) to isochores from granite samples. However, they are slightly steeper than isochores from QF Pegmatites and other types of quartz veins and produce relatively high Pt values (4600–7600 bar), particularly compared to Type (II) (skarn) Quartz Veins.

Type (II) (wallrock) Quartz Veins – Although fluid inclusion assemblages are sparse in the two samples of Type (II) Quartz Veins in unmineralized metasedimentary wallrock, Type (A) or Type (B) inclusions are in total equal abundances in a population of three

assemblages. For Type (A) inclusions, mean T_{eutectic} values are similar to mean values for all Type (A) inclusions. Compared to mean values for all Type (A) inclusions, mean T_{mice} , salinity, and density values are significantly higher, while T_{htot} are significantly lower. For the one assemblage of Type (B) inclusions, the T_{mCO_2} value is approximately the same as the mean value for all aquo-carbonic inclusions, while T_{eutectic} , $T_{\text{mclathrate}}$, and CO_2 values are lower, and the T_{hCO_2} (v), salinity, and density values are higher. T_{htot} values for both aqueous and aquo-carbonic inclusions are the lowest of any feature type. Although only three isochores were calculated for this feature type, they are all significantly steeper than most other isochores (mean slope = 16.28 bar/°C), indicating lower minimum T_{t} values.

Type (IV) Microcrystalline Quartz Veins – The population of five assemblages from the three samples of Type (IV) Microcrystalline Quartz Veins contains almost exclusively Type (A) aqueous fluid inclusions, with only one aquo-carbonic assemblage analyzed in this feature type. For Type (A) inclusions, mean T_{eutectic} values are slightly higher, while mean T_{mice} and density values are significantly higher than corresponding mean values for these data for all Type (A) inclusions. Mean T_{htot} and salinity values are significantly lower than mean values for these data for all Type (A) inclusions. For the one assemblage of aquo-carbonic Type (B) inclusions, the mean T_{eutectic} value is significantly higher, while T_{htot} values are significantly lower than corresponding mean data for all aquo-carbonic inclusions. The mean T_{hCO_2} (v) value is only slightly higher than the mean value for all aquo-carbonic inclusions. Isochores from Type (IV) Microcrystalline Quartz Veins are similar in slope to Type (II) (wallrock) Quartz Veins (mean slope = 15.40 bar/°C), which is significantly steeper than isochores from other feature types. This is due to higher densities and lower T_{t} values.

3.4.2.4 SPATIAL AND TEMPORAL TRENDS IN MICROTHERMOMETRY DATA

Additional perspectives from which to compare HPP microthermometry data are based on distinctions between orthomagmatic and hydrothermal features related to fluid activity, between individual intrusive units, and between the early and late stage intrusive suites that comprise the pluton. The following sections describe microthermometric variation based on these criteria by presenting select scatter plots, isochore plots, and maps. See Table 3.2 for mean microthermometric data for orthomagmatic and hydrothermal feature types and intrusive units. See Figure 3.14 for maps illustrating spatial variation in T_{tot} and salinity values.

Comparison Between Orthomagmatic, Hydrothermal, and Post-Intrusion Hydrothermal Feature Types

Comparison between microthermometry data derived from the populations of fluid inclusions in orthomagmatic features and hydrothermal features also provides insight into the style and conditions of fluid activity during key junctures in the emplacement of the HPP (see Table 3.2). Orthomagmatic features, (defined as veins, structures, and crystal zones that form by crystallization from a magma), include granites, (M)QF Pegmatites, and all types of aplites. The population of 26 fluid inclusion assemblages from orthomagmatic features analyzed by microthermometry is comprised of 9 Type (A) assemblages, 8 Type (B) assemblages, and 9 Type (C) assemblages. Hydrothermal features, (defined as veins, structures, crystal aggregates, vugs, and alteration zones formed by fluids primarily derived from magmatic exsolution), include miarolitic cavities, Type (I), (II) (skarn), and (III) Quartz Veins. The population of 40 fluid inclusion assemblages from hydrothermal features is comprised of 20 Type (A) assemblages, 13 Type (B) assemblages, and 7 Type (C)

assemblages. The remaining feature types (Type (II) (wallrock) Quartz Veins and Type (IV) and (V) Microcrystalline Quartz Veins) can be genetically separated from the other hydrothermal feature types due to low mean $T_{h_{tot}}$ values and significantly steeper isochore slopes, indicating entrapment at lower temperatures (see Figures 3.13 and 3.15). The formation of these features may have been largely independent from the primary orthomagmatic-hydrothermal system represented by the other feature types and likely formed much later in the history of the HPP. Microthermometry measurements from these features are not included in calculations for mean values for the comparison between orthomagmatic features or in the comparison between intrusive units below. However, they are discussed in some detail at the end of this section.

Mean values for microthermometry measurements from fluid inclusion assemblages from orthomagmatic and hydrothermal features (further subdivided between aqueous Type (A) and aquo-carbonic Type (B) and (C) assemblages) demonstrate an inconsistent pattern of variation. For aqueous Type (A) inclusions, mean $T_{m_{ice}}$, and density values are higher in orthomagmatic feature types than in hydrothermal feature types. However, $T_{eutectic}$, $T_{h_{tot}}$, and salinity values are lower in orthomagmatic feature types than in hydrothermal feature types. For Type (B) and (C) aquo-carbonic assemblages, mean $T_{m_{CO_2}}$, $T_{m_{clathrate}}$, and density values are similar between orthomagmatic and hydrothermal feature types, while mean $T_{eutectic}$, $T_{h_{CO_2}}(v)$, and salinity values are higher in hydrothermal feature types than in orthomagmatic feature types. The opposite is true for mean $T_{h_{CO_2}}(l)$, $T_{h_{tot}}$ and CO_2 values. Isochores for orthomagmatic features have an average slope value of 13.29 bar/ $^{\circ}C$, and a unimodal Pt range of ~ 3600 – 7100 bar, with a mode of ~ 5200 bar. Isochores for hydrothermal features (excluding Type (II) (wallrock) Quartz Veins and Type

(IV) Microcrystalline Quartz Veins) display a generally similar average slope value of 12.70 bar/°C, but a non-normal distribution of calculated Pt values (~3200–6800 bar) with no apparent modal value (Figure 3.15, Figure 3.16).

Fluid inclusions from post-intrusion hydrothermal feature types demonstrate generally distinct microthermometry values from the orthomagmatic and hydrothermal feature types. Type (A) assemblages are generally vapor-poor, and demonstrate lower salinities and $T_{h_{tot}}$ values than inclusions of this type in orthomagmatic and hydrothermal feature types. Aquo-carbonic assemblages are also relatively vapor-poor, and have lower $T_{eutectic}$, $T_{m_{clathrate}}$, and $T_{h_{tot}}$ values and lower CO_2 concentrations than corresponding assemblages in orthomagmatic or hydrothermal feature types. However, densities and salinities are slightly higher than corresponding values for orthomagmatic and hydrothermal feature types. Isochores for all fluid inclusion assemblages from post-intrusion hydrothermal feature types are significantly steeper (mean slope: 16 bar/°C) than isochores from orthomagmatic and hydrothermal feature types (Figure 3.15C). Although entrapment conditions for this group of feature types cannot be calculated using the wet granite solidus curve, they can be estimated using the minimum Pt values for hydrothermal feature types (~3200 bar), yielding Tt values of ~310–400 °C.

Comparison Between Intrusive Units

Although the possibility exists that orthomagmatic and hydrothermal features may not necessarily originate from their host intrusive units, field observations of veins and crystal zones with exposed strike lengths greater than ~10 m are almost nonexistent. Furthermore, descriptions and distributions of orthomagmatic and hydrothermal features indicate a significant difference in the styles of fluid activity between early and late stage

intrusive units (see Chapter 2 for full descriptions and discussion). Thus, it is appropriate to assume that the microthermometric data generated for each sample are reflective of the chemical compositions and the thermodynamic conditions of the surrounding intrusive unit. Scatter plots of $T_{h_{tot}}$ vs. salinity for intrusive units are included in Figure 3.12.

Compiled isochore plots for early and late stage fluid inclusion assemblages are displayed in Figure 3.17. Compiled mean and raw microthermometry data for intrusive units can be found in Table 3.2 and Appendix E.3.4, respectively.

Ttc – A relatively small population of three assemblages (two Type (A) and one Type (B); each containing only one inclusion) was analyzed by microthermometry for three samples from the early stage *Ttc* granodiorite. It should be noted that due to the limited sample size, the microthermometric data from the *Ttc* are not conducive to statistically significant comparisons with data from other intrusive units. For Type (A) inclusions in the *Ttc*, the mean $T_{eutectic}$ value is the lowest of any inclusion type in any of the intrusive units in the HPP. The mean $T_{m_{ice}}$ and density values are within the range of other units. The mean $T_{h_{tot}}$ and salinity value for the Type (A) inclusions is lower than the late stage units, but is only slightly higher than the corresponding mean values for the *Tcc*. For the single Type (B) inclusion, the measured $T_{m_{CO_2}}$ and $T_{m_{clathrate}}$ value is low compared to mean values for other units and the range observed in the *Tcc*, but is within the range of the *Tmg* and *Tgm* units. The $T_{eutectic}$ and $T_{h_{CO_2}}$ (v) values are within the range for aquo-carbonic inclusions from other units. The $T_{h_{tot}}$, salinity, density, and CO_2 values for this single inclusion are also within the range for other units. Although the population of isochores for this unit is too small and widely scattered to make an independent *Pt* estimate, it is within the scatter of *Tcc* isochores.

Tcc – A population of 16 assemblages (14 Type (A), and two Type (B); a total of 79 inclusions) was analyzed by microthermometry for 8 samples from the early stage *Tcc* monzogranite. For aqueous Type (A) inclusions, the mean T_{eutectic} and T_{mice} values are the highest of any of the intrusive units for this inclusion type. The mean T_{htot} and salinity values for Type (A) inclusions are the lowest for this type of inclusions in any intrusive unit. For aquo-carbonic Type (B) and (C) inclusions, the mean T_{mCO_2} value is similar to values for the *Tmg* and *Tgm*, but is higher than values for the *Ttc*. The mean T_{eutectic} , T_{mice} , T_{htot} , and CO_2 values for aquo-carbonic inclusions are the lowest for this inclusion type in any intrusive unit. However, the mean T_{htot} value is similar to the T_{htot} value for aqueous inclusions in this unit. Mean $T_{\text{mclathrate}}$, T_{hCO_2} (v), and salinity values for these inclusions in the *Tcc* are similar to aquo-carbonic inclusions in other units. The mean density value for aquo-carbonic inclusions in the *Tcc* is higher than mean values for any inclusion type in any intrusive unit. Isochores from the *Tcc* demonstrate a bimodal distribution of calculated P_t values based on the intersection with the wet granite solidus. The range of P_t values for these two populations are ~3400–4800 bar and ~5200–6800 bar with modal values of ~4100 and ~6000 bar, respectively.

Tmg – A relatively large population of 41 assemblages (13 Type (A), 16 Type (B), 12 Type (C); a total of 155 inclusions) was analyzed by microthermometry for 17 samples from the late stage *Tmg* monzogranite. For Type (A) inclusions, the mean T_{eutectic} and T_{mice} values are the highest for any inclusion type in any intrusive unit. The mean T_{htot} value is higher than both early stage units, but is lower than the single T_{htot} value for the *Tgm*, (although this may be a product of the small population size for the *Tgm*). The mean salinity and density values are within the range of other units. For Type (B) and (C) aquo-carbonic

inclusions, the T_{mCO_2} value is very similar to the mean values for other intrusive units, except for the T_{tc} , (which is lower). The mean $T_{eutectic}$ value is higher than the T_{cc} and T_{mg} , but is the same as the T_{tc} . The mean $T_{mclathrate}$ and T_{hCO_2} (v & l) values are higher than the corresponding mean values for other intrusive units. The mean T_{htot} values are within the range of mean values for other aquo-carbonic inclusions, but it should be noted that it is significantly higher than the mean value for the early stage T_{cc} . Mean salinity and density values are also within the range of corresponding mean values for aquo-carbonic inclusions in other intrusive units, although the mean salinity value is similar to the T_{gm} , but is lower than both early stage units. A normal, unimodal population of isochores yield a calculated range for P_t for this unit of $\sim 4800\text{--}7600$ bar, with a modal value of ~ 6200 bar.

Tgm – A relatively small population of six assemblages (one Type (A), five Type (B); a total of 25 inclusions) was analyzed by microthermometry for three samples from the late stage T_{gm} two-mica monzogranite. Similar to the T_{tc} microthermometry data, caution should be exercised in making comparisons with other intrusive units due to the limited population size, particularly for Type (A) inclusions. For the single Type (A) aqueous inclusion, the $T_{eutectic}$, T_{mice} values are within the range of other units. The values for T_{htot} and salinity are higher than the corresponding mean values for Type (A) inclusions in other intrusive units, but are still within the ranges. Conversely, the density value for the single Type (A) inclusion in the T_{gm} is lower than corresponding mean values for other intrusive units, but is also still within the ranges. For the population of Type (B) aquo-carbonic inclusions, the mean T_{mCO_2} , $T_{eutectic}$, $T_{mclathrate}$, density, and CO_2 values are within the range of other units. The mean T_{hCO_2} , However, it should be noted that the mean salinity value is similar to the other late stage unit (T_{gm}), but is lower than salinity values for both early stage units. The

mean Th_{CO_2} (v & l) values are lower than the mean values for aquo-carbonic inclusions in other intrusive units, while the mean Th_{tot} value is higher. Although the population of isochores for this unit is too small and widely scattered to make an independent Pt estimate, it is within the scatter of Tmg isochores.

Comparison Between Early Stage and Late Stage Intrusive Units

Microthermometry data from the early stage intrusive units demonstrates several key characteristics and trends that illustrate key similarities and differences from late stage units (see compiled mean microthermometry data in Table 3.2). Aqueous Type (A) inclusions are in much higher abundances in early stage units than aquo-carbonic Type (B) and (C) inclusions, representing 22 of the 27 assemblages. Conversely, aquo-carbonic Type (B) and (C) inclusions are much more common in late stage units, representing 33 of the 47 assemblages. However, mean CO_2 values for aquo-carbonic inclusions are only slightly higher in late stage units than early stage units.

Compared to data for corresponding inclusion types in late stage units, mean Tm_{CO_2} and $Tm_{clathrate}$ values are lower, while the mean Th_{CO_2} (v) value are higher for early stage Type (B) and (C) inclusions. Only CO_2 homogenization to vapor was observed in early stage inclusions, while homogenization to vapor and liquid was observed in late stage inclusions. Mean $T_{eutectic}$ and Th_{tot} values are lower for all inclusion types in early stage units than the mean values for corresponding inclusion types from late stage units. However, mean Tm_{ice} and density values are higher for all inclusion types in early stage units than in late stage units. Comparison of salinity values is less straightforward: mean salinity values are lower for Type (A) inclusions and higher for Type (B) and (C) inclusions in early stage units than corresponding mean values in late stage units. The bimodal population of early stage

assemblages has a calculated Pt range of ~3400–6800 bar, with modes at ~4200 bar and ~6000 bar. Late stage assemblages have a generally unimodal population (~4800–7600 bar) (range of T_{mg}). The mode of Pt values for the normal late stage population (~5200 bar) is between the modes for the early stage population (see Figure 3.16).

3.4.3 MULTI-ELEMENT GEOCHEMISTRY

To determine multi-element compositions of fluid inclusions in igneous and hydrothermal quartz in the HPP, LA-ICP-MS analyses were conducted on inclusions in 18 sample chips that were previously characterized by petrography and microthermometry. Quartz from two of these samples was also analyzed for oxygen stable isotopes (see Section 3.4.4). This sample suite consists of one sample of granitic rock, three QF Pegmatites, one MQF Pegmatite, two Aplites, two samples from a Mirolitic Cavity, three Type (I) Quartz Veins, one Type (II) Quartz Veins, three Type (III) Quartz Veins, and two Type (IV) Microcrystalline Quartz Veins. Location data, brief descriptions, and select microthermometry data can be found in Table 3.3.

LA-ICP-MS analyses were performed at the USGS Crustal Geophysics and Geochemistry Science Center under the supervision of Erin Marsh and Alan Koenig. Inclusions were selected based on size, optical clarity, and petrographic setting. Due to optical and analytical constraints of LA-ICP-MS methodology, large inclusions (typically >10 μm) were preferentially selected for analysis. Between 5 and 12 individual inclusions were ablated on each sample chip, typically with each inclusion representing a different fluid inclusion assemblage in order to assess homogeneity of inclusions within the sample. Annotated photomicrographs of analyzed fluid inclusions are included in Appendix F.1.

Instrument calibrations were performed using NIST610 and NIST612 glass standards.

Analytical procedures are described in detail in Appendix A.2.1.

In these analyses, 26 elements (including two isotopes for Ca, Fe, and Zn) were selected for detection (atomic weights of each isotope): Li (7); B (11); Mg (24); Al (27); Si (29); Cl (37); K (39); Ca (43) (44); Fe (54) (57); Co (59); Ni (60); Cu (65); Zn (66) (68); As (75); Rb (85); Sr (88); Mo (95); Ag (107); Sn (118); Sb (121); Cs (133); Ba (137); La (139); W (192); Pb (208); Bi (209). However, only the 15 following elements were detected in a significant fraction (>~40%) of analyzed inclusions: Li, B, Al, Cl, K, Ca (44), Fe (54), Ni, Cu, Zn (68), Rb, Sr, Sn, Cs, and Pb. Data reduction procedures in Iolite (v3) are described in Appendix A.2.2. Limits of detection vary between inclusions as well; concentrations below limits of detection were discarded. One sample (HPP-3-15) contained exceptionally large inclusions (20–40 μm) and permitted quantification of elements not detected or not present in the majority of analyzed inclusions.

3.4.3.1 FIRST PASS RESULTS

An initial qualitative inspection of analytical spectra for the >175 analyzed inclusions revealed elemental associations and relative abundances that focused further data reduction and eventual calculation of concentrations for select inclusions with “high quality” spectra. Analytical spectra for all 111 inclusions that contained a Na anomaly of any kind were described. This “first pass” is useful for the presentation of multi-element data because it provides a link between the quantitative data generated from the 31 inclusions with “high-quality” spectra (i.e. those with pronounced, non-transient Na peaks that correlate well with other elements) and the other 80 inclusions which yielded spectra that were rejected for various reasons (i.e. transient or abnormal Na peaks, presumed

interference from sample chipping, or simultaneous analysis of mineral inclusions). Furthermore, the “first pass” includes observations of anomalous elements that may be present, but unique to a certain feature type or locality. However, these observations are fundamentally qualitative and useful primarily for determination of basic elemental relationships between different analyzed inclusions. “First pass” data (including analytical notes, spectral observations, and lists of elements closely and possibly associated with Na) are included in Appendix F.3).

In addition to identification of the 37 inclusions with high quality spectra and readily apparent elemental associations, several key trends can be recognized from “first pass” observations. First, it is observed that relatively few trace element species were detected in samples from granites, aplites, miarolitic cavities, and Type (IV) Microcrystalline Quartz Veins. In fact, two samples (HPP-1-20 and HPP-1-36a) show little indication that any trace elements are present in detectable abundances within their fluid inclusions. Conversely, (M)QF Pegmatites and Type (II) (skarn) Quartz Veins, are observed to contain the highest abundances and most diversity of trace element species. Second, it is obvious that peaks of Li, B, Cs, Rb, Sr, are most commonly observed with Na in analytical spectra across assemblage types, feature types, and samples. Third, although potassium peaks are occasionally observed in spectra from other samples, they are significantly more intense in HPP-3-15, (which may be due the significantly larger size of inclusions in this sample). Where K peaks are correlated with Al, it is likely that this signals the ablation of a mineral inclusion. Lastly, the most common ore metals observed are Pb and Cu, (although Sn and W are observed more rarely).

3.4.3.2 MULTI-ELEMENT DATA

Multi-element geochemical data for 13 elements from selected “high-quality” analyzed inclusions is presented in Figure 3.18, where it is organized by fluid inclusion compositional type. Raw multi-element data for all analyzed inclusions can be found in Appendix F.2.1. In addition to sodium concentrations calculated from microthermometry, values for lithium, boron, potassium, iron (57), nickel, copper, arsenic, rubidium, strontium, tin, cesium, and lead are selected due to several factors, including frequency, abundance, and relevance to hydrothermal ore deposits. Elemental concentrations are divided by sample and feature type. Data for most elements contain outlier values, although varying limits of detection indicate that certain concentrations within the analytical scatter may also not be meaningful. Generalized descriptions for the multi-element data from the host quartz and the results of a qualitative subtraction from inclusion data are presented in Section 3.4.3.5. Although several individual inclusions produced anomalous data for numerous elements, the compositions of most inclusions are generally homogeneous with regards to the element groups summarized here. However, a number of relatively minor trends and relationships are apparent that can provide information about the fluid history of the HPP. Due to the general homogeneity in multi-element data, the inconsistent detection of certain elements, and the relatively large number of different feature types in this dataset, only select, significant trends and associations in element concentrations between feature types will be presented in this section.

Major Elements

Na, K: Sodium and potassium are the most and second most abundant cations, respectively, detected in samples from the HPP. Sodium concentrations were determined from salinity

values (wt % eq. NaCl) calculated from microthermometric measurements (see Section 3.4.2 and Appendix A.1.3 for description of salinity calculations) and were used as the internal standard in the concentration calculations performed in Iolite (see Appendix A.2.2 for description of data reduction procedures). With the exception of one outlier (HPP-2-62), sodium concentrations are generally similar between feature and assemblage types (~8000–11000 ppm). Potassium concentrations are consistently lower (~500–3000 ppm) if three anomalously high values are ignored (LOD: 10–180 ppm). As noted in section 3.4.3.1, potassium is slightly higher in one QF Pegmatite sample (HPP-3-15) than other samples, while it is not detected in the single MQF Pegmatite sample (HPP-3-01b).

Molar K:Na ratios (displayed in Table 3.8) range from 0.01 to 0.19, with three anomalously high values of 0.79, 1.48, and 3.10 (which can be discarded) (Table 3.4). The K:Na geothermometer of Fournier & Truesdel (1973) can be used to postulate the mineral assemblage that equilibrated with a given fluid up to temperatures of ~350 °C, although studies by Orville (1963) and Rusk et al. (2004) allow the applicable temperature range to be extended. However, calculated ratios are only qualitatively useful here due to inconsistencies in these studies and the relatively small population size in this study. There exists no distinguishable correlation between K:Na molar ratios and T_{tot} values. The highest K:Na ratio calculated within the normal distribution (0.19) belongs to a Type (A) aqueous inclusion from a miarolitic cavity, while the second highest value (0.13) belongs to a Type (B) aquo-carbonic inclusion in a Type (I) Quartz Vein. Some of the lowest K:Na ratios were calculated for the two inclusions from aplite samples, while QF Pegmatite samples exhibited the widest spread of ratios. No other strong correlations between K:Na ratios and other characteristics or data were observed.

Ca: Although calcium (43) and (44) were detected in many analyzed inclusions, the two orders of magnitude spread in concentrations (1000–600000 ppm) appears spuriously large, particularly because of the low crustal abundances of these isotopes relative to Ca (40). This extreme variation is likely due to high limits of detection (LOD: 5000–50000 ppm) and the occasional analysis of mineral inclusions.

Fe, Mg: Iron (57) and magnesium are present in concentrations of ~200–800 ppm and <200 ppm, respectively, in approximately a quarter to a third of analyzed inclusions (Fe (57) LOD: ~20–400 ppm; Mg LOD: 1–40 ppm). Two samples (one miarolitic cavity and one Type (III) Quartz Vein) yield significantly higher concentrations (1300 ppm and 1800 ppm) for iron (57), in addition to one clearly anomalous value that is greater by two orders of magnitude. Iron is also not detected in Type (I) Quartz Veins. Magnesium is most common in inclusions from QF Pegmatite samples. There are two anomalously high magnesium values from a miarolitic cavity (5700 ppm) and a QF Pegmatite (1300 ppm).

Minor & Trace Elements

B: Boron is present in many analyzed inclusions in typical abundances of 80–1100 ppm, although outlier values up to two orders of magnitude higher have been recorded in some samples (LOD: 60–200 ppm). Boron is notably absent from all but one inclusion in one heavily analyzed QF Pegmatite sample (HPP-3-15). Of all feature types, miarolitic cavities display the highest boron concentrations.

Li: Lithium is a minor element that is observed in almost all analyzed inclusions in typical abundances of ~100–1000 ppm with few outliers (LOD: 1–35 ppm). Lithium values are remarkably similar across all samples, regardless of feature type, location, or assemblage type. The only exception is the one inclusion analyzed from HPP-2-10, which yielded an

anomalously low lithium concentration of 21 ppm. However, the ease with which this element diffuses through the crystal lattice of host quartz suggest that the concentrations detected for this element are not representative of the original magmatic-hydrothermal fluids.

Rb, Sr, Cs: The minor lithophile elements rubidium, strontium, and cesium were detected in consistent concentrations of <100 ppm in most analyzed inclusions (LOD: 1–5 ppm). For the majority of inclusions, cesium is present in the highest abundances, but no clear relationship between rubidium and strontium was observed. Concentrations of these elements were slightly, but consistently lower in aplites and Type (I) Quartz Veins than in other feature types. The results of calculated Na:Cs, K:Cs, and Rb:Cs molar ratios as indicators of magmatic fractionation are presented in Section 3.4.3.6.

La: Lanthanum was only rare earth element that was analyzed for in these samples (LOD: 0–1 ppm). However, it was detected rarely and in very low concentrations (<6 ppm), except for one outlier that yielded 140 ppm, (which may indicate a mineral inclusion).

Ore & Related Elements

Cu: Copper was detected in 13 of the 37 analyzed inclusions, (representing all seven analyzed feature types) in typical concentrations of ~50–150 ppm (LOD: 1–65 ppm). However, two outliers of 450 ppm and 410 ppm were also detected in a miarolitic cavity and a Type (III) Quartz Vein, respectively. No consistent relationship was observed between copper concentrations and other ore and related elements or feature types.

Pb: Curiously, lead is present in 12 of the 37 analyzed inclusions in typical abundances of <30 ppm (LOD: 0–22 ppm). Two outlier inclusions yielded Pb concentrations of 61 ppm and 900 ppm, from two different samples of Type (III) Quartz Veins. However, the second

value is likely spurious due to significantly lower concentrations detected in other inclusions from the same sample. Also, detected concentrations for Pb are generally lowest in QF Pegmatites.

Sn: Tin is consistently the most common and abundant ore element detected in samples from the HPP. Concentrations range from 10 to 1000 ppm (LOD: 5–350 ppm), with the lowest values observed in the QF Pegmatite sample HPP-3-15 and in Type (I) Quartz Veins. However, some of the highest tin concentrations were detected in other QF Pegmatite samples. Due to the consistent detection of tin in the host quartz (see Section 3.4.3.5), it is interpreted that the fluid inclusions contained little, if any, of this element.

As: Arsenic, an element of interest due to its association with numerous ore deposit types, was detected in 12 of the 37 analyzed inclusions in typical abundances of ~50–250 ppm (LOD: 0–60 ppm). However, no clear correlation between arsenic concentrations and feature type, location, or assemblage type was observed, (although it should be noted that arsenic was below the limit of detection in both analyzed inclusions from the Tgm).

Other Ore Elements (Ni, Zn, Mo, W, Ag, Bi)

Other ore elements were detected in several analyzed inclusions, but did not demonstrate any systematic variation. Nickel and zinc (66) were among the most common metals detected in HPP samples (present in ~25% of analyzed inclusions). These elements exhibit ranges of ~50–700 ppm, with several extreme (likely spurious) outliers (LOD: 5–500 ppm). Molybdenum, tungsten, silver, and bismuth were all detected in concentrations of <50 ppm in several inclusions from a variety of samples, but no relationship was observed between these elements (LOD: 0–10 ppm). Predictably, two inclusions from Type (II) (skarn) Quartz Veins yield the highest tungsten concentrations (28 and 41 ppm), while

the other two inclusions with measurable tungsten values originated from QF Pegmatites. The highest value for silver detected in these samples (18 ppm) was also from the same Type (II) (skarn) Quartz Vein that yielded measurable concentrations of copper, arsenic, tungsten and bismuth. The highest value for bismuth was also detected in an inclusion from another Type (II) (skarn) Quartz Vein sample.

3.4.3.3 BACKGROUND QUARTZ COMPOSITIONS

Subtraction of the “background” values for elements in host quartz from fluid inclusion data and is important for establishing the true compositions of fluid compositions (see Heinrich et al., 2003). Host quartz compositions are shown in Figure 3.19, and raw multi-element data can be found in Appendix F.2.2. Lithium, magnesium, silicon, potassium, and tin are consistently present in significant abundances (>1 ppm) in these inclusions. Lithium and tin are invariably present in abundances of 4–12 ppm and 3–9 ppm, respectively (LOD: 1–9 ppm). However, examination of the analytical spectra reveals no corresponding increase in tin counts during ablation of inclusions. Potassium and magnesium are detected in some analyses in abundances of 10–50 ppm, (with several outliers). Magnesium was not detected in quartz in all aplites and Type (III) Quartz Veins, all but one Type (II) (skarn) Quartz Veins, and some (M)QF Pegmatites and all aplites. Potassium also is absent from all Type (III) Quartz Veins and some (M)QF Pegmatites. Potassium concentrations are also lower in Type (II) (skarn) Quartz Veins than other vein types. Boron and iron (57) are also included in Table GG, but were only detected in two analyses. Rubidium, strontium, and cesium were detected in numerous analyses, but in very low abundances (<1 ppm) and are not included (LOD: 0–0.2 ppm).

While a quantitative subtraction of multi-element concentrations in host quartz from fluid inclusion concentrations is not viable due to uncertainty in the mechanics of simultaneous ablation of inclusions and quartz, a qualitative assessment of “background” values is useful for estimating the quality of data generated by these analyses. The most important comparisons are that of lithium and tin, which, due to the lack of variability of analytical counts during ablation, indicates that much, if not all, of the calculated concentrations of these elements originate from host quartz. Also, based on variability in analytical spectra, up to ~5% of measured potassium concentrations in fluid inclusions may also originate from host quartz.

3.4.3.4 SPATIAL AND TEMPORAL COMPOSITIONAL TRENDS

Assemblage Types

Again, due to the overall homogeneity of multi-element data, the inconsistent detection of several elements, and the limited sample size, few, if any, significant correlations between element abundances and assemblage type (i.e. Type (A), (B), or (C)) were observed (see Figure 3.18). Potassium values are typically slightly lower in Type (B) and (C) aquo-carbonic assemblages (~800–1200 ppm) than in Type (A) aqueous assemblages (~1000–5000 ppm), whereas lead (when detected) was typically higher (>10 ppm vs. <10 ppm). The minor lithophile elements strontium and cesium are generally higher in Type (A) aqueous assemblages (Sr: >6 ppm; Cs: >12 ppm) than in Type (B) and (C) aquo-carbonic assemblages (Sr: <6 ppm; Cs: <12 ppm). In fact, strontium is notably absent from many aquo-carbonic assemblages.

Na:Cs, K:Cs, and Rb:Cs molar ratios have been demonstrated as a viable indicators of magma fractionation in intrusive systems, characterized with smaller values (due to

increased Cs) in the more highly fractionated components of a magmatic suite (Audétat et al., 2008). These ratios are used here to describe the relative degrees of fractionation for the different fluid inclusion types, (correlation with the fractionation of host intrusive units is discussed in Section 3.5.5.2). See Table 3.4 for a compilation of relevant element ratio data. Na:Cs ratios range from ~132 to ~72750 (mean: ~7085), K:Cs ratios range from ~7 to ~8444 (mean: ~970), and Rb:Cs ratios range from ~0.1 to ~11 (mean: ~2). The aggregated multi-element data reveals higher mean Na:Cs and K:Cs molar ratios for the aquo-carbonic fluid inclusion assemblages (Type (B) and Type (C) inclusions) than for aqueous assemblages (Type (A) inclusions). Mean values for Rb:Cs molar ratios between inclusion types were similar.

Igneous and Hydrothermal Features

Only two minor trends were observed during comparison between multi-element data from orthomagmatic and hydrothermal features (Figure 3.20). Boron was detected with more frequency in hydrothermal features, and strontium concentrations may be slightly higher in orthomagmatic features than in hydrothermal features. However, these trends are neither consistent nor compelling.

Intrusive Units

Due to the very small populations of analyzed inclusions for the Ttc and Tgm units, comparison of multi-element data between intrusive units will be based only on comparison of early (Ttc and Tcc) and late stage (Tmg and Tgm) units (Figure 3.21). The only trends observed in the raw multi-element geochemical data are that boron and cesium concentrations appear to be in slightly higher concentrations in early stage units. The range of calculated K:Cs molar ratios in all analyzed fluid inclusions (~7 to ~8444) demonstrates

consistently lower values in the late stage units (mean: ~ 56) than in the early units (mean: ~ 256). A similar trend is observed in Na:Cs molar ratio values, which are also generally lower in the later stage units (mean: ~ 1014) than in the early stage units (mean: ~ 972). However, the difference between mean values for calculated Rb:Cs molar ratios from early stage intrusive units (mean: ~ 0.85) and late stage intrusive units (mean ~ 0.58) is equivocal.

3.4.4 STABLE ISOTOPE DATA

Ten representative vein samples were selected for analysis of oxygen and hydrogen stable isotopes in quartz using the methods of Sharp (1990) and Sharp et al. (2001). In order to accurately characterize the isotopic variation in orthomagmatic and hydrothermal features across the HPP with a limited sample set, the ten samples were chosen from all four of the major intrusive units and represent five of the nine major vein types. Relevant descriptive information and calibrated oxygen isotopic compositions for all samples are shown in Table 3.5. Four samples originated from early stage units, (one from the Ttc, two from the Tcc, and one from a mineralized skarn on the Tcc contact), and six samples originated from late stage units, (five from the Tmg, and one from the Tgm). Of the ten samples, three were QF Pegmatites one was a QF-cored Aplite, and six were Quartz Veins (three Type (I) Quartz Veins, one Type (II) (skarn) Quartz Vein, and two Type (III) Quartz Veins). Sample preparation and analytical methods are described in Appendix A.3. Although sample material was submitted for bulk hydrogen stable isotope analysis of fluid inclusions, it was determined that there was insufficient inclusion volume in all samples to generate meaningful data, and thus only oxygen stable isotope data are presented here.

Orthomagmatic features (QF Pegmatites and Aplites) were selected to determine magmatic isotopic values in the early and late stage intrusive units and to generate a baseline for determining the fluid origin of hydrothermal veins. Primary hydrothermal features (Types (I), (II) (skarn), and (III) quartz veins) were selected due to the inherent ambiguity in the nature of their fluid origin and, in some cases, their association with skarn mineralization. Alteration zones were excluded due to the unavoidable presence of multiple generations of quartz crystals. Types (IV) and (V) quartz veins were also excluded due to evidence of brittle emplacement after primary magmatic-hydrothermal activity had ceased.

Calibrated $\delta^{18}\text{O}$ values for all analyzed samples range between +7.5‰ and +11.1‰, with a mean of +9.8‰. Several systematic variations are apparent for $\delta^{18}\text{O}$ values between sampled feature types. Values for the orthomagmatic samples exhibit very little scatter, ranging from +9.7‰ to +10.2‰ with a mean of +10.0‰. The $\delta^{18}\text{O}$ values for all hydrothermal features are more widely scattered, ranging from +7.5‰ to +11.1‰ with an average of +9.7‰. However, ignoring the one anomalously low value (+7.5‰), yields a mean value of +10.2‰ for hydrothermal features. Type (I) Quartz Veins consistently yielded values within or higher than the range of orthomagmatic features, and also higher than Type (III) Quartz Veins. There are also a number of observed patterns in $\delta^{18}\text{O}$ values between early and late stage units and between the individual units. Early stage orthomagmatic features display very similar values to late stage orthomagmatic features. Hydrothermal veins from the early stage Tcc exhibit the largest variation (+7.5‰ to +11.1‰), while values for the hydrothermal vein samples from all other intrusive units are relatively tightly grouped between +9.5‰ and +10.3‰.

3.5 DISCUSSION

An in-depth analysis and synthesis of the field, petrographic, microthermometric, multi-element geochemical, and isotopic data presented in Sections 3.3 and 3.4 are required to understand the nature and activity of magmatic-hydrothermal fluids in the HPP. This section is divided into the following sections: (1) an overview of the characteristics of all magmatic-hydrothermal fluid types, (2) a classification and discussion of the distinct types of magmatic-hydrothermal fluid types entrapped in fluid inclusions in and around the HPP and interpretations of their conditions of entrapment, (3) a discussion of the spatial variation of these fluid types within the HPP, (4) a synthesis and comparison of the most significant characteristics of these fluid types, and (5) a detailed integration with relevant data from other studies of the HPP. The fluid type classification scheme, and spatial, temporal, and genetic relationships described in this section are the basis of the fluid history presented in Section 3.6.

3.5.1 OVERALL CHARACTERISTICS OF MAGMATIC-HYDROTHERMAL FLUIDS

With the exception of fluid inclusions from Type (II) (wallrock) Quartz Veins and Type (IV) Microcrystalline Quartz Veins (discussed in Section 3.4.2.3), samples in this study exhibit a relatively narrow, well-defined range for microthermometry measurements and multi-element geochemistry data. From these data, two classes of fluids are apparent: aqueous and aquo-carbonic. Characteristics are generally similar within these two classes of fluids, indicating that magma chemistry and any additional inputs did not vary significantly for this system. Homogenization temperatures ($T_{h_{tot}}$) range from ~150 to >375°C and salinities range from 0 to 8 wt % eq. NaCl. Density ranges from ~0.7 to 1.1

g/cm³. Inspection of microthermometry data for all primary inclusions reveals a generally positive correlation between Th_{tot} and salinity, a relationship that has been well documented in intrusive and subvolcanic systems (i.e. Heinrich, 2005). Aquo-carbonic inclusions typically exhibit higher Th_{tot} values than aqueous inclusions, which is a trend discussed in the following section. Multi-element data indicates consistent detection of Na, K, B, Li, Rb, Sr, and Cs (in decreasing abundance), and the inconsistent detection of Fe, Mg, Cu, As, and Pb, (in decreasing frequency). Calibrated $\delta^{18}O$ values for fluid inclusions from a representative suite of orthomagmatic and hydrothermal features range between +7.5‰ and +11.1‰, with a mean of +9.8‰, indicating a dominantly magmatic source.

3.5.2 CLASSIFICATION OF MAGMATIC-HYDROTHERMAL FLUIDS

From the field, petrographic, microthermometric, multi-element geochemical, and isotopic data generated in this study, the identities of at least four distinct magmatic-hydrothermal fluids have emerged. Distinctions between these four fluids can be made primarily on the basis of fluid inclusion petrography of internal phase relations and microthermometry measurements, (particularly Th_{tot} , salinity, and density), but are supported by other data, including correlations with certain feature types and localities, and subtle differences in multi-element concentrations. Type (A) aqueous inclusions are subdivided into three populations, which are identified as three distinct aqueous fluid types likely entrapped at different P-T conditions: A1, A2, and A3. Type (B) and (C) aquo-carbonic inclusions are combined into one population, which is identified as the one fluid type entrapped at approximately the same P-T conditions: BC. See Figure 3.22 compiled isochores and interpreted entrapment conditions. Entrapment conditions generated using $\pm 50^{\circ}C$ zones around isochore intersections with the experimentally determined wet

granite solidus curve are described and discussed for each fluid type (see justification for this method in Section 3.4.2.2). The following sections will provide further discussion and justification for this classification.

3.5.2.1 (A1) AQUEOUS FLUID TYPE

The bimodal distribution of T_{tot} values for all aqueous inclusions and the difference between mean values for these two populations ($\sim 290^\circ\text{C}$ vs. $\sim 220^\circ\text{C}$), clearly demonstrates that two distinct populations exist. The A1 fluid type is identified as the H_2O -NaCl-KCl aqueous fluids entrapped in the “high temperature” population of Type (A) aqueous fluid inclusions ($T_{\text{tot}} > 260^\circ\text{C}$) in orthomagmatic and hydrothermal samples in the HPP. A1 fluid inclusions are much less common than the low T_{tot} fluid inclusions. In this fluid type, there is no relationship between T_{tot} and salinity (range: 0–7.02 wt % eq. NaCl; mean: 2.56 wt % eq. NaCl). The mean T_{eutectic} value (-24.7°C) indicates that NaCl and KCl were major cation species in this fluid type. Bimodality in isochore slope for all Type (A) inclusions also indicates that densities are consistently and significantly lower in A1 fluids (mean density: 0.74 g/cm^3) than in A2 fluids (mean density: 0.86 g/cm^3). Isochore intersections with the wet granite solidus constrain entrapment conditions to ~ 2400 – 3600 bar and ~ 620 – 700°C . Based on these characteristics, it is interpreted that the A1 fluid type was a volumetrically minor, H_2O -NaCl-(KCl) fluid of predominantly magmatic origin. It was entrapped at high temperatures and relatively low pressures in several orthomagmatic and primary hydrothermal feature types throughout the HPP and in adjacent skarn deposits.

3.5.2.2 (A2) AQUEOUS FLUID TYPE

The A2 fluid type is identified as the H_2O -NaCl-KCl aqueous fluids entrapped in the “intermediate temperature” population of Type (A) aqueous fluid inclusions in

orthomagmatic and hydrothermal samples in the HPP. This fluid type is apparent from a population in the distribution of total homogenization values at ~180–260°C (mean = ~220 °C). The mean T_{eutectic} value is -25.2 °C, which is slightly lower than the other aqueous fluid types. This likely indicates complex fluid compositions with multiple cation species. Salinity (mean: 3.09 wt % eq. NaCl; range: 0.35–6.16 wt % eq. NaCl) is very similar to that of the A1 fluid type. Density is intermediate (mean: 0.86 g/cm³) between A1 and A3 fluid types. It is interpreted that the entrapment of this fluid type occurred at ~3200–7600 bar and ~590–690°C. Thus, the A2 fluid type is interpreted as being of H₂O-NaCl-KCl composition, predominantly magmatic origin, and more volumetrically more significant than the A1 fluid type. It was entrapped at similar but slightly lower temperatures, and distinctly higher pressures than the A1 fluid type. Entrapment occurred in the full suite of orthomagmatic and hydrothermal feature types, (particularly Type (III) Quartz Veins and QF Pegmatite zones), as well as in skarn deposits.

In this study, the most comprehensive multi-element dataset was generated for the A2 fluid type (analysis of 19 individual fluid inclusions). This fluid type is characterized by the following elemental suite: Na and K as major elements (>1000 ppm), and Li, Rb, Sr, and Cs as minor elements (10–1000 ppm). B was detected as a minor element in miarolitic cavities (with the highest concentrations measured) and Type (II) (skarn) Quartz Veins, but rarely in QF Pegmatites. Pb, Mg, As, Fe (57), Cu, and Ni (listed in decreasing frequency) were detected as minor or trace elements (<100 ppm) in some inclusions. See Section 3.4.3 for a comprehensive description of the multi-element geochemistry data in this study. Generally, the A2 fluid type contains higher concentrations of K, Sr, and Cs than the BC fluid type, but concentrations of Pb (when detected) are lower. The mean Na:Cs and K:Cs molar

ratios for this fluid type are ~ 1824 and ~ 124 , respectively. These values are both an order of magnitude higher than the corresponding mean values for the BC fluid type. The mean Rb:Cs molar ratio is 0.59, which is similar to the corresponding value for the BC fluid type. For all other elements and element ratios, there are no systematic differences between the A2 and BC fluid types. This overall similarity is discussed below in Section 3.5.2.4 after the characterization of the BC fluid type.

3.5.2.3 (A3) AQUEOUS FLUID TYPE

The A3 fluid type is identified as the H₂O-NaCl-KCl aqueous fluids entrapped in Type (II) (wallrock) Quartz Veins and Type (IV) Microcrystalline Quartz Veins. These features likely formed after intrusion and crystallization of the HPP, as indicated by their crosscutting morphologies, fine-grained crystal morphology, and general lack of fluid inclusions. This is supported by trends in microthermometry data, such as low T_{tot} (mean: $\sim 180^\circ\text{C}$), low salinity (range: 0.35–2.41 wt % eq. NaCl, mean: ~ 1.42 wt % eq. NaCl) and high density (mean: 0.90 g/cm³). However, T_{eutectic} values are similar to the A1 fluid type (mean: -24.6°C), also indicating that Na was the dominant cation, but additional species were present. Furthermore, isochores for these feature types display anomalously steep slopes, further indicating that fluid entrapment occurred at drastically different conditions than the A1 and A2 fluid type. T_{tot} values for inclusions in these feature types are consistently at or near the lower limit of the analytical scatter for all aqueous inclusions, but are similar to some inclusions interpreted to belong to the A2 fluid type. The interpretation that the A3 fluid type was circulating after the cessation of magmatic and primary hydrothermal activity excludes estimation of entrapment conditions using the wet granite solidus curve. Instead, the minimum Pt value (~ 2400 bar) for the three magmatic

fluid types is used as an upper bound of Pt for this fluid type, resulting in calculated maximum Tt values of ~220–400°C. However, it is possible that entrapment occurred at lower pressures and temperatures. Thermochronology of the HPP by Kistler et al. (1981) and Burton (1997) demonstrate that temperatures rapidly cooled to below this upper temperature limit within ~5 Ma, indicating that this fluid type was entrapped relatively soon after intrusion. Based on these characteristics, the A3 fluid type is interpreted as being of H₂O-NaCl-KCl composition, locally volumetrically major (although few inclusions were entrapped), and entrapped at significantly lower temperatures and pressures than all other fluid types recognized in this study.

Although LA-ICP-MS analysis of two fluid inclusion assemblages from a Type (IV) Microcrystalline Quartz Vein was attempted, the characteristically small size of inclusions hosted by this feature type (and by Type (II) (wallrock) Quartz Veins) prevented collection of multi-element data. Thus, it is impossible to characterize the chemistry of the A3 fluid type beyond what can be determined from microthermometry, which indicates that dissolved major cation species were in relatively low concentrations. Consistent association with zones of chlorite-sericite hydrothermal alteration also indicates that multi-element compositions of this fluid type could be markedly different from the A1, A2, and BC fluid types, likely due to the difference in source.

3.5.2.4 (BC) AQUO-CARBONIC FLUID TYPE

Type (BC) fluids are identified as the H₂O-CO₂-NaCl-(KCl) fluids entrapped in Type (B) and (C) aquo-carbonic fluid inclusions in orthomagmatic and hydrothermal samples in the HPP and in skarn deposits on the pluton contact. Although CO₂ concentrations are inherently lower in Type (C) inclusions than in Type (B) inclusions, the similarity between

mean salinity and density values, visual comparison of isochore populations, and the coexistence of both inclusion types in the same samples and petrographic settings provide strong support for their equivalency. Considered as the BC fluid type, these two fluid inclusion populations are the most abundant of any of the fluid types observed in this study. CO₂ concentrations are moderate, ranging from 2.6 to 10.5 mol%, with an average value of 5.2 mol%. Ignoring one anomalously low value, Th_{tot} values are among the highest of any fluid type (range: 191.3–375°C; mean: 277.3°C). Approximately 4–8 mol% CO₂ is present in these inclusions, but Tm_{CO2} values (mean: -57.1°C) indicate that the CO₂ is slightly impure. Clathrate melting temperatures indicate relatively high aqueous phase salinities (range: 0.18–8.00 wt % eq. NaCl; mean: 3.70 wt % eq. NaCl), compared to other fluid types. This fluid type has many similarities with the A1 fluid type (including mean Th_{tot} and salinity), and displays higher Th_{tot} and salinity values than the A2 and A3 aqueous fluid types. However, density values for BC fluid inclusions (mean: 0.91 g/cm³) are significantly higher than the densities for A1 fluids, and are most similar to the A3 fluid type. However, compositional differences between aqueous and aquo-carbonic fluid inclusions makes direct density comparisons difficult. Thus, the BC fluid type is a volumetrically major magmatic fluid of dominantly H₂O-CO₂-NaCl-KCl composition that was entrapped in orthomagmatic and hydrothermal feature types in late stage intrusive units. Slightly bimodal isochore populations indicate that the majority of entrapment occurred between 570–680°C and 3200–7400 bar.

A total of 18 individual fluid inclusions of the BC fluid type were analyzed by LA-ICP-MS. To reiterate, there exists only minor systematic variation in the multi-element fluid compositions between the A2 and the BC fluid types. This fluid type is characterized by the

following elemental suite: Na and K as major elements (>1000 ppm), and Li, B, Rb, Sr, and Cs as minor elements (10–1000 ppm). Cu, As, Pb, Mg, Fe, and Ni (listed in decreasing frequency) were detected as minor or trace elements (<100 ppm) in some inclusions. See section 3.4.3 for a comprehensive description of the multi-element geochemistry data in this study. As noted earlier as well, BC fluids generally contain slightly lower K, Sr, and Cs, but higher Pb (when detected) than A2 fluids. In order to discuss Na:Cs, K:Cs, and Rb:Cs molar ratios for the BC fluid type, correlations with magmatic stages/units must first be addressed. The BC fluid type was observed almost exclusively in late stage intrusive units, resulting in significant overlap and overall similarity between these two datasets. Mean Na:Cs and K:Cs molar ratios are ~825 and ~40, respectively, both representing an order of magnitude decrease from the corresponding mean values for the A2 fluid type. The mean Rb:Cs molar ratio is 0.73, which is similar to the mean value for the A2 fluid type.

3.5.3 REVIEW OF FEATURE TYPE DISTRIBUTION

A detailed presentation and discussion of the distribution of feature types throughout the HPP can be found in Chapter 2, (including field and petrographic descriptions, spatial trends, and relationships). Clear differences in the evidence of MVP saturation, exsolution, and migration were observed between early and late stage intrusive units, which is supportive of the incremental assembly of the HPP argued by Barnes et al. (2001). Early stage units are characterized by localized swarms of aplite veins and dikes, sparse miarolitic cavities (indicative of magmatic fluid saturation and exsolution), zones of hydrothermal alteration, and skarn/carbonate replacement Pb-Zn-Ag-W-(Cu) mineralization in wallrock units adjacent to the pluton roof zone. It was interpreted in Chapter 2 that the bulk of metal deposition and hydrothermal alteration were caused by

hydrothermal fluids sourced from early stage units. Late stage units are characterized by abundant aplites and pegmatites, but display limited evidence of fluid exsolution, migration, and hydrothermal skarn mineralization.

3.5.4 SPATIAL AND CATEGORICAL VARIATION IN FLUID TYPES

Fluid inclusions containing Type A1, A2, and BC fluids are observed in orthomagmatic and hydrothermal features throughout the HPP and in adjacent skarn deposits and wallrock units. However, spatial trends in these three populations indicate that certain fluids were more prevalent in some intrusive units than others and that variation of T and P at the time of fluid exsolution and migration existed in the HPP. No systematic spatial variation was observed for T_{mCO_2} , $T_{eutectic}$, T_{mice} , $T_{mclathrate}$, T_{hCO_2} , or salinity values. However, patterns in T_{htot} and density allow limited conclusions to be drawn about the thermal regime of the HPP during the magmatic-hydrothermal transition. Furthermore, correlations with the distributions of orthomagmatic and hydrothermal feature types in and around the HPP provide indications of the immediate settings of these fluids and their relative timing in the fluid history of the HPP. It should be noted that the A1, A2, and BC fluid types coexist in nearly all feature types, thus making any genetic inferences between these fluid types and their host feature types tentative at best.

Although significant variation is apparent from microthermometry data, the multi-element geochemistry data indicates general geochemical homogeneity across fluid and feature types and intrusive units. Certain element ratios (i.e. Na:Cs, K:Cs) demonstrate some spatial variation, but this is interpreted as primarily a function of fluid type distribution (see Section 3.5.5.2 for full discussion). As a result of the overall homogeneity of the data, multi-element geochemical variation is not addressed in this section.

3.5.4.1 AQUEOUS FLUID TYPES

Although it was observed in fluid inclusions from all intrusive units except the Ttc, the overall rarity of the A1 fluid type in the HPP indicates that it was a volumetrically minor fluid. It was most commonly observed in hydrothermal features (i.e. Type (I), (II) (skarn), and (III) Quartz Veins), and rarely in orthomagmatic features (i.e. a single QF Pegmatite). This suggests that the dominantly magmatic A1 fluid type largely escaped entrapment in orthomagmatic features and that the hydrothermal quartz veins listed above were at least partially crystallized from this aqueous magmatic fluid type. The recognition of this fluid type in quartz from skarn and carbonate replacement deposits provides a possible upper limit of $\sim 640^{\circ}\text{C}$ (from sample HPP-4-02b) for the temperature of formation for these deposits.

The A2 fluid type was entrapped in all intrusive units (and skarn localities) in and around the HPP. However, it was slightly more prevalent in early stage units. Hydrothermal feature types hosted the majority of A2 fluid inclusion assemblages in early stage units, while both orthomagmatic and hydrothermal feature types hosted equal numbers of A2 fluid inclusion assemblages in late stage units. It should be noted that A2 fluid inclusion assemblages are notably absent from aplites from early and late stage units, but was observed in pegmatites. Thus, it is likely that the A2 fluid type was exsolved from both early and late stage units, but a slightly larger proportion of this fluid was entrapped in orthomagmatic features in late stage units than in early stage units. The uniformity of T_{tot} values indicates that the orthomagmatic and hydrothermal feature types that host these fluid inclusions crystallized at similar temperatures and pressures.

A3 fluids are observed throughout the HPP, but are generally restricted to discrete zones of fluid flow, commonly characterized by microcrystalline quartz and alteration. Although relatively few A3 fluid inclusions were analyzed by microthermometry, the data from these inclusions can be extrapolated for all features interpreted to have formed during post-intrusion hydrothermal activity (i.e. Type (IV) and (V) Microcrystalline Quartz Veins, and Type (II) (wallrock) Quartz Veins). As such, the A3 fluid type is present in all intrusive units, but was completely uncoupled from any magmatic processes.

3.5.4.2 AQUO-CARBONIC FLUID TYPE

Unlike the A1 and A2 fluid types, the BC fluid type was almost exclusively present in orthomagmatic and hydrothermal feature types in late stage intrusive units. The rare BC fluid inclusions observed in early stage units are hosted by a Mirolitic Cavity and a QF Pegmatite zone. This distribution is one of the most significant differences between early and late stage units and provides strong support for widespread magmatic exsolution and migration of aquo-carbonic fluids during intrusion of late stage magmas. BC fluid inclusion assemblages coexist with A1 and A2 fluid inclusion assemblages in late stage units, but provide no petrographic indications of their relative timing. Only one BC fluid inclusion assemblage was observed in a Type (II) (skarn) Quartz Vein. Also, BC fluid inclusion assemblages were only rarely observed in Type (II) (wallrock) Quartz Veins and Type (IV) Microcrystalline Quartz Veins, which are features interpreted to have formed during post-intrusion hydrothermal activity. These occurrences could be at least partially explained by the minor remobilization of aquo-carbonic fluids from other orthomagmatic and hydrothermal features by other, later fluids.

3.5.5 DISCUSSION OF FLUID TYPES

Although the characterizations of the four major fluid types are not exhaustive in nature, they do effectively demonstrate that these fluid types are similar, but compositionally distinct and entrapped at different P-T conditions. Certain fluid inclusion microthermometry data and LA-ICP-MS multi-element data show compositional disparities and trends, while calculated entrapment conditions and spatial distributions display P-T and temporal differences. The interpretations and comparisons made in this section will be synthesized with a discussion of external data (Section 3.5.5) to construct a detailed fluid history in Section 3.6.

3.5.5.1 MICROTHERMOMETRY

Overall similarities and overlap in the ranges for major microthermometric measurements (i.e. T_{HCO_2} , T_{eutectic} , T_{mice} , $T_{\text{mclathrate}}$, T_{HCO_2} , and T_{Htot}) and resulting calculated values (i.e. salinity) indicate that the magmatic fluids exsolved from the HPP belong to two compositional groups: low salinity aqueous and low salinity aquo-carbonic. Differences between fluid types in T_{Htot} and density values are addressed indirectly in the following paragraph on emplacement condition. The A1 and A2 magmatic aqueous fluid types demonstrate very similar thermal and compositional characteristics. Generally low salinities ($\sim < 4.5$ wt % eq. NaCl) are only slightly higher in the A2 fluid type. T_{eutectic} values are also lower ($\sim -25^\circ\text{C}$), (confirming the component of KCl detected by LA-ICP-MS), with the A2 fluid type containing the lowest values. Thus, it is interpreted that the A2 fluid type contained more dissolved species than the A1 fluid type. The A3 fluid type demonstrates lower salinity but similar T_{eutectic} values to the A1 fluid type. Finally, the BC fluid type

contains intermediate salinities and low Th_{CO_2} values, indicating an impure CO_2 -bearing fluid system with possibly multiple minor dissolved and vapor species.

3.5.5.2 CONDITIONS OF ENTRAPMENT

The Tt and Pt values for the three magmatic fluid types (A1, A2, BC) demonstrate a progression that is permissible within the existing model for the two-stage emplacement of the HPP. Interpreted Tt values are similar for these three fluid types, but the A1 fluid type demonstrates slightly higher Tt values than the other two fluid types. Pt values vary much more significantly. For aqueous fluids, the entrapment of the A2 fluid type occurred at generally higher pressures (3200–7600 bar) than the A1 fluid type (2400–3600 bar). Despite a lack of petrographic evidence for relative timing, this disparity is interpreted as evidence of the relatively isothermal, overlapping transition from saturation, exsolution, and expulsion of the A2 fluid type to the A1 fluid type during emplacement of the HPP at progressively higher structural levels. Based on hydrothermal textures and crosscutting morphologies, it can be assumed that the A3 fluid type was entrapped at lower temperatures and lower pressures than the magmatic fluid types. If the lower limit of emplacement pressures for magmatic fluid types are used as an upper bound, calculated Tt values (~220–400°C) are significantly lower for the A3 fluid type.

The relatively large range Pt recorded for the BC fluid type (~3200–7400 bar) can be reduced based on the assumption that this fluid was entrapped during late stage intrusive activity. The Pt histogram for late stage assemblages in Figure 3.16 demonstrates that the bulk of entrapment occurred between ~4800–7200 bar. These high Pt values could be the result of (1) fundamental variations in the equations of state used in isochore calculations, (2) pre-emplacement fluid entrapment in late stage units at depth, or (3)

overpressuring of the late stage magmatic system. The effects of different equations of state in isochore calculations for different fluid types are unclear since the rare carbonic fluid inclusions observed in early stage units demonstrate pressures similar to coexisting aqueous fluid inclusions (ex: HPP-1-03). However, a significant disparity exists in T_t between some coexisting aqueous and aquo-carbonic fluid inclusions in late stage units (ex: HPP-2-35, HPP-2-40). Pre-emplacment entrapment at depth is considered unlikely due to the relatively high magmatic pressures for early stage units compared to late stage units determined by Barnes et al. (2001). In that study, thermobarometry of magmatic hornblende demonstrated that deeper partial crystallization was only an operative process in early stage units. Overpressuring is considered the most attractive explanation, since increases of ~ 2 kbar above normal lithostatic pressures within cooling magmatic systems have been recorded by (Fowler & Spera, 2010). The lower pressures recorded by late stage magmatic hornblende from Barnes et al. (2001) are likely due to crystallization of these phases prior to overpressuring at the final stages of emplacement. Rapid reduction of the melt phase proportion, as evidenced by the abundance of aplitic zones in late stage units, has been described as a mechanism for such pronounced pressure increases in near-solidus granitic intrusions (Thomas, 1994).

3.5.5.3 MULTI-ELEMENT GEOCHEMISTRY

The fact that the A2 and BC fluid types demonstrate only minor overall variation in most element concentrations provides evidence for several key aspects of their origin and evolution. First, it is clear that the fluids generated from the two magmatic suites and their constituent units remained generally geochemically constant over space and time. Also, this spatial and temporal geochemical homogeneity indicates that interaction between

magmatic and meteoric fluids was volumetrically minor and localized, and therefore must not be represented in the limited multi-element geochemical data from this study.

However, order of magnitude differences in fluid inclusion K:Cs and Na:Cs molar ratios between the A2 and BC fluid types indicate that that BC fluids were more highly fractionated. This disparity provides some indication of relative timing, since Barnes et al. (2001) demonstrated from whole-rock geochemistry that late stage units were more strongly fractionated. Further discussion of the relationship between fluid type, fractionation, and intrusive units can be found in Section 3.5.5.2.

3.5.5.4 DISTRIBUTION

Several trends are apparent from inspection of the spatial distribution of these fluid types and the orthomagmatic and hydrothermal feature types in which they are hosted. First, it is clear that no correlation exists between specific feature types and fluid types, with the exception of the A3 fluid type and Type (II) (wallrock) Quartz Veins and Type (IV) Microcrystalline Quartz Veins. The three magmatic fluid types (A1, A2, and BC) are observed in almost all feature types and often coexist. However, it should be noted that the vast majority of fluid inclusions observed in aplites belong to the BC fluid type, which is suggestive that these features also crystallized at the higher P_t calculated for this fluid type. The BC fluid type demonstrates a strong relationship with the late stage intrusive units, providing strong evidence that this fluid type was exsolved by these magmas and did not migrate far from its source. The A1 and A2 fluid types are observed in all intrusive units, suggesting that they migrated more extensively.

3.5.6 INTEGRATION WITH EXTERNAL DATA

3.5.6.1 FLUID INCLUSION DATA

The work of Musekamp (2012) to characterize the evidence of hydrothermal fluid flow in the contact metamorphic aureole of the HPP using fluid inclusions and stable isotopes provides useful supplementary data that will aid in the construction of a comprehensive fluid history. Musekamp (2012) identified three hydrothermal fluids from trends in the microthermometry data. Here, comparison of microthermometry data permits correlation with the specific fluid types described in Section 3.5.2 for the purpose of linking the hydrothermal activity around and within the HPP. Remarkable similarities exist between these two datasets, with different sampling biases accounting for apparent differences. The maps in Figure 3.14 permit spatial integration of these datasets. Comparison between these two datasets is complicated by the coexistence of multiple fluid types (particularly aqueous and aquo-carbonic) in the majority of samples in this study, a condition less frequently observed by Musekamp (2012). In the following paragraphs, the fluids identified by Musekamp (2012) are referenced in quotations to avoid confusion with the fluid types identified by this study.

The A1 fluid type recognized in this study is broadly correlative with the higher temperature range ($>250^{\circ}\text{C}$) of the vapor-rich “Type II” aqueous fluid inclusions recognized by Musekamp (2012). “Type II” inclusions were classified as a distinct magmatic fluid type based on Th_{tot} values ($\text{Th}_{\text{tot}} > 200^{\circ}\text{C}$) and were present in quartz and hydrogrossular within the HPP, on the contact, and in adjacent metasedimentary wallrock units. Reexamination of the Th_{tot} data for “Type II” inclusions reveals a previously unrecognized bimodality that is very similar to the distributions observed in the

population of aqueous inclusions in this study, reinforcing the distinction made between the A1 and A2 fluid types in this study. Similar salinities (<6 wt % eq. NaCl) and densities ($\sim 0.78 \text{ g/cm}^3$) between the two populations further support this correlation between populations. T_{eutectic} values for “Type II” inclusions exhibit a wider range than observed for the A1 fluid type, but are generally slightly higher ($\sim 21^\circ\text{C}$). The correlation between lower T_{eutectic} values and the A2 fluid type is not observed in the “Type II” fluid inclusion data. However, this disagreement could easily be the product of different workers rather than a significant difference in fluid inclusion compositions. As in this study, “Type II” inclusions were observed coexisting with inclusions apparently entrapped at lower temperatures and pressures.

The A2 fluid type is broadly correlative with the lower temperature sub-population (<250°C) of the vapor-rich “Type II” aqueous fluid inclusions recognized by Musekamp (2012). As mentioned above, “Type II” fluid inclusions were interpreted to be of magmatic origin, and were recognized in quartz and hydrogrossular crystals in multiple settings in and around the HPP. In this study, salinities are broadly similar between the two populations (<6 wt % eq. NaCl), but demonstrate a weak positive trend with T_{tot} values. Density values for the lower temperature sub-population of “Type II” inclusions are similarly high ($\sim 0.86 \text{ g/cm}^3$) relative to the high-temperature sub-population. The similarity in the variation of these measurements between the two populations of “Type II” inclusions in Musekamp (2012) further demonstrates the equivalency of these two sets of fluid inclusion populations.

Based on associated vein types, the A3 fluid type correlates with the vapor-poor “Type I” aqueous fluid inclusions recognized by Musekamp (2012), which exhibited

markedly lower T_{tot} values than “Type II” inclusions ($T_{\text{tot}} < 200^\circ\text{C}$) and were primarily present in quartz vugs in large milky quartz veins (i.e. Type (IV) and (V) Microcrystalline Quartz Veins) within the HPP, and calcite veins away from the plutonic contact in metasedimentary wallrock units. The mean T_{tot} value for “Type I” inclusions was reported as $\sim 160^\circ\text{C}$ by Musekamp (2012), which is somewhat lower than the mean value for A3 fluid inclusions in this study ($\sim 180^\circ\text{C}$). “Type I” fluid inclusions also have a wide spread of salinities (0.35–9.73 wt% eq. NaCl). However, the mean salinity (3.02 wt % eq. NaCl) is lower than mean values other inclusion types in Musekamp (2012), but is higher than the mean value for A3 fluid inclusions in this study. Despite this dissimilarity, the high densities for “Type I” inclusions (mean: 0.92 g/cm^3) match very closely with values for A3 inclusions, providing support for this correlation. A range of T_t values was calculated by Musekamp (2012) using the HPP emplacement pressure estimates of 1600–3200 bar from Burton (1997). These temperatures (~ 200 – 388°C) for “Type I” fluid inclusions are similar to the T_t range of 320 – 410°C determined independently by this study. Fluid inclusions of the A3 fluid type were also observed in Type (II) (wallrock) Quartz Veins near the plutonic contact in this study, although this was not documented by Musekamp (2012).

The BC fluid type correlates well with the “Type III” aquo-carbonic fluid inclusions observed by Musekamp (2012). T_{tot} values ranged from 240 – 480°C (mean: 327°C) for “Type III” inclusions, which is generally higher than the scatter of T_{tot} values was observed for aquo-carbonic fluid inclusions in this study. A similar trend is observed in salinity values, which are also higher in “Type III” inclusions (mean: 5.6 wt% eq. NaCl) than in BC inclusions. The biggest disparity between the two populations is apparent in density values, which are significantly lower in “Type III” inclusions (mean: 0.74 g/cm^3) than in BC

inclusions. However, relative to other fluid types in both studies, “Type III” and BC inclusions demonstrate the highest Th_{tot} and salinity values, and the lowest densities. Also, the similarity in Th_{tot} between “Type II” and “Type III” inclusions in Musekamp (2012) correlates well with the similarity between the A1 and BC fluid types in this study. Many of the differences between these populations can be explained by the fact that the small population of “Type III” inclusions was only observed in miarolitic cavities by Musekamp (2012), whereas inclusions of aquo-carbonic composition were observed in all feature types in this study. Lastly, significantly higher concentrations for the carbonic phase were calculated for BC fluid inclusions in this study (mean mol% CO_2 : 4.6) than were calculated by Musekamp (2012) for “Type III” inclusions (mean mol% CO_2 : ~ 1). However, this disparity is significantly reduced when the comparison is made only between data from fluid inclusions from miarolitic cavities.

3.5.6.2 MULTI-ELEMENT GEOCHEMISTRY DATA

Whole-rock multi-element geochemical data and relevant element ratios from Barnes et al. (2001) were compiled, inspected, calculated (when necessary), and compared with the fluid inclusion multi-element data generated in this study. It should be noted again that the paucity of fluid inclusion multi-element data for certain units generally restricts discussion of trends to between the early and late stage groups. Barnes et al. (2001) argued that, on the basis of rare earth patterns, the intrusive units of the HPP demonstrate increasing fractionation from early to late stage units. Certain element ratios, (Na:Cs, K:Cs, Rb:Cs), permit discrimination between different intrusive units (and possibly fluid types) using relative degrees of magmatic fractionation (Audètat et al., 2008). Spatial comparisons were performed to assess the nature and strength of the relationship between the magma

chemistry of the two main intrusive pulses that assembled the HPP and magmatic-hydrothermal fluids entrapped within them. Comparisons between whole-rock element ratios and the A2 and BC fluid type ratios were performed to determine if these fluid types exhibited significantly disparate degrees of fractionation, possibly providing indications of relative timing.

Direct comparison of multi-element data between fluid inclusion and whole rock geochemical analyses is complicated by the coefficients that control element partitioning between the melt, crystal, and fluid phases. However, calculation of the fluid inclusion/whole rock (FI/WR) element ratios is useful for a basic discussion of mass balance (see Figure 3.23 and Table 3.6). Two common elements, Na and Ca, have mean FI/WR ratios of ~ 1 . K, Rb, and Sr generally have FI/WR ratios of < 1 , which is consistent with the abundance of alkali feldspar in the HPP. Two other compatible elements, Mg and La, demonstrate a wide range of FI/WR ratios, but have mean values that are < 1 . Highly incompatible elements, such as Cs, have FI/WR ratios that are consistently > 1 . Cu, when detected, also exhibited generally high FI/WR ratios, which is consistent with some models of metal partitioning for reduced granitic intrusions (i.e. Cline & Bodnar, 1991; Frank et al., 2011).

The fluid inclusion multi-element data in this study demonstrates a statistically significant decrease in the mean Na:Cs and K:Cs molar ratios from early to late stage intrusive units of approximately an order of magnitude (from ~ 260 to ~ 60 , and from ~ 1700 to ~ 1000 , respectively). However, Rb:Cs molar ratios demonstrate only slight and statistically insignificant increases from early to late stage intrusive units (within the same order of magnitude). This similarity between mean Rb:Cs molar ratios for early and late

stage intrusive units is also observed in whole-rock Rb:Cs ratios from Barnes et al. (2001). The mean whole-rock K:Cs molar ratios of Barnes et al. (2001) demonstrate a very similar decrease of an order of magnitude from early to late stage intrusive units (~16000 to ~9000). This disparity is similar for Na:Cs molar ratios as well. A summary of these data is presented in Table 3.6. It should be noted that mean whole-rock K:Cs molar ratios for both early stage units (T_{tc} and T_{cc}) and the late stage T_{mg} are very similar, with the T_{gm} population as the clear outlier. This pattern is not reflected in the data from this study, which demonstrates a clear disparity between the mean T_{cc} and T_{mg} K:Cs ratios. Thus, it is possible that relative degrees of bulk magmatic fractionation between intrusive units directly affected the compositions of the magmatic-hydrothermal fluids hosted therein, but that this relationship was obscured in the data of Barnes et al. (2001) by unrecognized zones of cryptic magmatic fractionation.

Since fluid inclusion microthermometry and oxygen stable isotope data suggest that both the A2 and BC fluid types were predominantly derived from magmas, it is expected that certain element patterns would be similar in intrusive units and the fluids they presumably produced. Direct comparison of multi-element data confirms typical fractionation behavior of elements detected in both Barnes et al. (2001) and this study. Gross trends in K:Cs and Na:Cs molar ratios indicate a correlation between fluid inclusion and host whole-rock compositions. However, certain intrusive units (T_{tc} and T_{gm}) are not adequately represented in the fluid inclusion LA-ICP-MS dataset from this study. Furthermore, as noted earlier, inspection of whole-rock values for individual intrusive units lack of a clear progression in fractionation from the early to the late stage. Thus, it is interpreted that the differences between early and late stage K:Cs and Na:Cs molar ratios in

fluid inclusion data are primarily a product of the distribution of fluid types, rather than the product of a strong causative relationship between magmatic and hydrothermal fluid features and their host rocks. This permits the possibility that these features may contain fluid types (particularly A1 and A2) that originated from other localities within the HPP. Fundamental to these hypotheses is the interpretation that the BC fluid type (which was observed almost exclusively in the late stage units) was more fractionated than the A2 fluid type (which was observed in all intrusive units).

3.5.6.3 STABLE ISOTOPE DATA

It has been well documented that many upper-crustal magmatic intrusions are open systems with regard to fluid inputs, and that oxygen isotope exchange occurs through the interaction of rock and fluids of both magmatic and meteoric origin. A commonly observed decrease in $\delta^{18}\text{O}$ values from the core of an intrusion into adjacent wallrock units provides strong evidence for progressive meteoric water infiltration from external sources (Nabelek, 1991; Taylor, 1974; 1977). Oxygen isotope data for a representative suite of orthomagmatic and hydrothermal features related to fluid saturation, exsolution, and migration are discussed here and compared to whole-rock and quartz separate oxygen isotope data collected for the HPP by Barnes et al. (2001).

The oxygen stable isotope data presented in Section 3.4.4 demonstrates important characteristics of the fluids involved in the crystallization of various orthomagmatic and hydrothermal features in the HPP. No consistent variation exists in $\delta^{18}\text{O}$ values between orthomagmatic and hydrothermal features throughout the HPP. There is considerable overlap in the analytical scatter for both populations, and mean $\delta^{18}\text{O}$ values for orthomagmatic and hydrothermal features are within 0.3‰ of each other (+10.0‰ and

+9.7‰, respectively). Thus, it is interpreted that primary hydrothermal features were crystallized from fluids of dominantly magmatic origin that were in equilibrium with the surrounding rocks. However, the one anomalously low $\delta^{18}\text{O}$ value in the analyzed population of hydrothermal features (+7.5‰) originates from the early stage Tcc, indicating that local mixing with meteoric fluids may have been spatially restricted to this unit.

Quartz separate and whole-rock $\delta^{18}\text{O}$ values of +9.7‰ to +11.1‰, and +8.7‰ to +10.1‰, respectively, were reported for early stage intrusive units by Barnes et al. (2001) and interpreted as magmatic. This clustering is consistent with all early stage orthomagmatic features and some early stage hydrothermal features analyzed in this study. Barnes et al. (2001) also reported that late stage units yielded $\delta^{18}\text{O}$ values of +7.1‰ to +11.6‰ and +0.6 to +10.0‰ for quartz separate and whole-rock analysis, respectively. However, with the exception of four samples, all values fell within or above the same range reported for early stage quartz separate and whole-rock analyses. Barnes et al. (2001) interpreted anomalously low whole-rock oxygen isotope values ($\delta^{18}\text{O} < +7.8‰$) as evidence of interaction with $\delta^{18}\text{O}$ -depleted meteoric fluids. Only one sample from this study (HPP-1-30), (a Type (III) Quartz Vein from the Tcc), yielded similarly low values.

This comparison between oxygen stable isotope data from this study and Barnes et al. (2001) yields several helpful clues for describing the transition from supersolidus magmatic crystallization to primary hydrothermal activity in the HPP and determining the role of later meteoric fluid infiltration. First, it is apparent that relatively minor infiltration and mixing of lower-temperature meteoric fluids occurred in all intrusive units. In early stage units, it appears that this process did not significantly affect the host granite and

orthomagmatic fluid features (i.e. pegmatites, aplites), and was localized along a minority of hydrothermal veins during primary hydrothermal activity. In late stage units, the quartz separate and whole-rock values reported by Barnes et al. (2001) reveal that interaction with meteoric fluids was more widespread in the host granite, while orthomagmatic and hydrothermal fluid features from the same areas yield undiluted magmatic values in this study. It is possible that meteoric fluids infiltrated after primary hydrothermal activity had ceased and exploited later, brittle microfracture networks. This would result in isotopic exchange occurring preferentially in the granitic host rock, instead of in the orthomagmatic and hydrothermal features, which would have been effectively “sealed” from further fluid flow.

Musekamp (2012) is additional source of stable isotope data for the HPP. However, the carbon and oxygen stable isotope data were collected from carbonate veins and metasedimentary wallrock units around the HPP, and thus provide, at best, diluted magmatic isotopic signatures. All data from Musekamp (2012) represent $\delta^{18}\text{O}$ values recalculated using corrections for oxygen isotope fractionation, and pressure corrected temperatures (Tt) that were determined from fluid inclusions and pressure estimates from Burton (1997). Calcite veins from skarn deposits on the HPP contact exhibit a scatter of $\delta^{18}\text{O}$ values interpreted to be magmatic (mean: +8.6‰, range: 2.3–14.7‰) with linear data arrays indicating some mixing with meteoric fluids. However, carbonate veins in unmineralized wallrock units on the HPP contact (classified as “Type B” carbonate veins “on” by Musekamp (2012)) exhibited a much wider range of $\delta^{18}\text{O}$ values (mean: +13.9‰, range: 1.1–25.9‰), which was interpreted as evidence of both meteoric-magmatic and meteoric-connate fluid mixing. Unaltered metasedimentary rocks and two populations of

calcite veins >2 km from the HPP (classified as “Type A” carbonate veins “away” by Musekamp (2012)) have variably connate and meteoric-connate $\delta^{18}\text{O}$ signatures (mean: +27.0‰, +29.5‰, and +6.9‰, respectively), with little to no influence from the HPP.

The data from these carbonate vein populations and unaltered wallrock units indicate that multiple end-member fluids existed around the margins of the HPP. The wide range of calculated $\delta^{18}\text{O}$ values is most plausibly explained by mixing of magmatic, meteoric, metamorphic, and connate fluids. When viewed in conjunction with the isotopic data in this study, it is clear that $\delta^{18}\text{O}$ values for orthomagmatic and hydrothermal features within the HPP are consistently higher and in a narrower range than hydrothermal features on the contact, supporting the hypothesis that magmatic fluids were expelled from the HPP and experienced progressively higher degrees of dilution with increased distance from the intrusive center. Furthermore, the single Type (II) (skarn) Quartz Vein analyzed in this study yielded a $\delta^{18}\text{O}$ value (+10.2‰) that is within the range determined for calcite veins in skarn deposits (2.3–14.7‰), indicating that these two types of veins (and the deposits themselves) were likely formed by fluids of similar, dominantly magmatic origin.

3.6 FLUID HISTORY

As a central research goal of this thesis, the orthomagmatic-hydrothermal fluid history of the HPP is reconstructed by synthesizing several different types of new and existing data. Here, the fluid history is divided into early and late pulses that correlate with the two-stage magmatic assembly of the HPP described by Barnes et al. (2001). The exsolution, migration, and entrapment of specific fluid types are described within this

context and related to the hydrothermal fluid activity in the contact metamorphic aureole examined by Musekamp (2012) and the formation of ore deposits along the pluton margin. Also, certain trends in thermodynamic and compositional data are also cited as evidence for the temporal, spatial, and compositional variation of different fluid types in the HPP.

3.6.1 EARLY STAGE

The HPP was first intruded into the transition zone between the igneous and metamorphic infrastructural core of the RMEHR core complex and its suprastructural carapace of Paleozoic sedimentary strata at ~36 Ma during a period of profuse regional magmatism. Mineral thermobarometry and stratigraphic reconstructions indicate that emplacement occurred at depths of 4–12 km with calculated peak temperatures of crystallization of ~760°C (Burton, 1997; Barnes et al., 2001; Colgan et al., 2010; Deans, 2010). Emplacement of the early stage magmatic suite, (which consists of the granodioritic Ttc, monzogranitic Tcc units, and volumetrically minor porphyritic and equigranular roof dikes), was accommodated by diking, stoping, and brittle/ductile wallrock deformation. It was in the context of this emplacement that the first magmatic volatile phase(s) reached saturation and were exsolved as distinct fluid phases.

The first pulse of fluid activity in the HPP involved the exsolution of aqueous fluids and was a result of the intrusion of the early stage magmas, but as early stage fluids are preserved in late stage units, circulation of these fluids is interpreted to have continued throughout the magmatic evolution of the pluton. This pulse of fluid activity was characterized by the initial exsolution of the A2 fluid type, followed by the exsolution of the A1 fluid type, as illustrated in Figure 3.23. These fluids were B-Na-K-Rb-Sr-Cs-bearing, but generally ore metal-poor, (despite association with skarn mineralization). Large volumes of

the low salinity (~3.1 wt % eq. NaCl), aqueous A2 fluid type were entrapped at 590–690°C and 3200–7600 bar in QF Pegmatites, miarolitic cavities, and all quartz vein types, (including Type (II) (skarn) Quartz Veins). Following entrapment of A2 fluids, smaller volumes of the low salinity (~2.6 wt % eq. NaCl), aqueous A1 fluid type were exsolved and entrapped 620–700°C and 2400–3600 bar. This relatively rare fluid type continued to circulate during late stage intrusive activity, and was entrapped in QF Pegmatites and in Type (I) and (III) Quartz Veins from all intrusive units and in Type (II) (skarn) Quartz Veins. While it is possible that the aqueous fluids entrapped in late stage units were exsolved separately from the late stage intrusive units, similarities in compositions and entrapment conditions with the A1 and A2 fluid inclusions entrapped in early stage units indicate that they originate from the early fluid pulse. Ignoring the fractions of these fluids entrapped during late stage emplacement, the bulk of these aqueous fluid types were entrapped between 3400–6800 bar (see Figure 3.17).

A1 and A2 fluids were generated by magmatic volatile phase saturation, as evidenced by their presence in miarolitic cavities preserved exclusively in early stage units. A minority of fluid inclusions in miarolitic cavities, which likely crystallized from end-member unmixed magmatic-hydrothermal fluids, contain detectable but low CO₂ concentrations. However, the volumetric bulk of early stage fluids belong to the aqueous A1 and A2 fluid types described above. After exsolution, these aqueous fluids migrated throughout the HPP, resulting in entrapment in crystallizing orthomagmatic features, and forming hydrothermal quartz veins. Dominantly, but not exclusively, magmatic δ¹⁸O values in all host feature types within the HPP indicate, at most, only minor meteoric fluid mixing during entrapment of the A1 and A2 fluid types. Typically there is a strong pressure

gradient between crystallizing magmas and surrounding wallrock. Observations of magmatic Tt and $\delta^{18}\text{O}$ values outside of the HPP demonstrate that such a pressure gradient allowed these fluids to migrate outward and upward towards the roof zone and margins of the HPP (Musekamp, 2012). During expulsion from the HPP, the A1 and A2 fluid types were responsible for potassic and phyllic alteration of early stage granitic rocks and wallrock units, as well as the formation of skarn and possibly Pb-Sn-W-(Cu) deposits on the pluton contact. Outside the HPP, these fluids interacted with impure carbonate strata and formed quartz and calcite veins.

3.6.2 LATE STAGE

Radiometric dating indicates that emplacement of the late stage biotite and two-mica Tmg monzogranite, the two-mica Tgm monzogranite, and minor mafic dikes occurred <2 My after the intrusion of early stage magmas (Burton, 1997; Colgan et al., 2010). Despite extensive interaction between the sheets and dikes of the volumetrically major Tmg and its dismembered Ttc host, very little evidence of back-melting or chilled intrusive margins has been observed. This demonstrates that the temperature differential between early and late stage units was minor, and further indicates that the late stage magmas intruded early stage units soon after their emplacement. This model of relatively rapid, but fundamentally incremental pluton assembly provides a setting for the thermal development of late stage fluids described below.

Late stage intrusive activity in the HPP was accompanied by a compositionally distinct episode of magmatic-hydrothermal fluid activity, as illustrated in Figure 3.24. Exsolution of the intermediate volume (relative to the abundance of other fluid types), low salinity (~ 3.7 wt % eq. NaCl), B-Na-K-Rb-Sr-Cs-bearing, ore metal-poor, magmatic BC fluid

type signaled a shift from dominantly aqueous to aquo-carbonic fluid compositions. CO₂ concentrations range from 2.6 to 10.5 mol%, (mean: 4.6 mol%). Despite overall similarity in minor and trace element geochemistry, the BC fluid type was derived from a later, distinctly more evolved magma than aqueous fluid types. Entrapment of this fluid occurred across a range of similar temperatures (570–680°C) and pressures (3200–7400 bar) to other magmatic fluids. However, the bulk of this fluid type was entrapped at 4800–7200 bar (see Figure 3.17). These fluids were entrapped in quartz in (M)QF Pegmatites, aplites (texturally homogeneous, QF-cored, and layered Aplite/Pegmatite), and Type (I) and (III) Quartz Veins.

Moderate overpressuring of the late stage magmatic system driven by rapid crystallization of the melt phase was largely responsible for relatively high Pt for the BC fluid type (compared to the A1 fluid type). Isothermal fluid entrapment is evidenced by clearly magmatic $\delta^{18}\text{O}$ values for all feature types. The distinct lack of miarolitic cavities and the abundance of aplites in late stage units in the HPP are supportive of very late fluid saturation caused by rapid crystallization and overpressuring (Thomas, 1994; Candela, 1997). However, as late stage magmas ascended, cooled, and interacted with early stage magmas, a transition from an overpressured system to a negative fluid pressure gradient from early to late stage units may have allowed relatively low volumes of the A1 and A2 fluid types to be introduced. This transition to a negative pressure gradient is also supported by the lack of carbonic fluids outside of late stage units.

3.6.3 POST-INTRUSION

The final stage of hydrothermal activity in the HPP occurred after all magmatic activity had ceased and was characterized by the influx of large volumes of cooler, aqueous

hydrothermal fluids, as illustrated in Figure 3.25. The initial period of rapid cooling of the fully assembled HPP from magmatic temperatures of ~615–760°C at ~36 Ma to ~270–300°C at 33.3 Ma was followed by a relatively steady temperature decline at a rate of ~8.5°C/My (Burton, 1997; Deans, 2010). The transition between these two thermal regimes was likely facilitated by the introduction of cooler, deeply circulating, surface-derived fluids driven by extension on the RMSZ and an elevated regional geotherm. The brittle-ductile RMSZ forms the western margin of the HPP, indicating that extension was initiated shortly after plutonic assembly. Wickham et al. (1993) documented evidence of meteoric fluid infiltration fronts (δD : -125 to -175‰; $\delta^{18}O$ down to -4.4‰) at paleodepths of 5–10 km in mylonites on this regional, low-angle structure.

At the locality of the HPP, these fluids (identified as the A3 fluid type) are interpreted to be the products of mixing of deeply circulating meteoric groundwater with the magmatic fluids, possibly the A1 and A2 fluid types. These low temperature (320–410°C), low salinity (within the HPP: <4.0 wt % eq. NaCl; outside the HPP: <6.5 wt % eq. NaCl) aqueous fluids were likely entrapped at pressures of <2400 bar and temperatures of ~220–400°C. Consistently high $\delta^{18}O$ values within the HPP and generally lower values within the contact metamorphic aureole indicate that the bulk of fluid mixing occurred outside the HPP. Expelled magmatic fluids interacted with infiltrating meteoric inputs, resulting in the entrapment of A3 fluids in calcite veins in metasedimentary wallrock units and in calcite veins and Type (II) (wallrock) Quartz Veins on the HPP contact. Large volumes of A3 fluids then entered the HPP by exploiting large-scale, crosscutting, brittle fault systems, forming Type (V) and subsidiary Type (IV) Microcrystalline Quartz Veins. Multiple intersecting vuggy zones in many of these features indicate that fluid flow was

relatively long-lived. They were also responsible for localized zones of pervasive silicification and chlorite-sericite alteration around these faults, indicating significant thermal and chemical disequilibrium with the subsolidus host granitic rocks of the HPP and the metasedimentary rocks in the contact metamorphic aureole. The entry of these mixed meteoric fluids into the HPP is also indicated by their entrapment in secondary fluid inclusions in quartz crystals in skarn deposits (Musekamp, 2012).

3.7 IMPLICATIONS FOR THE RMEHR METAMORPHIC CORE COMPLEX DEVELOPMENT

Pressure and temperature constraints on magmatic fluid exsolution in the early and late stage intrusive units of the HPP have important implications for the depth of emplacement of the HPP. Several workers have addressed this question to varying degrees and using different methods (Willden & Kistler, 1979; Hudec, 1992; Wright & Snoke, 1993; Burton, 1997; Barnes et al., 2001; Colgan et al., 2010). This study provides the additional perspective of fluid entrapment pressures and lends support for the relatively deep emplacement estimates from the thermobarometry data of Burton (1997) and Barnes et al. (2001), and challenges emplacement depths determined from simple stratigraphic reconstructions by Burton (1997) and Colgan et al. (2010). The depth interpretation comes to bear on current understandings of the thermal and structural development of the RMEHR metamorphic core complex. Most significantly, the results of this study are suggestive of a now-eroded overlying rock package that was ~9 km thick at the time of emplacement. Discrepancies between these estimates and stratigraphic reconstructions are likely due to either (1) regional variation or erosional gaps in the composite

stratigraphic column, or (2) cryptic Mesozoic orogenic events. Additionally, the amount of post-intrusion vertical exhumation that was accomplished by slip on the low-angle RMSZ is estimated to be at least 9 km.

3.7.1 REVIEW OF HPP EMPLACEMENT DEPTHS

Existing estimates of the depth of emplacement for the HPP have been based on several methods of inquiry: (1) field relationships, (2) barometry of equilibrium mineral assemblages, and (3) reconstructing overlying stratigraphy. Field observations by Hudec (1992) and Burton (1997) of miarolitic cavities in early stage units and the narrow width (<1.5 km) of the andalusite-bearing contact metamorphic mineral assemblage suggest relatively shallow emplacement of the roof zone (<4 kbar). The Al-in-hornblende barometer used by Burton (1997) and recalculated by Barnes et al. (2001) yielded deeper estimates for early stage units (4.6–6.9 kbar) than late stage units (3.3–4.0 kbar). This systematic disparity was explained by crystallization of analyzed hornblendes at depth prior to emplacement at higher structural levels. Emplacement depths of ~9–18 km beneath the Eocene land surface were calculated from pressure estimates using bulk density estimates of 2.68 g/cm³ for the overlying carbonate siliciclastic rock package which was modified from the regional gravity study of Gibbs et al. (1968). Densities for individual rock units were determined using open-hole geophysical well logs from Huntington Valley west of the RMEHR. Hudec (1990; 1992) documented late Jurassic metamorphic depths of 13–18 km in the igneous complex north of the HPP (~5 km structurally below the HPP roof zone).

A generally east-dipping, >8 km composite sequence of Neoproterozoic to Mississippian strata can be reconstructed from exposures throughout the southern

RMEHR. Integration of regionally exposed upper Paleozoic units by Burton (1997) and Colgan et al. (2010) with the immediate stratigraphic framework into which the HPP was intruded yielded relatively shallow emplacement depths of 6–13 km and 4–12 km, respectively. The minimum values from these studies are based on the position of the HPP roof zone in the Ordovician Pogonip Group and the assumption that only negligible thicknesses of Mesozoic and Cenozoic strata existed above the Paleozoic section at the time of intrusion. However, there are few constraints on the maximum thickness of Eocene units, which Colgan et al. (2010) simply states as 1000 m, (producing a margin of error of ± 1 km). Observations from adjacent ranges of Eocene lava flows overlying granites that resided at shallow depths in the Cretaceous suggest that there are not significant gaps in the stratigraphy (Colgan et al., 2010). Although Colgan et al. (2010) cited agreement with the emplacement pressures of <3–4 kbar of Barnes et al. (2001), the resulting depth estimates for these values are approximately <8–11 km. Since these values are significantly deeper than the minimum estimates of Colgan et al. (2010), it appears that the agreement between these studies is overstated.

3.7.2 NEW HPP EMPLACEMENT DEPTH ESTIMATES

The assumption that entrapment of three distinct aqueous and aquo-carbonic fluid types occurred within 50°C of the wet granite solidus is supported by observations of these fluids in both orthomagmatic and hydrothermal feature types with unequivocal magmatic isotopic signatures. The criteria for selection of inclusions entrapped during primary crystal growth are described in Section 3.4.1. Also, no systematic variation between orthomagmatic and hydrothermal features exists for Th_{tot} values for each respective fluid type, further demonstrating that thermodynamic conditions were generally similar for

fluid entrapment in both settings. Thus, the pressures of entrapment derived from the intersection of fluid inclusion isochores with the experimentally determined wet granite solidus curve can serve as estimates of the overall pressure regime for the HPP at the approximate solidus temperature.

In this study, entrapment pressures for the bulk of the aqueous (A2 and A1) and aquo-carbonic (BC) fluid types were determined to be ~3400–6800 bar, and ~4800–7200 bar, respectively (see Sections 3.6.1 and 3.6.2). However, due to the interpretation that trapping of the BC fluid type occurred in an overpressured system (see Section 3.5.5.2), only pressure estimates from the A1 and A2 fluid type will be used to determine the minimum crustal depth of the HPP and surrounding rocks at 36–38 Ma. It can reasonably be assumed that the effects of magmatic overpressuring in early stage units (if any) were negligible, since there exists general agreement with pressure estimates from other studies. Using the conversion of Burton (1997) (described above), the entrapment pressures of aqueous fluids (A2 and A1) generate emplacement depths of ~8.9–17.8 km. The emplacement depths of the A2 and A1 fluid type demonstrate general agreement with the thermobarometric depths of 9–16 km determined by Barnes et al. (2001). However, these estimates are, at minimum, 2.9 km and 4.9 km deeper than the shallowest depths indicated by the stratigraphic reconstructions of Burton (1997) and Colgan et al. (2010), respectively, and suggest that simple interpretations of the overlying Paleozoic rock package are insufficient. The HPP emplacement depths determined by this study indicate that at least 9 km of total vertical exhumation has occurred in the southern RMEHR since the late Eocene. It is clear that the magmatic-hydrothermal fluid system of the HPP

supports models of pre-intrusion tectonic burial of the southern RMEHR to greater than stratigraphic depths.

3.7.3 REVIEW OF RMEHR METAMORPHIC CORE CORE COMPLEX DEVELOPMENT

Current models for the development of the RMEHR metamorphic core complex require burial of the infrastructural migmatites and gneisses in the northern RMEHR to mid- or lower-crustal depths (~9 kbar equivalent) and burial of equivalent suprastructural rocks in the southern RMEHR to poorly-defined but progressively shallower levels southward to achieve observed metamorphic grades (Howard, 1980; Dallmeyer et al., 1986; Hodges et al., 1992; Camilleri & Chamberlain, 1997; McGrew et al., 2000). These rocks were returned to the surface by episodic extension that was most extreme during the Miocene, but may have begun as early as the Eocene (Dallmeyer et al., 1986; McGrew & Snee, 1994). Extension occurred on the RMSZ, a ~20° west-dipping, brittle fault which superimposed on a 100–1000 m wide extensional mylonitic shear zone that extends for ~150 km along the western margin of the range (see Snoke & Miller, 1988 for review). Estimates of total E–W lateral extension accommodated by the RMSZ have ranged from 4 km to as much as 65–70 km (see review by Howard, 2003). This feature sharply crosscuts the HPP, where mylonitic and cataclastic textures are weakly and locally developed (Dokka et al., 1986; Hurlow et al., 1991). Disparity between HPP emplacement pressures and the metamorphic pressures from Jurassic granites adjacent to the northern margin of the HPP and minor Paleogene hanging wall basin deposits are permissive of ~2–3 km of extensional uplift prior to intrusion (Hudec, 1992; Satarugsa & Johnson, 2000; Colgan et al., 2010). Although minor deformation has been observed within hydrothermal veins in this study, the absence of any major penetrative fabrics in the HPP indicates that syn-intrusion

extension was relatively minor and that brittle faulting did not begin until after magmatic crystallization (Burton, 1997).

Exhumation of the RMEHR metamorphic core complex by extensional slip on the RMSZ is generally interpreted to have occurred episodically from the Eocene to the middle Miocene (McGrew et al., 2000; Dokka et al., 1986; Dallmeyer et al., 1986; Wright & Snoke, 1993; Burton, 1997; MacCready et al., 1997; Colgan et al., 2010; Haines & van der Pluijm, 2010). Several radiogenic age datasets from the HPP and surrounding localities have been interpreted to record rapid, west-directed ductile-to-brittle slip on the RMSZ and exhumation of the RMEHR metamorphic core complex. Biotite K-Ar and zircon and apatite fission track data range from ~35–9 Ma, with an obvious west-younging trend (Kistler et al., 1981; Reese, 1986; Burton, 1997; Colgan et al., 2010). Miocene-recent tilting of the RMEHR horst block by ~30° was first suggested by Blackwell et al. (1985) on the basis of west-younging apatite fission track data and confirmed with field evidence by Burton (1997). Colgan et al. (2010) argued that the oldest of these dates (37–20 Ma) represent partial resetting rather than extension-driven cooling and restricted extension to a relatively brief period between 17–16 Ma and 10–12 Ma.

3.7.4 THE HPP AND RMEHR METAMORPHIC CORE COMPLEX

As determined by the entrapment conditions of magmatic-hydrothermal fluids in this study, the crystallization of early stage HPP magmas at pressures of 3400–6800 bar (~9–17 km) broadly supports the deeper thermobarometric and stratigraphic estimates of Burton (1997) and Barnes et al. (2001), while challenging the shallower stratigraphic estimates of Colgan et al. (2010). The emplacement pressure estimates demonstrate that the thickness of the overlying rock package (and thus the syn-plutonic depths of RMEHR

transition zone rock units) was at least 9 km, and that the bulk of vertical exhumation occurred after intrusion. Numerous studies have also documented geochronological and thermobarometric evidence for burial of the RMEHR to as great as three times stratigraphic depths at the northern extent of the range (reviewed by Howard, 2003). Here, two of the most plausible explanations for RMEHR crustal thickening and intrusion at depths greater than stratigraphic reconstructions are considered, (see Figure 3.26 for visual representation of HPP emplacement depth and possible explanations). However, since the data and conclusions of this study are permissive of both, endorsement of either explanation is withheld.

The first explanation for the disparity between stratigraphic and analytical determinations of HPP emplacement depths invokes uncertainties in the thicknesses of units and the effects of erosion in the overlying rock package at the time of intrusion. Although a complete sequence between the Neoproterozoic McCoy Group and the Ordovician Pogonip Group is preserved locally at the HPP, inferences of thicknesses must be made for the rest of the section from units exposed in fault-bounded blocks in the central RMEHR, in adjacent ranges, and regionally (Willden & Kistler, 1979). As noted earlier, few constraints are placed on the thicknesses of now-eroded Eocene units that overlaid Paleozoic stratigraphy in the RMEHR at the time of HPP intrusion. Thus, variations in depositional environments and post-deposition erosion are difficult to constrain and to incorporate into the reconstructed stratigraphy. As a result, even the most confident studies contain margins of error of at least 1 km for HPP emplacement depths (i.e. Colgan et al., 2010). Although these uncertainties would likely not satisfactorily explain the large disparities (i.e. ~5 km) between HPP emplacement depths and the reconstructed

stratigraphy of Colgan et al. (2010), it is conceivable that the differences of ~3 km observed between this study and Burton (1997) could be accommodated.

The second explanation for burial of the southern RMEHR to greater-than-stratigraphic depths argues for more significant tectonic complexity at the scale of the RMEHR and the northern Great Basin (see Howard, 2003). Published arguments for Mesozoic structural thickening and burial by the emplacement of cryptic allochthon(s) and fold nappes onto the Paleozoic strata in the region of the RMEHR prior to Eocene intrusion of the HPP remain the most prevalent explanation for disagreement between calculated pressures in the RMEHR and reconstructions of overlying stratigraphy (Smith & Ketner, 1976a, 1978; Snoke & Lush, 1984; Thorman et al., 1991; Hodges et al., 1992; Smith et al., 1993; Miller & Hoisch, 1995; Camilleri & McGrew, 1997; Jones, 1999; Taylor et al., 2000; Howard, 2003). The Elko Orogeny, proposed and described by Thorman et al. (1990; 1991; 2003), is one of several Mesozoic orogenic events that could explain the high emplacement pressures of the HPP. Evidence of late Jurassic southeast-directed imbrication and crustal thickening has been recognized regionally and in the RMEHR by several authors (reviewed by Thorman et al., 1990). Hudec (1992) determined a coeval increase in metamorphic pressures of ~1 kbar for the RMEHR, with peak values corresponding to depths of 13–18 km. Although evidence of subsequent extension in the Cretaceous exists, thermobarometry from the HPP and other localities in the RMEHR (i.e. Lamoille Canyon) demonstrates that rapid exhumation did not begin until the Eocene, hence the southern RMEHR was still overthickened at the time of HPP intrusion (Kistler et al., 1981; Hodges & Walker, 1992; Hodges et al., 1992; Hudec, 1992; Burton, 1997).

3.8 IMPLICATIONS FOR CARLIN-TYPE AU DEPOSITS

Although disseminated, sediment-hosted, hydrothermal CTD's have been recognized as the most significant source of Au in the Great Basin for decades, the origin and evolution of mineralizing fluids remain contested (see review by Hofstra & Cline, 2000). The debate centers on whether felsic intrusive magmatism (exemplified by the HPP) or deep crustal metamorphic reactions generated the fluids and ore elements, or deeply circulating meteoric fluids scavenged Au from preexisting crustal anomalies. More recently, Muntean et al. (2011) proposed a variant of the traditional magmatic model that argues for mixing of Au-bearing magmatic fluids with meteoric inputs as a critical process in the formation of CTD's. This model specifically incorporates the HPP as an example of an exposed source pluton for CTD ore fluids, and, thus, the results of this study are discussed in that context. The thermal, isotopic, and compositional characteristics of the magmatic fluid types described in this study do not provide conclusive evidence for the origin of CTD's, but do suggest a less significant role for magmatism than proposed by some authors. Despite some overall similarities in basic fluid properties and stable isotope values with CTD's, the data demonstrate that the HPP was likely not enriched in Au and other Carlin "pathfinder" elements. Furthermore, there is little evidence for several key components of the magmatic fluid mixing model of Muntean et al. (2011).

3.8.1 REVIEW OF CTD'S

The two end-member models for the origin of CTD's that have dominated discussion in recent years both derive support from a large, diverse body of research. The general thermal, geochemical, and volumetric characteristics of main ore-stage fluids have been

defined by several studies of CTD's from the most prolific localities in the northeastern Great Basin. Fluid inclusion studies and thermal modeling have constrained ore fluid trapping temperatures to 180–240°C, salinities to 2–4 wt % eq. NaCl, and CO₂, H₂S, and CH₄ concentrations to <0.83 wt %, 10⁻¹–10⁻² mol, and <0.4 mol%, respectively (Lamb, 1995; Hofstra & Cline, 2000; Cline & Hofstra, 2000; Lubben, 2004; Lubben et al., 2012). Some studies have interpreted the presence of two distinct ore fluids: a vapor-rich, moderate salinity phase, and a vapor-poor, low-salinity phase (Kuehn & Rose, 1995; Arehart, 1996). The pH of ore fluids transitioned from neutral to acidic (pH = 3.0–3.5) as they cooled, creating porosity by dissolution in reactive carbonate horizons (Cline et al., 2005). Sulfidation of Fe-bearing host rocks and/or pyrite surface reactions are generally believed to be responsible for Au deposition, while no evidence exists for fluid immiscibility or boiling (e.g. Hofstra et al., 1991; Kesler et al., 2003). Characteristically high S:Cl ratios in ore fluids resulted in depressed base metal solubility, and enhanced bisulfide complexing and transport of Au (Hofstra, 1994; Emsbo et al., 2003).

Many studies have reconstructed the multi-element compositional character of CTD ore fluids from mineral chemistry and deposit-scale mass balance, although published fluid inclusion LA-ICP-MS data is lacking. Nevertheless, it has been demonstrated that in addition to Au, a suite of Carlin-type pathfinder elements (As, Hg, Sb, Tl) are consistently elevated above local and regional background levels within and around the deposit footprint (Kuehn et al., 1992; Albino, 1994; Emsbo et al., 2003; Fortuna et al., 2003; Heitt et al., 2003; Kesler et al., 2003; de Almeida et al., 2010; Vaughan, 2013). Like Au, As and Sb can be transported by bisulfide complexes. A recently documented correlation between Au grade and elevated K/Al and Rb at the Banshee deposit and other CTD's indicates that illite

alteration was caused by ore fluids, and that these fluids were enriched in K and Rb (Vaughan, 2013). Other elements that are inconsistently enriched in CTD's, (and therefore display an unclear relationship with ore fluids), include W, Te, Cu, Mo, Se, Fe, Ag, Pb, Si, Ba, Cs, Zn (Cline et al., 2005). However, several elements (As, Se, Ag, Zn, Au) may have been added to CTD host rocks by non-hydrothermal, syn-sedimentary processes (Vaughan, 2013).

Although much of the stable isotope data for CTD ore fluids indicates a primarily meteoric origin, a discernable magmatic/metamorphic fluid component has been documented at several localities (Hofstra et al., 1999; Yigit, 2001; Emsbo et al., 2003; Heitt et al., 2003; Lubben, 2004; Cline et al., 2005; Lubben et al., 2012). This is most apparent in stable isotope data from pre-ore and ore-stage clay minerals and calcite at Getchell, which contain evidence of magmatic-meteoric fluid mixing ($\delta^{18}\text{O}_{\text{H}_2\text{O}}$: 4 to 9‰; δD : -77 to -114‰) (Cline & Hofstra, 2000). Variable $\delta^{18}\text{O}$ depletion has been interpreted as being proportional to the amount of fluid-rock interaction, and is spatially correlative to Au grade (Veizer, 1999; Cline & Hofstra, 2000; Nutt & Hofstra, 2003; Arehart & Donelick, 2006; Vaughan, 2013). Mantle-derived helium isotopes from ore-stage fluid inclusions from Getchell are also supportive of a possible deep crustal fluid source (Cline et al., 2003). Despite analytical problems, the wide range of sulfur isotope values observed in ore-stage pyrites was likely a product of multiple sedimentary sources (Hofstra, 1997; Emsbo et al., 2003). However, some data from Getchell and the Northern Carlin Trend demonstrate a small scatter and values indicative of a magmatic source (Cline et al., 2003; Kesler et al., 2003a; Henkelman, 2004; Cline et al., 2005). The variability in all isotopic results from the mineral to the district scale has been described by several authors and has been interpreted by some as

evidence for deep crustal ore fluids of magmatic or metamorphic origin mixing with infiltrating meteoric fluids during or shortly after the bulk of Au deposition (see Cline & Hofstra, 2000; Hofstra & Cline, 2000; Cline et al., 2005).

3.8.2 COMPARISON BETWEEN THE HPP AND CTD ORE FLUIDS

Despite significant differences in entrapment conditions precluding comparison of certain fluid inclusion characteristics between CTD ore fluids and HPP magmatic fluids, some useful evaluations can be made. First, it is apparent that salinities for the magmatic fluid types at the HPP and at the majority of CTD's are similarly low (<4 wt % eq. NaCl). Ore fluids at Getchell and Deep Star are permissive of a fluid component with the $\delta^{18}\text{O}$ values determined for the magmatic fluid types at the HPP. Although δD values were not determined for fluids at the HPP, values for ore fluids from Getchell are also permissive of a magmatic component. The carbon and oxygen stable isotopes data of Musekamp (2012) from calcite veins and skarn deposits around the HPP also plot along lines of mixing between various end-member fluid sources (including the magmatic fluid types of this study) and demonstrate some agreement with the isotope values for late ore-stage calcite veins in CTD's (Hofstra & Cline, 2000). However, this mixing of end member fluids has not been documented at many other CTD's (i.e. Carlin, Meikle, Jerritt Canyon, and Alligator Ridge), where only exchanged meteoric signatures have been detected for ore fluids (see review by Hofstra & Cline, 2000). These basic similarities between fluid types demonstrate that certain components of CTD ore fluids (i.e. water, CO_2 , major cations) may have been sourced from intrusions such as the HPP.

The restriction of the aquo-carbonic BC fluid type to late stage units, (and absence in early stage units and wallrock units), demonstrates that the late stage intrusive units of the

HPP did not significantly contribute to the local or regional Eocene crustal fluid budget or to the formation of CTD's. This is also consistent with the lack of skarn and carbonate replacement mineralization directly related to late stage magmatism. The low concentrations of CO₂ detected in ore stage fluid inclusions from CTD's (<2–4 mol%) could not have originated from these fluids. However, CO₂ is soluble in aqueous fluids (and thus invisible during petrographic inspection and microthermometry) below ~4 mol% CO₂ (Bodnar, 1993). Thus, it remains possible that the A1 and A2 aqueous fluid types contained low, but sufficient concentrations of CO₂ to generate CTD ore fluids of appropriate composition.

Although there currently exist no published LA-ICP-MS data for ore-stage fluid inclusions from CTD's in the Great Basin (largely due to their rarity), several such studies from CTD's in China allow a more detailed characterization of ore fluid chemistry. The 140–75 Ma Chinese deposits are also characterized by enrichment in Carlin pathfinder elements, Au-hosting microscopic As-rich pyrite, alteration styles typical of CTD's (i.e. decarbonitization, argillization, silicification), and impure carbonate host rocks (see Hu et al., 2002; Zhang et al., 2003; Hofstra et al., 2005; Su et al., 2008; 2009). Three groups of fluids have been identified at several CTD's in Guizhou, China representing the pre-ore, ore-stage, and post-ore fluid fluxes (Hu et al., 2002; Hofstra et al., 2005; Su et al., 2009). Main ore-stage inclusions are of aquo-carbonic composition (~6.3–8.4 mol% CO₂), demonstrate Tt values of 150–250°C, moderate acidity, lower salinities (0.9–2.3 wt % eq. NaCl) than aqueous pre-ore inclusions (5.0–6.9 wt % eq. NaCl), and densities of 0.97–0.99 g/cm³, and measurable concentrations of B, Na, K, Sr, Cs, Sb, As, and Au (Gao, 1992; Hu et al., 2002; Su et al., 2009). Relevant ore fluid stable isotope values (calculated from fluid inclusions) are

generally indicative of a magmatic fluid source (δD : -87 to -47‰; $\delta^{18}O$: -2.1–16.2‰).

Carbon and sulfur stable isotopes indicate a sedimentary fluid source (Hu et al., 2002).

The general similarity in fluid characteristics between CTD's in China and the Great Basin demonstrates that these deposits, (despite differences in age, tectonic setting, and Au endowment), can be treated as crudely equivalent for the purposes of this discussion. It is therefore assumed that, in the absence of fluid inclusion multi-element data from CTD's in the Great Basin, the multi-element geochemistry of ore-stage fluid inclusions from Chinese CTD's (as determined by Su et al. (2009)) can serve as a viable proxy. The three fluid types of Su et al. (2009) demonstrate decreasing trace element abundances (except for As and Sb) across the ore depositional event. No clear evolution in trace element geochemistry is observed between fluid types in this study. Na, K, and Cs concentrations are generally higher in this study (but within an order of magnitude). Sr concentrations are significantly higher in this study when compared to ore-stage inclusions (at least an order of magnitude), but are similar to concentrations in pre-ore inclusions. Concentrations of B are similar between these datasets. Although Cu and Pb were detected in a fraction of inclusions in this study, they are almost completely absent from the data of Su et al. (2009), whereas the converse is true for Sb. Where detected, As concentrations are also similar. However, As was below the limit of detection in significantly more inclusions in this study than in Su et al. (2009), which may either be due to either lower absolute concentrations or to analytical differences (i.e. inclusion size, beam size, sample depth).

This qualitative comparison demonstrates that HPP magmatic fluid types contained consistently higher concentrations of major dissolved species (supported by slightly higher overall salinities) and base metals, but generally lower concentrations of CTD pathfinder

elements. The discrepancy in salinities can be explained by varying concentrations of chloride or dilution during fluid transport and mixing with meteoric inputs. Also, it is plausible that base metals largely precipitated in more proximal deposit types along or near the plutonic margins (as observed at the HPP). However, the data suggest that although the HPP contained slightly elevated As and Sb, it did not possess sufficient concentrations of these elements to act as the primary source of ore fluids for CTD mineralizing systems.

3.8.3 THE MAGMATIC-HYDROTHERMAL PHASE SEPARATION MODEL

The traditional magmatic-hydrothermal fluid model is based on spatial and temporal associations between Au deposits and regional felsic magmatic activity, isotopic evidence from select deposits, and similarities with porphyry and orogenic Au systems. The model of Muntean et al. (2011) presented new oxygen and hydrogen stable isotope data, and LA-ICP-MS and microprobe multi-element data from synthetic glasses and argued for magmatic-hydrothermal fluid phase separation as a critical process in the evolution of CTD ore fluids. Additional fundamental components of this model are the reactivated extensional tectonic setting, an SCLM fertilized and hydrated by subduction, and Fe-rich carbonate upper crustal host rocks. Delamination of the Farallon plate beneath western North America during the Eocene initiated interaction between asthenospheric melts and the SCLM the voluminous production of Au-S-CO₂-enriched, hydrous, intermediate, calc-alkaline magmas. At an unspecified depth in the middle to upper crust (10–20 km), transitory magma chambers (of which the HPP is cited as an example) experienced partitioning of copper into mono-sulfide solid solution, resulting in very high Au:Cu ratios in the remaining melt.

It is proposed that at higher levels in the crust, the unmixed, CO₂-H₂S-Au-bearing magmatic fluids experienced density-driven phase separation after saturation and expulsion from crustal intrusions such as the HPP. This primitive fluid was likely aqueous and of moderate-low salinity (2–12 wt % eq. NaCl). A base metal-bearing, high salinity fluid stalled at depth, while a low-salinity (~3–5 wt % eq. NaCl), (Au-As-Sb-Tl-Hg)-bearing vapor phase ascended through the crust away from source intrusions. Interaction and mixing with meteoric fluids at relatively shallow crustal levels (<10 km) caused rapid cooling of the vapor phase. The resulting fluid mixture (~220–250°C, ~2–3 wt % eq. NaCl) ascended along high-angle feeder faults before intersecting favorable carbonate horizons and precipitating Au and other trace elements by sulfidation and other water-rock reactions.

3.8.4 THE HPP AND THE MAGMATIC-HYDROTHERMAL PHASE SEPARATION MODEL

The HPP was described by Muntean et al. (2011) as an example of an exposed mid to upper-crustal intrusive body that may have released primitive CTD ore fluids during emplacement. Calculated crystallization depths of 9–16 km for magmatic hornblende, as interpreted by Barnes et al. (2001), contain some indications that emplacement may have been preceded by accumulation of early stage magmas at deeper midcrustal depths, a process that is correlative with the emplacement of the transitory magma chambers described above in the model of Muntean et al. (2011). Emplacement depth estimates from this study generally support this interpretation. Some of the orthomagmatic features observed at the roof zone of the HPP by Burton (1997) and Barnes et al. (2001), (i.e. porphyritic and equigranular roof dikes and leucocratic cupolas) were described by Muntean et al. (2001) as evidence of fault-driven upward expulsion of fluids and magma, and proposed to be equivalent to deep roots of syn-ore dikes in CTD's and erupted volcanic

centers such as the Tuscarora and Emigrant Pass volcanic fields. The presence and distribution of other features in early and late stage units, including abundant aplites and pegmatites, sparse miarolitic cavities, quartz veins, and adjacent skarn mineralization also provide evidence for a robust syn- and post-intrusion fluid system.

As the integration with the data of Musekamp (2012) in Section 3.5.5, and the fluid history described in Section 3.6 have shown, there is evidence of a spatially, temporally, and compositionally evolving magmatic-hydrothermal fluid system within and immediately around the HPP. The low density, low salinity A1 fluid type and the intermediate density, low salinity A2 fluid types proposed in Section 3.5.2 are the best evidence for the low salinity magmatic vapor phase described as the primitive CTD ore fluid in the model of Muntean et al. (2011). Thus, the dominance of these fluid types in early stage units is consistent with the similar distribution of miarolitic cavities and skarn deposits. The lack of a high salinity fluid phase in the fluid inclusion data of Musekamp (2012) and of this study is problematic for the application of the Muntean et al. (2011) magmatic-hydrothermal phase separation model. In that model, such a fluid would be expected to be present in the base metal-bearing skarn and carbonate replacement deposits. However, there exists no consistent variation in fluid inclusion thermal or compositional data between these deposits and other feature types.

The lack of evidence for a high salinity aqueous fluid in this study and in Musekamp (2012) is in strong disagreement with the model of Muntean et al. (2011). Since the HPP was cited by Muntean et al. (2011) as the best example of an exposed source intrusion for CTD ore fluids, it is assumed here that this model is generally dependent on compatibility with data from the HPP. It is possible that low initial copper concentrations in HPP magmas

could potentially eliminate the need for a high salinity phase to explain the high Au:Cu ratios in CTD's. Whole-rock multi-element data from Barnes et al. (2001) demonstrates very low, sub-chondritic Cu concentrations (<15 ppm) that could be explained by deeper magmatic fractionation and removal of Cu from ascending magmas. However, multiple instances of copper and base metal mineralization around the HPP are still problematic for this explanation. Thus, it is more likely that neither high salinity fluids nor elevated Au concentrations existed during syn-emplacement magmatic-hydrothermal fluid activity. The model of Muntean et al. (2011) must be revised to reflect this fundamental difference in magma chemistry.

Compositionally, the A2 and BC magmatic fluid types demonstrate several significant inconsistencies with the predictions of Muntean et al. (2001). Although Au was not in the suite of elements analyzed for by LA-ICP-MS in this study, two bisulfide complexing proxy elements (As, Sb) and two related elements (Cu, Pb) were detected in concentrations consistently higher than corresponding whole-rock concentrations from the HPP recorded by Barnes et al. (2001). However, a lack in elemental variation between the A2 and BC fluid types clearly indicates that neither of these fluids can be favored as a primitive CTD ore fluid. If one fluid type were to be considered equivalent to the primitive CTD ore fluid, it would be expected to have significantly higher concentrations of these elements than other magmatic fluids. Furthermore, the model of Muntean et al. (2011) predicts extremely efficient partitioning of metals into magmatic fluids, a process not reflected by a difference in Cu values between fluids and whole-rock values of only one order of magnitude.

If the magmatic-hydrothermal phase separation model of Muntean et al. (2011) is to be adopted, the A3 fluid type may be treated as an analog for CTD ore fluids, which also exhibit evidence of formation by magmatic-meteoric mixing processes. The A3 fluid type was generated by mixing at depth between magmatic fluid types and cooler meteoric fluids within ~5 Ma of HPP emplacement. Both fluid types exhibit generally low salinities ($\ll 4$ wt % eq. NaCl), and relatively low $\delta^{18}\text{O}$ values indicative of magmatic and meteoric fluid mixing. Interpreted temperatures of entrapment for the A3 fluid type (320–410°C) are somewhat higher than the temperatures determined for CTD ore fluids (180–240°C), but were also entrapped at considerably deeper crustal levels (Cline & Hofstra, 2000; Hofstra & Cline, 2000). Also, the values for the A3 fluid type represent an upper temperature limit; actual fluid temperatures may have been significantly lower. It was also interpreted that the A3 fluid type was responsible for chlorite-sericite (and possibly phyllic) alteration and localized pervasive silicification. Pre- and ore stage quartz veins and silicification and late and post-ore stage calcite veins are ubiquitous features of CTD's (Hofstra & Cline, 2000; Cline et al., 2005; Lubben et al., 2012). However, other features, most notably geochemical anomalies of Carlin pathfinder elements (As, Sb, Tl, Hg), are lacking within the end member magmatic fluid types of the HPP.

3.8.5 PROPOSED FLUID MODELS

The fluid model for the magmatic-hydrothermal fluid system of the HPP based on the observations and data from this study and Musekamp (2012) provides important implications for the magmatic-hydrothermal phase separation model of Muntean et al. (2011) and the role of magmatism in the formation of CTD's. Tt values, salinities, and carbon and oxygen stable isotope values indicative of magmatic-meteoric fluid mixing in

and around the HPP were first recognized by Musekamp (2012) and are generally supported by this study. As stated earlier, the A3 fluid type is interpreted to be the most significant product of this process and can be treated as broadly analogous to CTD ore fluids. However, the lack of evidence for a high salinity aqueous fluid and consistently low fluid inclusion concentrations of CTD pathfinder elements provide strong indications that the model of Muntean et al. (2011) requires revision and that the HPP is an unlikely source for ore and related elements in CTD's. Nevertheless, application of this model to the data and fluid history presented in this study is useful for fully understanding the inconsistencies and agreements between them. Here, we explore several models that propose different relationships between the A3 fluid type and CTD ore fluids and discuss the viability of each.

Generally similar Tt values, salinities, (Musekamp, 2012; this study), and stable isotope values (from Musekamp, 2012) support the treatment of the A3 fluid type as a deeply entrapped, near-source analog for CTD ore fluids. Three different models would provide explanations for the relationship between them. First, it may be that the A3 fluid type is a thermally equivalent, but compositionally distinct, analog for CTD ore fluids. In this model, CTD ore fluids underwent a similar evolution as observed at the HPP, but were sourced from Au-As-Sb-Tl-Hg-enriched intrusions. The geochemical heterogeneity of the Mojave basement province beneath this region of the Great Basin lends credibility to this interpretation (Bennett & DePaolo, 1987; Wooden & Miller, 1990). However, this model, if valid, requires a new base metal partitioning mechanism to explain the Au-only character of CTD's. In the second model, primitive metal-enriched fluids ascended along faults to favorable host rock units during and after mixing with meteoric fluids, while the A3 fluid

type represents an Au-As-Sb-poor fraction that locally formed calcite and quartz veins. However, no evidence for the enriched fluid fraction has been observed in or around the HPP.

Finally, the similarities between the A3 fluid type and CTD ore fluids can be explained by the meteoric fluid model for CTD formation, in which Au originates from preexisting crustal Au anomalies rather than intrusions. In this scenario, the A3 fluid type represents a non-mineralizing aqueous fluid of mixed magmatic-meteoric origin (but dominantly meteoric) that had the potential to become enriched in Au and Carlin pathfinder elements if it had circulated through Au-As-Sb-rich rocks in the crust. This model is supported by the basic similarities observed between the HPP magmatic fluids and CTD ore fluids and the inconsistent and/or weak magmatic isotope signatures observed at some deposits. Although the first model cannot be entirely discounted, the data and conclusions of this study clearly favor this explanation.

Based on the relationships between the fluid types observed in and around the HPP, the known characteristics of CTD ore fluids, and the magmatic fluid mixing model of Muntean et al. (2011), it is proposed here that the HPP is a low-salinity, Au-poor intrusion that was, at most, a possible heat and minor fluid source for CTD's in the Great Basin during the Eocene. However, it remains conceivable that the HPP represents a relatively infertile end-member of a regional flux of magmas, represented by geophysically imaged plutons beneath the Carlin Trend and erupted silicic calderas of similar age. In such a scenario, the HPP still serves as a viable, (albeit geochemically distinct), analog for Au and Carlin pathfinder element-enriched source plutons if a novel base-metal partitioning mechanism

can be invoked. Regardless, it can be reasonably concluded that the HPP itself was not an Au source for the CTD's formed in the Great Basin during the Eocene.

3.9 SUMMARY

This study has reconstructed the magmatic-hydrothermal fluid history of a silicic intrusion that was emplaced in two stages into a major Cordilleran metamorphic core complex. Generation and intrusion of magmas occurred during southwestward migration of regional magmatic fronts and a coeval Au-rich crustal fluid flux that was responsible for the formation of CTD's. Field, petrographic, isotopic, and fluid inclusion microthermometric and geochemical data indicate that the crystallization of the HPP was accompanied by two distinct pulses of magmatic-hydrothermal fluid activity. The first pulse originated from early stage magmas and was dominated by low salinity, aqueous fluids. These fluids continuously circulated during and throughout the early and late stages of magmatic emplacement and were entrapped in pegmatites, aplites, miarolitic cavities, and quartz veins, and into the contact metamorphic aureole, where they were entrapped in skarn deposits, quartz veins, and calcite veins. The second pulse originated from late stage magmas, and was dominated by low salinity, aquo-carbonic fluids that were entrapped in pegmatites, aplites, and quartz veins within their source magmas. Despite generally similar compositions, the aquo-carbonic fluids from the second pulse demonstrate that they are derived from more fractionated magmas than the aqueous fluids from the first fluid pulse. Post-intrusion hydrothermal fluids were generated by mixing between aqueous magmatic

fluids from the first fluid pulse and cooler meteoric fluids within the contact metamorphic aureole and were largely entrapped within microcrystalline quartz-hosting structures.

Magmatic fluids offer a snapshot of the temperature and pressure conditions of this intrusion at near-solidus conditions, and thus suggest that emplacement occurred at depths greater than those inferred from stratigraphy. According to the pressures of entrapment determined for magmatic fluids in early stage intrusive units, emplacement of the HPP occurred at approximately ~9–18 km below the Eocene land surface. These values are similar to earlier estimates from mineral thermobarometry of the HPP and nearby igneous rocks. It is interpreted here that the roof zone of the HPP and structurally adjacent rock units resided at a minimum depth of ~9 km prior to the onset of tectonic exhumation brought on by brittle slip the N–S striking, west-rooted, low-angle Ruby detachment (as described by Snoke & Miller, 1988). Intermittent large-scale extension along this structure from ~35–9 Ma is recorded by published thermochronological data from the HPP, with episodes of rapid slip in the middle Miocene (Kistler et al., 1981; Blackwell, 1985; Reese, 1986; Burton, 1997; Colgan et al., 2010). This approximate emplacement depth is at least 5 km greater than expected depths calculated from overlying stratigraphy. Poorly-preserved, overriding Mesozoic thrust sheets or error in the thicknesses of specific overlying rock units may account for discrepancies between the emplacement depths determined in this study and existing stratigraphic reconstructions.

The compositions of HPP magmatic fluids also provide a critique of an existing model for the formation of Carlin-type Au deposits, and indicate that this intrusion was likely not a source of Au or associated elements. Key aspects of the magmatic-hydrothermal phase separation model for the origin of CTD's (proposed by Muntean et al. (2011)) are not

supported by the findings of this study. In addition to the low concentrations of Carlin pathfinder elements detected within magmatic fluids, no evidence of a high salinity, base metal-enriched fluid phase was encountered in this study. In light of these observations and data, a new mechanism for the separation of Au from base metals during fluid ascent must be proposed for the magmatic-meteoric fluid mixing model to remain viable. Since several of these elements are transported by the same complexing ligands as Au, low concentrations of Carlin pathfinder elements in the magmatic fluids from the HPP indicate that this intrusion was likely also not enriched in Au. However, similar salinities and stable isotope characteristics suggest that these fluids may represent the minor magmatic component of CTD ore fluids detected at certain deposits. Based on the findings of this study, it is proposed that mixing between magmatic and meteoric fluids, (similar to what occurred around the HPP), followed by enrichment in ore elements through crustal circulation are fundamental processes in the evolution of CTD ore fluids.

TABLE 3.1 – Sample locations, descriptions, and analytical designations.

Sample ID	Point East (UTM11 NAD27)	Point North (UTM11 NAD27)	Elevation (ft)	Intrusive Unit	Sample Lithology/ Feature Type	Thickness (cm)	Petrography	Fluid Inclusion Petrography & Microthermometry	Fluid Inclusion LA-ICP-MS	Oxygen Stable Isotope Analysis
HPP-1-03	626852	4460696	7822	Tcc	Type (II) (wallrock) Quartz Vein	10-12		Yes		
HPP-1-04	626579	4460844	7539	Tcc	Type (I) Quartz Vein	1		Yes		
HPP-1-17a	626334	4461936	7335	Tcc	Aplite	3	Yes			
HPP-1-20	625908	4461985	7505	Tcc	Granite (altered)	2 x 3.5		Yes		
HPP-1-24b	625877	4462000	7483	Tcc	Miarolitic Cavity			Yes		
HPP-1-25d	625760	4461981	7424	Tcc	Type (II) (skarn) Quartz Vein (Mineralized)		Yes			
HPP-1-27	626020	4462115	7447	Tcc	Type (IV) Microcrystalline Quartz Vein	0.5-1		Yes		
HPP-1-30	626260	4462440	7597	Tcc	Type (III) Quartz Vein	4-13		Yes		Yes
HPP-1-35a	626909	4461813	7541	Tcc	Aplite	3	Yes			
HPP-1-35b	626909	4461813	7541	Tcc	QF Pegmatite	5	Yes			
HPP-1-36a	626939	4461809	7568	Tcc	Type (IV) Microcrystalline Quartz Vein	1.5-2		Yes	Yes	
HPP-1-56	626755	4462847	7470	Tcc	QF Pegmatite	4-5		Yes		
HPP-1-59	626630	4463024	7536	Tcc	Granite (altered)		Yes			
HPP-1-63	626560	4463204	7683	Tcc	Type (IV) Microcrystalline Quartz Vein	2-5		Yes		
HPP-1-66	626598	4463302	7603	Tcc	Type (V) Microcrystalline Quartz Vein	5		Yes		
HPP-1-73	626613	4464196	7416	Tcc	Type (IV) Microcrystalline Quartz Vein	1-3		Yes	Yes	
HPP-1-76	626606	4464264	7372	Ttc	Type (III) Quartz Vein	6		Yes		
HPP-1-78	626585	4464452	7290	Ttc	QF Pegmatite	3-7		Yes		
HPP-2-02	621547	4466217	7147	Tmg	Aplite (QF-cored)	14		Yes		Yes

Sample ID	Point East (UTM11 NAD27)	Point North (UTM11 NAD27)	Elevation (ft)	Intrusive Unit	Sample Lithology/ Feature Type	Thickness (cm)	Petrography	Fluid Inclusion Petrography & Microthermometry	Fluid Inclusion LA-ICP-MS	Oxygen Stable Isotope Analysis
HPP-2-03	621585	4466221	7168	Tmg	Aplite (Q-cored)		Yes	Yes		
HPP-2-06	621722	4466156	7278	Tmg	Type (I) Quartz Vein	1-2		Yes	Yes	
HPP-2-08b	621693	4466134	7241	Tmg	Granite (Leuco)	12		Yes		
HPP-2-10	621951	4466253	7363	Tmg	Aplite	5-8		Yes	Yes	
HPP-2-19a	622271	4466164	7419	Tmg	Basalt/Microdiorite	45	Yes			
HPP-2-22	622313	4466070	7331	Tmg	Type (I) Quartz Vein	1-2		Yes		
HPP-2-27	622546	4466029	7229	Tmg	Aplite	20	Yes			
HPP-2-29	622607	4466038	7203	Tmg	QF Pegmatite	50-55		Yes		
HPP-2-35	623180	4466130	7091	Tmg	QF Pegmatite	10-15		Yes	Yes	Yes
HPP-2-38	623580	4466241	7099	Tmg	Type (I) Quartz Vein	7-8		Yes		
HPP-2-40	623703	4466230	7185	Tmg	QF Pegmatite	7		Yes		
HPP-2-41	623810	4466203	7232	Tmg	Type (III) Quartz Vein	11-15		Yes	Yes	
HPP-2-44	624176	4466273	7153	Tmg	Aplite (Layered QF Pegmatite)	45		Yes	Yes	
HPP-2-47	624291	4466300	7177	Tmg	Type (I) Quartz Vein	8		Yes		Yes
HPP-2-55	626232	4466222	7489	Ttc	Type (I) Quartz Vein	1.5-2		Yes		
HPP-2-56	626395	4466194	7522	Ttc	Type (III) Quartz Vein	15		Yes		
HPP-2-57	626662	4466197	7622	Ttc	QF Pegmatite	12-15		Yes		
HPP-2-62	627034	4466244	7599	Ttc	QF Pegmatite	13-15		Yes	Yes	Yes
HPP-2-65	627748	4466231	7609	Ttc	Type (I) Quartz Vein	1.5-2	Yes			

Sample ID	Point East (UTM11 NAD27)	Point North (UTM11 NAD27)	Elevation (ft)	Intrusive Unit	Sample Lithology/ Feature Type	Thickness (cm)	Petrography	Fluid Inclusion Petrography & Microthermometry	Fluid Inclusion LA-ICP-MS	Oxygen Stable Isotope Analysis
HPP-2-71a	629117	4466932	7380	Ttc	Metased (Marble, mineralized)		Yes			
HPP-3-01	625349	4468459	7580	Tmg	MQF Pegmatite	20		Yes	Yes	
HPP-3-03	625052	4468162	7408	Tmg	Type (IV) Microcrystalline Quartz Vein	10	Yes			
HPP-3-04	625045	4468106	7376	Tmg	Type (I) Quartz Vein	1.5-3		Yes		Yes
HPP-3-15	623600	4468115	7515	Tmg	QF Pegmatite	40		Yes	Yes	
HPP-3-19	622726	4468113	6699	Tgm	Type (I) Quartz Vein	1-2		Yes		
HPP-3-23	621919	4468293	6888	Tmg	Type (III) Quartz Vein	11-26.5		Yes	Yes	
HPP-3-27	621345	4468132	6550	Tmg	Type (IV) Microcrystalline Quartz Vein	7-8	Yes	Yes		
HPP-3-29	620979	4468164	6534	Tmg	MQF Pegmatite	5	Yes			
HPP-3-33	620858	4468021	6527	Tmg	QF Pegmatite	33-34		Yes		Yes
HPP-3-38	628227	4468357	8113	Ttc	Type (II) (wallrock) Quartz Vein	6		Yes		
HPP-3-39	628260	4468322	8090	Ttc	Type (I) Quartz Vein	1-3	Yes			
HPP-4-01	625757	4461970	7377	Tcc	Type (II) (skarn) Quartz Vein	1.5		Yes	Yes	
HPP-4-02	629519	4463081	6507	Tcc	Type (II) (skarn) Quartz Vein	3		Yes		Yes
HPP-4-06	627144	4469124	8353	Ttc	Skarn	5-10		Yes		
HPP-4-08	622379	4469686	7181	Tgm	Type (III) Quartz Vein	30		Yes	Yes	Yes
HPP-4-10	622576	4468576	7396	Tmg	QF Pegmatite	7-12		Yes		

TABLE 3.2 – Tabulated mean fluid inclusion microthermometry data for all fluid inclusion compositional types, feature types, and intrusive units.

Category	Petrographic Group(s)	Size (um)	H ₂ O Liquid Fraction (%)	T _{mCO₂} (°C)	T _{eutectic} (°C)	T _{mice} (°C)	T _{mclathrate} (°C)	Th _{CO₂} (V) (°C)	Th _{CO₂} (L) (°C)	Th _{tot} (°C)	Ph _{tot} (bar)	Salinity (wt % eq. NaCl)	Density (g/cm ³)	mol% CO ₂
A	2>1>3>4	13	88		-25.0	-1.6				229.8		2.7	0.8	
B	1>2>3	13	80	-57.1	-24.6		7.7	28.8	29.6	293.3	653	3.8	0.9	6.4
C	1>2>4	11	86	-56.9	-26.1		8.2	31.0		251.0	318	3.4	0.9	1.9
Aqueous	2>1>3>4	13	88		-25.0	-1.6				229.8		2.7	0.8	
Aquo-Carbonic	1>2>3>4	12	84	-57.2	-26.8		8.1	29.2	29.9	254.8	480	3.6	0.9	4.6
Granite (altered)	2	10	95		-25.4	-1.7				201.2		2.9	0.9	
Granite (Leuco) (CO ₂)	1>3	16	81	-56.5	-27.5		7.7		30.8	272.3	500	3.9	1.0	5.2
QF Pegmatite	2>1=4	16	90		-25.5	-1.7				244.7		2.6	0.8	
QF Pegmatite (CO ₂)	1>2=3	14	85	-56.9	-26.1	-1.3	7.9	28.5		244.8	482	3.5	0.9	4.6
MQF Peg (CO ₂)	2	14	84	-57.7	-24.1	-1.4	8.0			279.9	378	3.4	0.9	4.1
Aplite (Layered QF Pegmatite) (CO ₂)	1	16	89		-26.3	-2.3	11.1			191.3				
Aplite (QF-cored) (CO ₂)	1	6	63	-58.8	-24.4		7.4	25.5		326.1	613	4.3	0.8	7.6
Aplite (CO ₂)	1=4	8	86	-56.9	-26.3	-2.1	9.1			289.8	400	1.5	1.0	3.7
Miarolitic Cavity	2	32	88		-25.5	-2.2				239.3		4.1	0.8	
Miarolitic Cavity (CO ₂)	1=2	11	89	-56.8	-28.1	-1.4	7.1			225.6	305	2.4	0.9	2.8
Type (I) Quartz Vein	1>2	9	65		-24.5	-2.2				278.3		3.6	0.8	
Type (I) Quartz Vein (CO ₂)	1>2>3	15	80	-57.1	-27.1	-2.3	7.7	29.1	28.2	288.7	590	3.6	0.9	5.9
Type (II) (skarn) Quartz Vein	2>1	9	90		-23.9	-1.4				253.6		2.4	0.8	
Type (II) (skarn) Quartz Vein (CO ₂)	1	7	89		-27.4	-5.2				277.5	250	5.4	1.0	2.7
Type (II) (wallrock) Quartz Vein	2=3	5	96		-25.2	-0.7				172.9		1.2	0.9	
Type (II) (wallrock) Quartz Vein (CO ₂)	2	13	93	-57.1	-28.1		7.4	31.0		152.3	765	4.3	1.0	3.1
Type (III) Quartz Vein	1	13	86		-25.5	-2.1				238.7		3.5	0.8	
Type (III) Quartz Vein (CO ₂)	1	11	81	-57.1	-28.2		8.0	31.0	30.8	304.1	523	3.5	0.9	5.8
Type (IV) Microcrystalline Quartz Vein	1=2>4	12	96		-24.8	-0.8				210.0		1.3	0.9	
Type (IV) Microcrystalline Quartz Vein (CO ₂)	2	10	91		-28.4			29.7		204.8				
Orthomagmatic	2>1>4	13	92		-25.5	-1.7				223.0		2.8	0.9	
Orthomagmatic (CO ₂)	1>2>3=4	12	81	-57.3	-25.8	-1.8	8.5	27.0	30.8	267.4	474	3.3	0.9	5.1
Hydrothermal	1>2>3	16	82		-24.9	-2.0				252.5		3.4	0.8	
Hydrothermal (CO ₂)	1>2>3	11	85	-57.0	-27.7	-3.0	7.6	30.1	29.5	274.0	417	3.7	0.9	4.3
Post-Intrusion Hydrothermal	1=2>3=4	9	96		-25.0	-0.7				191.4		1.3	0.9	
Post-Intrusion Hydrothermal (CO ₂)	2	12	92	-57.1	-28.3		7.4	30.4		178.6	765	4.3	1.0	3.1
Tcc	2>1	14	87		-24.3	-1.5				232.1		2.6	0.8	
Tcc (CO ₂)	1	9	89	-56.8	-27.8	-3.3	7.1	30.4		251.6	278	3.9	0.9	2.7
Tgm	1	10	86		-27.5	-2.8				301.1		4.7	0.8	
Tgm (CO ₂)	1=2	9	79	-57.2	-27.5		7.9	31.0	30.1	293.7	742	3.1	0.9	7.5
Tmg	1>2	12	80		-25.2	-1.8				251.5		3.0	0.8	
Tmg (CO ₂)	1>2>3>4	15	82	-57.1	-26.1	-2.0	8.3	28.4	29.0	269.1	465	3.3	0.9	4.8
Ttc	4	22	91		-29.9	-3.1				255.1		5.1	0.8	
Ttc (CO ₂)	3	17	80	-58.2	-26.1	0.0	7.0	30.8		271.5	920	5.0	0.9	8.3
Early Stage	2>1>4>3	18	89		-27.1	-2.3				243.6		3.9	0.8	
Early Stage (CO ₂)	1=2>3	13	84	-57.5	-26.9	-1.7	7.1	30.6		261.5	599	4.4	0.9	5.5
Late Stage	1>2	11	83		-26.4	-2.3				276.3		3.8	0.8	
Late Stage (CO ₂)	1>2>3>4	12	81	-57.1	-26.8	-2.0	8.1	29.7	29.6	281.4	603	3.2	0.9	6.2

TABLE 3.3 – Descriptions of LA-ICP-MS fluid inclusion assemblages.

Assemblage ID	Feature Type	Number & Nature of Phases	Assemblage Interpretation	Shape of Inclusions	Size of Inclusions (μm)	T_{tot} ($^{\circ}\text{C}$)	Salinity (wt % eq. NaCl)
HPP-1-20-FIA2	Granite (altered)	2 (L+V)	Primary	Negative crystal	6-15	204.6	3.1
HPP-1-24b-FIA2	Miarolitic Cavity	2 (L+V)	Primary	Equant/geometric.	3-24	248.1	3.2
HPP-1-24b-FIA3	Miarolitic Cavity	3 (L+V)	Primary	Elongate/tabular	47-52	230.5	4.2
HPP-1-36a-FIA2	Type (IV) Microcrystalline Quartz Vein	2 (L+V)	Primary	Cubic to irregular	10-15	168.5	1.7
HPP-1-73-FIA1a	Type (IV) Microcrystalline Quartz Vein	3 (L1+L2+V)	Secondary	Rounded/irregular to tabular.	5-14	198.0	3.7
HPP-2-6-FIA3	Type (I) Quartz Vein	3 (L1+L2+V)	Primary	Irregular/equant.	4-16	325.1	2.9
HPP-2-6-FIA4	Type (I) Quartz Vein	3 (L1+L2+V)	Primary	Geometric/equant.	15	277.2	1.9
HPP-2-10-FIA2	Aplite	2 (L+V) w/ clathrate	Pseudo	Equant to elongate	5-10	204.6	0.2
HPP-2-22-FIA1	Type (I) Quartz Vein	3 (L1+L2+V)	Primary	Tabular, slightly irregular.	23-24	268.8	1.9
HPP-2-35-FIA3	QF Pegmatite	3 (L1+L2+V)	Primary/Pseudo	Tabular	16-19	228.7	2.2
HPP-2-41a-FIA3	Type (III) Quartz Vein	2 (L+V)	Primary	Tabular/negative crystal.	27	189.2	1.6
HPP-2-44-FIA3	Aplite (Layered QF Pegmatite)	3 (L1+L2+V)	Secondary	Varied; elongate irregular to equant/negative crystal.	7-44	203.8	3.2
HPP-2-62-FIA2	QF Pegmatite	3 (L1+L2+V)	Primary	Rounded, equant, one is nearly square.	17	271.5	5.0
HPP-3-1b-FIA1	MQF Pegmatite	2 (L+V) w/ clathrate	Primary	Negative crystal to tabular.	10-26	282.3	3.5
HPP-3-15-FIA2	QF Pegmatite	3 (L+V+S)	Primary	Tabular	20-40	202.1	3.9
HPP-3-23-FIA3a	Type (III) Quartz Vein	3 (L1+L2+V)	Primary	Equant to tabular/irregular	5-25	330.0	3.7
HPP-4-1-FIA3	Type (II) (skarn) Quartz Vein	2 (L+V)	Primary	Equant to tabular, irregular	9-17	243.5	3.5
HPP-4-8-FIA1	Type (III) Quartz Vein	3 (L1+L2+V)	Primary	Irregular cubic to negative crystal.	<8-14	310.9	3.5

TABLE 3.4 – Na, K, Rb, Cs concentrations from LA-ICP-MS with approximate K:Na, Na:Cs, K:Cs, and Rb:Cs molar element ratios from selected inclusions. Limits of detection (LOD) from fluid inclusion LA-ICP-MS analysis for these elements (in ppm) are as follows: Mg: 1-40; K: 10-180; Ca: 5000-50000; Cu: 1-65; As: 0-60; Rb: 1-5; Sr: 1-5; Sn: 5-350; Cs: 1-5; La: 0-1.

Full ID	Feature Type	Intrusive Unit	Assemblage Compositional Type	Assemblage Interpretation	Th _{tot} (°C)	Na (Mol)	K (Mol)	Rb (Mol)	Cs (Mol)
HPP-1-24b-FIA2_i1b	Miarolitic Cavity	Tcc	Type (A)	Primary	248.1	0.55	0.1	0.0003	0.0009
HPP-1-24b-FIA2_i3c	Miarolitic Cavity	Tcc	Type (A)	Primary	248.1	0.55		0.0001	0.0004
HPP-1-24b-FIA2_i4a	Miarolitic Cavity	Tcc	Type (A)	Primary	248.1	0.55			0.0005
HPP-2-06-FIA4_i1	Type (I) Quartz Vein	Tmg	Type (B)	Primary	277.2	0.33	0.01	0.0002	0.00002
HPP-2-06-FIA4_i2	Type (I) Quartz Vein	Tmg	Type (B)	Primary	277.2	0.33		0.0002	0.0002
HPP-2-10-FIA2_i5	Aplite	Tmg	Type (C)	Pseudosecondary	204.6	0.03	0.0007	0.0001	0.00004
HPP-2-22-FIA1_i13	Type (I) Quartz Vein	Tmg	Type (B)	Primary	268.8	0.33		0.0002	0.002
HPP-2-22-FIA1_i1b	Type (I) Quartz Vein	Tmg	Type (B)	Primary	268.8	0.33	0.02	0.0002	
HPP-2-22-FIA1_i6	Type (I) Quartz Vein	Tmg	Type (B)	Primary	268.8	0.33	0.04	0.0002	0.0001
HPP-2-35-FIA3_i1a	QF Pegmatite	Tmg	Type (B)	Primary/Pseudosecondary	228.7	0.38		0.0004	0.0001
HPP-2-35-FIA3_i2	QF Pegmatite	Tmg	Type (B)	Primary/Pseudosecondary	228.7	0.38	0.004	0.0004	0.0001
HPP-2-35-FIA3_i4	QF Pegmatite	Tmg	Type (B)	Primary/Pseudosecondary	228.7	0.38		0.0007	0.0003
HPP-2-35-FIA3_i6b	QF Pegmatite	Tmg	Type (B)	Primary/Pseudosecondary	228.7	0.38		0.0002	0.0006
HPP-2-44-FIA3_i9	Aplite (Layered QF Pegmatite)	Tmg	Type (C)	Secondary	203.8	0.55	0.02	0.0001	0.0001
HPP-2-62-FIA2_i6a	QF Pegmatite	Ttc	Type (B)	Primary	271.5	0.85	0.7	0.0002	0.0001
HPP-3-01b-FIA1_i3	MQF Pegmatite	Tmg	Type (C)	Primary	282.3	0.61		0.0004	
HPP-3-01b-FIA1_i5	MQF Pegmatite	Tmg	Type (C)	Primary	282.3	0.61		0.0002	0.0002
HPP-3-15-FIA2_i1	QF Pegmatite	Tmg	Type (A)	Primary	202.1	0.66	0.03	0.0001	0.0003
HPP-3-15-FIA2_i10	QF Pegmatite	Tmg	Type (A)	Primary	202.1	0.66	0.02	0.0001	0.0002
HPP-3-15-FIA2_i11	QF Pegmatite	Tmg	Type (A)	Primary	202.1	0.66	0.05	0.00002	0.0005
HPP-3-15-FIA2_i12	QF Pegmatite	Tmg	Type (A)	Primary	202.1	0.66	0.07	0.0001	0.0001
HPP-3-15-FIA2_i2	QF Pegmatite	Tmg	Type (A)	Primary	202.1	0.66	0.02	0.0002	0.0002
HPP-3-15-FIA2_i5	QF Pegmatite	Tmg	Type (A)	Primary	202.1	0.66		0.0002	0.0001
HPP-3-15-FIA2_i7	QF Pegmatite	Tmg	Type (A)	Primary	202.1	0.66	0.03	0.0003	0.001
HPP-3-15-FIA2_i8	QF Pegmatite	Tmg	Type (A)	Primary	202.1	0.66	0.04	0.0009	0.0002
HPP-3-15-FIA2_i9a	QF Pegmatite	Tmg	Type (A)	Primary	202.1	0.66	0.03	0.0001	0.0006
HPP-3-15-FIA2_i9b	QF Pegmatite	Tmg	Type (A)	Primary	202.1	0.66	2.1	0.0002	0.0005
HPP-3-23-FIA3a_i5a	Type (III) Quartz Vein	Tmg	Type (B)	Primary	330	0.63	0.04	0.0005	0.0002
HPP-3-23-FIA3a_i5b	Type (III) Quartz Vein	Tmg	Type (B)	Primary	330	0.63	0.02	0.0002	0.003
HPP-4-01-FIA3_i1a	Type (II) (skarn) Quartz Vein	Tcc	Type (A)	Primary	243.5	0.61	0.03		0.0001
HPP-4-01-FIA3_i1c	Type (II) (skarn) Quartz Vein	Tcc	Type (A)	Primary	243.5	0.61			0.00003
HPP-4-01-FIA3_i2a	Type (II) (skarn) Quartz Vein	Tcc	Type (A)	Primary	243.5	0.61	0.03		0.00001
HPP-4-01-FIA3_i4b	Type (II) (skarn) Quartz Vein	Tcc	Type (A)	Primary	243.5	0.61	0.05	0.0002	0.0001
HPP-4-01-FIA3_i5a	Type (II) (skarn) Quartz Vein	Tcc	Type (A)	Primary	243.5	0.61		0.0001	0.0000
HPP-4-01-FIA3_i8	Type (II) (skarn) Quartz Vein	Tcc	Type (A)	Primary	243.5	0.61	0.02	0.0002	0.0002
HPP-4-08-FIA1_i1b	Type (III) Quartz Vein	Tgm	Type (B)	Primary	310.9	0.61	0.9	0.0001	0.0004
HPP-4-08-FIA1_i4	Type (III) Quartz Vein	Tgm	Type (B)	Primary	310.9	0.61	0.04	0.0003	0.0002

Full ID	Feature Type	Intrusive Unit	Assemblage Compositional Type	Assemblage Interpretation	Th _{int} (°C)	Na (Mol)	K (Mol)	Rb (Mol)	Cs (Mol)
HPP-1-24b-FIA2_11b	Miarolitic Cavity	Tcc	Type (A)	Primary	248.1	0.55	0.1	0.0003	0.0009
HPP-1-24b-FIA2_13c	Miarolitic Cavity	Tcc	Type (A)	Primary	248.1	0.55		0.0001	0.0004
HPP-1-24b-FIA2_14a	Miarolitic Cavity	Tcc	Type (A)	Primary	248.1	0.55			0.0005
HPP-2-06-FIA4_11	Type (I) Quartz Vein	Tmg	Type (B)	Primary	277.2	0.33	0.01	0.0002	0.00002
HPP-2-06-FIA4_12	Type (I) Quartz Vein	Tmg	Type (B)	Primary	277.2	0.33		0.0002	0.0002
HPP-2-10-FIA2_15	Aplite	Tmg	Type (C)	Pseudosecondary	204.6	0.03	0.0007	0.0001	0.00004
HPP-2-22-FIA1_113	Type (I) Quartz Vein	Tmg	Type (B)	Primary	268.8	0.33		0.0002	0.002
HPP-2-22-FIA1_11b	Type (I) Quartz Vein	Tmg	Type (B)	Primary	268.8	0.33	0.02	0.0002	
HPP-2-22-FIA1_16	Type (I) Quartz Vein	Tmg	Type (B)	Primary	268.8	0.33	0.04	0.0002	0.0001
HPP-2-35-FIA3_11a	QF Pegmatite	Tmg	Type (B)	Primary/Pseudosecondary	228.7	0.38		0.0004	0.0001
HPP-2-35-FIA3_12	QF Pegmatite	Tmg	Type (B)	Primary/Pseudosecondary	228.7	0.38	0.004	0.0004	0.0001
HPP-2-35-FIA3_14	QF Pegmatite	Tmg	Type (B)	Primary/Pseudosecondary	228.7	0.38		0.0007	0.0003
HPP-2-35-FIA3_16b	QF Pegmatite	Tmg	Type (B)	Primary/Pseudosecondary	228.7	0.38		0.0002	0.0006
HPP-2-44-FIA3_19	Aplite (Layered QF Pegmatite)	Tmg	Type (C)	Secondary	203.8	0.55	0.02	0.0001	0.0001
HPP-2-62-FIA2_16a	QF Pegmatite	Ttc	Type (B)	Primary	271.5	0.85	0.7	0.0002	0.0001
HPP-3-01b-FIA1_13	MQF Pegmatite	Tmg	Type (C)	Primary	282.3	0.61		0.0004	
HPP-3-01b-FIA1_15	MQF Pegmatite	Tmg	Type (C)	Primary	282.3	0.61		0.0002	0.0002
HPP-3-15-FIA2_11	QF Pegmatite	Tmg	Type (A)	Primary	202.1	0.66	0.03	0.0001	0.0003
HPP-3-15-FIA2_110	QF Pegmatite	Tmg	Type (A)	Primary	202.1	0.66	0.02	0.0001	0.0002
HPP-3-15-FIA2_111	QF Pegmatite	Tmg	Type (A)	Primary	202.1	0.66	0.05	0.0002	0.0005
HPP-3-15-FIA2_112	QF Pegmatite	Tmg	Type (A)	Primary	202.1	0.66	0.07	0.0001	0.0001
HPP-3-15-FIA2_12	QF Pegmatite	Tmg	Type (A)	Primary	202.1	0.66	0.02	0.0002	0.0002
HPP-3-15-FIA2_15	QF Pegmatite	Tmg	Type (A)	Primary	202.1	0.66		0.0002	0.0001
HPP-3-15-FIA2_17	QF Pegmatite	Tmg	Type (A)	Primary	202.1	0.66	0.03	0.0003	0.001
HPP-3-15-FIA2_18	QF Pegmatite	Tmg	Type (A)	Primary	202.1	0.66	0.04	0.0009	0.0002
HPP-3-15-FIA2_19a	QF Pegmatite	Tmg	Type (A)	Primary	202.1	0.66	0.03	0.0001	0.0006
HPP-3-15-FIA2_19b	QF Pegmatite	Tmg	Type (A)	Primary	202.1	0.66	0.03	0.0002	0.0005
HPP-3-23-FIA3a_15a	Type (III) Quartz Vein	Tmg	Type (B)	Primary	330	0.63	0.04	0.0005	0.0002
HPP-3-23-FIA3a_15b	Type (III) Quartz Vein	Tmg	Type (B)	Primary	330	0.63	0.02	0.0002	0.003
HPP-4-01-FIA3_11a	Type (II) (skarn) Quartz Vein	Tcc	Type (A)	Primary	243.5	0.61	0.03		0.0001
HPP-4-01-FIA3_11c	Type (II) (skarn) Quartz Vein	Tcc	Type (A)	Primary	243.5	0.61			0.00003
HPP-4-01-FIA3_12a	Type (II) (skarn) Quartz Vein	Tcc	Type (A)	Primary	243.5	0.61	0.03		0.00001
HPP-4-01-FIA3_14b	Type (II) (skarn) Quartz Vein	Tcc	Type (A)	Primary	243.5	0.61	0.05	0.0002	0.0001
HPP-4-01-FIA3_15a	Type (II) (skarn) Quartz Vein	Tcc	Type (A)	Primary	243.5	0.61		0.0001	0.0000
HPP-4-01-FIA3_16	Type (II) (skarn) Quartz Vein	Tcc	Type (A)	Primary	243.5	0.61	0.02	0.0002	0.0002
HPP-4-08-FIA1_11b	Type (III) Quartz Vein	Tgm	Type (B)	Primary	310.9	0.61	0.9	0.0001	0.0004
HPP-4-08-FIA1_14	Type (III) Quartz Vein	Tgm	Type (B)	Primary	310.9	0.61	0.04	0.0003	0.0002

TABLE 3.5 – Descriptions and calibrated $\delta^{18}\text{O}$ values for stable isotope samples.

Sample ID	Feature Type	Intrusive Unit	Analyzed Mineral	$\delta^{18}\text{O}$ (Calibrated value)
HPP-1-04	Type (I) Quartz Vein	Tcc	Qtz	11.1
HPP-1-30	Type (III) Quartz Vein	Tcc	Qtz	7.5
HPP-2-02	Aplite (QF-cored)	Tmg	Qtz	10.0
HPP-2-35	QF Pegmatite	Tmg	Qtz	9.7
HPP-2-47	Type (I) Quartz Vein	Tmg	Qtz	10.3
HPP-2-62	QF Pegmatite	Ttc	Qtz	10.0
HPP-3-04a	Type (I) Quartz Vein	Tmg	Qtz	9.7
HPP-3-33	QF Pegmatite	Tmg	Qtz	10.2
HPP-4-02b	Type (II) (skarn) Quartz Vein	Skarn by Tcc	Qtz	10.2
HPP-4-08	Type (III) Quartz Vein	Tgm	Qtz	9.5

TABLE 3.6 – Comparison of selected mean fluid inclusion molar element ratios with the corresponding whole-rock data of Barnes et al. (2001). Limits of detection (LOD) from fluid inclusion LA-ICP-MS analysis for these elements (in ppm) are as follows: Mg: 1-40; K: 10-180; Ca: 5000-50000; Cu: 1-65; As: 0-60; Rb: 1-5; Sr: 1-5; Sn: 5-350; Cs: 1-5; La: 0-1. LOD values for whole-rock multi-element data from Barnes et al. (2001) are not available.

<i>Approximate Fluid Inclusion Molar Element Ratios (This Study)</i>						
	Ttc	Tcc	Early Stage	Tmg	Tgm	Late Stage
Rb:Cs	2.2	0.8	0.9	0.5	1.5	0.6
K:Cs	8400	220	260	50	290	60
Na:Cs	11000	1500	1700	970	2000	1000
K:Na	N/A	0.1	0.1	0.1	0.1	0.1
	Type (A)	A2 Fluid Type	Type (B)	Type (C)	BC Fluid Type	
Rb:Cs	0.6	0.6	0.7	1.2	0.7	
K:Cs	120	120	40	30	40	
Na:Cs	1800	1800	740	1600	830	
K:Na	0.07	0.07	0.06	0.03	0.05	
<i>Approximate Whole-Rock Molar Element Ratios (Barnes et al., 2001)</i>						
	Ttc	Tcc	Early Stage	Tmg	Tgm	Late Stage
Rb:Cs	60	90	70	90	50	70
K:Cs	14000	22000	16000	15000	4800	8900
Na:Cs	20000	27000	22000	15000	3000	6000
K:Na	0.7	0.9	0.8	1.1	1.4	1.2

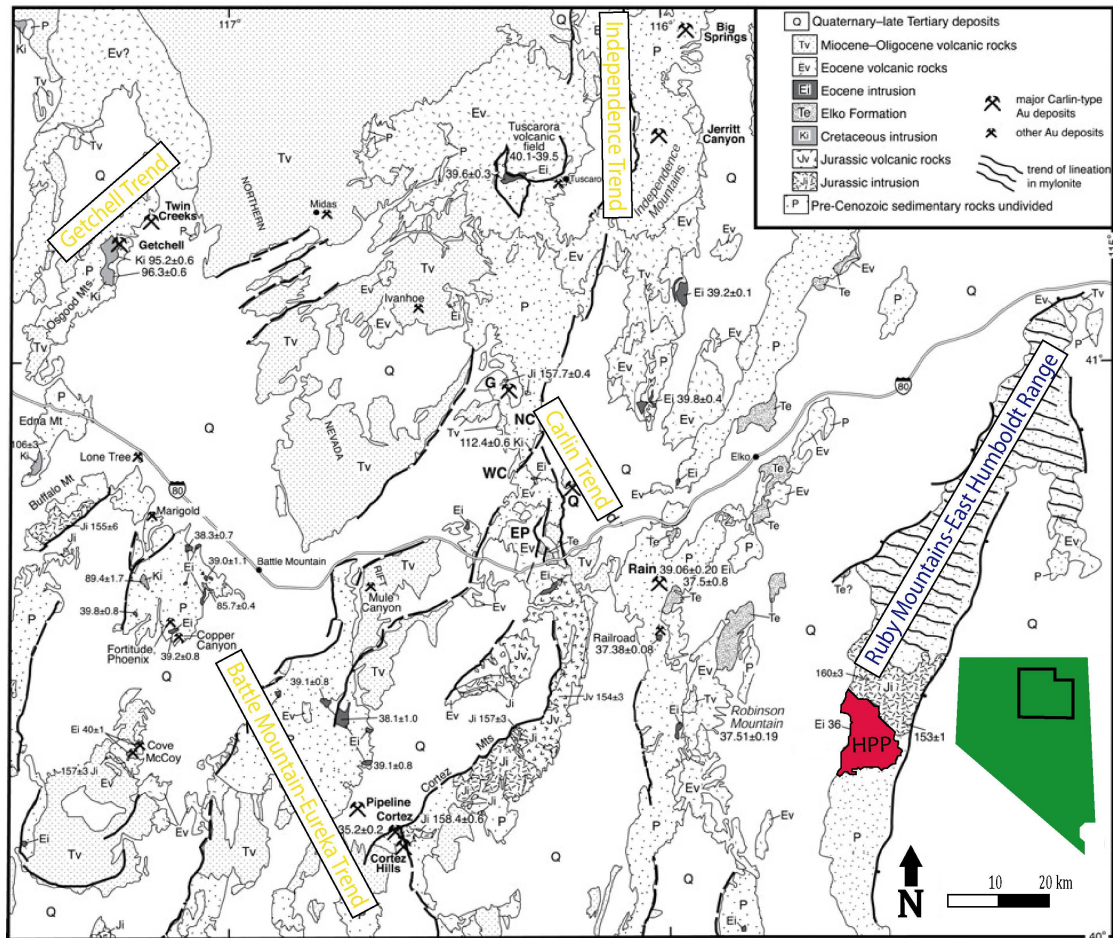


FIGURE 3.1 – Regional geological map adapted from Henry & Ressel (2006). The HPP, RMEHR, and major trends of CTD's are identified.

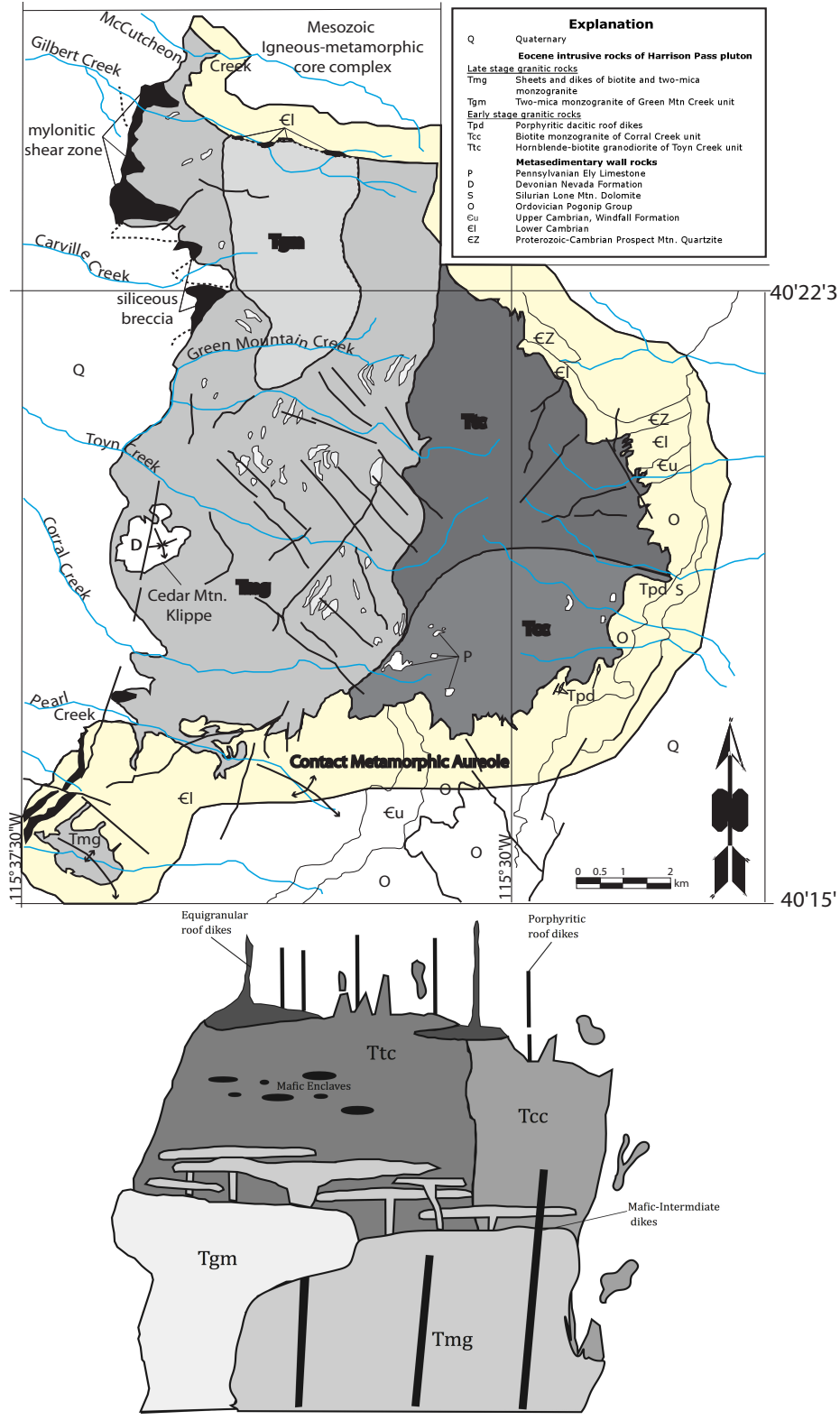


FIGURE 3.2 – Geologic map and schematic cross-section of the HPP showing constituent intrusive units. Map and cross-section adapted from Burton (1997) and Barnes et al. (2001), respectively.

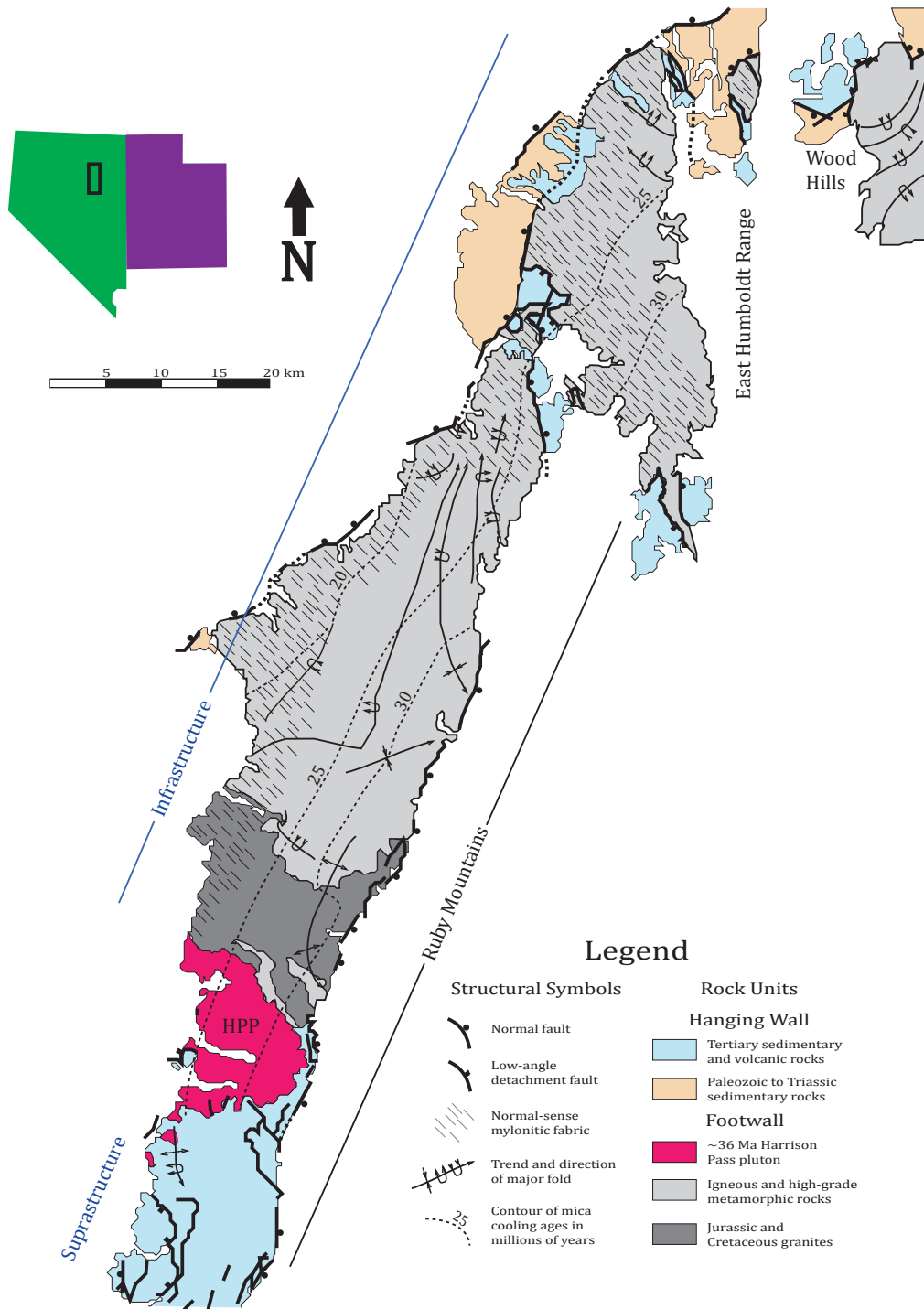


FIGURE 3.3 – Detailed geologic map of the RMEHR metamorphic core complex. The HPP is intruded into the transition zone between the infrastructural core of high-grade metamorphic and igneous rocks and the suprastructure of low-grade and unmetamorphosed sedimentary rocks. Adapted from Snoke & Lush (1984).

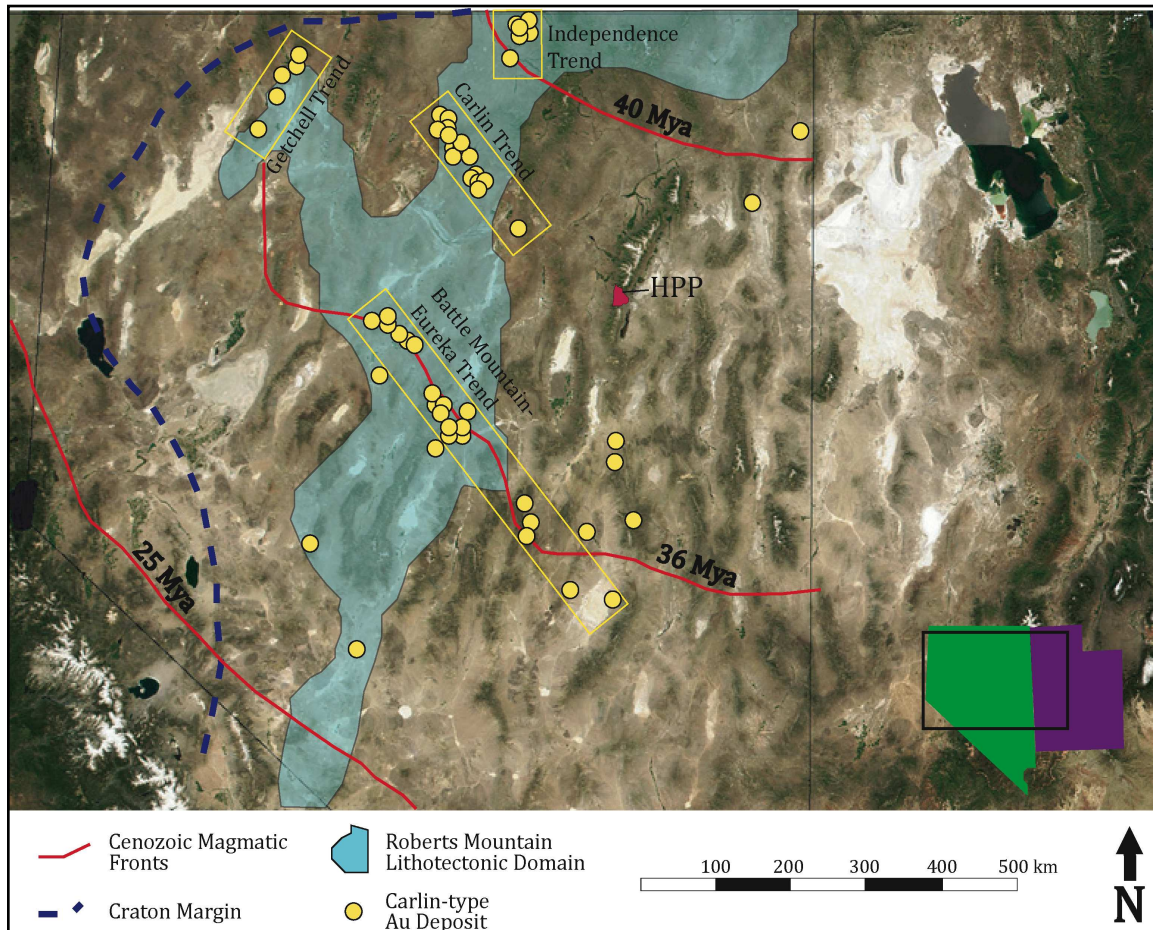


FIGURE 3.4 – Map showing the regional distribution of Carlin-Type Au Deposits in the Great Basin in relationship to the HPP. Also shown are other features relevant to the formation of these deposits, including the southward migration of Cenozoic silicic magmatic fronts, the Roberts Mountain lithotectonic domain, and the western margin of the North American craton. Adapted from Muntean et al. (2011) and Vaughan (2013).

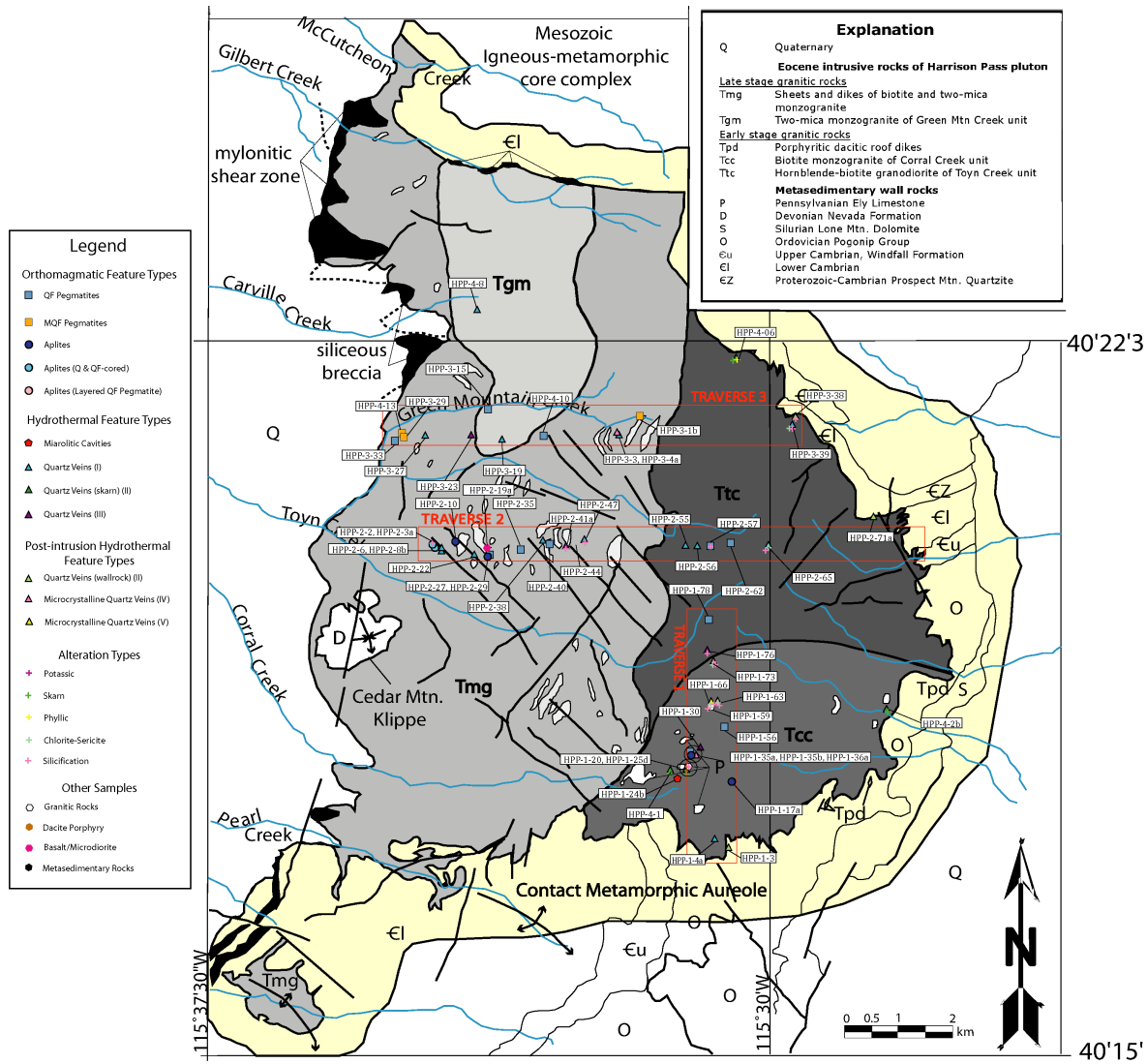


FIGURE 3.5 – Map of the HPP showing the locations of microthermometry samples. Adapted from Burton (1997).

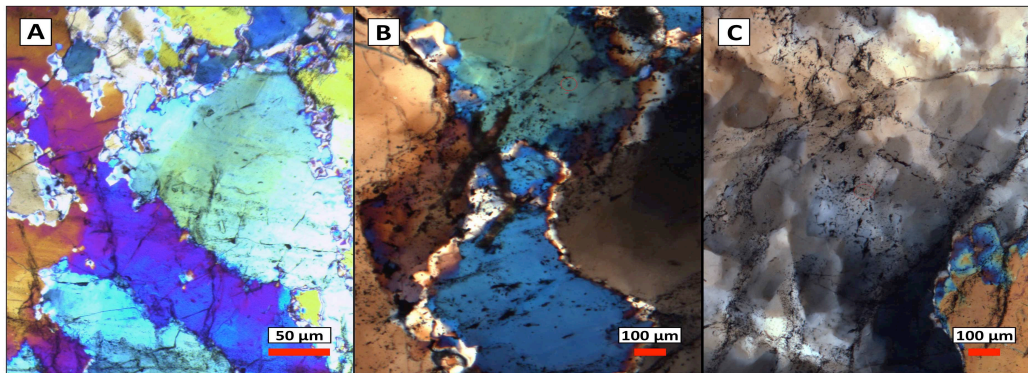


FIGURE 3.6 – Representative photomicrographs of major deformation microstructures in microthermometry samples. A: Inclusion-free neoblasts along grain boundaries. B: Sutured/recrystallized grain boundaries. C: Undulose extinction.

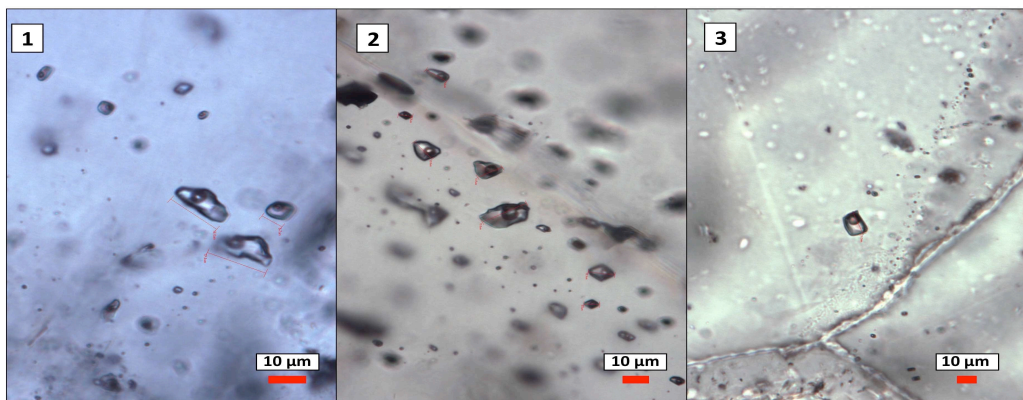


FIGURE 3.7 – Representative photomicrographs of fluid inclusion petrographic groups. 1: Diffuse, relatively isolated 3-dimensional clusters. 2: Planes within growth zones. 3: Isolated single inclusions.

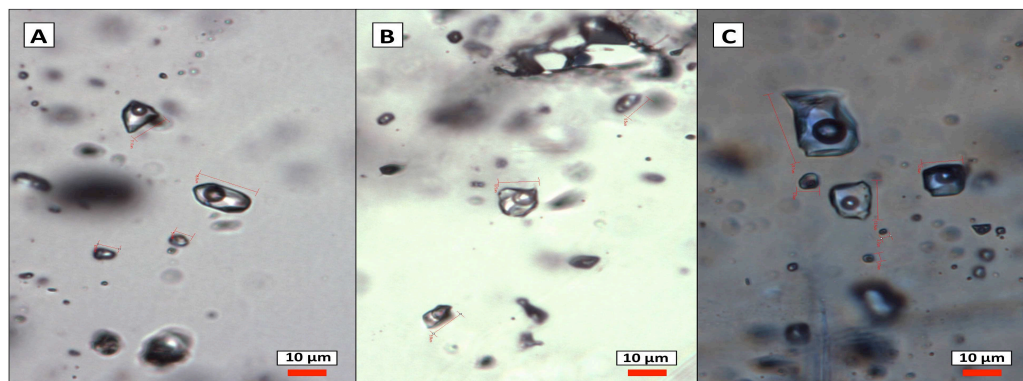


FIGURE 3.8 – Representative photomicrographs of fluid inclusion compositional types. A: Two-phase (liquid and vapor). B: Three-phase (wetting liquid, non-wetting liquid, and vapor). C: Two-phase (liquid and vapor) at ambient conditions, but three-phase (wetting liquid, non-wetting liquid, and vapor) upon cooling.

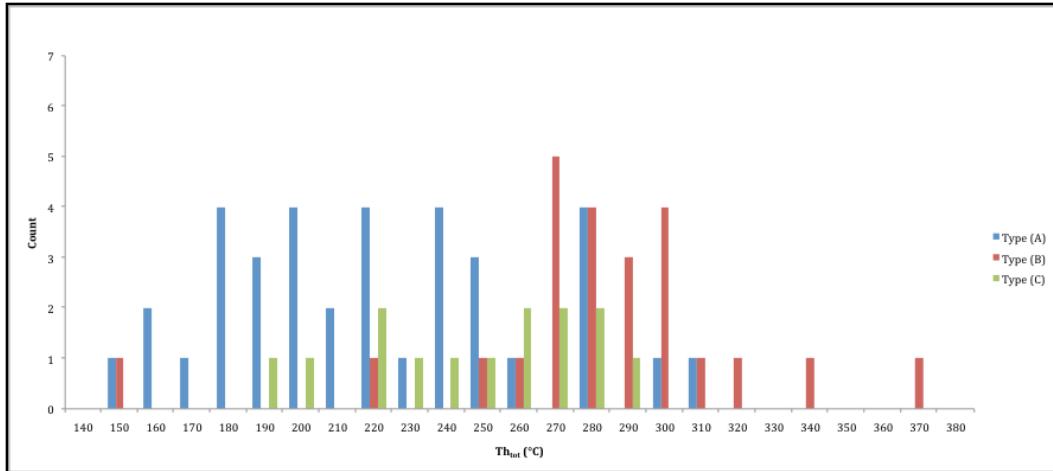


FIGURE 3.09 – Histogram of Th_{tot} values for fluid inclusion compositional types.

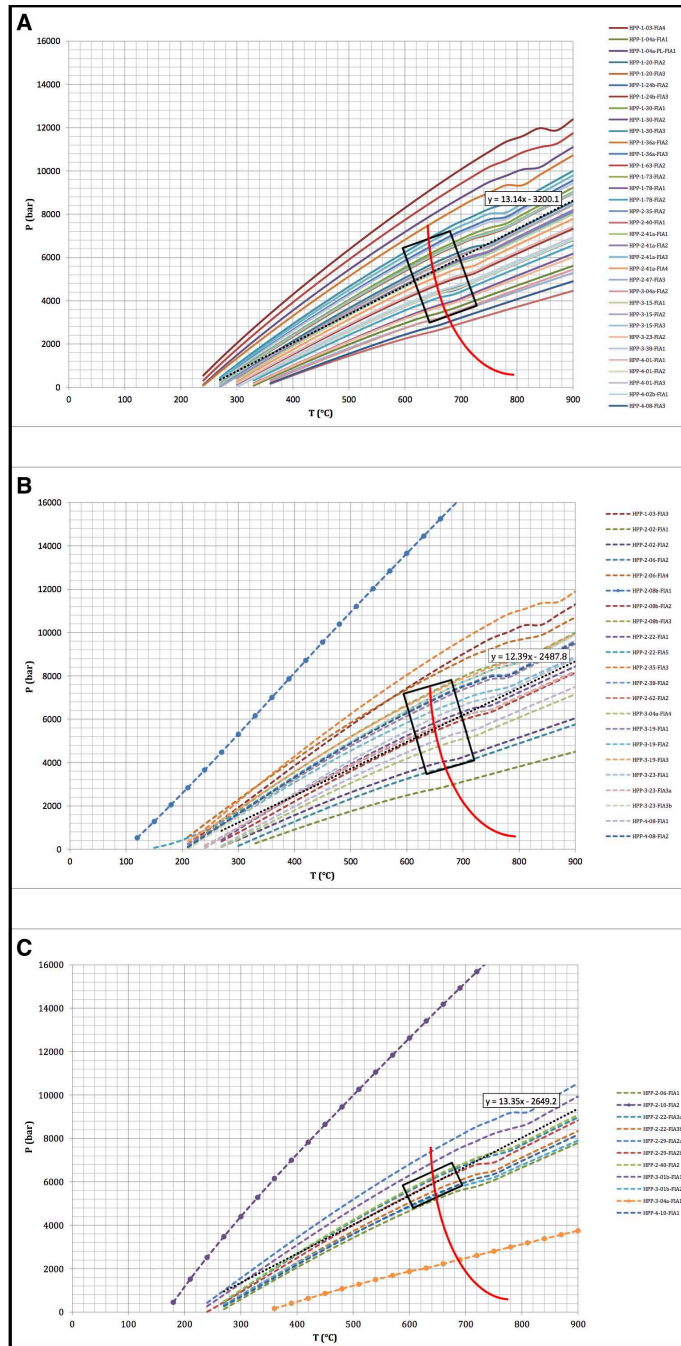


FIGURE 3.10 – Isochore plots subdivided by fluid inclusion compositional type. A: Type (A) aqueous fluid inclusion assemblages. B: Type (B) aquo-carbonic fluid inclusion assemblages. C: Type (C) aquo-carbonic fluid inclusion assemblages. Solid lines indicate aqueous fluid inclusions, while dashed lines indicate aquo-carbonic fluid inclusions. A trendline representing an idealized mean isochore is included as a black dotted line with equation. Anomalous isochores are marked by filled circles. The experimentally determined wet granite solidus is represented by a red curve with a black box delineating a $\pm 50^{\circ}\text{C}$ range for the intersections of isochores with this curve. This range is interpreted as the fluid entrapment conditions.

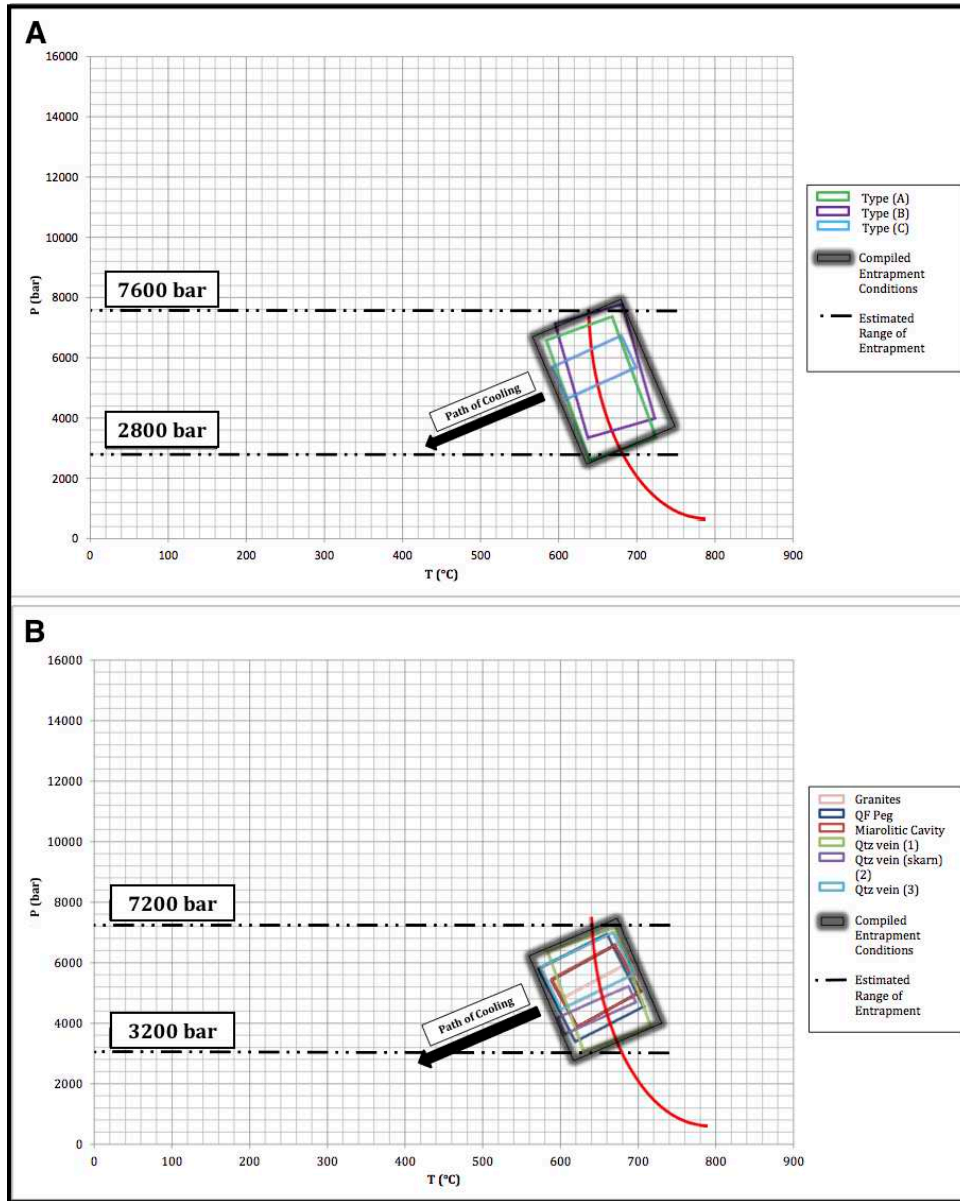


FIGURE 3.11 – Compiled fluid entrapment conditions with P_t estimates (between black dash-dotted lines). A: For fluid inclusion compositional type. B: For select feature types. The experimentally determined wet granite solidus is represented by a red curve. Colored boxes represent estimates of entrapment conditions for individual fluid inclusion compositional types (see Fig 3.10) and feature types (see Fig 3.11). Certain feature types are excluded due to a lack of sufficient data (i.e. MQF Pegmatites, Aplites) or because they formed independently of the magmatic crystallization of the HPP (i.e. Type (II) (wallrock) Quartz Veins and Type (IV) Microcrystalline Quartz Veins). Black blurred boxes represent the compiled entrapment conditions that are interpreted to represent the entire intrusive system.

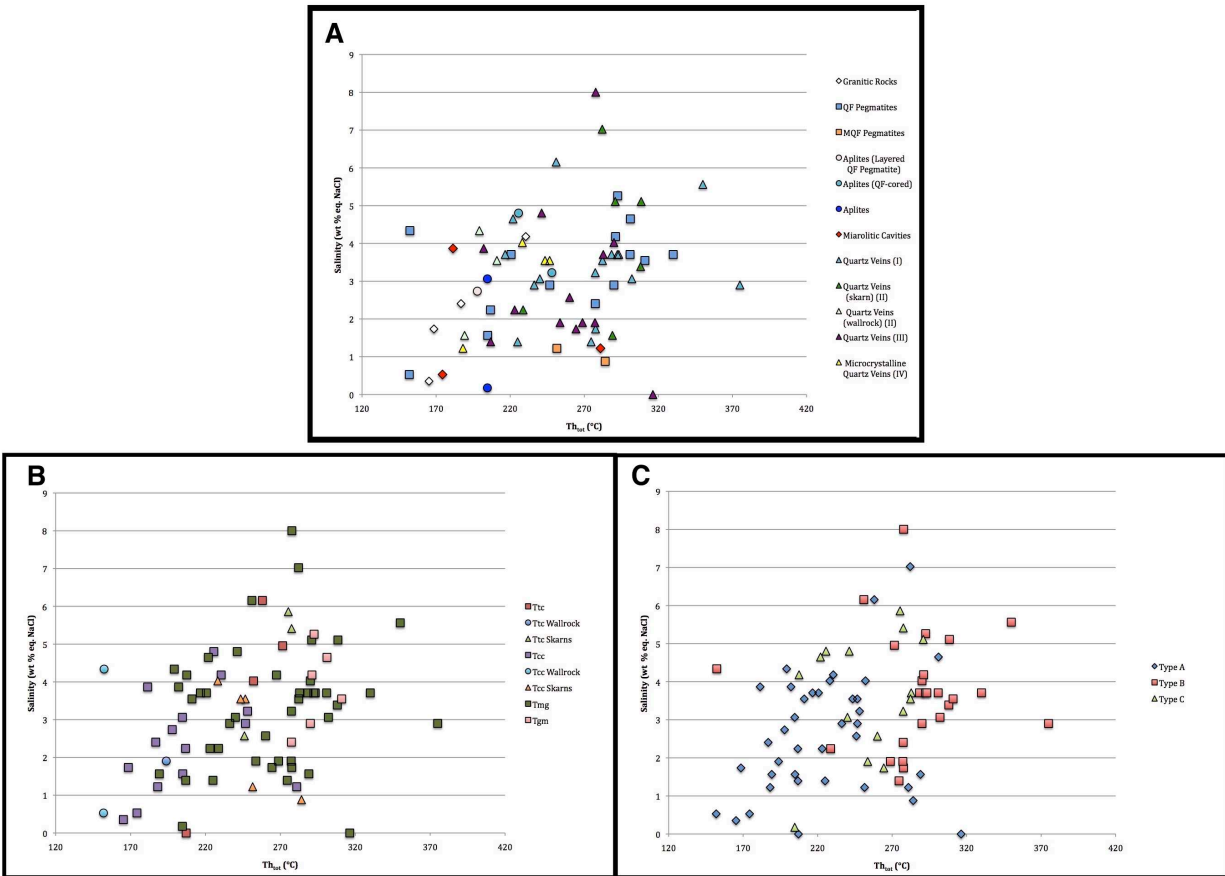


FIGURE 3.12 – Select Th_{tot} (°C) vs. Salinity (wt % eq. NaCl) scatter plots demonstrating spatial and temporal trends in microthermometry data. A: All values for primary fluid inclusion assemblages, subdivided by feature type. B: All values for primary fluid inclusion assemblages, subdivided by intrusive unit. C: All values for primary fluid inclusions, subdivided by fluid inclusion compositional type.

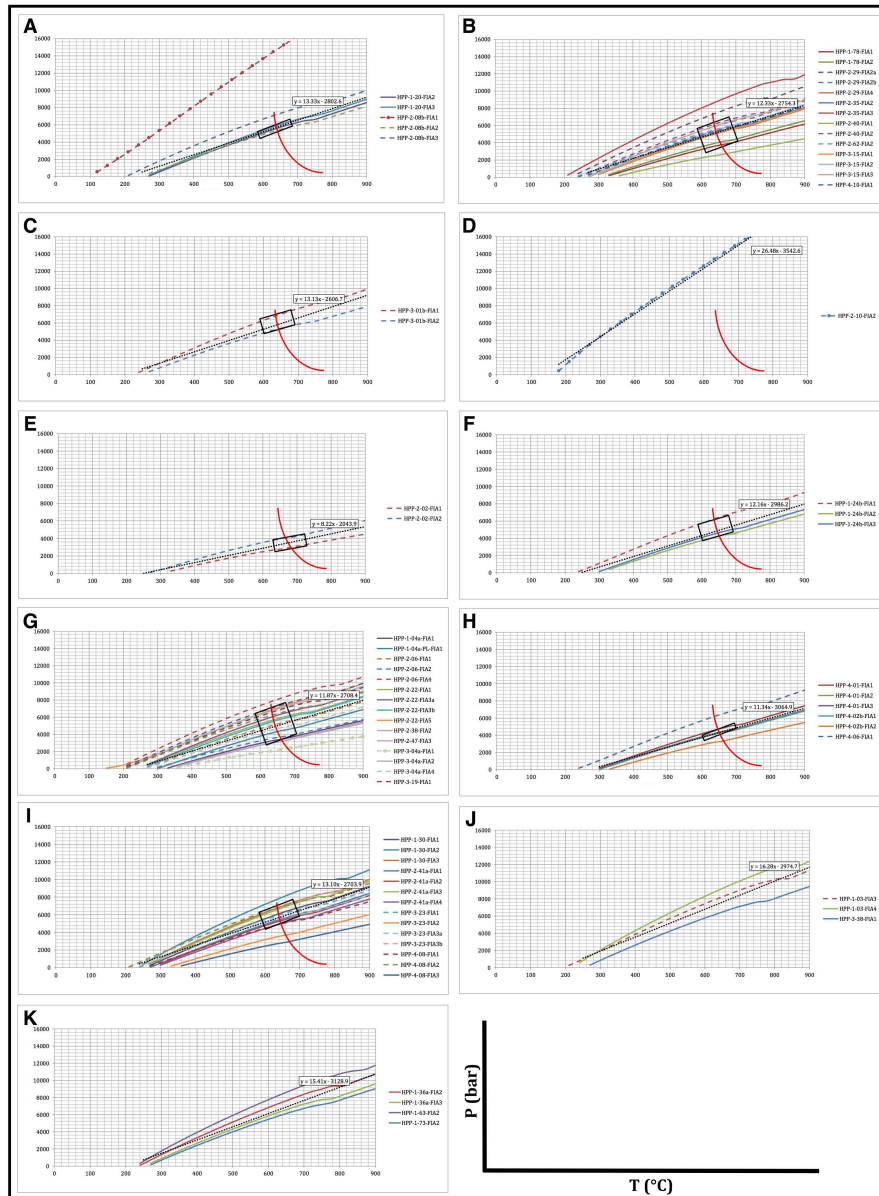
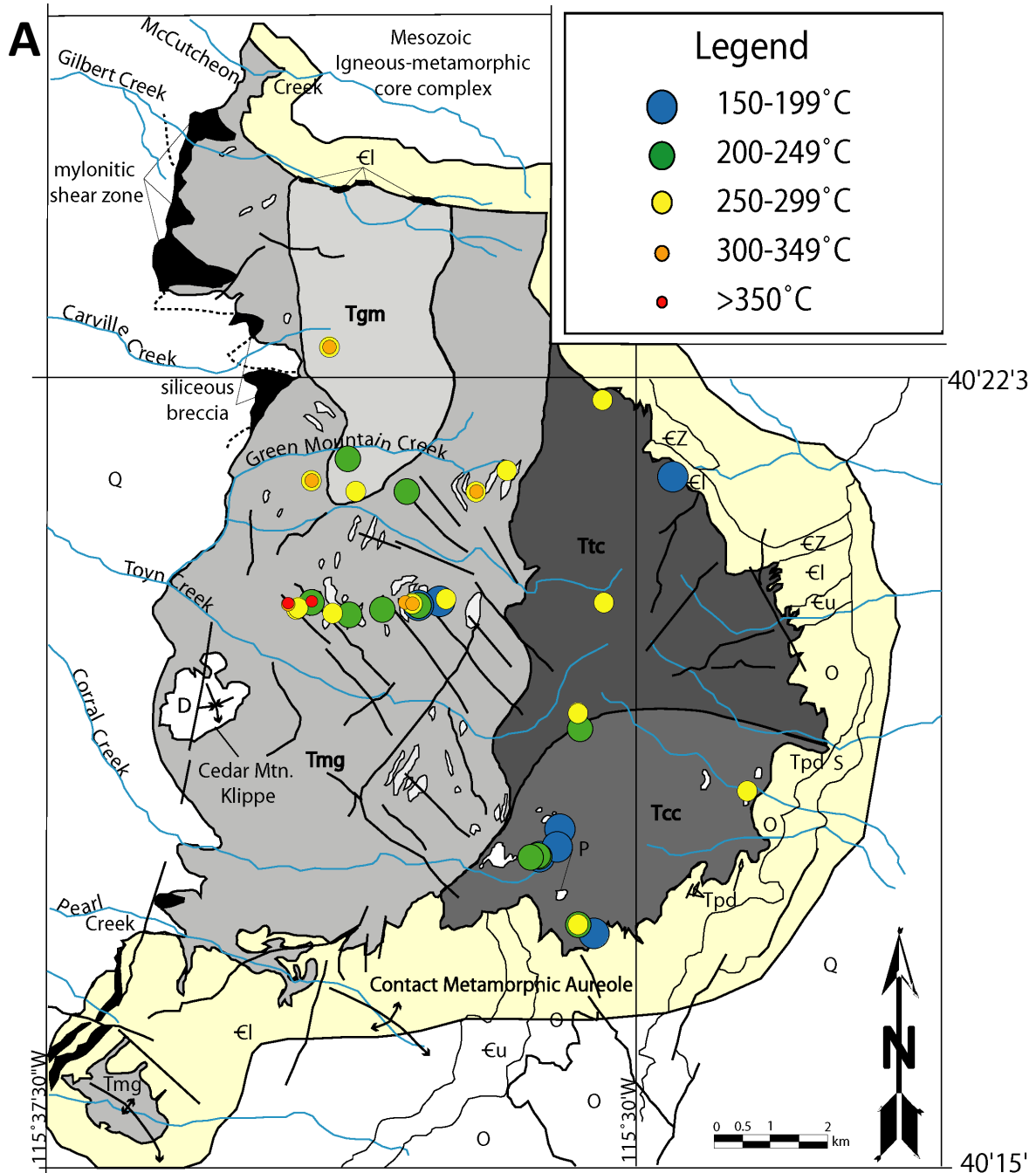


FIGURE 3.13 – Isochore plots subdivided by feature type. A: Granitic rocks. B: QF Pegmatites. C: MQF Pegmatites. D: Aplites. E: Aplites (Q and QF-cored). F: Mirolitic Cavities. G: Type (I) Quartz Veins. H: Type (II) (skarn) Quartz Veins. I: Type (III) Quartz Veins. J: Type (II) (wallrock) Quartz Veins. K: Type (IV) Microcrystalline Quartz Veins. Solid lines indicate aqueous fluid inclusions, while dashed lines indicate aquo-carbonic fluid inclusions. Trendline representing an idealized mean isochore is included as black dotted line with equation. Anomalous isochores are marked by filled circles. The experimentally determined wet granite solidus is represented by a red curve with a black box delineating a $\pm 50^{\circ}\text{C}$ range for the intersections of isochores with this curve. This range is interpreted as the fluid entrapment conditions. Solidus curve and intersection box are not included for feature types that formed independently of the magmatic crystallization of the HPP (i.e. Type (II) (wallrock) Quartz Veins and Type (IV) Microcrystalline Quartz Veins).



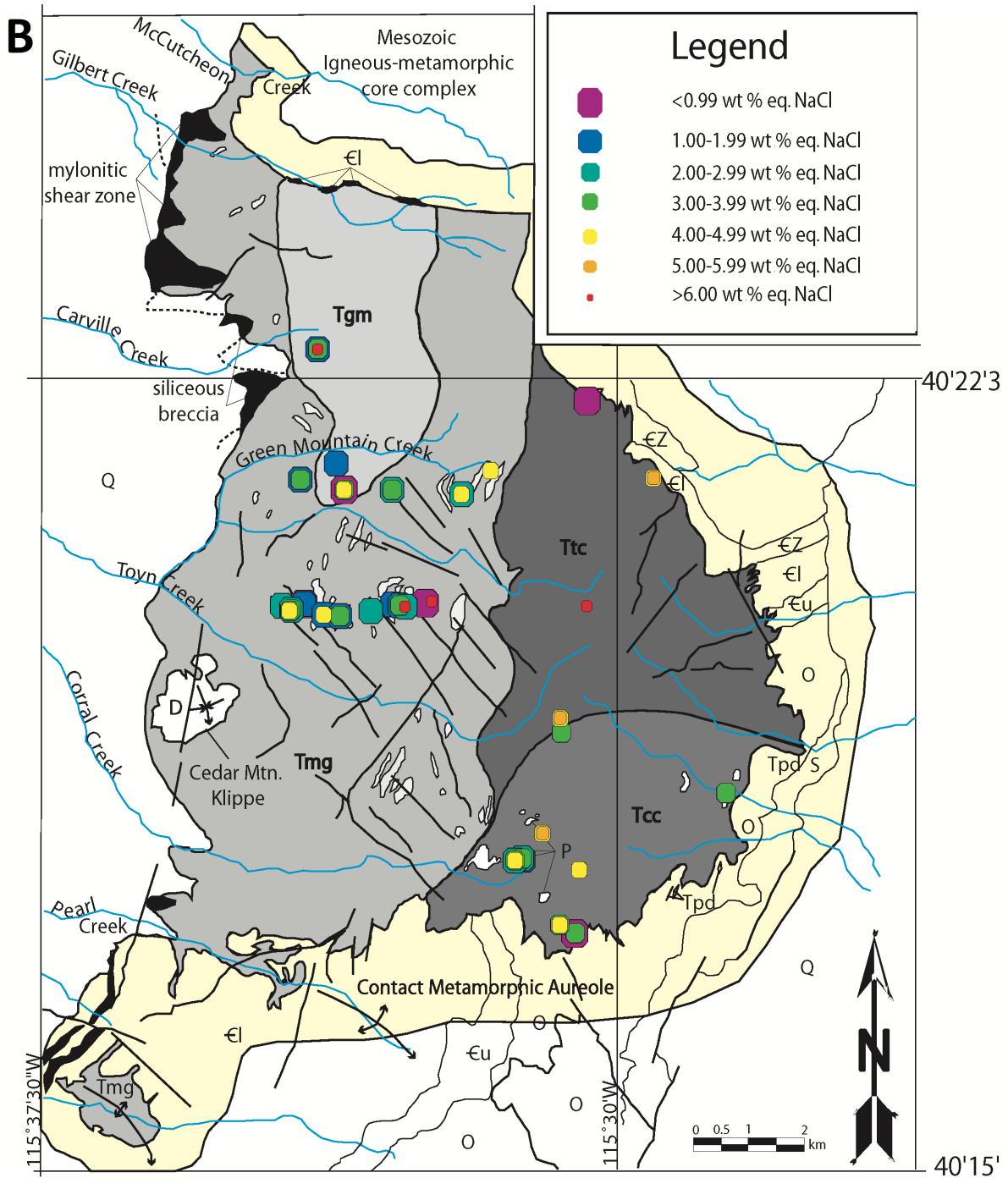


FIGURE 3.14 – Maps illustrating spatial variation in select microthermometry data throughout the HPP. A: T_{tot} ($^{\circ}\text{C}$). B: Salinity (wt % eq. NaCl). Adapted from Burton (1997).

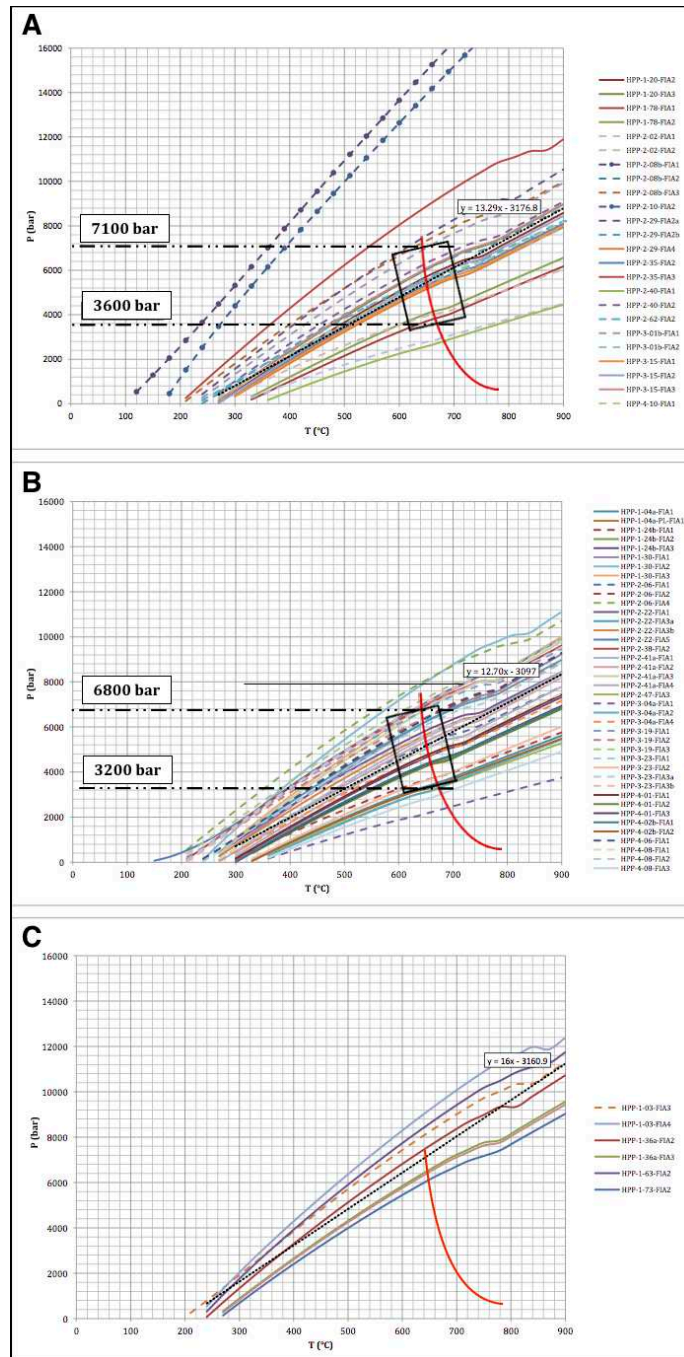


FIGURE 3.15 – Compiled isochore plots and entrapment conditions for the three major categories of feature type. A: Orthomagmatic feature types. B: Hydrothermal feature types. C: Post-intrusion hydrothermal feature types. Solid lines indicate aqueous fluid inclusions, while dashed lines indicate aquo-carbonic fluid inclusions. A trendline representing an idealized mean isochore is included as a black dotted line with equation. The experimentally determined wet granite solidus is represented by a red curve with a black box delineating a $\pm 50^{\circ}\text{C}$ range for the intersections of isochores with this curve. This range is interpreted as the fluid entrapment conditions.

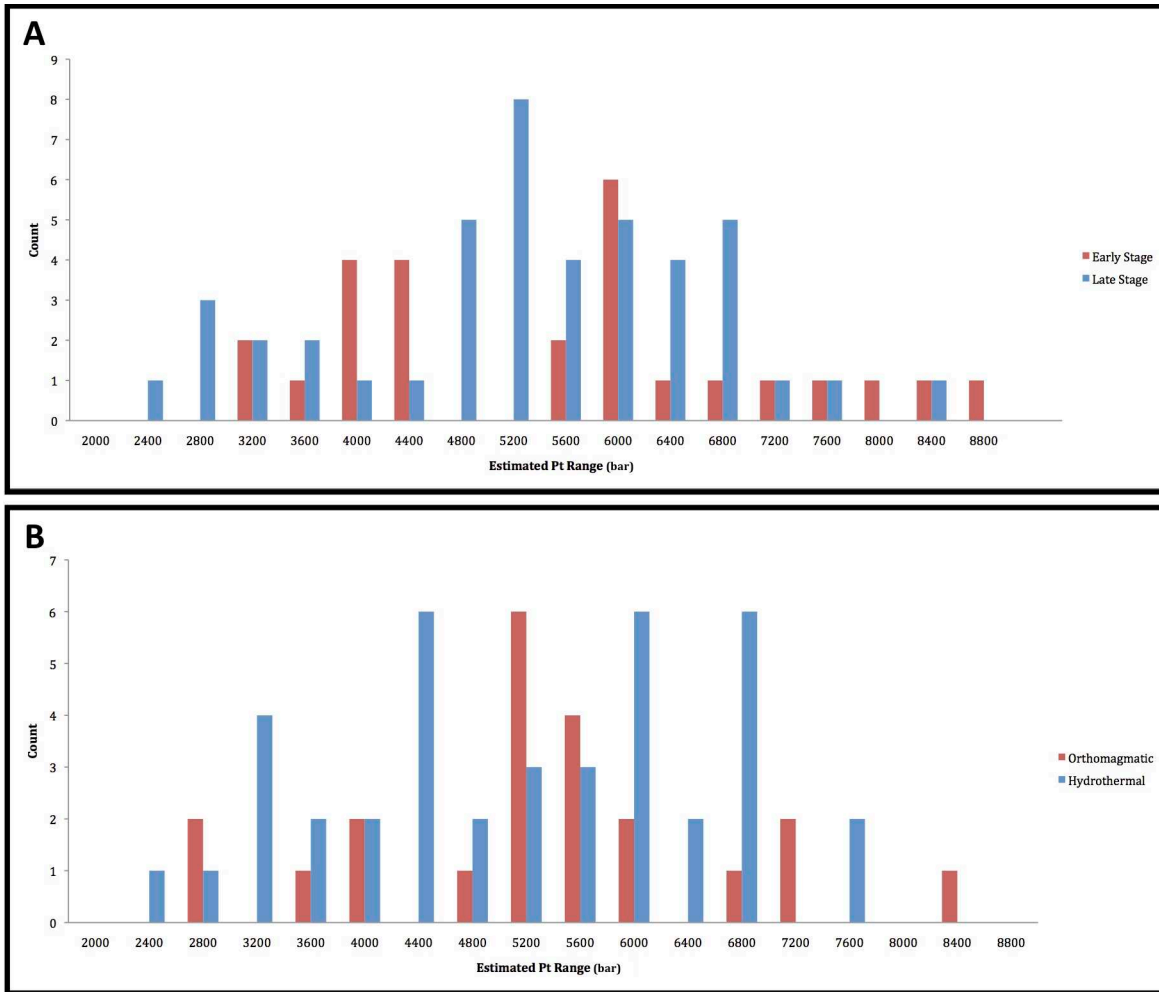


FIGURE 3.16 – Histograms of Pt values calculated from isochores. A: Early and late stages of intrusive activity. B: Orthomagmatic and hydrothermal feature types. Pt ranges for each bin represent one grid square in the isochore plots. Bin populations were determined by counting the number of isochores that intersect the experimentally determined wet granite solidus curve within the given Pt range for each bin.

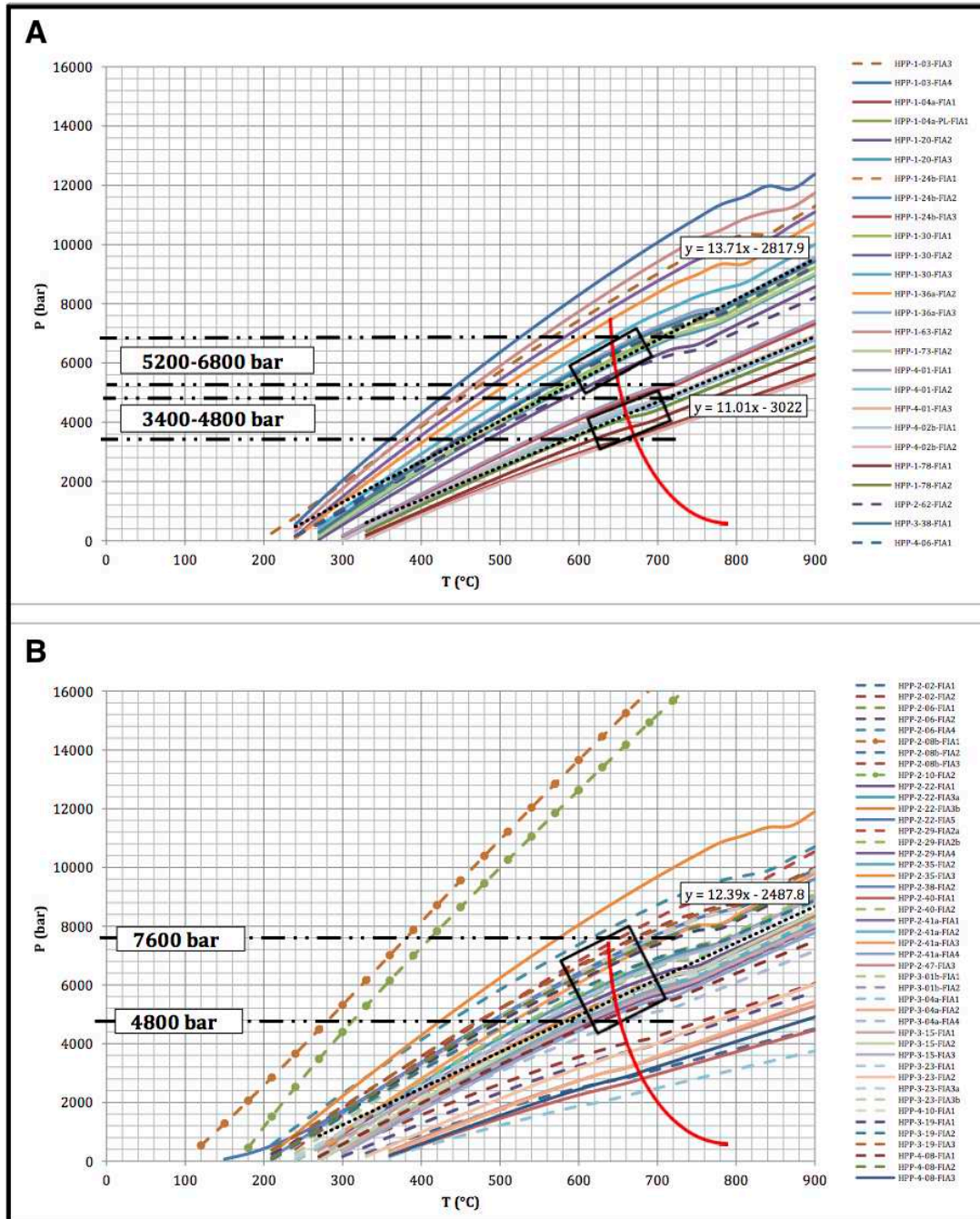


FIGURE 3.17 – Compiled isochore plots and entrapment conditions for the stages of intrusive activity with interpreted entrapment ranges (between black dash-dotted lines). A: Early stage. B: Late stage. Solid lines indicate aqueous fluid inclusions, while dashed lines indicate aquo-carbonic fluid inclusions. A trendline representing an idealized mean isochore is included as a black dotted line with equation. Anomalous isochores are marked by filled circles. The experimentally determined wet granite solidus is represented by a red curve with a black box delineating a $\pm 50^{\circ}\text{C}$ range for the intersections of isochores with this curve. This range is interpreted as the fluid entrapment conditions.

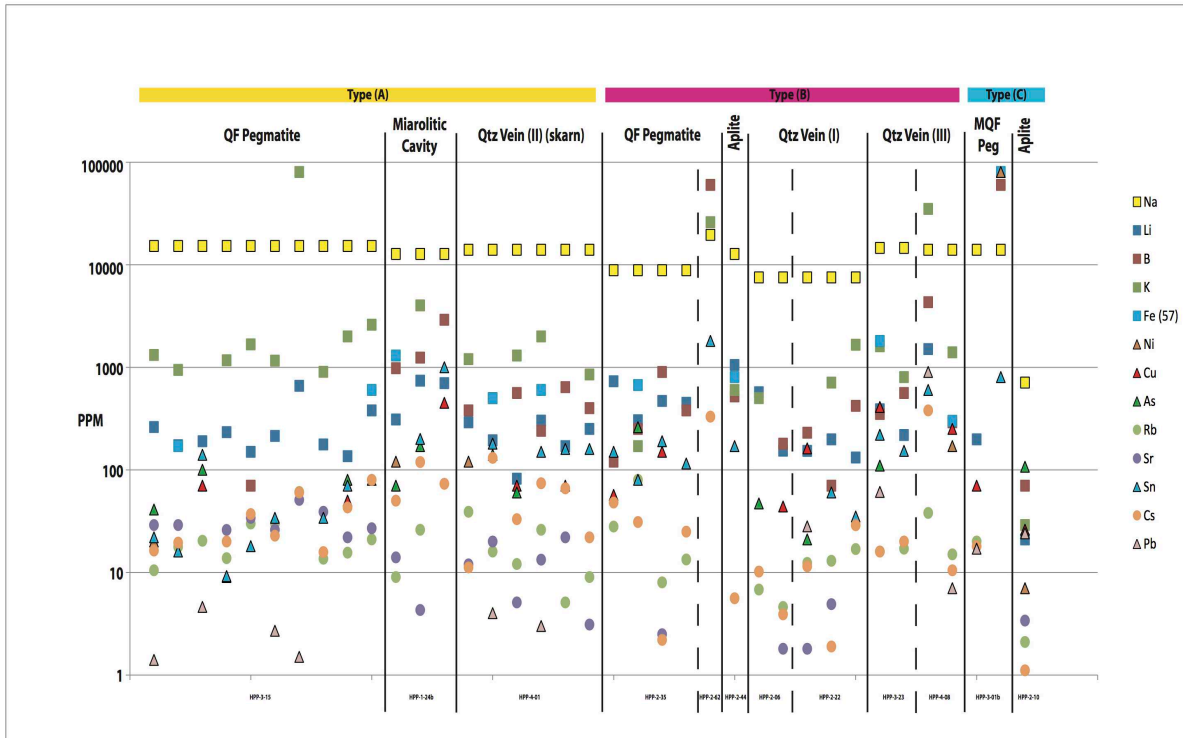


FIGURE 3.18 – LA-ICP-MS multi-element data for selected fluid inclusions, organized by fluid inclusion compositional type. Na concentrations were determined from fluid salinities. Limits of detection (LOD) for these elements (in ppm) are as follows: Li: 1-35; B: 60-200; K: 10-180; Fe(57): 20-400; Ni: 5-500; Cu: 1-65; As: 0-60; Rb: 1-5; Sr: 1-5; Sn: 5-350; Cs: 1-5; Pb: 0-22.

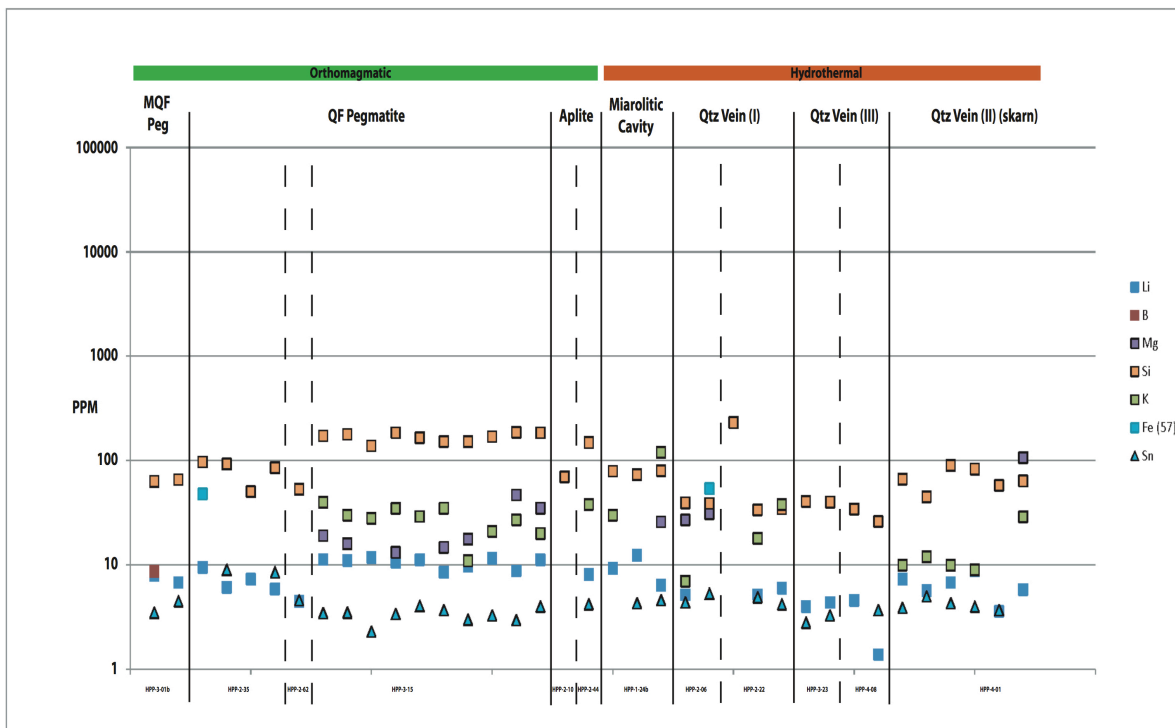


FIGURE 3.19 – LA-ICP-MS multi-element data for host quartz crystals, organized by fluid inclusion compositional type. Si concentration in pure quartz was used as an internal standard. Limits of detection (LOD) for these elements (in ppm) are as follows: Li: 1-35; B: 60-200; Mg: 1-40; K: 10-180; Fe(57): 20-400; Sn: 5-350.

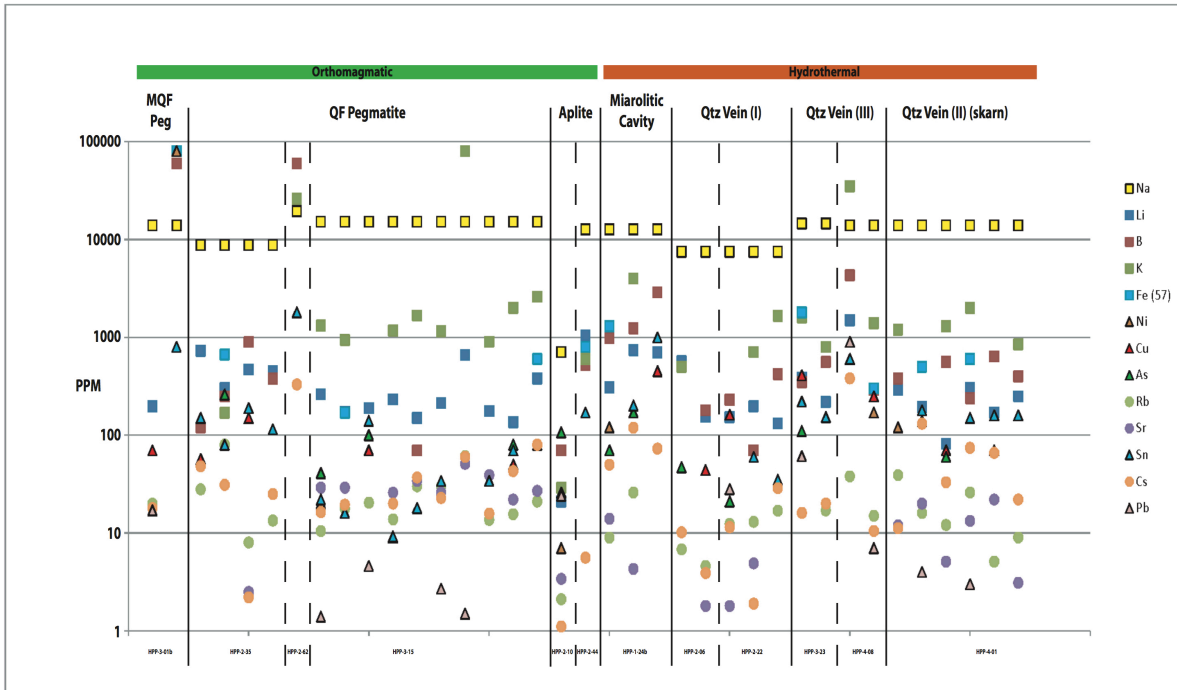


FIGURE 3.20 – LA-ICP-MS multi-element data for selected fluid inclusions, organized by feature type. Na concentrations were determined from fluid salinities. Limits of detection (LOD) for these elements (in ppm) are as follows: Li: 1-35; B: 60-200; K: 10-180; Fe(57): 20-400; Ni: 5-500; Cu: 1-65; As: 0-60; Rb: 1-5; Sr: 1-5; Sn: 5-350; Cs: 1-5; Pb: 0-22.

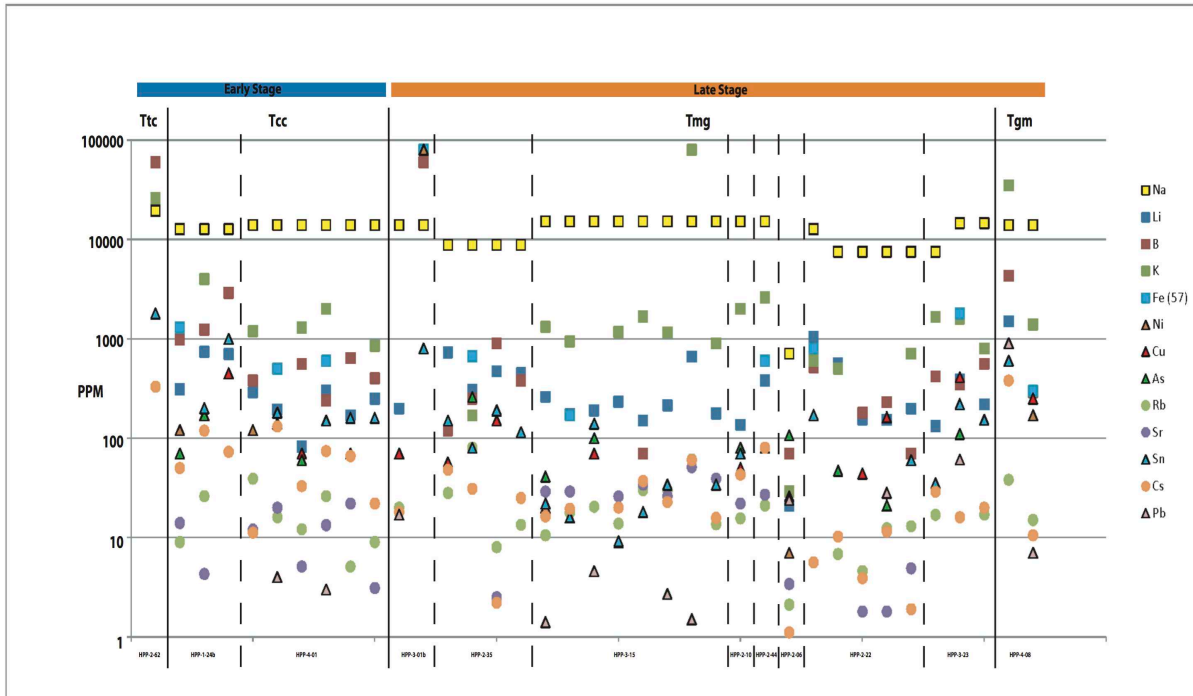


FIGURE 3.21 – LA-ICP-MS multi-element data for selected fluid inclusions, organized by intrusive unit. Na concentrations were determined from fluid salinities. Limits of detection (LOD) for these elements (in ppm) are as follows: Li: 1-35; B: 60-200; K: 10-180; Fe(57): 20-400; Ni: 5-500; Cu: 1-65; As: 0-60; Rb: 1-5; Sr: 1-5; Sn: 5-350; Cs: 1-5; Pb: 0-22.

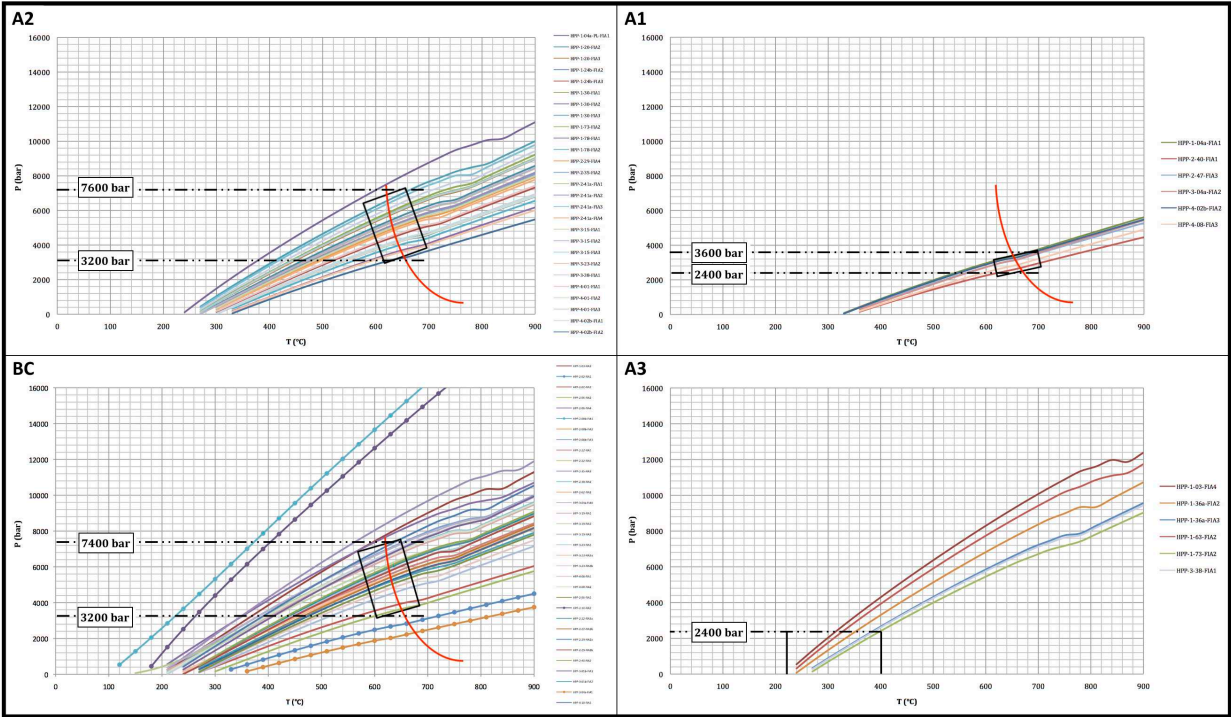


FIGURE 3.22 – Compiled isochore plots and estimated entrapment conditions (between black dash-dotted lines) for the A2, A1, BC, and A3 fluid types observed in the HPP. Anomalous isochores are marked by filled circles. The experimentally determined wet granite solidus is represented by a red curve with a black box delineating a $\pm 50^{\circ}\text{C}$ range for the intersections of isochores with this curve. This range is interpreted as the fluid entrapment conditions. For the A3 fluid type, the black dash-dotted and solid lines correspond to the maximum entrapment conditions for this fluid type, based on the minimum entrapment conditions of other fluid types.

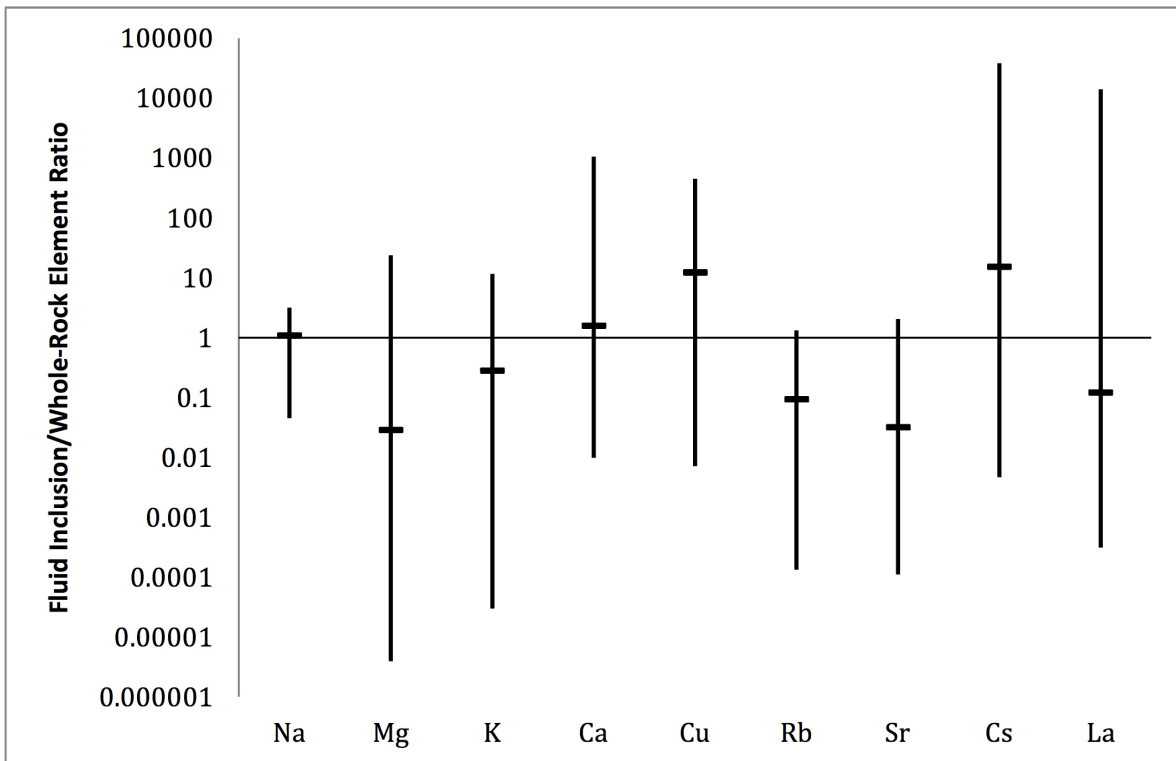


FIGURE 3.23 – Graphical comparison between multi-element compositions of fluid inclusions (this study) and host intrusive units (Barnes et al. (2001)). Vertical bar represent the range of element ratios and horizontal tick marks indicate the mean ratio. Na concentrations were determined from fluid salinities. Limits of detection (LOD) from fluid inclusion LA-ICP-MS analysis for these elements (in ppm) are as follows: Mg: 1-40; K: 10- 180; Ca: 5000-50000; Cu: 1-65; As: 0-60; Rb: 1-5; Sr: 1-5; Sn: 5-350; Cs: 1-5; La: 0-1. LOD values for whole-rock multi-element data from Barnes et al., (2001) are not available.

Early Stage

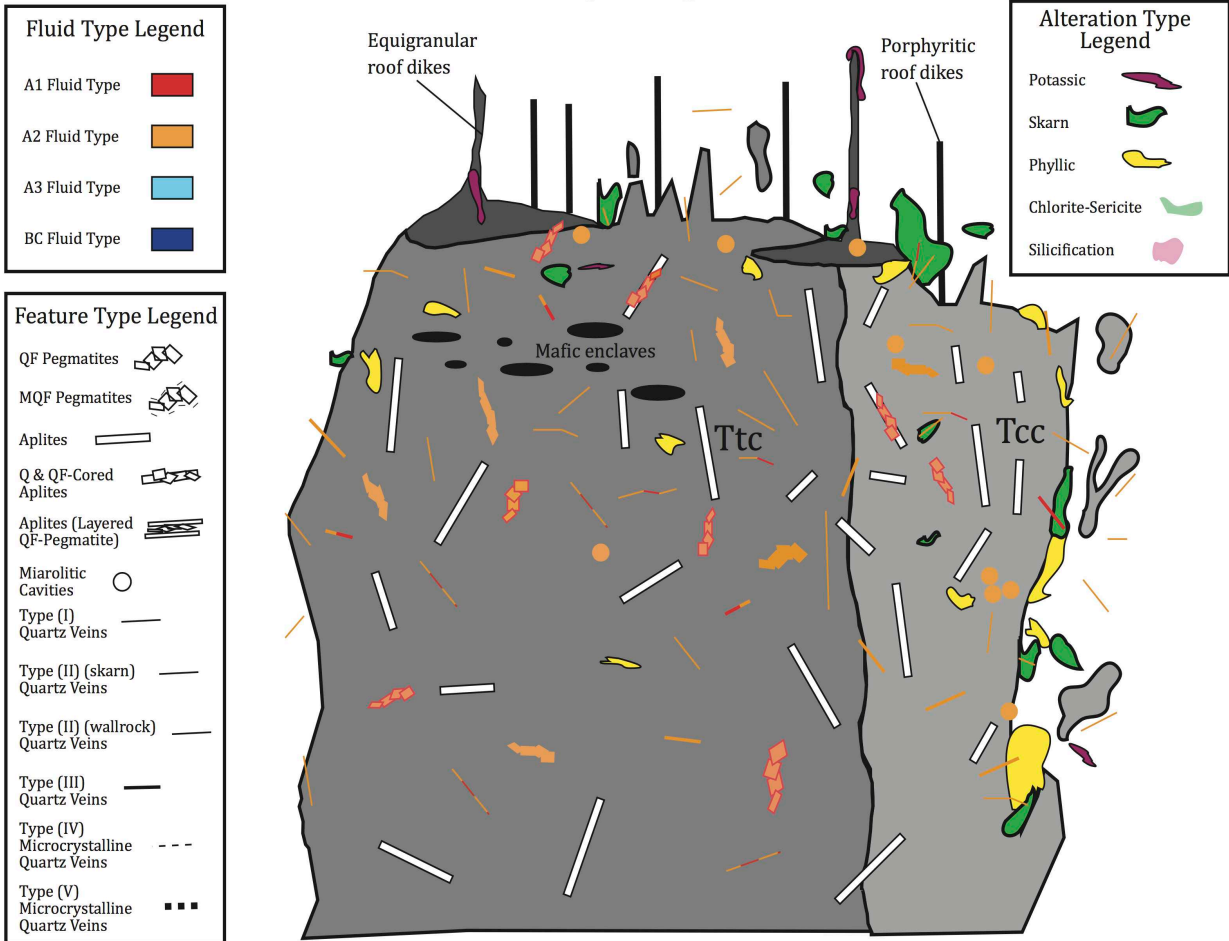


FIGURE 3.24 – Schematic cross section of the HPP illustrating exsolution, migration, and entrapment of early stage magmatic-hydrothermal fluids during the early stage of intrusive assembly. Feature types are colored to represent the fluid type(s) they host. Alteration types are colored for identification. Cross-section template adapted from Barnes et al. (2001).

Late Stage

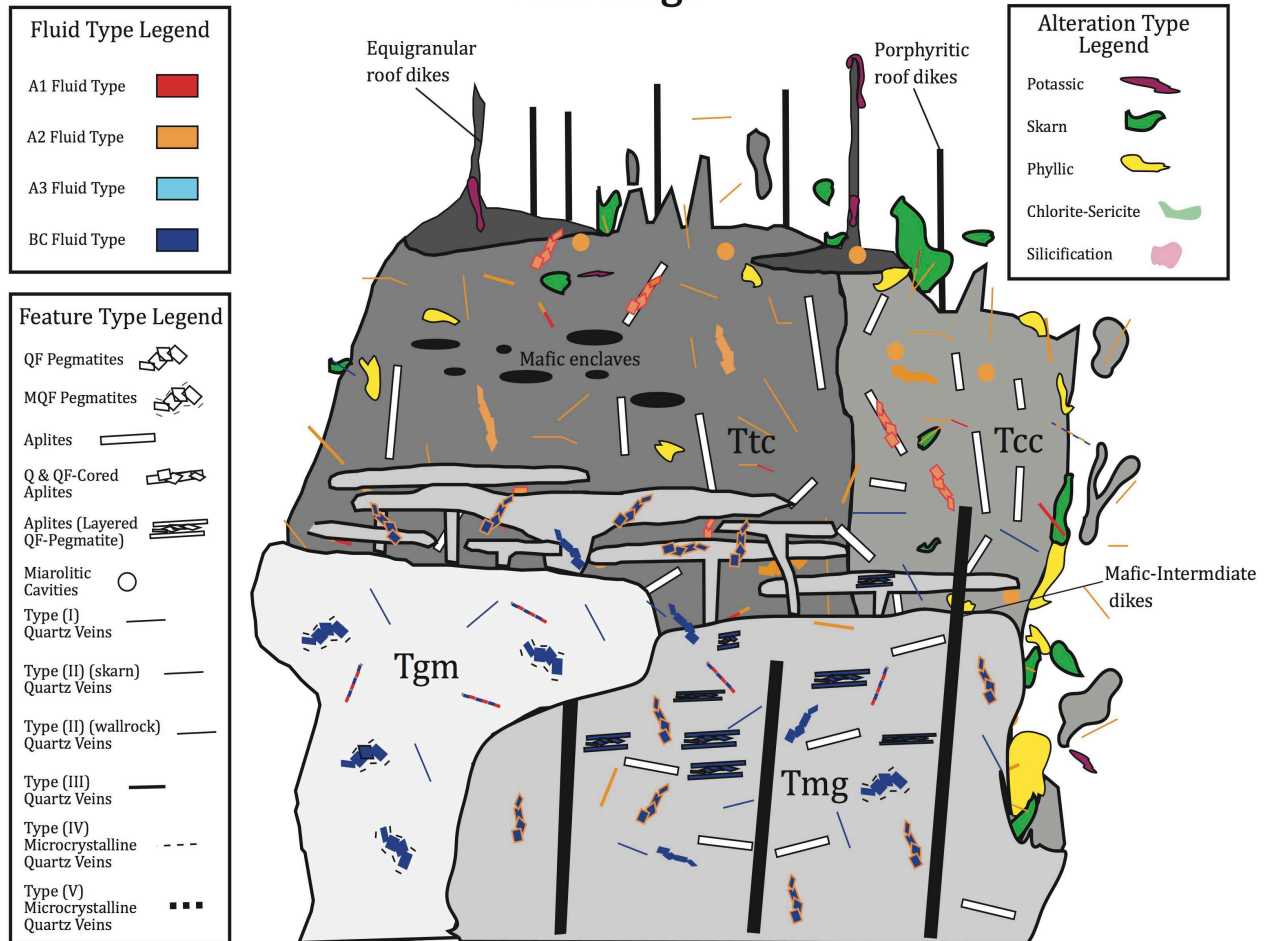


FIGURE 3.25 – Schematic cross section of the HPP illustrating exsolution, migration, and entrapment of late stage magmatic-hydrothermal fluids during the late stage of intrusive assembly. Feature types are colored to represent the fluid type(s) they host. Alteration types are colored for identification. Cross-section template adapted from Barnes et al. (2001).

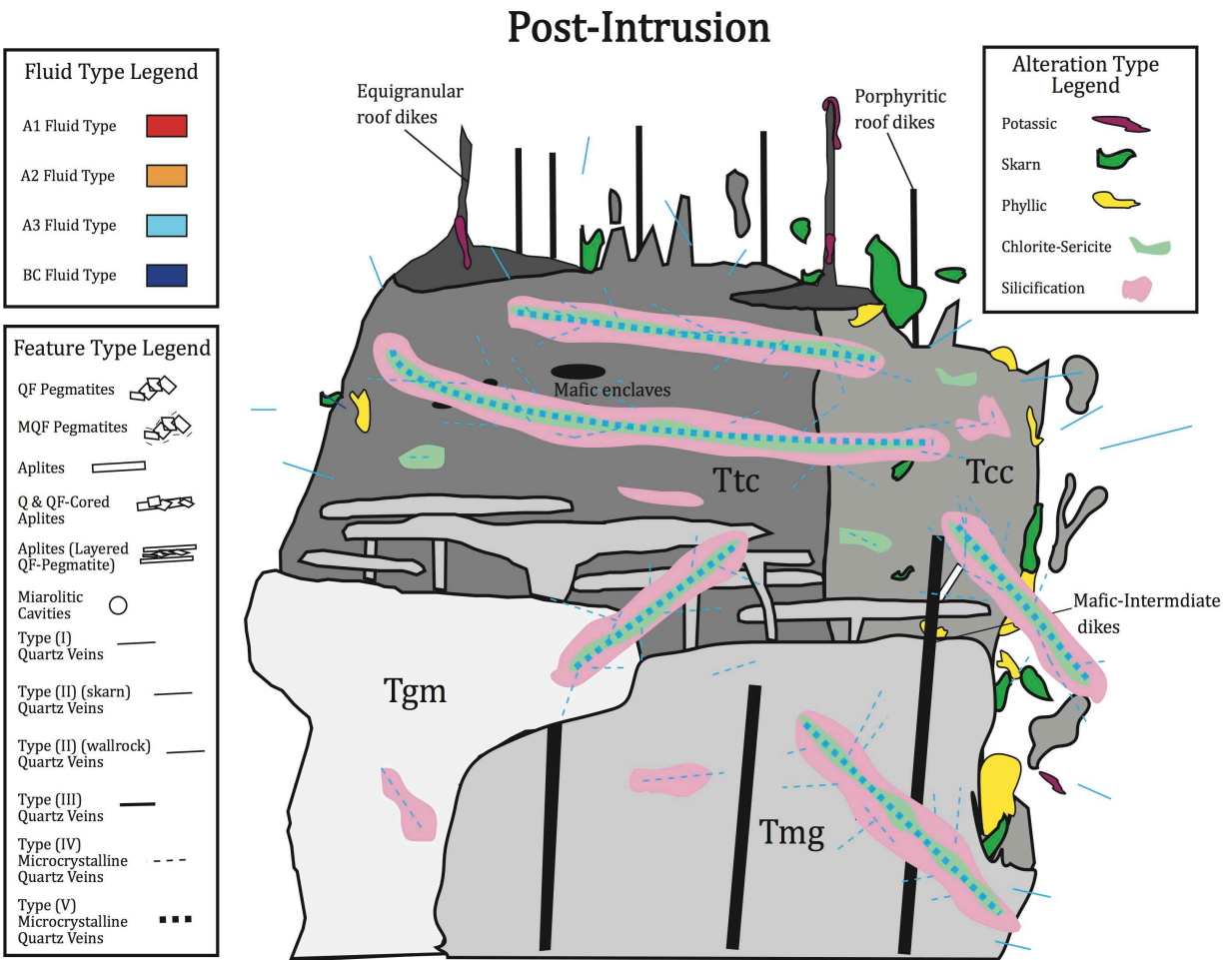


FIGURE 3.26 – Schematic cross section of the HPP illustrating the late influx and entrapment of post-intrusion hydrothermal fluids. Feature types are colored to represent the fluid type(s) they host. Alteration types are colored for identification. Cross-section template adapted from Barnes et al. (2001).

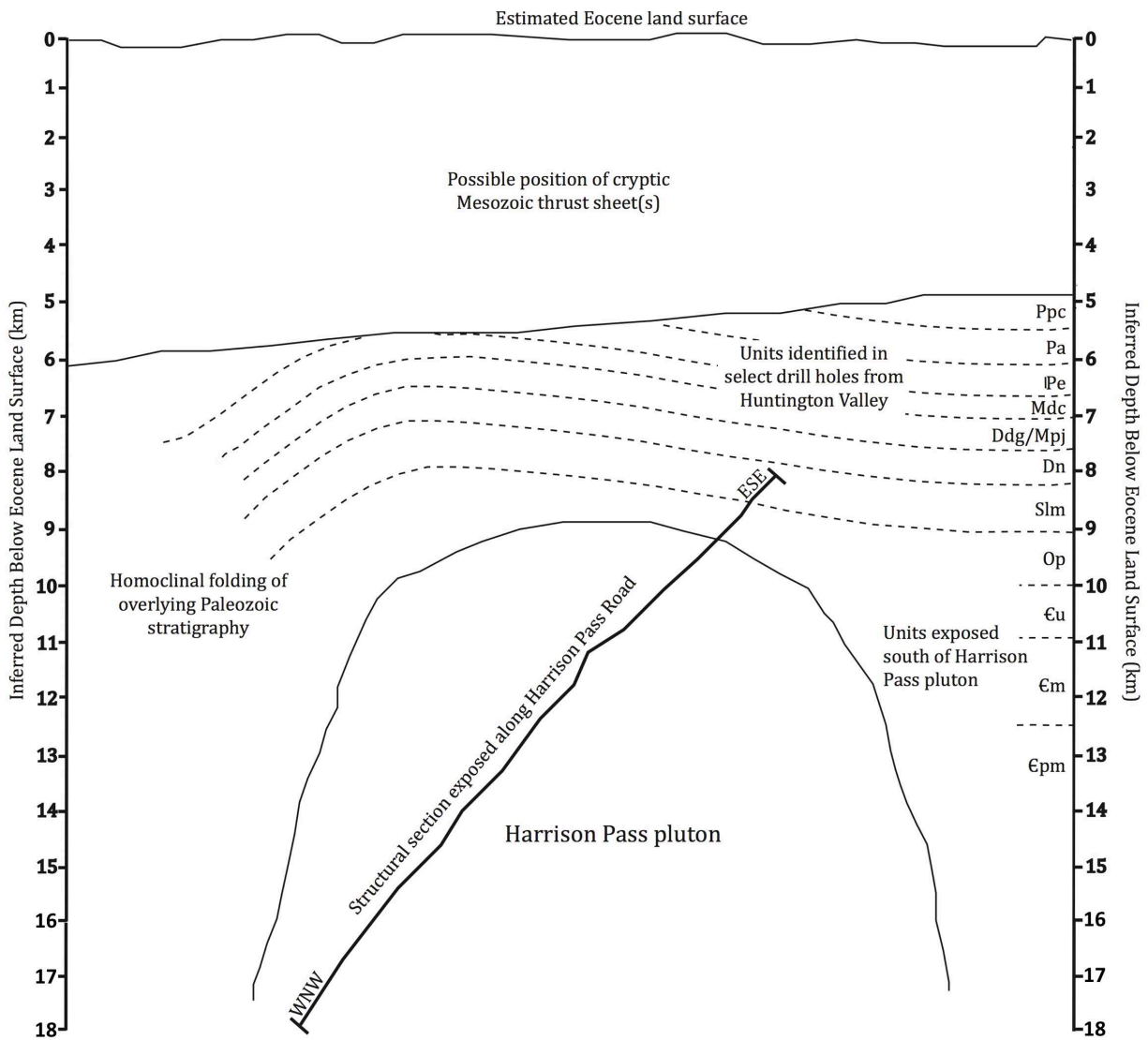


FIGURE 3.27 – Schematic WNW–ESE cross-section of the HPP and host stratigraphic/structural framework showing emplacement depths determined in this study. Also shown is the possible position of cryptic Mesozoic thrust sheet(s) as an explanation for burial of the HPP to greater than stratigraphic depths. See Colgan et al. (2010), and Burton (1997) for explanation and description of local stratigraphy. Adapted from Colgan et al. (2010).

3.10 REFERENCES

- Albino, G. V. (1994). Geology and lithogeochemistry of the Ren gold prospect, Elko County, Nevada—the role of rock sampling in exploration for deep Carlin-type deposits. *Journal of Geochemical Exploration*, 51(1), 37–58.
- Arehart, G. B. (1996). Characteristics and origin of sediment-hosted disseminated gold deposits: A review. *Ore Geology Reviews*, 11(6), 383–403.
- Arehart, G. B., Chakurian, A. M., Tretbar, D. R., Christensen, J. N., McInnes, B. A., & Donelick, R. A. (2003). Evaluation of radioisotope dating of Carlin-type deposits in the Great Basin, western North America, and implications for deposit genesis. *Economic Geology*, 98(2), 235–248.
- Arehart, G. B., & Donelick, R. A. (2006). Thermal and isotopic profiling of the Pipeline hydrothermal system: Application to exploration for Carlin-type gold deposits. *Journal of Geochemical Exploration*, 91(1), 27–40.
- Armstrong, R. L., Ekren, E. B., McKee, E. H., & Noble, D. C. (1969). Space-time relations of Cenozoic silicic volcanism in the Great Basin of the western United States. *American Journal of Science*, 267(4), 478–490.
- Armstrong, R. L. (1982). Cordilleran metamorphic core complexes—from Arizona to southern Canada. *Annual review of earth and planetary sciences*, 10, 129.
- Audétat, A., & Pettke, T. (2003). The magmatic-hydrothermal evolution of two barren granites: a melt and fluid inclusion study of the Rito del Medio and Canada Pinabete plutons in northern New Mexico (USA). *Geochimica et Cosmochimica Acta*, 67(1), 97–121.
- Audétat, A., Pettke, T., Heinrich, C. A., & Bodnar, R. J. (2008). Special paper: the composition of magmatic-hydrothermal fluids in barren and mineralized intrusions. *Economic Geology*, 103(5), 877–908.
- Bakken, B. M., & Einaudi, M. T. (1986). Spatial and temporal relations between wall rock alteration and gold mineralization, Main pit, Carlin gold mine, Nevada, USA. In *Gold*, 86, 388–403.
- Bakker, R. J. (1999). Adaptation of the Bowers and Helgeson (1983) equation of state to the H₂O–CO₂–CH₄–N₂–NaCl system. *Chemical Geology*, 154(1), 225–236.
- Bakker, R. J. (2003). Package FLUIDS 1. Computer programs for analysis of fluid inclusion data and for modeling bulk fluid properties. *Chemical Geology*, 194(1), 3–23.
- Barnes, C. G., Burton, B. R., Burling, T. C., Wright, J. E., & Karlsson, H. R. (2001). Petrology and Geochemistry of the Late Eocene Harrison Pass Pluton, Ruby Mountains Core Complex, Northeastern Nevada, 42(5), 901–929.

- Bennett, V. C., & DePaolo, D. J. (1987). Proterozoic crustal history of the western United States as determined by neodymium isotopic mapping. *Geological Society of America Bulletin*, 99(5), 674–685.
- Bettles, K. (2002). Overview of geology and exploration history at the Goldstrike property, Carlin Trend, Nevada, USA. *Giant Ore Deposit: Characteristics, Genesis and Exploration*. CODES Special Publication, 4, 175–189.
- Blackwell, D. D., Reese, N. M., & Kelley, S. A. (1985). Evolution of Basin and Range structure in the Ruby Mountains and vicinity, Nevada. In *Heat and Detachment in Crustal Extension on Continents and Planets*, 1, 12–14.
- Bowers, T. S., & Helgeson, H. C. (1983). Calculation of the thermodynamic and geochemical consequences of nonideal mixing in the system H₂O-CO₂-NaCl on phase relations in geologic systems: Equation of state for H₂O-CO₂-NaCl fluids at high pressures and temperatures. *Geochimica et Cosmochimica Acta*, 47(7), 1247–1275.
- Burton, B. R. (1997). Structural geology and emplacement history of the Harrison Pass pluton, central Ruby Mountains, Nevada. PhD Dissertation: University of Wyoming, Laramie, WY.
- Camilleri, P. A., & Chamberlain, K. R. (1997). Mesozoic tectonics and metamorphism in the Pequop Mountains and Wood Hills region, northeast Nevada: Implications for the architecture and evolution of the Sevier orogen. *Geological Society of America Bulletin*, 109(1), 74–94.
- Candela, P. A. (1997). A Review of Shallow, Ore-related Granites: Textures, Volatiles, and Ore Metals. *Journal of Petrology*, 38(12), 1619–1633.
- Cathles, L. M. (1981). Fluid flow and genesis of hydrothermal ore deposits. *Econ. Geol.*, 75, 424–457.
- Chakurian, A. M., Arehart, G. B., Donelick, R. A., Zhang, X., & Reiners, P. W. (2003). Timing constraints of gold mineralization along the Carlin Trend utilizing apatite fission-track, ⁴⁰Ar/³⁹Ar, and apatite (U-Th)/He methods. *Economic Geology*, 98(6), 1159–1171.
- Christiansen, R. L., & Lipman, P. W. (1972). Cenozoic volcanism and plate-tectonic evolution of the western United States. II. Late Cenozoic. *Philosophical Transactions of the Royal Society of London: Mathematical, Physical and Engineering Sciences*, 271(1213), 249–284.
- Christiansen, R. L., and Yeats, R. L. (1992) Post-Laramide geology of the U.S. Cordilleran region, in Burchfiel, B. C., Lipman, P. W., and Zoback, M. L., eds., *The Cordilleran Orogen: Conterminous U.S.: Boulder, CO, Geological Society of America, Geology of North America*, G-3, 261–406.
- Cline, J. S., & Bodnar, R. J. (1991). Can economic porphyry copper mineralization be generated by a typical calc-alkaline melt? *Journal of Geophysical Research: Solid Earth* (1978–2012), 96(B5), 8113–8126.

- Cline, J. S., Hofstra, A., Landis, G., & Rye, R. O. (1997). Ore fluids at the Getchell, Carlin-type Au deposit, north-central Nevada. *Society of Economic Geologists Field Trip Guidebook*, 28, 155–166.
- Cline, J. S., & Hofstra, A. A. (2000). Ore-fluid evolution at the Getchell Carlin-type Au deposit, Nevada, USA. *European Journal of Mineralogy*, 12(1), 195–212.
- Cline, J. S., Stuart, F. M., Hofstra, A. H., Premo, W., Riciputi, L., Tosdal, R. M., & Tretbar, D. R. (2003). Multiple sources of ore-fluid components at the Getchell Carlin-type Au deposit, Nevada, USA. *Mineral exploration and sustainable development*. Millpress, Rotterdam, 965–968.
- Cline, J. S., Hofstra, A. H., Muntean, J. L., Tosdal, R. M., & Hickey, K. A. (2005). Carlin-Type Au Deposits in Nevada: Critical Geologic Characteristics and Viable Models. *Economic Geology*, 100th Anniversary Volume, 451–484.
- Colgan, J. P., Howard, K. A., Fleck, R. J., & Wooden, J. L. (2010). Rapid middle Miocene extension and unroofing of the southern Ruby Mountains, Nevada. *Tectonics*, 29(6).
- Coney, P. J., & Harms, T. A. (1984). Cordilleran metamorphic core complexes: Cenozoic extensional relics of Mesozoic compression. *Geology*, 12(9), 550–554.
- Dallmeyer, R. D., Snoke, A. W., & McKee, E. H. (1986). The Mesozoic-Cenozoic tectonothermal evolution of the Ruby Mountains, East Humboldt Range, Nevada: A Cordilleran Metamorphic Core Complex. *Tectonics*, 5(6), 931–954.
- de Almeida, C. M., Olivo, G. R., Chouinard, A., Weakly, C., & Poirier, G. (2010). Mineral paragenesis, alteration, and geochemistry of the two types of gold ore and the host rocks from the Carlin-type deposits in the southern part of the Goldstrike property, northern Nevada: Implications for sources of ore-forming elements, ore genesis, and mineral exploration. *Economic Geology*, 105(5), 971–1004.
- Deans, J. R. (2010). Trace element and calculated temperature variation in quartz and titanite in the 36 Ma Harrison Pass pluton, Ruby Mountains NE Nevada. PhD Dissertation: Texas Tech University, (Doctoral dissertation, Texas Tech University, Lubbock, TX).
- Dickinson, W.R., 2006, Geotectonic Evolution of the Great Basin. *Geosphere*, v. 2, p. 353–368.
- Dohrenwend, J. C., Schell, B. A., Menges, C. M., Moring, B. C., & McKittrick, M. A. (1996). Reconnaissance photogeologic map of young (Quaternary and late Tertiary) faults in Nevada. *An Analysis of Nevada's Metal-Bearing Mineral Resources*, 96–2.
- Dokka, R. K., Mahaffie, M. J., & Snoke, A. W. (1986). Thermochronologic evidence of major tectonic denudation associated with detachment faulting, Northern Ruby Mountains-East Humboldt Range, Nevada. *Tectonics*, 5(7), 995–1006.
- Emsbo, P., Hofstra, A. H., Lauha, E. A., Griffin, G. L., & Hutchinson, R. W. (2003). Origin of high-grade gold ore, source of ore fluid components, and genesis of the Meikle and

neighboring Carlin-type deposits, northern Carlin trend, Nevada. *Economic Geology*, 98(6), 1069–1105.

Fortuna, J., Kesler, S. E., & Stenger, D. P. (2003). Source of iron for sulfidation and gold deposition, Twin Creeks Carlin-type deposit, Nevada. *Economic Geology*, 98(6), 1213–1224.

Fournier, R. O., & Truesdell, A. H. (1973). An empirical Na K Ca geothermometer for natural waters. *Geochimica et Cosmochimica Acta*, 37(5), 1255–1275.

Fowler, S. J., & Spera, F. J. (2010). A metamodel for crustal magmatism: phase equilibria of giant ignimbrites. *Journal of Petrology*, 51(9), 1783–1830.

Frank, M. R., Simon, A. C., Pettke, T., Candela, P. A., & Piccoli, P. M. (2011). Gold and copper partitioning in magmatic-hydrothermal systems at 800 C and 100MPa. *Geochimica et Cosmochimica Acta*, 75(9), 2470–2482.

Gans, P. B., Mahood, G. A., & Schermer, E. (1989). Synextensional magmatism in the Basin and Range Province; a case study from the eastern Great Basin. *Geological Society of America Special Papers*, 233, 1–53.

Gao, Z. (1992). The ore-forming conditions and ore predictions of sediment-hosted disseminated gold deposits in northwest Sichuan. I-88-92-02-2 research report of the Gold Administration of China.

Gibbs, J. F., Willden, R., & Carlson, J. E. (1968). Gravity anomalies in the Ruby Mountains, northeastern Nevada. *Geological Survey research*, B88–B94.

Haines, S. H., & van der Pluijm, B. A. (2010). Dating the detachment fault system of the Ruby Mountains, Nevada: Significance for the kinematics of low-angle normal faults. *Tectonics*, 29(4).

Hedenquist, J. W., & Lowenstern, J. B. (1994). The role of magmas in the formation of hydrothermal ore deposits. *Nature*, 370(6490), 519–527.

Heinrich, C. A., Pettke, T., Halter, W. E., Aigner-Torres, M., Audétat, A., Günther, D., Hattendorf, B., Bleiner, D., Guillong, M. & Horn, I. (2003). Quantitative multi-element analysis of minerals, fluid and melt inclusions by laser-ablation inductively-coupled-plasma mass-spectrometry. *Geochimica et Cosmochimica Acta*, 67(18), 3473–3497.

Heitt, D. G., Dunbar, W. W., Thompson, T. B., & Jackson, R. G. (2003). Geology and geochemistry of the Deep Star Au deposit, Carlin trend, Nevada. *Economic Geology*, 98(6), 1107–1135.

Henkelman, C. (2004). Variations in pyrite chemistry as clues to gold deposition at the Goldstrike system, Carlin trend, Nevada USA: Unpublished M. Sc (Doctoral dissertation, thesis, Las Vegas, University of Nevada).

- Henry, C. D., & Boden, D. R. (1998). Eocene magmatism: The heat source for Carlin-type gold deposits of northern Nevada. *Geology*, 26(12), 1067–1070.
- Henry, C. D., & Ressel, M. W. (2000). Interrelation of Eocene magmatism, extension, and Carlin-type Au deposits in northeastern Nevada. *Great Basin and Sierra Nevada: Boulder, Colorado, Geological Society of America Field Guide*, 2, 165–187.
- Hickey, K. A., Barker, S. L., Dipple, G. M., Arehart, G. B., & Donelick, R. A. (2014). The brevity of hydrothermal fluid flow revealed by thermal halos around giant gold deposits: implications for Carlin-type gold systems. *Economic Geology*, 109(5), 1461–1487.
- Hodges, K. V., & Walker, J. D. (1992). Extension in the Cretaceous Sevier orogen, North American Cordillera. *Geological Society of America Bulletin*, 104(5), 560–569.
- Hodges, K. V., Snoke, A. W., & Hurlow, H. A. (1992). Thermal evolution of a portion of the Sevier Hinterland: The Northern Ruby Mountains-East Humboldt Range and Wood Hills, northeastern Nevada. *Tectonics*, 11(1), 154–164.
- Hofstra, A. H., Leventhal, J. S., Northrop, H. R., Landis, G. P., Rye, R. O., Birak, D. J., & Dahl, A. R. (1991). Genesis of sediment-hosted disseminated-gold deposits by fluid mixing and sulfidization: Chemical-reaction-path modeling of ore-depositional processes documented in the Jerritt Canyon district, Nevada. *Geology*, 19(1), 36–40.
- Hofstra, A. H. (1997). Isotopic composition of sulfur in Carlin-type gold deposits: Implications for genetic models. In *Carlin-type gold deposits field conference: Society of Economic Geologists Guidebook Series* (Vol. 28, pp. 119–129).
- Hofstra, A. H., Snee, L. W., Rye, R. O., Folger, H. W., Phinisey, J. D., Loranger, R. J., Dahl, A. R., Naeser, C. W., Stein, H. J., & Lewchuk, M. T. (1999). Age constraints on Jerritt Canyon and other Carlin-type gold deposits in the Western United States; relationship to mid-Tertiary extension and magmatism. *Economic Geology*, 94(6), 769–802.
- Hofstra, A. H., & Cline, J. S. (2000). Characteristics and models for Carlin-type Au deposits. *Reviews in Economic Geology*, 13, 163–220.
- Hofstra, A. H., Emsbo, P., Christiansen, W. D., Theodorakos, P., Zhang, X. C., Hu, R. Z., ... & Fu, S. H. (2005). Source of ore fluids in Carlin-type gold deposits, China: Implications for genetic models. In *Mineral Deposit Research: Meeting the Global Challenge* (pp. 533–536). Springer Berlin Heidelberg.
- Howard, K. A. (1980). Metamorphic infrastructure in the northern Ruby Mountains, Nevada. *Geological Society of America Memoirs*, 153, 335–348.
- Howard, K. A. (2003). Crustal Structure in the Elko-Carlin Region, Nevada, during Eocene Au Mineralization: Ruby-East Humboldt Metamorphic Core Complex as a Guide to the Deep Crust. *Economic Geology*, 98, 249–268.

- Hu, R.Z., Wen-Chao, S., Xian-Wu, B., Guang-Zhi, T., & Hofstra, A. H. (2002). Geology and geochemistry of Carlin-type gold deposits in China. *Mineralium Deposita*, 37(3-4), 378-392.
- Hudec, M. R. (1990). The structural and thermal evolution of the central Ruby Mountains, Elko County, Nevada. (Doctoral Dissertation, thesis: University of Wyoming).
- Hudec, M. R. (1992). Mesozoic structural and metamorphic history of the central Ruby Mountains metamorphic core complex, Nevada. *Geological Society of America Bulletin*, 104(9), 1086-1100.
- Humphreys, E. D. (1995). Post-Laramide removal of the Farallon slab, western United States. *Geology*, 23(11), 987-4.
- Hurlow, H. A., Snoke, A. W., & Hodges, K. V. (1991). Temperature and pressure of mylonitization in a Tertiary extensional shear zone, Ruby Mountains-East Humboldt Range, Nevada: Tectonic implications. *Geology*, 19(1), 82-86.
- Jamtveit, B., & Yardley, B. W. (1997). Fluid flow and transport in rocks: an overview (pp. 1-14). Netherlands: Springer.
- Johnston, M. K., & Ressel, M. W. (2004). Controversies on the origin of world-class gold deposits, Pt. I: Carlin-type gold deposits in Nevada, II. Carlin-type and distal disseminated Au-Ag deposits: Related distal expressions of Eocene intrusive centers in north-central Nevada: *Society of Economic Geologists Newsletter*, 59, 12-14.
- Kesler, S. E., Fortuna, J., Ye, Z., Alt, J. C., Core, D. P., Zohar, P., & Chryssoulis, S. L. (2003). Evaluation of the role of sulfidation in deposition of gold, Screamer section of the Betze-Post Carlin-type deposit, Nevada. *Economic Geology*, 98(6), 1137-1157.
- Kistler, R. W., Ghent, E. D., & O'Neil, J. R. (1981). Petrogenesis of garnet two-mica granites in the Ruby Mountains, Nevada. *Journal of Geophysical Research: Solid Earth* (1978-2012), 86(B11), 10591-10606.
- Klepper, M. R., Wiese, J. W., Swinney, C. M., & Joralemon, P. (1944). Star tungsten mine and vicinity, Harrison Pass, Elko County, Nevada (No. 44-37).
- Kuehn, C. A., & Rose, A. W. (1992). Geology and geochemistry of wall-rock alteration at the Carlin gold deposit, Nevada. *Economic Geology*, 87(7), 1697-1721.
- Kuehn, C. A., & Rose, A. W. (1995). Carlin gold deposits, Nevada; origin in a deep zone of mixing between normally pressured and overpressured fluids. *Economic Geology*, 90(1), 17-36.
- Lamb, J. B. (1995). A petrographic and fluid inclusion study of the Purple Vein and Post-Betze orebodies, Carlin, Nevada. University of Nevada, Las Vegas (Doctoral dissertation, MS, thesis).

- Lapointe, D. D., Tingley, J. V., & Jones, R. B. (1991). Mineral resources of Elko County, Nevada (No. 106). Reno: University of Nevada, Reno, MacKay School of Mines.
- Lister, G. S., & Snoke, A. W. (1984). SC mylonites. *Journal of Structural Geology*, 6(6), 617–638.
- Lubben, J. D. (2004). Silicification Across the Betze-Post Carlin-type Au Deposit: Clues to Ore Fluid Properties and Sources, Northern Carlin Trend, Nevada (Doctoral dissertation, University of Nevada, Las Vegas).
- Lubben, J. D., Cline, J. S., & Barker, S. L. L. (2012). Ore Fluid Properties and Sources from Quartz-Associated Au at the Betze-Post Carlin-Type Au Deposit, Nevada, United States. *Economic Geology*, 107, 1351–1383.
- Lush, A. P., McGrew, A. J., Snoke, A. W., & Wright, J. E. (1988). Allochthonous Archean basement in the northern East Humboldt Range, Nevada. *Geology*, 16(4), 349–353.
- MacCready, T., Snoke, A. W., Wright, J. E., & Howard, K. A. (1997). Mid-crustal flow during Tertiary extension in the Ruby Mountains core complex, Nevada. *Geological Society of America Bulletin*, 109(12), 1576–1594.
- McGrew, A. J., & Snee, L. W. (1994). $^{40}\text{Ar}/^{39}\text{Ar}$ thermochronologic constraints on the tectonothermal evolution of the Northern East Humboldt range metamorphic core complex, Nevada. *Tectonophysics*, 238(1), 425–450.
- McGrew, A. J., Peters, M. T., & Wright, J. E. (2000). Thermobarometric constraints on the tectonothermal evolution of the East Humboldt Range metamorphic core complex, Nevada. *Geological Society of America Bulletin*, 112(1), 45–60.
- Muntean, J. L., Cline, J. S., Simon, A. C., & Longo, A. A. (2011). Magmatic-hydrothermal origin of Nevada's Carlin-type gold deposits. *Nature Geoscience*, 4(2), 122–127.
- Musekamp, C. O. J. (2012). Field, fluid inclusion and isotope chemistry evidence of fluids circulating around the Harrison Pass pluton during intrusion: A fluid model for Carlin-type deposits. (Masters thesis, Colorado State University)
- Nabelek, P. I. (1991). Stable isotope monitors. *Reviews in Mineralogy and Geochemistry*, 26(1), 395–435.
- Nutt, C. J., & Hofstra, A. H. (2003). Alligator Ridge district, east-central Nevada: Carlin-type gold mineralization at shallow depths. *Economic Geology*, 98(6), 1225–1241.
- Orville, P. M. (1963). Alkali ion exchange between vapor and feldspar phases. *American Journal of Science*, 261(3), 201–237.
- Petford, N., Cruden, A. R., McCaffrey, K. J. W., & Vigneresse, J. L. (2000). Granite magma formation, transport and emplacement in the Earth's crust. *Nature*, 408(6813), 669–673.
- Pitcher, W. S. (1979). The nature, ascent and emplacement of granitic magmas. *Journal of the Geological Society*, 136(6), 627–662.

- Radtke, A. S., Rye, R. O., & Dickson, F. W. (1980). Geology and stable isotope studies of the Carlin gold deposit, Nevada. *Economic Geology*, 75(5), 641–672.
- Reese, N. M. (1986). Cenozoic tectonic history of the Ruby Mountains and adjacent areas, northeastern Nevada: constraints from radiometric dating and seismic reflection profiles. M.S. thesis: Southern Methodist University, Dallas, TX.
- Reich, M., Kesler, S. E., Utsunomiya, S., Palenik, C. S., Chryssoulis, S. L., & Ewing, R. C. (2005). Solubility of gold in arsenian pyrite. *Geochimica et Cosmochimica Acta*, 69(11), 2781–2796.
- Ressel, M. W., Noble, D. C., Henry, C. D., & Trudel, W. S. (2000). Dike-hosted ores of the Beast deposit and the importance of Eocene magmatism in gold mineralization of the Carlin trend, Nevada. *Economic Geology*, 95(7), 1417–1444.
- Ressel, M. W., & Henry, C. D. (2006). Igneous Geology of the Carlin Trend, Nevada: Development of the Eocene Plutonic Complex and Significance for Carlin-Type Au Deposits. *Economic Geology*, 101, 347–383.
- Rusk, B. G., Reed, M. H., Dilles, J. H., Klemm, L. M., & Heinrich, C. A. (2004). Compositions of magmatic hydrothermal fluids determined by LA-ICP-MS of fluid inclusions from the porphyry copper–molybdenum deposit at Butte, MT. *Chemical Geology*, 210(1), 173–199.
- Satarugsa, P., & Johnson, R. A. (2000). Cenozoic tectonic evolution of the Ruby Mountains metamorphic core complex and adjacent valleys, northeastern Nevada. *Rocky Mountain Geology*, 35(2), 205–230.
- Schmidt, C., & Bodnar, R. J. (2000). Synthetic fluid inclusions: XVI. PVTX properties in the system H₂O-NaCl-CO₂ at elevated temperatures, pressures, and salinities. *Geochimica et Cosmochimica Acta*, 64(22), 3853–3869.
- Sharp, Z. D. (1990). A laser-based microanalytical method for the in situ determination of oxygen isotope ratios of silicates and oxides. *Geochimica et Cosmochimica Acta*, 54(5), 1353–1357.
- Sharp, Z. D. (1992). In situ laser microprobe techniques for stable isotope analysis. *Chemical Geology: Isotope Geoscience section*, 101(1), 3–19.
- Sillitoe, R. H., & Bonham, H. F. (1990). Sediment-hosted gold deposits: Distal products of magmatic-hydrothermal systems. *Geology*, 18(2), 157–161.
- Simon, G., Kesler, S. E., & Chryssoulis, S. (1999). Geochemistry and textures of gold-bearing arsenian pyrite, Twin Creeks, Nevada; implications for deposition of gold in Carlin-type deposits. *Economic Geology*, 94(3), 405–421.
- Smith Jr, J. K., Ketner, K. B., & Mabey, D. R. (1976). Stratigraphy of post-Paleozoic rocks and summary of resources in the Carlin-Piñon Range area, Nevada, with a section on aeromagnetic survey (No. 867-B).

Snoke, A. W. (1980). Transition from infrastructure to suprastructure in the northern Ruby Mountains, Nevada. *Geological Society of America Memoirs*, 153, 287–334.

Snoke, A. W., & Lush, A. P. (1984). Polyphase Mesozoic-Cenozoic deformational history of the northern Ruby Mountains-East Humboldt Range, Nevada. In *Western Geological Excursions*, prepared for the 1984 Annual Meetings of the Geological Society of America and affiliated societies at Reno, 232–260.

Snoke, A. W., & Miller, D. M. (1988). Metamorphic and tectonic history of the northeastern Great Basin. *Metamorphism and crustal evolution of the western United States*, Rubey, 7, 606–648.

Snoke, A. W., McGrew, A. J., Valasek, P. A., & Smithson, S. B. (1990). A crustal cross-section for a terrain of superimposed shortening and extension: Ruby Mountains-East Humboldt Range metamorphic core complex, Nevada. In *Exposed cross-sections of the Continental Crust*, 103–135. Netherlands: Springer.

Su, W., Xia, B., Zhang, H., Zhang, X., & Hu, R. (2008). Visible gold in arsenian pyrite at the Shuiyindong Carlin-type gold deposit, Guizhou, China: implications for the environment and processes of ore formation. *Ore Geology Reviews*, 33(3), 667–679.

Su, W., Heinrich, C. A., Pettke, T., Zhang, X., Hu, R., & Xia, B. (2009). Sediment-hosted gold deposits in Guizhou, China: products of wall-rock sulfidation by deep crustal fluids. *Economic Geology*, 104(1), 73–93.

Taylor, H. P. (1974). The application of oxygen and hydrogen isotope studies to problems of hydrothermal alteration and ore deposition. *Economic geology*, 69(6), 843–883.

Taylor, B. E., & O'Neil, J. R. (1977). Stable isotope studies of metasomatic Ca-Fe-Al-Si skarns and associated metamorphic and igneous rocks, Osgood Mountains, Nevada. *Contributions to Mineralogy and Petrology*, 63(1), 1–49.

Teal, L., & Jackson, M. (2002). Geologic overview of the Carlin trend gold deposits. *Gold deposits of the Carlin trend*. Nevada Bureau of Mines and Geology, Bulletin, 111, 9–19.

Thomas, R. (1994). Fluid evolution in relation to the emplacement of the Variscan granites in the Erzgebirge region: a review of the melt and fluid inclusion evidence. *Metallogeny of collisional orogens*. Czech Geological Survey, Prague, 70–81.

Thorman, C. H., Ketner, K. B., & Peterson, F. (1990). The Elko orogeny-Late Jurassic orogenesis in the Cordilleran miogeocline: Geological Society of America Cordilleran Meeting. *Programs with Abstract*, 22(3), 88.

Thorman, C. H., Ketner, K. B., Brooks, W. E., Snee, L. W., & Zimmerman, R. A. (1991). Late Mesozoic-Cenozoic tectonics in northeastern Nevada. In *Geology and ore deposits of the Great Basin: Symposium Proceedings*, Geological Society of Nevada, Reno, Nevada, 1, 25–45.

- Thorman, C. H., & Peterson, F. (2003). The Middle Jurassic Elko Orogeny-A Major Tectonic Event in Nevada-Utah. In Annual Meeting Expanded Abstracts, 12, 169–174.
- Tingley, J. V. (1981). Summary Report, Mineral Inventory of the Wells Resource Area, Elko District, Elko County, Nevada (Vol. 81, No. 4). NV Bureau of Mines & Geology.
- Vaughan, J. R. (2013). Tracing hydrothermal fluid flow in the rock record: geochemical and isotopic constraints on fluid flow in Carlin-type gold systems. PhD dissertation: University of British Columbia, Vancouver, BC.
- Veizer, J., Ala, D., Azmy, K., Bruckschen, P., Buhl, D., Bruhn, F., ... & Jasper, T. (1999). $^{87}\text{Sr}/^{86}\text{Sr}$, $\delta^{13}\text{C}$ and $\delta^{18}\text{O}$ evolution of Phanerozoic seawater. *Chemical geology*, 161(1), 59–88.
- Wells, M. L., Snee, L. W., & Blythe, A. E. (2000). Dating of major normal fault systems using thermochronology: An example from the Raft River detachment, Basin and Range, western United States. *Journal of Geophysical Research: Solid Earth (1978–2012)*, 105(B7), 16303–16327.
- Wells, M. L. (2001). Rheological control on the initial geometry of the Raft River detachment fault and shear zone, western United States. *Tectonics*, 20(4), 435–457.
- Wickham, S. M. (1987). The segregation and emplacement of granitic magmas. *Journal of the Geological Society*, 144(2), 281–297.
- Wickham, S. M., Peters, M. T., Fricke, H. C., & O'Neil, J. R. (1993). Identification of magmatic and meteoric fluid sources and upward-and downward-moving infiltration fronts in a metamorphic core complex. *Geology*, 21(1), 81–84.
- Willden, R., & Kistler, R. W. (1979). Precambrian and Paleozoic Stratigraphy in Central Ruby Mountains Elko County, Nevada.
- Wooden, J. L., & Miller, D. M. (1990). Chronologic and isotopic framework for Early Proterozoic crustal evolution in the eastern Mojave Desert region, SE California. *Journal of Geophysical Research: Solid Earth (1978–2012)*, 95(B12), 20133–20146.
- Wright, J. E., & Snoke, A. W. (1993). Tertiary magmatism and mylonitization in the Ruby-East Humboldt metamorphic core complex, northeastern Nevada: U-Pb geochronology and Sr, Nd, and Pb isotope geochemistry. *Geological Society of America Bulletin*, 105(7), 935–952.
- Yigit, O., Nelson, E. P., Hitzman, M. W., & Hofstra, A. H. (2003). Structural controls on Carlin-type gold mineralization in the Gold Bar district, Eureka County, Nevada. *Economic Geology*, 98(6), 1173–1188.
- Zhang, X. C., Spiro, B., Halls, C., Stanley, C. J., & Yang, K. Y. (2003). Sediment-hosted disseminated gold deposits in Southwest Guizhou, PRC: their geological setting and origin in relation to mineralogical, fluid inclusion, and stable-isotope characteristics. *International Geology Review*, 45(5), 407–470.

CHAPTER 4: CONCLUSIONS

Intrusion of the ~36 Ma, multi-phase, granodiorite-monzogranite HPP into the RMEHR metamorphic core complex in the northeastern Great Basin was accompanied by magmatic fluid saturation, exsolution, migration, and expulsion. Field mapping and sampling, petrography, isotope geochemistry, and fluid inclusion microthermometry and multi-element geochemistry have been employed in this research project to examine the spatial distribution, timing relationships, entrapment conditions, and geochemical compositions of these fluids. Results were interpreted in the context of the Cenozoic tectonic development of the RMEHR metamorphic core complex and the broadly synchronous formation of CTD's in the Great Basin. This chapter briefly summarizes the significant results of this research, the most salient industry applications, and possible avenues for future study of the HPP and similar coeval intrusions in the Great Basin.

4.1 SIGNIFICANT RESEARCH FINDINGS

Reconstruction of the dynamic, spatially variable, multi-stage magmatic-hydrothermal fluid history of the HPP is the most significant accomplishment of this research project. Although previous studies have examined the age (Kistler et al., 1981); field geology and emplacement dynamics (Burton, 1997); igneous petrology and geochemistry (Barnes et al., 2001); and the external, intrusion-driven hydrothermal system (Musekamp, 2011); this thesis is the first direct investigation of the magmatic-hydrothermal fluid system within the HPP. The central goals of this thesis, described in

Section 1.4, are to constrain the (1) thermodynamic conditions of the syn-emplacement magmatic-hydrothermal transition of the HPP, and (2) the chemistry of the hydrothermal fluids exsolved from crystallizing HPP magmas. Accomplishment of these two goals permits an independent determination of the emplacement depth of the HPP, and an assessment of potential genetic links between the HPP and CTD ore fluids, respectively.

Chapter 2 describes the field and petrographic observations of the evidence of magmatic-hydrothermal fluid activity in the HPP. This evidence is subdivided into 15 distinct “feature types.” It is demonstrated that the two-stage magmatic assembly of the HPP controlled the systematic variations in the evidence of fluid activity that exist between early and late stage intrusive units. It is also concluded that fluid exsolution was more substantial in early stage units than in late stage units, and that the hydrothermal ore deposits observed around the HPP were likely formed by fluids exsolved from early stage magmas.

Chapter 3 has explored the multi-element and isotope geochemistry and entrapment conditions of the fluids circulating within the HPP during emplacement, and has shown that three fluid types were exsolved from crystallizing magmas. Early stage magmas exsolved two low-salinity (~3 wt % eq. NaCl), B-Na-K-Rb-Sr-Cs-bearing, aqueous fluids that migrated throughout the HPP and were expelled into metasedimentary wallrock units, and were likely responsible for the formation of base metal skarn and carbonate replacement deposits. Overpressured late stage magmas exsolved one fluid that was ore element-poor, low-salinity (~3 wt % eq. NaCl), B-Na-K-Rb-Sr-Cs-bearing, and aquo-carbonic (~5 mol% CO₂). This fluid did not migrate extensively. This chapter also demonstrated that entrapment of the bulk of early stage fluids occurred at ~3400–6800

bar, which translate to depths of ~9–18 km, (assuming dominantly lithostatic fluid pressure). These pressures and depths are similar to those determined by previous studies based on mineral thermobarometry, indicating that the southern Ruby Mountains were likely buried to greater than stratigraphic depths. It is also concluded that the fluid model for the origin of CTD's proposed by Muntean et al. (2011) is not supported by this study, largely due to the fact that a high-salinity fluid was not observed. Comparison of fluid inclusion multi-element geochemical data from this study (demonstrating low concentrations of CTD ore elements, but some general bulk similarities), with the geochemical profiles constructed for ore fluids from CTD's in Nevada and China has also not provided strong indications that the HPP was the source of the ore elements.

4.2 APPLICATIONS OF RESEARCH FINDINGS

As described in Section 1.2.3, hydrothermal fluids derived from granitoid intrusions are directly related to the formation of several important ore deposit types (reviewed by Cox & Singer, 1986). Although the relationship between contemporaneous intrusive magmatism in the Great Basin and CTD's is still poorly understood, Eocene intrusions, such as the HPP, are frequently invoked as potential sources of fluids and ore elements for CTD's on the basis of field relationships, isotopic data, geochronology, and geochemical modeling (i.e. Ressel et al., 2000; Heitt et al., 2003; Ressel & Henry, 2006; Muntean et al., 2011). Proximity to coeval intrusive rocks in areas of CTD mineralization is an essential, or at least typical, component of several published theoretical deposit models (Sillitoe & Bonham, 1990; Henry & Boden, 1998; Cline et al., 2005; Ressel & Henry, 2006; Muntean et al., 2011).

At the Carlin Trend, these relatively low-volume coeval intrusive rocks have been described as evidence of a suite of underlying silicic plutons similar to the HPP (Ressel & Henry, 2006; Muntean et al., 2011).

This study has found that one such Eocene granitoid intrusion in the Great Basin, the HPP, exsolved aqueous and aquo-carbonic fluids with some overall similarities to CTD ore fluids. First, salinities for these fluids are similar to, but slightly higher than, CTD ore fluids. These fluids have oxygen stable isotope values similar to the magmatic component detected for ore fluids as several CTD's. However, the fluids exsolved from the HPP have concentrations of certain elements associated with CTD's (As, Sb) that are below the concentrations determined for CTD ore fluids. Thus, the findings of this study do not support a strong genetic link between the HPP and CTD's. This conclusion has significant implications for exploration for this deposit type. In the Great Basin and in areas of burgeoning CTD exploration (i.e. China, the Yukon) it is recommended that local or regional granitoid intrusive magmatism not be used as a primary targeting criterion for CTD exploration.

4.3 FUTURE RESEARCH FINDINGS

The conclusion of this research raises several possible avenues for future research into the magmatic-hydrothermal fluid history of the HPP, particularly in regard to the relationships with the RMEHR metamorphic core complex and CTD's discussed here. Specific unanswered questions pertaining to the fluid history of the HPP can be generally divided into two different categories: (1) areas of interest for further field study and

sampling and (2) additional geochemical analytical methods. In the first category, focused mapping and sampling of miarolitic cavities (with fluid inclusion microthermometry and LA-ICP-MS) would clarify the apparent disagreement between this study and Musekamp (2012) regarding the fluid compositions observed in this feature type. Similarly, more rigorous sampling of the late stage Tgm unit could reveal undetected compositional heterogeneities in the fluids exsolved from this geochemically distinct magma. In the second category, analysis of fluid inclusions by laser Raman spectroscopy or gas chromatography would better constrain the concentrations of minor gas components not detected in this study (H_2S , CH_4 , N_2). Also, quantitative geochemical analysis (i.e. XRF, EMP, LA-ICP-MS) of accessory minerals associated with fluid saturation within granitic rocks (i.e. muscovite, garnet, pyrite), as well as minerals in hydrothermal alteration zones and associated ore deposits, would permit quantitative mass balance calculations and detailed characterizations of the fluids of formation.

In addition to the questions pertaining directly to the HPP, potential opportunities for regional synthesis and comparison of magmatic-hydrothermal fluid geochemical data are raised by this research. It is recommended that future workers conduct investigations of the magmatic-hydrothermal fluid activity of other Eocene granitoid intrusions in the Great Basin (i.e. Lamoille Canyon, Railroad district, Mount Neva granodiorite, Welches Canyon, Swales Mountain, Lone Mountain, Hatter stock, McGinty monzogranite, Iapah Pluton, Gold Hill, Rosebud) using the methods employed here. Compilation, comparison, and integration of fluid inclusion data from this study, existing fluid inclusion datasets of Eocene granitoid intrusions (i.e. Bingham Canyon, Landtwing et al., 2005), and future work are essential for constructing a database of Eocene magmatic-hydrothermal fluid activity in

the Great Basin. Such a database would reveal if HPP fluid compositions are regionally representative, and, if not, what factors may have controlled regional heterogeneities. Finally, a robust geochemical profile for the magmatic component of the Eocene regional fluid flux could provide an authoritative assessment of the role of intrusive magmatism in the formation of CTD's.

4.4 REFERENCES

- Barnes, C. G., Burton, B. R., Burling, T. C., Wright, J. E., & Karlsson, H. R. (2001). Petrology and Geochemistry of the Late Eocene Harrison Pass Pluton, Ruby Mountains Core Complex, Northeastern Nevada, 42(5), 901–929.
- Burton, B. R. (1997). Structural geology and emplacement history of the Harrison Pass pluton, central Ruby Mountains, Nevada. Ph.D. Dissertation: University of Wyoming, Laramie, WY.
- Cline, J. S., Hofstra, A. H., Muntean, J. L., Tosdal, R. M., & Hickey, K. A. (2005). Carlin-type gold deposits in Nevada: critical geologic characteristics and viable models. *Economic Geology* 100th anniversary volume, 100, 451–484.
- Cox, D. P., & Singer, D. A. (1986). *Mineral deposit models* (Vol. 1693). Washington, DC, USA: US Government Printing Office.
- Heitt, D. G., Dunbar, W. W., Thompson, T. B., & Jackson, R. G. (2003). Geology and geochemistry of the Deep Star gold deposit, Carlin trend, Nevada. *Economic Geology*, 98(6), 1107–1135.
- Henry, C. D., & Boden, D. R. (1998). Eocene magmatism: The heat source for Carlin-type gold deposits of northern Nevada. *Geology*, 26(12), 1067–1070.
- Kistler, R. W., Ghent, E. D., & O'Neil, J. R. (1981). Petrogenesis of garnet two-mica granites in the Ruby Mountains, Nevada. *Journal of Geophysical Research: Solid Earth* (1978–2012), 86(B11), 10591–10606.
- Landtwing, M. R., Pettke, T., Halter, W. E., Heinrich, C. A., Redmond, P. B., Einaudi, M. T., & Kunze, K. (2005). Copper deposition during quartz dissolution by cooling magmatic–hydrothermal fluids: the Bingham porphyry. *Earth and Planetary Science Letters*, 235(1), 229–243.
- Muntean, J. L., Cline, J. S., Simon, A. C., & Longo, A. A. (2011). Magmatic-hydrothermal origin of Nevada's Carlin-type gold deposits. *Nature Geoscience*, 4(2), 122–127.
- Musekamp, C. O. J. (2012). Field, fluid inclusion and isotope chemistry evidence of fluids circulating around the Harrison Pass pluton during intrusion: A fluid model for Carlin-type deposits. (Masters thesis, Colorado State University)
- Ressel, M. W., Noble, D. C., Henry, C. D., & Trudel, W. S. (2000). Dike-hosted ores of the Beast deposit and the importance of Eocene magmatism in gold mineralization of the Carlin trend, Nevada. *Economic Geology*, 95(7), 1417–1444.
- Ressel, M. W., & Henry, C. D. (2006). *Igneous Geology of the Carlin Trend, Nevada: Development of the Eocene Plutonic Complex and Significance for Carlin-Type Au Deposits*. *Economic Geology*, 101, 347–383.

Sillitoe, R. H., & Bonham, H. F. (1990). Sediment-hosted gold deposits: Distal products of magmatic-hydrothermal systems. *Geology*, 18(2), 157-161.

APPENDICES

APPENDIX A: METHODS

A.1 FLUID INCLUSION PETROGRAPHY AND MICROTHERMOMETRY METHODS

A.1.1 FLUID INCLUSION PETROGRAPHY AND SAMPLE PREPARATION

45 samples were selected for the fluid inclusion analysis component of this study. Six ~120 μm double-polished thin sections were manufactured by Paula Leek Petrographics, and an additional 41 thin sections were manufactured by Mann Petrographics, with two duplicates. These samples include 1 miarolitic cavity, 17 crystalline quartz veins, 15 QF pegs, 2 microcrystalline quartz veins, 1 aplite, and 6 from the contact metamorphic aureole, (skarn/ carbonated replacement deposits and metasedimentary wallrock). Each of the 45 double-polished thin sections, (representing 43 samples), were carefully examined with a Leica DM2500 and/or an Olympus BX-51 petrographic microscope prior to microthermometric analyses. Using the Camex petrographic camera on the Leica DM2500 and the proprietary Captiva imaging software, complete thin section photo mosaics were created at 12.5x magnification. These photo mosaics were used to map the locations of fluid inclusion assemblages for convenient reference during analysis and can be found in Appendix E.2.

A total of 131 fluid inclusion assemblages were identified, mapped, and described in quartz crystals from 42 of the 47 double-polished thin sections with an average of three assemblages per sample. A detailed petrographic description of host mineral crystals, deformation, and fluid inclusion assemblage morphology and phase relations was compiled for each assemblage using the Olympus BX-51 petrographic microscope. Fluid inclusion

origin interpretations (primary, secondary, pseudosecondary) were assigned to assemblages according to the classification criteria of Roedder (1984). Annotated photomicrographs were taken with the proprietary Linksys imaging software at 40X and 400X magnifications for each assemblage. Appendix E.1 contains lists provides petrographic observations about each sample selected for microthermometry.

The locations of fluid inclusion assemblages selected for microthermometry were marked with a fine-tipped permanent marker on the surface of the thin section. To prepare the samples for microthermometry, the binding agent between the thin section slice and the glass slide was chemically dissolved in acetone. After thorough cleaning with ethyl alcohol, the thin section slices were cut using a razor blade in order to isolate the mapped fluid inclusion assemblages in $\sim 30 \text{ mm}^2$ pieces.

A.1.2 FLUID INCLUSION MICROTHERMOMETRY ANALYTICAL PROCEDURE

The following analytical procedure (modified after Roedder, 1984) was performed for 119 of the 124 mapped and described fluid inclusion assemblages, and was repeated as needed for assemblages when certain phase changes were not initially observed. The remaining six assemblages were discarded due to one or more of the optical factors listed earlier (i.e. sample opacity, insufficient inclusion size). For each analysis, individual sample chips containing at least one fluid inclusion assemblage were loaded into a Linkam 600 heating-freezing stage attached to an Olympus BX-51 petrographic microscope. Routine calibration of the stage is performed with synthetic pure $\text{H}_2\text{O}-\text{CO}_2$ and pure critical density H_2O fluid inclusions. When the desired fluid inclusion assemblage was located, samples were cooled from ambient temperatures (T_A) to $-100 \text{ }^\circ\text{C}$ (Step 1) and then heated stepwise to the total homogenization temperature ($T_{h_{\text{tot}}}$) or 350°C (whichever was reached first)

according to the sequence outlined in Steps 2–10. Precise temperatures at which expected phase changes occurred within their corresponding heating steps were recorded. Lastly, samples were cooled back to T_A according to Step 11 before being removed from the sample chamber.

TABLE A.1 – Fluid inclusion microthermometry analytical procedure.

Step No.	ΔT Range (°C)	Rate of ΔT (°C min ⁻¹)	Possible Phase Change Observed with T Range	Indication(s) of Phase Change
1	T_A to -100	35	¹ Freezing of H ₂ O + CO ₂	Vapor bubble suddenly becomes angular; ice crystals visible.
2	-100 to -65	35	None	
3	-65 to -55	2–3	Melting of CO₂ (T_{mCO_2})	Rapid rounding of angular frozen carbonic phase; movement of fluid.
4	-55 to -30	15	None	
5	-30 to -20	5	² First Melting of aqueous phase ($T_{eutectic}$)	Deformation of vapor bubble by intruding ice and salt-hydrate crystals/coarsening of crystals in aqueous phase.
6	-20 to -6	15	None	
7	-6 to 2	1	³ Final Melting of Aqueous Phase (T_{mice})	Sudden and most significant movement of vapor bubble.
8	2 to 10	2–3	<i>Melting of Clathrate ($T_{mclathrate}$)</i>	<i>Rounding of vapor bubble, possible movement.</i>
9	10 to 35	5	⁴CO₂-H₂O Homogenization (T_{hCO_2})	“Double-bubble” no longer visible; inner bubble either grows or shrinks.
10	35 to (T_{htot}) or 350	35	⁵ Total Homogenization (T_{htot})	Complete disappearance of vapor bubble.
11	(T_{htot}) or 350 to T_A	35, 3	None	

Steps in bold are only applicable for H₂O-CO₂-NaCl-(KCl) inclusions.

Steps in bold and italics are only applicable for H₂O-CO₂-NaCl-(KCl) inclusions, and associated phase changes may be the only indicator of low CO₂ concentrations in certain inclusions.

¹The freezing temperature of H₂O is only a qualitative value due to kinetic factors.

²This phase change is typically subtle and often requires one, if not several, repetitions from -100°C to observe.

³Final melting of H₂O is not an observable or quantitatively informative phase change in the H₂O-CO₂-NaCl-(KCl) system.

⁴CO₂-H₂O homogenization occurs either by the expansion (V) or shrinking (L) of the vapor phase. The type of homogenization is recorded.

⁵Due to the large range of possible T_{htot} values, this step is first performed at a high rate (~35°C min⁻¹), and then a much slower rate (~3°C min⁻¹) from approximately ($T_{htot} = -10^\circ\text{C}$) to determine a more accurate value.

A.1.3 CALCULATION AND MODELING OF FLUID PROPERTIES

Salinities were calculated using the depression of H₂O and clathrate melting points for aqueous and aquo-carbonic inclusions, respectively, and the formula of Bodnar, 2003:

$$\text{Salinity (wt \% eq. NaCl)} = 0.00 + 1.78\theta - 0.0442\theta^2 + 0.000557\theta^3$$

where θ is the freezing point depression (i.e. absolute value of $T_{m_{ice}}$) in degrees Celsius. For Type (B) and Type (C) carbonic inclusions, ten degrees were subtracted from the melting temperature of clathrate to yield an input for $T_{m_{ice}}$ (method after Diamond, 1992).

Microthermometry measurements from analyzed fluid inclusion assemblages were used as input values for the program BULK in the FLUIDS software suite developed by Bakker (2003) to determine compositions (in “amount of substance fractions”) and densities. For Type (A) H₂O-NaCl-(KCl) assemblages, equations of state after Zhang & Frantz (1987) were used in BULK to determine compositions and densities. For Type (B) and (C) H₂O-CO₂-NaCl-(KCl) inclusion assemblages, equations of state after Bodnar (1993) and Archer (1992) were used in BULK to determine compositions and densities. Isochores for all assemblages were constructed based on an “any gas mixture + NaCl” system and utilizing the equation of state of Bowers & Helgeson (1983) and Bakker (1999).

A.2: LA-ICP-MS METHODS

A.2.1 LA-ICP-MS ANALYTICAL PROCEDURE

LA-ICP-MS analysis was performed using a ThermoScientific XSeries II quadrupole mass spectrometer coupled with a 193nm ArF GeoLas (Lambda Physik, Germany) laser following a method adapted from Longerich et al. (1996). Sample chips (<30 mm² sections of 120 µm double-polished thin sections) were temporarily affixed to glass slides with a sugar-water mixture to prevent movement in the sample chamber. Using the 25X Schwarzschild ablation objective (193 µm), 5 to 20 individual inclusions were mapped on each chip prior to analysis with the aid of printed 10X photographs. Although these inclusions represent numerous fluid inclusion assemblages, all were determined to be primary or pseudosecondary in origin and are treated as equivalent to the representative assemblage that was measured by microthermometry prior to LA-ICP-MS analysis. Annotated images of these inclusions are included in Appendix F.1.

Three data acquisitions from both the NIST 610 and NIST 612 glass reference materials were performed at the beginning and end of each experimental run to quantify instrument drift. Experimental runs consisted of <20 analyses (i.e. 160-second, 700-pulse ablations of 1 or 2 individual inclusions). Helium gas background was collected for 30 seconds before the laser was fired at a selected inclusion for 30–130 seconds using a 32 µm spot size. The Schwarzschild objective was focused approximately ~5 µm above the surface of the sample at the start of ablation and focused at progressively deeper levels to match the depth of the ablation pit. In some cases where the selected inclusion was located more than ~50 µm below the surface of the sample chip, the sample was ablated by 1–7 pulses of

the laser using a 45 μm spot size to create a wider ablation pit, mitigating the possibility of incomplete fluid inclusion sampling and elemental fractionation that may result from deep laser drilling (see Guillong et al., 2011; Seo et al., 2011).

Count rates of several key elements (Si, Na, Al, and K) were monitored during ablation of fluid inclusions. Most analyses were characterized by an initial spike in multiple element counts (including Na) at the start of ablation, followed by a sustained elevated Si signal that progressively decreased until the end of the analysis. The initial spike may be attributed to either compounds on the surface of the sample or analytical noise created by fragments of quartz reaching the mass spectrometer. During ablation, a peak in Na counts is considered to be the best proxy for the ablation and analysis of a fluid inclusion due to the dominance of Na in geologic fluids (Heinrich et al., 2003). Analyses were typically terminated after detection of a Na peak that was interpreted as an inclusion, or if Si counts dropped below pre-ablation background values, indicating that the laser had reached the other side of the sample. It was not uncommon to observe two or more Na peaks in one analysis, indicating ablation of multiple fluid inclusions.

A.2.2 LA-ICP-MS DATA REDUCTION PROCEDURE

Processing of LA-ICP-MS data was performed with Iolite (v3) on the Igor Pro analytical software platform following a procedure modified from Hellstrom et al. (2008) and Paton et al. (2011). Raw experiment files (X-Series .csv type) were imported into Iolite in the “Import” tab. In the “Baseline” tab, an “average median” baseline subtraction was applied to segments of analytical spectra recorded during periods when the laser was not ablating. In the “Reference Materials” tab, analyses of the NIST610 and NIST612 reference materials were bracketed in order to apply a correction for instrumental drift throughout

the experimental run. In the “Samples” tab, spectra of analyzed elements for each inclusion were observed and compared to background values. A “first pass” inspection of elemental spectra for each inclusion was conducted to determine the location, relative intensity, and width of Na peaks and the identity of elements associated with Na. Due to interference from substances on the sample surface and from fragments of ablated quartz, Na peaks observed at the start of ablation are not included. “First pass” results (presented in Appendix F.3) permit a qualitative elemental characterization of the fluids in each sample and assist in selection of Na peaks for quantitative concentration calculations.

The next stage of the data processing procedure involves the selection and labeling of selected “high quality” spectral peaks interpreted to be fluid inclusions in the “Samples” tab. “High quality” Na peaks are designated based on relative intensity, width, and associated elements. Peaks that are exceedingly transient (i.e. only one count by the mass spectrometer), only marginally more intense than background levels (i.e. <200% background intensity), significantly irregular in shape (i.e. multiple narrow sub-peaks, no discernable apex), or associated with peaks of anomalous elements or elements not favored by the fluid phase (i.e. elements observed in only one inclusion, aluminum from surrounding quartz) are not selected for element concentration calculations. Additionally, Na peaks that occurred coeval with chipping of sample quartz during ablation (determined by consulting analytical notes) are discarded.

The final step in data processing of LA-ICP-MS data is the application of a data reduction scheme (DRS) and internal standards to the input data in the “DRS” tab. The DRS utilized for these data is the “Trace Element_IS” developed by Woodhead et al. (2007; 2008). The internal reference, or “index channel,” is the wt % Na calculated for each

selected fluid inclusion from salinities determined by microthermometry. Wt % Na was calculated from salinities (wt % eq. NaCl) using the mass proportion of Na in NaCl. Default settings are used for all other parameters in the DRS tab. The raw data tables in the “Results” tab were exported from Iolite as .txt files and compiled by sample, feature type, and intrusive unit in MS Excel. Elemental concentrations lower than the corresponding limits of detection were discarded.

A similar procedure as described in the previous two paragraphs was used for quantitative determination of the composition of the quartz ablated around each selected fluid inclusion in order to determine the degree of spectral interference from this source. Spectral segments interpreted to record “background” values from ablation of quartz above or below an inclusion were selected. These segments lack significant peaks of Na or other elements that would indicate a notable heterogeneity in the quartz. Elemental concentrations were calculated using the same DRS as the fluid inclusions, but wt % Si was used as the internal standard. The value used for wt % Si in pure quartz is 46.68% (Marsh, 2015, personal communication).

A.3: STABLE ISOTOPE METHODS

Ten quartz-bearing samples were selected for analysis of oxygen and hydrogen stable isotopes. These samples represent five feature types, (QF Pegmatite, QF-cored Aplite, and Type (I), (II) (skarn), and (III) Quartz Veins), from all four major intrusive phases in the HPP, (Tcc, Ttc, Tmg, and Tgm), as well as one hydrogrossular-diopside contact skarn sample from the site of the defunct Star Tungsten Mine at the roof contact of the pluton.

Petrographic examination and fluid inclusion microthermometry were also conducted on thin sections manufactured from these samples by the same techniques described in Appendix A.1.1 and A.1.2, respectively.

The sample preparation process was conducted in the rock cutting facility and the Petrology & Structure laboratory at Colorado State University. First, samples were cut to remove non-quartz material and then crushed in a hand-operated hammer impact mill. The disaggregated samples were sieved into six size fractions: (1) <180 μm , (2) 180–250 μm , (3) 250–300 μm , (4) 300–600 μm , (5) 600–850 μm , (6) >850 μm . Grains from size fractions (2) and (3) were selected for hydrogen and oxygen stable isotope analysis, respectively. The following procedure was performed twice to ensure that all additional material was removed from the samples: grains were rinsed twice with deionized water, and then ultrasonicated for 90 seconds. Cleaned grains were submerged in isopropyl alcohol and observed under a binocular microscope and selected for final isotope analysis based on clarity and cleanliness, (estimated visual clarity lower cutoff was 90%). Also, grains lacking in observable fluid inclusions were selected from size fraction (3) for oxygen isotope analysis, while fluid inclusion-rich grains were selected from size fraction (2) for hydrogen isotope analysis. Approximately 2 mg (12–16 grains) from each sample was selected for oxygen isotope analysis and approximately 20–40 mg from each sample was selected for hydrogen isotope analysis.

Samples were sent to Dr. Jaime Barnes at the Light Stable Isotope Laboratory at the University of Texas at Austin for stable isotope analysis of oxygen and hydrogen in silicates. Oxygen isotope ratios were determined using the method developed in Sharp (1990). Approximately 2 mg of quartz material from each sample was individually heated

with BrF_5 using a CO_2 laser. A silicate extraction line was used for cryogenic sample purification prior to being loaded into a ThermoElectron MAT 253 isotope ratio mass spectrometer (Chin et al, 2014). In order to check for precision and accuracy, in-house quartz standard Lausanne-1 ($\delta^{18}\text{O}=+18.1\text{‰}$) was run. All $\delta^{18}\text{O}$ values are reported relative to SMOW, where the $\delta^{18}\text{O}$ value of NBS-28 is $+9.65\text{‰}$. Error is $\pm 0.1\text{‰}$, (Barnes, personal comm., 2015).

δD values for fluid inclusions within quartz sample material were to be determined using the methods of Sharp et al. (2001). The samples were loaded into silver capsules, which were pyrolyzed in a ThermoElectron MAT TC-EA (high temperature conversion elemental analyzer). However, these analyses were unsuccessful due to a lack of sufficient fluid volume in the samples.

A.4 REFERENCES

- Archer, D. G. (1992). Thermodynamic Properties of the NaCl+ H₂O System. II. Thermodynamic Properties of NaCl (aq), NaCl·2H₂ (cr), and Phase Equilibria. *Journal of Physical and Chemical Reference Data*, 21(4), 793–829.
- Bakker, R. J. (1999). Adaptation of the Bowers and Helgeson (1983) equation of state to the H₂O–CO₂–CH₄–N₂–NaCl system. *Chemical Geology*, 154(1), 225–236.
- Bodnar, R. J. (2003). Introduction to aqueous-electrolyte fluid inclusions. *Fluid Inclusions: Analysis and Interpretation*, 32, 81–100.
- Bowers, T. S., & Helgeson, H. C. (1983). Calculation of the thermodynamic and geochemical consequences of nonideal mixing in the system H₂O–CO₂–NaCl on phase relations in geologic systems: Equation of state for H₂O–CO₂–NaCl fluids at high pressures and temperatures. *Geochimica et Cosmochimica Acta*, 47(7), 1247–1275.
- Chin, E. J., Lee, C. T. A., & Barnes, J. D. (2014). Thickening, refertilization, and the deep lithosphere filter in continental arcs: Constraints from major and trace elements and oxygen isotopes. *Earth and Planetary Science Letters*, 397, 184–200.
- Diamond, L. W. (1992). Stability of CO₂ clathrate hydrate+ CO₂ liquid+ CO₂ vapour+ aqueous KCl–NaCl solutions: Experimental determination and application to salinity estimates of fluid inclusions. *Geochimica et Cosmochimica Acta*, 56(1), 273–280.
- Guillong, M., Danyushevsky, L., Walle, M., & Raveggi, M. (2011). The effect of quadrupole ICPMS interface and ion lens design on argide formation. Implications for LA-ICP-MS analysis of PGE's in geological samples. *Journal of Analytical Atomic Spectrometry*, 26(7), 1401–1407.
- Heinrich, C. A., Pettke, T., Halter, W. E., Aigner-Torres, M., Audétat, A., Günther, D., Hattendorf, B., Bleiner, D., Guillong, M., & Horn, I. (2003). Quantitative multi-element analysis of minerals, fluid and melt inclusions by laser-ablation inductively-coupled-plasma mass-spectrometry. *Geochimica et Cosmochimica Acta*, 67(18), 3473–3497.
- Hellstrom, J., Paton, C., Woodhead, J., & Hergt, J. (2008). Iolite: software for spatially resolved LA-(quad and MC) ICPMS analysis. *Mineralogical Association of Canada short course series*, 40, 343–348.
- Longerich, H. P., Jackson, S. E., & Günther, D. (1996). Inter-laboratory note. Laser ablation inductively coupled plasma mass spectrometric transient signal data acquisition and analyte concentration calculation. *Journal of Analytical Atomic Spectrometry*, 11(9), 899–904.

Paton, C., Hellstrom, J., Paul, B., Woodhead, J., & Hergt, J. (2011). Iolite: Freeware for the visualization and processing of mass spectrometric data. *Journal of Analytical Atomic Spectrometry*, 26(12), 2508–2518.

Roedder, E. (1984). Fluid inclusions. P. H. Ribbe (Ed.). Washington, DC: Mineralogical Society of America, 12, 79–108.

Seo, J. H., Guillong, M., Aerts, M., Zajacz, Z., & Heinrich, C. A. (2011). Microanalysis of S, Cl, and Br in fluid inclusions by LA-ICP-MS. *Chemical Geology*, 284(1), 35–44.

Sharp, Z. D. (1990). A laser-based microanalytical method for the in situ determination of oxygen isotope ratios of silicates and oxides. *Geochimica et Cosmochimica Acta*, 54(5), 1353–1357.

Sharp, Z. D., Atudorei, V., & Durakiewicz, T. (2001). A rapid method for determination of hydrogen and oxygen isotope ratios from water and hydrous minerals. *Chemical Geology*, 178(1), 197–210.

Woodhead, J. D., Hellstrom, J., Hergt, J. M., Greig, A., & Maas, R. (2007). Isotopic and elemental imaging of geological materials by laser ablation inductively coupled plasma-mass spectrometry. *Geostandards and Geoanalytical Research*, 31(4), 331–343.

Woodhead, J., Hellstrom, J., Paton, C., Hergt, J., Greig, A., & Maas, R. (2008). A guide to depth profiling and imaging applications of LA-ICP-MS. *Laser Ablation ICP-MS in the Earth Sciences: Current Practices and Outstanding Issues*, 40.

Zhang, Y. G., & Frantz, J. D. (1987). Determination of the homogenization temperatures and densities of supercritical fluids in the system NaCl-KCl-CaCl-2H₂O using synthetic fluid inclusions. *Chemical Geology*, 64(3), 335–350.

APPENDIX B: FIELD SAMPLE DATA

Sample ID	Traverse #	Date	Waypoint ID	Point East	Point North	Point Elev. (ft)	Host Unit	Sample Lithology/Feature Type	Sample Description
HPP-1-01	1	5/27/14	1	626665	4460559		Tcc	Metased (marble/limestone)	Pure grey-white sparry marble/limestone. Fine-grained at contact. Some foliation?
HPP-1-02	1	5/27/14	2	626661	4460620		Tcc	QF Pegmatite	Pegmatitic quartz and orthoclase vein in granite, (QFbqGr).
HPP-1-03	1	5/27/14	3	626852	4460696	7822	Tcc	Type (II) (wallrock) Quartz Vein	Poorly exposed, milky qtz vein in metasedimentary marble, (same as HPP-1-1).
HPP-1-04	1	5/27/14	4	626579	4460844	7539	Tcc	Type (I) Quartz Vein	Milky, pure qtz vein. Linear, in finer-grained, feldspar-rich granite, (mm grain size), FMQGr.
HPP-1-05	1	5/27/14	5	626661	4461109	7468	Tcc	Type (III) Quartz Vein	Pure qtz segregation in aplite vein in med-grained homogeneous granite. Matrix is more qtz-rich than HPP 1-4. Avg. grain size = 6 mm in matrix, 1 mm in vein. Qtz is pegmatitic in segregations in vein.
HPP-1-06a	1	5/27/14	6	626544	4461220	7449	Tcc	Aplite	Two large, fine-grained aplitic veins in granite tor. Veins are subparallel.
HPP-1-06b	1	5/27/14	6	626544	4461220	7449	Tcc	Aplite	Two large, fine-grained aplitic veins in granite tor. Veins are subparallel.
HPP-1-06c	1	5/27/14	6	626544	4461220	7449	Tcc	Aplite	A third, smaller aplite vein is present.
HPP-1-07a	1	5/28/14	7	626642	4461235	7426	Tcc	Aplite	Aplite vein in weathered granite. Dominantly orthoclase with qtz, (mica poor).
HPP-1-07b	1	5/28/14	7	626642	4461235	7426	Tcc	Aplite	Aplite vein in weathered granite. Dominantly orthoclase with qtz, (mica poor).
HPP-1-08	1	5/28/14	8	626689	4461343	7449	Tcc	Aplite	Two closely-spaced, parallel aplite veins in Tcc granite. Veins join at top of outcrop. Irregular lenses of melanocratic (biotite?) material along vein margins.
HPP-1-09	1	5/28/14	9	626683	4461371	7439	Tcc	Aplite	Two large, aplite veins in Tcc unit. More resistant than surrounding rock. Southern vein bifurcates into two veins. Biotite-rich zones within and along vein margins. Multiple (not sampled) veins are parallel in a set.
HPP-1-10	1	5/28/14	10	626745	4461420	7449	Tcc	Aplite	One large, aplite vein with biotite-rich core, (1 cm wide). Matrix is typical Tcc. Biotite rich zone also on right margin. Crosscut by small (<1cm) aplite veinlet.
HPP-1-11	1	5/28/14	11	626630	4461465	7378	Tcc	Miarolitic Cavity	5 cm long, oblong miarolitic cavity with pegmatitic euhedrally terminated qtz crystals (>1cm in size). Cavity may already have been excavated. One smaller miarolitic cavity filled by several larger qtz crystals above first cavity (3 cm long, 1.5 cm wide).

Sample ID	Thickness (cm)	Potassic	Skarn	Phyllic	Chlorite-Sericite	Silicification	Jarosite	Strike	Dip	Dip Direction	Additional Notes
HPP-1-01											Contact Metamorphic Aureole
HPP-1-02	5-7							21	59	SE	
HPP-1-03	10-12										Contact Metamorphic Aureole
HPP-1-04	1							140	90		
HPP-1-05	4							110	80	NE	
HPP-1-06a	8							90	80	S	
HPP-1-06b	20							120	66	NE	
HPP-1-06c	4-6							90	80	S	
HPP-1-07a	4-5							95	63	NE	
HPP-1-07b	4-5							95	63	NE	
HPP-1-08	7 (combined); 4, 2 when separate							59	81	NW	
HPP-1-09	9-10							51	73	SW	
HPP-1-10	8-11							72	59	SE	
HPP-1-11	3 x 1.5										

Sample ID	Traverse #	Date	Waypoint ID	Point East	Point North	Point Elev. (ft)	Host Unit	Sample Lithology/Feature Type	Sample Description
HPP-1-12	1	5/28/14	12	626533	4461430	7324	Tcc	Granite (aplitic)	Massive fine-grained aplitic granite similar to previous vein samples. Massive. Avg. grain size 1-2 mm. Contains abundant biotite, qtz, and fspar. Contact nearby with coarse-grained granite?
HPP-1-13	1	5/28/14	14	626795	4461573	7327	Tcc	Aplite	Large granite outcrop with several large aplite veins. One large vein sampled in coarse-grained granite matrix. Some orange alteration in veins. Disseminated porphyritic biotite (1 mm) in nearly aphanitic matrix.
HPP-1-14	1	5/28/14	15	626775	4461545	7417	Tcc	Aplite	Another large vein sampled in coarse-grained granite matrix. Some orange alteration in veins. Disseminated porphyritic biotite (1 mm) in nearly aphanitic matrix.
HPP-1-15	1	5/28/14	16	626782	4461546	7517	Tcc	Aplite	Very large aplite dike, dominated by qtz in coarse-grained heavily weathered granite matrix. Biotite-rich segregations (1-1.5 cm) in vein and along margins. Possible alteration and removal of feldspars, leaving negative crystal voids.
HPP-1-16	1	5/28/14	17	626815	4461516	7523	Tcc	QF Pegmatite	Pegmatitic qtz and fspar vein with biotite-rich zones outside of vein margins in coarse-grained granite matrix. Three small microplitic cavities/vugs in vein containing euhedrally-terminated qtz and fspar veins (8 cm x 3 cm).
HPP-1-17a	1	5/29/14	19	626334	4461936	7335	Tcc	Aplite	Sample is from beneath weathering rind. Single pegmatitic feldspar vein with minor qtz in weathered coarse-grained granite outcrop. Matrix has abundant qtz.
HPP-1-17b	1	5/29/14	19	626334	4461936	7335	Tcc	Aplite	Sample is from surface of the outcrop. Single pegmatitic feldspar vein with minor qtz in weathered coarse-grained granite outcrop. Matrix has abundant qtz.
HPP-1-18	1	5/29/14	20	626292	4461976	7332	Tcc	Aplite	Single large, aplitic granular dike in coarse-grained granite. Orange/buff color with ~3cm-wide alteration zone on right (SE) margin. NW contact not exposed. Dike appears to curve and fractures parallel to margins.
HPP-1-19a	1	5/29/14	21	625938	4461971	7494	Tcc	Type (IV) Microcrystalline Quartz Vein	Milky qtz vein, pale orange alteration. Most qtz is anhedral massive with some cm-scale crystals visible. Eye-shaped void with alteration rim along vein, (30 cm x 12 cm). Extensive/pervasive alteration.

Sample ID	Thickness (cm)	Potassic	Skarn	Phyllic	Chlorite-Sericite	Silicification	Jarosite	Strike	Dip	Dip Direction	Additional Notes
HPP-1-12											
HPP-1-13	19						Yes	43	88	NE	
HPP-1-14	15						Yes	20	89	NE	
HPP-1-15	50							45	85	NE	
HPP-1-16	3							52	71	NE	
HPP-1-17a	3							110	65	NE	
HPP-1-17b	3							110	65	NE	
HPP-1-18	40						Yes	19	66	NW	
HPP-1-19a	8				Yes		Yes				

Sample ID	Traverse #	Date	Waypoint ID	Point East	Point North	Point Elev. (ft)	Host Unit	Sample Lithology/Feature Type	Sample Description
HPP-1-19b	1	5/29/14	21	625938	4461971	7494	Tcc	Granite (altered)	Wallrock is altered granite with apparent reaction fronts along vein margins.
HPP-1-20	1	5/29/14	22	625908	4461985	7505	Tcc	Granite (altered)	Isolated megaquartz segregations in heavily altered granite. Rock is almost completely silicified. Matte qtz with clear qtz intergrowths and aforementioned megaquartz segregations. No apparent veining here. Hard white matte mineral may not be qtz.
HPP-1-21	1	5/29/14	23	625904	4462020	7504	Tcc	Metased (silty dolostone)	Heavily metasomatized rock, metasedimentary roof pendant. Grey with white granular zones. Trend of foliation is 64°. Lenses and discontinuous pods of qtz. Very granular.
HPP-1-22	1	5/29/14	24	625893	4462020	7515	Tcc	QF Pegmatite	Large, irregular, elongate, pegmatitic segregation in unaltered granite. Large qtz (~2 cm) and feldspar grains in zones. Qtz in center of segregation. A second, smaller circular segregation proximal to the first, about 20 cm to the right. Crystals in first segregation range from <1 cm to ~4.5 cm. Euhedral, but no voids.
HPP-1-23	1	5/29/14	25	625892	4461970	7511	Tcc	Aplite	Pegmatitic quartz and feldspar in heavily altered granite, similar to previous sample. Forms a discontinuous vein-like trail.
HPP-1-24a	1	5/29/14	26	625877	4462000	7483	Tcc	Miarolitic Cavity	Large, (18 cm wide), pegmatitic qtz/feldspar zone, (possible sheeted/layered vein system). Intermixed with fine-grained (1-2 mm grains) granitic matrix. One large (7 cm) qtz crystal sampled.
HPP-1-24b	1	5/29/14	26	625877	4462000	7483	Tcc	Miarolitic Cavity	Oblate, rounded miarolitic cavity with large, pegmatitic, transparent qtz crystals, (subhedral). Minor microcline. Little to no mica. Little wall rock alteration. Also parallel to vein sampled in HPP-1-24a.
HPP-1-25a	1	5/29/14	27	625760	4461981	7424	Tcc	Type (III) Quartz Vein	Contact between mega-qtz and altered granite. Qtz is milky-white. Granite contains biotite.
HPP-1-25b	1	5/29/14	27	625760	4461981	7424	Tcc	Type (II) (wallrock) Quartz Vein	Opposite vein margins containing an echelon qtz (washboard) on both sides. Inner rock is fine-grained granular qtz and feldspar (?). Could be metasomatized limestone. Glassy qtz vein material (2-3 cm crystal size). Inner material matte white.
HPP-1-25c	1	5/29/14	27	625760	4461981	7424	Tcc	Type (II) (skarn) Quartz Vein	Thin qtz vein in metasomatized (contact metamorphosed), mineralized skarn, (protolith: silty dolostone?). Mineralized host rock (skarn) is dense, green/brown/red and granular.

Sample ID	Thickness (cm)	Potassic	Skarn	Phyllic	Chlorite-Sericite	Silicification	Jarosite	Strike	Dip	Dip Direction	Additional Notes
HPP-1-19b	2.5-3				Yes		Yes				
HPP-1-20	2 x 3.5			Yes		Yes					
HPP-1-21			Yes								
HPP-1-22	16-22 x ~87										
HPP-1-23	3-5			Yes				87			
HPP-1-24a	18							15	80	SE	
HPP-1-24b											Collected from mine tailings. Not in situ.
HPP-1-25a			Yes	Yes		Yes					Collected from mine tailings. Not in situ.
HPP-1-25b	3										Collected from mine tailings. Not in situ.
HPP-1-25c	0.5		Yes								Collected from mine tailings. Not in situ.

Sample ID	Traverse #	Date	Waypoint ID	Point East	Point North	Point Elev. (ft)	Host Unit	Sample Lithology/Feature Type	Sample Description
HPP-1-25d	1	5/29/14	27	625760	4461981	7424	Tcc	Type (II) (skarn) Quartz Vein (Mineralized)	Contact between matte white qtz vein and red/brown mineralized skarn, (protolith: silty dolostone).
HPP-1-25e	1	5/29/14	27	625760	4461981	7424	Tcc	Type (II) (skarn) Quartz Vein (Unmineralized)	Contact between mega-qtz vein and unmineralized, metasomatized, green/white diopside skarn/silty-sandy dolostone.
HPP-1-26	1	5/29/14	28	625849	4462028	7439	Tcc	QF Pegmatite	QF Peg vein in medium-grained white granite. Vein is relatively thin and discontinuous.
HPP-1-27	1	5/29/14	29	626020	4462115	7447	Tcc	Type (IV) Microcrystalline Quartz Vein	Heavily altered and fractured fine-grained granite with qtz vein, (milky white, massive qtz). Minor parallel to subparallel veins on either side. Rock also shows pervasive microfracturing and orange-red alteration staining around vein up to distances of 12 cm. Singes of pervasive fluid flow. Vuggy qtz cavity on vein margin.
HPP-1-28	1	5/29/14	30	626013	4462243	7480	Tcc	Granite (altered)	Silicified granite or aplite vein.
HPP-1-29	1	5/29/14	31	626255	4462431	7625	Tcc	Granite (altered)	Silicified granite or aplite vein with graphic intergrowth of quartz and feldspar.
HPP-1-30	1	5/29/14	32	626260	4462440	7597	Tcc	Type (III) Quartz Vein	Irregular, poorly exposed, pegmatitic qtz zone in bleached, altered granite. Qtz zone is truncated by a fracture and consists of several large crystals.
HPP-1-31	1	5/29/14	33	626391	4462619	7517	Tcc	Aplite	Aplite vein in coarse-grained, microcline-rich granite. All heavily altered with SO4 staining in linear patterns and zones. Rock appears silicified with no mica present. This zone of alteration extends south to mine prospect on hill.
HPP-1-32	1	5/30/14	34	626726	4461878	7380	Tcc	Type (IV) Microcrystalline Quartz Vein	Tabular qtz vein in weathered coarse-grained granite. Vein is massive, orange-stained milky-white qtz. Exposed area is 25 cm long. Small fractures crosscut but do not truncate vein.
HPP-1-33	1	5/30/14	35	626746	4461857	7421	Tcc	Aplite	Aplite vein in course-grained weathered granite outcrop. Granite matrix is 50% microcline, 50% glassy/grey qtz. Vein is aphanitic.
HPP-1-34	1	5/30/14	36	626725	4461820	7434	Tcc	QF Pegmatite	Pegmatitic qtz and fspar vein in weathered and possibly altered coarse-grained granite. Possible slip along vein? Milky qtz and microcline.
HPP-1-35a	1	5/30/14	37	626909	4461813	7541	Tcc	Aplite	Weathered grey/dark grey granular fine-grained aplite vein in weathered coarse-grained granite. Crosscuts HPP-1-35b

Sample ID	Thickness (cm)	Potassic	Skarn	Phyllic	Chlorite-Sericite	Silicification	Jarosite	Strike	Dip	Dip Direction	Additional Notes
HPP-1-25d			Yes								Collected from mine tailings. Not in situ.
HPP-1-25e			Yes								Collected from mine tailings. Not in situ.
HPP-1-26	3							5			
HPP-1-27	0.5-1			Yes			Yes				Block not in place.
HPP-1-28	7					Yes		16	60	SE	
HPP-1-29	8-12				Yes	Yes					
HPP-1-30	4-13			Yes		Yes	Yes				
HPP-1-31				Yes			Yes	125	70	NE	
HPP-1-32	0.5						Yes	160	85	NE	
HPP-1-33	5							98	59	NW	
HPP-1-34	2					Yes		42	58	SE	
HPP-1-35a	3										

Sample ID	Traverse #	Date	Waypoint ID	Point East	Point North	Point Elev. (ft)	Host Unit	Sample Lithology/Feature Type	Sample Description
HPP-1-35b	1	5/30/14	37	626909	4461813	7541	Tcc	QF Pegmatite	White, coarser-grained, pegmatitic vein/zone crosscut by HPP-1-35a. Mostly consists of microcline. Small, vuggy quartz pockets with unidentified silvery sulfide mineral (galena?).
HPP-1-36a	1	5/30/14	38	626939	4461809	7568	Tcc	Type (IV) Microcrystalline Quartz Vein	Pure microcrystalline white qtz stained orange in irregular zones. Parallel to HPP-1-36b.
HPP-1-36b	1	5/30/14	38	626939	4461809	7568	Tcc	Type (IV) Microcrystalline Quartz Vein	Pure microcrystalline white qtz. Parallel to HPP-1-36a.
HPP-1-37	1	5/30/14	39	627042	4461844	7665	Tcc	QF Pegmatite	Pegmatitic qtz and fspar vein in coarse-grained weathered granite. 10 cm wide alteration zone, (bleaching, orange), around vein.
HPP-1-38	1	5/30/14	41	627110	4461932	7665	Tcc	Aplite	Large, fine-grained, qtz core (19-20 cm) in aplite dike (2 m), in coarse-grained, weathered Tcc granite. Qtz core is eroded and poorly exposed. Qtz zone appears to have two distinct zones that are separated by a plane. The southern zone is stained red, while the northern zone is stained light green. Alteration of surrounding granite is strong, (bleaching, orange staining).
HPP-1-39	1	5/30/14	42	627066	4462071	7682	Tcc	Aplite	Large, resistant aplite dike in weathered granite, (50% qtz, 50% microcline). Vein is very granular/sucrosic, with red/orange staining on the surface.
HPP-1-40a	1	5/30/14	43	627057	4462108	7696	Tcc	Aplite	Large, aplite vein in weathered coarse-grained granite.
HPP-1-40b	1	5/30/14	43	627057	4462108	7696	Tcc	Aplite	Large, aplite vein in weathered coarse-grained granite.
HPP-1-40c	1	5/30/14	43	627057	4462108	7696	Tcc	Aplite	Large, aplite vein in weathered coarse-grained granite. Vein splits into two smaller veins at bottom of outcrop.
HPP-1-41	1	5/30/14	44	627074	4462123	7713	Tcc	Aplite	Fine-grained aplite vein. Wall rock is weathered coarse-grained granite.
HPP-1-42	1	5/30/14	45	627064	4462113	7700	Tcc	Aplite	Thin aplite vein in coarse-grained weathered granite.
HPP-1-43	1	5/30/14	46	627093	4462237	7730	Tcc	QF Pegmatite	Pegmatitic qtz-fspar vein. Fairly resistant, laterally continuous. Also has sections of fine-grained aplite similar to previous samples.
HPP-1-44	1	5/30/14	47	626680	4462351	7498	Tcc	Aplite	Large aplite vein/dike in weathered coarse-grained granite.
HPP-1-45	1	5/30/14	48	626807	4462233	7439	Tcc	Aplite	Medium-thickness aplite vein in coarse-grained, weathered granite. More of the same. Vein has a kink in it.
HPP-1-46	1	5/30/14	49	626827	4462184	7429	Tcc	Aplite	Aplite vein in coarse-grained granite.

Sample ID	Thickness (cm)	Potassic	Skarn	Phyllic	Chlorite-Sericite	Silicification	Jarosite	Strike	Dip	Dip Direction	Additional Notes
HPP-1-35b	5							47	28	SE	
HPP-1-36a	1.5-2						Yes	172	76	NE	
HPP-1-36b	0.5-1						Yes	172	76	NE	
HPP-1-37	7-9						Yes	98	75	SW	
HPP-1-38	19-20 (core), 200 (dike)					Yes	Yes	87	72	NE	Qtz core may be a separate vein hosted in the aplite dike.
HPP-1-39	17						Yes	93	54	SW	
HPP-1-40a	27						Yes	60	87	SE	
HPP-1-40b	52						Yes	81	64	SE	
HPP-1-40c	14						Yes	98	64	SW	
HPP-1-41	9						Yes	74	70	SE	
HPP-1-42	1-1.5							116	81	NE	
HPP-1-43	3-4							152	75	SW	
HPP-1-44	79							72	90		
HPP-1-45	11							89	74	SE	
HPP-1-46	15							92	83	SW	

Sample ID	Traverse #	Date	Waypoint ID	Point East	Point North	Point Elev. (ft)	Host Unit	Sample Lithology/Feature Type	Sample Description
HPP-1-47	1	5/30/14	50	626615	4461987	7424	Tcc	Aplite	Aplite vein in heavily-weathered, coarse-grained granite.
HPP-1-48	1	5/30/14	52	626567	4461962	7357	Tcc	Aplite	A set of at least three parallel aplite veins. Dominantly microcline. One vein pinches out at the top of the outcrop and another begins ~6 cm to the right.
HPP-1-49	1	5/31/14	53	626568	4461964	7313	Tcc	Aplite	A set of aplite veins in weathered, microcline-rich granite. All four veins are parallel.
HPP-1-50	1	5/31/14	54	626593	4462493	7510	Tcc	Aplite	An extensive set of at least six parallel aplite veins in weathered, coarse-grained, white/grey granite.
HPP-1-51	1	5/31/14	56	626623	4462512	7511	Tcc	Aplite	A series of parallel aplite veins in weathered coarse-grained granite. One large complex vein, (sampled), has zones of coarse-grained granite in it, causing the vein to split and rejoin.
HPP-1-52	1	5/31/14	57	626658	4462598	7487	Tcc	Aplite	Two aplite veins cutting through coarse-grained granite (weathered). The larger of the two veins (sampled) is to the north and has several parallel zones in it, (see sketch). Wall rock zonation indicates possible chill zone, (no biotites in chill zone).
HPP-1-53a	1	5/31/14	58	626563	4462722	7555	Tcc	Aplite	Aplite vein in coarse-grained granite. 0.3 m to the north of HPP-1-53b.
HPP-1-53b	1	5/31/14	58	626563	4462722	7555	Tcc	Aplite	Aplite vein in coarse-grained granite. 0.3 m to the south of HPP-1-53a
HPP-1-54	1	5/31/14	59	626616	4462774	7555	Tcc	Type (V) Microcrystalline Quartz Vein	Coarse-grained milky qtz vein in highly-altered granite. Evidence of pervasive fluid flow, possible silicification of granite. This outcrop represents a significant change in rock type from coarse-grained granite previously sampled.
HPP-1-55	1	5/31/14	60	626755	4462788	7473	Tcc	Aplite	Aplite vein in coarse-grained granite. Smaller aplite veins with parallel orientations nearby.
HPP-1-56	1	5/31/14	61	626755	4462847	7470	Tcc	QF Pegmatite	Pegmatitic qtz-fspar vein in unaltered coarse-grained granite. May be some aplite present, vein is very poorly exposed. Large feldspars (~2 cm) and smaller qtz crystals (<1 cm).
HPP-1-57	1	5/31/14	62	626503	4462890	7651	Tcc	Granite (altered)	Altered granite hosting aplite vein in less altered, (but still somewhat silicified/qtz-rich), granite. Poorly exposed. Large, pegmatitic qtz and feldspar crystals along vein selvages, (1-2 cm). Red/orange alteration bands on edges of vein.

Sample ID	Thickness (cm)	Potassic	Skarn	Phyllic	Chlorite-Sericite	Silicification	Jarosite	Strike	Dip	Dip Direction	Additional Notes
HPP-1-47	15							83	85	SE	
HPP-1-48	2							113	79	NW	
HPP-1-49	4-5							86	60	NW	
HPP-1-50	5							80	71	NW	
HPP-1-51	19-20							85	65	NW	
HPP-1-52	17-21							112	87	SW	
HPP-1-53a	17							83	81	NW	
HPP-1-53b	6							76	78	NW	
HPP-1-54	11-15				Yes	Yes	Yes	44	67	NW	vertical is continuous to the NE across the pluton, (as seen from ridge as a continuous line along strike with vein)
HPP-1-55	9							81	77	NW	
HPP-1-56	4-5							79	65	NW	
HPP-1-57	1.5-2					Yes	Yes	135	67	NE	

Sample ID	Traverse #	Date	Waypoint ID	Point East	Point North	Point Elev. (ft)	Host Unit	Sample Lithology/Feature Type	Sample Description
HPP-1-58	1	5/31/14	63	626629	4463032	7529	Tcc	Type (III) Quartz Vein	Pure, milky white, discontinuous qtz vein in silicified, coarse-grained granite. In highly altered granite.
HPP-1-59	1	5/31/14	64	626630	4463024	7536	Tcc	Granite (altered)	Possibly a laterally continuous zone of chlorite-sericite alteration in highly altered, silicified granite. Pale greenish grey, more friable than strongly silicified granite. Possible alignment of minerals (?).
HPP-1-60	1	5/31/14	65	626622	4463075	7582	Tcc	Miarolitic Cavity	Oblong milky-white qtz pod in silicified granite. May be part of a discontinuous vein. Several large, 2-4 cm qtz crystals in pod. Outcrop is poorly exposed.
HPP-1-61	1	5/31/14	66	626511	4462972	7695	Tcc	Granite (aplitic)	Silicified, fine-grained, aplitic granite, (fairly homogeneous), showing orange alteration lines indicating fluid flow. Extensively bleached and highly microfractured. Show some parallel fractures and curvature.
HPP-1-62	1	5/31/14	67	626494	4463134	7689	Tcc	Granite (altered)	High qtz content (?), containing some microfractures: qtz-rich granite. Almost entirely qtz, (maybe white fspar?). Typically green/grey with red staining. Still granular.
HPP-1-63	1	5/31/14	68	626560	4463204	7683	Tcc	Type (IV) Microcrystalline Quartz Vein	Highly altered, qtz-rich, numerous parallel qtz veins in silicified, vuggy, orange-stained granite. Rock is pervasively altered with significant mass removed. Vugs within veins are filled with cockade/colliform, euhedrally terminated qtz crystals, (2-5 mm). S04 staining. On contact with blocky, qtz-rich granite sampled in HPP-1-62.
HPP-1-64	1	5/31/14	69	626593	4463244	7610	Tcc	Aplite	Very fine-grained, white-green, poorly exposed aplite vein in coarse-grained granite. Vein material is very qtz-rich with 2-4 mm clear qtz crystals in a white/green granular, fine-grained matrix. Wallrock is coarser (2-3 mm), with a high qtz content. May represent another contact or a change in alteration zones. Still different from the Mammoth outcrops.
HPP-1-65	1	5/31/14	70	626536	4463250	7626	Tcc	Miarolitic Cavity	Pod of milky white qtz crystals in coarse-grained, silica-rich granite. A small area of fine-grained black crystals found in one sample piece, (biotite?).
HPP-1-66	1	5/31/14	71	626598	4463302	7603	Tcc	Type (V) Microcrystalline Quartz Vein	Pure, homogeneous, microcrystalline, milky-white qtz vein in silica-rich, weathered, coarse-grained grey-white granite, (biotite-poor).

Sample ID	Thickness (cm)	Potassic	Skarn	Phyllic	Chlorite-Sericite	Silicification	Jarosite	Strike	Dip	Dip Direction	Additional Notes
HPP-1-58	10				Yes	Yes	Yes	10	44	SE	
HPP-1-59					Yes	Yes					Alteration Zone
HPP-1-60	4 x 7										
HPP-1-61						Yes	Yes				
HPP-1-62				Yes		Yes					
HPP-1-63	2-5					Yes	Yes	26	85	SE	
HPP-1-64	8					Yes		0	43	E	Contact?
HPP-1-65	7 x 10					Yes					Two samples collected.
HPP-1-66	5				Yes	Yes		17	43	SE	

Sample ID	Traverse #	Date	Waypoint ID	Point East	Point North	Point Elev. (ft)	Host Unit	Sample Lithology/Feature Type	Sample Description
HPP-1-67	1	5/31/14	72	626739	4463202	7485	Tcc	Aplite	Microcrystalline, white qtz vein in coarse-grained, qtz-rich granite. Vein very similar to HPP-1-64. White and slightly light green. Granular, with no change in texture or mineralogy (?) at contacts.
HPP-1-68	1	5/31/14	73	626734	4463190	7488	Tcc	Aplite	One microcrystalline white, granular vein in weathered, silicified, coarse-grained granite. See description of HPP-1-67.
HPP-1-69	1	5/31/14	75	626611	4463381	7551	Tcc	Type (IV) Microcrystalline Quartz Vein	Discontinuous vein of milky white, microcrystalline qtz. Qtz crystals range from 1 cm -2.2 cm in size. Vein located in silicified, fractured, light-colored, weathered, fine-grained granite.
HPP-1-70	1	5/31/14	76	626618	4463366	7565	Tcc	Type (V) Microcrystalline Quartz Vein	Fine-grained, silica-rich, white vein in coarse-grained, granular weathered granite. Vein is tabular, crosscutting larger vein orthogonally.
HPP-1-71	1	5/31/14	77	626609	4463430	7538	Tcc	Type (IV) Microcrystalline Quartz Vein	Laterally continuous, exposed milky qtz vein. Vein is parallel and central to the ridge. Vein is occasionally discontinuous, exposed for ~15 m. Surrounding rock is silicified med-grained granite, (pink).
HPP-1-72	1	5/31/14	78	626617	4463866	7487	Tcc	Type (IV) Microcrystalline Quartz Vein	Discontinuous, milky-white qtz vein. Wallrock is fine-grained, white-light green, granular, silicified granite. Vein is continuously exposed for up to 5 m.
HPP-1-73	1	5/31/14	79	626613	4464196	7416	Tcc	Type (IV) Microcrystalline Quartz Vein	Discontinuous, anastomosing, microcrystalline qtz vein with smaller qtz veins on either side. Host rock is bleached, med-coarse-grained granite. Orange alteration zones on either side of the vein area.
HPP-1-74	1	5/31/14	80	626596	4464201	7425	Tcc	QF Pegmatite	Pegmatitic qtz-fspar vein with milky and transparent qtz crystals. Vein is continuous and is surrounded by zones of fine-grained and coarse-grained granitic material. Immediately adjacent to vein is coarse-grained granite, but fine-grained aplitic granite is within a meter.

Sample ID	Thickness (cm)	Potassic	Skarn	Phyllic	Chlorite-Sericite	Silicification	Jarosite	Strike	Dip	Dip Direction	Additional Notes
HPP-1-67	7-8				Yes	Yes		90	63	N	
HPP-1-68	2					Yes		106	64	NE	
HPP-1-69	3				Yes	Yes		11	57	SE	Fine-grained granite wallrock.
HPP-1-70	7-10							137	84	NE	
HPP-1-71	3				Yes	Yes		161	45	SE	
HPP-1-72	6				Yes			4	79	SE	
HPP-1-73	1-3					Yes	Yes	67	85	SE	
HPP-1-74	3							160	34	NE	

Sample ID	Traverse #	Date	Waypoint ID	Point East	Point North	Point Elev. (ft)	Host Unit	Sample Lithology/Feature Type	Sample Description
HPP-1-75	1	5/31/14	81	626707	4464234	7385	Ttc	Type (V) Microcrystalline Quartz Vein	Very large zone of microcrystalline, white, hydrothermally-precipitated Qtz. Very massive, wallrock is silicified, med-grained granite. Wall rock is poorly exposed in this outcrop. Mostly Qtz.
HPP-1-76	1	5/31/14	82	626606	4464264	7372	Ttc	Type (III) Quartz Vein	Beautiful, pegmatitic Qtz vein. Large (1-5 cm) glassy crystals of Qtz. Located in microcline-rich, coarse-grained, weathered granite. Also milky-white Qtz crystals.
HPP-1-77	1	5/31/14	83	626598	4463397	7335	Ttc	QF Pegmatite	Qtz-microcline pegmatite zone, (poorly exposed), with alteration zones, (bleaching, orange staining), on either side of zone for unknown distance. Unaltered rock nearby is very coarse-grained granite with large, porphyritic (1-2 cm) microcline phenocrysts. Appears to be laterally continuous across Harrison Pass (?).
HPP-1-78	1	5/31/14	84	626585	4464452	7290	Ttc	QF Pegmatite	Several fine-grained veins cutting through outcrop of very coarse-grained granite with 1-3 cm microcline phenocrysts. Sampled vein is pegmatitic Qtz-fspar with a ~2 cm core of pure, glassy grey/white Qtz. Several aplite veins in outcrop as well.
HPP-1-79	1	5/31/14	85	626628	4464722	7226	Ttc	QF Pegmatite	Pegmatitic Qtz-fspar vein in coarse-grained granite with 1-3 cm microcline phenocrysts in granite. Vein has 2 cm wide Qtz-rich core and crosscuts older pegmatitic zone obliquely. Qtz crystals are 1-2 cm and glassy.
HPP-2-01	2	6/2/14	87	621537	4466228	7145	Tmg	QF Pegmatite	Biotite granite. Large microclines.
HPP-2-02	2	6/2/14	88	621547	4466217	7147	Tmg	Aplite (QF-cored)	bqfgr(QF Peg)(Minor FeO). Aplite zone is 4 cm thick on either side of a 6-cm thick QF Peg core.
HPP-2-03	2	6/2/14	90	621585	4466221	7168	Tmg	Aplite (Q-cored)	bqfgr(Ap + Q)(SiO2, minor FeO)
HPP-2-04	2	6/2/14	91	621665	4466178	7251	Tmg	Basalt/Microdiorite	Dark grey/green, fine-grained highly altered, fine-grained, diorite/biotite-rich granite. 1-2 mm biotite phenocrysts and pervasive veins of leucocratic fine-grained granite with pegmatitic Qtz-feldspar cores. Contact with HPP-2-4.

Sample ID	Thickness (cm)	Potassic	Skarn	Phyllic	Chlorite-Sericite	Silicification	Jarosite	Strike	Dip	Dip Direction	Additional Notes
HPP-1-75	40					Yes		5	87	SE	
HPP-1-76	6					Yes		39	22	SE	
HPP-1-77	22						Yes	42	52	SE	Beginning of microcline megacrysts
HPP-1-78	3-7				Yes			40	40	SE	
HPP-1-79	11							72	73	SE	
HPP-2-01	6							13	49	SE	
HPP-2-02	14							150	70	SW	
HPP-2-03					Yes						
HPP-2-04											

Sample ID	Traverse #	Date	Waypoint ID	Point East	Point North	Point Elev. (ft)	Host Unit	Sample Lithology/Feature Type	Sample Description
HPP-2-05	2	6/2/14	91	621665	4466178	7251	Tmg	QF Pegmatite	Fine-grained bqfGr(QF Peg)(SiO2). Pegmatite veins, zones and one cavity (20 cm across). Source of leucocratic veins across contact. Contact with HPP-2-4.
HPP-2-06	2	6/2/14	92	621722	4466156	7278	Tmg	Type (I) Quartz Vein	(b)fqGr(QZ)(SO4, FeO) Glassy, continuous qtz veins with jarosite staining and minor iron oxide in medium-coarse grained granite. Fine-grained along vein margins. Veins oblique to each other.
HPP-2-07	2	6/2/14	93	621707	4466141	7250	Tmg	Aplite (Layered QF Pegmatite)	qfGr(QF Peg)(FeO). Altered fine-grained granite (silicified) surrounding bending, subparallel, qtz-fspar pegmatite veins. Some iron oxide staining.
HPP-2-08a	2	6/2/14	94	621693	4466134	7241	Tmg	Basalt/Microdiorite	Dark, fine-grained, platy, mafic rock. Numerous lenses, veins, and inclusions of felsic, granitic material. Likely a dike.
HPP-2-08b	2	6/2/14	94	621693	4466134	7241	Tmg	Granite (Leuco)	Qtz core in leucogranite dike cutting through basalt/microdiorite inclusion/dike in outcrop. A 4 cm core of larger, subhedral qtz crystals with microcrystalline vein edges. Some pink coloration/staining.
HPP-2-08c	2	6/2/14	94	621693	4466134	7241	Tmg	Granite (altered)	Bleached, fine-grained granite along contact with (meta?)-basalt dike. Possibly a chill zone or reaction front.
HPP-2-09	2	6/2/14	95	621850	4466222	7446	Tmg	QF Pegmatite	qfAp(QF Peg)(SiO2, SO4). Bleached, vuggy, large feldspars.
HPP-2-10	2	6/2/14	96	621951	4466253	7363	Tmg	Aplite	Several med-large aplite veins, parallel, in qbfGr with pegmatitic microcline phenocrysts. Some minor jarosite staining.
HPP-2-11	2	6/2/14	97	621956	4466294	7404	Tmg	Aplite	Large aplite vein with large zones of bleaching on either side, (18-22 cm wide each), in coarse-grained bqfGr with pegmatitic euhedral microcline phenocrysts. Obvious kink in vein.
HPP-2-12	2	6/2/14	98	621979	4466306	7453	Tmg	Aplite (Layered QF Pegmatite)	Complex QF Peg vein zone in bqfGr. Three distinct pegmatite zones. Qtz crystals <2 cm, feldspar crystals <5 cm. Minor FeO staining. Finer-grained, bleached zones on margins of pegmatitic zones.
HPP-2-13	2	6/2/14	99	621970	4466240	7383	Tmg	Aplite	Aplite vein in bqfGr. Vein is bleached, no distinct zoning. Thin (2 cm) QF Peg zone along upper margin of vein.

Sample ID	Thickness (cm)	Potassic	Skarn	Phyllic	Chlorite-Sericite	Silicification	Jarosite	Strike	Dip	Dip Direction	Additional Notes
HPP-2-05											
HPP-2-06	1-2						Yes	46	90		
HPP-2-07	3-5					Yes		36	21	NW	
HPP-2-08a											
HPP-2-08b	12							25	90		
HPP-2-08c											
HPP-2-09	3-5					Yes	Yes	32	28	SE	
HPP-2-10	5-8						Yes	32	64	SE	
HPP-2-11	22							4	77	SE	
HPP-2-12	80							129	9	NE	
HPP-2-13	56							21	19	SE	

Sample ID	Traverse #	Date	Waypoint ID	Point East	Point North	Point Elev. (ft)	Host Unit	Sample Lithology/Feature Type	Sample Description
HPP-2-14	2	6/2/14	100	621982	4466239	7418	Tmg	Type (I) Quartz Vein	(b)qfGr(QF Peg)(SO4, SiO2). Pegmatite vein in bleached zone, possibly silicified.
HPP-2-15	2	6/2/14	101	622061	4466192	7387	Tmg	Aplite	Large apfite vein in bqfGr. Granite is coarse-grained and unaltered. Vein has small pegmatite zone near upper margin.
HPP-2-16	2	6/2/14	102	622103	4466272	7430	Tmg	Aplite (Layered QF Pegmatite)	bmqfGr(SO4)(QF Peg). Altered fine-grained biotite-poor granite with multiple repeating sequences of parallel pegmatite and aplitic layers.
HPP-2-17	2	6/2/14	103	622129	4466250	7398	Tmg	QF Pegmatite	Complex pegmatitic vein in bleached qfGr(A3-SO4), very friable. Main pegmatite zone is composed of qtz and feldspar. Surrounding unaltered granite is coarse-grained.
HPP-2-18	2	6/3/14	105	622255	4466168	7392	Tmg	QF Pegmatite	bqfGr(QF Peg). Complex pegmatite vein dominated by large feldspars, minor qtz. Some apfite also.
HPP-2-19a	2	6/3/14	106	622271	4466164	7419	Tmg	Basalt/Microdiorite	Dark, fine-grained, mafic rock. Many veins, lenses, and inclusions of felsic material. Bounded and crosscut by one large felsic/apfite vein. Entire dark zone thickness = ~0.45 m, (tabular).
HPP-2-19b	2	6/3/14	106	622271	4466164	7419	Tmg	Aplite	Fine-grained aplitic inclusion, (relict vein material?) in larger mafic inclusion (HPP-2-19a).
HPP-2-19c	2	6/3/14	106	622271	4466164	7419	Tmg	QF Pegmatite	Large QF Peg zone in silicified granite near contact with major mafic inclusion. Dominated by feldspar, but with some aplitic material in zone.
HPP-2-20	2	6/3/14	107	622279	4466135	7386	Tmg	Aplite (Layered QF Pegmatite)	qfGr(SiO2,FeO,SO4)(QF Peg) Aplite hosting numerous parallel pegmatitic qtz-fspar veins.
HPP-2-21	2	6/3/14	108	622299	4466121	7364	Tmg	Aplite (Layered QF Pegmatite)	qfGr(FeO)(QF Peg) Numerous pegmatitic qtz-feldspar zones/veins.
HPP-2-22	2	6/3/14	109	622313	4466070	7331	Tmg	Type (I) Quartz Vein	bqfGr(QF Peg)(Q-glassy)(FeO3,SO42). Coarse-med grained bleached aplitic granite with strong FeO staining and some QF Peg zones. Sampled is a translucent qtz vein with FeO and SO4 staining.
HPP-2-23	2	6/3/14	110	622406	4466095	7341	Tmg	QF Pegmatite	qfGr(FeO,3SO41)(QF Peg)(Q-glassy). Medium-coarse grained, iron-stained granite with QF Pegmatitic veins. Also, small 1-2 cm glassy qtz veins, (not sampled).

Sample ID	Thickness (cm)	Potassic	Skarn	Phyllic	Chlorite-Sericite	Silicification	Jarosite	Strike	Dip	Dip Direction	Additional Notes
HPP-2-14	5					Yes	Yes	135	84	SW	
HPP-2-15	15							20	37	SE	
HPP-2-16	10-16						Yes	19	16	SE	
HPP-2-17	4						Yes	28	40	SE	
HPP-2-18	10							139	4	NE	
HPP-2-19a	45										
HPP-2-19b	10										
HPP-2-19c	16					Yes		73	34	SE	
HPP-2-20	7-17						Yes	55	39	SE	
HPP-2-21	9-15							28	32	SE	
HPP-2-22	1-2						Yes	62	76	SE	
HPP-2-23	11						Yes	35	69	SE	

Sample ID	Traverse #	Date	Waypoint ID	Point East	Point North	Point Elev. (ft)	Host Unit	Sample Lithology/Feature Type	Sample Description
HPP-2-24	2	6/3/14	112	622423	4466019	7273	Tmg	QF Pegmatite	qfGr(FeO, SO42)(QF Peg). Med-grained, bleached, granite with pervasive, QF Pegmatitic veins in two sets. The larger set is 9-12 cm thick, (sampled). The thinner set are 1-3 cm thick, and oriented 98°, 29°SW, (not sampled).
HPP-2-25	2	6/3/14	113	622500	4466119	7345	Tmg	QF Pegmatite	qfGr(FeO2)(QF Peg). Fine-medium grained granite, (iron-stained) with one large QF Peg vein crosscutting.
HPP-2-26	2	6/3/14	114	622542	4466107	7295	Tmg	Aplite (Layered QF Pegmatite)	bqfGr(QF Peg). Very large, complex, banded QF Peg zone with zones of aplite. At least two pegmatite zones with thicknesses of 10-30 cm.
HPP-2-27	2	6/3/14	116	622546	4466029	7229	Tmg	Aplite	bqfGr(Ap + QF Peg)(FeO). Megacrystic microcline phenocrysts in monzogranite matrix, relatively weathered. One large aplite vein (sampled) cutting through. Minor FeO staining on vein only. Small QF Peg veins in general area.
HPP-2-28	2	6/3/14	118	622590	4466036	7188	Tmg	Aplite (Layered QF Pegmatite)	bqfGr(QF Peg)(FeO). Complex zone of QF Pegmatites in FeO-stained, biotite monzogranite. Zone is 30 cm thick with several zones of fine-grained material alternating with petmatic crystals.
HPP-2-29	2	6/3/14	119	622607	4466038	7203	Tmg	QF Pegmatite	bqfGr(FQ-peg)3(SO4). Large fspar-qtz pegmatite zone with enormous (10-20 cm) qtz crystals, (grey-glassy). Some jarosite staining at vein margins. Some is poorly exposed.
HPP-2-30	2	6/4/14	120	622735	4466033	7182	Tmg	Aplite (Layered QF Pegmatite)	Poorly exposed bqfGr(SiO2, bleaching)(QF Peg)(SO4)(FeO)2. Repeating zones of QF Pegmatite and bleached, med-fine grained aplite zones.
HPP-2-31	2	6/4/14	121	622690	4465863	7128	Tmg	Aplite (Layered QF Pegmatite)	Thick zone of enormous (5-15 cm) qtz and feldspar crystals in qfGr(bleaching)3(FeO).
HPP-2-32	2	6/4/14	122	622851	4466144	7119	Tmg	Miarolitic Cavity	qfGr(QF Peg)(FeO). Possible QF Peg miarolitic cavity or poorly exposed/discontinuous vein with qtz-feldspar crystals 2-5 cm in size. QF Peg veins nearby as well. Cavity has no open space remaining.
HPP-2-33	2	6/4/14	123	622900	4466149	7072	Tmg	QF Pegmatite	qfGr(SO4)2(QF Peg) One large, qtz-dominated QF Peg vein with jarosite staining on either margin and throughout the host rock. Host rock is bleached, and weathered aplite with a med-coarse grain size.

Sample ID	Thickness (cm)	Potassic	Skarn	Phyllic	Chlorite-Sericite	Silicification	Jarosite	Strike	Dip	Dip Direction	Additional Notes
HPP-2-24	9-12						Yes	17	28	SE	
HPP-2-25	10-15							20	22	SE	
HPP-2-26	70							94	6	SW	
HPP-2-27	20							43	41	SE	
HPP-2-28	30							33	39	SE	
HPP-2-29	50-55						Yes	40	63	SE	
HPP-2-30	17						Yes	48	12	SE	
HPP-2-31	50							70	14	SE	
HPP-2-32	6 x 10										
HPP-2-33	7-9						Yes	19	44	SE	

Sample ID	Traverse #	Date	Waypoint ID	Point East	Point North	Point Elev. (ft)	Host Unit	Sample Lithology/Feature Type	Sample Description
HPP-2-34	2	6/4/14	124	623162	4466155	7125	Tmg	QF Pegmatite	bqGr(QF Peg)(FeO). Thick QF Peg zone in coarse-grained aplite, (lacking biotite).
HPP-2-35	2	6/4/14	126	623180	4466130	7091	Tmg	QF Pegmatite	qfGr(SO4)(QF Peg)(bleached). Med grained, iron-stained, aplitic granite with two large QF Peg veins, one 10-15 cm thick (sampled), and the other 7 cm thick. Very large, (5-9 cm), qtz and feldspar crystals.
HPP-2-36	2	6/4/14	127	623363	4466233	7241	Tmg	QF Pegmatite	qfGr(QF Peg)(SO4,FeO). One folded, Fq-peg vein with FeO, SO4-stained cavity near center of fold (see sketch). Vein is dominated by feldspar with minor qtz.
HPP-2-37	2	6/4/14	128	623389	4466241	7222	Tmg	Miarolitic Cavity	A large, poorly outcropping miarolitic cavity with massive qtz (1.5-2.5 cm) and microcline (5-15 cm). Host rock is qfGr(SiO2)3(QF Peg)(SO4). Possible sericitic alteration
HPP-2-38	2	6/4/14	129	623580	4466241	7099	Tmg	Type (I) Quartz Vein	qfGr(Q-peg)(QF Peg)(FeO). One glassy qtz vein (sampled) with QF Pegs nearby. Vein almost entirely qtz with minor fspars on margins.
HPP-2-39	2	6/4/14	130	623630	4466243	7118	Tmg	Type (I) Quartz Vein	qfGr(Q-peg, glassy)(SO4)3 One qtz vein, (glassy) with minor fspar in heavily bleached, altered/weathered granite with strong jarosite staining.
HPP-2-40	2	6/4/14	131	623703	4466230	7185	Tmg	QF Pegmatite	qfGr(QF Peg)(SO4)2(FeO)2 One QF Peg vein with jarosite staining along margins in med-grained, bleached, stained, aplitic granite.
HPP-2-41	2	6/4/14	132	623810	4466203	7232	Tmg	Type (III) Quartz Vein	Two large, irregular, discontinuous, elongate pods of pure, pegmatitic, milky-white qtz crosscutting intensely altered, (silicified, fractured, possibly argillically altered), crumbly/friable granite. Pods are about 1 m long each and show some jarosite staining.
HPP-2-42	2	6/4/14	133	623927	4466249	7181	Tmg	Aplite (QF-cored)	Relatively unaltered bqGr(QF-cored Aplite). Several aplite veins with QF Peg cores cutting through relatively unaltered granite. One large, complex aplite vein with a QF Peg core. Thin (4-5 cm), discontinuous QF Peg core. Unaltered granite is coarse-grained.

Sample ID	Thickness (cm)	Potassic	Skarn	Phyllic	Chlorite-Sericite	Silicification	Jarosite	Strike	Dip	Dip Direction	Additional Notes
HPP-2-34	20-25							170	39	SE	
HPP-2-35	10-15						Yes	38	24	SE	
HPP-2-36	6-8						Yes				
HPP-2-37	30 x 53					Yes	Yes				
HPP-2-38	7-8							79	57	SE	
HPP-2-39	2.5-13			Yes			Yes	143	87	NE	
HPP-2-40	7						Yes	123	44	SW	
HPP-2-41	11-15					Yes	Yes				
HPP-2-42	30							50	83	SE	Contact between Layered Aplite/QF Peg and coarse-grained granite.

Sample ID	Traverse #	Date	Waypoint ID	Point East	Point North	Point Elev. (ft)	Host Unit	Sample Lithology/Feature Type	Sample Description
HPP-2-43	2	6/4/14	135	624058	4466303	7130	Tmg	Type (I) Quartz Vein	qfAp(Arg.?) bleaching, SiO2(?)3(Q-peg, milky)2(QF Peg)(SO4)4 Extremely altered granite with gritty, friable texture (Arg.?) and pervasive jarosite staining along fronts and small vein. Also, one large, discontinuous, pegmatitic qtz vein comprised of massive milky qtz in pods, (sampled).
HPP-2-44	2	6/4/14	136	624176	4466273	7153	Tmg	Aplite (Layered QF Pegmatite)	qfAp(QF Peg)(SO4)2(FeO). Bleached aplite host rock has intermediate jarosite staining. Complex QF Peg zone with two QF-rich cores alternating with aplite. Upper QF Peg core thickness = ~25 cm. Some is relatively flat-lying with some offset from fractures.
HPP-2-45	2	6/5/14	137	624169	4466388	7233	Tmg	QF Pegmatite	qfGr(QF Peg)(SO4)3(FeO). One QF Pegmatite zone in med-coarse grained, jarosite stained, weathered granite. Zone is poorly exposed and may be discontinuous or offset.
HPP-2-46	2	6/5/14	138	624175	4466347	7195	Tmg	QF Pegmatite	Elongate pod/qtz-rich section of discontinuous QF Peg vein (32 cm) in qfGr(SiO2)2(QF Peg)(weathered+bleached). Pod contains mostly milky/grey qtz. Less altered than outcrops upslope.
HPP-2-47	2	6/5/14	139	624291	4466300	7177	Tmg	Type (I) Quartz Vein	qfGr(SiO2)(Q-milky, QF Peg)(SO4)(FeO). Moderately silicified granite with several pegmatitic veins crosscutting. One vein is dominated by massive milky qtz with few large feldspars.
HPP-2-48	2	6/5/14	140	624344	4466328	7185	Tmg	Type (I) Quartz Vein	qfGr(SiO2)3(Q-peg, QF Peg)(FeO). One massive qtz vein (white/grey-glassy). Nearby is a wide (40 cm) bleached QF Peg zone with possible argillic alteration and strong jarosite staining.
HPP-2-49	2	6/5/14	141	624436	4466396	7172	Tmg	QF Pegmatite	bqfGr(SiO2)(Q-peg, QF Peg)(SO4)2 Host rock is a moderately altered, silicified, biotite granite with rotten biotites and feldspars, (propylitic alt.?). Several pegmatite veins, including one qtz-dominated vein with large (5-9 cm) qtz crystals and minor feldspar. Other pegmatitic crystals randomly oriented in granite.

Sample ID	Thickness (cm)	Potassic	Skarn	Phyllic	Chlorite-Sericite	Silicification	Jarosite	Strike	Dip	Dip Direction	Additional Notes
HPP-2-43	5-15					Yes	Yes	89	35	SE	
HPP-2-44	45						Yes		0		
HPP-2-45	12						Yes	95	30	SW	
HPP-2-46	5-9										
HPP-2-47	8 cm					Yes	Yes	50	22	SE	
HPP-2-48	12-13						Yes	23	38	SE	
HPP-2-49	6-8					Yes	Yes	0	17	E	

Sample ID	Traverse #	Date	Waypoint ID	Point East	Point North	Point Elev. (ft)	Host Unit	Sample Lithology/Feature Type	Sample Description
HPP-2-50	2	6/5/14	142	624563	4466293	7146	Tmg	QF Pegmatite	Large pegmatitic FQ-peg vein surrounded by intensely altered granite zone (qfGr(SiO ₂) ₃ (SO ₄) ₃). Vein has very large, (3-7 cm) qtz crystals at core with large feldspars along margins. Rock that is 20 m to the east or west of this NE-SW zone is relatively unaltered bqfGr.
HPP-2-51	2	6/5/14	143	625701	4466206	7372	Ttc	Aplite	bqfGr(Ap-Qf Peg). Relatively unaltered granite with microcline megacrysts. One Aplite vein dominated by subhedral feldspars.
HPP-2-52	2	6/5/14	144	625847	4466348	7356	Ttc	Aplite	qbfgGr(Ap-Qf Peg). Relatively unaltered coarse-grained granite with pegmatitic microcline megacrysts (euhedral). One QF vein with med-fine grained feldspar and qtz (no biotite).
HPP-2-53	2	6/5/14	145	626071	4466347	7423	Ttc	QF Pegmatite	qbfgGr(SiO ₂ , bleaching) ₃ (Qf Peg,Ap)(FeO)(SO ₄) ₃ Surrounding rock is unaltered wbf monzogranite with microcline megacrysts. One QF Peg vein (sampled) with strongly bleached, altered, jarosite stained, aplitic zones on either side up to 1 m. Possible argillic alteration. Pegmatitic glassy qtz and matte fspars (3-4 cm) with strong orange staining.
HPP-2-54	2	6/5/14	146	626124	4466255	7465	Ttc	QF Pegmatite	bqfGr(SiO ₂ , bleaching) ₂ (Ap-Qf Peg)(SO ₄) ₂ One QF Peg vein with zones of altered aplitic (silicification and bleaching), on either margin (~35 cm each). Nearby rock is relatively unaltered biotite granite. Some aplitic material in core of vein. Dominated by feldspar with minor qtz.
HPP-2-55	2	6/5/14	147	626232	4466222	7489	Ttc	Type (I) Quartz Vein	qbfgGr(Q-glassy) ₂ (SO ₄)(FeO) ₂ Relatively unaltered biotite granite with megacrystic microclines cut by several FeO/SO ₄ -stained fractures. One fracture is filled by a solid, FeO/SO ₄ -stained, pure qtz vein. Host rock is relatively unaltered.
HPP-2-56	2	6/5/14	148	626395	4466194	7522	Ttc	Type (III) Quartz Vein	qbfgGr(SiO ₂)(Q-massive)(SO ₄) ₂ One large, massive milky white/grey qtz vein with strong SO ₄ staining on the margins cutting through moderately altered, med-coarse grained granite.

Sample ID	Thickness (cm)	Potassic	Skarn	Phyllic	Chlorite-Sericite	Silicification	Jarosite	Strike	Dip	Dip Direction	Additional Notes
HPP-2-50	15					Yes	Yes	31	41	SE	
HPP-2-51	4-5							83	74	SE	Megacrystic Microclines.
HPP-2-52	2-3							78	77	NW	Megacrystic Microclines.
HPP-2-53	3-5					Yes	Yes	18	41	SE	
HPP-2-54	7-10 (core)					Yes	Yes	52	48	SE	
HPP-2-55	1.5-2						Yes	124	72	SW	
HPP-2-56	15						Yes	53	61	SE	

Sample ID	Traverse #	Date	Waypoint ID	Point East	Point North	Point Elev. (ft)	Host Unit	Sample Lithology/Feature Type	Sample Description
HPP-2-57	2	6/5/14	149	626662	4466197	7622	Ttc	QF Pegmatite	bqfGr(SiO2)2(QF Peg, ap)2(SO4)2 One large, qtz-fspar pegmatite zone in coarse-grained, silicified, SO4-stained aplite. Zone is mostly removed and is observed as a tabular void. Some large (8-12 cm) crystals remain. Zone of alteration on one side is 70 cm wide. Unaltered granite is biotite-bearing.
HPP-2-58	2	6/5/14	150	626729	4466207	7674	Ttc	QF Pegmatite	bqfGr(QF Peg)(SO4)3 Intensively altered, aplitic, SO4-stained zones up to 50 cm on each side of a pegmatitic QF-vein with enormous qtz & fspar crystals (5-15 cm). Some macro-graphic texture (qtz-fspar intergrowth).
HPP-2-59	2	6/5/14	152	626843	4466176	7689	Ttc	Aplite (QF-cored)	bqfGr(QF Peg)(Ap)(Q)(SO4). Relatively unaltered, med grained, biotite-rich granite with 1-3 cm microcline megacrysts, (contact with Ttc?). QF Peg vein with qtz-rich core and fine-grained, SO4-stained margins, (3-5 cm each). Small (1-3 cm) qtz-lined vugs in vein core. Three other similar veins cutting parallel through outcrop.
HPP-2-60	2	6/5/14	153	626880	4466173	7621	Ttc	Aplite (Layered QF Pegmatite)	bqfGr(QF Peg, ap)2(SO4)2(FeO). Complex, 20 cm wide QF Pegmatite zone with two cores of qtz-fspar, surrounded by bleached, altered aplitic granite with SO4 staining. Unaltered granite is within 0.5 m.
HPP-2-61	2	6/5/14	154	626958	4466107	7691	Ttc	Aplite	qbfgGr(QF-vein). No alteration of granite. Granite contains megacrystic microclines. Tabular qtz-feldspar vein with unaltered margins and med (1-3 cm) grain size. Possible filled fracture, (split along core). Mafic enclaves (3 cm) in granite.
HPP-2-62	2	6/5/14	155	627034	4466244	7599	Ttc	QF Pegmatite	bqfGr(SiO2)(QF Peg)(minor SO4). Relatively unaltered granite with mafic enclaves (3-15 cm) with one QF Peg zone. Thin zone of silicification and minor jarosite staining (2-4 cm) on either side. Very large, pure qtz crystals, (fspars around the margins).

Sample ID	Thickness (cm)	Potassic	Skarn	Phyllic	Chlorite-Sericite	Silicification	Jarosite	Strike	Dip	Dip Direction	Additional Notes
HPP-2-57	12-15					Yes	Yes	114	74	SW	
HPP-2-58	20-23					Yes	Yes	134	55	NE	
HPP-2-59	10-12						Yes	23	77	NW	
HPP-2-60	20						Yes	149	75	SW	
HPP-2-61	7							14	5	SE	
HPP-2-62	13-15						Yes	36	56	SE	

Sample ID	Traverse #	Date	Waypoint ID	Point East	Point North	Point Elev. (ft)	Host Unit	Sample Lithology/Feature Type	Sample Description
HPP-2-63	2	6/6/14	156	627419	4466110	7726	Ttc	Aplite	qbfgGr(QF-vein). Unaltered biotite granite with large microcline megacrysts. One Qtz-fspar vein cutting through, very linear/tabular and dominated by fairly massive fsp. Qtz is fairly minor, with no biotite in vein. No alteration zones.
HPP-2-64	2	6/6/14	157	627663	4466201	7595	Ttc	QF Pegmatite	bqfGr(QF Peg)(SO4)(SiO2?) Several parallel, tabular, thin (1.5-6 cm) QF veins (some pegmatitic) cutting through relatively unaltered granite. Some SO4 staining on larger vein margins (sampled).
HPP-2-65	2	6/6/14	158	627748	4466231	7609	Ttc	Type (I) Quartz Vein	bqfGr(SiO2, chlorite-sericite(?), FeO)3(Qtz-micro, vuggy). Strongly altered granite (pervasive iron staining). Zone of 3+ microcrystalline Qtz veins, green with white crystals in fine-grained groundmass and small (2-3 mm) brown vugs. Veins are thin, anastomosing with FeO staining on margins. Possible chlorite?
HPP-2-66	2	6/6/14	159	627888	4460750	7549	Ttc	QF Pegmatite	bqfGr(QF-vein). Unaltered, slightly weathered, biotite granite with microcline megacrysts and several sheeted parallel QF veins, (very tabular/linear). Veins dominated by feldspars with some Qtz and no biotite.
HPP-2-67	2	6/6/14	160			Ttc		Type (V) Microcrystalline Quartz Vein	Massive, complex microcrystalline Qtz vein in intensely altered granite (bqfGr(SiO2, Chlorite-sericite)3(SO4)(Q-microcrystalline). Possibly the same vein system as that sampled in HPP-1-75 or HPP-1-77. Altered granite is green/grey, friable, intensely fractured/pulverized, and silicified (hard). Complex zone with clear alignment of fractures, same orientation of vein.
HPP-2-68	2	6/6/14	161	628251	4466123	7446	Ttc	Type (V) Microcrystalline Quartz Vein	Large, massive, milky-white microcrystalline Qtz zone with numerous smaller, near parallel, subsidiary Qtz veins. Wide (>2m) zone of pervasive microfracturing, silicification, and chlorite-sericite alteration. Forms a linear ridge parallel to HPP-2-67, possibly also Traverse 1. SO4 staining. Possible K alteration 25 m NW, (pink feldspar phenocrysts in silicified granite).

Sample ID	Thickness (cm)	Potassic	Skarn	Phyllic	Chlorite-Sericite	Silicification	Jarosite	Strike	Dip	Dip Direction	Additional Notes
HPP-2-63	5-6							129	60	SW	
HPP-2-64	1.5-6					Yes	Yes	114	62	SW	
HPP-2-65	1.5-2				Yes	Yes		9	74	NW	
HPP-2-66	1-6							104	73	SW	
HPP-2-67	200			Yes		Yes	Yes	9	45	NW	Large fault-hosted qtz vein.
HPP-2-68	80-100				Yes	Yes	Yes	21	77	NW	Large fault-hosted qtz vein.

Sample ID	Traverse #	Date	Waypoint ID	Point East	Point North	Point Elev. (ft)	Host Unit	Sample Lithology/Feature Type	Sample Description
HPP-2-69	2	6/6/14	163	628365	4466398	7235	Ttc	Type (V) Microcrystalline Quartz Vein	Large, milky-white, massive microcrystalline Qtz zone. Surrounding rock is intensely altered, microfractured, and silicified. Possibly part of the same SiO ₂ , chlorite-sericite alteration zone as HPP-2-67, or HPP-2-68, which may also correlate to localities in Traverse 1.
HPP-2-70	2	6/6/14	164	628614	4466574	7327	Ttc	Type (V) Microcrystalline Quartz Vein	Massive, complex microcrystalline Qtz vein in intensely altered granite (bqfGr(SiO ₂ , Chlorite-sericite) ₃ (SO ₄)(Q-microcrystalline). Possibly the same vein system as that sampled in HPP-1-75 or HPP-1-77. Altered granite is green/grey, friable, intensely fractured/pulverized, and silicified (hard). Complex zone with clear alignment of fractures, same orientation of vein.
HPP-2-71a	2	6/6/14	165	629117	4466932	7380	Ttc	Metased (Marble, mineralized)	Mineralized and non-mineralized (pyrite & chalcopyrite) banded marbles from mine prospect at contact between HPP and metasedimentary rocks. Large oxidized veins present.
HPP-2-71b	2	6/6/14	165	629117	4466932	7380	Ttc	Metased (Vein galena in banded marble)	Mineralized galena vein in banded marble, (ore zone).
HPP-2-72	2	6/6/14	166	629153	4466392	7031	Ttc	Type (V) Microcrystalline Quartz Vein	Large, massive, milky microcrystalline Qtz zone. Surrounding granite is intensely altered and silicified. FeO staining present in wallrock. At distances greater than 10 m away from the Qtz zone, granite is relatively unaltered bqfGr with megacrystic microclines. Outcrop is poorly preserved/not in place.
HPP-3-01	3	6/8/14	170	625349	4468459	7580	Tmg	MQF Pegmatite	bmqfGr(MQF Peg). Relatively unaltered two-mica granite, (med-grained) with 20 cm wide MQF Pegmatite vein with glassy Qtz core, (5 cm). Muscovite concentrated along margins, sometimes in mica books.
HPP-3-02	3	6/8/14	171	625280	4468377	7529	Tmg	Type (III) Quartz Vein	One massive, milky white Qtz vein, (poorly outcropping), with strong jarosite staining and slickenlines. Surrounding rock is bmqfGr(SO ₄)(layered QF Peg/aplite(?)) ₃ (Q-micro). Surrounding rock is aplitic granite with interlayered QF Pegmatites.

Sample ID	Thickness (cm)	Potassic	Skarn	Phyllic	Chlorite-Sericite	Silicification	Jarosite	Strike	Dip	Dip Direction	Additional Notes
HPP-2-69	100				Yes	Yes	Yes	45	69	NW	Large fault-hosted qtz vein.
HPP-2-70	200				Yes	Yes	Yes	40	49	NW	Large fault-hosted qtz vein.
HPP-2-71a			Yes								Contact Metamorphic Aureole
HPP-2-71b			Yes								Contact Metamorphic Aureole
HPP-2-72	200				Yes	Yes		79	74	NW	Large fault-hosted qtz vein.
HPP-3-01	20							178	56	NE	
HPP-3-02	10						Yes	175	49	SW	May not be in place.

Sample ID	Traverse #	Date	Waypoint ID	Point East	Point North	Point Elev. (ft)	Host Unit	Sample Lithology/Feature Type	Sample Description
HPP-3-03	3	6/8/14	172	625052	4468162	7408	Tmg	Type (IV) Microcrystalline Quartz Vein	Vuggy, complex microcrystalline qtz vein with some minor FeO staining along margins. Wallrock is bleached, med-grained granite with megacrystic microcline crystals.
HPP-3-04	3	6/8/14	173	625045	4468106	7376	Tmg	Type (I) Quartz Vein	One pure milky qtz vein in med-grained, bleached, muscovite-bearing granite. In addition, small (miarolitic?) cavities are present containing qtz and fspars (3 cm x 5 cm).
HPP-3-05	3	6/8/14	174	624998	4468126	7389	Tmg	Type (III) Quartz Vein	Med-fine grained muscovite-bearing granite with large QF Peg zones. Some SO4 and FeO staining, plus bleaching. One massive qtz pod (sampled) that may be part of a discontinuous vein. Solid qtz, no staining, or feldspars in pod.
HPP-3-06a	3	6/8/14	175	624839	4468019	7259	Tmg	Type (IV) Microcrystalline Quartz Vein	Large outcrop of silicified, hematite stained, variably bleached, faulted granite. Likely a fault zone. Sampled one small, roughly spherical, pure, milky qtz pod.
HPP-3-06b	3	6/8/14	175	624839	4468019	7259	Tmg	Granite (faulted)	Large outcrop of silicified, hematite stained, variably bleached, faulted granite. Parallel fractures are continuous and throughgoing for 10s of meters. Likely a large fault zone.
HPP-3-07	3	6/9/14	176	624504	4467961	7222	Tmg	MQF Pegmatite	bqfGr(MQF Peg)(FeO) Slightly bleached, aplitic granite with some FeO staining. One MFQ-peg vein with little to no alteration around margins.
HPP-3-08	3	6/9/14	178	624015	4468008	7429	Tmg	Basalt/Microdiorite	Unaltered two-mica granite with several aplite veins and MQF Peg zones. Contact between granite and dark grey (meta?)-basalt xenolith. Xenolith is poorly exposed with a minimum width of 36 cm. Large pegmatitic microcline megacrysts in granite. Small, coarse-grained granite veins injected into xenolith.
HPP-3-09	3	6/9/14	179	623924	4468141	7678	Tmg	Aplite	Unaltered two-mica granite with several sets of aplite veins crosscutting. Vein has a fine-grained, feldspar-rich core.
HPP-3-10	3	6/9/14	180	623886	4468231	7729	Tmg	MQF Pegmatite	Contact between megacrystic/porphyritic biotite granite and med-grained biotite granite with no microcline megacrysts. Numerous aplite veins and at least one MQF Peg vein with large (2-4 cm) qtz and feldspar crystals. Vein is poorly exposed.

Sample ID	Thickness (cm)	Potassic	Skarn	Phyllic	Chlorite-Sericite	Silicification	Jarosite	Strike	Dip	Dip Direction	Additional Notes
HPP-3-03	10							116	81	SW	Megacrystic Microclines.
HPP-3-04	1.5-3							94	63	NW	
HPP-3-05	8 x 13						Yes				
HPP-3-06a	5 x 9										
HPP-3-06b	2000					Yes		37	85	SE	
HPP-3-07	10-13							49	21	SE	
HPP-3-08	36										Megacrystic Microclines.
HPP-3-09	12							160	85	NE	
HPP-3-10	3-6							142	62	NE	Contact between granite units.

Sample ID	Traverse #	Date	Waypoint ID	Point East	Point North	Point Elev. (ft)	Host Unit	Sample Lithology/Feature Type	Sample Description
HPP-3-11	3	6/9/14	181	623841	4468159	7773	Tmg	Basalt/Microdiorite	Relatively unaltered granite with anomalous red-weathering fine-grained (meta?)-basalt dike(?) at the summit. Rock is black/grey, (unweathered) and weathers into corestones. No bedding.
HPP-3-12	3	6/9/14	182	623793	4468156	7719	Tmg	Aplite	bqfGr with numerous (at least 3) aplite veins. Veins are relatively siliceous (hard).
HPP-3-13	3	6/9/14	183	623739	4468177	7631	Tmg	Aplite	Several parallel aplite veins in bqfGr, (sampled). Rock shows parallel alignment of fspars with veins, (some). Numerous smaller aplite and milky qtz veins also present, intersecting larger set obliquely.
HPP-3-14	3	6/9/14	184	623709	4468189	7582	Tmg	QF Pegmatite	One wide (1 m) zone of bleached bqfGr, (removal of mica in bleached/altered zone), around a QF Peg vein with glassy qtz core. Aplite veins also present.
HPP-3-15	3	6/9/14	186	623600	4468115	7515	Tmg	QF Pegmatite	Unaltered bqfGr with large, poorly exposed QF Peg zone or pod with large (10-15 cm) crystal agglomerates, dominated (60%) by feldspar.
HPP-3-16	3	6/9/14	189	623399	4468149	7008	Tmg	Type (I) Quartz Vein	Silicified, jarosite and iron-stained, medium-grained, two-mica granite. One large, irregular, pure, glassy qtz vein. Found in large boulder in float next to large outcrop. Bleaching and staining increase with proximity to vein.
HPP-3-17	3	6/9/14	190	623385	4468093	6969	Tmg	Type (IV) Microcrystalline Quartz Vein	Four parallel, microcrystalline qtz veins with jarosite staining in strongly silicified two-mica granite with hematite and jarosite staining.
HPP-3-18	3	6/10/14	191	622665	4468047	6528	Tgm	Type (III) Quartz Vein	One large, milky, massive qtz pod, (or filled mirolitic cavity), with strong jarosite staining in aplitic, bleached, muscovite-bearing granite.
HPP-3-19	3	6/10/14	192	622726	4468113	6699	Tgm	Type (I) Quartz Vein	mbqfGr granite with some jarosite staining and one small, milky/glassy qtz vein.
HPP-3-20	3	6/10/14	193	623098	4468323	6819	Tgm	Type (I) Quartz Vein	Jarosite stained, two-mica granite with one pure/massive qtz vein, (also stained).
HPP-3-21	3	6/10/14	194	623165	4468230	6899	Tgm	QF Pegmatite	Bleached mbqfGr granite with pervasive leiseegang alteration/staining. Two parallel, tabula QF Peg veins with some pegmatitic qtz along core of the vein.

Sample ID	Thickness (cm)	Potassic	Skarn	Phyllic	Chlorite-Sericite	Silicification	Jarosite	Strike	Dip	Dip Direction	Additional Notes
HPP-3-11	250							65	90		Dike?
HPP-3-12	2.5-5							122	76	NE	
HPP-3-13	4-6							120	73	NE	
HPP-3-14	10-13							128	83	SW	
HPP-3-15	40										
HPP-3-16	3-18					Yes	Yes				End megacrystic microclines.
HPP-3-17	1.5-3.5					Yes	Yes	27	77	SE	
HPP-3-18	150 x 60						Yes				
HPP-3-19	1-2						Yes	67	72	SE	
HPP-3-20	3						Yes	52	21	NW	
HPP-3-21	4-5						Yes	131	62	NE	

Sample ID	Traverse #	Date	Waypoint ID	Point East	Point North	Point Elev. (ft)	Host Unit	Sample Lithology/Feature Type	Sample Description
HPP-3-22	3	6/10/14	198	621978	4468364	6986	Tmg	Type (IV) Microcrystalline Quartz Vein	Extremely weathered, leisegang (SO4) altered zone in bqfGr. Granite around SO4-stained qtz vein. Rock is more friable with some more resistant zones. Biotite still present in altered rock.
HPP-3-23	3	6/10/14	199	621919	4468293	6888	Tmg	Type (III) Quartz Vein	bqfGr(SO4)3(Q-massive). Bleached, leisegang altered granite with numerous jarosite-qtz veinlets and one large, discontinuous qtz pod/zone, possibly formed at the coalescence of several veinlets. Unusually large, massive milky white qtz with strong jarosite staining.
HPP-3-24	3	6/10/14	200	621829	4468262	6751	Tmg	Type (III) Quartz Vein	Bleached, leisegang altered two-mica granite in a zone around a massive, irregular, milky-white qtz vein with strong jarosite staining. Unaltered granite is unbleached and contains two micas.
HPP-3-25	3	6/10/14	201	621460	4468145	6658	Tmg	QF Pegmatite	One lone QF Peg vein in pervasively leisegang altered aplitic granite. Granite shows alteration of biotites and jarosite and iron staining. Entire area shows bleaching and leisegang alteration.
HPP-3-26	3	6/10/14	202	621382	4468081	6544	Tmg	MQF Pegmatite	Two mica granite with small QF Peg zone with iron and jarosite staining along bleached margins.
HPP-3-27	3	6/10/14	203	621345	4468132	6550	Tmg	Type (IV) Microcrystalline Quartz Vein	175 cm wide zone of bleaching and leisegang-alteration around a complex qtz vein system with at least two veins (4 cm, 2 cm thicknesses), converging to one VUGGY qtz vein approximately 7-8 cm wide. Strong SO4 staining in veins. Unaltered wall rock shows layered parallel QF Peg zones.
HPP-3-28	3	6/10/14	204	621113	4468204	6538	Tmg	Type (I) Quartz Vein	Moderately altered, bleached, jarosite-stained granite with one massive milky qtz vein crosscutting.
HPP-3-29	3	6/10/14	205	620979	4468164	6534	Tmg	MQF Pegmatite	Altered, weathered two-mica granite (med-grained, no pegmatitic megacrystic microclines). One MQF Peg zone, some jarosite staining in wall rock, but none in vein. Small red, somewhat round crystals (3-7 mm) in vein material. Looks like garnet.

Sample ID	Thickness (cm)	Potassic	Skarn	Phyllic	Chlorite-Sericite	Silicification	Jarosite	Strike	Dip	Dip Direction	Additional Notes
HPP-3-22	1-2						Yes	40	25	NW	
HPP-3-23	11-26.5						Yes	50	73	NW	
HPP-3-24	25-35						Yes	33	85	NE	
HPP-3-25	2						Yes	46	79	SE	
HPP-3-26	5-10						Yes	147	66	NE	
HPP-3-27	7-8					Yes	Yes	113	67	NE	
HPP-3-28	2.5-3.5						Yes	46	88	SE	
HPP-3-29	5						Yes	8	76	NW	

Sample ID	Traverse #	Date	Waypoint ID	Point East	Point North	Point Elev. (ft)	Host Unit	Sample Lithology/Feature Type	Sample Description
HPP-3-30	3	6/10/14	207	620996	4468110	6630	Tmg	MQF Pegmatite	Leisegang altered granite with few biotites, (mostly removed?), and one QF Peg zone. Both milky and glassy qtz crystals present. Vein is poorly exposed and eroded.
HPP-3-31	3	6/10/14	208	620951	4468047	6582	Tmg	Type (III) Quartz Vein	Stained, medium-grained biotite granite with discontinuous, pure, milky qtz vein. Iron staining around vein. Vein is perpendicular to dominant fracture set and foliation.
HPP-3-32	3	6/10/14	209	620931	4468054	6632	Tmg	Type (III) Quartz Vein	Weathered, bleached, stained, pervasively fractured two-mica granite similar to HPP-3-31. One massive qtz zone, (milky, pure), in a discontinuous MQF Peg zone. Zone of bleaching up to 35 cm to each side of qtz zone. Large (1-2 cm) mica books in MQF Peg zone.
HPP-3-33	3	6/10/14	210	620858	4468021	6527	Tmg	QF Pegmatite	Bleached, biotite-bearing granite with large microcline megacrysts. Numerous (at least 4) QF Peg zones. The largest, (sampled), is dominated by large (5-15 cm) grey glassy qtz phenocrysts. Zone of bleaching around veins up to 1.5 m wide (total).
HPP-3-34	3	6/10/14	211	620685	4468261	6482	Tmg	Type (IV) Microcrystalline Quartz Vein	Highly silicified granite with some iron oxide staining. A polished qtz surface, (microcrystalline grey qtz), possibly due to flexural slip/faulting. Very smooth. This surface appears to be the dip face of the qtz vein.
HPP-3-35	3	6/10/14	212	620250	4468238	6481	Tmg	Type (V) Microcrystalline Quartz Vein	Massive microcrystalline qtz zone, (dull white). Likely a massive qtz vein, (also possibly a zone of extremely silicified granite). Surrounding rock is bleached and FeO-stained. Zone is poorly exposed.
HPP-3-36	3	6/11/14	217	628574	4468110	8112	Ttc	Metased (Quartzite)	Massive, blocky, orange-red stained, buff colored quartzite. Prospect Mtn unit. Mica in quartzite? Lots of mica, some vuggy qtz crystal growth, and a cubic magnetite crystal (2 mm) in sample.

Sample ID	Thickness (cm)	Potassic	Skarn	Phyllic	Chlorite-Sericite	Silicification	Jarosite	Strike	Dip	Dip Direction	Additional Notes
HPP-3-30	20						Yes	29	46	NW	
HPP-3-31	12.5							2			
HPP-3-32	17							11			
HPP-3-33	33-34						Yes	53	50	SE	Megacrystic Microclines.
HPP-3-34	3-5					Yes		95	51	SW	
HPP-3-35	45										Fault-hosted qtz vein?
HPP-3-36											Contact metamorphic aureole.

Sample ID	Traverse #	Date	Waypoint ID	Point East	Point North	Point Elev. (ft)	Host Unit	Sample Lithology/Feature Type	Sample Description
HPP-3-37	3	6/11/14	218	628265	4468092	8222	Ttc	Type (V) Microcrystalline Quartz Vein	bqfGr(SiO ₂ , C-S)3(Qtz-micro)(green). Intensely altered, (partially reacted biotites), granite with 4-5 mm enmeshed, polygonal qtz and fspar crystals with small (1-3 mm) masses of biotite. Rock appears green/grey, (chloritization of biotites?). Two large, parallel(?) zones of MicroXL qtz. Forms linear ridge that is oriented subparallel to contact with metasedimentary rocks, (N-S).
HPP-3-38	3	6/11/14	219	628227	4468357	8113	Ttc	Type (II) (wallrock) Quartz Vein	Impure, banded marble/limestone in contact with bqfGr(SiO ₂ , Chlorite-sericite)3(Q-massive). Contact is irregular with zones of granite intruding into limestone/marble. Several massive milky qtz veins in limestone/marble, unclear if veins continue into granite.
HPP-3-39	3	6/11/14	220	628260	4468322	8090	Ttc	Type (I) Quartz Vein	bqfGr(SiO ₂ , chlorite-sericite)3(Qtz-glassy)(green). Silicified, chlorite-sericite altered granite with pervasive parallel green/grey fractures, (healed) and at least two parallel qtz veins, (stained green).
HPP-4-01	4	7/26/14	283	625757	4461970	7377	Tcc	Type (II) (skarn) Quartz Vein	Hydrothermal qtz vein in skarn wall rock. Vein has aplitic selvages and clear qtz core. Vein extends from aplitic granite on other side of contact. Vein is parallel to deformation foliation. Vein bifurcates into separate aplite and qtz veins in the skarn.
HPP-4-02	4	7/26/14	284	629519	4463081	6507	Tcc	Type (II) (skarn) Quartz Vein	Med-sized clear qtz vein cutting across diopside skarn. Skarn is approx 2 m wide on contact between granite and metasediments, (contains garnet and diopside). Metasediments are limestones and marbles.
HPP-4-03	4	7/26/14	285	629658	4462862	6692	Tcc	Type (II) (skarn) Quartz Vein	Contact skarn (weathered) with major thick (4-7 cm) qtz veining. Intergrowth of euhedral garnets along margins of qtz veins. Scheelite and ferberite-hubnerite present as ore minerals. Irregular contact, difficult to follow. Granite near contact is coarse-grained with large qtz megacrysts, (1 cm), with matrix of finer-grained feldspar.

Sample ID	Thickness (cm)	Potassic	Skarn	Phyllic	Chlorite-Sericite	Silicification	Jarosite	Strike	Dip	Dip Direction	Additional Notes
HPP-3-37	10-20				Yes	Yes		32	8	SE	
HPP-3-38	6				Yes	Yes		100	42	SW	Contact Metamorphic Aureole
HPP-3-39	1-3				Yes	Yes		20	52	SE	
HPP-4-01	1.5							45	80	NW	Pogonip LS roof pendant prospect.
HPP-4-02	3		Yes								Star Tungsten Mine
HPP-4-03	4-7		Yes								Star Tungsten Mine

Sample ID	Traverse #	Date	Waypoint ID	Point East	Point North	Point Elev. (ft)	Host Unit	Sample Lithology/Feature Type	Sample Description
HPP-4-04	4	7/26/14	286	629807	4462976	6400	Tcc	Rhyodacite	Porphyritic granodiorite dike intruding into limestone country rock. 2-3 mm qtz and euhedral fspar phenocrysts. Amphiboles in matrix. Unclear orientation. Thickness >5 m. Grey in color, at least more mafic than any other granitic unit.
HPP-4-05	4	7/26/14	287	626763	4466187	7692	Ttc	Granite	Contact between megacrystic/porphyritic biotite granite and med-grained biotite granite with no microcline megacrysts. Microdiorite xenoliths (5-15 cm) are present in both units. Contact is sharp and undulating. No obvious genetic relationship between units. At some locations, contact is gradational. Continuously visible for 15-20 m.
HPP-4-06	4	7/26/14	288	627144	4469124	8353	Ttc	Skarn	Small contact skarn at N margin of HPP (contact with impure white/grey banded ls). Skarn is a 5-10 cm zone on the edge of the outcrop and extends into outcrop (south). Skarn is red/brown with garnet-rich and diopside-rich zones. Large, (5-7 cm) qtz crystals along skarn contact with granite. Granite is aplitic, (subsolidus deformation), with no megacrysts. Some deformed aplites.
HPP-4-07	4	7/27/14	289	622531	4469575	7170	Tgm	MQF Pegmatite	bmqf monzogranite with muscovite-rich veins. Monzogranite has equal parts muscovite and biotite, with zones of S04 staining and an overall subhorizontal foliation and fracture pattern. Sampled vein is approx. 17 cm wide and is planar. Moderate (3-6 cm) splays of muscovite crystals and blocky fspar dominates veins. Also, large (7-12 cm) pods of milky qtz are found in veins.
HPP-4-08	4	7/27/14	291	622379	4469686	7181	Tgm	Type (III) Quartz Vein	Large, planar, massive milky qtz vein with jarosite staining in subvertically-foliated, fractured and stained monzogranite.
HPP-4-09	4	7/27/14	292	622291	4469944	7552	Tgm	Type (I) Quartz Vein	Strongly altered two-mica monzogranite with extreme jarosite staining near and as haloes around pure milky qtz veins. Qtz veins are vuggy in some locations with gypsum alteration in wall rock and extreme jarosite staining.
HPP-4-10	4	7/27/14	293	622576	4468576	7396	Tmg	QF Pegmatite	A lone, med-sized QF Peg vein in jarosite-stained two-mica Green Mtn. monzogranite.

Sample ID	Thickness (cm)	Potassic	Skarn	Phyllic	Chlorite-Sericite	Silicification	Jarosite	Strike	Dip	Dip Direction	Additional Notes
HPP-4-04	>500										
HPP-4-05	Visible for 1500-2000										
HPP-4-06	5-10		Yes	Yes							
HPP-4-07	17						Yes	63	69	NW	
HPP-4-08	30						Yes	135	57	NE	
HPP-4-09	2-4			Yes			Yes	85	77	NE	
HPP-4-10	7-12						Yes	107	61	NE	

Sample ID	Traverse #	Date	Waypoint ID	Point East	Point North	Point Elev. (ft)	Host Unit	Sample Lithology/Feature Type	Sample Description
HPP-4-11	4	7/27/14	294	622266	4468702	7160	Tmg	MQF Pegmatite	A large aplite zone with pegmatitic lenses and zones. Pegmatite contains milky qtz, fspar, and minor muscovite. Liesegang alteration (orange alteration haloes and bands), pervasively through outcrop.
HPP-4-12	4	7/27/14	295	622023	4467992	6593	Tmg	Type (IV) Microcrystalline Quartz Vein	A large, multi-zoned vuggy, pure milky qtz zone with individual zones (some parallel, some oblique), of pure qtz (2-3 cm wide). Host rock is two-mica monzogranite with no megacrysts and a dominant subhorizontal foliation.
HPP-4-13	4	7/27/14	296	621007	4468090	6619	Tmg	MQF Pegmatite	MQF Pegmatite vein in two-mica granite, (no microcline megacrysts). Vein contains vlarge Titanite (1-3 cm). There are three crystals of titanite. Some muscovite books (~1 cm).
HPP-5-01a	5	8/15/15		625108	4461461		Tcc	Granite (aplitic)	Equigranular, aplitic white (monzo?)granite with late, shreddy oxidized biotite phenocrysts. In contact with diopside, hypersthene-rich skarn. Quartz veins in skarn and dispersed throughout granite (thin + discontinuous, ~1 cm wide). Sample A is silicified, K-metasomatic?
HPP-5-01b	5	8/15/15		625108	4461461		Tcc	Skarn	Diopside, hypersthene-rich skarn containing thin Subtype 1 quartz veins (discontinuous, ~1 cm). Crystalline
HPP-5-02	5	8/15/15		624666	4461233	7374	Tcc	Miarolitic Cavity	
HPP-5-03	5	8/15/15		624640	4461182	7289	Tcc	Type (V) Microcrystalline Quartz Vein	Massive, discontinuous zone of pure microcrystalline hydrothermal quartz vein. Appears to extend farther than exposure, blebby near southern plutonic contact on backside of large tower-like outcrop. Two other exposures of zone, also large outcrops, approx 100 m (one WNW, the other S).

Sample ID	Thickness (cm)	Potassic	Skarn	Phyllic	Chlorite-Sericite	Silicification	Jarosite	Strike	Dip	Dip Direction	Additional Notes
HPP-4-11	100-150			Yes			Yes	171	61	NE	
HPP-4-12	30-40				Yes	Yes		119	68	NE	
HPP-4-13	7-10							178	73	NE	
HPP-5-01a						Yes					
HPP-5-01b	1		Yes								
HPP-5-02		Yes			Yes	Yes	Yes				
HPP-5-03	400-500							110	~90		

Sample ID	Traverse #	Date	Waypoint ID	Point East	Point North	Point Elev. (ft)	Host Unit	Sample Lithology/Feature Type	Sample Description
HPP-5-04	5	8/15/15		624406	4460683		Tcc	Granite (monzo)	Relatively unaltered monzogranite with alkali feldspar megacrysts and sparse mafic/microdioritic enclaves. Very slightly orientation of crystals N-S. No veining; very close to contact (~90 m). No sample.
HPP-5-05	5	8/15/15		625273	4460882	7634	Tcc	Granite (monzo)	Bleached, silicified, possibly sericite-altered monzogranite. Original igneous textures largely destroyed. Discrete bands of jarosite staining. No obvious veining. Isolated outcrop very close to or within carbonate country rock.
HPP-5-06	5	8/15/15		625411	4461305	7251	Tcc	Granite (monzo)	Within 70 m of contact with strongly folded, rhythmically-bedded limestone-shale/marble. Sample is of a strongly bleached, silicified, and possibly C-S altered monzogranite (light green color). Textures mostly destroyed. Qtz crystals still somewhat visible. Microfractured.
HPP-5-07	5	8/15/15		629814	4463520	6955	Tcc	Granodiorite	Granodiorite body in contact with silicified, aplitic monzogranite. Dike geometry is unclear; may be more than one dike. Somewhat discontinuous, up to 7-8 m wide. Weathers red/dark grey with abundant k-feldspar phenocrysts. Granodiorite/dacite is cut by one aplitic vein (~7 cm).
HPP-5-08	5	8/15/15		629803	4463323	7203	Tcc	Granite (altered)	Directly observed contact between bleached leucogranitic aplitic apophysis and texturally destroyed calc-silicate marble wallrock. Contact zone is approx. 35-40 cm-wide, tremolite-rich (light yellow color with band of grey/black directly adjacent to calc-silicate. Wallrock may also be a stope block entrained in aplitic granite. Sample is from contact zone.
HPP-5-09	5	8/15/15		629881	4463370	6911	Tcc	QF Pegmatite	Classic QF Pegmatite vein in intermixed granodiorite/dacite and aplitic monzogranite. Vein is discontinuous; with approximately equal abundances of glassy quartz and white alkali feldspar.
HPP-5-10	5	8/16/15		623526	4461750	6856	Tcc	Type (IV) Microcrystalline Quartz Vein	Very large, Type (IV), microcrystalline Qtz vein/dike approx 1 m wide. Vein has multiple cores; vuggy cockade/colliform textures. In contact with strongly sericitized granite with some jarosite staining.

Sample ID	Thickness (cm)	Potassic	Skarn	Phyllic	Chlorite-Sericite	Silicification	Jarosite	Strike	Dip	Dip Direction	Additional Notes
HPP-5-04											
HPP-5-05						Yes					
HPP-5-06					Yes	Yes					
HPP-5-07	700-800										
HPP-5-08			Yes								
HPP-5-09	6-8							135	90		
HPP-5-10	100							110	90		

Sample ID	Traverse #	Date	Waypoint ID	Point East	Point North	Point Elev. (ft)	Host Unit	Sample Lithology/Feature Type	Sample Description
HPP-5-11	5	8/16/15		623456	4460910	7507	Tcc	Type (IV) Microcrystalline Quartz Vein	Intensely altered and veined outcrop of granite near southern margin of HPP. Veins are Type (IV) microcrystalline qtz veins with many subsidiary cores that chaotically cut and crosscut each other. Granite is grey/green; may be C-S alteration. Characterized by addition of magnetite + sericite and removal of feldspar.
HPP-5-12	5	8/16/15		622957	4460571	7541	Tcc	Type (II) (wallrock) Quartz Vein	Large, complex, (micro?)crystalline quartz vein with two mine adits and obvious Cu mineralization (malachite). Qtz vein is stained strongly with jarosite; Cu minerals present as aggregates and fracture coatings and infill. Wallrock is sparry calc-silicate marble. Black hornfels (10-12 cm wide) at contact of vein and wallrock.
HPP-5-13	5	8/16/15		622831	4460582	7685	Tcc	Granite (monzo)	Phyllic altered granite in dumps from mine at S HPP contact. ~25 m downslope (N) from 5-12. At surface is a large (~2 m) microXL qtz vein in thinly to med-bedded silty calc-silicate marble, (±sparry). In dumps, there is (meta?) sandstone and kaolinite-rich marble units. Granite shows addition of biotite, sericite, and K-spar and kaolinite. Granite is white-grey with few original textures.
HPP-5-14	5	8/16/15		621801	4461993	6709	Tcc	Granite (monzo)	Another outcrop of highly altered, aplitic-granular monzogranite cut chaotically by Type (IV) microcrystalline quartz veins. Rock is white/green, with indications of C-S alteration. Quartz veins range from <1-40 cm. Similar to HPP-5-11.

Sample ID	Thickness (cm)	Potassic	Skarn	Phyllic	Chlorite-Sericite	Silicification	Jarosite	Strike	Dip	Dip Direction	Additional Notes
HPP-5-11	1-100			Yes							
HPP-5-12	200		Yes					0	29	W	
HPP-5-13	200			Yes							
HPP-5-14	1-40			Yes							

APPENDIX C: STEREAONETS

C.1 Master Stereonet

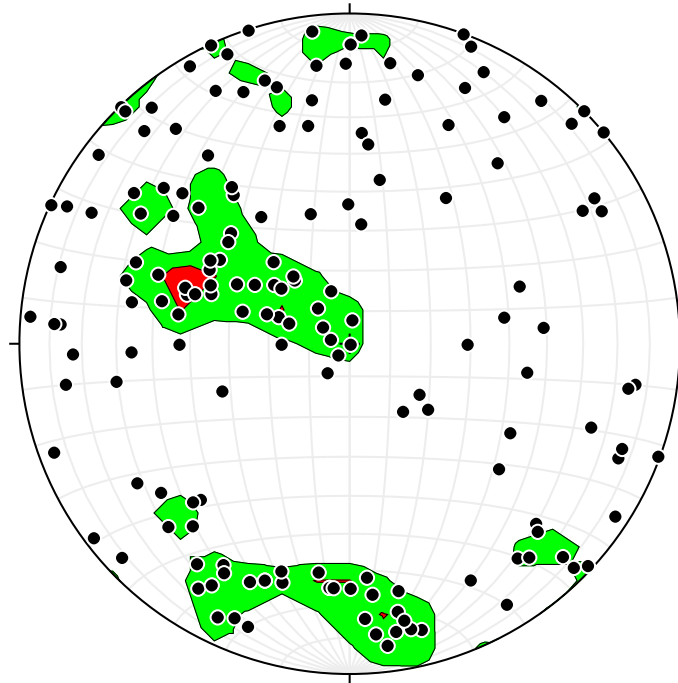


FIGURE C.1.1 - Compiled stereonet of orientations for all feature types in the HPP.

C.2 Stereonets for Intrusive Units

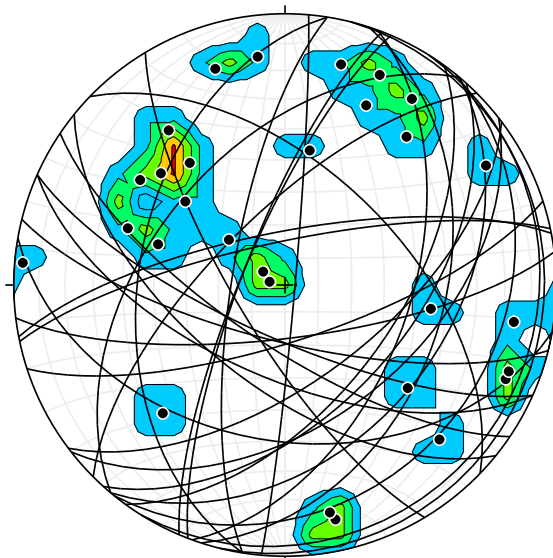


FIGURE C.2.1 - Stereonet for all feature types in the early stage Ttc granodiorite.

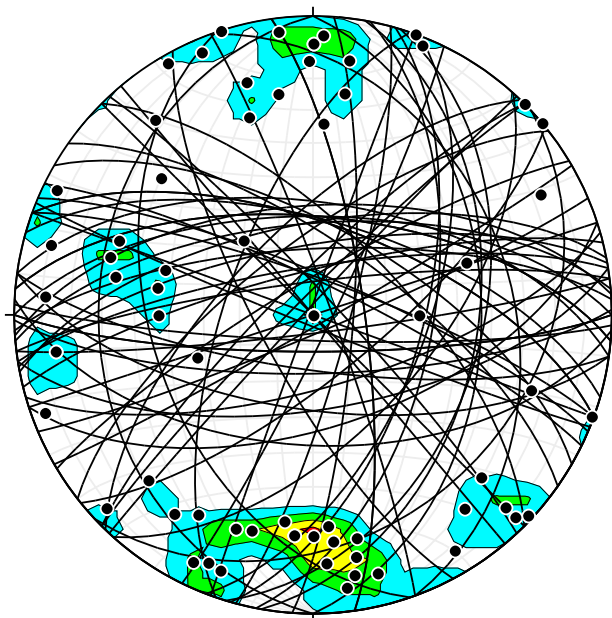


FIGURE C.2.2 - Stereonet for all feature types in the early stage Tcc monzogranite.

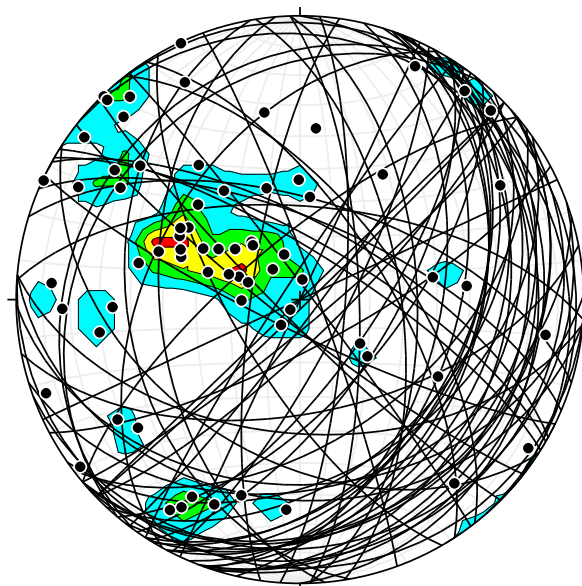


FIGURE C.2.3 - Stereonet for all feature types in the late stage Tmg biotite and two-mica monzogranite sheets and dikes.

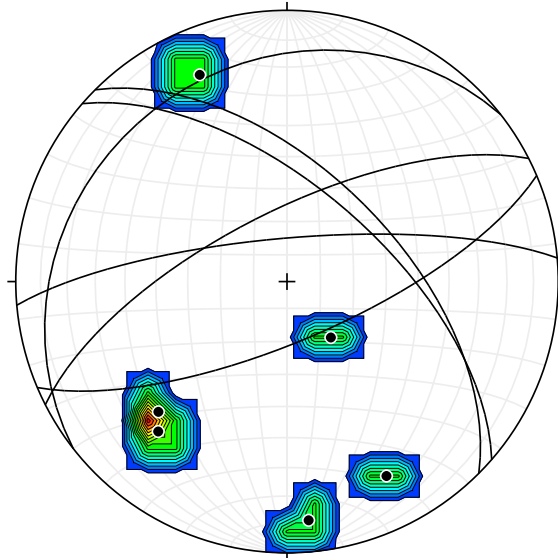


FIGURE C.2.4 - Stereonet for all feature types in the late stage Tgm two-mica monzogranite.

C.3 Stereonets for Feature Types

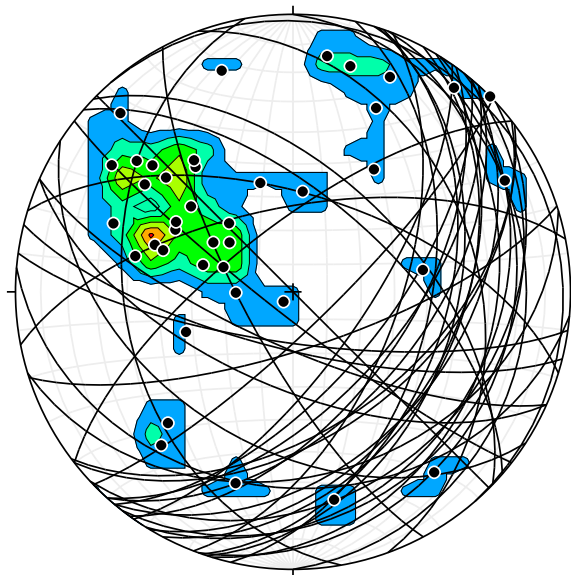


FIGURE C.3.1 - Stereonet for all QF Pegmatites.

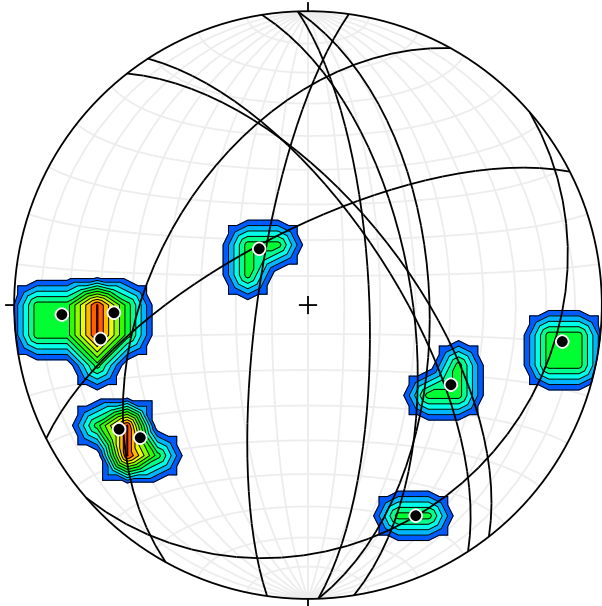


FIGURE C.3.2 - Stereonet for all MQF Pegmatites.

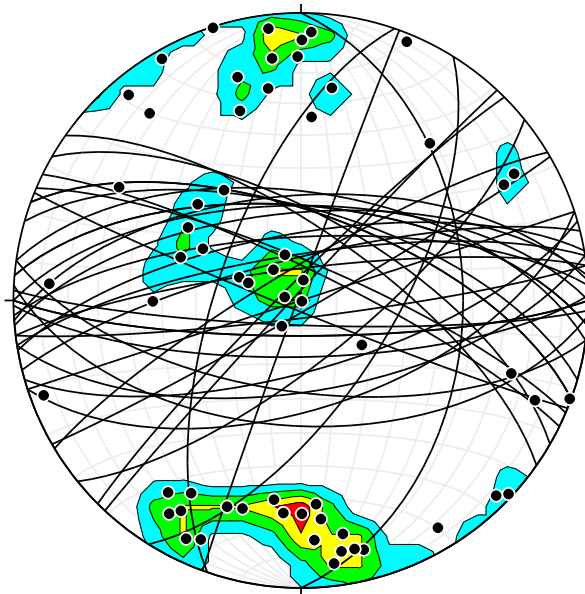


FIGURE C.3.3 - Stereonet for all Aplites (Homogeneous, QF-Cored, Layered QF-Pegmatite).

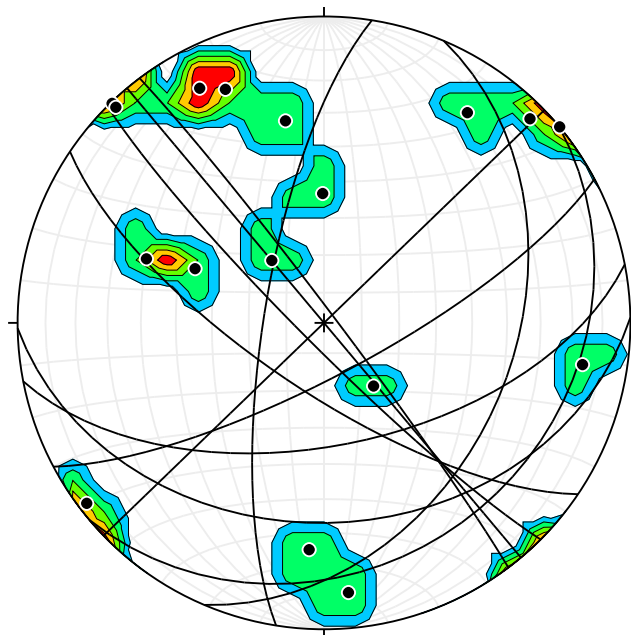


FIGURE C.3.4 - Stereonet for all Type (I) Quartz Veins.

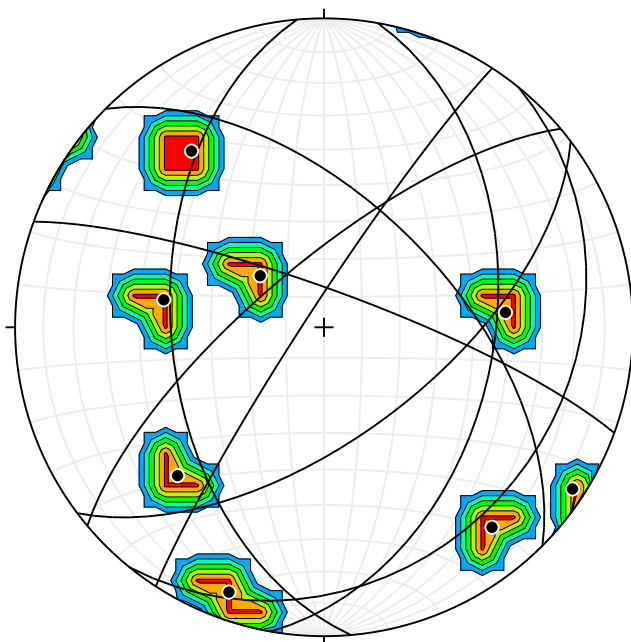


FIGURE C.3.5 - Stereonet for all Type (III) Quartz Veins.

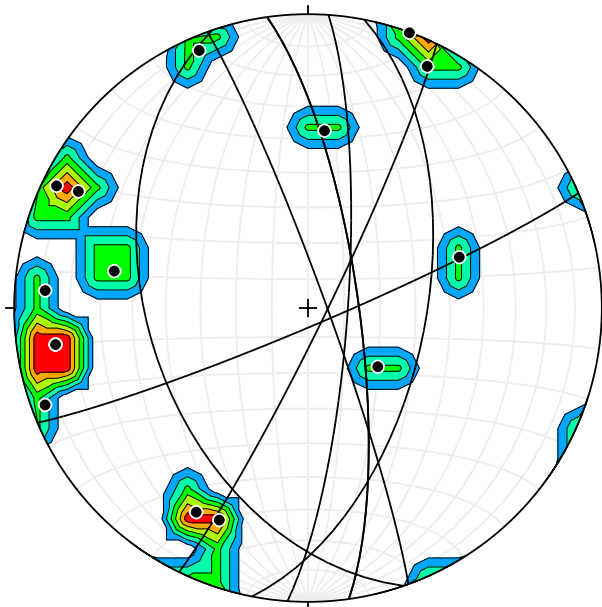


FIGURE C.3.6 - Stereonet for all Type (IV) Microcrystalline Quartz Veins.

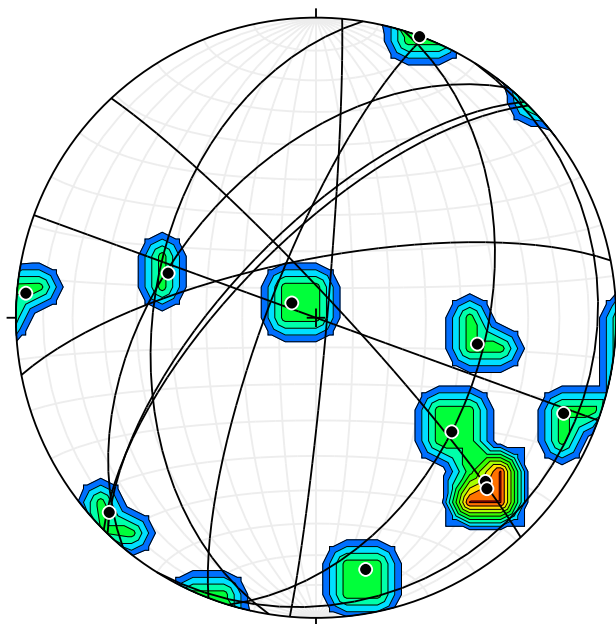


FIGURE C.3.7 - Stereonet for all Type (V) Microcrystalline Quartz Veins.

APPENDIX D: PETROGRAPHIC DESCRIPTIONS

HPP-1-03 Type (II) (wallrock) Quartz Vein

Sample is from a milky, crystalline, 10-12 cm-wide Type (II) (wallrock) quartz vein in contact metamorphosed Opm impure carbonate wallrock units at the contact with the early stage Tcc monzogranite. Mineral Assemblage: Quartz. Vein quartz crystals are coarse (200-2000 μm), generally anhedral (but also rarely subhedral). Deformation is almost entirely brittle; the sample is cut by numerous parallel fractures at the thin section scale, but offset is difficult to assess. Minor recrystallization along crystal contacts is observed. No associated alteration is observed in this outcrop.

HPP-1-04 Type (I) Quartz Vein

Sample is from a 1 cm-wide crystalline Type (I) Quartz Vein in fine-grained monzogranite in the early stage Tcc monzogranite near the pluton contact. Mineral Assemblage: Quartz. Vein quartz is coarse to very coarse (500-10000 μm) and generally anhedral-subhedral, with some crystals large enough to span the width of the vein. The vein-wallrock contact is very sharp and is generally curvilinear. Several brittle fractures orthogonally cutting the vein are observed. Recrystallization along crystal contacts is ubiquitous, while some large crystals exhibit undulose extinction. Host rock is generally fine-grained/aplitic (100-400 μm) and feldspar-rich, but shows no evidence of hydrothermal alteration.

HPP-1-17a Aplite

Sample is from a 3 cm-thick texturally homogeneous aplite in coarse-grained early phase Tcc monzogranite. Rock is covered with lichens, and highly weathered with a ~7 cm thick weathering rind. Mineral assemblage: Quartz + Alkali Feldspar + Biotite \pm Muscovite. Large (1000-4000 μm) weathered alkali feldspars within altered, weathered aplite vein with subhedral-anhedral crystalline quartz core. Fine-grained micas fill fractures. There exists a large population of small, anhedral, round quartz crystals within wallrock. Some silicification and late, hydrothermal mica growth is possible. Thin section has been overly thinned in places.

HPP-1-20 Granite (altered)

Sample is from an area of intense silicification and isolated hydrothermal quartz in the early stage Tcc monzogranite. Rock appears matte white with no clear distinctions between minerals. No veins observed. Mineral assemblage: Quartz + Alkali Feldspar. Sample is very coarse-grained to pegmatitic (0.1-2.5 cm), with intergrowth of early subhedral crystalline quartz with later subhedral alkali feldspar. On average, alkali feldspar crystals are larger than quartz. Additionally, round, anhedral crystal blebs (~1000 μm) and thin ribbons of crystalline quartz (~50-100 μm wide, ~200-1000 μm long) are observed in the cores of alkali feldspar crystals. Little evidence of deformation is observed in this sample, with the exception of several minor brittle fracture zones and isolated zones of recrystallization.

HPP-1-24b Mirolitic Cavity

Sample is from a ~700 cm², roughly oblate (in outcrop) mirolitic cavity in the early stage Tcc monzogranite. Mineral Assemblage: Quartz + Alkali Feldspar ± Muscovite ± Magnetite. No open space preserved in this mirolitic cavity. Contact with fine-grained, aplitic monzogranite wallrock is invariably sharp. Hydrothermal quartz and Alkali feldspar are both very coarse to pegmatitic (>1 cm), but quartz is generally subhedral, while alkali feldspar is euhedral-subhedral. Quartz crystals are generally smaller than alkali feldspar crystals, and demonstrate several zones of uniform extinction. Alkali feldspar exhibits well-developed lathes. No pervasive deformation fabrics or wallrock alteration are observed.

HPP-1-25d Type (II) (skarn) Quartz Vein

Sample is from a minor (<1.5 cm) crystalline quartz vein in a historically mined skarn/carbonate replacement deposit in a contact metamorphosed Opm impure carbonate roof pendant in the early stage Tcc monzogranite. Vein mineral assemblage: Quartz + Alkali Feldspar + Plagioclase ± Diopside ± Hydrogrossular ± Titanite. Skarn mineral assemblage: Diopside + Hydrogrossular + Sericite + Tremolite ± Calcite. Microgranular texture was observed around vein. Coarser (>700 μm), blocky, subhedral diopside grains are scattered throughout quartz-feldspar vein material. Two-stage reaction front observed between quartz and skarn. The primary (closest to quartz vein) reaction front is ~2500 μm wide and dominated by impure coarser crystalline quartz with sericite intergrowths (<15 μm) and minor coarse, diamond-shaped titanite (~500 μm). The secondary (closest to skarn) reaction front is a sublinear zone ~300 μm wide and dominated by subhedral blocky diopside (<200 μm). Large area between primary and secondary reaction fronts of feldspar demonstrates uniform extinction. Numerous small, altered diopside grains were observed along primary reaction front. Secondary reaction front characterized by dispersed, fine-grained white mica flecks in feldspar and quartz crystals.

HPP-1-27 Type (IV) Microcrystalline Quartz Vein

Sample is from a milky white, minor (0.5-1 cm) Type (IV) Microcrystalline Quartz Vein in the early stage Tcc monzogranite. Vein Mineral Assemblage: Quartz, Microcrystalline Quartz. Wallrock Mineral Assemblage: Alkali Feldspar + Quartz + Microcrystalline Quartz + Chlorite + Sericite (+ Jarosite). Vein contains a relatively fine-grained (200-1000 μm) crystalline quartz core (~1 cm wide) with evidence of intense recrystallization. Thin (~200-500 μm) zones of microcrystalline quartz bound both sides of the vein, and crosscut the vein and the surrounding wallrock. Monzogranitic wallrock is fine-grained, heavily C-S altered, and fractured. Minor parallel to subparallel veins on either side. Wallrock also shows pervasive microfracturing and orange-red jarosite staining around the vein up to distances of 12 cm. Signs of pervasive fluid flow throughout sample area. Some small (<5000 μm) vugs lined with drusy quartz are observed within microcrystalline quartz zones along vein margins.

HPP-1-30 Type (III) Quartz Vein

Sample is from a 4-13 cm-wide, poorly exposed, zone/pod of pure, milky, crystalline quartz in C-S altered, highly fractured monzogranite from the early stage Tcc monzogranite. Mineral Assemblage: Quartz. Zone is crosscut and offset by multiple fractures. Quartz crystals are pegmatitic (>2 cm), contain a very high density of fluid

inclusions, and exhibit several recrystallized fracture zones. Wallrock alteration was not observed petrographically, but altered rock appears grey/green, fine-grained/aplitic, and granular in hand sample.

HPP-1-35a Aplite

Sample is from a 3 cm-thick, weathered, grey/dark grey, granular, homogeneous aplite vein in weathered, coarse-grained, early stage monzogranite. Mineral assemblage: Quartz + Alkali Feldspar + Biotite ± Magnetite/Hematite. Vein material exhibits generally equigranular, coarse-grained, sucrosic textures. Relatively fine-grained (<300 μm), anhedral masses of opaque crystals (magnetite/hematite) disseminated throughout wallrock and vein, otherwise very homogenous.

HPP-1-35b QF Pegmatite

Sample is from a 5 cm wide, coarse-grained quartz-feldspar pegmatite zone crosscut by HPP-1-35a in the early stage Tcc Monzogranite. Fine to medium grained. Mineral assemblage: Quartz + Plagioclase + Alkali Feldspar + Biotite + Magnetite/Hematite ± Galena. Alkali feldspar is dominantly microcline with subordinate oligoclase. Small, vuggy quartz pockets (<2000 μm) were observed containing an anhedral opaque mineral determined to be galena from reflected light petrography (appears silver in hand sample). Microcline contains minor perthitic segregations.

HPP-1-36a Type (IV) Microcrystalline Quartz Vein

Sample is from a thin (1.5-2 cm) Type (IV) Microcrystalline Quartz Vein in the early stage Tcc monzogranite. Mineral Assemblage: Quartz + Microcrystalline Quartz + Magnetite/Hematite. At least three cores of crystalline quartz (1000-4000 μm) are observed within larger zones of relatively pure microcrystalline quartz (5000-9000 μm). These zones do contain parallel, thin (~150 μm), lenses of opaque material (likely magnetite partially or completely oxidized to hematite), and occasional, small crystalline quartz clasts (~200 μm). Quartz within crystalline cores is relatively coarse (50-2500 μm), subhedral, and appears to be truncated in some areas by the microcrystalline quartz. Several quartz crystals are heavily deformed and exhibit undulose extinction, while others appear almost completely undeformed. In hand sample, parallel zones of jarosite staining are visible within veins, corresponding to the lenses of opaque material observed in thin section. Wallrock is friable and may exhibit some evidence of C-S alteration.

HPP-1-56 QF Pegmatite

Sample is from a very poorly exposed, relatively thin (4-5 cm), Quartz-Feldspar pegmatite zone in unaltered, early stage Tcc monzogranite. Mineral assemblage: Alkali Feldspar + Quartz ± Muscovite. Vein appears to have at least one narrow (~1 cm) aplitic zone, however limited exposure precludes determinations of the continuity of this feature. Quartz crystals are large (<1 cm), typically subhedral, and often included in larger (~2 cm), subhedral-euhedral, alkali feldspar crystals. Some open space (~1000-5000 μm) is preserved on and around euhedral crystals. The contact with the coarse-grained, weathered, but relatively unaltered monzogranite wallrock ranges from sharp to gradational with respect to grain size. Alkali feldspar crystals exhibit myrmekitic textures. Minor recrystallization is observed in smaller quartz crystals.

HPP-1-59 Granite (altered)

Sample is from chlorite-sericite altered, silicified, and weathered granite in the Tcc monzogranite unit. Rock is crumbly and friable with some foliation (possibly fracture induced) visible. Some megacrystic alkali feldspar crystals observed in otherwise medium to fine-grained matrix. Mineral assemblage: Quartz + Microcrystalline Quartz + Plagioclase ± Biotite ± Chlorite ± Sericite. Lots of microcrystalline quartz, forming indistinct veins. Strong sericitization of feldspars; can be seen altering along twinning. Some feldspars are entirely destroyed by alteration. Chlorite entirely replaces most biotite crystals. Few very large quartz crystals along edges of section. Example of chlorite-sericite alteration and overprinting microcrystalline silicification and fracturing.

HPP-1-63 Type (IV) Microcrystalline Quartz Vein

Sample is from a large (35-45 cm), complex zone of Type (IV) Microcrystalline Quartz Veins with pervasive jarosite staining and silicification in the early stage Tcc monzogranite. Mineral Assemblage: Microcrystalline Quartz + Quartz. Multiple veins of microcrystalline quartz are accompanied by volumetrically significant, elongate vuggy zones lined with cockade/colliform, euhedrally-terminated crystalline quartz crystals (<500 µm). These features are hosted by strongly silicified, C-S altered, quartz-rich monzogranite. In thin section, small veinlets crosscut and form the matrix for crystalline quartz segregations and isolated crystals (<1000-5000 µm). It is apparent that crystalline quartz veins were crosscut and dismembered by microcrystalline quartz growth. At least one zone of relatively fine-grained crystalline quartz (<1000 µm) is continuous at the thin section scale and exhibits relatively minor evidence of recrystallization.

HPP-1-66 Type (V) Microcrystalline Quartz Vein

Sample is from a relatively small (5 cm wide), texturally complex, milky/matte white, Type (V) Microcrystalline Quartz Vein in heavily weathered, bleached, silicified, C-S altered, early stage Tcc monzogranite. Mineral assemblage: Quartz + Microcrystalline Quartz ± Magnetite ± Muscovite. Although apparently texturally homogeneous in the field, this vein contains discrete zones of crystalline quartz, small (<1-1.5 cm) vugs lined with muscovite blades (<1000-3000 µm), and disseminated, oxidized magnetite crystals (2000-4000 µm). In thin section, subhedral blocky quartz (5000-11000 µm) dominates vein material, but is crosscut (particularly near and along the vein margin) by veinlets and pockets of microcrystalline quartz (<2000 µm wide). Microcrystalline quartz veinlets are also observed parallel to vein margins in altered monzogranitic wallrock within 1 cm of the vein contact. Some subhedral quartz crystals contain abundant thin (<100 µm), vermicular inclusions of secondary quartz. Fluid inclusions are almost entirely absent from this sample.

HPP-1-73 Type (IV) Microcrystalline Quartz Vein

Sample is from a single, complex Type (IV) Microcrystalline Quartz Vein in the early stage Tcc monzogranite near the contact with the early stage Ttc granodiorite. Mineral Assemblage: Microcrystalline Quartz. Anastomosing, irregular zones and networks of white-green microcrystalline quartz (typically <1 cm wide) crosscut bleached, but relatively unaltered, medium-grained (<1 mm) leucomonzogranite. Highly irregular

contacts exist between microcrystalline quartz and host monzogranite, with abundant minor, subsidiary veinlets emanating from microcrystalline quartz zones. Numerous angular clasts of crystalline quartz and alkali feldspar (<10-1000 μm) are included throughout microcrystalline quartz zones.

HPP-1-76 Type (III) Quartz Vein

Sample is from a 6 cm wide, pegmatitic, Type (III) Quartz Vein in weathered, feldspar-rich, early stage Ttc granodiorite near the contact with the early stage Tcc monzogranite. Mineral Assemblage: Quartz. Vein is entirely composed of crystalline, glassy grey quartz crystals that range from <0.1 to >3 cm. The largest crystals are well-formed euhedral lathes (>1.5 cm), while smaller crystals are euhedral-subhedral and may be elongate or equant (<1-2 mm). Smaller quartz crystals are often oriented perpendicularly to larger lathes. Some relatively large alkali feldspars are present in the wallrock along the selvages of the vein and are intergrown with vein quartz crystals. Vein quartz exhibits pervasive recrystallization along crystal boundaries, but little evidence of fracturing.

HPP-1-78 QF Pegmatite

Sample is from a 3-7 cm-wide, linear Quartz-Feldspar Pegmatite zone with a ~2 cm wide crystalline quartz core in the coarse-grained, megacrystic, early stage Ttc granodiorite. Mineral Assemblage: Quartz + Alkali Feldspar. The margins of this feature are dominated by relatively equant, subhedral-anhedral alkali feldspar and quartz crystals (<1 cm). Quartz is often included in larger alkali feldspar crystals. Near the center of this pegmatite zone, there exists a ~2 cm-wide, discontinuous vein of pure crystalline quartz with an irregular margin and multiple crosscutting fractures. While quartz crystals in this zone are large (1000-9000 μm), quartz and alkali feldspar crystals are significantly smaller (<100 μm) along its margins. Additionally, undulose extinction and recrystallized grain boundaries are common deformation features in crystalline quartz throughout this sample.

HPP-2-02 Aplite (QF Cored)

Sample is from a linear, 14 cm-wide QF-cored aplite vein in unaltered, relatively unweathered, late stage Tmg biotite monzogranite. A 6 cm-wide core of muscovite and pegmatitic quartz and alkali feldspar is bounded on either side by 4 cm-wide muscovite-bearing aplite zones. The boundaries between these zones are sharp and marked by abrupt changes in average grain sizes. The pegmatite core is dominated by euhedral-subhedral alkali feldspar lathes (<1 cm), anhedral, fractured glassy quartz (<4500 μm), and rare blades of muscovite (<2000 μm). The aplitic zones are fine-grained (<250 μm), crudely equigranular, and contain anhedral quartz, alkali feldspar, and muscovite.

HPP-2-03 Aplite (Q Cored)

Sample is from a crystalline quartz-cored aplite vein in the late stage Tmg monzogranite. Fine to very fine grained (200-400 μm), equigranular, seriate, interlocking crystal texture. Mineral assemblage: Plagioclase + Quartz + Alkali Feldspar + Muscovite. Petrogenetic sequence demonstrates early alkali feldspar and muscovite growth with later plagioclase and quartz growth. Quartz is anhedral and demonstrates strong recrystallization and undulose extinction. The contact between the crystalline quartz and

aplitic zones is highly irregular. This sample is heavily fractured; some fracture zones contain microcrystalline quartz. Some silicification with iron oxide staining is observed.

HPP-2-06 Type (I) Quartz Vein

Sample is from a 1-2 cm-wide, laterally continuous, volumetrically minor, glassy, Type (I) Quartz Vein in bleached, strongly weathered, aplitic, late stage Tmg monzogranite. Mineral assemblage: Quartz. There exists at least one other, similar Type (I) Quartz Vein in this outcrop. Vein quartz is dominantly coarse (0.1-1.1 cm), subhedral, and demonstrates textures indicating inward growth from vein margins. Vein quartz is highly deformed (i.e. undulose extinction, recrystallized grain contacts) and crosscut by numerous parallel fractures. Coarse vein quartz is also cut by parallel and orthogonal veinlets of finer-grained (~50-150 μm) quartz. Strong jarosite and iron oxide staining observed around this vein and in host rock originates from small pyrites and magnetite crystals (<100 μm) along the vein margin. Host aplitic monzogranite is medium-coarse grained (<500 μm), and dominated by anhedral, strained quartz and subordinate alkali feldspars.

HPP-2-08b Granite (Leuco)

Sample is from a 12 cm-wide, crystalline quartz-cored, aplitic leucogranite dike intruding into a basalt/microdiorite body/dike in late-stage Tmg monzogranite. Mineral assemblage: Quartz + Alkali Feldspar. The quartz core is ~4 cm wide and consists of milky, flakey, crystalline quartz. Vein quartz is coarse (<3000 μm), and strongly recrystallized, as evidenced by sutured, ribbon-like grain boundaries, and small inclusions of recrystallized quartz (<50 μm). The margin between the crystalline quartz core is irregular and gradational, with a ~1.2 cm-wide zone of fine-grained aplite on either side. The leucogranite dike material beyond the aplitic zones is dominated by highly recrystallized, medium-grained quartz.

HPP-2-10 Aplite

Sample is from a single, 5-8 cm-wide, planar, texturally homogeneous aplite vein in weathered, megacrystic, late stage, Tmg biotite monzogranite. Mineral assemblage: Quartz + Alkali Feldspar. Aplite is dominated by fine-grained, anhedral quartz and alkali feldspar. The boundary with the coarser-grained (<1000 μm), strongly recrystallized host monzogranite is very sharp.

HPP-2-19a Basalt/Microdiorite

Sample is from the contact between a tabular ~45 cm-wide basalt/microdiorite dike and a 10 cm-wide crosscutting aplite vein in the late stage Tmg monzogranite. Basalt/microdiorite is very fine-grained (<150 μm), while aplite is fine-grained (~500 μm). Basalt/microdiorite mineral assemblage: Quartz + Plagioclase + Hornblende + Alkali feldspar + Titanite. Aplite mineral assemblage: Quartz + Plagioclase + Alkali feldspar \pm Titanite \pm Hornblende. Small titanites dispersed in microdiorite, some in aplite. Trails of zircon crystals in microdiorite. There exists a more mafic area in the microdiorite. Some hornblendes included in aplite. Distinct flow texture of hornblendes in basalt/microdiorite. Rare micrographic intergrowth of quartz and alkali feldspar observed. Some sericitization of feldspars and chloritization of hornblende and biotite is also present in this sample.

HPP-2-22 Type (I) Quartz Vein

Sample is from a discontinuous, 1-2 cm wide, irregular, deformed, and minorly folded Type (I) crystalline Quartz Vein in med-coarse grained, bleached, late stage Tmg two-mica monzogranite. Mineral assemblage: Quartz. A 3 cm-wide knot of crystalline quartz is observed in a folded kink in the vein. Vein quartz is very coarse (1000-9000 μm), generally anhedral, and exhibits strong evidence of recrystallization (including pervasive ribbon textures, sutured grain boundaries, and undulose extinction). Also, The vein is crosscut by multiple brittle fractures. The boundary between the vein and the surrounding monzogranite is sharp and well defined. Relatively small (<150 μm), oxidized pyrite and magnetite crystals are observed in monzogranite wallrock within several mm of vein contact.

HPP-2-27 Aplite

Sample is from a 20 cm wide texturally homogenous aplite vein in a weathered zone containing megacrystic microcline crystals in the late stage Tmg monzogranite. Small Quartz-Feldspar Pegmatite veins observed nearby. Mineral assemblage: Quartz + Microcline + Plagioclase + Biotite + Muscovite \pm Magnetite \pm Chlorite \pm Sericite. Medium to fine grained equigranular texture is observed within aplite. Minor chlorite-sericite alteration of host monzogranite. Quartz and muscovite included in larger plagioclase and microcline crystals. Rare, disaggregated opaque clusters intergrown with plagioclase. A large brittle fracture is observed cutting across the thin section.

HPP-2-29 QF Pegmatite

Sample is from a very large (50-55 cm) Quartz-Feldspar pegmatite zone in bleached early stage Tmg biotite monzogranite. Mineral Assemblage: Alkali Feldspar + Quartz. Pegmatite is composed of early euhedral-subhedral matte white alkali feldspar (5-25 cm) and subhedral-anhedral glassy grey quartz (5-20 cm). In thin section, quartz is highly recrystallized. All quartz crystals are characterized by sutured grain boundaries and pervasive undulose extinction. The contact between the pegmatite zone and the host monzogranite is sharp, and defined by 3-5 cm-wide zones of relatively small (<1.5 cm), inward-directed quartz and alkali feldspar crystals.

HPP-2-35 QF Pegmatite

Sample is from one of two large Quartz-Feldspar Pegmatite veins in weathered, aplitic, jarosite stained, med-grained, late stage Tmg monzogranite. Sampled vein is 10-15 cm wide, while the unsampled vein is \sim 7 cm wide. Mineral assemblage: Quartz + Alkali Feldspar. Vein contains very large (5-9 cm), euhedral-subhedral, glassy grey quartz crystals and subordinate, anhedral-subhedral matte white alkali feldspar. Numerous small (<1 cm) quartz inclusions are observed within later alkali feldspar crystals. Contact between pegmatite and host granite is sharp and marked by zones of inward-directed quartz crystal growth. There are relatively small segregations (<10 cm) of medium-grained leucogranite within this pegmatite zone. Surrounding host granite is much more heavily weathered than this pegmatite zone and appears orange (due to sulfide oxidation) and is friable. In thin section, pegmatitic quartz is undeformed, relatively unfractured, and contains abundant fluid inclusion trails.

HPP-2-38 Type (I) Quartz Vein

Sample is from a planar, 7-8 cm wide, Type (I) crystalline Quartz Vein in bleached, heavily weathered, aplitic, late stage Tmg monzogranite. Mineral assemblage: Quartz. Vein margins are sharp and planar and occasionally coarse alkali feldspar crystals (<1.5 cm) are observed in the immediately adjacent monzogranite wallrock. Vein quartz is strongly deformed and characterized by pervasive undulose extinction, ribbon textures, and recrystallized grain boundaries. Furthermore, numerous discontinuous brittle fractures are observed throughout. Individual ribbons range from <1000 μm to >2 cm in length. Fluid inclusions are relatively rare.

HPP-2-40 QF Pegmatite

Sample is from a poorly exposed, highly irregular, nonlinear, 7 cm wide, Quartz-Feldspar Pegmatite zone in medium-grained, bleached, jarosite stained, late stage Tmg muscovite monzogranite. Mineral assemblage: Quartz + Alkali Feldspar. Early coarse-pegmatitic (<1-3 cm), euhedral-subhedral, alkali feldspar crystal growth was followed by crystallization of coarse-pegmatitic (<1-4 cm), blocky, anhedral, glassy grey quartz. Boundaries between this pegmatite zone and the host monzogranite are irregular and indistinct, recognized only by a gradational increase in crystal size to pegmatite proportions. In thin section, alkali feldspar crystals exhibit well-formed crystal faces and are relatively undeformed. Conversely, quartz is generally anhedral and demonstrates evidence of deformation and recrystallization (i.e. undulose extinction and sutured grain boundaries). Several brittle fractures also crosscut this sample.

HPP-2-41 Type (III) Quartz Vein

Sample is from one of two discontinuous, 11-15 cm wide, pod-like, Type (III) crystalline Quartz Veins in an outcrop of silicified, bleached, and heavily weathered and friable, late stage Tmg monzogranite. Mineral assemblage: Quartz. Vein quartz is milky white, pegmatitic (>2 cm), and exhibits generally irregular, nonplanar contacts with host monzogranite. Other than silicification, no associated hydrothermal alteration is observed. In thin section, quartz is generally subhedral and is very rich in fluid inclusion planes. Very little evidence of internal deformation is observed, however there are several narrow (<500 μm), healed/recrystallized fractures crosscutting this sample.

HPP-2-44 Aplite (Layered Quartz-Feldspar Pegmatite)

Sample is from a relatively flat-lying, planar Quartz-Feldspar Pegmatite zone within a 45-cm high, layered Aplite-Pegmatite outcrop in the late stage Tmg leucomonzogranite. Mineral assemblage: Quartz + Alkali Feldspar. At least four Aplite-Pegmatite sequences (representing 8 individual zones between 4 and 25 cm wide) are observed, bounded by irregular but abrupt transitions in crystal size. Pegmatite zones contain approximately equal abundances of blocky subhedral matte white alkali feldspar and glassy, grey, crystalline quartz. One major brittle fracture zone is observed to crosscut this outcrop at an oblique angle. Only pegmatitic quartz was examined petrographically. In thin section, quartz is relatively undeformed and rich in crosscutting secondary fluid inclusion planes. Several narrow, minorly recrystallized fracture zones are observed.

HPP-2-47 Type (I) Quartz Vein

Sample is from an 8 cm wide, planar, Type (I) crystalline Quartz Vein in silicified, aplitic, late stage Tmg monzogranite near to several QF Pegmatite veins. Mineral assemblage: Quartz. Vein quartz is blocky and fractured, and exhibits sharp margins with host monzogranite. In thin section, quartz is pegmatitic (>2 cm), with minor recrystallization along grain boundaries and healed fracture zones. Countless discontinuous, minor brittle fractures are observed within larger quartz crystals.

HPP-2-55 Type (I) Quartz Vein

Sample is from a 1.5-2 cm, planar, Type (I) crystalline Quartz Vein in unaltered, megacrystic, early stage Ttc granodiorite near the contact with the late stage Tmg. Mineral assemblage: Quartz + Muscovite + Pyrite ± Magnetite. In thin section, this vein is characterized by irregular margins with surrounding granodiorite, with narrow selvages (1000-5000 µm) of coarse (1000-2000 µm) muscovite. Additionally, rare, relatively large, euhedral-subhedral, pyrite crystals (~500-1000 µm) are observed within vein quartz and in these selvages. Vein quartz is anhedral and fine-medium grained (<150-2000 µm), and highly recrystallized (as evidenced by sutured, recrystallized grain boundaries and undulose extinction).

HPP-2-56 Type (III) Quartz Vein

Sample is from a 15 cm wide, gently anastomosing, milky white/grey, blocky, Type (III) crystalline Quartz Vein with jarosite-stained margins in weathered, medium-grained, late stage Tmg biotite monzogranite. Mineral assemblage: Quartz ± Pyrite. The contact between this vein and the fine-grained, aplitic, host biotite monzogranite is sharp and characterized by <1.5 cm wide zones of pervasive jarosite staining. Vein quartz is anhedral, generally pegmatitic (>2 cm) and exhibits evidence of localized deformation (i.e. discontinuous mm-scale zones of ribbon texture, and crystals with undulose extinction). Although crosscutting planes of fluid inclusions are observed, a relatively low overall density of fluid inclusions is observed throughout this sample. Although sulfides were not observed in thin section, it is interpreted that the jarosite staining along the edges of this vein is the product of oxidized pyrites in the vein selvage (similar to HPP-2-55).

HPP-2-57 QF Pegmatite

Sample is from a 12-15 cm wide, partially eroded, Quartz-Feldspar Pegmatite zone in silicified, jarosite stained, heavily weathered, coarse-grained, aplitic, late stage Ttc granodiorite. Mineral assemblage: Quartz + Alkali Feldspar. Since only a minor volume of this pegmatite zone has not been eroded away (leaving a tabular void), only a cursory characterization of the vein-wallrock margin is permitted. This contact appears to be relatively sharp and planar. Host granodiorite is strongly silicified (appearing bleached and granular, with no clear distinctions between minerals) in a 70 cm zone on one side of this pegmatite. Milky white, blocky quartz is significantly more abundant than matte white alkali feldspar. Due to the large size of sampled quartz crystals (>2 cm), only two individual crystals were observed in thin section. These crystals are anhedral, cloudy (due to an abundance of crosscutting fluid inclusion trails), and moderately deformed (as evidenced by only minor zones of recrystallization, but some undulose extinction). Also, one major brittle fracture crosscuts this sample.

HPP-2-62 QF Pegmatite

Sample is from a 13-15 cm wide, generally planar Quartz-Feldspar Pegmatite zone in relatively unaltered, mafic enclave-bearing, early stage Ttc granodiorite. Mineral assemblage: Quartz + Alkali Feldspar. The core of the pegmatite is dominated by very large (5-15 cm), blocky, glassy grey quartz crystals, while the margins contain a higher abundance of smaller (<4 cm), matte white alkali feldspars. The boundary with surrounding granodiorite is irregular, (appearing to conform to the edges of pegmatitic crystals), but sharp. Minor silicification and jarosite staining are observed in narrow zones (2-4 cm) on either side of the pegmatite zone. In thin section, one pegmatitic quartz crystal (>2 cm) is characterized by a very high density of parallel, crosscutting fluid inclusion planes, but appears relatively internally undeformed. However, on the margin between the one quartz crystal that dominates the thin section and several euhedral-subhedral alkali feldspar crystals (5000-11000 μm), there exists a thin zone (1000-2000 μm) of smaller (1000-2000 μm), anhedral-subhedral, highly recrystallized quartz crystals. The contact between this zone and the larger quartz crystal appears serrated.

HPP-2-65 Type (I) Quartz Vein

Sample is from a 1.5-2 cm-wide Type (I) crystalline Quartz Vein in the early stage Ttc granodiorite. Sample is altered and cut by multiple smaller microcrystalline quartz veinlets with fine-grained groundmass. Mineral assemblage: Alkali feldspar + Quartz + Microcrystalline Quartz + Plagioclase + Muscovite + Chlorite + Sericite \pm Zircon. Microcrystalline quartz veins are not clearly defined because of pervasive chlorite-sericite alteration. Abundant white micas are observed as rims around and/or embayments in alkali feldspars. Coarse/megacrystic composite plagioclase crystals observed throughout. Coarse crystalline quartz vein material is unaffected by alteration. Several small (2-3 mm) brown, crystal-lined vugs have been observed. Veins are thin, anastomosing with FeO staining on margins.

HPP-2-71a Metased (Mineralized Marble)

Sample is from a relatively pure, banded, coarse-grained, sparry marble unit in the contact metamorphosed Opm carbonate unit that contains chalcopyrite and has been historically mined at the roof zone contact with the early stage Ttc granodiorite. Mineral assemblage: Calcite + Pyrite \pm Chalcopyrite \pm Muscovite \pm Zircon \pm Quartz. Well developed calcite twinning and euhedral pyrite and chalcopyrite showing some hematite oxidation. Some pyrite and chalcopyrite cubes are twinned as well and often exhibit calcite inclusions. Some muscovite and sericite around sulfides. Numerous fine zircon crystals may be present in this sample. Large (<7 cm) oxidized veins/horizons observed parallel to banding (not sampled).

HPP-3-01 MQF Pegmatite

Sample is from a large (~20 cm) Muscovite-Quartz-Feldspar Pegmatite crystal zone with a ~5 cm-wide crystalline quartz zone in weathered, but relatively unaltered, late stage Tmg monzogranite. Mineral assemblage: Quartz + Alkali Feldspar + Muscovite. Pegmatitic quartz and alkali feldspar are subhedral-anhedral. Quartz is highly recrystallized, as evidenced by undulose extinction and recrystallized grain boundaries. Large (<3000 μm)

books of muscovite are concentrated along the margins of the pegmatite zone. Boundary with host monzogranite is defined by ~17 cm wide zones of coarser monzogranite, (mean crystal size: ~1000-3000 μm).

HPP-3-03 Type (IV) Microcrystalline Quartz Vein

Sample is from a 10 cm-wide, vuggy, complex, Type (IV) Microcrystalline Quartz Vein in a bleached, medium-grained zone of megacrystic microcline crystals in the late stage Tmg monzogranite. Mineral assemblage: Quartz + Microcrystalline Quartz \pm Muscovite. The bulk of vein material is microcrystalline quartz, while coarser-grained, euhedrally-terminated quartz crystals form the most recent stage of cockade crystal growth along the linings of vugs. Several stages of quartz growth are observed, (marked by growth zones of muscovite).

HPP-3-04 Type (I) Quartz Vein

Sample is from a 1.5-3 cm-wide, pure, Type (I) crystalline Quartz Vein in medium-grained, bleached, late stage Tmg muscovite monzogranite. This vein is relatively well-exposed and continuous over 2 m. Mineral assemblage: Quartz. Vein quartz is medium-coarse (1000-9000 μm) and ubiquitously anhedral, with strong, pervasive evidence of recrystallization (i.e. sutured grain contacts and undulose extinction). Additionally, numerous orthogonal brittle fractures crosscut this quartz vein. The margin between the quartz vein and the host monzogranite is sharp and gently anastomosing. No associated hydrothermal alteration.

HPP-3-15 QF Pegmatite

Sample is from a 40 cm-wide, poorly exposed, Quartz-Feldspar Pegmatite zone or pod from the heavily weathered late stage Tmg biotite monzogranite. Mineral assemblage: Alkali Feldspar + Quartz. Sample is composed of ~60% early, pegmatitic (>7 cm), blocky, subhedral-euhedral alkali feldspar and ~40% late, pegmatitic (>6 cm), anhedral, glassy grey crystalline quartz. In thin section, quartz is completely deformed and recrystallized, as indicated by pervasive ribbon textures, undulose extinction, and sutured grain contacts. Numerous recrystallized fracture zones may indicate later influx of SiO_2 -bearing fluids. Fluid inclusions are rare. Contacts between this pegmatite zone and the surrounding monzogranite are very sharp.

HPP-3-19 Type (I) Quartz Vein

Sample is from a single, planar, 1-2 cm-wide, Type (I) crystalline Quartz Vein in bleached, weathered, jarosite-stained, aplitic late stage Tgm two-mica monzogranite. Mineral assemblage: Quartz. Vein quartz is strongly deformed and characterized by pervasive ribbon textures that are oblique or near-parallel to vein margins. This is consistent with observations of multiple brittle fractures that are similarly oblique to vein margins. Individual quartz ribbons range from <1 to 13 mm long. The contact between this vein and the host monzogranite is invariably sharp. Several tabular or rounded crystalline quartz clasts of various sizes (1500-5000 μm) are preserved amidst the flow texture of the deformed quartz ribbons. Minor jarosite staining is the product of oxidation of rare, small (<200 μm), cubic pyrite crystals in the monzogranite wallrock. There exists no hydrothermal alteration associated with this vein.

HPP-3-23 Type (III) Quartz Vein

Sample is from a large (11-26.5 cm), complex, strongly jarosite stained Type (III) crystalline Quartz Vein in bleached, aplitic, leisegang altered, late stage Tmg muscovite monzogranite near the contact with the late stage Tgm two-mica monzogranite. Several crystalline, jarosite-stained quartz veinlets (~1-2 cm) crosscut outcrop and appear to be subsidiary to, and originate from, the sampled major quartz vein. The bulk of jarosite staining is restricted to these veins. In thin section, a large population of rounded crystalline quartz clasts (<500 μm – 16.6 cm) is entrained in a matrix of fine-grained crystalline and microcrystalline quartz. It is possible that these textures are representative of a hydrothermal breccia. While there is some contact between these clasts, this sample is largely matrix-supported. Evidence of ductile deformation is rare, and only several brittle fractures are observed to crosscut this sample. Due to the mineralogical purity of this vein, it is interpreted that the jarosite staining was produced by oxidation of sulfides (likely pyrite).

HPP-3-27 Type (IV) Microcrystalline Quartz Vein

Sample is from a texturally unique, complex, 175 cm wide zone of bleaching, leisegang alteration, and microcrystalline quartz veins and veinlets in the late stage Tmg monzogranite. At least two veins exist within this zone (4 cm and 2 cm, respectively), converging to one vuggy microcrystalline quartz vein approximately 7-8 cm wide. Mineral assemblage: Quartz + Microcrystalline Quartz + Pyrite \pm Muscovite. Abundant well-formed, small (~100-500 μm) pyrite cubes concentrated within microcrystalline margins of quartz vein with a crystalline quartz vein core. Very minor deformed muscovite crystals associated with crystalline quartz in wallrock. Wallrock is silicified and strongly jarosite stained, but, where unaltered, exhibits multiple zones of layered QF pegmatites and aplites.

HPP-3-29 MQF Pegmatite

Sample is from a ~5 cm-wide, very coarse-grained MQF pegmatite crystal zone in a weathered, medium-grained zone within the late stage Tmg monzogranite unit. Mineral assemblage: Quartz \pm Alkali feldspar + Muscovite + Garnet. Texturally, this crystal zone displays interlocking, sutured textures with Alkali feldspar. Large (>1 cm) books of muscovite mica and a range of sizes of euhedral-subhedral dark red Fe-Mg garnets (0.25-1.5 cm) observed within crystal zone. Garnets of this size were not observed elsewhere in the HPP. Some jarosite staining is apparent in this area, but is not observed within the sampled crystal zone.

HPP-3-33 QF Pegmatite

Sample is from a 33-34 cm-wide Quartz-Feldspar Pegmatite zone (one of many in this outcrop) in bleached, megacrystic, late stage Tmg biotite monzogranite. Mineral assemblage: Quartz + Alkali Feldspar. Pegmatite zone is composed of ~20% early, matte white, subhedral alkali feldspar crystals and ~80% late, glassy grey, subhedral-anhedral, crystalline quartz. In thin section, this sample is highly deformed and nearly completely recrystallized. Vein quartz is characterized by ribbon textures and sutured grain contacts. Flow textures around several relatively small (<1 cm), rounded clasts of crystalline quartz

are preserved in larger, recrystallized zones. These clasts preserve fractures and fluid inclusion trails that formed before the recrystallization deformation event.

HPP-3-38 Type (II) (wallrock) Quartz Vein

Sample is from a 6 cm-wide, texturally massive, milky quartz vein in relatively pure, sparry white marble near the contact with the early stage Ttc granodiorite. Several of these veins crosscut metasedimentary marble in this outcrop, but it is unclear if these veins also intrude early stage granites. Mineral assemblage: Quartz. Vein quartz is sooty, but pure with respect to mineralogy. Quartz crystals are anhedral, heavily fractured, and rich with fluid inclusions. Multiple recrystallized fracture zones (~100-200 μm wide) crosscut vein quartz. The contact between this quartz vein and its host marble is sharp, but irregular, and marked by a ~2000 μm wide zone of opaque material.

HPP-3-39 Type (I) Quartz Vein

Sample is from a 1-3 cm-wide Type (I) crystalline Quartz Vein in the early stage Ttc granodiorite. Sample is strongly modified by chlorite-sericite alteration (appears green/grey) and crosscut by numerous healed fracture zones and by at least two central, parallel quartz veins and numerous veinlets. Mineral assemblage: Quartz + Plagioclase + Alkali Feldspar + Microcrystalline Quartz + Magnetite + Titanite + Muscovite + Chlorite + Sericite. Wallrock is relatively coarse, while hydrothermal minerals and alteration products are fine grained. Disaggregated opaque grain included in coarser quartz grain. Coarse, complex titanite grains intergrown with quartz, alkali feldspars. Veins of microcrystalline quartz are present, but poorly defined. Heavily altered, significant amounts of white mica overgrowth on alkali feldspars.

HPP-4-01 Type (II) (skarn) Quartz Vein

Sample is from a narrow (1.5 cm), anastomosing, two-stage, Type (II) (skarn) crystalline Quartz Vein in a historically mined, contact skarn in an Opm impure carbonate roof pendant in the early stage Tcc monzogranite. Vein mineral assemblage: Quartz \pm Plagioclase. Skarn mineral assemblage: Diopside + Quartz + Hydrogrossular + Tremolite + Sericite + Calcite. Skarn is relatively narrow (<3 m) and located around a central system of hydrothermal quartz veins (largely mined out), of which the sampled vein system is a subsidiary. The sampled vein system is characterized by two types of quartz: a ~1-1.25 cm core of pure, coarse-grained, crystalline quartz and two narrow (<1 cm each), selvages of matte white, fine-grained crystalline quartz. These two zones bifurcate into separate veins within the skarn after approximately 1 m. Crystalline vein quartz is coarse (500-5000 μm), generally anhedral, and exhibits some localized grain boundary recrystallization. The outer zones are dominated by anhedral, equant, fine-grained (~200 μm), seriate quartz with subordinate plagioclase that display uniform extinction. The host skarn contains abundant poorly formed, impure crystalline quartz and calcite (<1000-6000 μm) with high densities of skarn mineral inclusions. Some dextral offset of skarn minerals by laterally continuous, complex, veinlets of calcite (<50 μm) is observed. However, these veinlets do not crosscut crystalline vein quartz.

HPP-4-02b Type (II) (skarn) Quartz Vein

Sample is from a <3 cm wide, discontinuous, blebby, pure Type (II) (skarn) crystalline Quartz Vein in a volumetrically major, historically mined Star Tungsten contact skarn in the metamorphosed Opu carbonate unit on the roof zone of the early stage Tcc monzogranite. Vein mineral assemblage: Quartz. Skarn mineral assemblage (in sampled area): Hydrogrossular + Diopside + Tremolite ± Quartz. Vein quartz is coarse (>1.5 cm), pure, internally undeformed, and anhedral. Extremely irregular vein margins with the surrounding skarn minerals, (including isolated quartz blebs (<1000 µm) and discontinuous veinlets parallel to vein) indicates that quartz crystallization occurred late. Linear zones (1000-3000 µm wide) of skarn minerals are commonly included in vein quartz. Several brittle fractures orthogonally crosscut this vein. Due to the thickness of the double-polished thin section, petrographic investigation of skarn minerals (which appear opaque) is largely impossible. However, small quartz crystals (<200 µm) are a minor component away from the vein.

HPP-4-06 Type (II) (skarn) Quartz Vein

Sample is from pegmatitic quartz segregations in a volumetrically minor (5-10 cm wide) contact skarn hosted by impure white/banded contact metamorphosed carbonate at the northern margin of the early stage Ttc granodiorite. Skarn mineral assemblage: Hydrogrossular + Diopside + Tremolite + Quartz + Magnetite/Hematite. Cobbles of pure iron oxide gossan were observed in nearby float. This skarn is characterized by very homogeneous segregations of constituent minerals; irregular zones of relatively pure diopside up to 20 cm wide exist adjacent to similar zones of hydrogrossular or quartz. Minor intergrowth of these minerals along contacts between zones demonstrate that, like other skarns at the HPP, quartz crystallization likely occurred last. Oxidized magnetite and hematite coatings on skarn minerals were observed throughout, (possibly the sites of now-eroded gossans). Only quartz from this skarn was examined petrographically. Quartz is pegmatitic (>2 cm), subhedral-anhedral, intergrown with other skarn minerals, and demonstrates relatively minor evidence of post-crystallization deformation. Some relatively small (<1000 µm) segments of crystal boundaries appear to be recrystallized, and undulose extinction is only observed in one quartz crystal. However, numerous fluid inclusion planes crosscut this sample, in addition to several partially recrystallized, discontinuous fracture zones.

HPP-4-08 Type (III) Quartz Vein

Sample is from a large (~30 cm), pure, matte white, Type (III) crystalline Quartz Vein in weathered, subvertically foliated, fractured, jarosite stained, late stage, Tgm two-mica monzogranite (muscovite rich). Mineral assemblage: Quartz ± Muscovite. This vein is pure crystalline quartz with rare, coarse books of muscovite, and is minorly stained by jarosite. The vein changes thickness over the 2 m exposure. Vein boundary with host granite is sharp. In thin section, quartz is pervasively deformed. Indications of strain, including ribbon textures, undulose extinction, and recrystallized grain boundaries, are observed throughout this sample. Individual crystals are coarse to pegmatitic (1000 µm – 1.6 cm). Several healed brittle-plastic fracture zones (<250 µm wide) crosscut quartz ribbons and are also offset by later, similar healed fractures. At least one of these fracture zones is dextrally offset by a later deformation event

HPP-4-10 QF Pegmatite

Sample is from a moderately large (7-12 cm), poorly exposed, Quartz-Feldspar Pegmatite vein in the strongly weathered, jarosite stained, late stage Tmg two-mica monzogranite. Mineral assemblage: Quartz + Alkali Feldspar. Glassy grey, pegmatitic (<1-9 cm), fluid inclusion-rich quartz dominates this vein, while early, coarse to pegmatitic (<1-3 cm), euhedral-subhedral alkali feldspar is a relatively minor component (<15%). The boundary with the host granite is irregular and poorly defined, but was not observed in thin section. Also, only quartz was observed in thin section. Vein quartz is strongly recrystallized and exhibits ubiquitous ribbon textures and sutured grain boundaries. However, a pervasive fabric indicative of a sustained stress regime is lacking. Several crosscutting brittle fractures are also observed.

APPENDIX E: FLUID INCLUSION PETROGRAPHY AND MICROTHERMOMETRY DATA

E.1: FLUID INCLUSION PETROGRAPHY DATA

Sample ID	Feature Type	Petrographic Description of Host Mineral Grain(s)	Petrographic Group	Number & Nature of Phases (for each assemblage)	# of Assemblages Investigated
HPP-1-03	Type (II) (wallrock) Quartz Vein	Fractured, med-fine grained (0.5-2 mm), anhedral-subhedral quartz in crystalline vein. High fluid inclusion density; many crosscutting trails. Zones of recrystallization, healed fractures, and amorphous zones throughout sample.	Group 1; Group 5	FIA1: 3-phase (L1+L2+V) & 2-phase (L+V) (Group 1) FIA2: 2-phase (L+V) (Group 5) FIA3: 3-phase (L1+L2+V) (Group 1) FIA4: 2-phase (L+V) (Group 1)	4
HPP-1-04a	Type (I) Quartz Vein	Anhedral-subhedral quartz, (1-5 mm), in pure, tabular quartz vein, (translucent). Sutured grain contacts with evidence of dynamic recrystallization.	Group 2/4; Group 5	FIA1: 2-phase (L+V) (Group 2/4) FIA2: 2-phase (L+V) (Group 5)	2
HPP-1-04a-PL	Type (I) Quartz Vein	Anhedral-subhedral quartz, (1-5 mm), in pure, tabular quartz vein, (translucent). Sutured grain contacts with evidence of dynamic recrystallization.	Group 2/4; Group 5	FIA1: 2-phase (L+V) & 3-phase (L+V+S) (Group 2/4) FIA2: 3-phase (L+V+S) (Group 5)	2
HPP-1-20	Granite (altered)	Large (2-5 mm) quartz crystals with feldspars in a QF-pegmatite. Fairly low fluid inclusion density except in a few grains	Group 2/4; Group 1	FIA1: 2-phase (L+V) (Group 2/4) FIA2: 2-phase (L+V) (Group 1) FIA3: 2-phase (Group 1)	3
HPP-1-20-PL	Granite (altered)	N/A	N/A	N/A	N/A
HPP-1-24b	Miarolitic Cavity	Fractured, coarse, subhedral quartz with pegmatitic microcline near miarolitic cavity. Generally high fluid inclusion density with multiple cross-cutting trails. Some recrystallization along fractures of shattered quartz crystals.	Group 1; Group 5	FIA1: 2-phase (L+V) (w/ clathrate) (Group 1) FIA2: 2-phase (L+V) (Group 1) FIA3: 2-phase (L+V) (Group 1) FIA4: 2-phase (L1+L2+V) (Group 5)	4

Sample ID	Size of Inclusions (µm) (for each assemblage)	Shape of Inclusions (for each assemblage)	Relative Volume Proportions for Phases (homogeneous or heterogeneous) (for each assemblage)	Interpretation of Assemblages (with brief explanation)
HPP-1-03	FIA1: 4.1-11.6 µm (only 3 inclusions) FIA2: 3.4-13.2 µm (elongate) FIA3: 10.4-16.5 µm FIA4: 3.3-8.5 µm	FIA1: Geometric/irregular. FIA2: Elongate FIA3: Irregular, elongate. FIA4: Equant/irregular to tabular.	FIA1: 2%-3.5% (V); 0%-0.5% (L2); 96%-98% (L); (Homogeneous) FIA2: 2%-7% (V); 93%-98% (L); (Homogeneous) FIA3: 4%-7% (V); 1%-2% (L2); 91%-95% (L1); (Homogeneous). FIA4: 6% (V); 94% (L); (Homogeneous)	FIA1: Secondary; somewhat aligned trail/cluster of inclusions that does not continue in surrounding grains. FIA2: Secondary; trail of inclusions crosscut grain boundaries. FIA3: Primary; diffuse cluster; somewhat aligned, of inclusions not near grain boundaries. FIA4: Primary; 3D cluster of relatively large inclusions.
HPP-1-04a	FIA1: 3.1-9.3 µm FIA2: <2.8-19.4 µm	FIA1: Ovoid, rounded, few irregular FIA2: Elongate/irregular	FIA1: 75%-85% (L); 15-25% (V); (Heterogeneous) FIA2 85%-90% (L); 10%-15% (V); (Homogeneous)	FIA1: Primary/Pseudosecondary; high inclusion density patch on FI trail, larger inclusions than elsewhere. FIA2: Secondary; clearly defined fluid inclusion trails crosscutting grain boundaries and other mineral textures. Evidence of deformation, recrystallization.
HPP-1-04a-PL	FIA1: 6-8.3 µm FIA2: 2-7.7 µm	FIA1: Large, negative crystal (3 phase); and elongate/irregular (2-phase). FIA2: Negative crystal-irregular.	FIA1: 0%-4% (S); 8%-20% (V); 80%-92% (L) (Heterogeneous). FIA2: 1%-2% (S); 15%-20% (V); 78%-84% (L); (Homogeneous).	FIA1: Primary/Pseudosecondary; short, discontinuous trail of relatively large inclusions in large quartz grain, isolated from recrystallized edges and other trails. FIA2: Secondary; trail crosscuts grain boundaries, associated with recrystallized areas.
HPP-1-20	FIA1: 3.75-11 µm FIA2: 6.2-15.1 µm FIA3: 8.8-10.6 µm	FIA1: Irregular/equant. FIA2: Negative crystal. FIA3: Irregular, negative crystal.	FIA1: 4%-6% (V); 94%-96% (L); (Homogeneous). FIA2: 3%-5% (V); 95%-97% (L); (Homogeneous). FIA3: 4%-7% (V); 93%-96% (L1); (Homogeneous)	FIA1: Pseudosecondary/secondary; trail of relatively large inclusions is truncated at grain boundaries, (although grain borders feldspars). FIA2: Primary; cluster of med-sized inclusions away from grain contact. FIA3: Primary; cluster of three inclusions orthogonal to nearby cross-cutting trail.
HPP-1-20-PL	N/A	N/A	N/A	N/A
HPP-1-24b	FIA1: 5.3-16.6 µm FIA2: 2.7-24.1 µm FIA3: 47.1-52.1 µm FIA4: 3.8-17.2 µm	FIA1: Negative crystal/equant. FIA2: Equant/geometric. FIA3: Elongate/tabular. FIA4: Elongate/irregular.	FIA1: 10%-13% (V); 87%-90% (L); (Homogeneous). FIA2: 7%-12% (V); 88%-93% (L); (Homogeneous) FIA3: 12%-17% (V); 83%-88% (L1); (Homogeneous) FIA4: 10%-12% (V); 2%-4% (L2); 84%-88% (L1); (Homogeneous)	FIA1: Primary; high fluid inclusion density in center of quartz crystal. FIA2: Primary; high fluid inclusion density area away from crystal edge. FIA3: Primary; 3D cluster not on crosscutting FI trail. FIA4: Secondary; large inclusions in high inclusion density trail.

Sample ID	Feature Type	Petrographic Description of Host Mineral Grain(s)	Petrographic Group	Number & Nature of Phases (for each assemblage)	# of Assemblages Investigated
HPP-1-24b-PL	Miarolitic Cavity	Fractured, coarse, subhedral quartz with pegmatitic microcline near miarolitic cavity (?). Generally high fluid inclusion density with multiple cross-cutting trails. Recrystallization along fractures of shattered quartz crystals.	Group 1	FIA1: 3-phase (L1+L2+V) (Group 1)	1
HPP-1-27	Type (IV) Microcrystalline Quartz Vein	N/A	N/A	N/A	N/A
HPP-1-30	Type (III) Quartz Vein	Large (5-15 mm), subhedral, glassy quartz from pegmatite zone. Healed fracture zones with small (0.25-1 mm) recrystallized Qtz crystals.	Group 1; Group 5	FIA1: 3-phase (L+V+S), solid is tabular and slightly birefringent, (Ca-salt?) (Group 1) FIA2: 2-phase (L+V) (Group 1) FIA3: 2-phase (L+V) (Group 1) FIA4: 2-phase (L+V) (Group 5)	4
HPP-1-36a	Type (IV) Microcrystalline Quartz Vein	A vein of subhedral quartz and feldspar, (4-5 mm wide). Quartz and fsp are intergrown with multiple through-going fractures and strong recrystallization along grain boundaries within vein.	Group 5; Group 1	FIA1: 2-phase (L+V) (Group 5) FIA2: 2-phase (L+V) (Group 1) FIA3: 2-phase (L+V) (Group 1)	3
HPP-1-56	QF Pegmatite	N/A	N/A	N/A	N/A
HPP-1-63	Type (IV) Microcrystalline Quartz Vein	Highly recrystallized subhedral quartz (0.1-0.5 mm) in crystalline-microcrystalline vuggy vein system. Several quartz crystals are not recrystallized and may contain primary inclusions.	Group 1; Group 5	FIA1: 3-phase (L1+L2+V) (Group 5) FIA2: 2-phase (L+V) (Group 1) FIA3: 2-phase (L+V) & 3-phase (L1+L2+V) (Group 5)	3
HPP-1-66	Microcrystalline Qtz (5)	N/A	N/A	N/A	N/A

Sample ID	Size of Inclusions (µm) (for each assemblage)	Shape of Inclusions (for each assemblage)	Relative Volume Proportions for Phases (homogeneous or heterogeneous) (for each assemblage)	Interpretation of Assemblages (with brief explanation)
HPP-1-24b-PL	FIA1: 8.6-14.4 µm	FIA1: Negative crystal	FIA1: 3%-8% (V); 3%-6% (L2); 86%-94% (L1); (Heterogeneous)	FIA1: Primary; 3D cluster of negative crystal inclusions.
HPP-1-27	N/A	N/A	N/A	N/A
HPP-1-30	FIA1: 7.4-11 µm FIA2: 14.4-19.6 µm FIA3: 21.5 µm FIA4: 21.8 µm	FIA1: tabular, negative crystal FIA2: tabular/irregular. FIA3: Tabular/irregular. FIA4: Irregular to somewhat tabular.	FIA1: 35%-70% (L); 15%-40% (V); 1% (S) (Heterogeneous) FIA2: 6%-7% (V); (6%-97% (L); (Homogeneous) FIA3: 88% (L); 12% (V) (Single inclusion) FIA4: 6% (V); 94% (L); (Single inclusion)	FIA1: Primary; relatively isolated inclusions, not in recrystallized fracture zone or along a single trail. FIA2: Primary; Large, isolated inclusions. FIA3: Primary; very large single inclusion in low FI density area. FIA4: Secondary; cluster is located in healed fracture zone.
HPP-1-36a	FIA1: 3.3-16.3 µm FIA2: 9.6-15.3 µm FIA3: 12-36.2 µm	FIA1: Elongate to equant/irregular. FIA2: Highly irregular. FIA3: elongate, tabular.	FIA1: 4%-8% (V); 92%-95% (L); (Homogeneous). FIA2: 5% (V); 95% (L); (Homogeneous) FIA3: 5%-9% (V); 91%-95% (L); (Slightly heterogeneous)	FIA1: Secondary; inclusions are on a FI trail, also associated with a discontinuous crack. FIA2: Primary; cluster is not associated with a grain boundary or fracture, no nearby recrystallization textures. FIA3: Primary; 3D cluster away from secondary trails.
HPP-1-56	N/A	N/A	N/A	N/A
HPP-1-63	FIA1: 24.8 µm FIA2: 8.8-15.6 µm FIA3: > 17.3 µm	FIA1: Highly irregular. FIA2: Highly irregular FIA3: Irregular/equant to elongate.	FIA1: 4%-5% (V); 1% (L2); 94%-95% (L1); (Homogeneous). FIA2: 3%-7% (V); 93%-97% (L); (Heterogeneous) FIA3: 2%-5% (V); 95%-98% (L1); (Heterogeneous)	FIA1: Secondary; fracture/inclusion trail follows possible crystal growth zone perpendicular to edge. FIA2: Primary; inclusion cluster is 3D and not associated with trails or recrystallized zones. FIA3: Secondary; cluster is very close to grain boundary with plagioclase (however, boundary appears to be euhedral).
HPP-1-66	N/A	N/A	N/A	N/A

Sample ID	Feature Type	Petrographic Description of Host Mineral Grain(s)	Petrographic Group	Number & Nature of Phases (for each assemblage)	# of Assemblages Investigated
HPP-1-73	Type (IV) Microcrystalline Quartz Vein	Small (<0.25-2.5 mm) anhedral quartz crystals in aplite zones crosscut by recrystallized microcrystalline qtz veins. Quartz crystals show med-strong evidence of recrystallization along boundaries.	Group 1; Group 4	FIA1: 3-phase (L1+L2+V); (Group 1) FIA2: 2-phase (L+V); (Group 4)	2
HPP-1-76	Type (III) Quartz Vein	A complex quartz-feldspar vein with large (0.1-2 cm) quartz crystals and feldspars. Two very large, (>1 cm) elongate quartz crystals in vein. Relatively little recrystallization or fracturing. Some opaques (<0.1 mm) distributed in fracture zones.	Group 5	FIA1: 2-phase (L+V) (Group 5) FIA2: 2-phase (L+V) (Group 5)	2
HPP-1-78	QF Pegmatite	Coarse-grained (0.3-1 cm) pure, crystalline qtz vein with aplitic material along selvages. Minor recrystallization of vein qtz, some fracturing.	Group 1; Group 5	FIA1: 3-phase (L+V+S) (Group 1) FIA2: 2-phase (L+V) (Group 1) FIA3: 2-phase (L+V) (Group 5)	3
HPP-2-02	Aplite (QF-cored)	Several large (4-10 mm) quartz crystals in core of QF-aplite). Generally low fluid inclusion density. Some localized grain suturing and recrystallization.	Group 2; Group 1; Group 5	FIA1: 3-phase (L1+L2+V) (Group 2) FIA2: 3-phase (L1+L2+V) (Group 1) FIA3: 2-phase (L+V). (Group 5). FIA4: 3-phase (L1+L2+V) (Group 2)	4
HPP-2-03a-PL	Aplite (Q-cored)	Aplite vein with quartz core. Evidence for recrystallization of qtz and numerous cross-cutting fractures.	Group 5; Group 1	FIA1: 2-phase (L+V) (Group 5) FIA2: 2-phase (L+V) (Group 1) FIA3: 3-phase (L1+L2+V) (Group 1) FIA4: 3-phase (L1+L2+V) & 2-phase (L+V) (Group 1)	4

Sample ID	Size of Inclusions (µm) (for each assemblage)	Shape of Inclusions (for each assemblage)	Relative Volume Proportions for Phases (homogeneous or heterogeneous) (for each assemblage)	Interpretation of Assemblages (with brief explanation)
HPP-1-73	FIA1: 5-14.1 µm FIA2: 3.8-9.1 µm	FIA1: Rounded/irregular to tabular. FIA2: Cubic-rounded to tabular.	FIA1: 2%-15% (V); 0%-1% (L2); 84%-98% (L1); (Heterogeneous) FIA2: 1-3% (V); 97%-99% (L); (Heterogeneous)	FIA1: Primary, cluster contains inclusions of much greater size than nearby trail, forms 3D geometry. FIA2: Pseudosecondary(?); inclusion trail is truncated by grain boundaries, however surrounding grains may be recrystallized.
HPP-1-76	FIA1: 3.3-16.6 µm FIA2: 7.8-10.3 µm	FIA1: Irregular/equant, geometric. FIA2: Tabular/negative crystal.	FIA1: 5%-7% (V); 93%-95% (L); (Homogeneous). FIA2: 6%-9% (V); 91%-94% (L); (Homogeneous).	FIA1: Secondary; trail is in an area of high FI-density at a zone of recrystallization near a major fracture. FIA2: Secondary; trail crosscuts grain boundaries and other textures.
HPP-1-78	FIA1: 16.3 µm FIA2: 27.8 µm FIA3: 7.4-10.2 µm (only two inclusions)	FIA1: Equant to negative crystal. FIA2: Tabular, irregular. FIA3: Ovoid, irregular.	FIA1: 1% (S); 10% (V); 89% (L) (Single Inclusion). FIA2: 8% (V); 92% (L-1); (Single Inclusion) FIA3: 4% (V); 96% (L); (Homogeneous).	FIA1: Primary/Pseudosecondary; off but associated with FI trail that terminates at grain boundary. FIA2: Primary? Near high FI density trails; though. FIA3: Secondary; short FI trail may have formed along growth zone of crystal.
HPP-2-02	FIA1: 3.3-6.8 µm FIA2: 3.5-7.6 µm FIA3: 19.9 µm FIA4: 7.7-9.5 µm	FIA1: Cubic-tabular; but some are irregular. FIA2: Equant-tabular. FIA3: Tabular/negative crystal. FIA4: Equant/irregular.	FIA1: 45%-65% (L1); 20%-30% (V); 10%-15% (L2) (Homogeneous) FIA2: 15%-20% (V1); 10%-15% (L2); 65%-75% (L1), (Heterogeneous). FIA3: 1% (V); 99% (L); (Single inclusion). FIA4: 10%-12% (V); 10%-25% (L2) 63%-80% (L); (Homogeneous)	FIA1: Primary; near, but not on a grain boundary, some negative crystal shapes. FIA2: Primary; near, but not on a secondary trail. Relatively large, but a range of FI sizes. Large vapor bubbles! FIA3: Secondary; Very large inclusion associated with discontinuous FI trail that terminates at grain boundary. FIA4: Primary; off of FI trail, may be growth zone-related.
HPP-2-03a-PL	FIA1: 3.4-6.2 µm FIA2: 3-6.6 µm FIA3: 3.9-7 µm FIA4: 6.1-17.5 µm	FIA1: Irregular equant. FIA2: Oblong, Equant. FIA3: Tabular to irregular. FIA4: Elongate irregular.	FIA1: 20%-35% (V); 65%-80% (L) (Heterogeneous) FIA2: 10%-14% (V); 86%-90% (L); (Homogeneous) FIA3: 10%-15% (L2); 10%-15% (V); 70%-80% (L1); (Homogeneous) FIA4: 0%-5% (L2); 5%-10% (V); 90% (L-1); (Heterogeneous)	FIA1: Secondary; Cluster is in highly recrystallized zone. FIA2: Primary/magmatic; found within apite qtz. 3D cluster is contained within grain boundaries. FIA3: Primary; 3-dimensional cluster of relatively large inclusions, although it is in recrystallized zone. FIA4: Primary; cluster is 3D and located in protected, unrecrystallized qtz grain.

Sample ID	Feature Type	Petrographic Description of Host Mineral Grain(s)	Petrographic Group	Number & Nature of Phases (for each assemblage)	# of Assemblages Investigated
HPP-2-06	Type (I) Quartz Vein	Pure quartz vein in biotite granodiorite. Vein is very coarse-grained and shows minor recrystallization and deformation.	Group 1	FIA1: 2-phase (L+V) (Group 1) FIA2: 3-phase (L1+L2+V) (Group 1) FIA3: 2-phase (L+V) & 3-phase (L1+L2+V) (Group 1) FIA4: 3-phase (L1+L2+V) (Group 1) FIA5: 3-phase (L1+L2+V) (Group 1)	5
HPP-2-08b	Granite (Leuco)	Pure quartz vein in melanocratic microdiorite/biotite tonalite. Qtz crystals are subhedral-anhedral with significant evidence of recrystallization along crystal boundaries. Some undulose extinction indicating deformation.	Group 1; Group 3	FIA1: 3-phase (L1+L2+V) (Group 1) FIA2: 3-phase (L1+L2+V) (Group 3) FIA3: 3-phase (L1+L2+V); (Group 3)	3
HPP-2-10	Aplite	Variably strained, minorly recrystallized subhedral quartz crystals with feldspar at core of pegmatite vein. Some grains are highly fractured, (possibly due to polishing). Some grains exhibit strong undulose extinction = deformation?	Group 5; Group 1/3; Group 4	FIA1: 2-phase (L+V) (Group 5) FIA2: 2-phase (L+V) (Group 4) FIA3: 3-phase (L1+L2+V) (Group 1/3)	3
HPP-2-22	Type (I) Quartz Vein	Large (1-15 cm) subhedral quartz crystals in pure quartz vein. Multiple parallel fractures orthogonal or oblique to vein direction.	Group 1; Group 5; Group 4	FIA1: 3-phase (L1+L2+V) (Group 1) FIA2: 3-phase (L+V) (Group 5) FIA3: 3-phases (L1+L2+V) (Group 1) FIA4: 3-phase (L1+L2+V) (Group 4) FIA5: 3-phase (L1+L2+V) & 4-phase (L1+L2+V+S) (Group 1/5)	5
HPP-2-29	QF Pegmatite	Very coarse (1-5 cm), deformed quartz crystals in qf-pegmatite. Undulose extinction and sutured grain contacts.	Group 1; Group 5	FIA1: 2-phase (L+V) (Group 1) FIA2: 3-phase (L1+L2+V) (Group 5) FIA3: 2-phase (L+V) (Group 1) FIA4: 2-phase (L+V) (Group 5)	4

Sample ID	Size of Inclusions (µm) (for each assemblage)	Shape of Inclusions (for each assemblage)	Relative Volume Proportions for Phases (homogeneous or heterogeneous) (for each assemblage)	Interpretation of Assemblages (with brief explanation)
HPP-2-06	FIA1: 11.7-12.9 µm (only 2 inclusions) FIA2: 14 µm FIA3: 4-15.6 µm FIA4: 14.7 µm FIAS: 7.3-30 µm	FIA1: Equant, negative crystal? FIA2: Tabular/irregular. FIA3: Irregular/equant. FIA4: Geometric/equant. FIA5: Elongate.	FIA1: 15%-22% (V); 78%-85% (L); (Heterogeneous) FIA2: 23% (V); 6% (L2); 72% (L1); (Single inclusion) FIA3: 20%-40% (V); 0%-6% (L2); 60%-74% (L1); (Heterogeneous) FIA4: 18% (V); 5% (L2); 77% (L1); (Single inclusion) FIAS: 15%-35% (V); 3-6% (L2); 59%-72% (L1); (Heterogeneous).	FIA1: Primary: isolated large inclusions in quartz crystals in vein; not near fractures. FIA2: Primary: isolated large inclusion in vein qtz. FIA3: Primary FIA4: Primary; not on trail, isolated inclusion. FIA5: Primary; irregular, 3D cluster of large inclusions within crystal.
HPP-2-08b	FIA1: 8.9-10.5 µm FIA2: 25.5 µm FIA3: 18 µm	FIA1: Equant to tabular. FIA2: Elongate, irregular/tabular FIA3: Negative crystal/tabular	FIA1: 10%-25% (V); 3%-6% (L2); 69%-87% (L1); (Heterogeneous) FIA2: 4% (V); 11% (L2); 85% (L1); (Single inclusion) FIA3: 7% (V); 14% (L2); 79% (L1); (Single inclusion)	FIA1: Primary: 3D cluster of fairly large, regularly-shaped 3-phase inclusions. FIA2: Primary: isolated single inclusion. FIA3: Primary: isolated single inclusion.
HPP-2-10	FIA1: 34 µm FIA2: 4.5-10 µm FIA3: 7.2-8.9 µm	FIA1: Elongate, slightly irregular. FIA2: Equant to elongate. FIA3: Irregular elongate.	FIA1: 3% (V); 97% (L); (Single inclusion) FIA2: 5%-10% (V); 90%-95% (L); (Mostly homogeneous) FIA3: 11% (V); 9% (L2); 80% (L1); (Homogeneous)	FIA1: Secondary; single, isolated, large, highly irregular inclusion. May be associated with fracture. FIA2: Pseudosecondary; trail is truncated by grain boundaries. FIA3: Primary; isolated group of inclusions.
HPP-2-22	FIA1: 22.9-24.2 µm FIA2: 17.2-20.6 µm FIA3: 7.7-18.2 µm FIA4: 5.1-10.3 µm FIAS: 12.1-32.7 µm	FIA1: Tabular, slightly irregular. FIA2: Very irregular, equant. FIA3: Tabular/negative crystal. FIA4: Equant to negative crystal. FIA5: Elongate to equant to highly irregular.	FIA1: 15% (V); 4% (L2); 81% (L1); (Homogeneous) FIA2: 10% (V); 90% (L); (Homogeneous) FIA3: 13% (V); 2%-3% (L2); 84%-85% (L1); (Homogeneous) FIA4: 18%-22% (V); 3%-6% (L2); 72%-79% (L1); (Homogeneous) FIA5: 6%-19% (V); 1%-2% (L2); 0%-0.5% (S); 78.5%-93% (L1); (Heterogeneous)	FIA1: Primary, 2 isolated, large inclusions not on trail or in high FI density area. FIA2: Secondary; inclusion trail crosscuts grain boundaries. FIA3: Primary; inclusions isolated from grain boundaries, other inclusions. FIA4: Pseudosecondary/Secondary, discontinuous FI trail near crosscutting FI trails. FIA5: Primary & Secondary(?); A primary assemblage that may have been modified by a crosscutting FI trail.
HPP-2-29	FIA1: 6.1-16.4 µm FIA2: 12.3-19.9(12.7) µm FIA3: 6.7-17.4 µm FIA4: 3.3-13.3 µm	FIA1: Tabular/irregular. FIA2: Cubic/equant and (highly) irregular FIA3: Elongate or equant. FIA4: Equant to tabular.	FIA1: 10%-12% (V); 88%-90% (L); (Homogeneous) FIA2: 3% or 10% (V); 7% or 3% (L2); 90% or 87% (L1) (respectively); (2 inclusions: heterogeneous) FIA3: 7%-12% (V); 88%-93% (L1); (Heterogeneous) FIA4: 9% (V); 91% (L); (Homogeneous)	FIA1: Secondary; inclusions associated with fracture zone. FIA2: Primary; may be either sparse, loosely spaced heterogeneous assemblage or two separate assemblages. FIA3: Secondary; 3D cluster of relatively large inclusions associated with nearby crosscutting FI trail. FIA4: Primary; 3D cluster of 4-phase inclusions.

Sample ID	Feature Type	Petrographic Description of Host Mineral Grain(s)	Petrographic Group	Number & Nature of Phases (for each assemblage)	# of Assemblages Investigated
HPP-2-35	QF Pegmatite	Part of one large quartz crystal with numerous fluid inclusion trails cutting across it. Areas of very low fluid inclusion density.	Group 1; Group 4	FIA1: 3-phase (L1+L2+V+S), single tabular daughter crystal (Group 1) FIA2: 2-phase (L+V) (Group 1) FIA3: 3-phase (L1+L2+V) (Group 1/4)	3
HPP-2-38	Type (I) Quartz Vein	Highly recrystallized, fractured, and deformed quartz vein. Crystals show undulose extinction, variable birefringence patterns and recrystallization textures along fractures and grain boundaries.	Group 5; Group 1; Group 3	FIA1: 2-phase (L+V) (Group 5) FIA2: 3-phase (L1+L2+V) (Group 1/3)	2
HPP-2-40	QF Pegmatite	Subhedral quartz with euhedral alkali feldspar in pegmatite vein. Quartz is variably strained and/or recrystallized, with one zone showing variable birefringence and undulose extinction with complex fracture patterns.	Group 1; Group 4; Group 5	FIA1: 2-phase (L+V) and 3-phase (L1+L2+V), (Group 1) FIA2: 2-phase (L+V) (Group 1) FIA3: 2-phase (L+V) (Group 5) FIA4: 2-phase (L+V) (Group 4/5)	4
HPP-2-41a	Type (III) Quartz Vein	Extremely FI-rich quartz (almost entirely one crystal) from pod. Several recrystallized fractures, and minor patches (<100 μm) showing localized deformation and recrystallization.	Group 1	FIA1: 2-phase (L+V) (Group 1) FIA2: 2-phase (L+V) (Group 1) FIA3: 2-phase (L+V) (Group 1) FIA4: 2-phase (L+V) (Group 1)	4
HPP-2-44	Aplite (Layered QF Pegmatite)	One large quartz crystal from QF-peg zone, crosscut by numerous (sub)-parallel FI trails. One half FI-rich, the other half is relatively FI-poor. Largely undeformed, with little to no evidence for fracturing and recrystallization.	Group 1; Group 5	FIA1: 2-phase (L+V) (Group 1) FIA2: 3-phase (L1+L2+V) (Group 5) FIA3: 3-phase (L1+L2+V) (Group 5)	3

Sample ID	Size of Inclusions (µm) (for each assemblage)	Shape of Inclusions (for each assemblage)	Relative Volume Proportions for Phases (homogeneous or heterogeneous) (for each assemblage)	Interpretation of Assemblages (with brief explanation)
HPP-2-35	FIA1: 3-10 µm FIA2: 4-7-15 µm FIA3: 16-18.6 µm	FIA1: Irregular to somewhat rounded. FIA2: Rounded, equant, one is nearly square. FIA3: Tabular.	FIA1: 2%-3% (S); 10%-15% (V); 74%-83% (L1); 5%-8% (L2); (Heterogeneous) FIA2: 10%-16% (V); 3%-4% (L2); 80%-87% (L1) (Heterogeneous) FIA3: 5%-8% (V); 2%-3% (L2); 89%-93% (L); (heterogeneous)	FIA1: Primary; irregular cluster of large inclusions not near secondary inclusion trail or grain boundary. FIA2: Primary; isolated inclusions, relatively large. FIA3: Primary or Pseudosecondary; isolated, large inclusions along trail that ends within the larger crystal boundaries.
HPP-2-38	FIA1: <3.1-8.6 µm FIA2: 23.6 µm	FIA1: Equant/negative crystal. FIA2: Tabular/irregular.	FIA1: 16% (V); 84% (L); (Homogeneous) FIA2: 15% (V); 5% (L2); 80% (L1); (Homogeneous)	FIA1: Secondary; FI trail near fracture zone in highly recrystallized, FI-poor qtz. FIA2: Primary; isolated pair of 3-phase inclusions.
HPP-2-40	FIA1: 7.8-25.1 µm FIA2: 3.8-10.3 µm FIA3: 4.2-9 µm FIA4: 4.1-10.7 µm	FIA1: Elongate, irregular. FIA2: Equant to tabular. FIA3: Equant/negative crystal to tabular. FIA4: Equant to tabular.	FIA1: 3-23% (V); 0%-2% (L2); 77%-95% (L1); (Very heterogeneous) FIA2: 10%-20% (V); 80%-90% (L); (Heterogeneous) FIA3: 8%-10% (V); 90%-92% (L); (Homogeneous) FIA4: 16% (V); 84% (L); (Homogeneous)	FIA1: Primary; Large, partially deformed inclusion cluster. FIA2: Primary; 3D cluster not on a trail, regular shapes. FIA3: Secondary; at intersection of two FI trails. FIA4: Secondary/Pseudosecondary; trail terminates well within grain boundaries, not secondary or pseudosecondary.
HPP-2-41a	FIA1: 6.5-17.4 µm FIA2: 3.4-12.4 µm FIA3: 26.8 µm FIA4: 14.4-18.1 µm	FIA1: Elongate. FIA2: Equant to slightly elongate. FIA3: Tabular/negative crystal. FIA4: Elongate/tabular.	FIA1: 5%-8% (V); 92%-95% (L); (Homogeneous) FIA2: 2%-6% (V); 94%-98% (L); (Heterogeneous) FIA3: 4% (V); 96% (L); (Single inclusion) FIA4: 7%-8% (V); 92%-93% (L); (Homogeneous)	FIA1: Primary; somewhat continuous 3D cluster of relatively large inclusions in area of low FI density. FIA2: Primary; somewhat continuous 3D cluster of relatively large inclusions in area of low FI density. FIA3: Primary; 3D cluster in high FI density area; no trails. FIA4: Primary; three isolated inclusions as part of 3D cluster in low FI-density area.
HPP-2-44	FIA1: 5.5-26.5 µm FIA2: 6.9-35.6 µm FIA3: 6.5-44.3 µm	FIA1: Tabular, slightly irregular. FIA2: Highly irregular, deformed. FIA3: Varied; elongate irregular to equant/negative crystal.	FIA1: 10%-12% (V); 88%-90% (L); (Homogeneous) FIA2: 2%-3% (L2); 4%-7% (V); 90%-94% (L1); (Homogeneous) FIA3: 2% (L2); 3%-4% (V); 94%-95% (L1); (Homogeneous)	FIA1: Primary; isolated 3D cluster, shows some evidence of deformation, though (irregularly elongated tabular inclusions). FIA2: Secondary; highly irregular shape near and on convergence of FI trails. FIA3: Secondary; on crosscutting FI trail.

Sample ID	Feature Type	Petrographic Description of Host Mineral Grain(s)	Petrographic Group	Number & Nature of Phases (for each assemblage)	# of Assemblages Investigated
HPP-2-47	Type (I) Quartz Vein	Large, (1-2 cm) anhedral quartz crystals in vein with strong fracturing and microcrystalline quartz along grain contacts, (deformation?). High fluid inclusion density.	Group 1; Group 5	FIA1: 2-phase (L+V) (Group 5) FIA2: 2-phase (L+V) (Group 5) FIA3: 2-phase (L+V) (Group 1)	3
HPP-2-55	Type (I) Quartz Vein	Highly deformed (strained and recrystallized) anhedral-subhedral quartz in pure quartz vein with muscovite selvages. Very low FI density, most are found in diffuse zones and crosscutting FI trails.	Group 5	FIA1: 3-phase (L1+L2+V) (Group 5)	1
HPP-2-56	Type (III) Quartz Vein	Anhedral/subhedral, large (1mm-2.5< cm), sutured quartz crystals from large, crystalline quartz vein. Some deformation and recrystallization along grain boundaries; most inclusions are located on crosscutting FI trails.	Group 5; Group 4	FIA1: 2-phase (L+V) (Group 5) FIA2: 2-phase (L+V) (Group 5) FIA3: 2-phase (L+V) (Group 4/5)	3
HPP-2-57	QF Pegmatite	Highly fractured and recrystallized quartz with very low FI density. Inclusions only visible in two areas of less deformed quartz.	Group 5	FIA1: 2-phase (L+V) (Group 5) FIA2: 2-phase (L+V) (Group 5)	2
HPP-2-62	QF Pegmatite	One large (>3 cm ²) quartz crystal with numerous parallel fluid inclusion trails crosscutting thin section. One area of relatively low fluid inclusion density.	Group 5; Group 3	FIA1: 3-phase (L1+L2+V) (Group 5) FIA2: 3-phase (L1+L2+V) (Group 3) FIA3: 2-phase (L+V) (Group 5)	3

Sample ID	Size of Inclusions (µm) (for each assemblage)	Shape of Inclusions (for each assemblage)	Relative Volume Proportions for Phases (homogeneous or heterogeneous) (for each assemblage)	Interpretation of Assemblages (with brief explanation)
HPP-2-47	FIA1: 7.8 µm FIA2: <4.8-9.2 µm FIA3: 7.3-9.0 µm	FIA1: Irregular, somewhat geometric/negative crystal. FIA2: Tabular, negative crystal. FIA3: Tabular, negative crystal.	FIA1: 5%-15% (V); 85%-95% (L); (Heterogeneous) FIA2: 8%-10% (V); 90%-92% (L); (Homogeneous) FIA3: 15%-25% (V); 75%-85% (L); (Only 2 inclusions; heterogeneous)	FIA1: Secondary; crosscutting FI trail. FIA2: Secondary; located on trail that crosscuts grain boundaries. FIA3: Primary; Two relatively large inclusions completely isolated from any trails or grain boundaries or other inclusions.
HPP-2-55	FIA1: 6-26 µm	FIA1: Highly irregular and elongate.	FIA1: 5%-8% (V); 92%-95% (L); (Homogeneous)	FIA2: Secondary; Highly deformed, irregular inclusions.
HPP-2-56	FIA1: 4.7-18.9 µm FIA2: <4.8-15.5 µm FIA3: 21.6 µm	FIA1: Tabular FIA2: Cubic to elongate, irregular. FIA3: Equant/irregular to tabular/irregular.	FIA1: 4%-6% (V), 94%-96% (L); (Homogeneous) FIA2: 5% (V), 95% (L); (Homogeneous) FIA3: 6% (V); 94% (L); (Single Inclusion)	FIA1: Secondary; crosscutting FI trail. FIA2: Secondary; crosscutting FI trail. FIA3: Secondary/Pseudosecondary; unclear if FI trail crosscuts crystal edges.
HPP-2-57	FIA1: 8.6-21.7 µm FIA2: <10.7-16.7 µm	FIA1: Irregular to negative crystal. FIA2: Equant to tabular/negative crystal.	FIA1: 5%-7% (V); 93%-95% (L); (Homogeneous) FIA2: 5% (V); 95% (L); (Homogeneous)	FIA1: Secondary; on diffuse trail in partially recrystallized qtz. FIA2: Secondary; on crosscutting FI trail.
HPP-2-62	FIA1: 3.1-11.6 µm FIA2: 17.2 µm FIA3: <2.4-29 µm (elongate)	FIA1: Irregular/negative crystal. FIA2: Irregular, geometric. FIA3: Elongate, negative crystal.	FIA1: 10%-14% (L2); 5%-8% (V); 78%-85% (L1); (Homogeneous). FIA2: 15% (V); 5% (L2); 80% (L); (Single Inclusion). FIA3: 10%-15% (V); 85%-90% (L1) (Heterogeneous)	FIA1: Secondary; trails crosscut entire thin section. FIA2: Primary; isolated inclusion, no inclusions nearby. FIA3: Secondary; located on longer trail.

Sample ID	Feature Type	Petrographic Description of Host Mineral Grain(s)	Petrographic Group	Number & Nature of Phases (for each assemblage)	# of Assemblages Investigated
HPP-3-01b	MQF Pegmatite	Euhedral-subhedral, fractured, partially recrystallized quartz filling space between euhedral alkali feldspar crystals in mfg-peg vein. Most inclusions found in wide, linear swatches.	Group 2; Group 5	FIA1: 3-phase (L1+L2+V) (Group 2) FIA2: 2-phase (L+V) (Group 2) FIA3: 3-phase (L1+L2+V) (Group 5)	3
HPP-3-04a	Type (I) Quartz Vein	Medium-grained (1-2 mm) anhedral quartz with strong deformation features, recrystallized grain boundaries, sutured grain contacts. Some feldspars and opaques in vein.	Group 4; Group 5; Group 1	FIA1: 2-phase (L+V) (Group 4) FIA2: 2-phase (L+V) (Group 1) FIA3: 2-phase (L+V) (Group 5) FIA4: 3-phase (L1+L2+V) (Group 1)	4
HPP-3-15	QF Pegmatite	Massive anhedral, minorly recrystallized vein quartz with very high FI density. Numerous wide, extremely FI dense trails crosscutting section. Anomalous low 1st order interference colors, (overthinned?).	Group 2; Group 5; Group 1	FIA1: 2-phase (L+V) (Group 2) FIA2: 3-phase (L+V+S) (Group 5) FIA3: 2-phase (L+V) (Group 1)	3
HPP-3-19	Type (I) Quartz Vein	Highly deformed (strained & recrystallized) quartz in pure quartz vein forming elongate crystals and ribbons. Overall, very low FI density.	Group 4	FIA1: 3-phase (L1+L2+V) (Group 4) FIA2: 3-phase (L1+L2+V) (Group 4) FIA3: 3-phase (L1+L2+V) (Group 4)	3
HPP-3-23	Type (III) Quartz Vein	Brecciated and recrystallized quartz vein showing microcrystalline qtz cement and FI-rich crystalline quartz clasts (1-10 mm). Relatively minor internal deformation to clasts.	Group 1	FIA1: 3-phase (L1+L2+V) (Group 1) FIA2: 2-phase (L+V) (Group 1) FIA3: 3-phase (L1+L2+V) (Group 1)	3
HPP-3-27-PL	Type (IV) Microcrystalline Quartz Vein	N/A	N/A	N/A	N/A

Sample ID	Size of Inclusions (µm) (for each assemblage)	Shape of Inclusions (for each assemblage)	Relative Volume Proportions for Phases (homogeneous or heterogeneous) (for each assemblage)	Interpretation of Assemblages (with brief explanation)
HPP-3-01b	FIA1: 10-26 µm FIA2: <4.3-14.9 µm FIA3: 4.0-35.3 µm	FIA1: Negative crystal to tabular. FIA2: Equant/irregular to negative crystal. FIA3: Highly irregular.	FIA1: 11% (V); 89% (L); (Homogeneous) FIA2: 9%-35% (V); 65%-91% (L); (Heterogeneous) FIA3: 3%-5% (V); 95%-97% (L); (Heterogeneous)	FIA1: Primary; growth zone trail. FIA2: Primary; growth zone trail. FIA3: Secondary; highly deformed inclusions along crosscutting trail.
HPP-3-04a	FIA1: 4-18.1 µm (elongate) FIA2: 3.2-9.8 µm FIA3: 4.5-7.4 µm FIA4: 7.8-13.4 µm	FIA1: Irregular, elongate & negative crystal FIA2: Irregular, ovoid. FIA3: Irregular, geometric, slightly negative crystal. FIA4: Cubic to tabular.	FIA1: 10%-26% (V); 74%-90% (L); (Heterogeneous) FIA2: 7% (V); 93% (L1); (Homogeneous) FIA3: 10%-11% (V); 89%-90% (L) (Homogeneous) FIA4: 12% (V); 8% (L2); 80% (L1); (Homogeneous)	FIA1: Primary/Pseudosecondary; very heterogeneous, high FI density crystal. FIA2: Primary FIA3: Secondary; FI trail crosscuts grain boundaries. FIA4: Primary; no trail geometry, large cubic inclusions.
HPP-3-15	FIA1: 4.4-36.1 µm FIA2: ~20-40 µm FIA3: 15.9-29.3 µm	FIA1: Cubic/negative crystal to tabular. FIA2: Tabular FIA3: Equant to elongate.	FIA1: 9%-11% (V); 89%-91% (L); (Homogeneous) FIA2: 1% (S); 9%-10% (V); 89%-90% (L); (Homogeneous) FIA3: 6%-8% (V); 92%-94% (L); (Homogeneous)	FIA1: Primary; wide trail of inclusions that appears to crosscut by later fractures. Likely growth zone. FIA2: Primary; large, parallel-oriented negative crystal-shaped inclusions. FIA3: Secondary; crosscutting FI trail.
HPP-3-19	FIA1: 5.4-10.4 µm FIA2: 5.9-10.9 µm FIA3: 9-14.2 µm	FIA1: Equant/irregular to tabular/irregular. FIA2: Equant/irregular to tabular/negative crystal. FIA3: Equant to tabular/irregular.	FIA1: 4%-7% (V); 12%-14% (L2); 79%-84% (L1); (Heterogeneous) FIA2: 1.6% (V); 9%-11% (L2); 73%-75% (L1); (Heterogeneous) FIA3: 2%-3% (V); 1.6%-1.9% (L2); 78%-82% (L1); (Homogeneous)	FIA1: Pseudosecondary; associated with FI trail that truncates at grain boundaries in highly deformed quartz. FIA2: Pseudosecondary; FI trail is truncated by grain boundaries. FIA3: Pseudosecondary; trail terminates well within grain boundaries in recrystallized quartz.
HPP-3-23	FIA1: 5.1-20.6 µm FIA2: 7.6-22.4 µm FIA3: 4.9-24.9 µm	FIA1: Tabular/irregular. FIA2: Tabular/negative crystal. FIA3: Equant to tabular/irregular.	FIA1: 7%-15% (V); 3%-5% (L2); 80%-90% (L1); (Heterogeneous) FIA2: 15%-17% (V); 83%-85% (L); (Heterogeneous) FIA3: 9%-14% (V); 6%-8% (L2); 78%-85% (L1); (Heterogeneous)	FIA1: Primary; 3D cluster away from grain edges and fractures. FIA2: Primary; 3D cluster away from grain edges and fractures. FIA3: Primary; 3D cluster away from grain edges and fractures.
HPP-3-27-PL	N/A	N/A	N/A	N/A

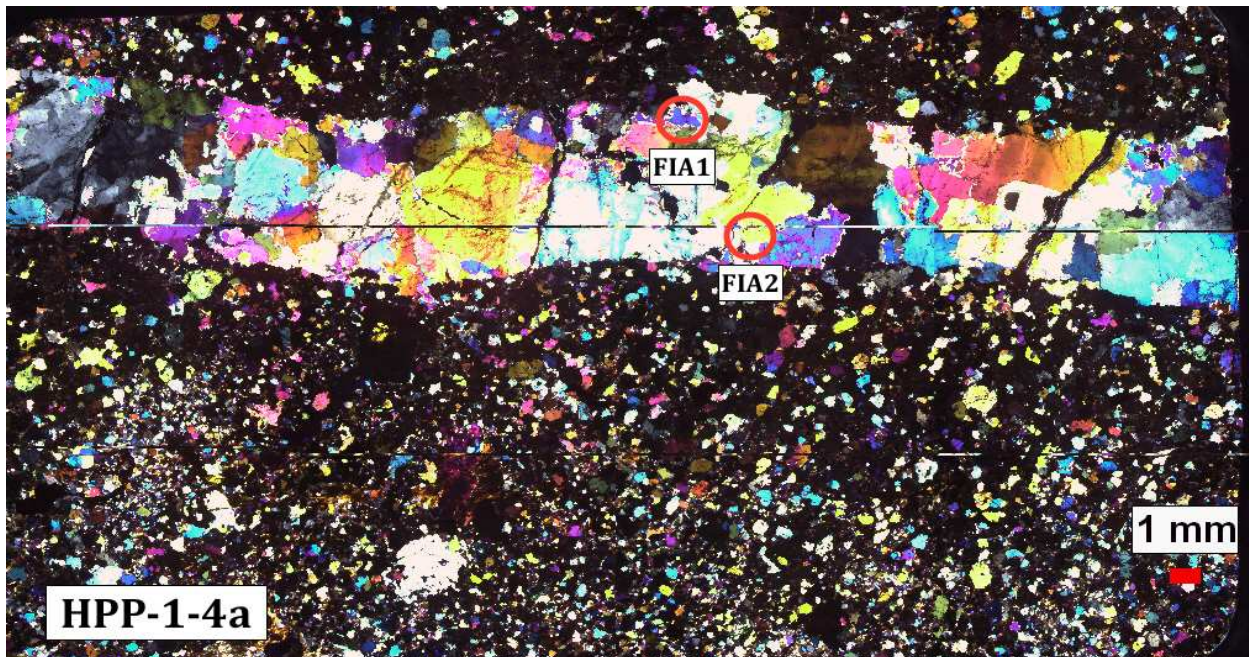
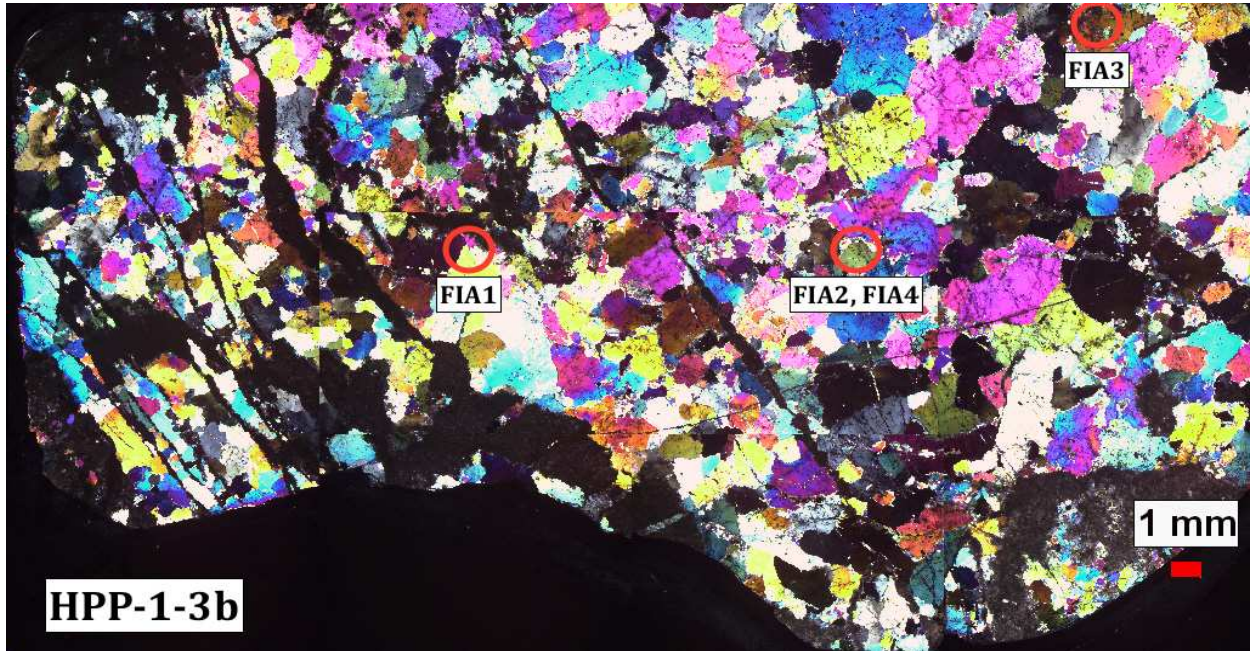
Sample ID	Feature Type	Petrographic Description of Host Mineral Grain(s)	Petrographic Group	Number & Nature of Phases (for each assemblage)	# of Assemblages Investigated
HPP-3-33	QF Pegmatite	Strongly recrystallized quartz grains (0.5-2 mm) with strain indicators, (parallel-oriented recrystallized grains); at least two resistant quartz clasts (0.75 cm) with surrounding flow textures.	Group 5	FIA1: 2-phase (L+V) & 3-phase (L1+L2+V) (Group 5) FIA2: 2-phase (L1+L2+V) (Group 5) FIA3: 3-phase (L+V+S) (Group 5)	3
HPP-3-38	Type (II) (wallrock) Quartz Vein	Highly fractured and recrystallized quartz at contact with metacarbonate. Very low FI density.	Group 3	FIA1: 2-phase (L+V) (Group 3) FIA2: 2-phase (L+V) (Group 3)	2
HPP-4-01	Type (III) (skarn) Quartz Vein	Subhedral-anhedral quartz in quartz-calcite vein (qtz core) with intense zones of recrystallization along grain boundaries.	Group 1	FIA1: 2-phase (L+V) (Group 1) FIA2: 2-phase (L+V) (Group 1) FIA3: 2-phase (L+V) (Group 1)	3
HPP-4-02b	Type (II) (skarn) Quartz Vein	Anhedral massive quartz vein (2 crystals) cutting through diopside skarn, numerous fractures, only small recrystallization features (minor deformation). Smaller veinlets intruding into skarn, with small diopside segregations within vein margins as well.	Group 1	FIA1: 2-phase (L+V) (Group 1) FIA2: 2-phase (L+V) (Group 1)	2
HPP-4-06	Type (II) (skarn) Quartz Vein	Very large (>2 cm) quartz crystals from contact skarn. Numerous crosscutting FI trails and several recrystallized fractures.	Group 2; Group 4; Group 5	FIA1: 2-phase (L+V) (Group 2) FIA2: 2-phase (L+V) (Group 4/5) FIA3: 2-phase (L+V) (Group 4/5)	3

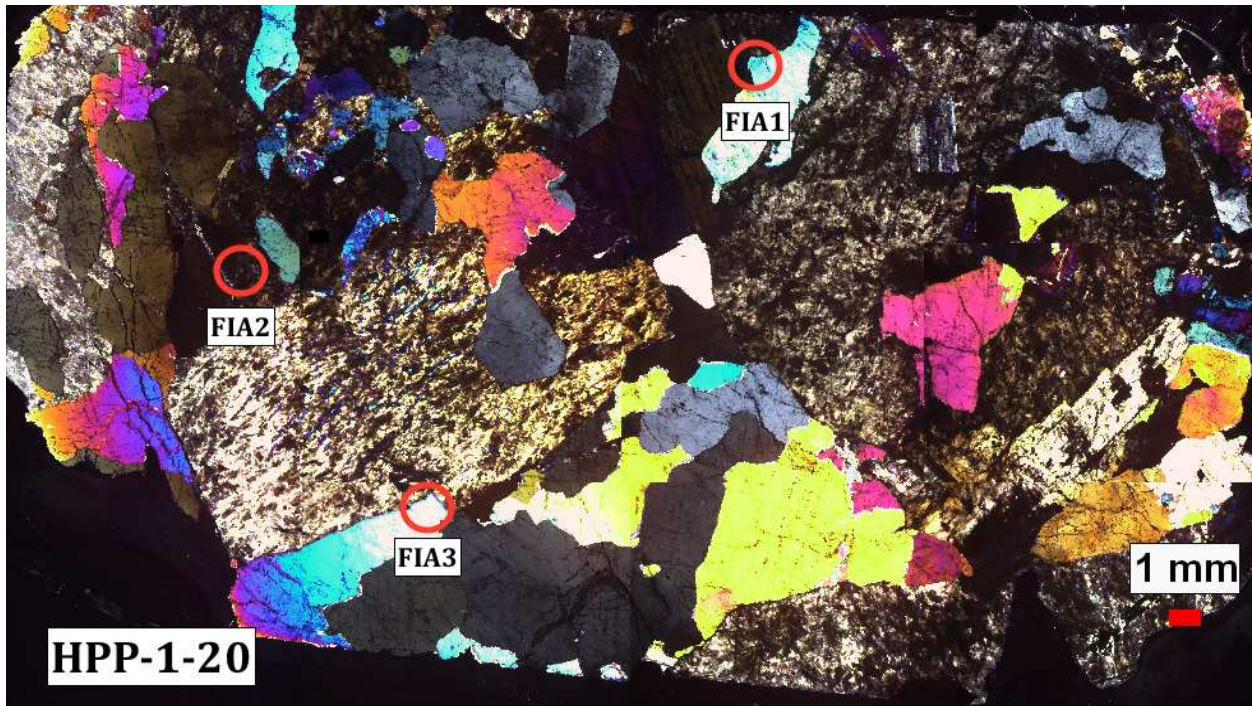
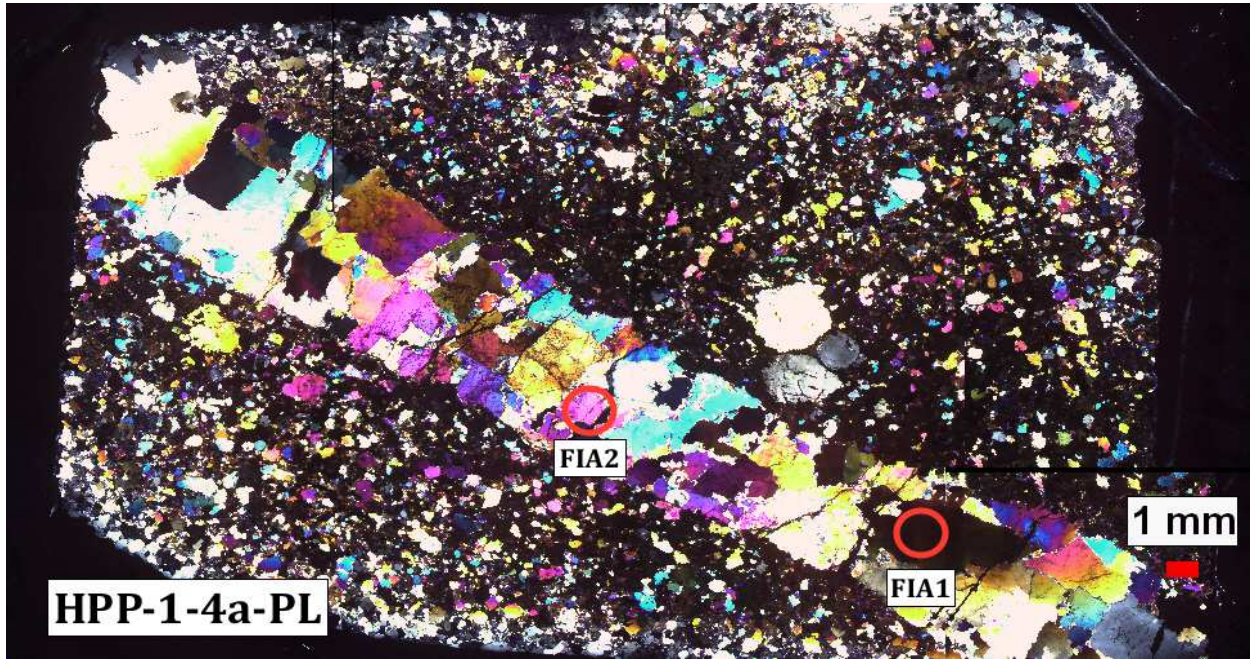
Sample ID	Size of Inclusions (µm) (for each assemblage)	Shape of Inclusions (for each assemblage)	Relative Volume Proportions for Phases (homogeneous or heterogeneous) (for each assemblage)	Interpretation of Assemblages (with brief explanation)
HPP-3-33	FIA1: 5.3-8.5 µm FIA2: 6.7 -11 µm FIA3: 4.7-11.6 µm (longest elongate)	FIA1: Negative crystal/tabular. FIA2: Irregular/negative crystal. FIA3: Irregular, negative crystal.	FIA1: 15%-20% (V); 80% (L1); 0%-5% (L2); (Homogeneous) FIA2: 15% (V); 5% (L2); 80% (L1); (Homogeneous) FIA3: 1%-2% (S); 8%-14% (V); 85%-90% (L); (Homogeneous)	FIA1: Secondary: FI trail crosscuts grain boundaries in highly recrystallized quartz. FIA2: Secondary: FI trail crosscuts grain boundaries in highly recrystallized quartz. FIA3: Secondary: FI trail crosscuts grain boundaries.
HPP-3-38	FIA1: 4.6 µm (single inclusion) FIA2: 6.6 µm (single inclusion)	FIA1: Irregular/elongate. FIA2: Tabular	FIA1: 3% (V); 97% (L); (Single inclusion) FIA2: 5% (V); 95% (L); (Single inclusion)	FIA1: Primary: isolated single inclusion. FIA2: Primary/Secondary?; no crosscutting trails nearby, several associated unresolvable small inclusions nearby, all parallel-oriented.
HPP-4-01	FIA1: 4.7-9.3 µm FIA2: 8.1-18.8 µm FIA3: 9.4-17.3 µm	FIA1: Equant to tabular. FIA2: Equant to negative crystal. FIA3: Equant to tabular, irregular.	FIA1: 5% (V); 95% (L); (Homogeneous) FIA2: 9% (V); 1-2% (L2); 89%-90% (L1); (Homogeneous) FIA3: 6% (V); 94% (L); (Homogeneous)	FIA1: Primary: 3D cluster of relatively large inclusions, not on FI trail. FIA2: Primary: 3D cluster. FIA3: Primary: 3D cluster.
HPP-4-02b	FIA1: 3.3-10.5 µm (longest elongate) FIA2: <5-8.7 µm	FIA1: Irregular, elongate. FIA2: Cubic/irregular to tabular/irregular.	FIA1: 10%-30% (V); 70%-90% (L) (Heterogeneous) FIA2: 4%-8% (V); 92%-96% (L); (Heterogeneous)	FIA1: Primary: cluster away from secondary trails, but in high FI-density area. FIA2: Primary: cluster in high FI density sample.
HPP-4-06	FIA1: 2.9-11.3 µm FIA2: 8.4-15.8 µm FIA3: 8.9-23.6 µm	FIA1: Cubic or tabular. FIA2: Tabular to irregular. FIA3: Cubic to elongate or irregular.	FIA1: 7%-8% (V); 3%-4% (L2); 88%-90% (L1); (Homogeneous) FIA2: 10% (V); 90% (L); (Homogeneous; may be two assemblages) FIA3: 3%-8% (V); 92%-97% (L); (Heterogeneous)	FIA1: Primary: FI trail terminates well within crystal boundaries and is in low FI-density area. FIA2: Secondary/Pseudosecondary; Trail crosscuts at least one crystal boundary. FIA3: Secondary/Pseudosecondary; Trail crosscuts at least one fracture zone.

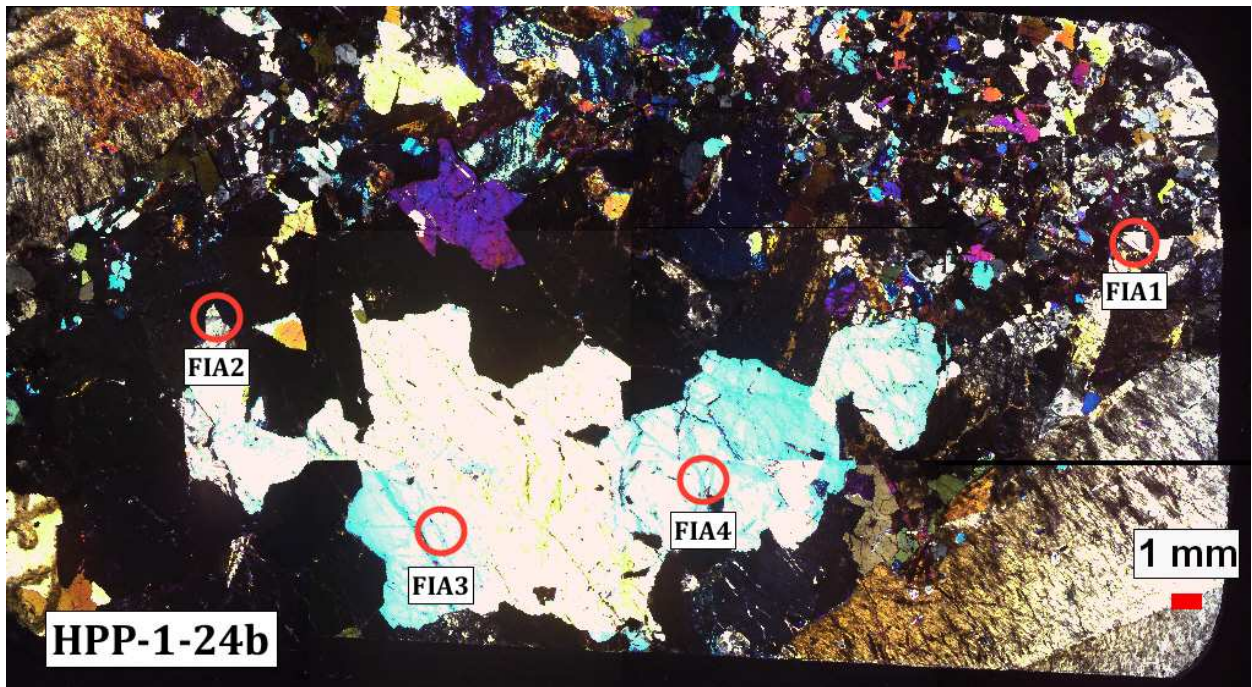
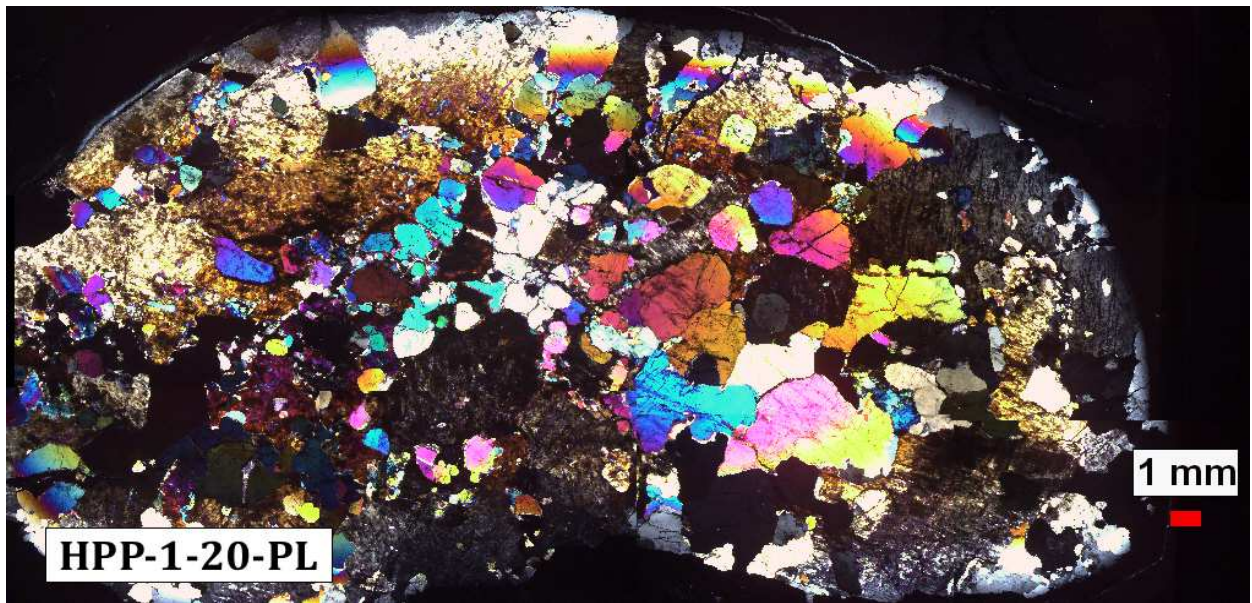
Sample ID	Feature Type	Petrographic Description of Host Mineral Grain(s)	Petrographic Group	Number & Nature of Phases (for each assemblage)	# of Assemblages Investigated
HPP-4-08	Type (III) Quartz Vein	Anhedra, somewhat parallel-oriented FI-rich, quartz crystals (1-10 mm) in pure milky quartz vein. Zones of recrystallization between grains as well as discrete fracture zones showing minor offset and strong fluid-free recrystallization.	Group 1	FIA1: 3-phase (L1+L2+V) (Group 1) FIA2: 3-phase (L1+L2+V) (Group 1) FIA3: 2-phase (L+V) (Group 1)	3
HPP-4-10	QF Pegmatite	Recrystallized, anhedral quartz with numerous fractures and FI trails crosscutting from QF-peg vein.	Group 1; Group 5	FIA1: 2-phase (L+V) (Group 1) FIA2: 2-phase (L+V) (Group 5) FIA3: 3-phase (L1+L2+V) (Group 5)	3

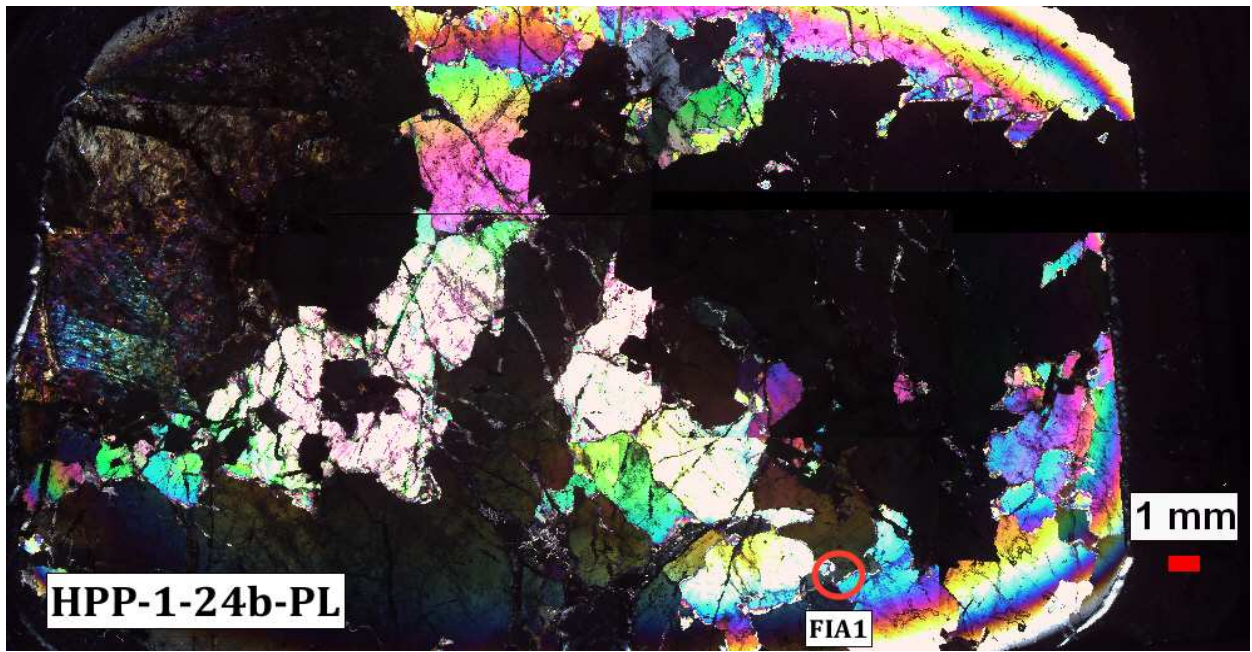
Sample ID	Size of Inclusions (µm) (for each assemblage)	Shape of Inclusions (for each assemblage)	Relative Volume Proportions for Phases (homogeneous or heterogeneous) (for each assemblage)	Interpretation of Assemblages (with brief explanation)
HPP-4-08	FIA1: <7-6-13.5 µm FIA2: 5.7-6 µm FIA3: 8.3-11.8 µm	FIA1: Irregular cubic to negative crystal. FIA2: Irregular, roughly equant/negative crystal. FIA3: Tabular/irregular.	FIA1: 10% (V); 10% (L2); 80% (L1) (Homogeneous) FIA2: 11%-15% (V); 6%-10% (L2); 75%-83% (L1); (Heterogeneous) FIA3: 10%-18% (V); 82%-90% (L1); (Heterogeneous).	FIA1: Primary; larger inclusions than surrounding trails, large vapor phase, irregular shape. FIA2: Primary; Larger inclusions, not associated with cross-cutting trail. FIA3: Primary; Larger inclusions not associated with cross-cutting trail.
HPP-4-10	FIA1: <3.9-13.7 µm FIA2: <3.3-29.7 µm FIA3: 4.6-13.1 µm	FIA1: Tabular/negative crystal to elongate/irregular. FIA2: Equant to highly elongate/irregular FIA3: Tabular to elongate/highly irregular.	FIA1: 15% (V); 85% (L); (Homogeneous) FIA2: 6-13% (V); 87%-94% (L); (Heterogeneous) FIA3: 4%-8% (V); 1%-3% (L2); 89%-95% (L1); (Homogeneous)	FIA1: Primary; 3D cluster in less recrystallized zone. FIA2: Secondary; located in crosscutting FI trail. FIA3: Secondary, diffuse cluster, may be a trail. Highly deformed, though.

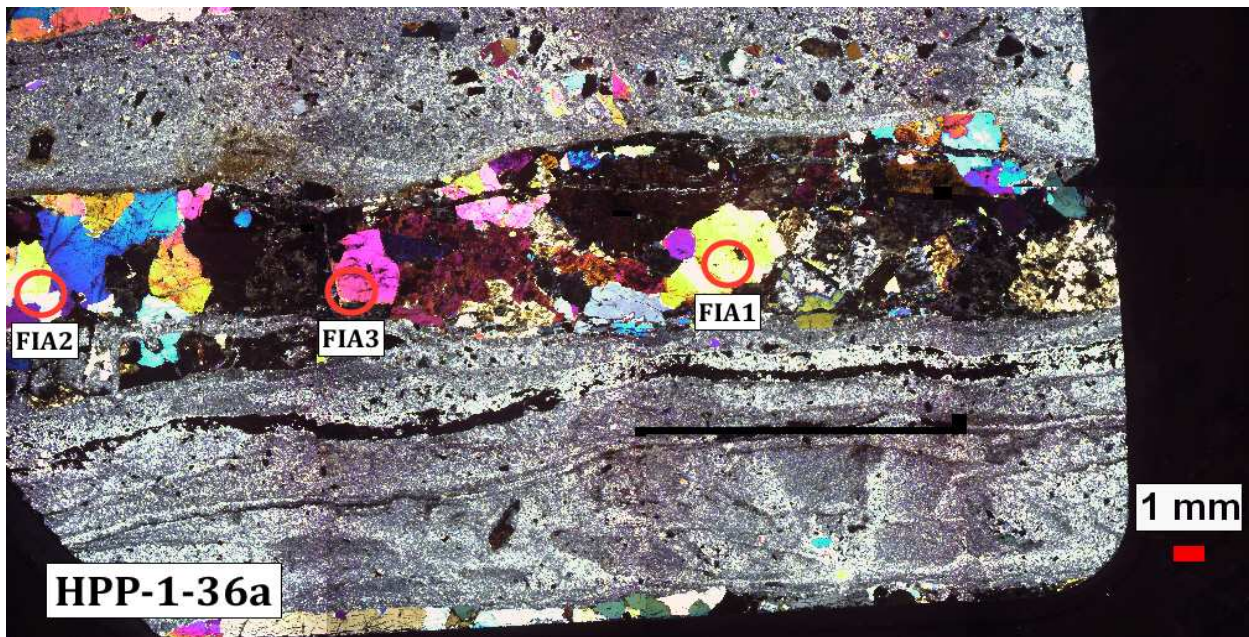
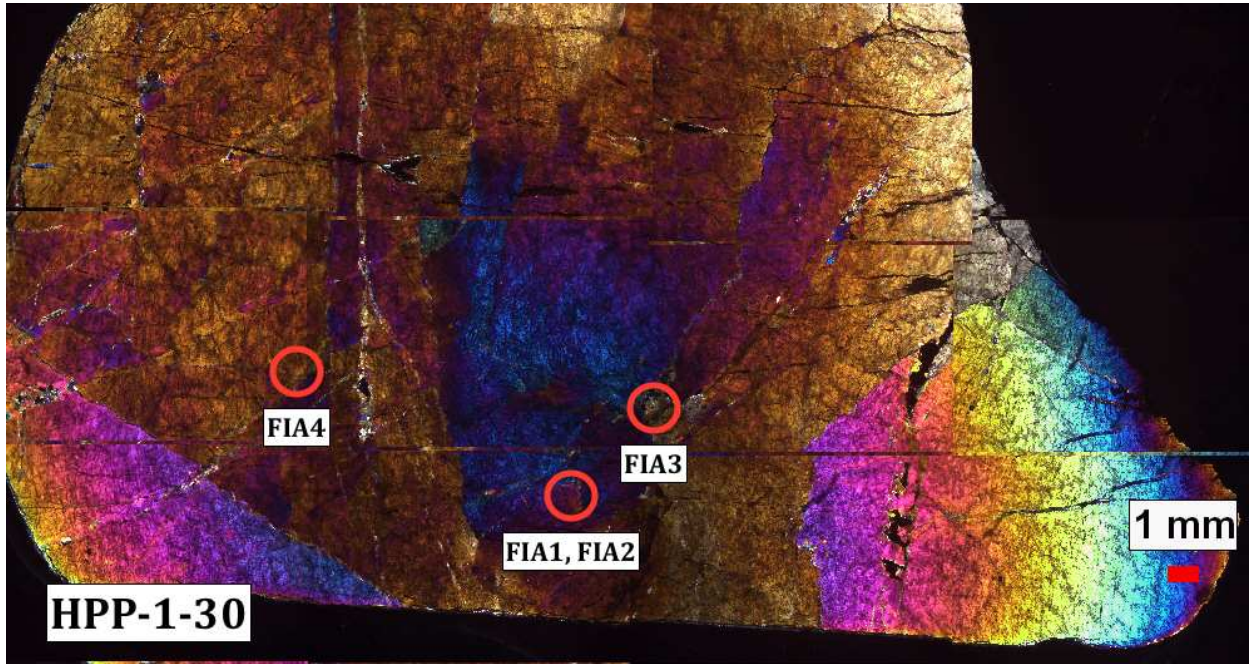
APPENDIX E.2: ANNOTATED FLUID INCLUSION THIN SECTION MOSAICS

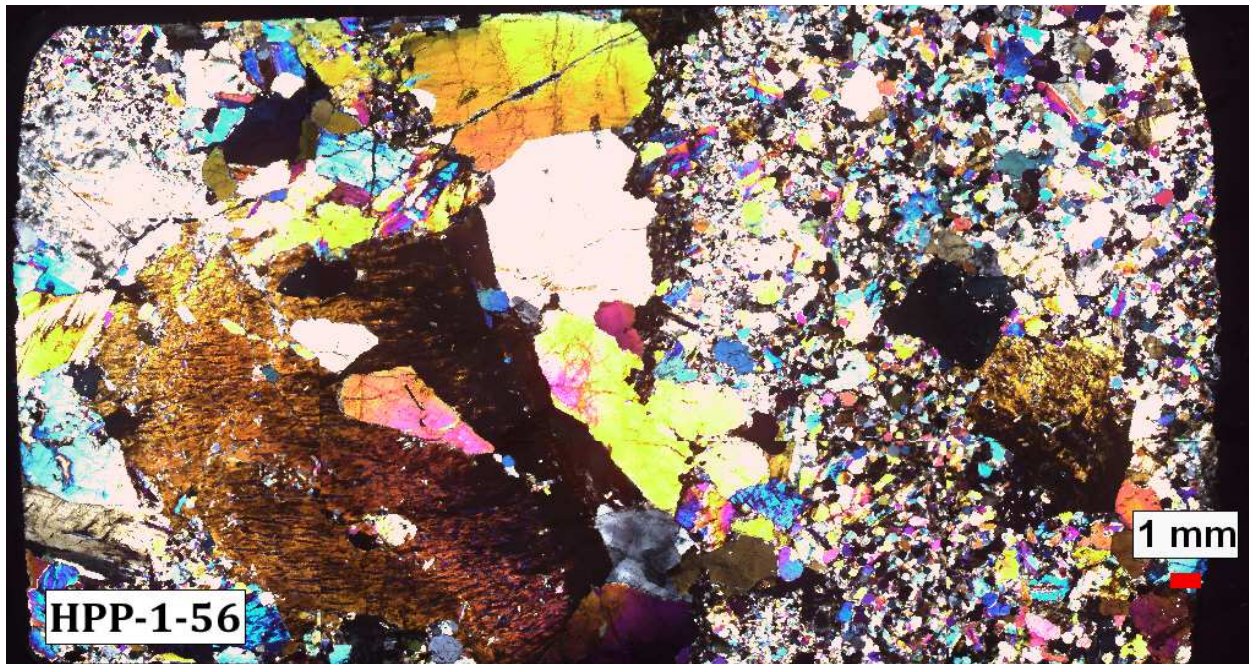


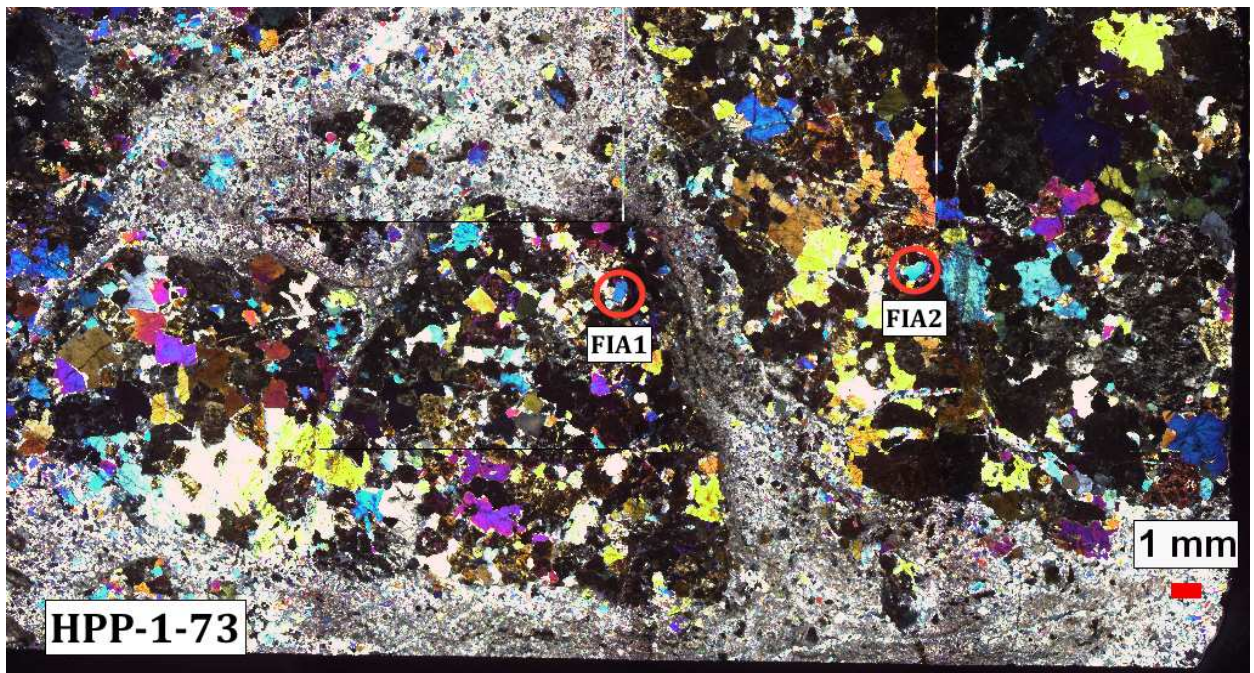


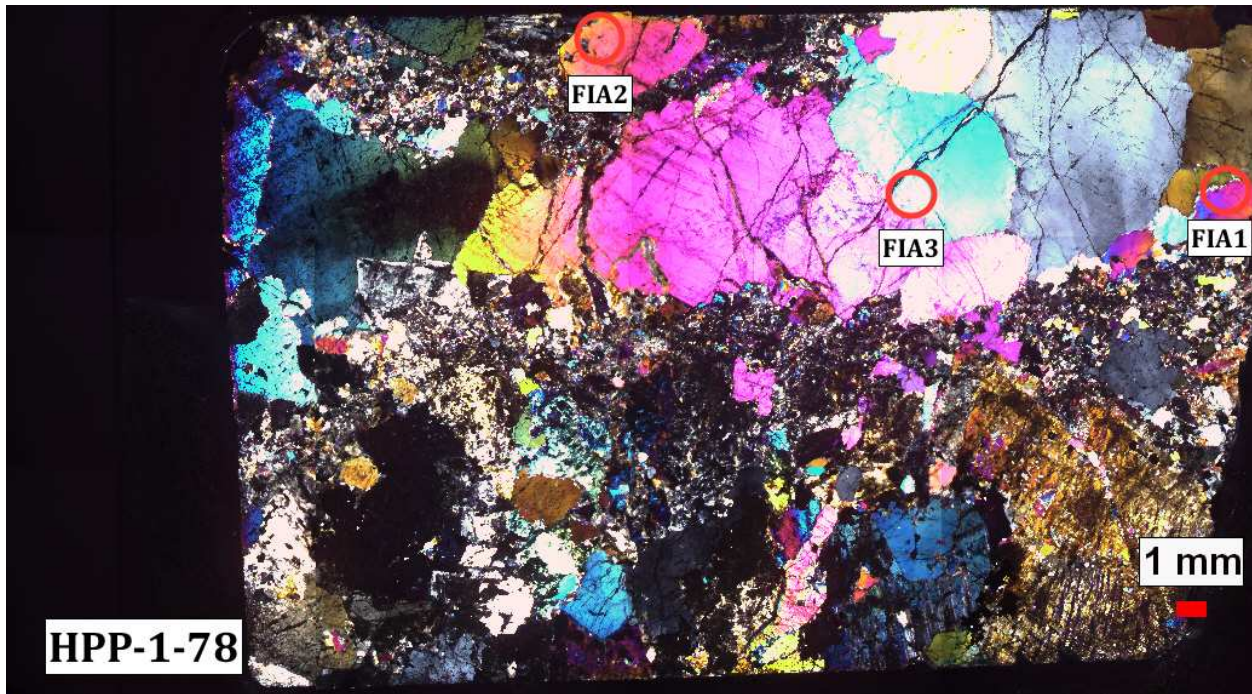
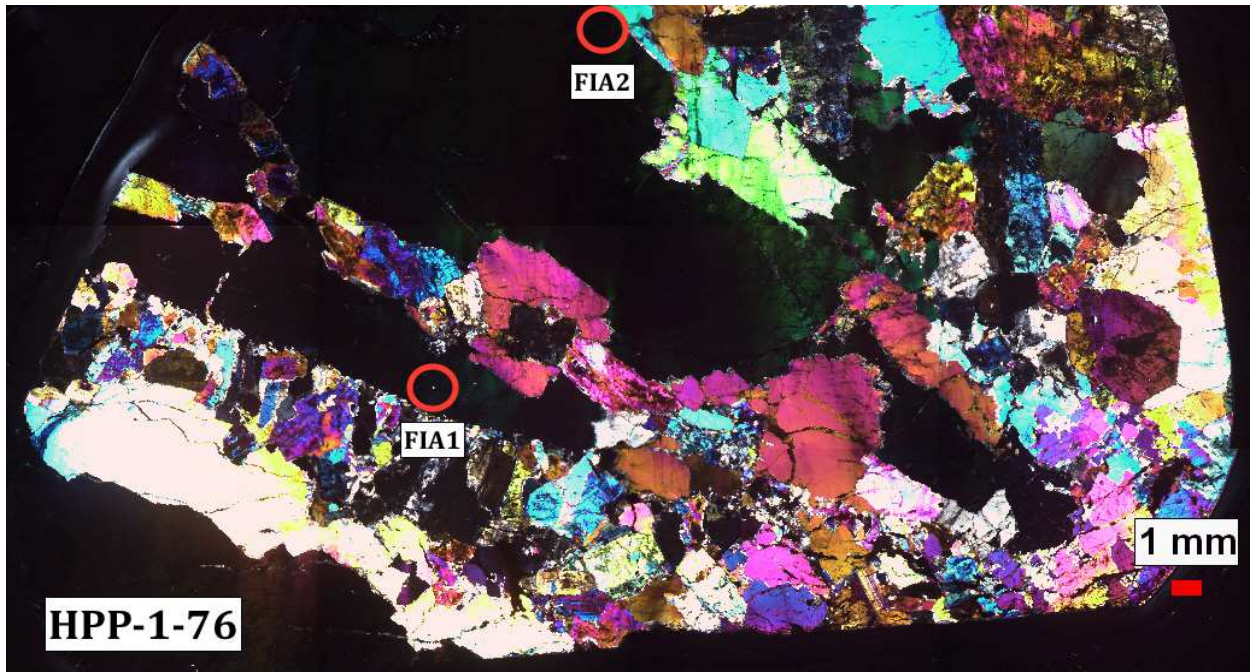


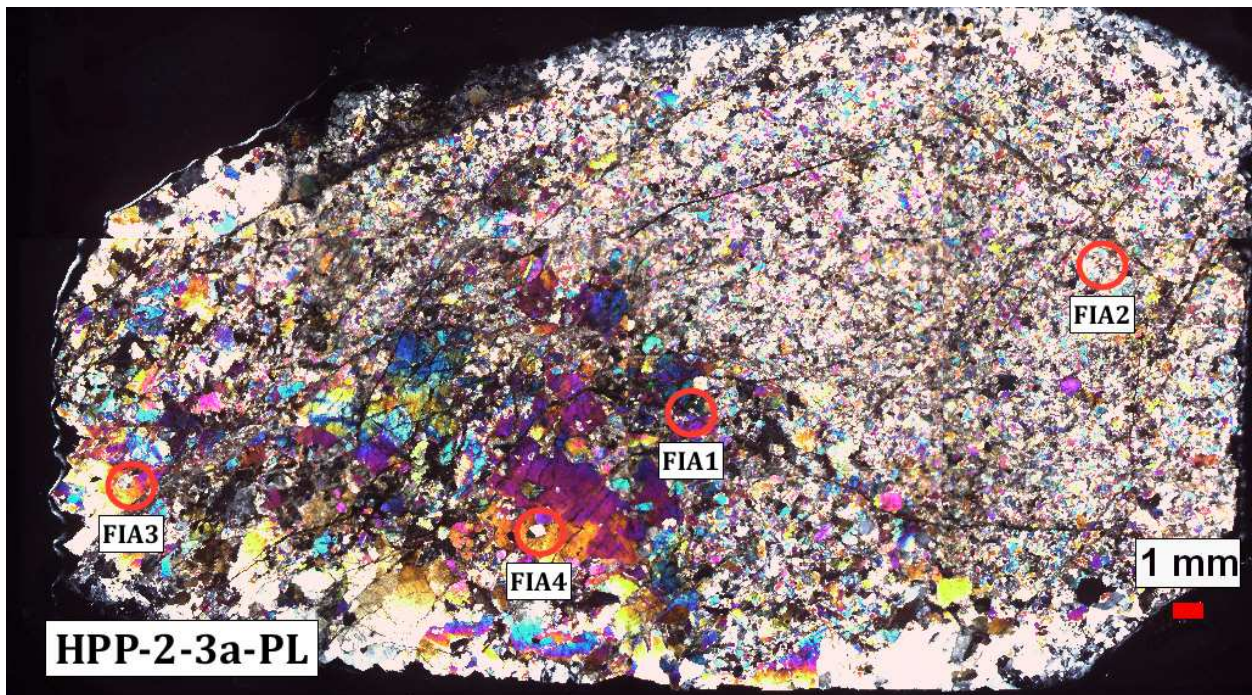
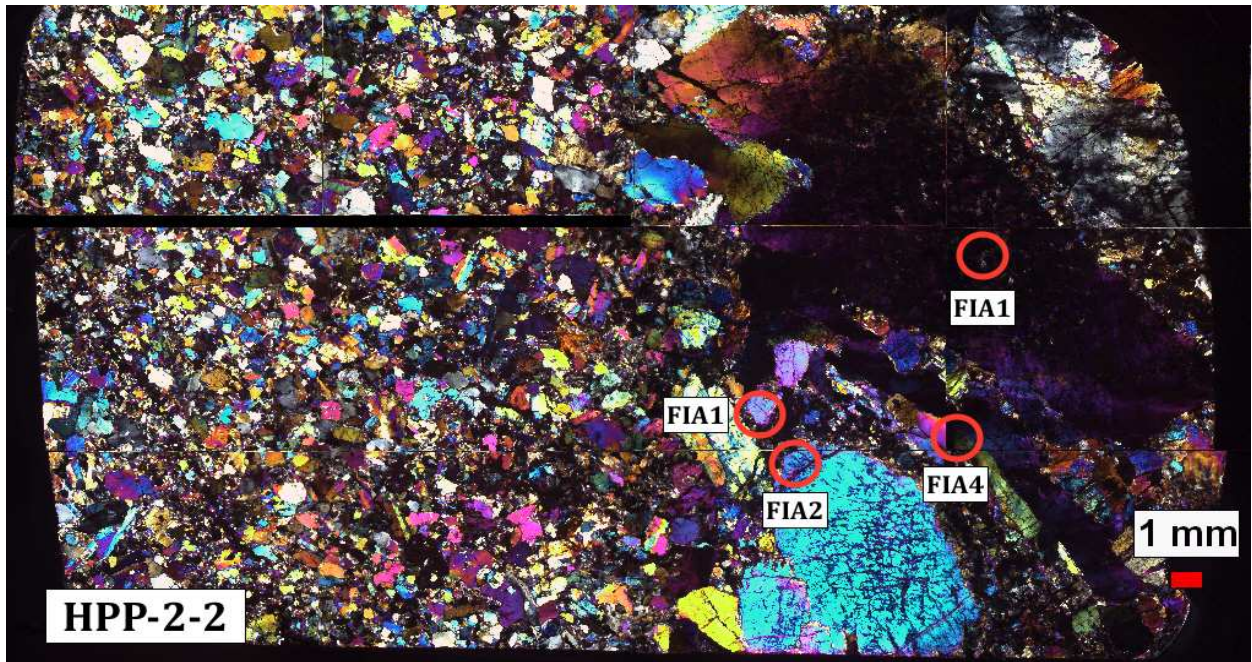


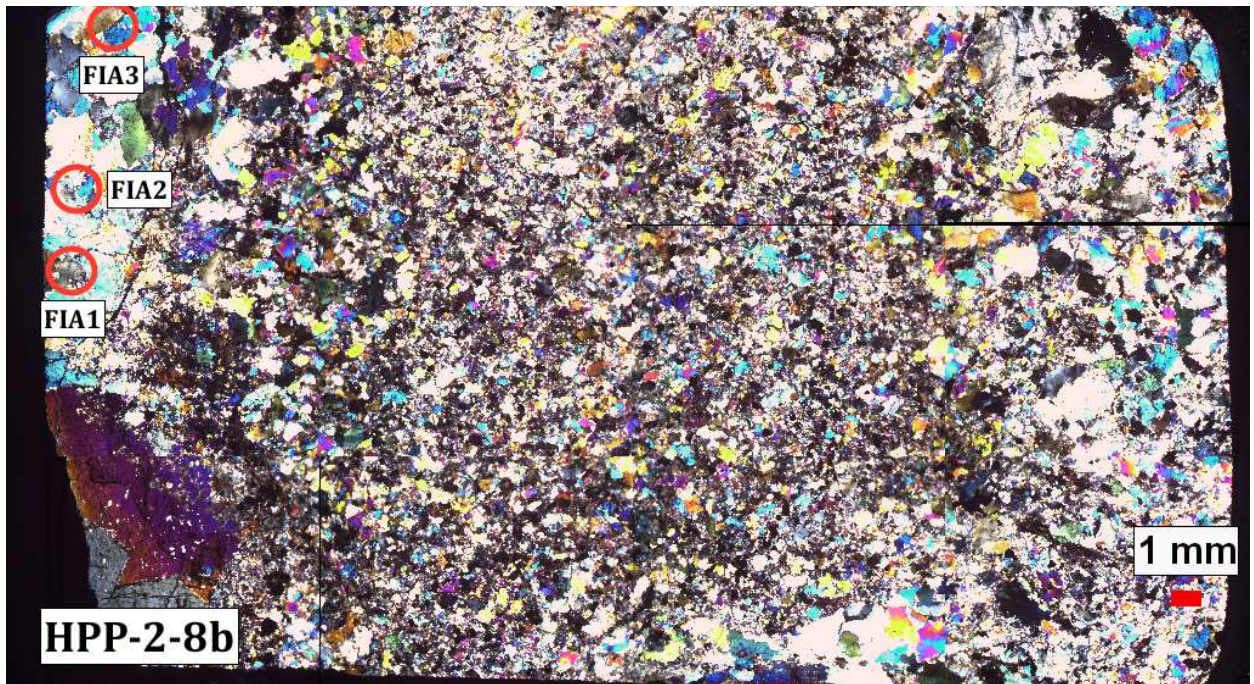
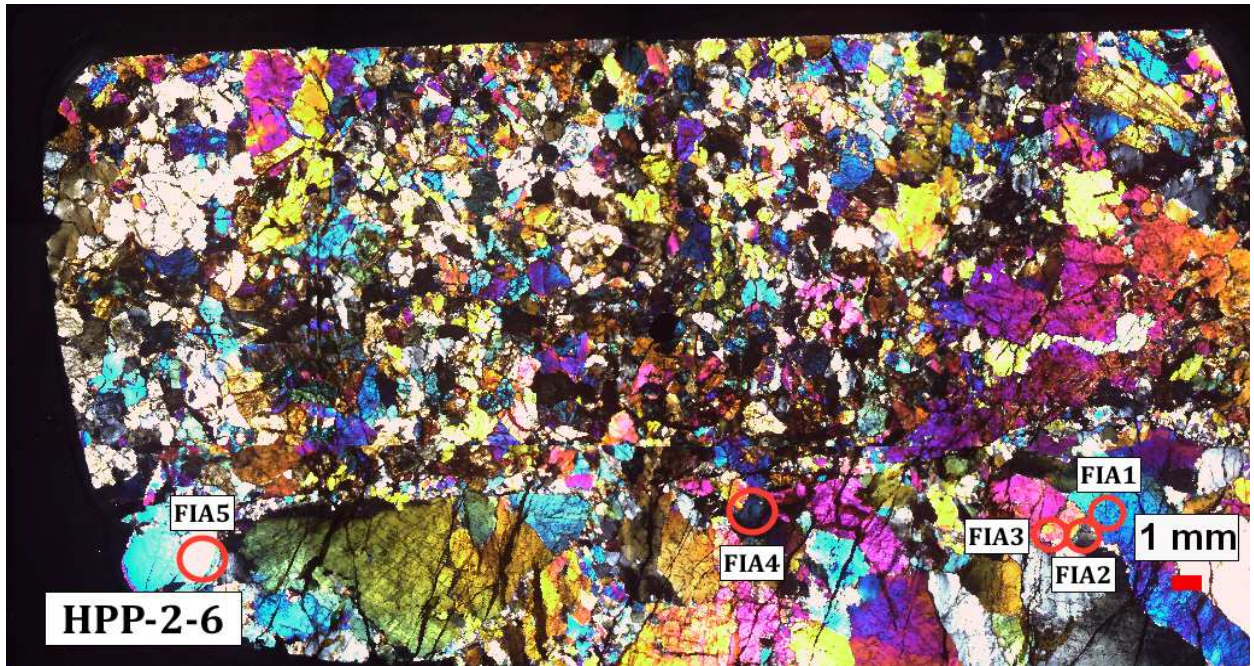


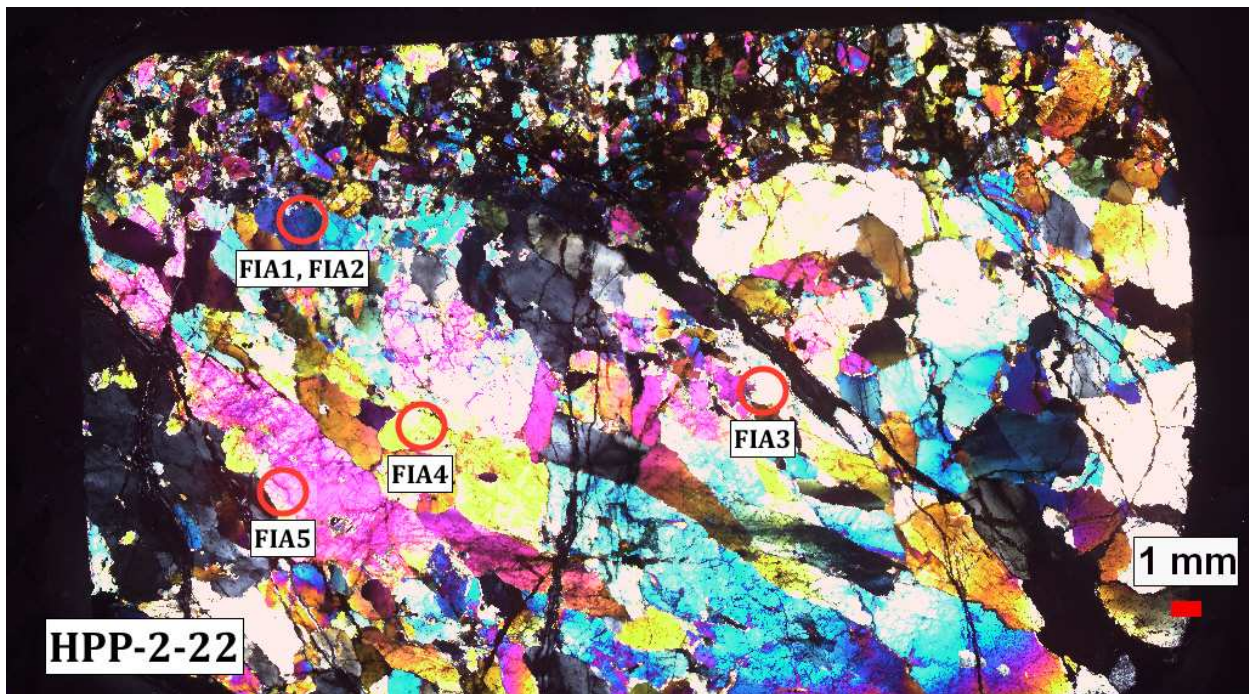
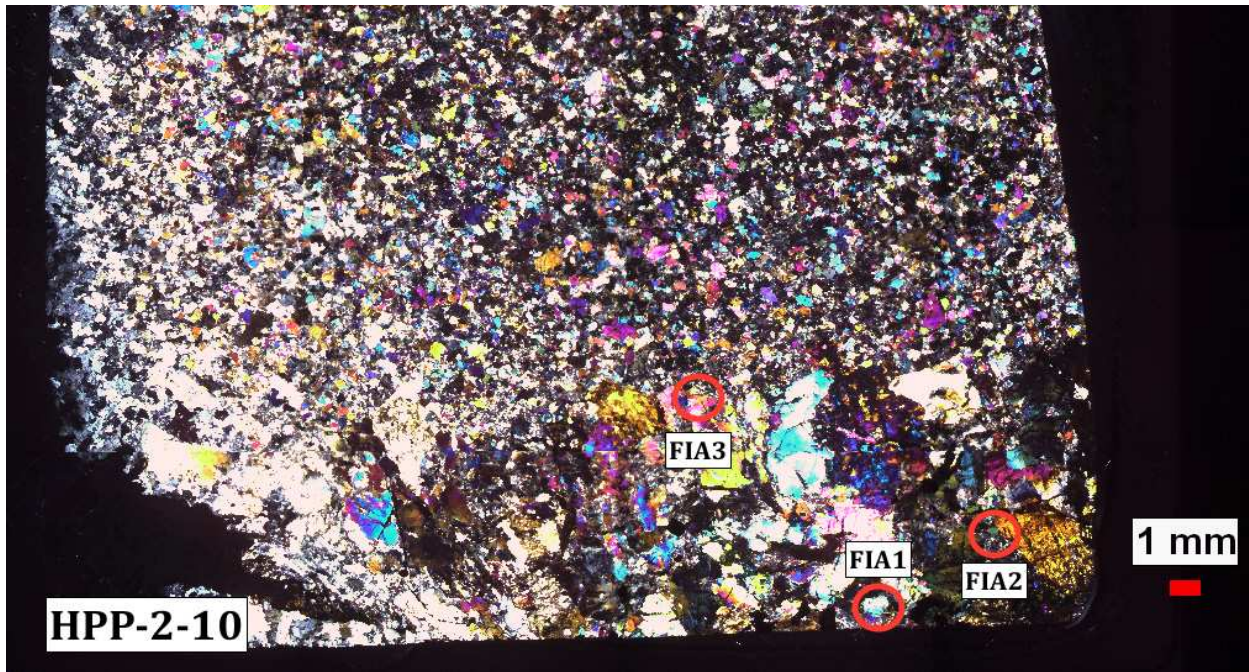


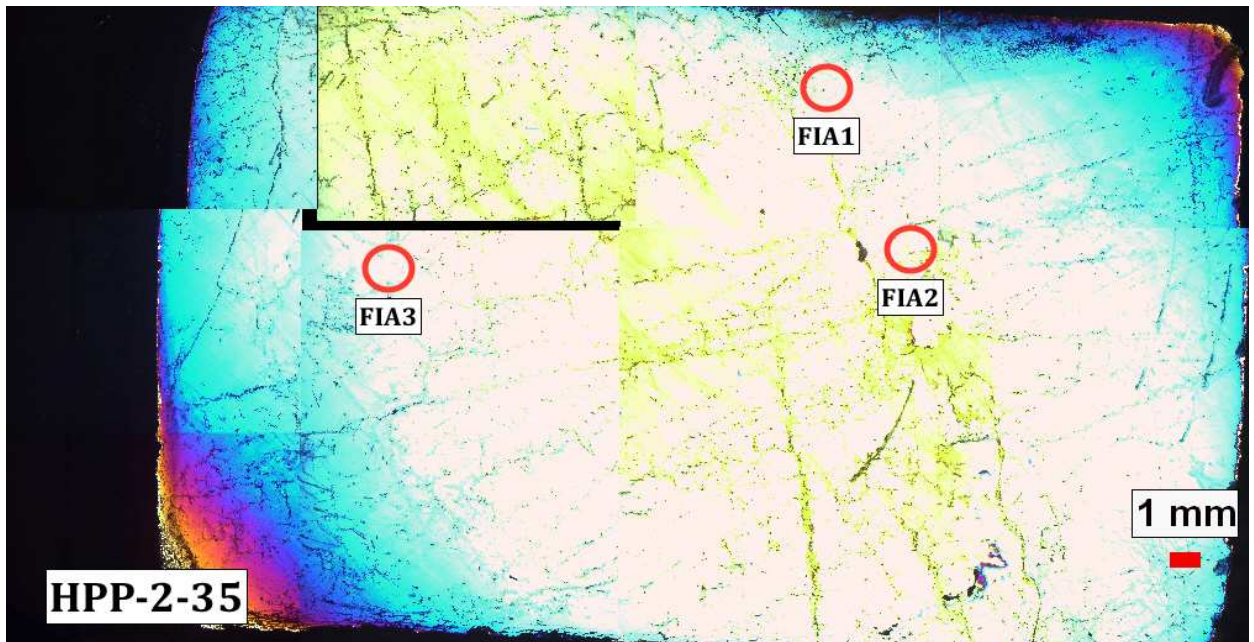
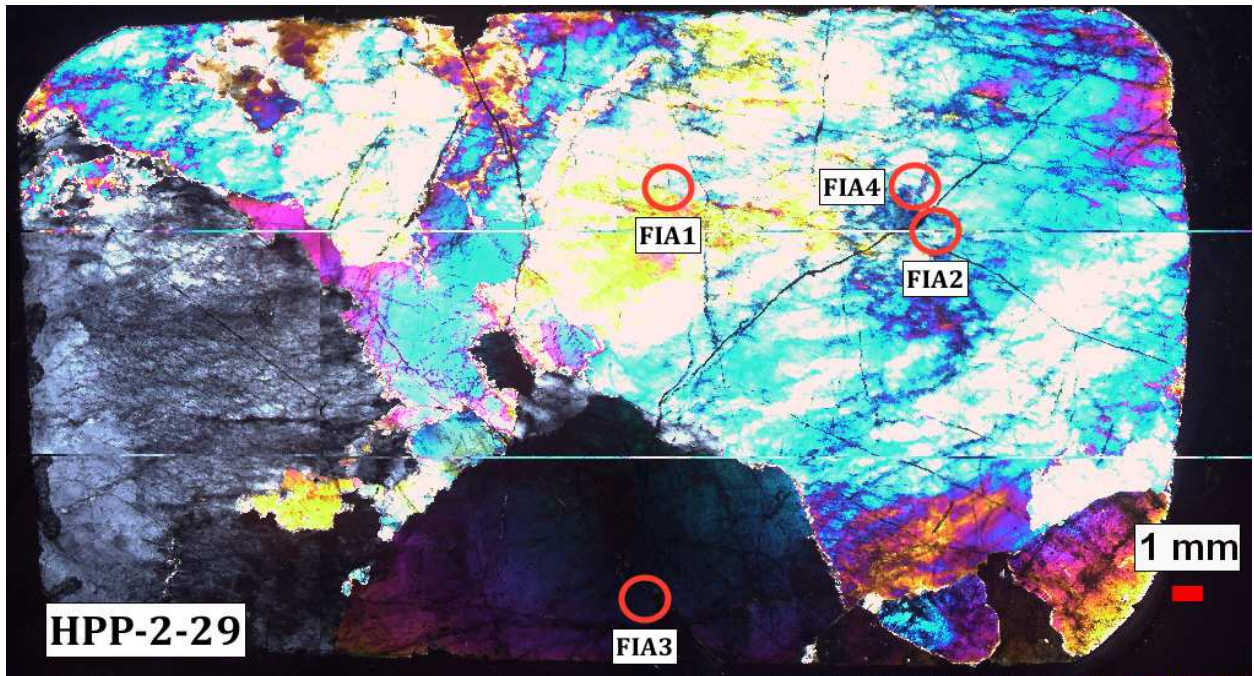


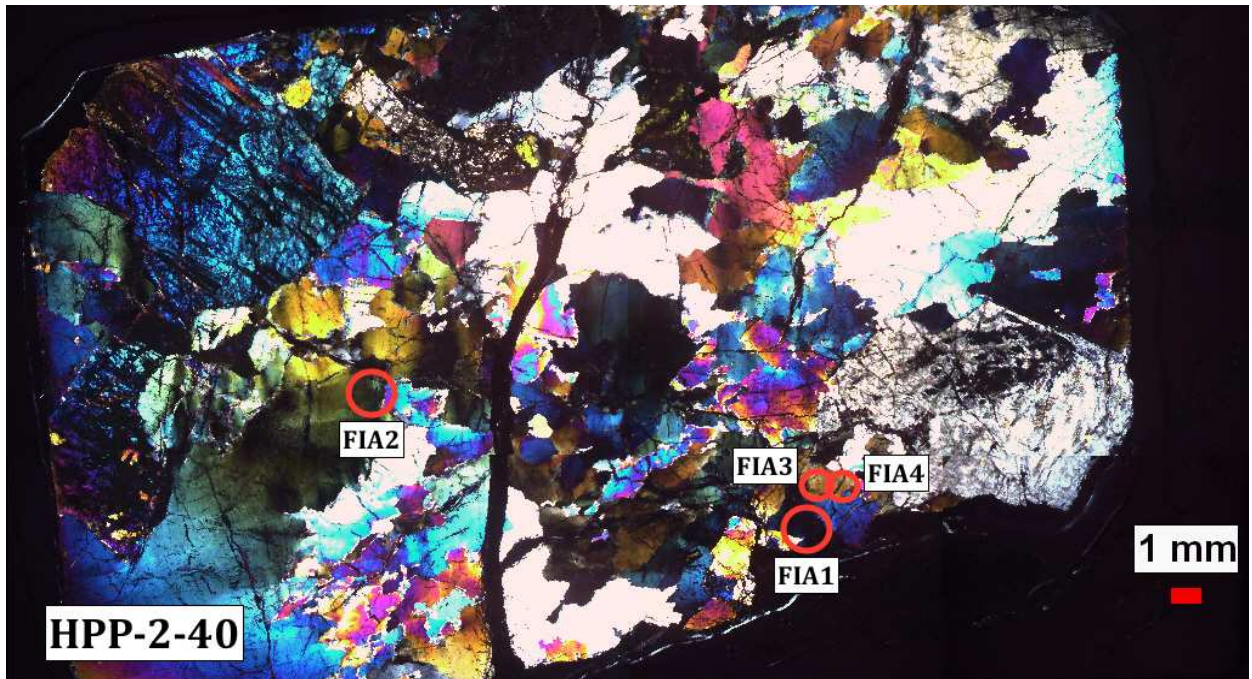
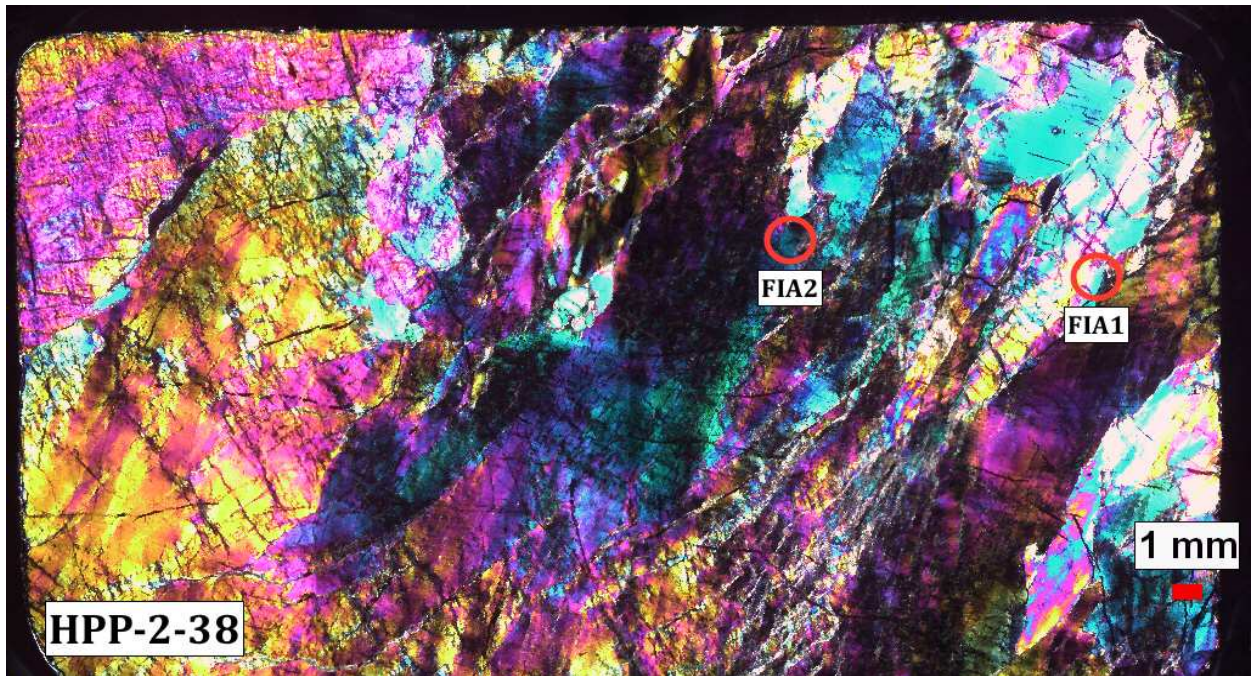


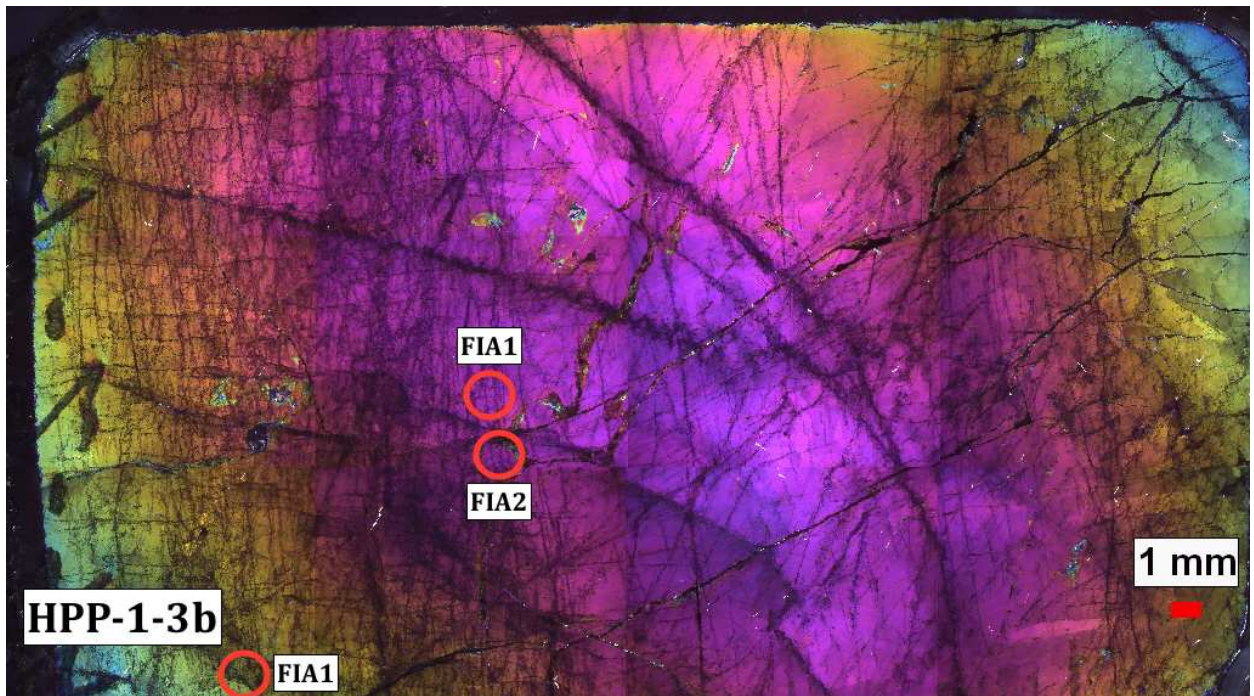
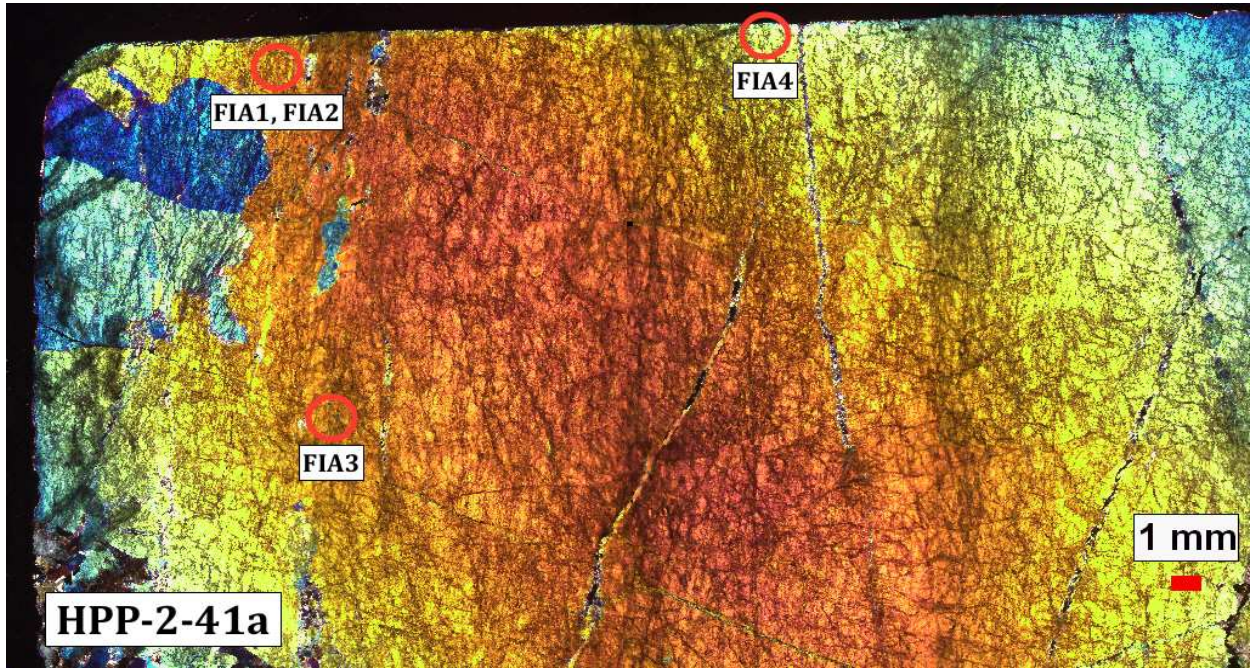


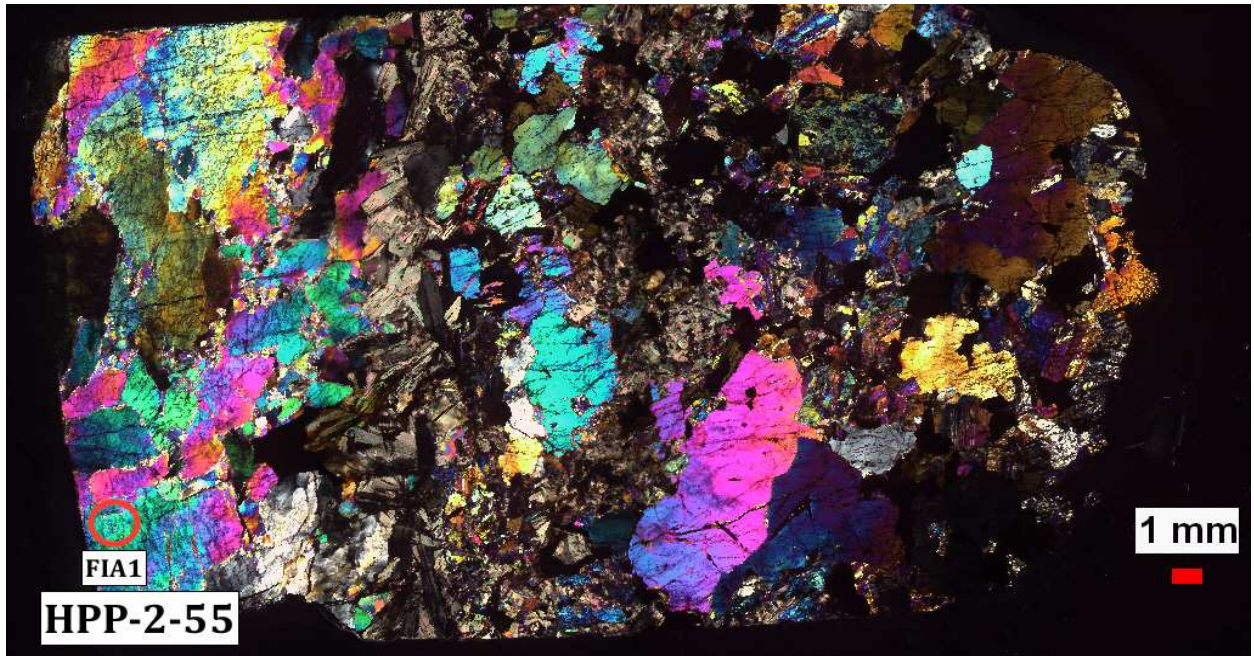
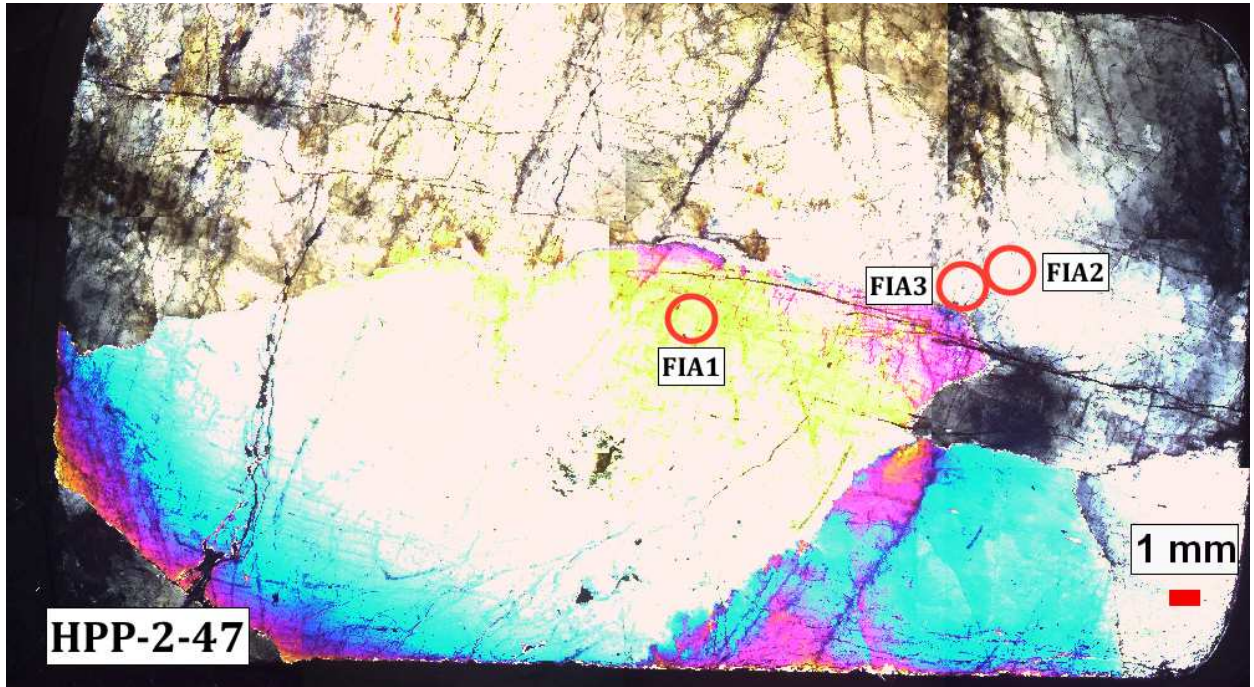


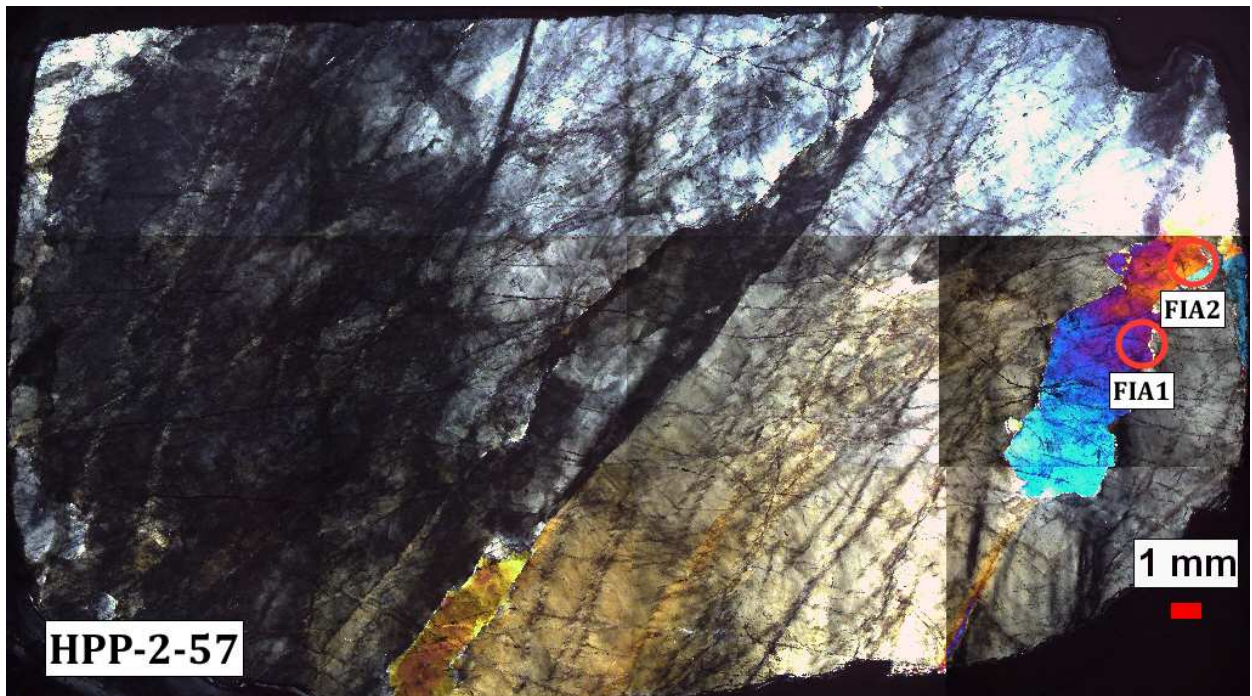
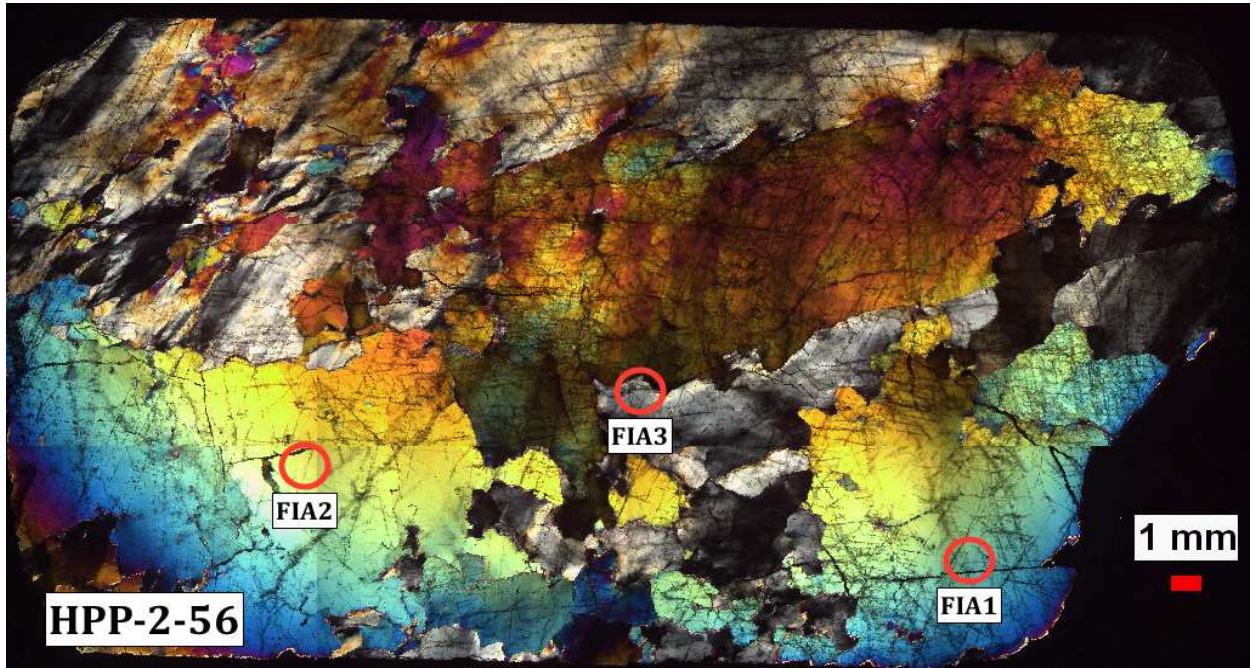


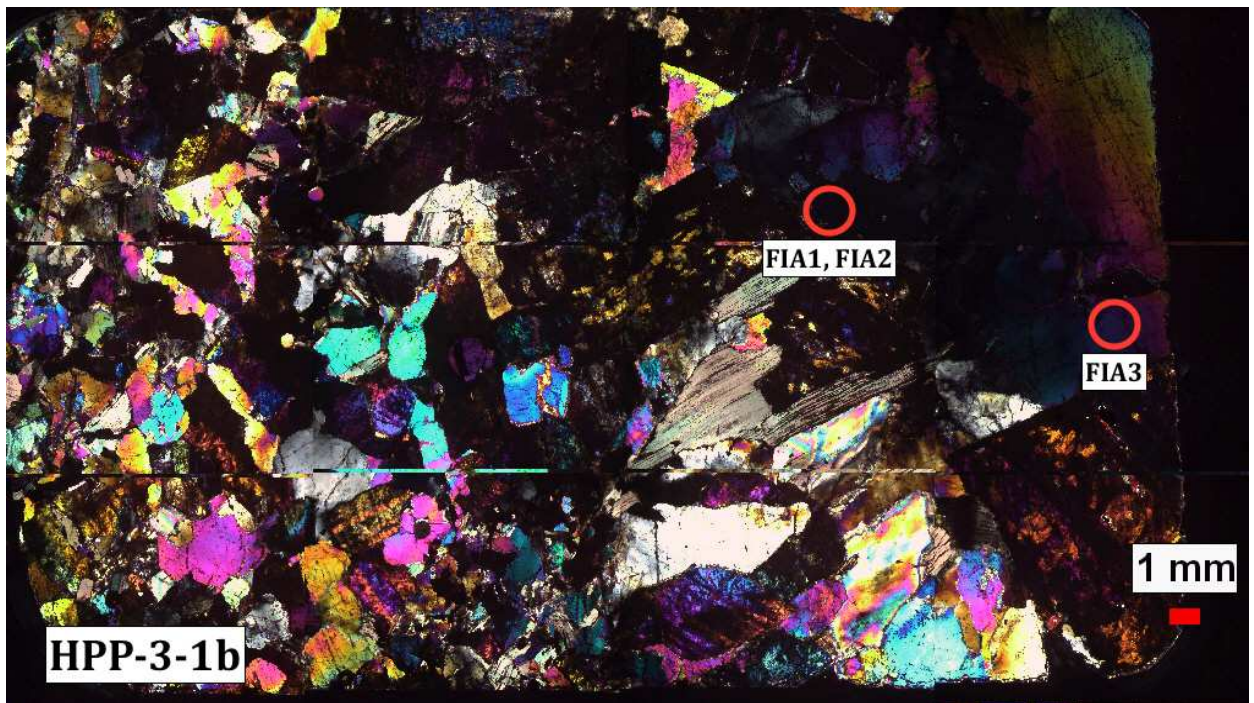
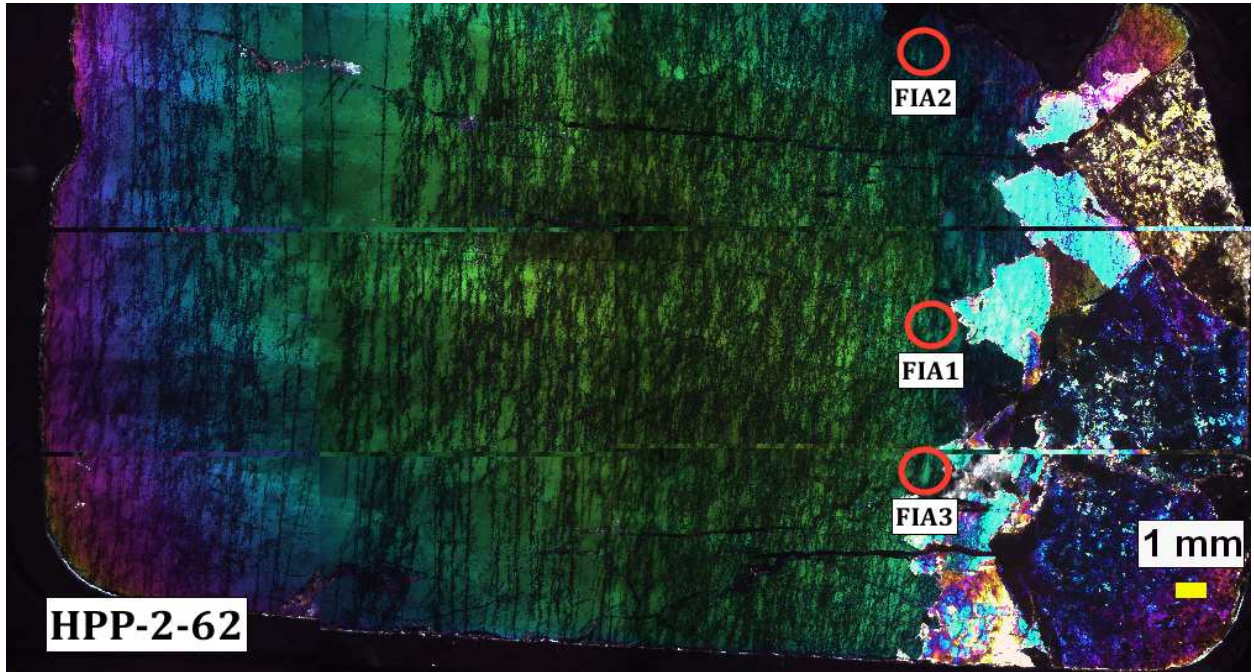


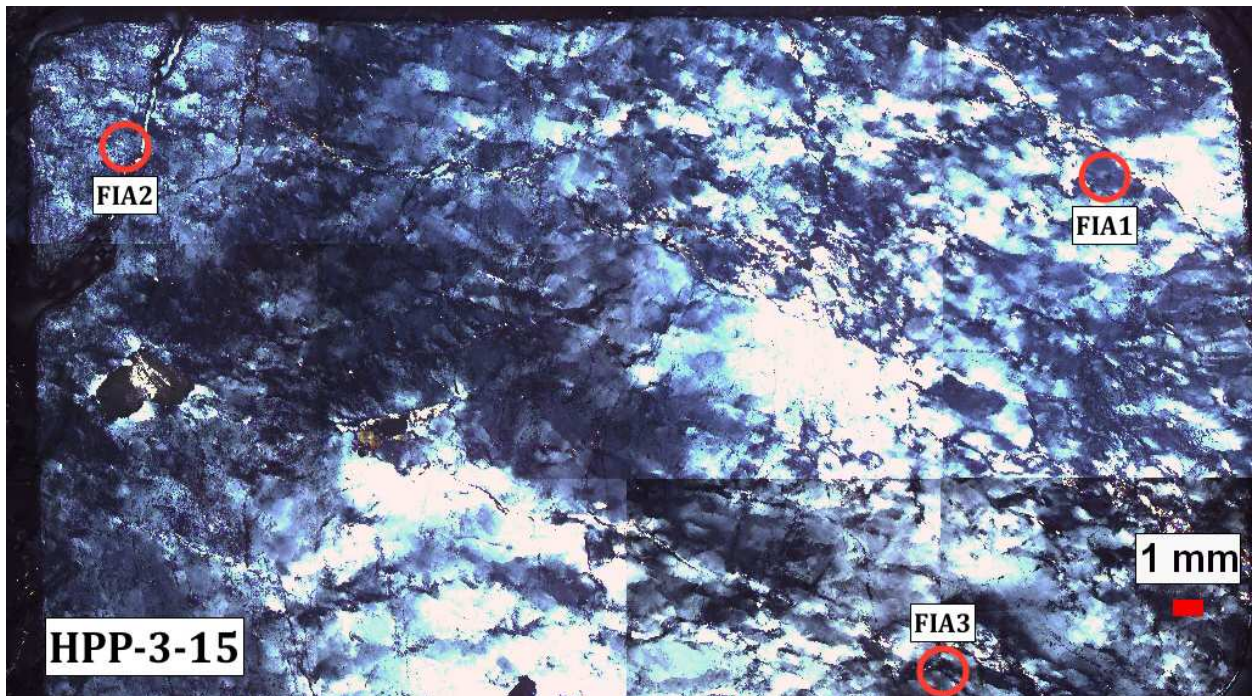
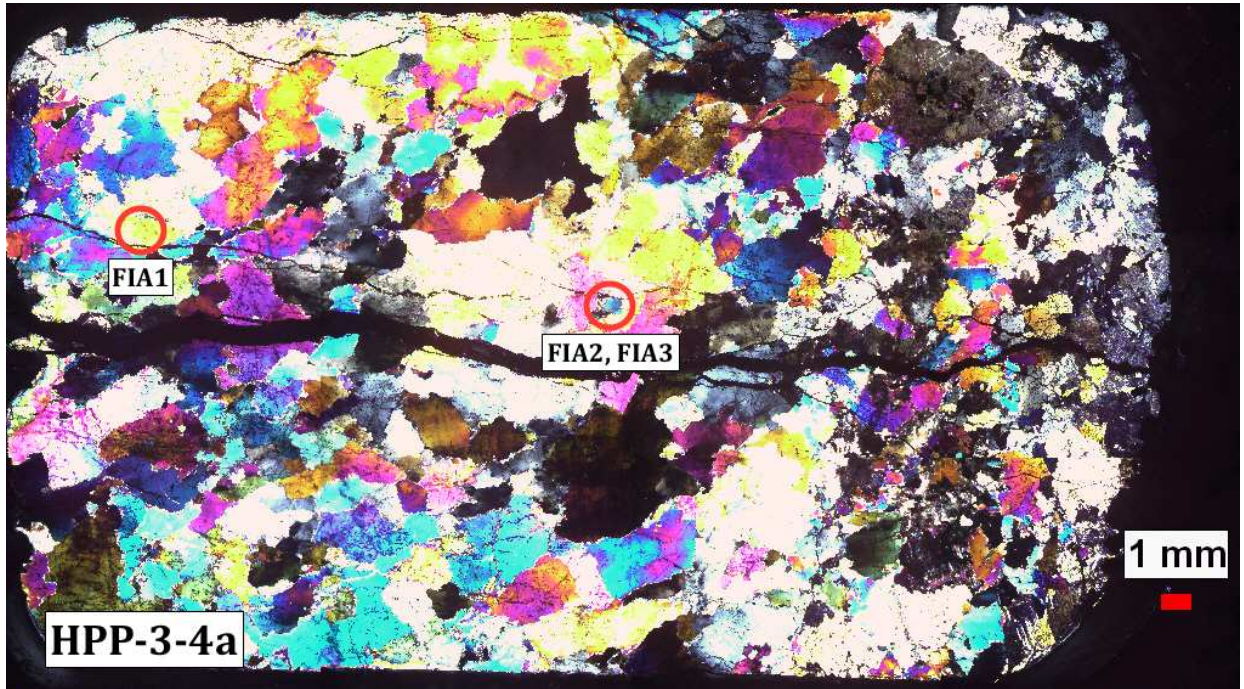


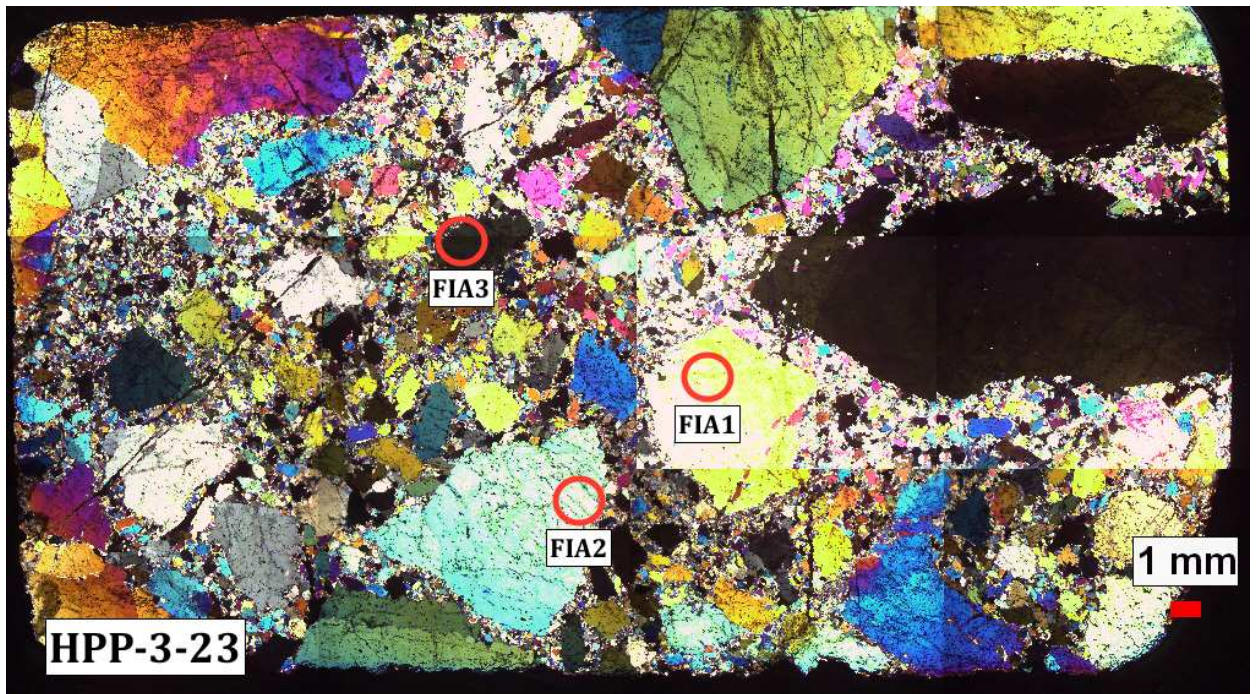
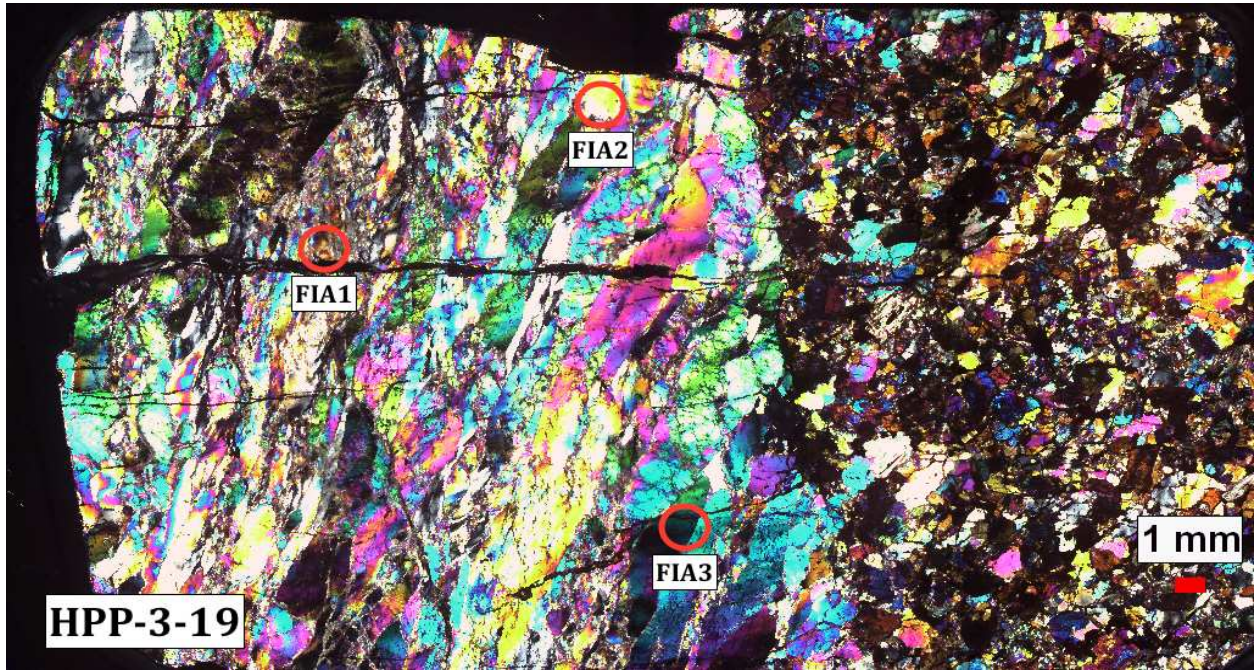


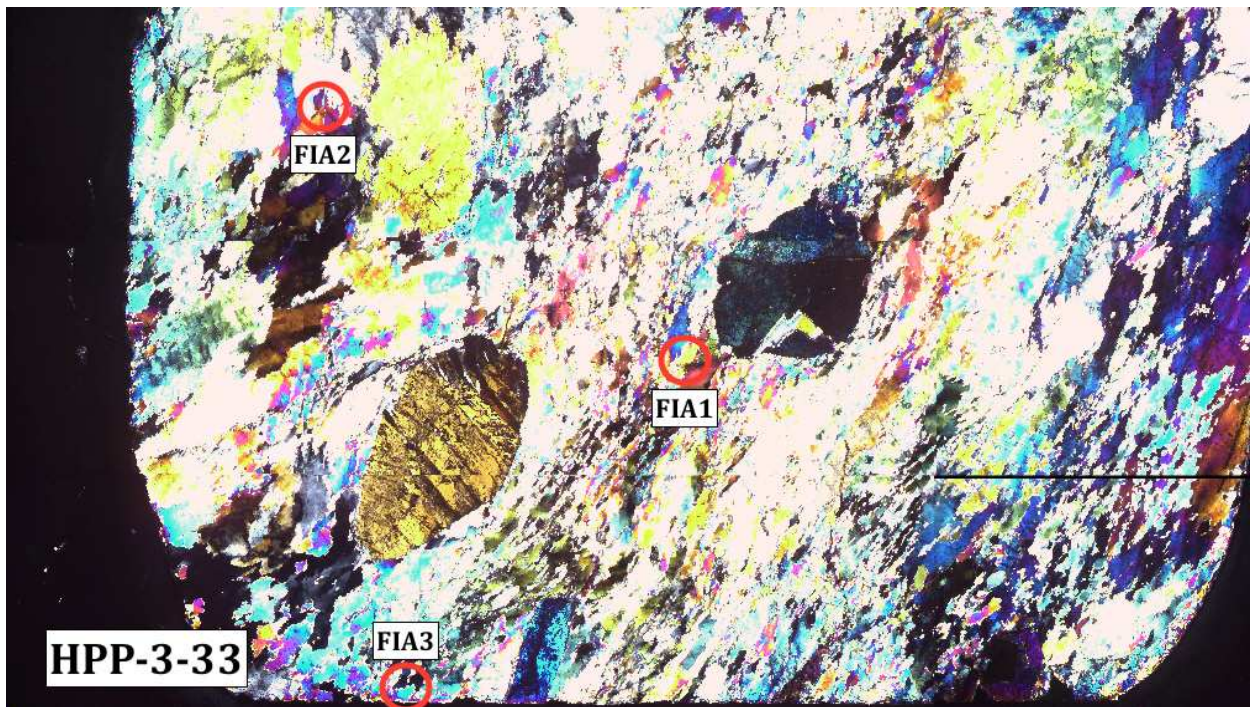
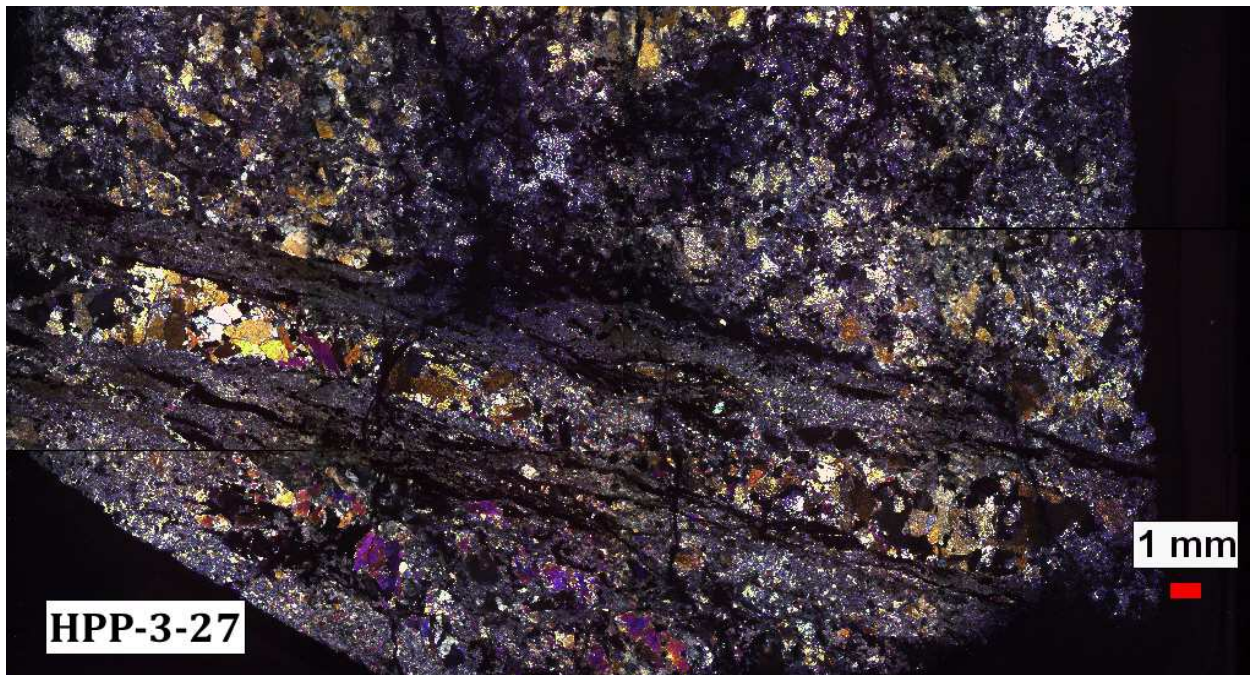


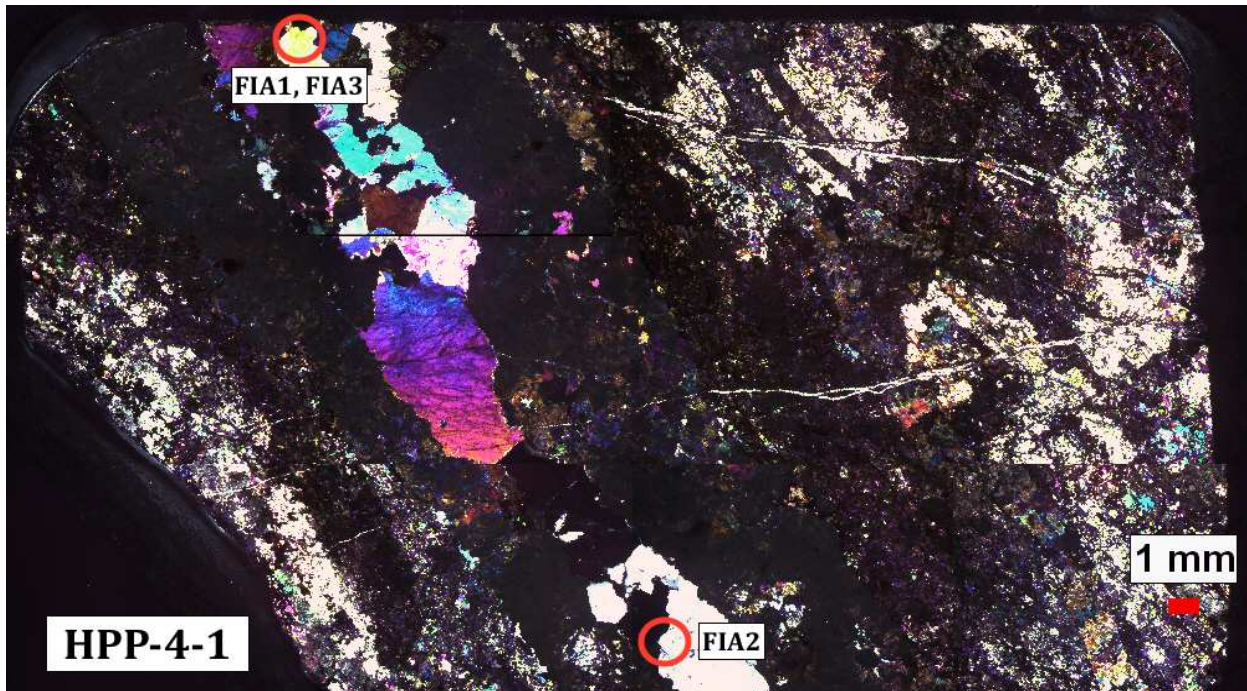
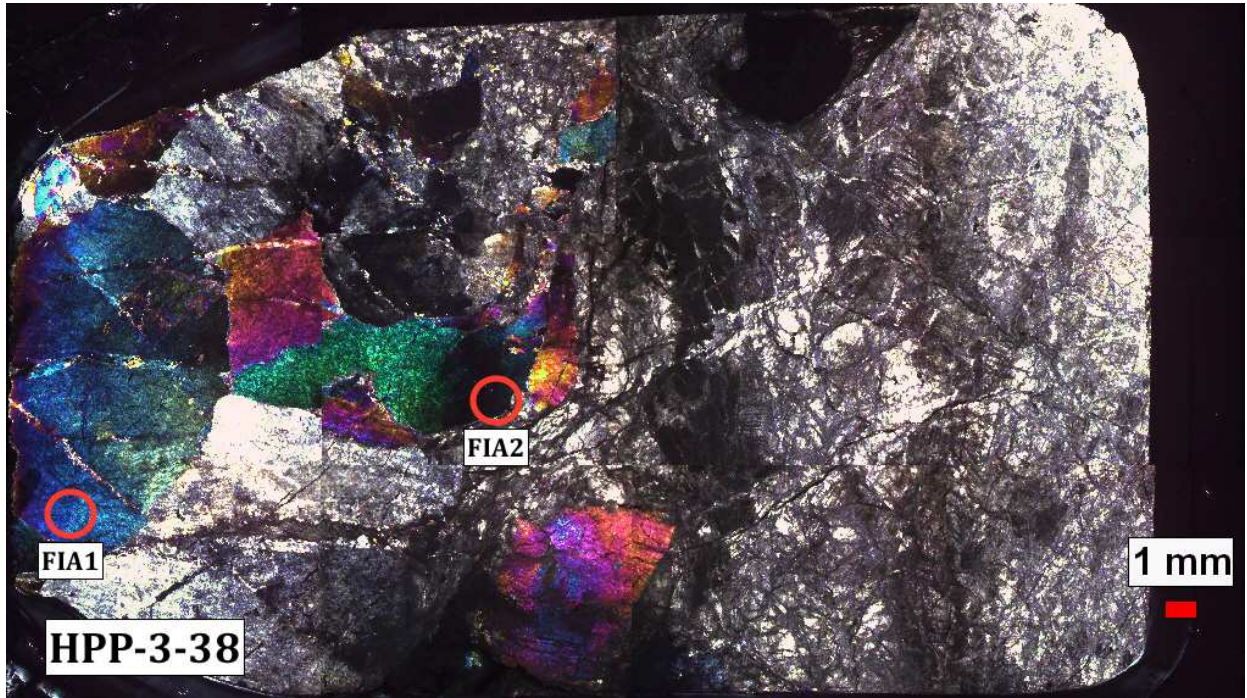


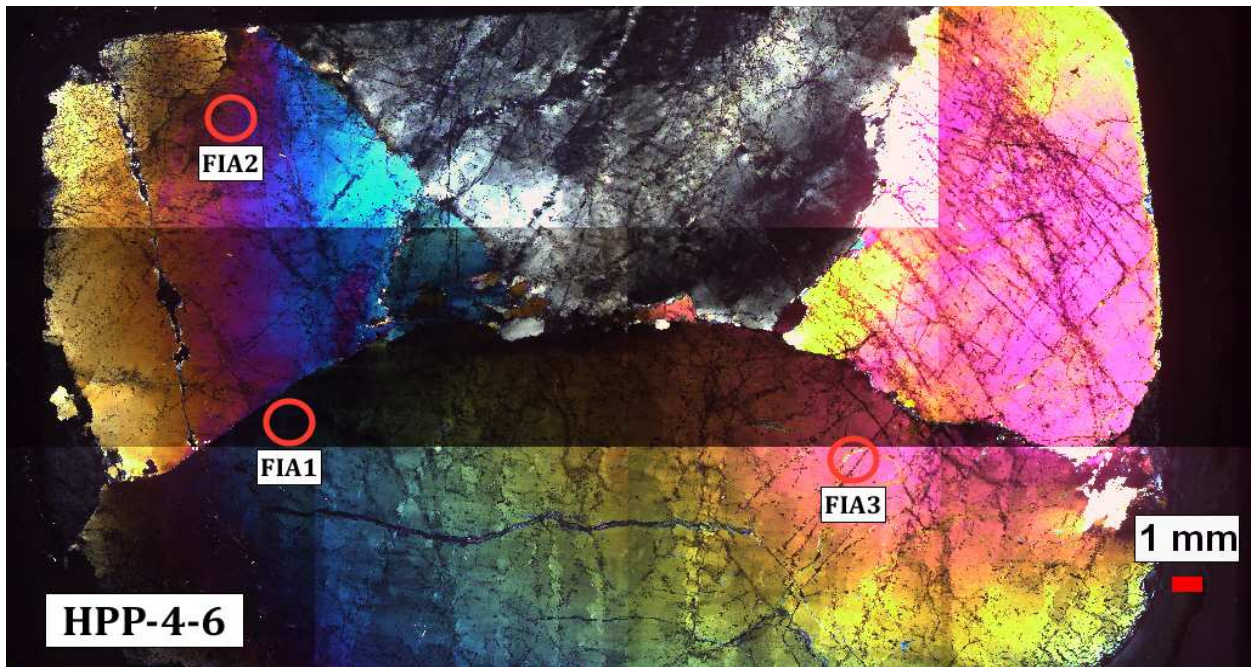
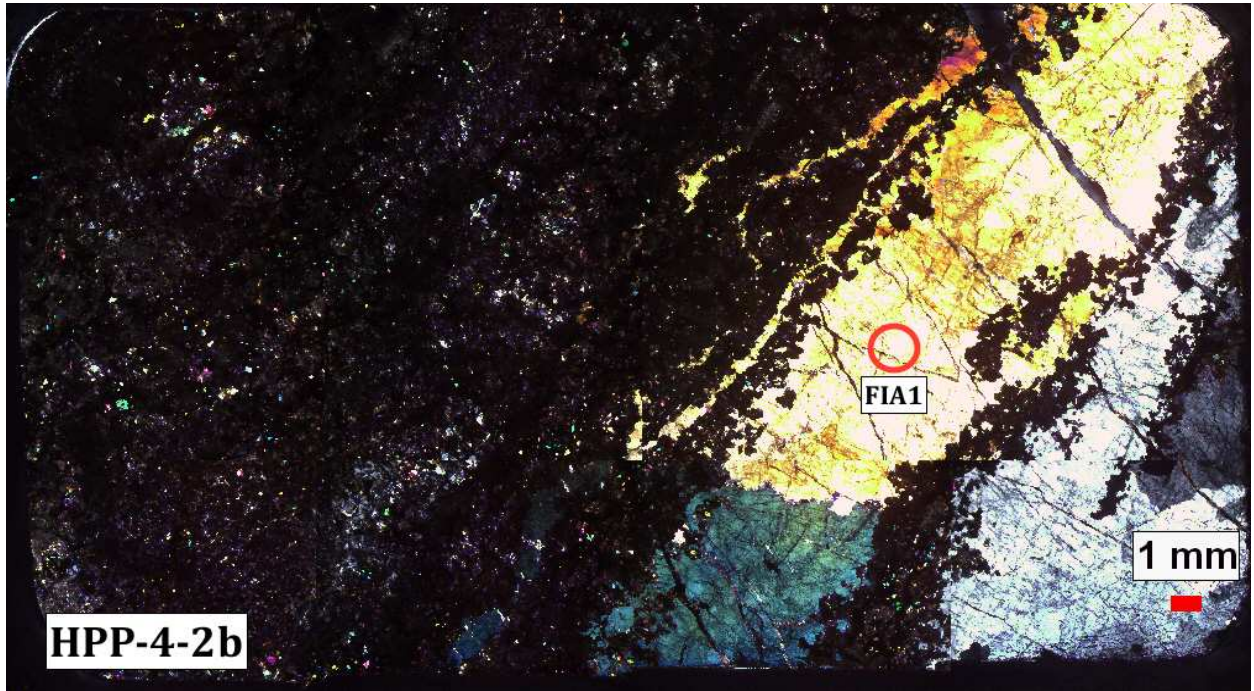


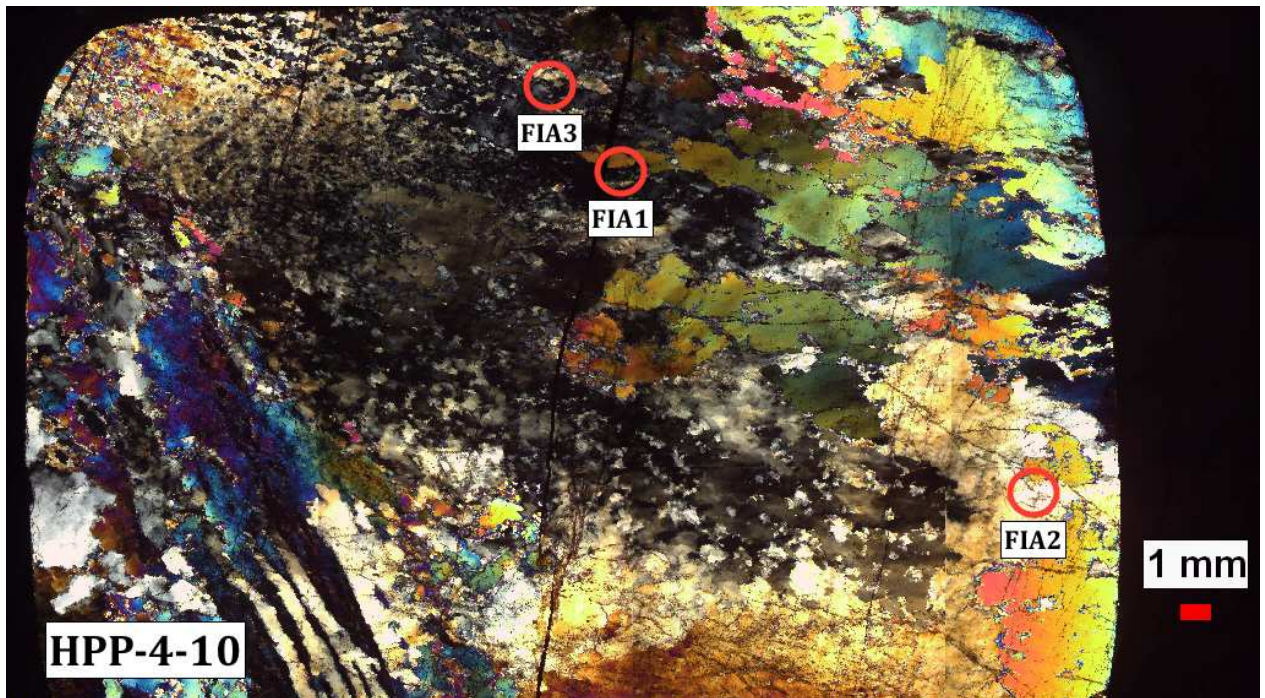
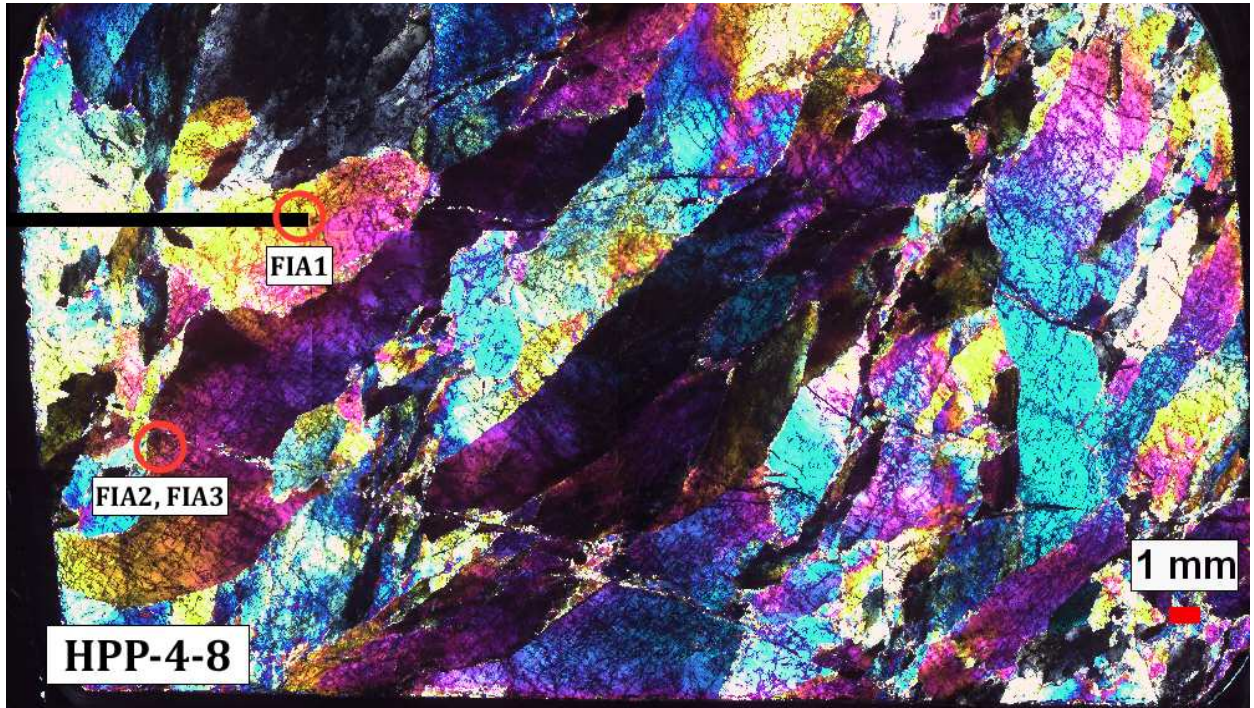












APPENDIX E.3: FLUID INCLUSION MICROTHERMOMETRY DATA

APPENDIX E.3.1: RAW MICROTHERMOMETRY DATA

Assemblage ID	Feature Type	Intrusive Unit	Assemblage Number	Number & Nature of Phases	Assemblage Interpretation	T _{mCO2} (°C)	T _{eutectic} (°C)	T _{mice} (°C)	Freezing point depression for H ₂ O (°C)	T _{mclathrate} (°C)
HPP-1-03-FIA1	Type (II) (wallrock) Quartz Vein	Tcc	FIA1	2 (L+V)	S		-22.7	-0.2	0.2	
HPP-1-03-FIA2	Type (II) (wallrock) Quartz Vein	Tcc	FIA2	2 (L+V)	S		-23.2	-0.1	0.1	
HPP-1-03-FIA3	Type (II) (wallrock) Quartz Vein	Tcc	FIA3	3 (L1+L2+V)	P	-57.1	-38.1			7.4
HPP-1-03-FIA4	Type (II) (wallrock) Quartz Vein	Tcc	FIA4	2 (L+V)	P		-25.2	-0.3	0.3	
HPP-1-04a-FIA1	Type (I) Quartz Vein	Tcc	FIA1	2 (L+V)	P		-25.7	-0.7	0.7	
HPP-1-04a-FIA2	Type (I) Quartz Vein	Tcc	FIA2	3 (L+V+S)	S		-23.4	-0.6	0.6	
HPP-1-04a-PL-FIA1	Type (I) Quartz Vein	Tcc	FIA1	2 (L+V)	P/Pseudo		-22.2	-1.7	1.7	
HPP-1-04a-PL-FIA2	Type (I) Quartz Vein	Tcc	FIA2	2 (L+V)	S		-24.1	-1.4	1.4	
HPP-1-20-FIA1	Granite (altered)	Tcc	FIA1	2 (L+V)	S/Pseudo		-23.6	-1.3	1.3	
HPP-1-20-FIA2	Granite (altered)	Tcc	FIA2	2 (L+V)	P		-26.5	-1.8	1.8	
HPP-1-20-FIA3	Granite (altered)	Tcc	FIA3	2 (L+V)	P		-24.3	-1.6	1.6	
HPP-1-24b-FIA1	Miarolitic Cavity	Tcc	FIA1	2 (L+V) w/ clath	P	-56.8	-28.1	-1.4	1.4	7.1
HPP-1-24b-FIA2	Miarolitic Cavity	Tcc	FIA2	2 (L+V)	P		-25.1	-1.9	1.9	
HPP-1-24b-FIA3	Miarolitic Cavity	Tcc	FIA3	2 (L+V)	P		-25.9	-2.5	2.5	
HPP-1-24b-FIA4	Miarolitic Cavity	Tcc	FIA4	2 (L+V)	S		-24.1	-1.7	1.7	
HPP-1-30-FIA1	Type (III) Quartz Vein	Tcc	FIA1	2 (L+V)	P		-23.1	-2.3	2.3	
HPP-1-30-FIA2	Type (III) Quartz Vein	Tcc	FIA2	2 (L+V)	P		-22	-0.3	0.3	
HPP-1-30-FIA3	Type (III) Quartz Vein	Tcc	FIA3	2 (L+V)	P		-23.6	-0.7	0.7	
HPP-1-30-FIA4	Type (III) Quartz Vein	Tcc	FIA4	2 (L+V)	S		-22.1	-1	1	
HPP-1-36a-FIA1	Type (IV) Microcrystalline Quartz Vein	Tcc	FIA1	2 (L+V) w/ clath	S	-59.5	-26.2	-1.7	1.7	11.4
HPP-1-36a-FIA2	Type (IV) Microcrystalline Quartz Vein	Tcc	FIA2	2 (L+V)	P		-23	-1	1	
HPP-1-36a-FIA3	Type (IV) Microcrystalline Quartz Vein	Tcc	FIA3	2 (L+V)	P		-23.6	-1.4	1.4	
HPP-1-63-FIA1	Type (IV) Microcrystalline Quartz Vein	Tcc	FIA1	2 (L+V) w/ clath	S		-28.3			5.3
HPP-1-63-FIA2	Type (IV) Microcrystalline Quartz Vein	Tcc	FIA2	2 (L+V)	P		-26.7	-0.2	0.2	
HPP-1-63-FIA3	Type (IV) Microcrystalline Quartz Vein	Tcc	FIA3	2 (L+V)	S			2.8	-2.8	
HPP-1-73-FIA1a	Type (IV) Microcrystalline Quartz Vein	Tcc	FIA1a	3 (L1+L2+V)	S	-57.2	-32.3			7.8
HPP-1-73-FIA1b	Type (IV) Microcrystalline Quartz Vein	Tcc	FIA1b	3 (L1+L2+V)	P		28.4			
HPP-1-73-FIA2	Type (IV) Microcrystalline Quartz Vein	Tcc	FIA2	2 (L+V)	Pseudo		-24.5	-0.9	0.9	
HPP-1-76-FIA1	Type (III) Quartz Vein	Ttc	FIA1	2 (L+V)	S		-27	-3.7	3.7	
HPP-1-76-FIA2a	Type (III) Quartz Vein	Ttc	FIA2a	2 (L+V) w/ clath	S		-24.8	0	0	
HPP-1-76-FIA2b	Type (III) Quartz Vein	Ttc	FIA2b	2 (L+V) w/clath	S					5.8

Assemblage ID	Freezing point depression for clathrate (°C)	Th _{CO2} (°C)	Type of CO ₂ Homogenization (L/V?)	Final Dissolution of Solid (°C)	Th _{tot} (°C)	Salinity (wt % eq. NaCl)
HPP-1-03-FIA1					163.3	0.4
HPP-1-03-FIA2					188.3	0.2
HPP-1-03-FIA3	2.6	31	V		152.3	4.3
HPP-1-03-FIA4					151.9	0.5
HPP-1-04a-FIA1					280.9	1.2
HPP-1-04a-FIA2					276.6	1.1
HPP-1-04a-PL-FIA1					246.7	2.9
HPP-1-04a-PL-FIA2					212.5	2.4
HPP-1-20-FIA1					206.7	2.2
HPP-1-20-FIA2					204.6	3.1
HPP-1-20-FIA3					197.8	2.7
HPP-1-24b-FIA1	2.9				225.6	4.8
HPP-1-24b-FIA2					248.1	3.2
HPP-1-24b-FIA3					230.5	4.2
HPP-1-24b-FIA4					254.5	2.9
HPP-1-30-FIA1					181.4	3.9
HPP-1-30-FIA2					174.3	0.5
HPP-1-30-FIA3					188.1	1.2
HPP-1-30-FIA4					148.2	1.7
HPP-1-36a-FIA1	-1.4				162.4	
HPP-1-36a-FIA2					168.5	1.7
HPP-1-36a-FIA3					186.8	2.4
HPP-1-63-FIA1	4.7				153.7	7.4
HPP-1-63-FIA2					165.2	0.4
HPP-1-63-FIA3					138.8	
HPP-1-73-FIA1a	2.2	9.1	V		198	3.7
HPP-1-73-FIA1b		29.7	V		287.1	
HPP-1-73-FIA2					204.8	1.6
HPP-1-76-FIA1					207.6	6.0
HPP-1-76-FIA2a					154.1	0
HPP-1-76-FIA2b	4.2				175.6	6.7

Assemblage ID	Feature Type	Intrusive Unit	Assemblage Number	Number & Nature of Phases	Assemblage Interpretation	T _{mCO2} (°C)	T _{eutectic} (°C)	T _{mice} (°C)	Freezing point depression for H ₂ O (°C)	T _{mclathrate} (°C)
HPP-1-78-FIA1	QF Pegmatite	Ttc	FIA1	3 (L+V+S)	P/Pseudo		-30.3	-3.8	3.8	
HPP-1-78-FIA2	QF Pegmatite	Ttc	FIA2	2 (L+V)	P/Pseudo		-29.5	-2.4	2.4	
HPP-1-78-FIA3	QF Pegmatite	Ttc	FIA3	2 (L+V)	S		-22.9	-0.7	0.7	
HPP-2-02-FIA1	Aplite (QF-cored)	Tmg	FIA1	3 (L1+L2+V)	P	-59.1	-23.4			8.2
HPP-2-02-FIA2	Aplite (QF-cored)	Tmg	FIA2	3 (L1+L2+V)	P	-58.4	-25.3			6.6
HPP-2-02-FIA3	Aplite (QF-cored)	Tmg	FIA3	2 (L+V)	S		-20.1	-0.4	0.4	
HPP-2-02-FIA4	Aplite (QF-cored)	Tmg	FIA4	2 (L+V)	S		-22.4			
HPP-2-03a-PL-FIA1	Aplite (Q-cored)	Tmg	FIA1							
HPP-2-03a-PL-FIA2	Aplite (Q-cored)	Tmg	FIA2							
HPP-2-03a-PL-FIA3	Aplite (Q-cored)	Tmg	FIA3							
HPP-2-03a-PL-FIA4	Aplite (Q-cored)	Tmg	FIA4							
HPP-2-06-FIA1	Type (I) Quartz Vein	Tmg	FIA1	2 (L+V) w/clath	P		-25.4	-1.2	1.2	8.5
HPP-2-06-FIA2	Type (I) Quartz Vein	Tmg	FIA2	3 (L1+L2+V)	P	-57.3	-27.6			7.6
HPP-2-06-FIA3	Type (I) Quartz Vein	Tmg	FIA3	3 (L1+L2+V)	S	-57.8	-27.2			8.3
HPP-2-06-FIA4	Type (I) Quartz Vein	Tmg	FIA4	3 (L1+L2+V)	P	-56.6	-28.3			8.9
HPP-2-06-FIA5	Type (I) Quartz Vein	Tmg	FIA5							
HPP-2-08b-FIA1	Granite (Leuco)	Tmg	FIA1	3 (L1+L2+V)	P	-56.6	-29			7.8
HPP-2-08b-FIA2	Granite (Leuco)	Tmg	FIA2	3 (L1+L2+V)	P	-56.4	-26			6.2
HPP-2-08b-FIA3	Granite (Leuco)	Tmg	FIA3	3 (L1+L2+V)	P	-56.5	-27.4			9
HPP-2-10-FIA1	Aplite	Tmg	FIA1	2 (L+V)	S		-27.8	-1.5	1.5	
HPP-2-10-FIA2	Aplite	Tmg	FIA2	2 (L+V) w/ clath	Pseudo		-24.8	-2.1	2.1	9.9
HPP-2-10-FIA3	Aplite	Tmg	FIA3	3 (L1+L2+V)	P	-56.9	-28.2			8.3
HPP-2-22-FIA1	Type (I) Quartz Vein	Tmg	FIA1	3 (L1+L2+V)	P	-57.2	-25.6			8.9
HPP-2-22-FIA2	Type (I) Quartz Vein	Tmg	FIA2	2 (L+V) w/ clath	S		-24.9	-1.6	1.6	7.5
HPP-2-22-FIA3a	Type (I) Quartz Vein	Tmg	FIA3a	2 (L+V) w/ clath	P	-56.8	-26.8			9
HPP-2-22-FIA3b	Type (I) Quartz Vein	Tmg	FIA3b	2 (L+V) w/ clath	P	-57.5	-27.4	-0.6	0.6	7.8
HPP-2-22-FIA4a	Type (I) Quartz Vein	Tmg	FIA4	3 (L1+L2+V)	S/Pseudo	-56.8	-27.4			7.8
HPP-2-22-FIA4b	Type (I) Quartz Vein	Tmg	FIA4b	3 (L1+L2+V)	S/Pseudo		-25.3			9.2
HPP-2-22-FIA5	Type (I) Quartz Vein	Tmg	FIA5	3 (L1+L2+V)	P	-56.7	-29.1			4.9
HPP-2-29-FIA1a	QF Pegmatite	Tmg	FIA1a	2 (L+V)	S		-24.4			
HPP-2-29-FIA1b	QF Pegmatite	Tmg	FIA1b	2 (L+V)	S		-24.4	-2.1	2.1	
HPP-2-29-FIA2a	QF Pegmatite	Tmg	FIA2a	2 (L+V) w/ clath	P	-56.4	-25.4			8.2
HPP-2-29-FIA2b	QF Pegmatite	Tmg	FIA2b	2 (L+V) w/ clath	P	-56.4	-25.4			7.2
HPP-2-29-FIA3	QF Pegmatite	Tmg	FIA3	2 (L+V)	S		-23.3	-0.7	0.7	
HPP-2-29-FIA4	QF Pegmatite	Tmg	FIA4	2 (L+V)	P		-24.8	-2.2	2.2	
HPP-2-35-FIA1	QF Pegmatite	Tmg	FIA1	2 (L+V)	S		-24.1	-3.8	3.8	
HPP-2-35-FIA2	QF Pegmatite	Tmg	FIA2	2 (L+V)	P		-28.4	-0.8	0.8	
HPP-2-35-FIA3	QF Pegmatite	Tmg	FIA3	3 (L1+L2+V)	P/Pseudo	-56.5	-22.3			8.7
HPP-2-38-FIA1	Type (I) Quartz Vein	Tmg	FIA1	2 (L+V) w/ clath	S	-58.4	-27.5			7.8
HPP-2-38-FIA2	Type (I) Quartz Vein	Tmg	FIA2	3 (L1+L2+V)	P	-56.6	-28.5			8
HPP-2-40-FIA1	QF Pegmatite	Tmg	FIA1	2 (L+V)	P		-22.2	0	0	
HPP-2-40-FIA2	QF Pegmatite	Tmg	FIA2	2 (L+V) w/ clath	P	-56.4	-26.9	-1.3	1.3	8.9

Assemblage ID	Freezing point depression for clathrate (°C)	Th _{CO₂} (°C)	Type of CO ₂ Homogenization (L/V?)	Final Dissolution of Solid (°C)	Th _{tot} (°C)	Salinity (wt % eq. NaCl)
HPP-1-78-FIA1				>258	258	6.2
HPP-1-78-FIA2					252.1	4.0
HPP-1-78-FIA3					152.5	1.2
HPP-2-02-FIA1	1.8	20.8	V		302.1	3.1
HPP-2-02-FIA2	3.4	30.2	V		350	5.6
HPP-2-02-FIA3					224.9	0.7
HPP-2-02-FIA4					28.6	0
HPP-2-03a-PL-FIA1						
HPP-2-03a-PL-FIA2						
HPP-2-03a-PL-FIA3						
HPP-2-03a-PL-FIA4						
HPP-2-06-FIA1	1.5	31	V		260.1	2.6
HPP-2-06-FIA2	2.4	31	V		290	4.0
HPP-2-06-FIA3	1.7	26			325.1	2.9
HPP-2-06-FIA4	1.1	24.6	L		277.2	1.9
HPP-2-06-FIA5						
HPP-2-08b-FIA1	2.2	30.8	L		288.4	3.7
HPP-2-08b-FIA2	3.8	31	L		251	6.2
HPP-2-08b-FIA3	1	30.5	L		277.6	1.7
HPP-2-10-FIA1					170.8	2.6
HPP-2-10-FIA2	0.1				204.6	0.2
HPP-2-10-FIA3	1.7				375	2.9
HPP-2-22-FIA1	1.1	25.2	V		268.8	1.9
HPP-2-22-FIA2	2.5				242.5	4.2
HPP-2-22-FIA3a	1				264.4	1.7
HPP-2-22-FIA3b	2.2				282.8	3.7
HPP-2-22-FIA4a	2.2	29.6	L		293.3	3.7
HPP-2-22-FIA4b	0.8	31	L		274.6	1.4
HPP-2-22-FIA5	5.1	28.1	L		277.7	8.0
HPP-2-29-FIA1a					241.3	
HPP-2-29-FIA1b					210.2	3.5
HPP-2-29-FIA2a	1.8				240	3.1
HPP-2-29-FIA2b	2.8				221.9	4.6
HPP-2-29-FIA3					201.1	1.2
HPP-2-29-FIA4					216.6	3.7
HPP-2-35-FIA1					213.6	6.2
HPP-2-35-FIA2					225	1.4
HPP-2-35-FIA3	1.3	26.1	V		228.7	2.2
HPP-2-38-FIA1	2.2				263.3	3.7
HPP-2-38-FIA2	2	30.6	L		308	3.4
HPP-2-40-FIA1					316.3	0
HPP-2-40-FIA2	1.1				253.6	1.9

Assemblage ID	Feature Type	Intrusive Unit	Assemblage Number	Number & Nature of Phases	Assemblage Interpretation	T _{mCO₂} (°C)	T _{eutectic} (°C)	T _{mice} (°C)	Freezing point depression for H ₂ O (°C)	T _{mclathrate} (°C)
HPP-2-40-FIA3	QF Pegmatite	Tmg	FIA3	2 (L+V)	S		-21.6	0	0	
HPP-2-40-FIA4	QF Pegmatite	Tmg	FIA4	2 (L+V)	S/Pseudo		-22.5	-1.7	1.7	
HPP-2-41a-FIA1	Type (III) Quartz Vein	Tmg	FIA1	2 (L+V)	P		-28.1	-2.6	2.6	
HPP-2-41a-FIA2	Type (III) Quartz Vein	Tmg	FIA2	2 (L+V)	P		-21.1	-2.1	2.1	
HPP-2-41a-FIA3	Type (III) Quartz Vein	Tmg	FIA3	2 (L+V)	P		-24.1	-0.9	0.9	
HPP-2-41a-FIA4	Type (III) Quartz Vein	Tmg	FIA4	2 (L+V)	P		-26.2	-2.2	2.2	
HPP-2-44-FIA1	Aplite (Layered QF-Pegmatite)	Tmg	FIA1	2 (L+V) w/ clath	P		-26.3	-2.3	2.3	11.1
HPP-2-44-FIA2a	Aplite (Layered QF-Pegmatite)	Tmg	FIA2a	3 (L1+L2+V)	S	-57.6	-27.4	-2.2	2.2	
HPP-2-44-FIA2b	Aplite (Layered QF-Pegmatite)	Tmg	FIA2b	3 (L1+L2+V)	S	-46.6	-27.4	-0.7	0.7	
HPP-2-44-FIA3	Aplite (Layered QF-Pegmatite)	Tmg	FIA3	3 (L1+L2+V)	S	-57.3	-27.1	-2.2	2.2	8.1
HPP-2-47-FIA1	Type (I) Quartz Vein	Tmg	FIA1	2 (L+V)	S		-21.5	-0.1	0.1	
HPP-2-47-FIA2	Type (I) Quartz Vein	Tmg	FIA2	2 (L+V)	S		-22.1	-0.1	0.1	
HPP-2-47-FIA3	Type (I) Quartz Vein	Tmg	FIA3	2 (L+V)	P		-21.6	-0.9	0.9	
HPP-2-55-FIA1	Type (I) Quartz Vein	Ttc	FIA1	2 (L+V)	S		-25.2	-0.2	0.2	
HPP-2-56-FIA1	Type (III) Quartz Vein	Ttc	FIA1	2 (L+V)	S		-25.4	-0.2	0.2	
HPP-2-56-FIA2	Type (III) Quartz Vein	Ttc	FIA2	2 (L+V)	S		-21.3	0	0	
HPP-2-56-FIA3	Type (III) Quartz Vein	Ttc	FIA3	2 (L+V)	S/Pseudo		-23.2	0	0	
HPP-2-57-FIA1	QF Pegmatite	Ttc	FIA1	2 (L+V)	S		-21.1	0	0	
HPP-2-57-FIA2	QF Pegmatite	Ttc	FIA2	2 (L+V)	S		-21.1	0	0	
HPP-2-62-FIA1	QF Pegmatite	Ttc	FIA1	3 (L1+L2+V)	S	-58.4	-23.2			8.8
HPP-2-62-FIA2	QF Pegmatite	Ttc	FIA2	3 (L1+L2+V)	P	-58.2	-26.1			7
HPP-2-62-FIA3	QF Pegmatite	Ttc	FIA3	2 (L+V)	S		-30.3	-3.7	3.7	
HPP-3-01b-FIA1	MQF Pegmatite	Tmg	FIA1	2 (L+V) w/ clath	P		-23.7	-1.4	1.4	7.9
HPP-3-01b-FIA2	MQF Pegmatite	Tmg	FIA2	2 (L+V) w/clath	P	-57.7	-24.5			8.1
HPP-3-01b-FIA3	MQF Pegmatite	Tmg	FIA3	2 (L+V) w/ clath	S/Pseudo	-56.3	-26.9	-0.3	0.3	7.5
HPP-3-04a-FIA1	Type (I) Quartz Vein	Tmg	FIA1	2 (L+V) w/ clath	P		-25.7	-5.2	5.2	6.9
HPP-3-04a-FIA2	Type (I) Quartz Vein	Tmg	FIA2	2 (L+V)	P		-27.8	-4.4	4.4	
HPP-3-04a-FIA3	Type (I) Quartz Vein	Tmg	FIA3	2 (L+V)	S		-22.9	-0.5	0.5	
HPP-3-04a-FIA4	Type (I) Quartz Vein	Tmg	FIA4	3 (L1+L2+V)	P	-57.8	-28.1			6.9
HPP-3-15-FIA1	QF Pegmatite	Tmg	FIA1	2 (L+V)	P		-25.3	-1.3	1.3	
HPP-3-15-FIA2	QF Pegmatite	Tmg	FIA2	3 (L+V+S)	P		-25.4	-2.3	2.3	
HPP-3-15-FIA3	QF Pegmatite	Tmg	FIA3	2 (L+V)	P		-24.8	-0.8	0.8	
HPP-3-19-FIA1	Type (I) Quartz Vein	Tgm	FIA1	3 (L1+L2+V)	Pseudo	-57.2	-25.4			6.8
HPP-3-19-FIA2	Type (I) Quartz Vein	Tgm	FIA2	3 (L1+L2+V)	Pseudo	-57.1	-25.8			8.6
HPP-3-19-FIA3	Type (I) Quartz Vein	Tgm	FIA3	3 (L1+L2+V)	Pseudo	-56.8	-26			7.5
HPP-3-23-FIA1	Type (III) Quartz Vein	Tmg	FIA1	3 (L1+L2+V)	P	-56.7	-27.1			7.8
HPP-3-23-FIA2	Type (III) Quartz Vein	Tmg	FIA2	2 (L+V)	P		-26.9	-2.5	2.5	
HPP-3-23-FIA3a	Type (III) Quartz Vein	Tmg	FIA3a	3 (L1+L2+V)	P	-57	-27.1			7.8

Assemblage ID	Freezing point depression for clathrate (°C)	Th _{CO2} (°C)	Type of CO ₂ Homogenization (L/V?)	Final Dissolution of Solid (°C)	Th _{tot} (°C)	Salinity (wt % eq. NaCl)
HPP-2-40-FIA3					221.6	0
HPP-2-40-FIA4					236.2	2.9
HPP-2-41a-FIA1					199.2	4.3
HPP-2-41a-FIA2					211	3.5
HPP-2-41a-FIA3					189.2	1.6
HPP-2-41a-FIA4					220.6	3.7
HPP-2-44-FIA1	-1.1				191.3	
HPP-2-44-FIA2a		28.2	V		203	3.7
HPP-2-44-FIA2b					203.6	1.2
HPP-2-44-FIA3	1.9				203.8	3.2
HPP-2-47-FIA1					191.1	0.2
HPP-2-47-FIA2					190.3	0.2
HPP-2-47-FIA3					289	1.6
HPP-2-55-FIA1					185.5	0.4
HPP-2-56-FIA1					185.5	0.4
HPP-2-56-FIA2					179.4	0
HPP-2-56-FIA3					207.1	0
HPP-2-57-FIA1					172.4	0
HPP-2-57-FIA2					163.5	0
HPP-2-62-FIA1	1.2	25.2	V		255.2	2.1
HPP-2-62-FIA2	3	30.8	V		271.5	5.0
HPP-2-62-FIA3					238.8	6.0
HPP-3-01b-FIA1	2.1				282.3	3.5
HPP-3-01b-FIA2	1.9				277.4	3.2
HPP-3-01b-FIA3	2.5				207.5	4.2
HPP-3-04a-FIA1	3.1				290.9	5.1
HPP-3-04a-FIA2					282.1	7.0
HPP-3-04a-FIA3					215.6	0.9
HPP-3-04a-FIA4	3.1	31	V		308.4	5.1
HPP-3-15-FIA1					223	2.2
HPP-3-15-FIA2				>250	202.1	3.9
HPP-3-15-FIA3					206.8	1.4
HPP-3-19-FIA1	3.2	30.3	L		292.5	5.3
HPP-3-19-FIA2	1.4	30.1	L		277.4	2.4
HPP-3-19-FIA3	2.5	28.4	L		291.1	4.2
HPP-3-23-FIA1	2.2	31	L		300.9	3.7
HPP-3-23-FIA2					267.4	4.2
HPP-3-23-FIA3a	2.2	30.9	V		330	3.7

Assemblage ID	Feature Type	Intrusive Unit	Assemblage Number	Number & Nature of Phases	Assemblage Interpretation	T _{mCO2} (°C)	T _{eutectic} (°C)	T _{mice} (°C)	Freezing point depression for H ₂ O (°C)	T _{mclathrate} (°C)
HPP-3-23-FIA3b	Type (III) Quartz Vein	Tmg	FIA3b	3 (L1+L2+V)	P	-57	-27.1			7.8
HPP-3-33-FIA1	QF Pegmatite	Tmg	FIA1	2 (L+V)	S		-23.9	-0.3	0.3	
HPP-3-33-FIA2	QF Pegmatite	Tmg	FIA2	2 (L+V)	S		-22.9	-0.3	0.3	
HPP-3-33-FIA3	QF Pegmatite	Tmg	FIA3	2 (L+V)	S		-24	-0.2	0.2	
HPP-3-38-FIA1	Type (II) (wallrock) Quartz Vein	Ttc	FIA1	2 (L+V)	P			-1.1	1.1	
HPP-3-38-FIA2	Type (II) (wallrock) Quartz Vein	Ttc	FIA2	2 (L+V)	S/P		-24.7	-0.9	0.9	
HPP-4-01-FIA1	Type (II) (skarn) Quartz Vein	Tcc	FIA1	2 (L+V)	P		-24.1	-2.4	2.4	
HPP-4-01-FIA2	Type (II) (skarn) Quartz Vein	Tcc	FIA2	2 (L+V)	P		-26.1	-2.1	2.1	
HPP-4-01-FIA3	Type (II) (skarn) Quartz Vein	Tcc	FIA3	2 (L+V)	P		-24.6	-2.1	2.1	
HPP-4-02b-FIA1	Type (II) (skarn) Quartz Vein	Tcc	FIA1	2 (L+V)	P		-22.5	-0.7	0.7	
HPP-4-02b-FIA2	Type (II) (skarn) Quartz Vein	Tcc	FIA2	2 (L+V)	P		-23.4	-0.5	0.5	
HPP-4-06-FIA1	Type (II) (skarn) Quartz Vein	Ttc	FIA1	2 (L+V) w/clath	P/Pseudo		-27.4	-5.2	5.2	6.7
HPP-4-06-FIA2	Type (II) (skarn) Quartz Vein	Ttc	FIA2	2 (L+V) w/clath	S/Pseudo		-27.2	-4.4	4.4	6.4
HPP-4-06-FIA3	Type (II) (skarn) Quartz Vein	Ttc	FIA3	2 (L+V)	S/Pseudo		-26	-1.5	1.5	
HPP-4-08-FIA1	Type (III) Quartz Vein	Tgm	FIA1	3 (L1+L2+V)	P	-58.7	-30.7			7.9
HPP-4-08-FIA2	Type (III) Quartz Vein	Tgm	FIA2	3 (L1+L2+V)	P	-56	-27.7			8.3
HPP-4-08-FIA3	Type (III) Quartz Vein	Tgm	FIA3	2 (L+V)	P		-27.5	-2.8	2.8	
HPP-4-10-FIA1	QF Pegmatite	Tmg	FIA1	2 (L+V) w/clath	P		-26.9	-1.8	1.8	7.1
HPP-4-10-FIA2	QF Pegmatite	Tmg	FIA2	2 (L+V)	S		-25.7	-2.6	2.6	
HPP-4-10-FIA3	QF Pegmatite	Tmg	FIA3	2 (L+V)	S		-26.5	-2.4	2.4	

Assemblage ID	Freezing point depression for clathrate (°C)	Th _{CO2} (°C)	Type of CO ₂ Homogenization (L/V?)	Final Dissolution of Solid (°C)	Th _{tot} (°C)	Salinity (wt % eq. NaCl)
HPP-3-23-FIA3b	2.2	30.9	V		292.3	3.7
HPP-3-33-FIA1					221.3	0.5
HPP-3-33-FIA2					208.7	0.5
HPP-3-33-FIA3					190	0.4
HPP-3-38-FIA1					193.8	1.9
HPP-3-38-FIA2					163.2	1.6
HPP-4-01-FIA1					228.2	4.0
HPP-4-01-FIA2					246.6	3.5
HPP-4-01-FIA3					243.5	3.5
HPP-4-02b-FIA1					251.5	1.2
HPP-4-02b-FIA2					284.1	0.9
HPP-4-06-FIA1	3.3				277.5	5.4
HPP-4-06-FIA2	3.6				275.3	5.9
HPP-4-06-FIA3					246	2.6
HPP-4-08-FIA1	2.1	32.2	V		310.9	3.5
HPP-4-08-FIA2	1.7	30.6	L		290	2.9
HPP-4-08-FIA3					301.1	4.6
HPP-4-10-FIA1	2.9				241.2	4.8
HPP-4-10-FIA2					229.9	4.3
HPP-4-10-FIA3					226.1	4.0

APPENDIX E.3.2: STATISTICAL COMPILATION OF MICROTHERMOMETRY DATA FOR
PRIMARY FLUID INCLUSIONS BY SAMPLE

Sample ID	Feature Type	Intrusive Unit	Number of Assemblages	Number of Inclusions	Petrographic Group(s)	Assemblage Compositional Type(s)	Size (min) (µm)
HPP-1-03	Type (II) (wallrock) Quartz Vein	Tcc	1	4	2	A	3
HPP-1-03 (CO ₂)	Type (II) (wallrock) Quartz Vein	Tcc	1	5	2	B	10
HPP-1-04	Type (I) Quartz Vein	Tcc	2	13	2	A	3
HPP-1-20	Granite (altered)	Tcc	2	13	2	A	6
HPP-1-24b	Miarolitic Cavity	Tcc	2	9	2	A	3
HPP-1-24b (CO ₂)	Miarolitic Cavity	Tcc	1	7	1	C	5
HPP-1-30	Type (III) Quartz Vein	Tcc	3	10	1	A	7
HPP-1-36a	Type (IV) Microcrystalline Quartz Vein	Tcc	2	10	1=2	A	10
HPP-1-63	Type (IV) Microcrystalline Quartz Vein	Tcc	1	6	1	A	9
HPP-1-73	Type (IV) Microcrystalline Quartz Vein	Tcc	1	4	4	A	4
HPP-1-73 (CO ₂)	Type (IV) Microcrystalline Quartz Vein	Tcc	1	2	2	B	5
HPP-1-78	QF Pegmatite	Ttc	2	2	4	A	16
HPP-2-02 (CO ₂)	Aplite (QF-cored)	Tmg	2	10	1	B	3
HPP-2-06 (CO ₂)	Type (I) Quartz Vein	Tmg	3	4	1>3	B>C	4
HPP-2-08b (CO ₂)	Granite (Leuco)	Tmg	3	5	1>3	B	9
HPP-2-10 (CO ₂)	Aplite	Tmg	2	6	1=4	B=C	5
HPP-2-22 (CO ₂)	Type (I) Quartz Vein	Tmg	4	9	1>2	B=C	5
HPP-2-29	QF Pegmatite	Tmg	1	7	1	A	3
HPP-2-29 (CO ₂)	QF Pegmatite	Tmg	2	3	2	C	12
HPP-2-35	QF Pegmatite	Tmg	1	3	1	A	5
HPP-2-35 (CO ₂)	QF Pegmatite	Tmg	1	2	1	B	16
HPP-2-38	Type (I) Quartz Vein	Tmg	1	1	3	B	24
HPP-2-40	QF Pegmatite	Tmg	1	6	2	A	4
HPP-2-40 (CO ₂)	QF Pegmatite	Tmg	1	10	1	C	8
HPP-2-41a	Type (III) Quartz Vein	Tmg	4	20	1	A	3
HPP-2-44 (CO ₂)	Aplite (Layered QF Pegmatite)	Tmg	1	3	1	C	6
HPP-2-47	Type (I) Quartz Vein	Tmg	1	2	1	A	7
HPP-2-62 (CO ₂)	QF Pegmatite	Ttc	1	1	3	B	17
HPP-3-01b (CO ₂)	MQF Pegmatite	Tmg	2	10	2	C	4
HPP-3-04a	Type (I) Quartz Vein	Tmg	1	3	1	A	4
HPP-3-04a (CO ₂)	Type (I) Quartz Vein	Tmg	2	10	1	B=C	8
HPP-3-15	QF Pegmatite	Tmg	3	19	2	A	4
HPP-3-19 (CO ₂)	Type (I) Quartz Vein	Tgm	3	13	2>1	B	5
HPP-3-23	Type (III) Quartz Vein	Tmg	1	6	1	A	8
HPP-3-23 (CO ₂)	Type (III) Quartz Vein	Tmg	3	12	1	B	5
HPP-3-38	Type (II) (wallrock) Quartz Vein	Ttc	1	1	3	A	5
HPP-4-01	Type (II) (skarn) Quartz Vein	Tcc	3	14	1>2	A	5
HPP-4-02b	Type (II) (skarn) Quartz Vein	Tcc	2	8	2	A	3
HPP-4-06 (CO ₂)	Type (II) (skarn) Quartz Vein	Tcc	1	5	1	C	3
HPP-4-08	Type (III) Quartz Vein	Tgm	1	3	1	A	8
HPP-4-08 (CO ₂)	Type (III) Quartz Vein	Tgm	2	9	1	B	6
HPP-4-10 (CO ₂)	QF Pegmatite	Tmg	1	4	1	C	4

Sample ID	Size (max) (um)	Size (mean of assemblage ranges) (um)	H ₂ O Liquid Fraction (%)	H ₂ O Liquid Fraction (min) (%)	H ₂ O Liquid Fraction (max) (%)	H ₂ O Liquid Fraction (mean) (%)
HPP-1-03	9	6	94	94	94	94
HPP-1-03 (CO ₂)	17	13	93	93	93	93
HPP-1-04	9	7	80	80	86	83
HPP-1-20	15	10	95	95	96	95
HPP-1-24b	52	32	86	86	91	88
HPP-1-24b (CO ₂)	17	11	89	89	89	89
HPP-1-30	22	15	53	53	94	78
HPP-1-36a	36	18	93	93	95	94
HPP-1-63	16	12	96	96	96	96
HPP-1-73	9	6	98	98	98	98
HPP-1-73 (CO ₂)	14	10	91	91	91	91
HPP-1-78	28	22	89	89	92	91
HPP-2-02 (CO ₂)	10	6	55	55	70	63
HPP-2-06 (CO ₂)	30	14	72	72	82	77
HPP-2-08b (CO ₂)	26	16	78	78	85	81
HPP-2-10 (CO ₂)	10	8	80	80	93	86
HPP-2-22 (CO ₂)	33	17	81	81	86	84
HPP-2-29	13	8	91	91	91	91
HPP-2-29 (CO ₂)	20	16	87	87	90	89
HPP-2-35	15	10	84	84	84	84
HPP-2-35 (CO ₂)	19	17	91	91	91	91
HPP-2-38	24	24	80	80	80	80
HPP-2-40	10	7	86	86	86	86
HPP-2-40 (CO ₂)	25	16	85	85	85	85
HPP-2-41a	27	14	93	93	96	95
HPP-2-44 (CO ₂)	27	16	89	89	89	89
HPP-2-47	9	8	20	20	20	20
HPP-2-62 (CO ₂)	17	17	80	80	80	80
HPP-3-01b (CO ₂)	26	14	78	78	89	84
HPP-3-04a	18	11	93	93	93	93
HPP-3-04a (CO ₂)	13	11	80	80	82	81
HPP-3-15	40	25	90	90	93	91
HPP-3-19 (CO ₂)	14	9	74	74	82	79
HPP-3-23	22	15	84	84	84	84
HPP-3-23 (CO ₂)	25	14	78	78	85	83
HPP-3-38	5	5	97	97	97	97
HPP-4-01	19	11	90	90	95	93
HPP-4-02b	11	7	80	80	94	87
HPP-4-06 (CO ₂)	11	7	89	89	89	89
HPP-4-08	12	10	86	86	86	86
HPP-4-08 (CO ₂)	14	8	79	79	80	80
HPP-4-10 (CO ₂)	14	9	85	85	85	85

Sample ID	CO ₂ Liquid Fraction (min) (%)	CO ₂ Liquid Fraction (max) (%)	CO ₂ Liquid Fraction (mean) (%)	T _{m,CO₂} (min) (°C)	T _{m,CO₂} (max) (°C)	T _{m,CO₂} (mean) (°C)
HPP-1-03	0	0	0			
HPP-1-03 (CO ₂)	1.5	1.5	1.5	-57.1	-57.1	-57.1
HPP-1-04	0	0	0			
HPP-1-20	0	0	0			
HPP-1-24b	0	0	0			
HPP-1-24b (CO ₂)	0	0	0	-56.8	-56.8	-56.8
HPP-1-30	0	0	0			
HPP-1-36a	0	0	0			
HPP-1-63	0	0	0			
HPP-1-73	0	0	0			
HPP-1-73 (CO ₂)	0.5	0.5	0.5			
HPP-1-78	0	0	0			
HPP-2-02 (CO ₂)	12.5	20	16.3	-59.1	-58.4	-58.8
HPP-2-06 (CO ₂)	0	6	3.7	-57.3	-56.6	-57.0
HPP-2-08b (CO ₂)	4	7	5.2	-56.4	-56.6	-56.5
HPP-2-10 (CO ₂)	0	9	4.5	-56.9	-56.9	-56.9
HPP-2-22 (CO ₂)	1.5	4	2.6	-57.5	-56.7	-57.1
HPP-2-29	0	0	0			
HPP-2-29 (CO ₂)	3	7	5	-56.4	-56.4	-56.4
HPP-2-35	3.5	3.5	3.5			
HPP-2-35 (CO ₂)	2.5	2.5	2.5	-56.5	-56.5	-56.5
HPP-2-38	5	5	5	-56.6	-56.6	-56.6
HPP-2-40	0	0	0			
HPP-2-40 (CO ₂)	0	0	0	-56.4	-56.4	-56.4
HPP-2-41a	0	0	0			
HPP-2-44 (CO ₂)	0	0	0			
HPP-2-47	0	0	0			
HPP-2-62 (CO ₂)	5	5	5	-58.2	-58.2	-58.2
HPP-3-01b (CO ₂)	0	0	0	-57.7	-57.7	-57.7
HPP-3-04a	0	0	0			
HPP-3-04a (CO ₂)	0	8	4	-57.8	-57.8	-57.8
HPP-3-15	0	0	0			
HPP-3-19 (CO ₂)	2.5	16	10.5	-57.2	-56.8	-57.0
HPP-3-23	0	0	0			
HPP-3-23 (CO ₂)	4	8	6	-57	-56.7	-56.9
HPP-3-38	0	0	0			
HPP-4-01	0	0	0			
HPP-4-02b	0	0	0			
HPP-4-06 (CO ₂)	3.5	3.5	3.5			
HPP-4-08	0	0	0			
HPP-4-08 (CO ₂)	8	10	9	-58.7	-56	-57.4
HPP-4-10 (CO ₂)	0	0	0			

Sample ID	T _{eutectic} (min) (°C)	T _{eutectic} (max) (°C)	T _{eutectic} (mean) (°C)	T _{m,ice} (min) (°C)	T _{m,ice} (max) (°C)	T _{m,ice} (mean) (°C)
HPP-1-03	-25.2	-25.2	-25.2	-0.3	-0.3	-0.3
HPP-1-03 (CO ₂)	-28.1	-28.1	-28.1			
HPP-1-04	-25.7	-22.2	-24.0	-1.7	-0.7	-1.2
HPP-1-20	-26.5	-24.3	-25.4	-1.8	-1.6	-1.7
HPP-1-24b	-25.9	-25.1	-25.5	-2.5	-1.9	-2.2
HPP-1-24b (CO ₂)	-28.1	-28.1	-28.1	-1.4	-1.4	-1.4
HPP-1-30	-23.6	-22	-22.9	-2.3	-0.3	-1.1
HPP-1-36a	-23.6	-23	-23.3	-1.4	-1	-1.2
HPP-1-63	-26.7	-26.7	-26.7	-0.2	-0.2	-0.2
HPP-1-73	-24.5	-24.5	-24.5	-0.9	-0.9	-0.9
HPP-1-73 (CO ₂)	-28.4	-28.4	-28.4			
HPP-1-78	-30.3	-29.5	-29.9	-3.8	-2.4	-3.1
HPP-2-02 (CO ₂)	-25.3	-23.4	-24.4			
HPP-2-06 (CO ₂)	-28.3	-25.4	-27.1	-1.2	-1.2	-1.2
HPP-2-08b (CO ₂)	-29	-26	-27.5			
HPP-2-10 (CO ₂)	-28.2	-24.4	-26.3	-2.1	-2.1	-2.1
HPP-2-22 (CO ₂)	-29.1	-25.6	-27.2	-0.6	-0.6	-0.6
HPP-2-29	-24.8	-24.8	-24.8	-2.2	-2.2	-2.2
HPP-2-29 (CO ₂)	-25.4	-25.4	-25.4			
HPP-2-35	-28.4	-28.4	-28.4	-0.8	-0.8	-0.8
HPP-2-35 (CO ₂)	-22.3	-22.3	-22.3			
HPP-2-38	-28.5	-28.5	-28.5			
HPP-2-40	-22.2	-22.2	-22.2	0	0	0.0
HPP-2-40 (CO ₂)	-26.9	-26.9	-26.9	-1.3	-1.3	-1.3
HPP-2-41a	-28.1	-21.1	-24.9	-2.6	-0.9	-2.0
HPP-2-44 (CO ₂)	-26.3	-26.3	-26.3	-2.3	-2.3	-2.3
HPP-2-47	-21.6	-21.6	-21.6	-0.9	-0.9	-0.9
HPP-2-62 (CO ₂)	-26.1	-26.1	-26.1			
HPP-3-01b (CO ₂)	24.5	23.7	-24.1	-1.4	-1.4	-1.4
HPP-3-04a	-27.8	-27.8	-27.8	-4.4	-4.4	-4.4
HPP-3-04a (CO ₂)	-28.1	-25.7	-26.9	-5.2	-5.2	-5.2
HPP-3-15	-25.4	-24.8	-25.2	-2.3	-0.8	-1.5
HPP-3-19 (CO ₂)	-26	-25.4	-25.7			
HPP-3-23	-26.9	-26.9	-26.9	-2.5	-2.5	-2.5
HPP-3-23 (CO ₂)	-27.1	-27.1	-27.1			
HPP-3-38	N/A	N/A	N/A	-1.1	-1.1	-1.1
HPP-4-01	-26.1	-24.1	-24.9	-2.4	-2.1	-2.2
HPP-4-02b	-23.4	-22.5	-23.0	-0.7	-0.5	-0.6
HPP-4-06 (CO ₂)	-27.4	-27.4	-27.4	-5.2	-5.2	-5.2
HPP-4-08	-27.5	-27.5	-27.5	-2.8	-2.8	-2.8
HPP-4-08 (CO ₂)	-30.7	-27.7	-29.2			
HPP-4-10 (CO ₂)	-26.9	-26.9	-26.9	-1.8	-1.8	-1.8

Sample ID	Tm _{diathrate} (min) (°C)	Tm _{diathrate} (max) (°C)	Tm _{diathrate} (mean) (°C)	Th _{CO₂} (V) (min) (°C)	Th _{CO₂} (V) (max) (°C)	Th _{CO₂} (V) (mean) (°C)
HPP-1-03						
HPP-1-03 (CO ₂)	7.4	7.4	7.4	31.0	31.0	31.0
HPP-1-04						
HPP-1-20						
HPP-1-24b						
HPP-1-24b (CO ₂)	7.1	7.1	7.1			
HPP-1-30						
HPP-1-36a						
HPP-1-63						
HPP-1-73						
HPP-1-73 (CO ₂)				29.7	29.7	29.7
HPP-1-78						
HPP-2-02 (CO ₂)	6.6	8.2	7.4	20.8	30.2	25.5
HPP-2-06 (CO ₂)	7.6	8.9	8.3	31.0	31.0	31.0
HPP-2-08b (CO ₂)	6.2	9.0	7.7			
HPP-2-10 (CO ₂)	8.3	9.9	9.1			
HPP-2-22 (CO ₂)	4.9	9.0	7.7	25.2	25.2	25.2
HPP-2-29						
HPP-2-29 (CO ₂)	7.2	8.2	7.7			
HPP-2-35						
HPP-2-35 (CO ₂)	8.7	8.7	8.7	26.1	26.1	26.1
HPP-2-38	8.0	8.0	8.0			
HPP-2-40						
HPP-2-40 (CO ₂)	8.9	8.9	8.9			
HPP-2-41a						
HPP-2-44 (CO ₂)	11.1	11.1	11.1			
HPP-2-47						
HPP-2-62 (CO ₂)	7.0	7.0	7.0	30.8	30.8	30.8
HPP-3-01b (CO ₂)	7.9	8.1	8.0			
HPP-3-04a						
HPP-3-04a (CO ₂)	6.9	6.9	6.9	31.0	31.0	31.0
HPP-3-15						
HPP-3-19 (CO ₂)	6.8	8.6	7.6			
HPP-3-23						
HPP-3-23 (CO ₂)	7.8	7.8	7.8	31.0	31.0	31.0
HPP-3-38						
HPP-4-01						
HPP-4-02b						
HPP-4-06 (CO ₂)						
HPP-4-08						
HPP-4-08 (CO ₂)	7.9	8.3	8.1	31.0	31.0	31.0
HPP-4-10 (CO ₂)	7.1	7.1	7.1			

Sample ID	Th _{CO2} (L) (min) (°C)	Th _{CO2} (L) (max) (°C)	Th _{CO2} (L) (mean) (°C)	Th _{tot} (min) (°C)	Th _{tot} (max) (°C)	Th _{tot} (mean) (°C)
HPP-1-03				151.9	151.9	151.9
HPP-1-03 (CO ₂)				152.3	152.3	152.3
HPP-1-04				246.7	280.9	263.8
HPP-1-20				197.8	204.6	201.2
HPP-1-24b				230.5	248.1	239.3
HPP-1-24b (CO ₂)				225.6	225.6	225.6
HPP-1-30				174.3	188.1	181.3
HPP-1-36a				168.5	186.8	177.7
HPP-1-63				165.2	165.2	165.2
HPP-1-73				287.1	287.1	287.1
HPP-1-73 (CO ₂)				204.8	204.8	204.8
HPP-1-78				252.1	258.0	255.1
HPP-2-02 (CO ₂)				302.1	350.0	326.1
HPP-2-06 (CO ₂)	24.6	24.6	24.6	260.1	290.0	275.8
HPP-2-08b (CO ₂)	30.5	31.0	30.8	251.0	288.4	272.3
HPP-2-10 (CO ₂)				204.6	375.0	289.8
HPP-2-22 (CO ₂)	28.1	28.1	28.1	264.4	282.8	273.4
HPP-2-29				216.6	216.6	216.6
HPP-2-29 (CO ₂)				221.9	240.0	231.0
HPP-2-35				225.0	225.0	225.0
HPP-2-35 (CO ₂)				228.7	228.7	228.7
HPP-2-38	30.6	30.6	30.6	308.0	308.0	308.0
HPP-2-40				316.3	316.3	316.3
HPP-2-40 (CO ₂)				253.6	253.6	253.6
HPP-2-41a				189.2	220.6	205.0
HPP-2-44 (CO ₂)				191.3	191.3	191.3
HPP-2-47				289.0	289.0	289.0
HPP-2-62 (CO ₂)				271.5	271.5	271.5
HPP-3-01b (CO ₂)				277.4	282.3	279.9
HPP-3-04a				282.1	282.1	282.1
HPP-3-04a (CO ₂)				290.2	308.4	299.3
HPP-3-15				202.1	223.0	210.6
HPP-3-19 (CO ₂)	28.4	30.3	29.6	277.4	292.5	287.0
HPP-3-23				267.4	267.4	267.4
HPP-3-23 (CO ₂)	30.9	30.9	30.9	292.3	330.0	307.7
HPP-3-38				193.8	193.8	193.8
HPP-4-01				228.2	246.6	239.4
HPP-4-02b				251.5	284.1	267.8
HPP-4-06 (CO ₂)				277.5	277.5	277.5
HPP-4-08				301.1	301.1	301.1
HPP-4-08 (CO ₂)	30.6	30.6	30.6	290.0	310.9	300.5
HPP-4-10 (CO ₂)				241.2	241.2	241.2

Sample ID	Ph _{tot} (min) (bar)	Ph _{tot} (max) (bar)	Ph _{tot} (mean) (bar)	Salinity (min) (wt % eq. NaCl)	Salinity (max) (wt % eq. NaCl)	Salinity (mean) (wt % eq. NaCl)
HPP-1-03				0.5	0.5	0.5
HPP-1-03 (CO ₂)	800	800	800	4.3	4.3	4.3
HPP-1-04				1.2	2.9	2.1
HPP-1-20				2.7	3.1	2.9
HPP-1-24b				3.2	4.2	4.1
HPP-1-24b (CO ₂)	305	305	305	2.4	2.4	2.4
HPP-1-30				0.5	3.9	1.9
HPP-1-36a				1.7	2.4	2.1
HPP-1-63				0.4	0.4	0.4
HPP-1-73				1.6	1.6	1.6
HPP-1-73 (CO ₂)						
HPP-1-78				4.0	6.2	5.1
HPP-2-02 (CO ₂)	590	635	613	3.1	5.6	4.3
HPP-2-06 (CO ₂)	330	1200	675	4.0	1.9	2.8
HPP-2-08b (CO ₂)	390	965	655	1.7	6.2	3.9
HPP-2-10 (CO ₂)	335	335	335	0.2	2.9	1.5
HPP-2-22 (CO ₂)	285	620	418	1.7	8.0	3.8
HPP-2-29				3.1	4.7	3.9
HPP-2-29 (CO ₂)	330	330	330	3.7	3.7	3.7
HPP-2-35				1.4	1.4	1.4
HPP-2-35 (CO ₂)	430	430	430	2.2	2.2	2.2
HPP-2-38	640	640	640	3.4	3.4	3.4
HPP-2-40				0.0	0.0	0.0
HPP-2-40 (CO ₂)	310	310	310	1.9	1.9	1.9
HPP-2-41a				1.6	3.6	3.3
HPP-2-44 (CO ₂)						
HPP-2-47				1.6	1.6	1.6
HPP-2-62 (CO ₂)	920	920	920	5.0	5.0	5.0
HPP-3-01b (CO ₂)	250	505	378	3.2	3.6	3.4
HPP-3-04a				7.0	7.0	7.0
HPP-3-04a (CO ₂)	295	365	330	5.1	5.1	5.1
HPP-3-15				1.4	3.9	2.5
HPP-3-19 (CO ₂)	700	1100	888	2.4	4.2	3.1
HPP-3-23				4.2	4.2	4.2
HPP-3-23 (CO ₂)	320	550	450	3.7	3.7	3.7
HPP-3-38				1.9	1.9	1.9
HPP-4-01				3.6	4.0	3.7
HPP-4-02b				0.9	1.2	1.1
HPP-4-06 (CO ₂)	250	250	250	5.4	5.4	5.4
HPP-4-08				4.7	4.7	4.7
HPP-4-08 (CO ₂)	390	830	595	2.9	3.6	3.2
HPP-4-10 (CO ₂)	310	310	310	4.8	4.8	4.8

Sample ID	Density (min) (g/cm ³)	Density (max) (g/cm ³)	Density (mean) (g/cm ³)	mol% CO ₂ (min)	mol% CO ₂ (max)	mol% CO ₂ (mean)
HPP-1-03	0.92	0.92	0.92			
HPP-1-03 (CO ₂)	0.98	0.98	0.98	3.07	3.1	3.1
HPP-1-04	0.75	0.83	0.79			
HPP-1-20	0.89	0.89	0.89			
HPP-1-24b	0.83	0.86	0.85			
HPP-1-24b (CO ₂)	0.94	0.94	0.94	2.78	2.8	2.8
HPP-1-30	0.89	0.92	0.90			
HPP-1-36a	0.90	0.92	0.91			
HPP-1-63	0.91	0.91	0.91			
HPP-1-73	0.87	0.87	0.87			
HPP-1-73 (CO ₂)						
HPP-1-78	0.83	0.85	0.84			
HPP-2-02 (CO ₂)	0.72	0.85	0.79	7.13	8.1	7.6
HPP-2-06 (CO ₂)	0.81	0.96	0.88	3.45	10.5	6.5
HPP-2-08b (CO ₂)	0.93	1.10	0.98	3.70	6.7	5.2
HPP-2-10 (CO ₂)	0.98	0.98	0.98	2.59	4.8	3.7
HPP-2-22 (CO ₂)	0.88	1.02	0.92	3.13	6.3	4.2
HPP-2-29	0.93	0.94	0.92			
HPP-2-29 (CO ₂)	0.88	0.88	0.88	2.82	2.9	2.9
HPP-2-35	0.84	0.84	0.84			
HPP-2-35 (CO ₂)	0.96	0.96	0.96	3.56	7.8	5.7
HPP-2-38	0.94	0.94	0.94	6.24	6.2	6.2
HPP-2-40	0.67	0.67	0.67			
HPP-2-40 (CO ₂)	0.89	0.89	0.89	3.24	3.2	3.2
HPP-2-41a	0.87	0.90	0.89			
HPP-2-44 (CO ₂)						
HPP-2-47	0.74	0.74	0.74			
HPP-2-62 (CO ₂)	0.92	0.92	0.92	8.31	8.3	8.3
HPP-3-01b (CO ₂)	0.68	0.94	0.81	2.85	5.4	4.1
HPP-3-04a	0.82	0.82	0.82			
HPP-3-04a (CO ₂)	0.88	0.88	0.88	3.19	4.3	3.8
HPP-3-15	0.86	0.90	0.87			
HPP-3-19 (CO ₂)	0.92	0.97	0.95	7.38	10.2	8.7
HPP-3-23	0.81	0.81	0.81			
HPP-3-23 (CO ₂)	0.90	0.95	0.92	3.83	7.0	5.4
HPP-3-38	0.89	0.89	0.89			
HPP-4-01	0.83	0.87	0.85			
HPP-4-02b	0.74	0.80	0.77			
HPP-4-06 (CO ₂)	0.95	0.95	0.95	2.71	2.7	2.7
HPP-4-08	0.76	0.76	0.76			
HPP-4-08 (CO ₂)	0.91	0.94	0.92	4.40	8.2	6.3
HPP-4-10 (CO ₂)	0.91	0.91	0.91	3.01	3.0	3.0

APPENDIX E.3.3: STATISTICAL COMPILATION OF MICROTHERMOMETRY DATA FOR
PRIMARY FLUID INCLUSIONS BY FEATURE TYPE

Feature Type	Number of Samples	Number of Assemblages	Number of Inclusions	Petrographic Group(s)	Assemblage Compositional Type(s)	Size (min) (µm)	Size (max) (µm)	Size (mean of assemblage ranges) (µm)
Granite (altered)	1	2	13	2	A	6	15	10
Granite (Lencro) (CO ₂)	1	3	5	1>3	B	9	26	16
QF Pegmatite	5	7	34	2>1=4	A	3	40	16
QF Pegmatite (CO ₂)	5	7	23	1>2=3	C>B	3	25	14
MQF Peg (CO ₂)	1	2	10	2	C	4	26	14
Aplite (Layered QF Pegmatite) (CO ₂)	1	1	3	1	C	6	27	16
Aplite (QF-cored) (CO ₂)	1	2	10	1	B	3	10	6
Aplite (CO ₂)	1	2	6	1=4	B=C	5	10	8
Miarolitic Cavity	1	2	9	2	A	3	52	32
Miarolitic Cavity (CO ₂)	1	1	7	1=2	C	5	17	11
Type (I) Quartz Vein	3	4	18	1>2	A	3	18	9
Type (I) Quartz Vein (CO ₂)	5	13	37	1>2>3	B>C	4	33	15
Type (II) (skarn) Quartz Vein	2	5	22	2>1	A	3	19	9
Type (II) (skarn) Quartz Vein (CO ₂)	1	1	5	1	C	3	11	7
Type (II) (wallrock) Quartz Vein	2	2	5	2=3	A	3	9	5
Type (II) (wallrock) Quartz Vein (CO ₂)	1	1	5	2	B	10	17	13
Type (III) Quartz Vein	4	9	39	1	A	3	27	13
Type (III) Quartz Vein (CO ₂)	2	5	21	1	B	5	25	11
Type (IV) Microcrystalline Quartz Vein	3	4	20	1=2>4	A	4	36	12
Type (IV) Microcrystalline Quartz Vein (CO ₂)	1	1	2	2	B	5	14	10

Orthomagmatic	6	9	47	2>1>4	A	3	40	13
Orthomagmatic (CO ₂)	10	17	57	1>2>3=4	C>B	3	27	12
Hydrothermal	10	20	88	1>2>3	A	3	52	16
Hydrothermal (CO ₂)	9	20	70	1>2>3	B>C	3	33	11
Post-intrusion Hydrothermal	5	6	25	1=2>3=4	A	3	36	9
Post-intrusion Hydrothermal (CO ₂)	2	2	7	2	B	5	17	12

Feature Type	H ₂ O Liquid Fraction (min) (%)	H ₂ O Liquid Fraction (max) (%)	H ₂ O Liquid Fraction (mean) (%)	Tm _{CO2} (min) (°C)	Tm _{CO2} (max) (°C)	Tm _{CO2} (mean) (°C)	T _{eutectic} (min) (°C)	T _{eutectic} (max) (°C)	T _{eutectic} (mean) (°C)
Granite (altered)	95	96	95				-26.5	-24.3	-25.4
Granite (Leuco) (CO ₂)	78	85	81	-56.4	-56.6	-56.5	-29.0	-26.0	-27.5
QF Pegmatite	86	93	90				-30.3	-22.2	-25.5
QF Pegmatite (CO ₂)	80	91	85	-58.2	-56.4	-56.9	-28.4	-22.3	-26.1
MQF Peg (CO ₂)	78	89	84	-57.7	-57.7	-57.7	24.5	23.7	-24.1
Aplite (Layered QF Pegmatite) (CO ₂)	89	89	89				-26.3	-26.3	-26.3
Aplite (QF-cored) (CO ₂)	55	70	63	-59.1	-58.4	-58.8	-25.3	-23.4	-24.4
Aplite (CO ₂)	80	93	86	-56.9	-56.9	-56.9	-28.2	-24.4	-26.3
Miarolitic Cavity	86	91	88				-25.9	-25.1	-25.5
Miarolitic Cavity (CO ₂)	89	89	89	-56.8	-56.8	-56.8	-28.1	-28.1	-28.1
Type (I) Quartz Vein	20	93	65				-27.8	-21.6	-24.5
Type (I) Quartz Vein (CO ₂)	72	86	80	-57.8	-56.6	-57.1	-29.1	-25.4	-27.1
Type (II) (skarn) Quartz Vein	80	95	90				-26.1	-22.5	-23.9
Type (II) (skarn) Quartz Vein (CO ₂)	89	89	89				-27.4	-27.4	-27.4
Type (II) (wallrock) Quartz Vein	94	97	96				-25.2	-25.2	-25.2
Type (II) (wallrock) Quartz Vein (CO ₂)	93	93	93	-57.1	-57.1	-57.1	-28.1	-28.1	-28.1
Type (III) Quartz Vein	53	96	86				-28.1	-21.1	-25.5
Type (III) Quartz Vein (CO ₂)	78	85	81	-58.7	-56.0	-57.1	-30.7	-27.1	-28.2
Type (IV) Microcrystalline Quartz Vein	93	98	96				-26.7	-23.0	-24.8
Type (IV) Microcrystalline Quartz Vein (CO ₂)	91	91	91				-28.4	-28.4	-28.4
Orthomagmatic	86	96	92				-30.3	-22.2	-25.5
Orthomagmatic (CO ₂)	55	93	81	-59.1	-56.4	-57.3	-29.0	23.7	-25.8
Hydrothermal	20	96	82				-28.1	-21.1	-24.9
Hydrothermal (CO ₂)	72	89	85	-58.7	-56.0	-57.0	-30.7	-25.4	-27.7
Post-Intrusion Hydrothermal	93	98	96				-26.7	-23.0	-25.0
Post-Intrusion Hydrothermal (CO ₂)	91	93	92	-57.1	-57.1	-57.1	-28.4	-28.1	-28.3

Feature Type	Tm _{ice} (min) (°C)	Tm _{ice} (max) (°C)	Tm _{ice} (mean) (°C)	Tm _{clathrate} (min) (°C)	Tm _{clathrate} (max) (°C)	Tm _{clathrate} (mean) (°C)	Th _{CO₂} (V) (min) (°C)	Th _{CO₂} (V) (max) (°C)	Th _{CO₂} (V) (mean) (°C)
Granite (altered)	-1.8	-1.6	-1.7						
Granite (Leuco) (CO ₂)				6.2	9.0	7.7			
QF Pegmatite	-3.8	0	-1.7						
QF Pegmatite (CO ₂)	-1.8	-0.8	-1.3	7.0	8.9	7.9	26.1	30.8	28.5
MQF Peg (CO ₂)	-1.4	-1.4	-1.4	7.9	8.1	8.0			
Aplite (Layered QF Pegmatite) (CO ₂)	-2.3	-2.3	-2.3	11.1	11.1	11.1			
Aplite (QF-cored) (CO ₂)				6.6	8.2	7.4	20.8	30.2	25.5
Aplite (CO ₂)	-2.1	-2.1	-2.1	8.3	9.9	9.1			
Miarolitic Cavity	-2.5	-1.9	-2.2						
Miarolitic Cavity (CO ₂)	-1.4	-1.4	-1.4	7.1	7.1	7.1			
Type (I) Quartz Vein	-4.4	-0.7	-2.2						
Type (I) Quartz Vein (CO ₂)	-5.2	-0.6	-2.3	4.9	9.0	7.7	25.2	31.0	29.1
Type (II) (skarn) Quartz Vein	-2.4	-0.5	-1.4						
Type (II) (skarn) Quartz Vein (CO ₂)	-5.2	-5.2	-5.2						
Type (III) (wallrock) Quartz Vein	-1.1	-0.3	-0.7						
Type (II) (wallrock) Quartz Vein (CO ₂)				7.4	7.4	7.4	31.0	31.0	31.0
Type (III) Quartz Vein	-2.8	-0.3	-2.1						
Type (III) Quartz Vein (CO ₂)				7.8	8.3	8.0	31.0	31.0	31.0
Type (IV) Microcrystalline Quartz Vein	-1.4	-0.2	-0.8						
Type (IV) Microcrystalline Quartz Vein (CO ₂)							29.7	29.7	29.7

Orthomagmatic	-3.8	0.0	-1.7						
Orthomagmatic (CO ₂)	-2.3	-0.8	-1.8	6.2	11.1	8.5	20.8	30.8	27.0
Hydrothermal	-4.4	-0.3	-2.0						
Hydrothermal (CO ₂)	-5.2	-0.6	-3.0	4.9	9.0	7.6	25.2	31.0	30.1
Post-Intrusion Hydrothermal	-1.4	-0.2	-0.7						
Post-Intrusion Hydrothermal (CO ₂)				7.4	7.4	7.4	29.7	31	30.4

Feature Type	Th _{CO2} (L) (min) (°C)	Th _{CO2} (L) (max) (°C)	Th _{CO2} (L) (mean) (°C)	Th _{hot} (min) (°C)	Th _{hot} (max) (°C)	Th _{hot} (mean) (°C)	Ph _{hot} (min) (bar)	Ph _{hot} (max) (bar)	Ph _{hot} (mean) (bar)
Granite (altered)				197.8	204.6	201.2			
Granite (Leuco) (CO ₂)	30.5	31.0	30.8	251.0	288.4	272.3	390	610	500
QF Pegmatite				202.1	316.3	244.7			
QF Pegmatite (CO ₂)				221.9	271.5	244.8	310	920	482
MQF Peg (CO ₂)				277.4	282.3	279.9	250	505	378
Aplite (Layered QF Pegmatite) (CO ₂)				191.3	191.3	191.3			
Aplite (QF-cored) (CO ₂)				302.1	350.0	326.1	590	635	613
Aplite (CO ₂)				204.6	375.0	289.8	335	465	400
Miarolitic Cavity				230.5	248.1	239.3			
Miarolitic Cavity (CO ₂)				225.6	225.6	225.6	305	305	305
Type (I) Quartz Vein				246.7	289.0	278.3			
Type (I) Quartz Vein (CO ₂)	24.6	30.6	28.2	260.1	308.4	288.7	285	1200	590
Type (II) (skarn) Quartz Vein				228.2	284.1	253.6			
Type (II) (skarn) Quartz Vein (CO ₂)				277.5	277.5	277.5	250	250	250
Type (II) (wallrock) Quartz Vein				151.9	193.8	172.9			
Type (II) (wallrock) Quartz Vein (CO ₂)				152.3	152.3	152.3	765	765	765
Type (III) Quartz Vein				174.3	301.1	238.7			
Type (III) Quartz Vein (CO ₂)	30.6	30.9	30.8	290.0	330.0	304.1	320	800	523
Type (IV) Microcrystalline Quartz Vein				165.2	287.1	210.0			
Type (IV) Microcrystalline Quartz Vein (CO ₂)				204.8	204.8	204.8			
Orthomagmatic				197.8	316.3	223.0			
Orthomagmatic (CO ₂)	30.5	31.0	30.8	191.3	375.0	267.4	250	920	474
Hydrothermal				174.3	301.1	252.5			
Hydrothermal (CO ₂)	24.6	30.9	29.5	225.6	330.0	274.0	250	1200	417
Post-Intrusion Hydrothermal				151.9	287.1	191.4			
Post-Intrusion Hydrothermal (CO ₂)				152.3	204.8	178.6	765	765	765

Feature Type	Salinity (min) (wt % eq. NaCl)	Salinity (max) (wt % eq. NaCl)	Salinity (mean) (wt % eq. NaCl)	Density (min) (g/cm ³)	Density (max) (g/cm ³)	Density (mean) (g/cm ³)	mol% CO ₂ (min)	mol% CO ₂ (max)	mol% CO ₂ (mean)
Granite (altered)	2.7	3.1	2.9	0.89	0.89	0.89			
Granite (Leuco) (CO ₂)	1.7	6.2	3.9	0.93	1.10	0.98	6.7	0.1	5.2
QF Pegmatite	0.0	6.2	2.6	0.67	0.94	0.83			
QF Pegmatite (CO ₂)	1.4	5.0	3.5	0.88	0.96	0.91	8.3	0.0	4.6
MQF Peg (CO ₂)	3.2	3.6	3.4	0.88	0.94	0.91	5.4	0.0	4.1
Aplite (Layered QF Pegmatite) (CO ₂)									
Aplite (QF-cored) (CO ₂)	3.1	5.6	4.3	0.72	0.85	0.79	8.1	0.1	7.6
Aplite (CO ₂)	0.2	2.9	1.5	0.98	0.98	0.98	4.8	0.0	3.7
Miarolitic Cavity	3.2	4.2	4.1	0.83	0.86	0.85			
Miarolitic Cavity (CO ₂)	2.4	2.4	2.4	0.94	0.94	0.94	2.8	0.0	2.8
Type (I) Quartz Vein	1.2	7.0	3.6	0.74	0.83	0.78			
Type (I) Quartz Vein (CO ₂)	1.7	8.0	3.6	0.81	1.02	0.92	10.5	0.1	5.9
Type (II) (skarn) Quartz Vein	0.9	4.0	2.4	0.74	0.87	0.81			
Type (II) (skarn) Quartz Vein (CO ₂)	5.4	5.4	5.4	0.95	0.95	0.95	2.7	0.0	2.7
Type (II) (wallrock) Quartz Vein	0.5	1.9	1.2	0.89	0.92	0.91			
Type (II) (wallrock) Quartz Vein (CO ₂)	4.3	4.3	4.3	0.98	0.98	0.98	3.1	0.0	3.1
Type (III) Quartz Vein	0.5	4.7	3.5	0.76	0.90	0.84			
Type (III) Quartz Vein (CO ₂)	2.9	3.7	3.5	0.90	0.95	0.92	8.2	0.1	5.8
Type (IV) Microcrystalline Quartz Vein	0.4	2.4	1.3	0.87	0.92	0.90			
Type (IV) Microcrystalline Quartz Vein (CO ₂)									

Orthomagmatic	0.0	6.2	2.8	0.67	0.94	0.86			
Orthomagmatic (CO ₂)	0.2	6.2	3.3	0.72	1.10	0.92	8.3	0.1	5.1
Hydrothermal	0.5	7.0	3.4	0.74	0.90	0.82			
Hydrothermal (CO ₂)	1.7	8.0	3.7	0.81	1.02	0.93	10.5	0.0	4.3
Post-Intrusion Hydrothermal	0.4	2.4	1.3	0.87	0.92	0.90			
Post-Intrusion Hydrothermal (CO ₂)	4.3	4.3	4.3	0.98	0.98	0.98	3.1	0.0	3.1

APPENDIX E.3.4: STATISTICAL COMPILATION OF MICROTHERMOMETRY DATA FOR
PRIMARY FLUID INCLUSIONS BY INTRUSIVE UNIT

Intrusive Unit	Number of Samples	Number of Assemblages	Number of Inclusions	Petrographic Group(s)	Assemblage Compositional Type(s)	Size (min) (um)	Size (max) (um)	Size (mean of assemblage ranges) (um)
<i>T_{cc}</i>	6	14	67	2>1	A	3	52	14
<i>T_{cc} (CO₂)</i>	2	2	12	1	C	3	17	9
<i>T_{gm}</i>	1	1	3	1	A	8	12	10
<i>T_{gm} (CO₂)</i>	2	5	22	1=2	B	5	14	9
<i>T_{mg}</i>	14	13	66	1>2	A	3	40	12
<i>T_{mg} (CO₂)</i>	8	28	89	1>2>3>4	B>C	3	33	15
<i>T_{tc}</i>	1	2	2	4	A	16	28	22
<i>T_{tc} (CO₂)</i>	1	1	1	3	B	17	17	17
Early Stage	7	16	69	2>1>4>3	A	3	52	18
Early Stage (CO ₂)	3	3	13	1=2>3	B>C	3	17	13
Late Stage	15	14	69	1>2	A	3	40	11
Late Stage (CO ₂)	10	33	111	1>2>3>4	B>C	3	33	12

Intrusive Unit	H ₂ O Liquid Fraction (min) (%)	H ₂ O Liquid Fraction (max) (%)	H ₂ O Liquid Fraction (mean) (%)	Tm _{CO2} (min) (°C)	Tm _{CO2} (max) (°C)	Tm _{CO2} (mean) (°C)	T _{entectic} (min) (°C)	T _{entectic} (max) (°C)	T _{entectic} (mean) (°C)
Tcc	53	96	87				-26.5	-22	-24.3
Tcc (CO ₂)	89	89	89	-56.8	-56.8	-56.8	-28.1	-27.4	-27.8
Tgm	86	86	86				-27.5	-27.5	-27.5
Tgm (CO ₂)	74	82	79	-58.7	-56	-57.2	-30.7	-25.4	-27.5
Tmg	20	96	80				-28.4	-21.1	-25.2
Tmg (CO ₂)	55	93	82	-59.1	-56.4	-57.1	-29.1	23.7	-26.1
Ttc	89	92	91				-30.3	-29.5	-29.9
Ttc (CO ₂)	80	80	80	-58.2	-58.2	-58.2	-26.1	-26.1	-26.1
Early Stage	53	96	89				-30.3	-22	-27.1
Early Stage (CO ₂)	80	89	84	-58.2	-56.8	-57.5	-28.1	-26.1	-26.9
Late Stage	20	96	83				-28.4	-21.1	-26.4
Late Stage (CO ₂)	55	93	81	-59.1	-56	-57.1	-30.7	23.7	-26.8

Intrusive Unit	Tm _{ice} (min) (°C)	Tm _{ice} (max) (°C)	Tm _{ice} (mean) (°C)	Tm _{clathrate} (min) (°C)	Tm _{clathrate} (max) (°C)	Tm _{clathrate} (mean) (°C)	Th _{CO2} (V) (min) (°C)	Th _{CO2} (V) (max) (°C)	Th _{CO2} (V) (mean) (°C)
Tcc	-2.5	-0.3	-1.5						
Tcc (CO ₂)	-5.2	-1.4	-3.3	7.1	7.1	7.1	29.7	31.0	30.4
Tgm	-2.8	-2.8	-2.8						
Tgm (CO ₂)				6.8	8.6	7.9	31.0	31.0	31.0
Tmg	-4.4	0	-1.8						
Tmg (CO ₂)	-5.2	-0.6	-2.0	4.9	11.1	8.3	25.2	31.0	28.4
Ttc	-3.8	-2.4	-3.1						
Ttc (CO ₂)	0	0	0	7.0	7.0	7.0	30.8	30.8	30.8
Early Stage	-3.8	-0.3	-2.3						
Early Stage (CO ₂)	-5.2	0	-1.7	7	7.1	7.1	29.7	31	30.6
Late Stage	-4.4	0	-2.3						
Late Stage (CO ₂)	-5.2	-0.6	-2.0	4.9	11.1	8.1	25.2	31	29.7

Intrusive Unit	Salinity (min) (wt % eq. NaCl)	Salinity (max) (wt % eq. NaCl)	Salinity (mean) (wt % eq. NaCl)	Density (min) (g/cm ³)	Density (max) (g/cm ³)	Density (mean) (g/cm ³)	mol% CO ₂ (min)	mol% CO ₂ (max)	mol% CO ₂ (mean)
T _{cc}	0.5	4.2	2.6	0.74	0.92	0.84			
T _{cc} (CO ₂)	2.4	5.4	3.9	0.94	0.95	0.95	2.7	2.8	2.7
T _{gm}	4.7	4.7	4.7	0.76	0.76	0.76			
T _{gm} (CO ₂)	2.4	4.2	3.1	0.91	0.97	0.94	4.4	10.2	7.5
T _{mg}	0.0	7.0	3.0	0.67	0.94	0.82			
T _{mg} (CO ₂)	0.2	8.0	3.3	0.68	1.10	0.90	2.6	10.5	4.8
T _{tc}	4.0	6.2	5.1	0.83	0.85	0.84			
T _{tc} (CO ₂)	5.0	5.0	5.0	0.92	0.92	0.92	8.3	8.3	8.3

Early Stage	0.5	6.2	3.9	0.74	0.92	0.84			
Early Stage (CO ₂)	2.4	5.4	4.4	0.92	0.95	0.93	2.7	8.3	5.5
Late Stage	0.0	7.0	3.8	0.67	0.94	0.79			
Late Stage (CO ₂)	0.2	8.0	3.2	0.68	1.10	0.92	2.6	10.5	6.2

Intrusive Unit	Th _{CO2} (L) (min) (°C)	Th _{CO2} (L) (max) (°C)	Th _{CO2} (L) (mean) (°C)	Th _{tot} (min) (°C)	Th _{tot} (max) (°C)	Th _{tot} (mean) (°C)	Ph _{tot} (min) (bar)	Ph _{tot} (max) (bar)	Ph _{tot} (mean) (bar)
T _{cc}				174.3	284.1	232.1			
T _{cc} (CO ₂)				225.6	277.5	251.6	250	305	278
T _{gm}				301.1	301.1	301.1			
T _{gm} (CO ₂)	28.4	30.6	30.1	277.4	310.9	293.7	390	1100	742
T _{mg}				189.2	316.3	251.5			
T _{mg} (CO ₂)	24.6	31.0	29.0	191.3	375	269.1	250	1200	465
T _{tc}				252.1	258	255.1			
T _{tc} (CO ₂)				271.5	271.5	271.5	920	920	920

Early Stage				174.3	284.1	243.6			
Early Stage (CO ₂)				225.6	277.5	261.5	250	920	599
Late Stage				189.2	316.3	276.3			
Late Stage (CO ₂)	24.6	31	29.6	191.3	375	281.4	250	1200	603

APPENDIX E.3.5: STATISTICAL COMPILATION OF MICROTHERMOMETRY DATA FOR
PRIMARY FLUID INCLUSIONS BY FLUID INCLUSION COMPOSITIONAL TYPE

Assemblage Compositional Type/Class	Number of Samples	Number of Assemblages	Number of Inclusions	Petrographic Group(s)	Size (min) (μm)	Size (max) (μm)	Size (mean of assemblage ranges) (μm)	H ₂ O Liquid Fraction (min) (%)	H ₂ O Liquid Fraction (max) (%)
A	21	36	163	2>1>3>4	3	52	13	20	98
B	14	24	74	1>2>3	3	33	13	55	93
C	11	14	57	1>2>4	3	27	11	78	93

Aqueous	21	36	163	2>1>3>4	3	52	13	20	98
Aqueo-Carbonic	25	38	131	1>2>3>4	3	33	12	55	93

Assemblage Compositional Type/Class	H ₂ O Liquid Fraction (mean) (%)	Tm _{CO2} (min) (°C)	Tm _{CO2} (max) (°C)	Tm _{CO2} (mean) (°C)	T _{eutectic} (min) (°C)	T _{eutectic} (max) (°C)	T _{eutectic} (mean) (°C)	Tm _{ice} (min) (°C)	Tm _{ice} (max) (°C)	Tm _{ice} (mean) (°C)
A	88				-30.3	-21.1	-25.0	-4.4	0.0	-1.6
B	80	-59.1	-56	-57.1	-30.7	28.4	-24.6			
C	86	-57.7	-56.4	-56.9	-28.1	-23.7	-26.1			

Aqueous	88				-30.3	-21.1	-25.0	-4.4	0.0	-1.6
Aquo-Carbonic	84	-59.1	-56.0	-57.2	-30.7	23.7	-26.8			

Assemblage Compositional Type/Class	T _{m-clathrate} (min) (°C)	T _{m-clathrate} (max) (°C)	T _{m-clathrate} (mean) (°C)	Th _{CO₂} (V) (min) (°C)	Th _{CO₂} (V) (max) (°C)	Th _{CO₂} (V) (mean) (°C)	Th _{CO₂} (L) (min) (°C)	Th _{CO₂} (L) (max) (°C)
A								
B	4.9	9.0	7.7	20.8	31	28.8	24.6	31
C	6.7	11.1	8.2	31	31	31		

Aqueous								
Aqueo-Carbonic	4.9	11.1	8.1	20.8	31	29.2	24.6	31

Assemblage Compositional Type/Class	Th _{CO2} (L) (mean) (°C)	Th _{tot} (min) (°C)	Th _{tot} (max) (°C)	Th _{tot} (mean) (°C)	Ph _{tot} (min) (bar)	Ph _{tot} (max) (bar)	Ph _{tot} (mean) (bar)	Salinity (min) (wt % eq. NaCl)	Salinity (max) (wt % eq. NaCl)	Salinity (mean) (wt % eq. NaCl)
A		151.9	316.3	229.8				0	7.0	2.7
B	29.6	228.7	375.0	293.3	320	1200	653	1.7	8.0	3.8
C		191.3	290.9	251.0	250	505	318	0.2	5.4	3.4

Aqueous		151.9	316.3	229.8				0	7.0	2.7
Aqueo-Carbonic	29.9	152.3	375.0	254.8	250	1200	480	0.2	8.0	3.6

Assemblage Compositional Type/Class	Density (min) (g/cm ³)	Density (max) (g/cm ³)	Density (mean) (g/cm ³)	mol% CO ₂ (min)	mol% CO ₂ (max)	mol% CO ₂ (mean)
<i>A</i>	0.7	0.9	0.8			
<i>B</i>	0.7	1.1	0.9	3.1	10.5	6.4
<i>C</i>	0.7	1.0	0.9	2.6	5.4	1.9

Aqueous	0.7	0.9	0.8			
<i>Aqueo-Carbonic</i>	0.7	1.1	0.93	2.6	10.5	4.6

APPENDIX E.4: ISOCHORE CALCULATION DATA

FLUIDS, package of computer programs for fluid inclusion studies
 Program 2: ISOC, version 01/03
 Product development Ronald J. Bakker

Filename : HPP-1-03-FIA3

Equation of state : Bakker (1999), Bowers & Helgeson (1983)
 Host Mineral : Quartz

Bulk fluid composition:

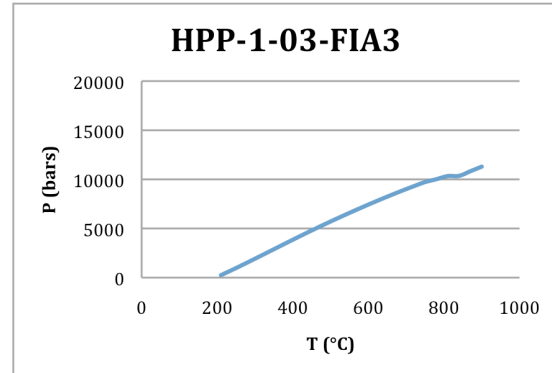
x(H₂O) = 0.887387
 x(CO₂) = 0.029423
 x(Na⁺) = 0.041595
 x(Cl⁻) = 0.041595

Salinity Aqueous Phase (associated molecules)

	Mass%	Molality
NaCl	13.2028	2.60186

Molar Volume = 20.062251 cc/mol
 Density = 0.982600 g/cc

T(K)	T(°C)	P(MPa)	P(bar)	V(cc/mol)
298.15	25	0.1	1	20.0623
298.15	25	0.1	1	20.0623
298.15	25	0.1	1	20.0623
298.15	25	0.1	1	20.0623
298.15	25	0.1	1	20.0623
298.15	25	0.1	1	20.0623
298.15	25	0.1	1	20.0623
483.15	210	25.0782	250.782	20.202
513.15	240	79.2051	792.051	20.198
543.15	270	135.159	1351.59	20.1927
573.15	300	192.332	1923.32	20.1869
603.15	330	250.214	2502.14	20.1813
633.15	360	308.339	3083.39	20.1764
663.15	390	366.262	3662.62	20.1729
693.15	420	423.573	4235.73	20.171
723.15	450	479.94	4799.4	20.1711
753.15	480	535.14	5351.4	20.1735
783.15	510	589.073	5890.73	20.1782
813.15	540	641.728	6417.28	20.1854
843.15	570	693.137	6931.37	20.1953
873.15	600	743.313	7433.13	20.2081
903.15	630	792.219	7922.19	20.2243
933.15	660	839.758	8397.58	20.2443
963.15	690	885.774	8857.74	20.2687
993.15	720	930.06	9300.6	20.2983
1023.15	750	972.367	9723.67	20.334
1053.15	780	1001.56	10015.6	20.4273
1083.15	810	1033.45	10334.5	20.5034
1113.15	840	1035.75	10357.5	20.7163
1143.15	870	1082.74	10827.4	20.7108
1173.15	900	1129.6	11296	20.7052



FLUIDS, package of computer programs for fluid inclusion studies
 Program 2: ISOC, version 01/03
 Product development Ronald J. Bakker

Filename : HPP-1-03-FIA4

Equation of state : Bakker (1999), Bowers & Helgeson (1983)

Host Mineral : Quartz

Bulk fluid composition:

x(H₂O) = 0.989456

x(Na⁺) = 0.005272

x(Cl⁻) = 0.005272

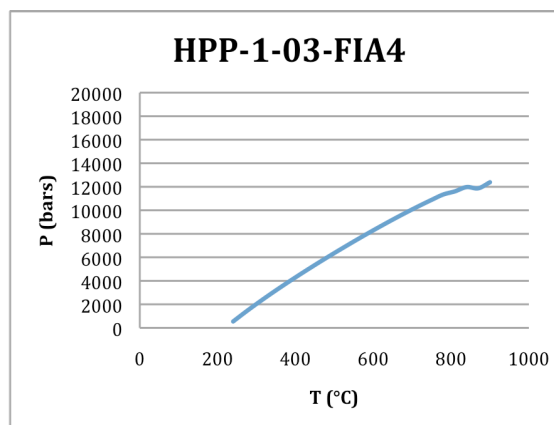
Salinity Aqueous Phase (associated molecules)

	Mass%	Molality
NaCl	1.69971	0.29576

Molar Volume = 19.637479 cc/mol

Density = 0.923415 g/cc

T(K)	T(°C)	P(MPa)	P(bar)	V(cc/mol)
298.15	25	0.1	1	19.6375
298.15	25	0.1	1	19.6375
298.15	25	0.1	1	19.6375
298.15	25	0.1	1	19.6375
298.15	25	0.1	1	19.6375
298.15	25	0.1	1	19.6375
298.15	25	0.1	1	19.6375
298.15	25	0.1	1	19.6375
513.15	240	54.5931	545.931	19.7854
543.15	270	130.778	1307.78	19.7678
573.15	300	203.628	2036.28	19.7529
603.15	330	273.767	2737.67	19.7407
633.15	360	341.646	3416.46	19.731
663.15	390	407.601	4076.01	19.7235
693.15	420	471.88	4718.8	19.7183
723.15	450	534.666	5346.66	19.7152
753.15	480	596.091	5960.91	19.7142
783.15	510	656.244	6562.44	19.7151
813.15	540	715.174	7151.74	19.718
843.15	570	772.887	7728.87	19.7231
873.15	600	829.35	8293.5	19.7307
903.15	630	884.483	8844.83	19.7409
933.15	660	938.162	9381.62	19.7543
963.15	690	990.213	9902.13	19.7715
993.15	720	1040.41	10404.1	19.7931
1023.15	750	1088.49	10884.9	19.82
1053.15	780	1134.12	11341.2	19.8531
1083.15	810	1161.04	11610.4	19.9526
1113.15	840	1197.36	11973.6	20.0129
1143.15	870	1187.03	11870.3	20.2477
1173.15	900	1238.28	12382.8	20.2418



FLUIDS, package of computer programs for fluid inclusion studies
 Program 2: ISOC, version 01/03
 Product development Ronald J. Bakker

Filename : HPP-1-04a-FIA1

Equation of state : Bakker (1999), Bowers & Helgeson (1983)

Host Mineral : Quartz

Bulk fluid composition:

x(H₂O) = 0.975894

x(Na⁺) = 0.012053

x(Cl⁻) = 0.012053

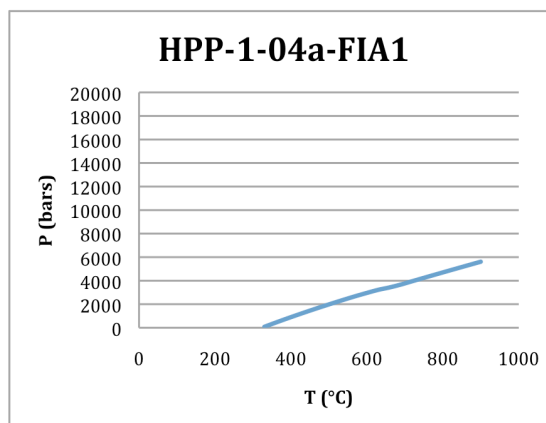
Salinity Aqueous Phase (associated molecules)

	Mass%	Molality
NaCl	3.85354	0.68557

Molar Volume = 24.489929 cc/mol

Density = 0.746660 g/cc

T(K)	T(°C)	P(MPa)	P(bar)	V(cc/mol)
298.15	25	0.1	1	24.4899
298.15	25	0.1	1	24.4899
298.15	25	0.1	1	24.4899
298.15	25	0.1	1	24.4899
298.15	25	0.1	1	24.4899
298.15	25	0.1	1	24.4899
298.15	25	0.1	1	24.4899
298.15	25	0.1	1	24.4899
298.15	25	0.1	1	24.4899
298.15	25	0.1	1	24.4899
298.15	25	0.1	1	24.4899
298.15	25	0.1	1	24.4899
603.15	330	7.84038	78.4038	24.8309
633.15	360	43.8292	438.292	24.8405
663.15	390	78.6881	786.881	24.8525
693.15	420	112.534	1125.34	24.8678
723.15	450	145.444	1454.44	24.8869
753.15	480	177.465	1774.65	24.9106
783.15	510	208.616	2086.16	24.9397
813.15	540	238.898	2388.98	24.9751
843.15	570	268.292	2682.92	25.0174
873.15	600	295.95	2959.5	25.0887
903.15	630	322.201	3222.01	25.1777
933.15	660	342.751	3427.51	25.3867
963.15	690	367.487	3674.87	25.4747
993.15	720	395.78	3957.8	25.4691
1023.15	750	423.835	4238.35	25.464
1053.15	780	451.672	4516.72	25.4591
1083.15	810	479.312	4793.12	25.4545
1113.15	840	506.77	5067.7	25.4499
1143.15	870	534.062	5340.62	25.4455
1173.15	900	561.201	5612.01	25.4411



FLUIDS, package of computer programs for fluid inclusion studies
 Program 2: ISOC, version 01/03
 Product development Ronald J. Bakker

Filename : HPP-1-04a-PL-FIA1

Equation of state : Bakker (1999), Bowers & Helgeson (1983)

Host Mineral : Quartz

Bulk fluid composition:

x(H₂O) = 0.943635

x(Na⁺) = 0.028183

x(Cl⁻) = 0.028183

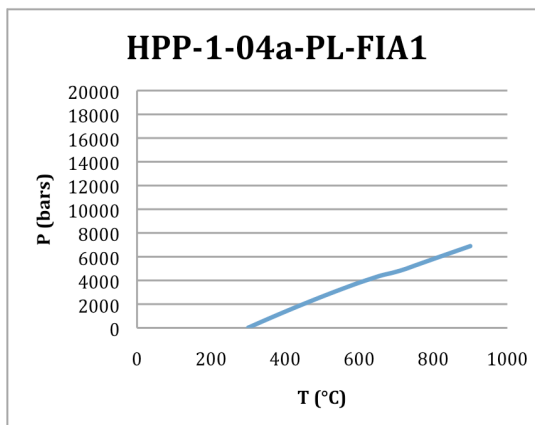
Salinity Aqueous Phase (associated molecules)

	Mass%	Molality
NaCl	8.83568	1.65782

Molar Volume = 22.536452 cc/mol

Density = 0.827436 g/cc

T(K)	T(°C)	P(MPa)	P(bar)	V(cc/mol)
298.15	25	0.1	1	22.5365
298.15	25	0.1	1	22.5365
298.15	25	0.1	1	22.5365
298.15	25	0.1	1	22.5365
298.15	25	0.1	1	22.5365
298.15	25	0.1	1	22.5365
298.15	25	0.1	1	22.5365
298.15	25	0.1	1	22.5365
298.15	25	0.1	1	22.5365
298.15	25	0.1	1	22.5365
298.15	25	0.1	1	22.5365
573.15	300	1.40338	14.0338	22.8173
603.15	330	42.842	428.42	22.8209
633.15	360	83.6072	836.072	22.8258
663.15	390	123.661	1236.61	22.8325
693.15	420	162.971	1629.71	22.8418
723.15	450	201.506	2015.06	22.8542
753.15	480	239.229	2392.29	22.8703
783.15	510	276.103	2761.03	22.8907
813.15	540	312.081	3120.81	22.916
843.15	570	347.11	3471.1	22.9469
873.15	600	381.127	3811.27	22.9839
903.15	630	412.401	4124.01	23.0532
933.15	660	442.275	4422.75	23.1318
963.15	690	464.634	4646.34	23.3084
993.15	720	491.449	4914.49	23.4065
1023.15	750	524.942	5249.42	23.4012
1053.15	780	558.201	5582.01	23.3961
1083.15	810	591.248	5912.48	23.3912
1113.15	840	624.099	6240.99	23.3863
1143.15	870	656.772	6567.72	23.3815
1173.15	900	689.28	6892.8	23.3767



FLUIDS, package of computer programs for fluid inclusion studies
 Program 2: ISOC, version 01/03
 Product development Ronald J. Bakker

Filename : HPP-1-20-FIA2

Equation of state : Bakker (1999), Bowers & Helgeson (1983)

Host Mineral : Quartz

Bulk fluid composition:

x(H₂O) = 0.940617

x(Na⁺) = 0.029691

x(Cl⁻) = 0.029691

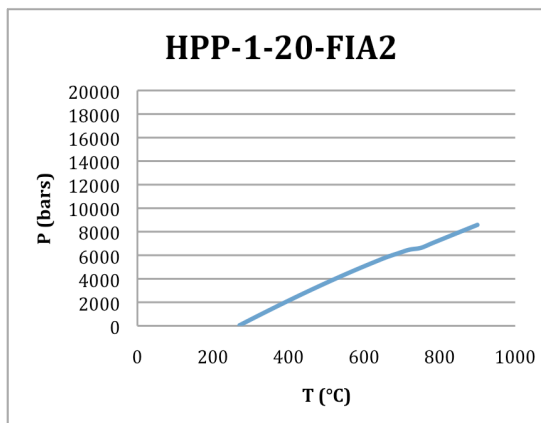
Salinity Aqueous Phase (associated molecules)

	Mass%	Molality
NaCl	9.29182	1.75218

Molar Volume = 21.084078 cc/mol

Density = 0.886039 g/cc

T(K)	T(°C)	P(MPa)	P(bar)	V(cc/mol)
298.15	25	0.1	1	21.0841
298.15	25	0.1	1	21.0841
298.15	25	0.1	1	21.0841
298.15	25	0.1	1	21.0841
298.15	25	0.1	1	21.0841
298.15	25	0.1	1	21.0841
298.15	25	0.1	1	21.0841
298.15	25	0.1	1	21.0841
298.15	25	0.1	1	21.0841
298.15	25	0.1	1	21.0841
543.15	270	4.28377	42.8377	21.3103
573.15	300	53.6998	536.998	21.3079
603.15	330	102.576	1025.76	21.3062
633.15	360	150.808	1508.08	21.3057
663.15	390	198.318	1983.18	21.307
693.15	420	245.043	2450.43	21.3105
723.15	450	290.929	2909.29	21.3166
753.15	480	335.924	3359.24	21.3258
783.15	510	379.979	3799.79	21.3384
813.15	540	423.037	4230.37	21.3548
843.15	570	465.036	4650.36	21.3754
873.15	600	505.904	5059.04	21.4006
903.15	630	545.553	5455.53	21.431
933.15	660	583.883	5838.83	21.4672
963.15	690	616.417	6164.17	21.5483
993.15	720	647.214	6472.14	21.6365
1023.15	750	662.377	6623.77	21.8536
1053.15	780	701.942	7019.42	21.8483
1083.15	810	741.288	7412.88	21.8431
1113.15	840	780.434	7804.34	21.8379
1143.15	870	819.4	8194	21.8327
1173.15	900	858.199	8581.99	21.8275



FLUIDS, package of computer programs for fluid inclusion studies
 Program 2: ISOC, version 01/03
 Product development Ronald J. Bakker

Filename : HPP-1-20-FIA3

Equation of state : Bakker (1999), Bowers & Helgeson (1983)
 Host Mineral : Quartz

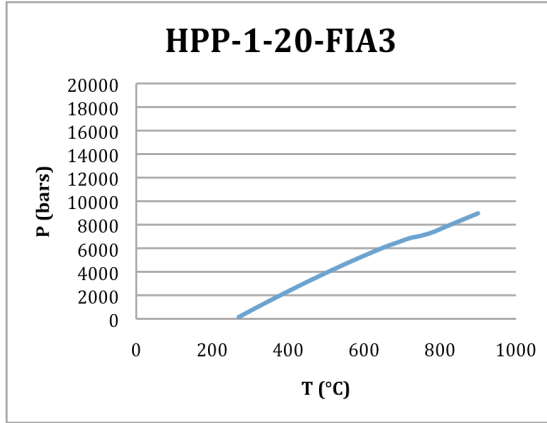
Bulk fluid composition:
 $x(\text{H}_2\text{O}) = 0.946661$
 $x(\text{Na}^+) = 0.026669$
 $x(\text{Cl}^-) = 0.026669$

Salinity Aqueous Phase (associated molecules)

	Mass%	Molality
NaCl	8.37644	1.56378

Molar Volume = 20.882395 cc/mol
 Density = 0.891350 g/cc

T(K)	T(°C)	P(MPa)	P(bar)	V(cc/mol)
298.15	25	0.1	1	20.8824
298.15	25	0.1	1	20.8824
298.15	25	0.1	1	20.8824
298.15	25	0.1	1	20.8824
298.15	25	0.1	1	20.8824
298.15	25	0.1	1	20.8824
298.15	25	0.1	1	20.8824
298.15	25	0.1	1	20.8824
298.15	25	0.1	1	20.8824
298.15	25	0.1	1	20.8824
543.15	270	15.128	151.28	21.0987
573.15	300	66.9756	669.756	21.0947
603.15	330	118.049	1180.49	21.0916
633.15	360	168.304	1683.04	21.0899
663.15	390	217.704	2177.04	21.09
693.15	420	266.218	2662.18	21.0924
723.15	450	313.813	3138.13	21.0974
753.15	480	360.457	3604.57	21.1053
783.15	510	406.11	4061.1	21.1165
813.15	540	450.725	4507.25	21.1313
843.15	570	494.247	4942.47	21.15
873.15	600	536.607	5366.07	21.1731
903.15	630	577.718	5777.18	21.2011
933.15	660	617.478	6174.78	21.2346
963.15	690	651.609	6516.09	21.3075
993.15	720	685.236	6852.36	21.3771
1023.15	750	706.429	7064.29	21.5376
1053.15	780	735.214	7352.14	21.6302
1083.15	810	775.853	7758.53	21.625
1113.15	840	816.294	8162.94	21.6197
1143.15	870	856.555	8565.55	21.6144
1173.15	900	896.651	8966.51	21.6091



FLUIDS, package of computer programs for fluid inclusion studies
 Program 2: ISOC, version 01/03
 Product development Ronald J. Bakker

Filename : HPP-1-24b-FIA1

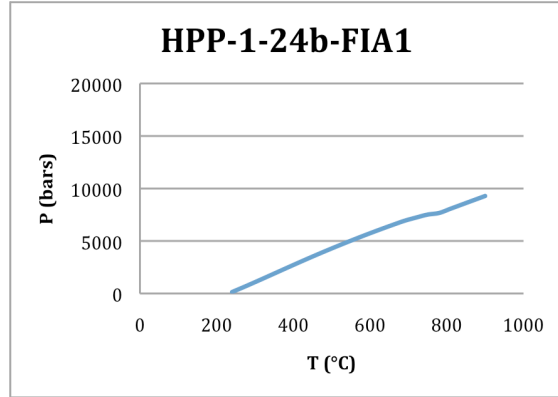
Equation of state : Bakker (1999), Bowers & Helgeson (1983)
 Host Mineral : Quartz

Bulk fluid composition:
 $x(\text{H}_2\text{O}) = 0.881830$
 $x(\text{CO}_2) = 0.026561$
 $x(\text{Na}^+) = 0.045804$
 $x(\text{Cl}^-) = 0.045804$

Salinity Aqueous Phase (associated molecules)

	Mass%	Molality
NaCl	14.4247	2.88324

Molar Volume = 20.950416 cc/mol
 Density = 0.941900 g/cc



T(K)	T(°C)	P(MPa)	P(bar)	V(cc/mol)
298.15	25	0.1	1	20.9504
298.15	25	0.1	1	20.9504
298.15	25	0.1	1	20.9504
298.15	25	0.1	1	20.9504
298.15	25	0.1	1	20.9504
298.15	25	0.1	1	20.9504
298.15	25	0.1	1	20.9504
298.15	25	0.1	1	20.9504
298.15	25	0.1	1	20.9504
513.15	240	13.7525	137.525	21.1356
543.15	270	60.1755	601.755	21.1359
573.15	300	108.084	1080.84	21.1351
603.15	330	156.91	1569.1	21.1339
633.15	360	206.144	2061.44	21.1333
663.15	390	255.31	2553.1	21.1339
693.15	420	303.979	3039.79	21.1364
723.15	450	351.807	3518.07	21.1414
753.15	480	398.57	3985.7	21.1492
783.15	510	444.171	4441.71	21.1601
813.15	540	488.599	4885.99	21.1746
843.15	570	531.874	5318.74	21.1928
873.15	600	573.995	5739.95	21.2152
903.15	630	614.917	6149.17	21.2422
933.15	660	654.548	6545.48	21.2745
963.15	690	692.754	6927.54	21.3127
993.15	720	723.225	7232.25	21.4031
1023.15	750	751.439	7514.39	21.5034
1053.15	780	766.887	7668.87	21.692
1083.15	810	807.578	8075.78	21.6869
1113.15	840	848.105	8481.05	21.6818
1143.15	870	888.481	8884.81	21.6767
1173.15	900	928.717	9287.17	21.6715

FLUIDS, package of computer programs for fluid inclusion studies
 Program 2: ISOC, version 01/03
 Product development Ronald J. Bakker

Filename : HPP-1-24b-FIA2

Equation of state : Bakker (1999), Bowers & Helgeson (1983)

Host Mineral : Quartz

Bulk fluid composition:

x(H₂O) = 0.937421

x(Na⁺) = 0.031289

x(Cl⁻) = 0.031289

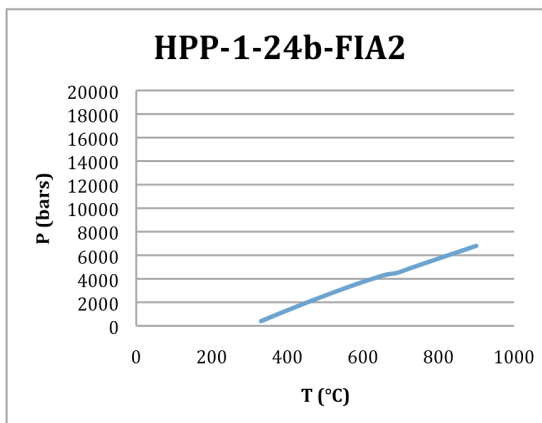
Salinity Aqueous Phase (associated molecules)

	Mass%	Molality
NaCl	9.77313	1.85277

Molar Volume = 22.581402 cc/mol

Density = 0.828875 g/cc

T(K)	T(°C)	P(MPa)	P(bar)	V(cc/mol)
298.15	25	0.1	1	22.5814
298.15	25	0.1	1	22.5814
298.15	25	0.1	1	22.5814
298.15	25	0.1	1	22.5814
298.15	25	0.1	1	22.5814
298.15	25	0.1	1	22.5814
298.15	25	0.1	1	22.5814
298.15	25	0.1	1	22.5814
298.15	25	0.1	1	22.5814
298.15	25	0.1	1	22.5814
298.15	25	0.1	1	22.5814
298.15	25	0.1	1	22.8588
603.15	330	39.5137	395.137	22.8692
633.15	360	79.5471	795.471	22.8747
663.15	390	118.98	1189.8	22.8819
693.15	420	157.752	1577.52	22.8916
723.15	450	195.809	1958.09	22.9044
753.15	480	233.101	2331.01	22.921
783.15	510	269.579	2695.79	22.9419
813.15	540	305.19	3051.9	22.9677
843.15	570	339.873	3398.73	22.9992
873.15	600	373.564	3735.64	23.0369
903.15	630	404.514	4045.14	23.108
933.15	660	433.951	4339.51	23.1904
963.15	690	450.193	4501.93	23.4613
993.15	720	483.646	4836.46	23.4557
1023.15	750	516.845	5168.45	23.4504
1053.15	780	549.812	5498.12	23.4453
1083.15	810	582.567	5825.67	23.4404
1113.15	840	615.128	6151.28	23.4355
1143.15	870	647.511	6475.11	23.4307
1173.15	900	679.728	6797.28	23.4259



FLUIDS, package of computer programs for fluid inclusion studies
 Program 2: ISOC, version 01/03
 Product development Ronald J. Bakker

Filename : HPP-1-24b-FIA3

Equation of state : Bakker (1999), Bowers & Helgeson (1983)

Host Mineral : Quartz

Bulk fluid composition:

x(H₂O) = 0.919754

x(Na⁺) = 0.040123

x(Cl⁻) = 0.040123

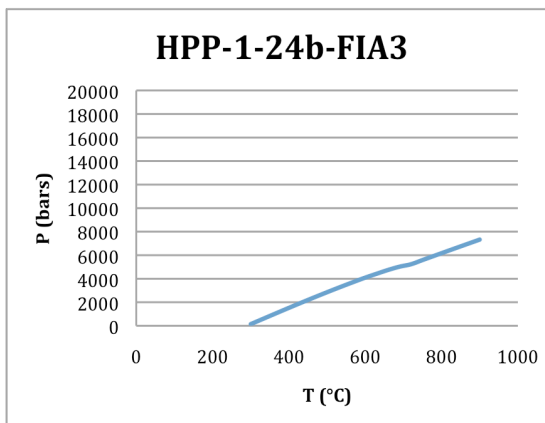
Salinity Aqueous Phase (associated molecules)

	Mass%	Molality
NaCl	12.401	2.42147

Molar Volume = 21.901468 cc/mol

Density = 0.863655 g/cc

T(K)	T(°C)	P(MPa)	P(bar)	V(cc/mol)
298.15	25	0.1	1	21.9015
298.15	25	0.1	1	21.9015
298.15	25	0.1	1	21.9015
298.15	25	0.1	1	21.9015
298.15	25	0.1	1	21.9015
298.15	25	0.1	1	21.9015
298.15	25	0.1	1	21.9015
298.15	25	0.1	1	21.9015
298.15	25	0.1	1	21.9015
298.15	25	0.1	1	21.9015
298.15	25	0.1	1	21.9015
573.15	300	14.1607	141.607	22.1643
603.15	330	55.8394	558.394	22.1677
633.15	360	97.4259	974.259	22.1718
663.15	390	138.71	1387.1	22.1775
693.15	420	179.536	1795.36	22.1853
723.15	450	219.78	2197.8	22.1959
753.15	480	259.344	2593.44	22.2099
783.15	510	298.139	2981.39	22.2279
813.15	540	336.086	3360.86	22.2504
843.15	570	373.105	3731.05	22.2779
873.15	600	409.115	4091.15	22.3111
903.15	630	442.357	4423.57	22.3728
933.15	660	474.622	4746.22	22.4372
963.15	690	502.398	5023.98	22.5484
993.15	720	523.079	5230.79	22.7371
1023.15	750	558.519	5585.19	22.7318
1053.15	780	593.723	5937.23	22.7266
1083.15	810	628.712	6287.12	22.7215
1113.15	840	663.503	6635.03	22.7165
1143.15	870	698.113	6981.13	22.7115
1173.15	900	732.554	7325.54	22.7066



FLUIDS, package of computer programs for fluid inclusion studies
 Program 2: ISOC, version 01/03
 Product development Ronald J. Bakker

Filename : HPP-1-30-FIA1

Equation of state : Bakker (1999), Bowers & Helgeson (1983)

Host Mineral : Quartz

Bulk fluid composition:

$x(\text{H}_2\text{O}) = 0.925484$

$x(\text{Na}^+) = 0.037258$

$x(\text{Cl}^-) = 0.037258$

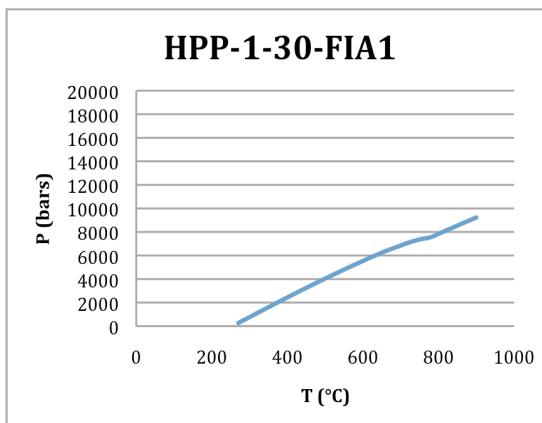
Salinity Aqueous Phase (associated molecules)

	Mass%	Molality
NaCl	11.5548	2.23466

Molar Volume = 20.547045 cc/mol

Density = 0.917458 g/cc

T(K)	T(°C)	P(MPa)	P(bar)	V(cc/mol)
298.15	25	0.1	1	20.547
298.15	25	0.1	1	20.547
298.15	25	0.1	1	20.547
298.15	25	0.1	1	20.547
298.15	25	0.1	1	20.547
298.15	25	0.1	1	20.547
298.15	25	0.1	1	20.547
298.15	25	0.1	1	20.547
298.15	25	0.1	1	20.547
298.15	25	0.1	1	20.547
543.15	270	26.4584	264.584	20.7519
573.15	300	76.8723	768.723	20.7491
603.15	330	127.336	1273.36	20.7466
633.15	360	177.571	1775.71	20.745
663.15	390	227.373	2273.73	20.745
693.15	420	276.586	2765.86	20.7469
723.15	450	325.093	3250.93	20.7513
753.15	480	372.796	3727.96	20.7584
783.15	510	419.611	4196.11	20.7685
813.15	540	465.459	4654.59	20.7821
843.15	570	510.26	5102.6	20.7994
873.15	600	553.928	5539.28	20.8208
903.15	630	596.364	5963.64	20.8468
933.15	660	637.454	6374.54	20.878
963.15	690	672.894	6728.94	20.9463
993.15	720	708.45	7084.5	21.0068
1023.15	750	736.369	7363.69	21.1168
1053.15	780	756.467	7564.67	21.2771
1083.15	810	798.337	7983.37	21.2718
1113.15	840	840.009	8400.09	21.2665
1143.15	870	881.501	8815.01	21.2611
1173.15	900	922.828	9228.28	21.2557



FLUIDS, package of computer programs for fluid inclusion studies
 Program 2: ISOC, version 01/03
 Product development Ronald J. Bakker

Filename : HPP-1-30-FIA2

Equation of state : Bakker (1999), Bowers & Helgeson (1983)
 Host Mineral : Quartz

Bulk fluid composition:

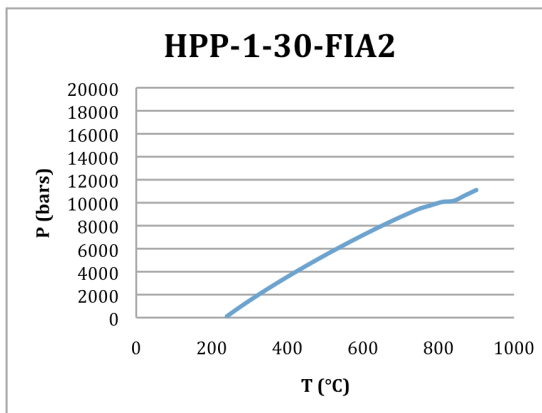
x(H₂O) = 0.989456
 x(Na⁺) = 0.005272
 x(Cl⁻) = 0.005272

Salinity Aqueous Phase (associated molecules)

	Mass%	Molality
NaCl	1.69971	0.29576

Molar Volume = 20.131448 cc/mol
 Density = 0.900757 g/cc

T(K)	T(°C)	P(MPa)	P(bar)	V(cc/mol)
298.15	25	0.1	1	20.1314
298.15	25	0.1	1	20.1314
298.15	25	0.1	1	20.1314
298.15	25	0.1	1	20.1314
298.15	25	0.1	1	20.1314
298.15	25	0.1	1	20.1314
298.15	25	0.1	1	20.1314
298.15	25	0.1	1	20.1314
513.15	240	11.6229	116.229	20.3108
543.15	270	81.7712	817.712	20.2957
573.15	300	148.709	1487.09	20.2831
603.15	330	213.039	2130.39	20.2729
633.15	360	275.198	2751.98	20.2652
663.15	390	335.5	3355	20.2599
693.15	420	394.171	3941.71	20.257
723.15	450	451.375	4513.75	20.2566
753.15	480	507.221	5072.21	20.2586
783.15	510	561.779	5617.79	20.2631
813.15	540	615.082	6150.82	20.2703
843.15	570	667.127	6671.27	20.2802
873.15	600	717.879	7178.79	20.2933
903.15	630	767.264	7672.64	20.3098
933.15	660	815.171	8151.71	20.3303
963.15	690	861.452	8614.52	20.3554
993.15	720	905.916	9059.16	20.3858
1023.15	750	948.333	9483.33	20.4224
1053.15	780	977.403	9774.03	20.5192
1083.15	810	1006.67	10066.7	20.6101
1113.15	840	1016.32	10163.2	20.7925
1143.15	870	1063.37	10633.7	20.7869
1173.15	900	1110.28	11102.8	20.7812



FLUIDS, package of computer programs for fluid inclusion studies
 Program 2: ISOC, version 01/03
 Product development Ronald J. Bakker

Filename : HPP-1-30-FIA3

Equation of state : Bakker (1999), Bowers & Helgeson (1983)
 Host Mineral : Quartz

Bulk fluid composition:

x(H₂O) = 0.975894

x(Na⁺) = 0.012053

x(Cl⁻) = 0.012053

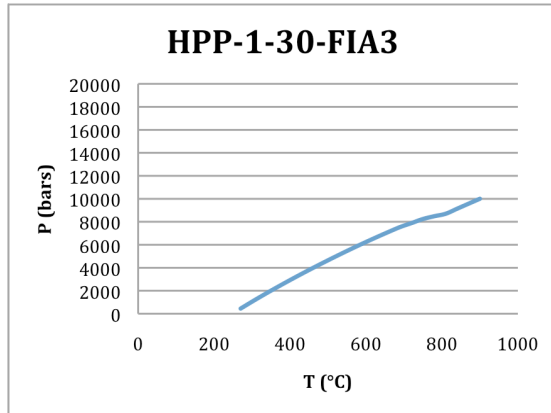
Salinity Aqueous Phase (associated molecules)

	Mass%	Molality
NaCl	3.85354	0.68557

Molar Volume = 20.534946 cc/mol

Density = 0.890465 g/cc

T(K)	T(°C)	P(MPa)	P(bar)	V(cc/mol)
298.15	25	0.1	1	20.5349
298.15	25	0.1	1	20.5349
298.15	25	0.1	1	20.5349
298.15	25	0.1	1	20.5349
298.15	25	0.1	1	20.5349
298.15	25	0.1	1	20.5349
298.15	25	0.1	1	20.5349
298.15	25	0.1	1	20.5349
298.15	25	0.1	1	20.5349
298.15	25	0.1	1	20.5349
543.15	270	44.7688	447.688	20.7272
573.15	300	104.903	1049.03	20.7181
603.15	330	163.072	1630.72	20.7108
633.15	360	219.546	2195.46	20.7056
663.15	390	274.52	2745.2	20.7028
693.15	420	328.129	3281.29	20.7023
723.15	450	380.463	3804.63	20.7044
753.15	480	431.581	4315.81	20.7093
783.15	510	481.509	4815.09	20.7171
813.15	540	530.251	5302.51	20.7281
843.15	570	577.784	5777.84	20.7424
873.15	600	624.06	6240.6	20.7604
903.15	630	669.003	6690.03	20.7827
933.15	660	712.51	7125.1	20.8096
963.15	690	754.448	7544.48	20.8419
993.15	720	788.691	7886.91	20.9175
1023.15	750	824.032	8240.32	20.9801
1053.15	780	848.474	8484.74	21.1041
1083.15	810	869.941	8699.41	21.2406
1113.15	840	913.604	9136.04	21.2352
1143.15	870	957.095	9570.95	21.2298
1173.15	900	1000.43	10004.3	21.2243



FLUIDS, package of computer programs for fluid inclusion studies

Program 2: ISOC, version 01/03

Product development Ronald J. Bakker

Filename : HPP-1-36a-FIA2

Equation of state : Bakker (1999), Bowers & Helgeson (1983)

Host Mineral : Quartz

Bulk fluid composition:

x(H2O) = 0.965795

x(Na+) = 0.017102

x(Cl-) = 0.017102

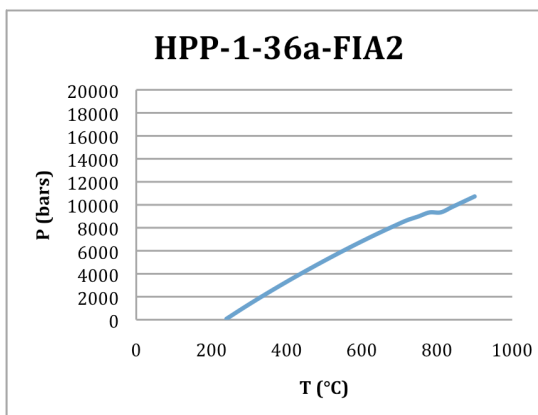
Salinity Aqueous Phase (associated molecules)

	Mass%	Molality
NaCl	5.43428	0.98295

Molar Volume = 20.101013 cc/mol

Density = 0.915323 g/cc

T(K)	T(°C)	P(MPa)	P(bar)	V(cc/mol)
298.15	25	0.1	1	20.101
298.15	25	0.1	1	20.101
298.15	25	0.1	1	20.101
298.15	25	0.1	1	20.101
298.15	25	0.1	1	20.101
298.15	25	0.1	1	20.101
298.15	25	0.1	1	20.101
298.15	25	0.1	1	20.101
298.15	25	0.1	1	20.101
513.15	240	7.62339	76.2339	20.2828
543.15	270	71.5686	715.686	20.2716
573.15	300	133.694	1336.94	20.2618
603.15	330	194.222	1942.22	20.2537
633.15	360	253.313	2533.13	20.2475
663.15	390	311.08	3110.8	20.2434
693.15	420	367.602	3676.02	20.2416
723.15	450	422.933	4229.33	20.2421
753.15	480	477.104	4771.04	20.2451
783.15	510	530.126	5301.26	20.2506
813.15	540	581.992	5819.92	20.2589
843.15	570	632.667	6326.67	20.2702
873.15	600	682.098	6820.98	20.2847
903.15	630	730.198	7301.98	20.3029
933.15	660	776.852	7768.52	20.3253
963.15	690	821.911	8219.11	20.3524
993.15	720	865.191	8651.91	20.3851
1023.15	750	898.224	8982.24	20.4673
1053.15	780	933.473	9334.73	20.5325
1083.15	810	934.262	9342.62	20.7755
1113.15	840	980.562	9805.62	20.7699
1143.15	870	1026.7	10267	20.7643
1173.15	900	1072.68	10726.8	20.7587



FLUIDS, package of computer programs for fluid inclusion studies

Program 2: ISOC, version 01/03

Product development Ronald J. Bakker

Filename : HPP-1-36a-FIA3

Equation of state : Bakker (1999), Bowers & Helgeson (1983)

Host Mineral : Quartz

Bulk fluid composition:

x(H₂O) = 0.952934

x(Na⁺) = 0.023533

x(Cl⁻) = 0.023533

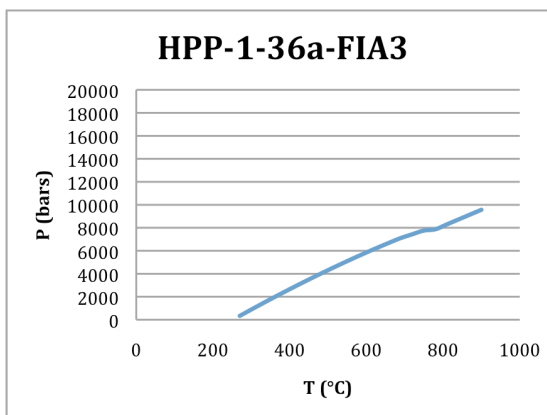
Salinity Aqueous Phase (associated molecules)

	Mass%	Molality
NaCl	7.41939	1.37079

Molar Volume = 20.579098 cc/mol

Density = 0.901068 g/cc

T(K)	T(°C)	P(MPa)	P(bar)	V(cc/mol)
298.15	25	0.1	1	20.5791
298.15	25	0.1	1	20.5791
298.15	25	0.1	1	20.5791
298.15	25	0.1	1	20.5791
298.15	25	0.1	1	20.5791
298.15	25	0.1	1	20.5791
298.15	25	0.1	1	20.5791
298.15	25	0.1	1	20.5791
298.15	25	0.1	1	20.5791
298.15	25	0.1	1	20.5791
543.15	270	33.3873	333.873	20.7795
573.15	300	88.6724	886.724	20.7735
603.15	330	142.926	1429.26	20.7686
633.15	360	196.165	1961.65	20.7652
663.15	390	248.4	2484	20.7637
693.15	420	299.632	2996.32	20.7646
723.15	450	349.855	3498.55	20.7679
753.15	480	399.054	3990.54	20.774
783.15	510	447.205	4472.05	20.7832
813.15	540	494.271	4942.71	20.7956
843.15	570	540.204	5402.04	20.8116
873.15	600	584.938	5849.38	20.8316
903.15	630	628.388	6283.88	20.856
933.15	660	670.445	6704.45	20.8854
963.15	690	710.976	7109.76	20.9204
993.15	720	743.783	7437.83	21.0031
1023.15	750	775.736	7757.36	21.0849
1053.15	780	786.983	7869.83	21.3021
1083.15	810	829.647	8296.47	21.2968
1113.15	840	872.115	8721.15	21.2914
1143.15	870	914.407	9144.07	21.2861
1173.15	900	956.538	9565.38	21.2806



FLUIDS, package of computer programs for fluid inclusion studies

Program 2: ISOC, version 01/03

Product development Ronald J. Bakker

Filename : HPP-1-63-FIA2

Equation of state : Bakker (1999), Bowers & Helgeson (1983)

Host Mineral : Quartz

Bulk fluid composition:

x(H₂O) = 0.993024

x(Na⁺) = 0.003488

x(Cl⁻) = 0.003488

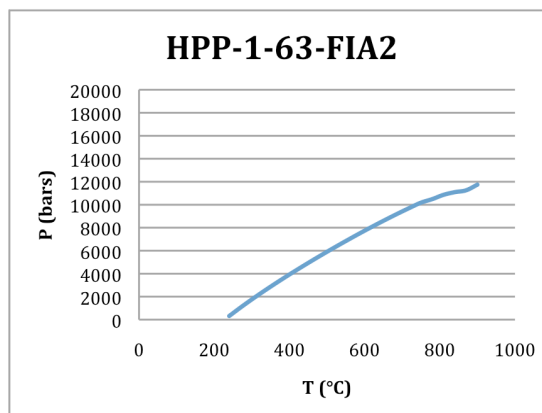
Salinity Aqueous Phase (associated molecules)

	Mass%	Molality
NaCl	1.12695	0.19496

Molar Volume = 19.900788 cc/mol

Density = 0.909186 g/cc

T(K)	T(°C)	P(MPa)	P(bar)	V(cc/mol)
298.15	25	0.1	1	19.9008
298.15	25	0.1	1	19.9008
298.15	25	0.1	1	19.9008
298.15	25	0.1	1	19.9008
298.15	25	0.1	1	19.9008
298.15	25	0.1	1	19.9008
298.15	25	0.1	1	19.9008
298.15	25	0.1	1	19.9008
513.15	240	31.4714	314.714	20.0653
543.15	270	105.34	1053.4	20.0484
573.15	300	175.723	1757.23	20.0343
603.15	330	243.292	2432.92	20.0228
633.15	360	308.533	3085.33	20.0139
663.15	390	371.801	3718.01	20.0075
693.15	420	433.354	4333.54	20.0034
723.15	450	493.38	4933.8	20.0015
753.15	480	552.011	5520.11	20.002
783.15	510	609.335	6093.35	20.0047
813.15	540	665.397	6653.97	20.0097
843.15	570	720.203	7202.03	20.0172
873.15	600	773.721	7737.21	20.0275
903.15	630	825.877	8258.77	20.0409
933.15	660	876.555	8765.55	20.0578
963.15	690	925.594	9255.94	20.0789
993.15	720	972.788	9727.88	20.1049
1023.15	750	1017.89	10178.9	20.1366
1053.15	780	1048.64	10486.4	20.2258
1083.15	810	1085.96	10859.6	20.2825
1113.15	840	1109.32	11093.2	20.3943
1143.15	870	1125.38	11253.8	20.5339
1173.15	900	1174.41	11744.1	20.5281



FLUIDS, package of computer programs for fluid inclusion studies
 Program 2: ISOC, version 01/03
 Product development Ronald J. Bakker

Filename : HPP-1-73-FIA2

Equation of state : Bakker (1999), Bowers & Helgeson (1983)
 Host Mineral : Quartz

Bulk fluid composition:

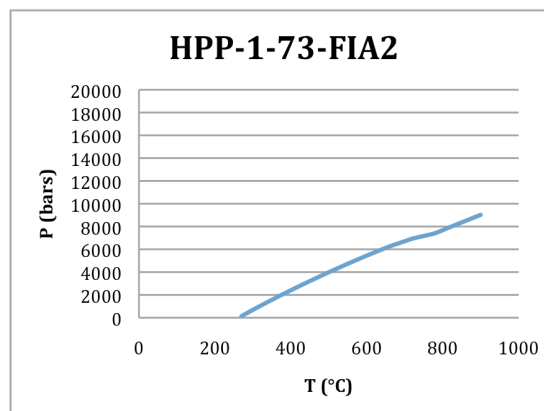
$x(\text{H}_2\text{O}) = 0.969085$
 $x(\text{Na}^+) = 0.015457$
 $x(\text{Cl}^-) = 0.015457$

Salinity Aqueous Phase (associated molecules)

	Mass%	Molality
NaCl	4.92143	0.88538

Molar Volume = 21.033214 cc/mol
 Density = 0.873001 g/cc

T(K)	T(°C)	P(MPa)	P(bar)	V(cc/mol)
298.15	25	0.1	1	21.0332
298.15	25	0.1	1	21.0332
298.15	25	0.1	1	21.0332
298.15	25	0.1	1	21.0332
298.15	25	0.1	1	21.0332
298.15	25	0.1	1	21.0332
298.15	25	0.1	1	21.0332
298.15	25	0.1	1	21.0332
298.15	25	0.1	1	21.0332
298.15	25	0.1	1	21.0332
543.15	270	13.9303	139.303	21.2519
573.15	300	68.7477	687.477	21.2458
603.15	330	121.931	1219.31	21.2412
633.15	360	173.676	1736.76	21.2385
663.15	390	224.118	2241.18	21.238
693.15	420	273.35	2733.5	21.24
723.15	450	321.431	3214.31	21.2447
753.15	480	368.391	3683.91	21.2525
783.15	510	414.24	4142.4	21.2636
813.15	540	458.965	4589.65	21.2783
843.15	570	502.534	5025.34	21.2969
873.15	600	544.894	5448.94	21.32
903.15	630	585.973	5859.73	21.3479
933.15	660	625.675	6256.75	21.3813
963.15	690	659.75	6597.5	21.4538
993.15	720	693.526	6935.26	21.5213
1023.15	750	717.214	7172.14	21.6604
1053.15	780	741.848	7418.48	21.7846
1083.15	810	782.394	7823.94	21.7794
1113.15	840	822.744	8227.44	21.7742
1143.15	870	862.916	8629.16	21.7689
1173.15	900	902.924	9029.24	21.7636



FLUIDS, package of computer programs for fluid inclusion studies
 Program 2: ISOC, version 01/03
 Product development Ronald J. Bakker

Filename : HPP-1-78-FIA1

Equation of state : Bakker (1999), Bowers & Helgeson (1983)
 Host Mineral : Quartz

Bulk fluid composition:

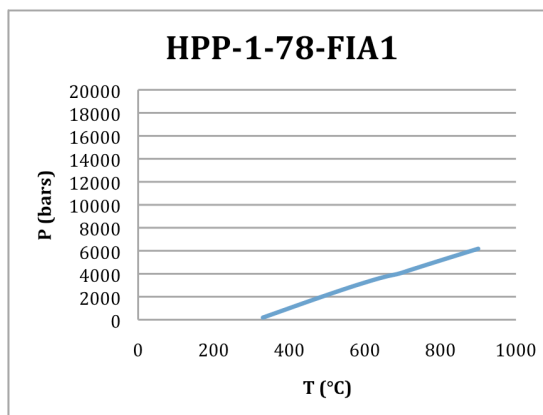
x(H₂O) = 0.883949
 x(Na⁺) = 0.058026
 x(Cl⁻) = 0.058026

Salinity Aqueous Phase (associated molecules)

	Mass%	Molality
NaCl	17.5614	3.64378

Molar Volume = 22.825721 cc/mol
 Density = 0.846278 g/cc

T(K)	T(°C)	P(MPa)	P(bar)	V(cc/mol)
273.15	0	103.217	1032.17	22.7505
298.15	25	0.1	1	22.8257
298.15	25	0.1	1	22.8257
298.15	25	0.1	1	22.8257
298.15	25	0.1	1	22.8257
298.15	25	0.1	1	22.8257
298.15	25	0.1	1	22.8257
298.15	25	0.1	1	22.8257
298.15	25	0.1	1	22.8257
298.15	25	0.1	1	22.8257
298.15	25	0.1	1	22.8257
298.15	25	0.1	1	22.8257
298.15	25	0.1	1	22.8257
603.15	330	18.6352	186.352	23.1342
633.15	360	53.3842	533.842	23.1442
663.15	390	88.4377	884.377	23.1552
693.15	420	123.494	1234.94	23.1683
723.15	450	158.328	1583.27	23.1843
753.15	480	192.766	1927.66	23.204
783.15	510	226.67	2266.7	23.2282
813.15	540	259.924	2599.24	23.2577
843.15	570	292.425	2924.25	23.2932
873.15	600	323.208	3232.08	23.3531
903.15	630	352.885	3528.85	23.4221
933.15	660	379.072	3790.72	23.544
963.15	690	400.869	4008.69	23.732
993.15	720	432.474	4324.74	23.7263
1023.15	750	463.844	4638.44	23.7209
1053.15	780	494.993	4949.93	23.7157
1083.15	810	525.937	5259.37	23.7108
1113.15	840	556.692	5566.92	23.706
1143.15	870	587.27	5872.7	23.7012
1173.15	900	617.684	6176.84	23.6965



FLUIDS, package of computer programs for fluid inclusion studies
 Program 2: ISOC, version 01/03
 Product development Ronald J. Bakker

Filename : HPP-1-78-FIA2

Equation of state : Bakker (1999), Bowers & Helgeson (1983)
 Host Mineral : Quartz

Bulk fluid composition:

$x(\text{H}_2\text{O}) = 0.922522$

$x(\text{Na}^+) = 0.038739$

$x(\text{Cl}^-) = 0.038739$

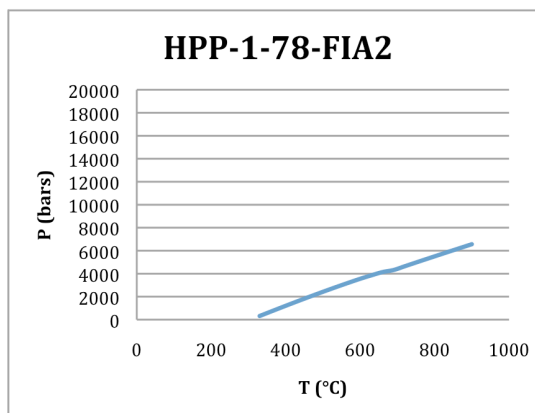
Salinity Aqueous Phase (associated molecules)

	Mass%	Molality
NaCl	11.9929 2.33093	

Molar Volume = 22.707506 cc/mol

Density = 0.831631 g/cc

T(K)	T(°C)	P(MPa)	P(bar)	V(cc/mol)
298.15	25	0.1	1	22.7075
298.15	25	0.1	1	22.7075
298.15	25	0.1	1	22.7075
298.15	25	0.1	1	22.7075
298.15	25	0.1	1	22.7075
298.15	25	0.1	1	22.7075
298.15	25	0.1	1	22.7075
298.15	25	0.1	1	22.7075
298.15	25	0.1	1	22.7075
298.15	25	0.1	1	22.7075
298.15	25	0.1	1	22.7075
298.15	25	0.1	1	22.7075
603.15	330	31.5528	315.528	23.0035
633.15	360	69.8113	698.113	23.0105
663.15	390	107.731	1077.31	23.019
693.15	420	145.182	1451.82	23.0299
723.15	450	182.062	1820.62	23.0438
753.15	480	218.288	2182.88	23.0616
783.15	510	253.783	2537.83	23.0837
813.15	540	288.477	2884.77	23.1109
843.15	570	322.298	3222.98	23.1439
873.15	600	355.173	3551.73	23.1834
903.15	630	385.294	3852.94	23.2595
933.15	660	413.584	4135.84	23.3532
963.15	690	431.801	4318.01	23.5986
993.15	720	464.507	4645.07	23.5929
1023.15	750	496.964	4969.64	23.5876
1053.15	780	529.194	5291.94	23.5825
1083.15	810	561.214	5612.14	23.5776
1113.15	840	593.041	5930.41	23.5727
1143.15	870	624.691	6246.91	23.5679
1173.15	900	656.175	6561.75	23.5632



FLUIDS, package of computer programs for fluid inclusion studies
 Program 2: ISOC, version 01/03
 Product development Ronald J. Bakker

Filename : HPP-2-02-FIA2

Equation of state : Bakker (1999), Bowers & Helgeson (1983)
 Host Mineral : Quartz

Bulk fluid composition:

x(H₂O) = 0.818018

x(CO₂) = 0.076639

x(Na⁺) = 0.052671

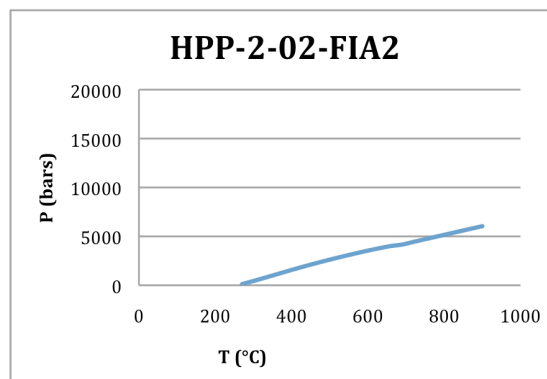
x(Cl⁻) = 0.052671

Salinity Aqueous Phase (associated molecules)

	Mass%	Molality
NaCl	17.2838	3.57414

Molar Volume = 25.069797 cc/mol

Density = 0.845200 g/cc



T(K)	T(°C)	P(MPa)	P(bar)	V(cc/mol)
298.15	25	0.1	1	25.0698
298.15	25	0.1	1	25.0698
298.15	25	0.1	1	25.0698
298.15	25	0.1	1	25.0698
298.15	25	0.1	1	25.0698
298.15	25	0.1	1	25.0698
298.15	25	0.1	1	25.0698
298.15	25	0.1	1	25.0698
298.15	25	0.1	1	25.0698
298.15	25	0.1	1	25.0698
543.15	270	11.681	116.81	25.3324
573.15	300	43.7567	437.567	25.3446
603.15	330	77.1646	771.646	25.3557
633.15	360	111.319	1113.19	25.367
663.15	390	145.505	1455.05	25.3797
693.15	420	179.016	1790.16	25.3951
723.15	450	211.335	2113.35	25.4143
753.15	480	242.249	2422.49	25.4384
783.15	510	271.828	2718.28	25.4679
813.15	540	300.283	3002.83	25.5035
843.15	570	327.808	3278.08	25.546
873.15	600	354.5	3545	25.596
903.15	630	378.81	3788.1	25.6879
933.15	660	401.261	4012.61	25.8074
963.15	690	416.783	4167.83	26.0592
993.15	720	443.98	4439.8	26.0547
1023.15	750	471.036	4710.36	26.0505
1053.15	780	497.96	4979.6	26.0463
1083.15	810	524.758	5247.58	26.0423
1113.15	840	551.438	5514.38	26.0383
1143.15	870	578.006	5780.06	26.0342
1173.15	900	604.469	6044.69	26.0302

FLUIDS, package of computer programs for fluid inclusion studies
 Program 2: ISOC, version 01/03
 Product development Ronald J. Bakker

Filename : HPP-2-06-FIA1

Equation of state : Bakker (1999), Bowers & Helgeson (1983)
 Host Mineral : Quartz

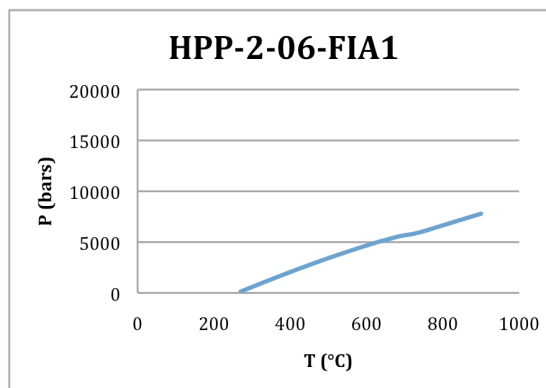
Bulk fluid composition:

x(H₂O) = 0.916281
 x(CO₂) = 0.033605
 x(Na⁺) = 0.025057
 x(Cl⁻) = 0.025057

Salinity Aqueous Phase (associated molecules)

	Mass%	Molality
NaCl	8.15095	1.51795

Molar Volume = 22.507417 cc/mol
 Density = 0.864200 g/cc



T(K)	T(°C)	P(MPa)	P(bar)	V(cc/mol)
298.15	25	0.1	1	22.5074
298.15	25	0.1	1	22.5074
298.15	25	0.1	1	22.5074
298.15	25	0.1	1	22.5074
298.15	25	0.1	1	22.5074
298.15	25	0.1	1	22.5074
298.15	25	0.1	1	22.5074
298.15	25	0.1	1	22.5074
298.15	25	0.1	1	22.5074
298.15	25	0.1	1	22.5074
543.15	270	12.8711	128.711	22.7422
573.15	300	58.4753	584.753	22.7427
603.15	330	103.421	1034.21	22.7439
633.15	360	147.665	1476.65	22.7464
663.15	390	191.133	1911.33	22.7507
693.15	420	233.729	2337.29	22.7574
723.15	450	275.352	2753.52	22.7672
753.15	480	315.91	3159.1	22.7804
783.15	510	355.331	3553.31	22.7976
813.15	540	393.568	3935.68	22.8192
843.15	570	430.592	4305.92	22.8459
873.15	600	466.382	4663.82	22.8782
903.15	630	500.912	5009.12	22.9166
933.15	660	531.504	5315.04	22.9925
963.15	690	560.892	5608.92	23.0727
993.15	720	579.199	5791.99	23.269
1023.15	750	607.155	6071.55	23.3457
1053.15	780	641.94	6419.4	23.341
1083.15	810	676.544	6765.44	23.3363
1113.15	840	710.985	7109.85	23.3316
1143.15	870	745.277	7452.77	23.3269
1173.15	900	779.432	7794.32	23.3222

FLUIDS, package of computer programs for fluid inclusion studies
 Program 2: ISOC, version 01/03
 Product development Ronald J. Bakker

Filename : HPP-2-06-FIA2

Equation of state : Bakker (1999), Bowers & Helgeson (1983)
 Host Mineral : Quartz

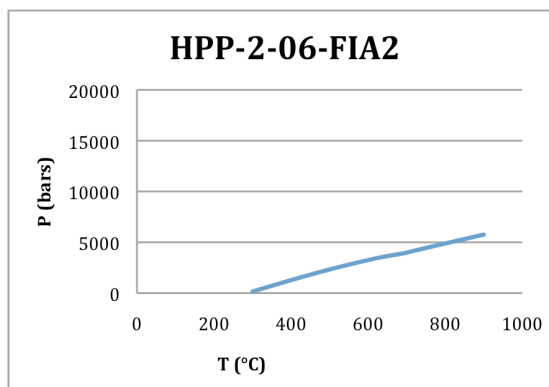
Bulk fluid composition:

x(H2O) = 0.870614
 x(CO2) = 0.051908
 x(Na+) = 0.038739
 x(Cl-) = 0.038739

Salinity Aqueous Phase (associated molecules)

	Mass%	Molality
NaCl	12.6177	2.4699

Molar Volume = 25.100598 cc/mol
 Density = 0.806100 g/cc



T(K)	T(°C)	P(MPa)	P(bar)	V(cc/mol)
298.15	25	0.1	1	25.1006
298.15	25	0.1	1	25.1006
298.15	25	0.1	1	25.1006
298.15	25	0.1	1	25.1006
298.15	25	0.1	1	25.1006
298.15	25	0.1	1	25.1006
298.15	25	0.1	1	25.1006
298.15	25	0.1	1	25.1006
298.15	25	0.1	1	25.1006
298.15	25	0.1	1	25.1006
298.15	25	0.1	1	25.1006
573.15	300	15.8286	158.286	25.4003
603.15	330	49.4354	494.354	25.4115
633.15	360	83.0983	830.983	25.4233
663.15	390	116.512	1165.12	25.4369
693.15	420	149.362	1493.62	25.4531
723.15	450	181.378	1813.78	25.473
753.15	480	212.375	2123.75	25.4976
783.15	510	242.274	2422.74	25.5277
813.15	540	271.09	2710.9	25.5641
843.15	570	298.88	2988.8	25.6077
873.15	600	324.934	3249.34	25.6785
903.15	630	349.859	3498.59	25.761
933.15	660	371.243	3712.43	25.9117
963.15	690	390.223	3902.23	26.1013
993.15	720	417.189	4171.89	26.0964
1023.15	750	443.985	4439.85	26.0919
1053.15	780	470.624	4706.24	26.0876
1083.15	810	497.116	4971.16	26.0833
1113.15	840	523.472	5234.72	26.0792
1143.15	870	549.701	5497.01	26.0751
1173.15	900	575.811	5758.11	26.071

FLUIDS, package of computer programs for fluid inclusion studies
 Program 2: ISOC, version 01/03
 Product development Ronald J. Bakker

Filename : HPP-2-06-FIA4

Equation of state : Bakker (1999), Bowers & Helgeson (1983)
 Host Mineral : Quartz

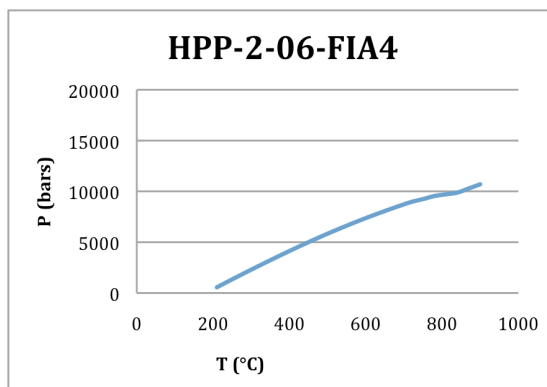
Bulk fluid composition:

x(H₂O) = 0.859189
 x(CO₂) = 0.103326
 x(Na⁺) = 0.018742
 x(Cl⁻) = 0.018742

Salinity Aqueous Phase (associated molecules)

	Mass%	Molality
NaCl	6.61089	1.21084

Molar Volume = 22.102994 cc/mol
 Density = 0.955600 g/cc



T(K)	T(°C)	P(MPa)	P(bar)	V(cc/mol)
298.15	25	0.1	1	22.103
298.15	25	0.1	1	22.103
298.15	25	0.1	1	22.103
298.15	25	0.1	1	22.103
298.15	25	0.1	1	22.103
298.15	25	0.1	1	22.103
298.15	25	0.1	1	22.2391
483.15	210	56.0695	560.695	22.236
513.15	240	115.07	1150.7	22.2286
543.15	270	172.9	1729	22.2219
573.15	300	229.802	2298.02	22.2162
603.15	330	285.87	2858.7	22.2116
633.15	360	341.087	3410.87	22.2085
663.15	390	395.351	3953.51	22.2072
693.15	420	448.515	4485.15	22.2078
723.15	450	500.414	5004.14	22.2107
753.15	480	550.899	5508.99	22.216
783.15	510	599.857	5998.57	22.2241
813.15	540	647.219	6472.19	22.2352
843.15	570	692.957	6929.57	22.2497
873.15	600	737.068	7370.68	22.2679
903.15	630	779.552	7795.52	22.2903
933.15	660	820.39	8203.9	22.3176
963.15	690	859.521	8595.21	22.3504
993.15	720	896.832	8968.32	22.3896
1023.15	750	924.069	9240.69	22.4829
1053.15	780	954.438	9544.38	22.5531
1083.15	810	971.205	9712.05	22.6973
1113.15	840	988.158	9881.58	22.8365
1143.15	870	1029.11	10291.1	22.8317
1173.15	900	1069.99	10699.9	22.8269

FLUIDS, package of computer programs for fluid inclusion studies
 Program 2: ISOC, version 01/03
 Product development Ronald J. Bakker

Filename : HPP-2-08b-FIA1

Equation of state : Bakker (1999), Bowers & Helgeson (1983)
 Host Mineral : Quartz

Bulk fluid composition:

$x(\text{H}_2\text{O}) = 0.863755$

$x(\text{CO}_2) = 0.064700$

$x(\text{Na}^+) = 0.035773$

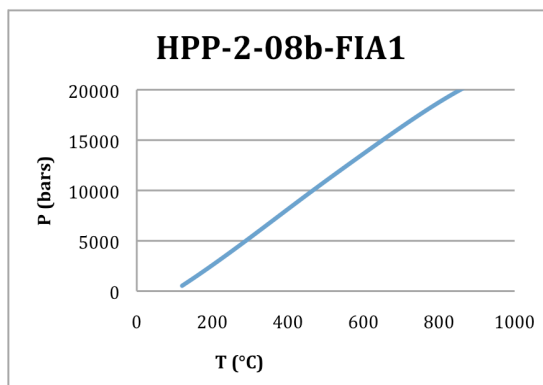
$x(\text{Cl}^-) = 0.035773$

Salinity Aqueous Phase (associated molecules)

	Mass%	Molality
NaCl	11.8477	2.29891

Molar Volume = 19.090677 cc/mol

Density = 1.073800 g/cc



T(K)	T(°C)	P(MPa)	P(bar)	V(cc/mol)
298.15	25	0.1	1	19.0907
298.15	25	0.1	1	19.0907
298.15	25	0.1	1	19.0907
298.15	25	0.1	1	19.0907
393.15	120	53.1046	531.046	19.128
423.15	150	127.956	1279.56	19.1137
453.15	180	205.202	2052.02	19.0989
483.15	210	284.498	2844.98	19.0836
513.15	240	365.508	3655.08	19.0684
543.15	270	447.947	4479.47	19.0533
573.15	300	531.553	5315.53	19.0387
603.15	330	616.04	6160.4	19.0243
633.15	360	701.065	7010.65	19.0103
663.15	390	786.231	7862.31	18.9965
693.15	420	871.129	8711.29	18.9828
723.15	450	955.412	9554.12	18.9692
753.15	480	1038.87	10388.7	18.9556
783.15	510	1121.45	11214.5	18.942
813.15	540	1203.27	12032.7	18.9285
843.15	570	1284.47	12844.7	18.9152
873.15	600	1365.19	13651.9	18.9023
903.15	630	1445.42	14454.2	18.8903
933.15	660	1525.01	15250.1	18.8796
963.15	690	1603.65	16036.5	18.8708
993.15	720	1680.9	16809	18.8646
1023.15	750	1756.25	17562.5	18.8617
1053.15	780	1829.18	18291.8	18.8626
1083.15	810	1899.16	18991.6	18.868
1113.15	840	1965.7	19657	18.8783
1143.15	870	2028.38	20283.8	18.8937
1173.15	900	2086.82	20868.2	18.9147

FLUIDS, package of computer programs for fluid inclusion studies
 Program 2: ISOC, version 01/03
 Product development Ronald J. Bakker

Filename : HPP-2-08b-FIA2

Equation of state : Bakker (1999), Bowers & Helgeson (1983)
 Host Mineral : Quartz

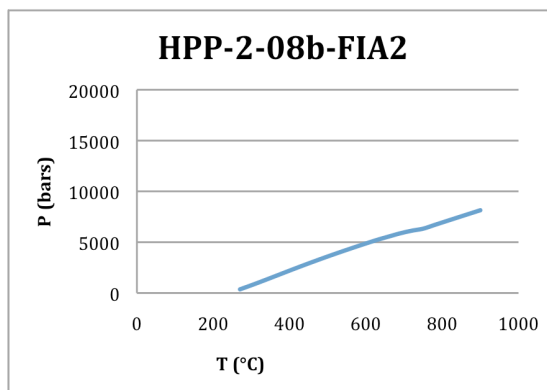
Bulk fluid composition:

x(H₂O) = 0.849096
 x(CO₂) = 0.034853
 x(Na⁺) = 0.058026
 x(Cl⁻) = 0.058026

Salinity Aqueous Phase (associated molecules)

	Mass%	Molality
NaCl	18.1514	3.79334

Molar Volume = 21.733362 cc/mol
 Density = 0.930500 g/cc



T(K)	T(°C)	P(MPa)	P(bar)	V(cc/mol)
298.15	25	0.1	1	21.7334
298.15	25	0.1	1	21.7334
298.15	25	0.1	1	21.7334
298.15	25	0.1	1	21.7334
298.15	25	0.1	1	21.7334
298.15	25	0.1	1	21.7334
298.15	25	0.1	1	21.7334
298.15	25	0.1	1	21.7334
298.15	25	0.1	1	21.9316
543.15	270	36.0885	360.885	21.9431
573.15	300	76.6051	766.051	21.9473
603.15	330	118.92	1189.2	21.9505
633.15	360	162.27	1622.7	21.9536
663.15	390	205.902	2059.02	21.9577
693.15	420	249.143	2491.43	21.9638
723.15	450	291.514	2915.14	21.9727
753.15	480	332.785	3327.85	21.9848
783.15	510	372.939	3729.39	22.0006
813.15	540	412.055	4120.55	22.0206
843.15	570	450.193	4501.93	22.045
873.15	600	487.349	4873.49	22.0744
903.15	630	523.455	5234.55	22.1093
933.15	660	555.762	5557.62	22.178
963.15	690	587.477	5874.77	22.2451
993.15	720	613.06	6130.6	22.3663
1023.15	750	633.044	6330.44	22.5352
1053.15	780	669.682	6696.82	22.5303
1083.15	810	706.149	7061.49	22.5255
1113.15	840	742.456	7424.56	22.5207
1143.15	870	778.616	7786.16	22.5158
1173.15	900	814.639	8146.39	22.5109

FLUIDS, package of computer programs for fluid inclusion studies
 Program 2: ISOC, version 01/03
 Product development Ronald J. Bakker

Filename : HPP-2-08b-FIA3

Equation of state : Bakker (1999), Bowers & Helgeson (1983)
 Host Mineral : Quartz

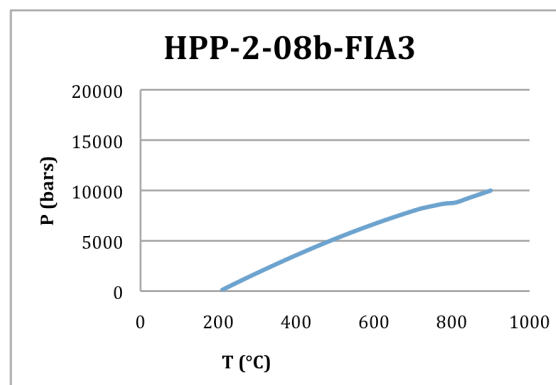
Bulk fluid composition:

x(H2O) = 0.884116
 x(CO2) = 0.081679
 x(Na+) = 0.017102
 x(Cl-) = 0.017102

Salinity Aqueous Phase (associated molecules)

	Mass%	Molality
NaCl	5.90667	1.07376

Molar Volume = 22.090550 cc/mol
 Density = 0.929000 g/cc



T(K)	T(°C)	P(MPa)	P(bar)	V(cc/mol)
298.15	25	0.1	1	22.0906
298.15	25	0.1	1	22.0906
298.15	25	0.1	1	22.0906
298.15	25	0.1	1	22.0906
298.15	25	0.1	1	22.0906
298.15	25	0.1	1	22.0906
298.15	25	0.1	1	22.0906
483.15	210	11.7989	117.989	22.2536
513.15	240	69.4968	694.968	22.2467
543.15	270	125.716	1257.16	22.2405
573.15	300	180.731	1807.31	22.2354
603.15	330	234.684	2346.84	22.2316
633.15	360	287.616	2876.16	22.2294
663.15	390	339.492	3394.92	22.229
693.15	420	390.236	3902.36	22.2308
723.15	450	439.749	4397.49	22.2351
753.15	480	487.936	4879.36	22.2421
783.15	510	534.715	5347.15	22.2521
813.15	540	580.029	5800.29	22.2654
843.15	570	623.842	6238.42	22.2824
873.15	600	666.129	6661.29	22.3035
903.15	630	706.867	7068.67	22.3292
933.15	660	746.014	7460.14	22.3602
963.15	690	783.498	7834.98	22.3972
993.15	720	819.208	8192.08	22.4411
1023.15	750	844.974	8449.74	22.5458
1053.15	780	868.212	8682.12	22.6614
1083.15	810	880.284	8802.84	22.8468
1113.15	840	919.897	9198.97	22.8422
1143.15	870	959.407	9594.07	22.8374
1173.15	900	998.825	9988.25	22.8326

FLUIDS, package of computer programs for fluid inclusion studies
 Program 2: ISOC, version 01/03
 Product development Ronald J. Bakker

Filename : HPP-2-10-FIA2

Equation of state : Bakker (1999), Bowers & Helgeson (1983)
 Host Mineral : Quartz

Bulk fluid composition:

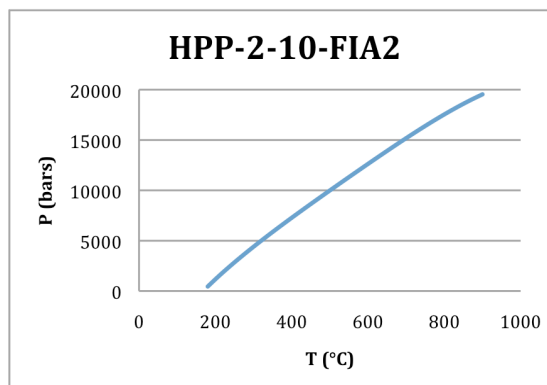
x(H2O) = 0.970553
 x(CO2) = 0.025853
 x(Na+) = 0.001797
 x(Cl-) = 0.001797

Salinity Aqueous Phase (associated molecules)

	Mass%	Molality
NaCl	0.59718	0.10276

Molar Volume = 19.028280 cc/mol

Density = 0.984200 g/cc



T(K)	T(°C)	P(MPa)	P(bar)	V(cc/mol)
298.15	25	0.1	1	19.0283
298.15	25	0.1	1	19.0283
298.15	25	0.1	1	19.0283
298.15	25	0.1	1	19.0283
298.15	25	0.1	1	19.0283
298.15	25	0.1	1	19.0283
453.15	180	44.8431	448.431	19.1218
483.15	210	151.508	1515.08	19.0898
513.15	240	251.98	2519.8	19.0626
543.15	270	347.649	3476.49	19.0393
573.15	300	439.536	4395.36	19.0194
603.15	330	528.411	5284.11	19.0021
633.15	360	614.877	6148.77	18.9869
663.15	390	699.42	6994.2	18.9732
693.15	420	782.443	7824.43	18.9605
723.15	450	864.277	8642.77	18.9485
753.15	480	945.191	9451.91	18.9368
783.15	510	1025.39	10253.9	18.9253
813.15	540	1105.01	11050.1	18.914
843.15	570	1184.11	11841.1	18.9029
873.15	600	1262.65	12626.5	18.8924
903.15	630	1340.53	13405.3	18.8827
933.15	660	1417.53	14175.3	18.8745
963.15	690	1493.34	14933.4	18.8683
993.15	720	1567.58	15675.8	18.8647
1023.15	750	1639.81	16398.1	18.8644
1053.15	780	1709.55	17095.5	18.8681
1083.15	810	1776.3	17763	18.8764
1113.15	840	1839.57	18395.7	18.8898
1143.15	870	1898.89	18988.9	18.909
1173.15	900	1953.82	19538.2	18.9343

FLUIDS, package of computer programs for fluid inclusion studies

Program 2: ISOC, version 01/03

Product development Ronald J. Bakker

Filename : HPP-2-22-FIA1

Equation of state : Bakker (1999), Bowers & Helgeson (1983)

Host Mineral : Quartz

Bulk fluid composition:

x(H₂O) = 0.915031

x(CO₂) = 0.047488

x(Na⁺) = 0.018740

x(Cl⁻) = 0.018740

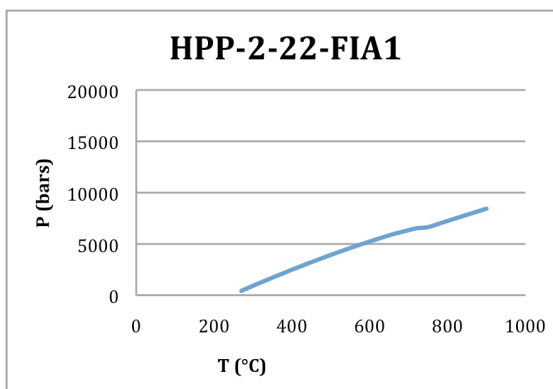
Salinity Aqueous Phase (associated molecules)

	Mass%	Molality
NaCl	6.23202	1.13683

Molar Volume = 22.390543 cc/mol

Density = 0.878500 g/cc

T(K)	T(°C)	P(MPa)	P(bar)	V(cc/mol)
298.15	25	0.1	1	22.3905
298.15	25	0.1	1	22.3905
298.15	25	0.1	1	22.3905
298.15	25	0.1	1	22.3905
298.15	25	0.1	1	22.3905
298.15	25	0.1	1	22.3905
298.15	25	0.1	1	22.3905
298.15	25	0.1	1	22.3905
298.15	25	0.1	1	22.3905
298.15	25	0.1	1	22.3905
543.15	270	42.3314	423.314	22.6019
573.15	300	91.5502	915.502	22.5999
603.15	330	139.707	1397.07	22.599
633.15	360	186.858	1868.58	22.5996
663.15	390	233.002	2330.02	22.6022
693.15	420	278.102	2781.02	22.6073
723.15	450	322.098	3220.98	22.6152
753.15	480	364.927	3649.27	22.6264
783.15	510	406.531	4065.31	22.6413
813.15	540	446.864	4468.64	22.6603
843.15	570	485.892	4858.92	22.6839
873.15	600	523.584	5235.84	22.7126
903.15	630	559.907	5599.07	22.747
933.15	660	594.814	5948.14	22.7878
963.15	690	624.166	6241.66	22.875
993.15	720	651.854	6518.54	22.9696
1023.15	750	663.796	6637.96	23.2073
1053.15	780	700.06	7000.6	23.2027
1083.15	810	736.145	7361.45	23.1981
1113.15	840	772.076	7720.76	23.1934
1143.15	870	807.869	8078.69	23.1887
1173.15	900	843.536	8435.36	23.1839



FLUIDS, package of computer programs for fluid inclusion studies

Program 2: ISOC, version 01/03

Product development Ronald J. Bakker

Filename : HPP-2-22-FIA3a

Equation of state : Bakker (1999), Bowers & Helgeson (1983)

Host Mineral : Quartz

Bulk fluid composition:

x(H2O) = 0.933458

x(CO2) = 0.032337

x(Na+) = 0.017102

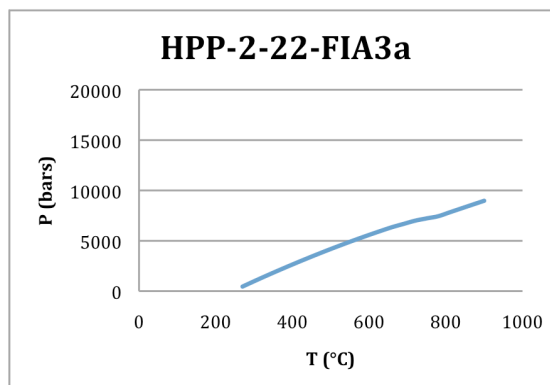
x(Cl-) = 0.017102

Salinity Aqueous Phase (associated molecules)

	Mass%	Molality
NaCl	5.61198	1.017

Molar Volume = 21.717477 cc/mol

Density = 0.885900 g/cc



T(K)	T(°C)	P(MPa)	P(bar)	V(cc/mol)
298.15	25	0.1	1	21.7175
298.15	25	0.1	1	21.7175
298.15	25	0.1	1	21.7175
298.15	25	0.1	1	21.7175
298.15	25	0.1	1	21.7175
298.15	25	0.1	1	21.7175
298.15	25	0.1	1	21.7175
298.15	25	0.1	1	21.7175
298.15	25	0.1	1	21.7175
298.15	25	0.1	1	21.7175
543.15	270	45.1576	451.576	21.9205
573.15	300	97.8117	978.117	21.9161
603.15	330	149.167	1491.67	21.9131
633.15	360	199.332	1993.32	21.9117
663.15	390	248.357	2483.57	21.9124
693.15	420	296.252	2962.52	21.9155
723.15	450	343.003	3430.03	21.9213
753.15	480	388.582	3885.82	21.9302
783.15	510	432.956	4329.56	21.9425
813.15	540	476.089	4760.89	21.9585
843.15	570	517.945	5179.45	21.9786
873.15	600	558.482	5584.82	22.0034
903.15	630	597.649	5976.49	22.0333
933.15	660	635.376	6353.76	22.0689
963.15	690	667.571	6675.71	22.1444
993.15	720	699.551	6995.51	22.214
1023.15	750	722.329	7223.29	22.3517
1053.15	780	743.777	7437.77	22.4928
1083.15	810	782.433	7824.33	22.4879
1113.15	840	820.92	8209.2	22.483
1143.15	870	859.258	8592.58	22.478
1173.15	900	897.459	8974.59	22.473

FLUIDS, package of computer programs for fluid inclusion studies

Program 2: ISOC, version 01/03

Product development Ronald J. Bakker

Filename : HPP-2-22-FIA3b

Equation of state : Bakker (1999), Bowers & Helgeson (1983)

Host Mineral : Quartz

Bulk fluid composition:

x(H2O) = 0.898274

x(CO2) = 0.030180

x(Na+) = 0.035773

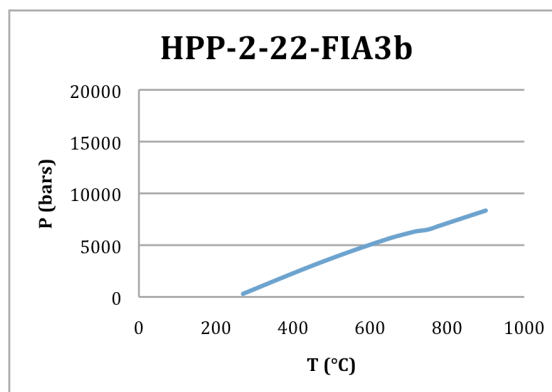
x(Cl-) = 0.035773

Salinity Aqueous Phase (associated molecules)

	Mass%	Molality
NaCl	11.4445	2.21057

Molar Volume = 21.819073 cc/mol

Density = 0.898400 g/cc



T(K)	T(°C)	P(MPa)	P(bar)	V(cc/mol)
298.15	25	0.1	1	21.8191
298.15	25	0.1	1	21.8191
298.15	25	0.1	1	21.8191
298.15	25	0.1	1	21.8191
298.15	25	0.1	1	21.8191
298.15	25	0.1	1	21.8191
298.15	25	0.1	1	21.8191
298.15	25	0.1	1	21.8191
298.15	25	0.1	1	21.8191
298.15	25	0.1	1	21.8191
543.15	270	29.6959	296.959	22.0343
573.15	300	75.662	756.62	22.0346
603.15	330	121.739	1217.39	22.035
633.15	360	167.665	1676.65	22.0363
663.15	390	213.173	2131.73	22.0392
693.15	420	258.008	2580.08	22.0442
723.15	450	301.945	3019.45	22.052
753.15	480	344.814	3448.14	22.063
783.15	510	386.517	3865.17	22.0776
813.15	540	427.015	4270.15	22.0964
843.15	570	466.307	4663.07	22.1196
873.15	600	504.396	5043.96	22.1479
903.15	630	541.262	5412.62	22.1817
933.15	660	576.849	5768.49	22.2217
963.15	690	606.748	6067.48	22.3102
993.15	720	634.356	6343.56	22.4125
1023.15	750	650.255	6502.55	22.619
1053.15	780	687.385	6873.85	22.6141
1083.15	810	724.335	7243.35	22.6093
1113.15	840	761.121	7611.21	22.6044
1143.15	870	797.756	7977.56	22.5995
1173.15	900	834.251	8342.51	22.5946

FLUIDS, package of computer programs for fluid inclusion studies
 Program 2: ISOC, version 01/03
 Product development Ronald J. Bakker

Filename : HPP-2-22-FIA5

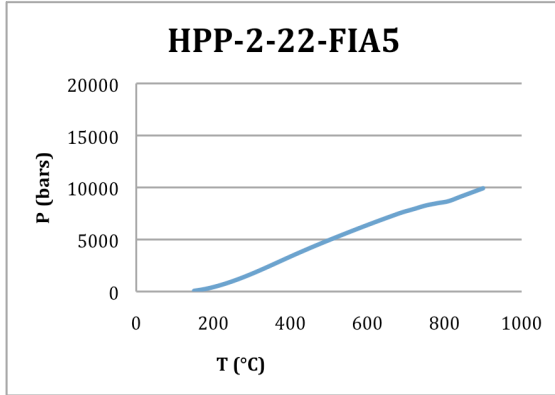
Equation of state : Bakker (1999), Bowers & Helgeson (1983)
 Host Mineral : Quartz

Bulk fluid composition:
 $x(\text{H}_2\text{O}) = 0.793426$
 $x(\text{CO}_2) = 0.058426$
 $x(\text{Na}^+) = 0.074074$
 $x(\text{Cl}^-) = 0.074074$

Salinity Aqueous Phase (associated molecules)

	Mass%	Molality
NaCl	23.2521	5.18226

Molar Volume = 20.878306 cc/mol
 Density = 1.015200 g/cc



T(K)	T(°C)	P(MPa)	P(bar)	V(cc/mol)
298.15	25	0.1	1	20.8783
298.15	25	0.1	1	20.8783
298.15	25	0.1	1	20.8783
298.15	25	0.1	1	20.8783
298.15	25	0.1	1	20.9498
423.15	150	6.53274	65.3274	20.9746
453.15	180	25.3135	253.135	20.9929
483.15	210	52.4399	524.399	21.0062
513.15	240	86.5091	865.091	21.0149
543.15	270	126.31	1263.1	21.0197
573.15	300	170.781	1707.81	21.0215
603.15	330	218.762	2187.62	21.0215
633.15	360	268.818	2688.18	21.0209
663.15	390	319.354	3193.54	21.0212
693.15	420	369.024	3690.24	21.0235
723.15	450	417.133	4171.33	21.0283
753.15	480	463.677	4636.77	21.036
783.15	510	508.997	5089.97	21.0465
813.15	540	553.393	5533.93	21.06
843.15	570	596.965	5969.65	21.0768
873.15	600	639.652	6396.52	21.0971
903.15	630	681.323	6813.23	21.1215
933.15	660	721.818	7218.18	21.1507
963.15	690	760.956	7609.56	21.1853
993.15	720	792.814	7928.14	21.2637
1023.15	750	825.857	8258.57	21.3289
1053.15	780	848.301	8483.01	21.4573
1083.15	810	868.32	8683.2	21.5962
1113.15	840	909.834	9098.34	21.5913
1143.15	870	951.234	9512.34	21.5863
1173.15	900	992.526	9925.26	21.5811

FLUIDS, package of computer programs for fluid inclusion studies

Program 2: ISOC, version 01/03

Product development Ronald J. Bakker

Filename : HPP-2-29-FIA2a

Equation of state : Bakker (1999), Bowers & Helgeson (1983)

Host Mineral : Quartz

Bulk fluid composition:

x(H2O) = 0.913254

x(CO2) = 0.027363

x(Na+) = 0.029691

x(Cl-) = 0.029691

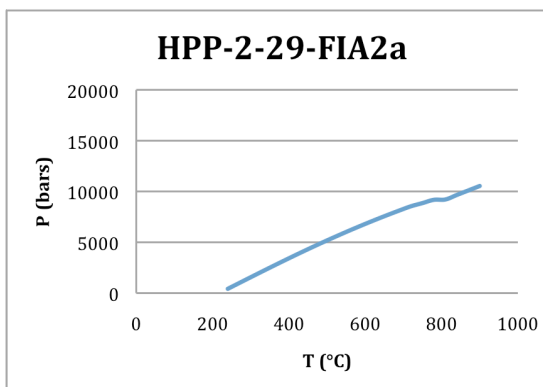
Salinity Aqueous Phase (associated molecules)

	Mass%	Molality
NaCl	9.54365	1.80467

Molar Volume = 20.536478 cc/mol

Density = 0.944300 g/cc

T(K)	T(°C)	P(MPa)	P(bar)	V(cc/mol)
298.15	25	0.1	1	20.5365
298.15	25	0.1	1	20.5365
298.15	25	0.1	1	20.5365
298.15	25	0.1	1	20.5365
298.15	25	0.1	1	20.5365
298.15	25	0.1	1	20.5365
298.15	25	0.1	1	20.5365
298.15	25	0.1	1	20.5365
298.15	25	0.1	1	20.5365
513.15	240	42.3637	423.637	20.6991
543.15	270	99.4687	994.687	20.6926
573.15	300	156.382	1563.82	20.6863
603.15	330	212.943	2129.43	20.6809
633.15	360	268.985	2689.85	20.6767
663.15	390	324.334	3243.34	20.6741
693.15	420	378.814	3788.14	20.6735
723.15	450	432.266	4322.66	20.6752
753.15	480	484.561	4845.61	20.6793
783.15	510	535.614	5356.14	20.6861
813.15	540	585.377	5853.77	20.6958
843.15	570	633.827	6338.27	20.7086
873.15	600	680.945	6809.45	20.7249
903.15	630	726.694	7266.94	20.7451
933.15	660	770.999	7709.99	20.7696
963.15	690	813.742	8137.42	20.7992
993.15	720	854.755	8547.55	20.8347
1023.15	750	885.8	8858	20.9214
1053.15	780	918.195	9181.95	20.9952
1083.15	810	921.314	9213.14	21.2289
1113.15	840	965.707	9657.07	21.2236
1143.15	870	1009.96	10099.6	21.2183
1173.15	900	1054.09	10540.9	21.2129



FLUIDS, package of computer programs for fluid inclusion studies

Program 2: ISOC, version 01/03

Product development Ronald J. Bakker

Filename : HPP-2-29-FIA2b

Equation of state : Bakker (1999), Bowers & Helgeson (1983)

Host Mineral : Quartz

Bulk fluid composition:

x(H2O) = 0.883516

x(CO2) = 0.027616

x(Na+) = 0.044434

x(Cl-) = 0.044434

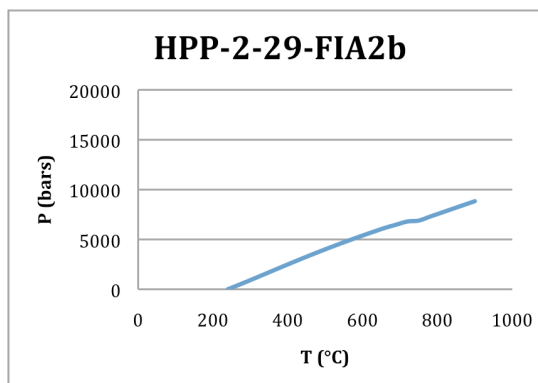
Salinity Aqueous Phase (associated molecules)

	Mass%	Molality
NaCl	14.0307	2.79163

Molar Volume = 21.281282 cc/mol

Density = 0.927100 g/cc

T(K)	T(°C)	P(MPa)	P(bar)	V(cc/mol)
298.15	25	0.1	1	21.2813
298.15	25	0.1	1	21.2813
298.15	25	0.1	1	21.2813
298.15	25	0.1	1	21.2813
298.15	25	0.1	1	21.2813
298.15	25	0.1	1	21.2813
298.15	25	0.1	1	21.2813
298.15	25	0.1	1	21.2813
298.15	25	0.1	1	21.2813
513.15	240	0.7675	7.67495	21.4785
543.15	270	45.7646	457.646	21.4798
573.15	300	92.0576	920.576	21.4799
603.15	330	139.134	1391.34	21.4798
633.15	360	186.53	1865.3	21.4802
663.15	390	233.807	2338.07	21.4819
693.15	420	280.566	2805.66	21.4856
723.15	450	326.48	3264.8	21.4919
753.15	480	371.336	3713.36	21.5011
783.15	510	415.035	4150.35	21.5138
813.15	540	457.564	4575.64	21.5302
843.15	570	498.942	4989.42	21.5507
873.15	600	539.172	5391.72	21.5757
903.15	630	578.217	5782.17	21.6057
933.15	660	615.992	6159.92	21.6414
963.15	690	648.329	6483.29	21.7176
993.15	720	680.039	6800.39	21.7921
1023.15	750	689.098	6890.98	22.0503
1053.15	780	728.294	7282.94	22.0453
1083.15	810	767.309	7673.09	22.0403
1113.15	840	806.159	8061.59	22.0353
1143.15	870	844.857	8448.57	22.0303
1173.15	900	883.414	8834.14	22.0252



FLUIDS, package of computer programs for fluid inclusion studies
 Program 2: ISOC, version 01/03
 Product development Ronald J. Bakker

Filename : HPP-2-29-FIA4

Equation of state : Bakker (1999), Bowers & Helgeson (1983)
 Host Mineral : Quartz

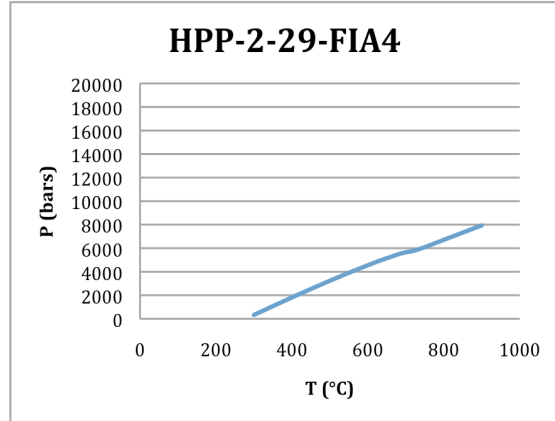
Bulk fluid composition:
 $x(\text{H}_2\text{O}) = 0.928454$
 $x(\text{Na}^+) = 0.035773$
 $x(\text{Cl}^-) = 0.035773$

Salinity Aqueous Phase (associated molecules)

	Mass%	Molality
NaCl	11.1138	2.13871

Molar Volume = 21.455859 cc/mol
 Density = 0.877044 g/cc

T(K)	T(°C)	P(MPa)	P(bar)	V(cc/mol)
298.15	25	0.1	1	21.4559
298.15	25	0.1	1	21.4559
298.15	25	0.1	1	21.4559
298.15	25	0.1	1	21.4559
298.15	25	0.1	1	21.4559
298.15	25	0.1	1	21.4559
298.15	25	0.1	1	21.4559
298.15	25	0.1	1	21.4559
298.15	25	0.1	1	21.4559
298.15	25	0.1	1	21.4559
573.15	300	32.6285	326.285	21.6993
603.15	330	77.6802	776.802	21.7002
633.15	360	122.419	1224.19	21.702
663.15	390	166.687	1666.87	21.7054
693.15	420	210.36	2103.6	21.711
723.15	450	253.344	2533.44	21.7193
753.15	480	295.556	2955.56	21.7308
783.15	510	336.921	3369.21	21.746
813.15	540	377.37	3773.7	21.7654
843.15	570	416.828	4168.28	21.7893
873.15	600	455.216	4552.16	21.8184
903.15	630	492.448	4924.48	21.8532
933.15	660	525.64	5256.4	21.9242
963.15	690	557.612	5576.12	21.9991
993.15	720	577.697	5776.97	22.1894
1023.15	750	608.739	6087.39	22.2546
1053.15	780	646.113	6461.13	22.2493
1083.15	810	683.268	6832.68	22.2442
1113.15	840	720.225	7202.25	22.2391
1143.15	870	756.998	7569.98	22.234
1173.15	900	793.604	7936.04	22.2289



FLUIDS, package of computer programs for fluid inclusion studies

Program 2: ISOC, version 01/03

Product development Ronald J. Bakker

Filename : HPP-2-35-FIA2

Equation of state : Bakker (1999), Bowers & Helgeson (1983)

Host Mineral : Quartz

Bulk fluid composition:

x(H₂O) = 0.972387

x(Na⁺) = 0.013807

x(Cl⁻) = 0.013807

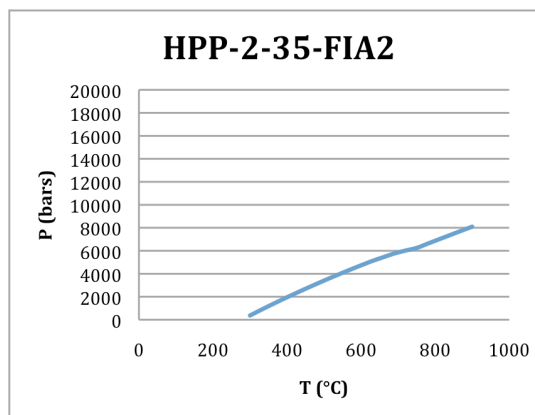
Salinity Aqueous Phase (associated molecules)

	Mass%	Molality
NaCl	4.40477	0.78815

Molar Volume = 21.712074 cc/mol

Density = 0.844000 g/cc

T(K)	T(°C)	P(MPa)	P(bar)	V(cc/mol)
298.15	25	0.1	1	21.7121
298.15	25	0.1	1	21.7121
298.15	25	0.1	1	21.7121
298.15	25	0.1	1	21.7121
298.15	25	0.1	1	21.7121
298.15	25	0.1	1	21.7121
298.15	25	0.1	1	21.7121
298.15	25	0.1	1	21.7121
298.15	25	0.1	1	21.7121
298.15	25	0.1	1	21.7121
298.15	25	0.1	1	21.7121
573.15	300	36.8539	368.539	21.9552
603.15	330	86.0128	860.128	21.9531
633.15	360	133.71	1337.1	21.9528
663.15	390	180.105	1801.05	21.9547
693.15	420	225.306	2253.06	21.9593
723.15	450	269.383	2693.83	21.967
753.15	480	312.373	3123.73	21.978
783.15	510	354.289	3542.89	21.9927
813.15	540	395.124	3951.24	22.0117
843.15	570	434.847	4348.47	22.0353
873.15	600	473.412	4734.12	22.064
903.15	630	510.753	5107.53	22.0984
933.15	660	544.059	5440.59	22.1675
963.15	690	576.476	5764.76	22.2369
993.15	720	601.546	6015.46	22.3716
1023.15	750	624.737	6247.37	22.5156
1053.15	780	662.118	6621.18	22.5104
1083.15	810	699.28	6992.8	22.5054
1113.15	840	736.243	7362.43	22.5003
1143.15	870	773.026	7730.26	22.4952
1173.15	900	809.644	8096.44	22.4902



FLUIDS, package of computer programs for fluid inclusion studies
 Program 2: ISOC, version 01/03
 Product development Ronald J. Bakker

Filename : HPP-2-35-FIA3

Equation of state : Bakker (1999), Bowers & Helgeson (1983)
 Host Mineral : Quartz

Bulk fluid composition:

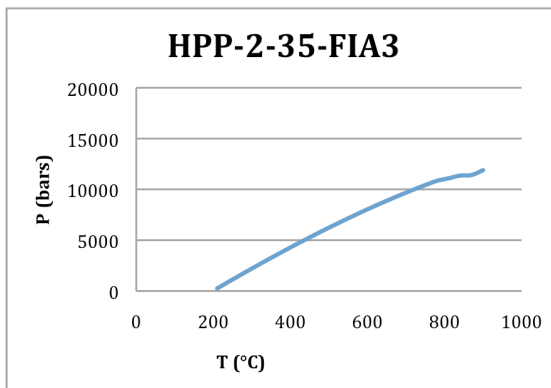
x(H2O) = 0.921362
 x(CO2) = 0.034820
 x(Na+) = 0.021909
 x(Cl-) = 0.021909

Salinity Aqueous Phase (associated molecules)

	Mass%	Molality
NaCl	7.16391	1.31995

Molar Volume = 20.216492 cc/mol

Density = 0.960200 g/cc



T(K)	T(°C)	P(MPa)	P(bar)	V(cc/mol)
298.15	25	0.1	1	20.2165
298.15	25	0.1	1	20.2165
298.15	25	0.1	1	20.2165
298.15	25	0.1	1	20.2165
298.15	25	0.1	1	20.2165
298.15	25	0.1	1	20.2165
298.15	25	0.1	1	20.2165
483.15	210	25.018	250.18	20.3574
513.15	240	91.5484	915.484	20.3457
543.15	270	156.94	1569.4	20.3348
573.15	300	221.306	2213.06	20.325
603.15	330	284.693	2846.93	20.3165
633.15	360	347.095	3470.95	20.3097
663.15	390	408.466	4084.66	20.3046
693.15	420	468.74	4687.4	20.3014
723.15	450	527.845	5278.45	20.3002
753.15	480	585.713	5857.13	20.301
783.15	510	642.293	6422.93	20.3039
813.15	540	697.548	6975.48	20.3092
843.15	570	751.449	7514.49	20.3168
873.15	600	803.964	8039.64	20.3273
903.15	630	855.04	8550.4	20.3408
933.15	660	904.594	9045.94	20.358
963.15	690	952.491	9524.91	20.3794
993.15	720	998.549	9985.49	20.4057
1023.15	750	1042.53	10425.3	20.4378
1053.15	780	1084.14	10841.4	20.4768
1083.15	810	1108.71	11087.1	20.5834
1113.15	840	1135.82	11358.2	20.6753
1143.15	870	1141.46	11414.6	20.8558
1173.15	900	1189.53	11895.3	20.8502

FLUIDS, package of computer programs for fluid inclusion studies
 Program 2: ISOC, version 01/03
 Product development Ronald J. Bakker

Filename : HPP-2-38-FIA2

Equation of state : Bakker (1999), Bowers & Helgeson (1983)
 Host Mineral : Quartz

Bulk fluid composition:

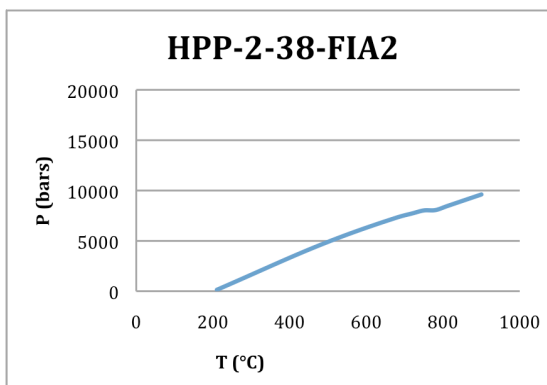
x(H₂O) = 0.858897
 x(CO₂) = 0.075532
 x(Na⁺) = 0.032785
 x(Cl⁻) = 0.032785

Salinity Aqueous Phase (associated molecules)

	Mass%	Molality
NaCl	11.0219	2.11883

Molar Volume = 21.968536 cc/mol
 Density = 0.942900 g/cc

T(K)	T(°C)	P(MPa)	P(bar)	V(cc/mol)
298.15	25	0.1	1	21.9685
298.15	25	0.1	1	21.9685
298.15	25	0.1	1	21.9685
298.15	25	0.1	1	21.9685
298.15	25	0.1	1	21.9685
298.15	25	0.1	1	21.9685
298.15	25	0.1	1	21.9685
483.15	210	13.5138	135.138	22.1295
513.15	240	63.2976	632.976	22.128
543.15	270	113.52	1135.2	22.1259
573.15	300	164.094	1640.94	22.1237
603.15	330	214.845	2148.45	22.1217
633.15	360	265.501	2655.01	22.1207
663.15	390	315.704	3157.04	22.1212
693.15	420	365.06	3650.6	22.1238
723.15	450	413.206	4132.06	22.1289
753.15	480	459.874	4598.74	22.1369
783.15	510	504.932	5049.32	22.1482
813.15	540	548.375	5483.75	22.1631
843.15	570	590.284	5902.84	22.1819
873.15	600	630.757	6307.57	22.205
903.15	630	669.859	6698.59	22.2329
933.15	660	707.587	7075.87	22.2662
963.15	690	743.866	7438.66	22.3055
993.15	720	772.972	7729.72	22.3923
1023.15	750	802.321	8023.21	22.4715
1053.15	780	805.64	8056.4	22.7351
1083.15	810	844.634	8446.34	22.7305
1113.15	840	883.516	8835.16	22.7259
1143.15	870	922.294	9222.94	22.7211
1173.15	900	960.976	9609.76	22.7163



FLUIDS, package of computer programs for fluid inclusion studies
 Program 2: ISOC, version 01/03
 Product development Ronald J. Bakker

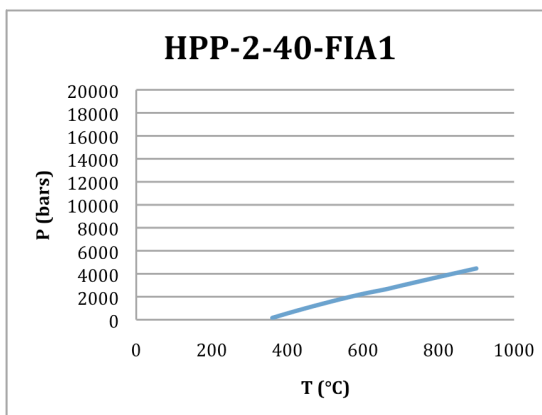
Filename : HPP-2-40-FIA1

Equation of state : Bakker (1999), Bowers & Helgeson (1983)
 Host Mineral : Quartz

Bulk fluid composition:
 x(H2O) = 1.000000

Molar Volume = 27.066348 cc/mol
 Density = 0.665597 g/cc

T(K)	T(°C)	P(MPa)	P(bar)	V(cc/mol)
298.15	25	0.1	1	27.0663
298.15	25	0.1	1	27.0663
298.15	25	0.1	1	27.0663
298.15	25	0.1	1	27.0663
298.15	25	0.1	1	27.0663
298.15	25	0.1	1	27.0663
298.15	25	0.1	1	27.0663
298.15	25	0.1	1	27.0663
298.15	25	0.1	1	27.0663
298.15	25	0.1	1	27.0663
298.15	25	0.1	1	27.0663
298.15	25	0.1	1	27.0663
298.15	25	0.1	1	27.0663
633.15	360	15.9579	159.579	27.483
663.15	390	45.3874	453.874	27.5024
693.15	420	73.726	737.26	27.5256
723.15	450	101.109	1011.09	27.5536
753.15	480	127.628	1276.28	27.5872
783.15	510	153.337	1533.37	27.6276
813.15	540	178.263	1782.63	27.6758
843.15	570	202.128	2021.28	27.7466
873.15	600	224.92	2249.2	27.8386
903.15	630	245.072	2450.72	28.0175
933.15	660	264.539	2645.39	28.1937
963.15	690	287.905	2879.05	28.1876
993.15	720	311.04	3110.4	28.1821
1023.15	750	333.963	3339.63	28.1771
1053.15	780	356.695	3566.95	28.1725
1083.15	810	379.252	3792.52	28.1681
1113.15	840	401.649	4016.49	28.164
1143.15	870	423.898	4238.98	28.1599
1173.15	900	446.011	4460.11	28.1559



FLUIDS, package of computer programs for fluid inclusion studies
 Program 2: ISOC, version 01/03
 Product development Ronald J. Bakker

Filename : HPP-2-40-FIA2

Equation of state : Bakker (1999), Bowers & Helgeson (1983)

Host Mineral : Quartz

Bulk fluid composition:

x(H₂O) = 0.930723

x(CO₂) = 0.031793

x(Na⁺) = 0.018742

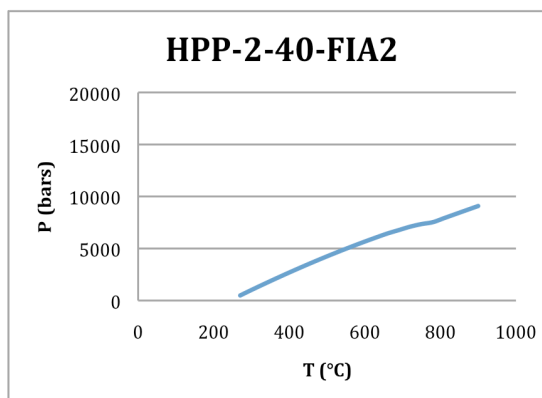
x(Cl⁻) = 0.018742

Salinity Aqueous Phase (associated molecules)

	Mass%	Molality
NaCl	6.13396	1.11778

Molar Volume = 21.606435 cc/mol

Density = 0.891500 g/cc



T(K)	T(°C)	P(MPa)	P(bar)	V(cc/mol)
298.15	25	0.1	1	21.6064
298.15	25	0.1	1	21.6064
298.15	25	0.1	1	21.6064
298.15	25	0.1	1	21.6064
298.15	25	0.1	1	21.6064
298.15	25	0.1	1	21.6064
298.15	25	0.1	1	21.6064
298.15	25	0.1	1	21.6064
298.15	25	0.1	1	21.8045
543.15	270	48.9083	489.083	21.8057
573.15	300	101.739	1017.39	21.8013
603.15	330	153.388	1533.88	21.7981
633.15	360	203.931	2039.31	21.7965
663.15	390	253.392	2533.92	21.797
693.15	420	301.759	3017.59	21.7997
723.15	450	349	3490	21.8052
753.15	480	395.075	3950.75	21.8137
783.15	510	439.94	4399.4	21.8256
813.15	540	483.557	4835.57	21.8411
843.15	570	525.889	5258.89	21.8606
873.15	600	566.895	5668.95	21.8847
903.15	630	606.527	6065.27	21.9138
933.15	660	644.716	6447.16	21.9485
963.15	690	677.35	6773.5	22.0222
993.15	720	710.038	7100.38	22.0881
1023.15	750	734.989	7349.89	22.2085
1053.15	780	753.223	7532.23	22.3751
1083.15	810	792.326	7923.26	22.3702
1113.15	840	831.262	8312.62	22.3653
1143.15	870	870.051	8700.51	22.3603
1173.15	900	908.704	9087.04	22.3553

FLUIDS, package of computer programs for fluid inclusion studies
 Program 2: ISOC, version 01/03
 Product development Ronald J. Bakker

Filename : HPP-2-41a-FIA1

Equation of state : Bakker (1999), Bowers & Helgeson (1983)

Host Mineral : Quartz

Bulk fluid composition:

x(H₂O) = 0.916810

x(Na⁺) = 0.041595

x(Cl⁻) = 0.041595

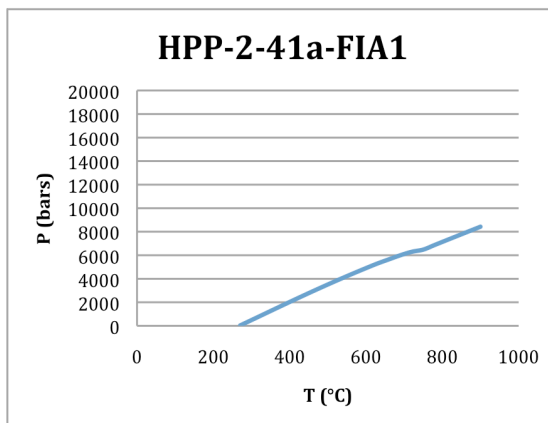
Salinity Aqueous Phase (associated molecules)

	Mass%	Molality
NaCl	12.8335	2.51836

Molar Volume = 20.994380 cc/mol

Density = 0.902543 g/cc

T(K)	T(°C)	P(MPa)	P(bar)	V(cc/mol)
298.15	25	0.1	1	20.9944
298.15	25	0.1	1	20.9944
298.15	25	0.1	1	20.9944
298.15	25	0.1	1	20.9944
298.15	25	0.1	1	20.9944
298.15	25	0.1	1	20.9944
298.15	25	0.1	1	20.9944
298.15	25	0.1	1	20.9944
298.15	25	0.1	1	20.9944
298.15	25	0.1	1	20.9944
543.15	270	2.98415	29.8415	21.2206
573.15	300	48.9024	489.024	21.2207
603.15	330	95.1741	951.741	21.2208
633.15	360	141.448	1414.48	21.2216
663.15	390	187.467	1874.67	21.2239
693.15	420	233.04	2330.4	21.2281
723.15	450	278.02	2780.2	21.2348
753.15	480	322.289	3222.89	21.2445
783.15	510	365.747	3657.47	21.2576
813.15	540	408.303	4083.03	21.2745
843.15	570	449.872	4498.72	21.2957
873.15	600	490.361	4903.61	21.3215
903.15	630	529.674	5296.74	21.3525
933.15	660	564.932	5649.32	21.4155
963.15	690	599.748	5997.48	21.4747
993.15	720	629.262	6292.62	21.5743
1023.15	750	647.821	6478.21	21.7647
1053.15	780	687.14	6871.4	21.7594
1083.15	810	726.24	7262.4	21.7542
1113.15	840	765.14	7651.4	21.749
1143.15	870	803.857	8038.57	21.7438
1173.15	900	842.406	8424.06	21.7385



FLUIDS, package of computer programs for fluid inclusion studies
 Program 2: ISOC, version 01/03
 Product development Ronald J. Bakker

Filename : HPP-2-41a-FIA2

Equation of state : Bakker (1999), Bowers & Helgeson (1983)

Host Mineral : Quartz

Bulk fluid composition:

x(H₂O) = 0.931434

x(Na⁺) = 0.034283

x(Cl⁻) = 0.034283

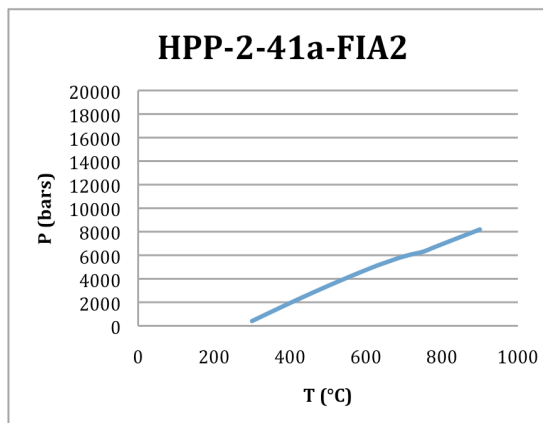
Salinity Aqueous Phase (associated molecules)

	Mass%	Molality
NaCl	10.6699 2.04308	

Molar Volume = 21.285388 cc/mol

Density = 0.882498 g/cc

T(K)	T(°C)	P(MPa)	P(bar)	V(cc/mol)
298.15	25	0.1	1	21.2854
298.15	25	0.1	1	21.2854
298.15	25	0.1	1	21.2854
298.15	25	0.1	1	21.2854
298.15	25	0.1	1	21.2854
298.15	25	0.1	1	21.2854
298.15	25	0.1	1	21.2854
298.15	25	0.1	1	21.2854
298.15	25	0.1	1	21.2854
298.15	25	0.1	1	21.5144
573.15	300	40.8072	408.072	21.5208
603.15	330	87.2215	872.215	21.5208
633.15	360	133.244	1332.44	21.5217
663.15	390	178.732	1787.32	21.5243
693.15	420	223.577	2235.77	21.529
723.15	450	267.692	2676.92	21.5365
753.15	480	311.002	3110.02	21.547
783.15	510	353.437	3534.37	21.5612
813.15	540	394.929	3949.29	21.5793
843.15	570	435.408	4354.08	21.6018
873.15	600	474.796	4747.96	21.6293
903.15	630	513.003	5130.03	21.6623
933.15	660	547.183	5471.83	21.7289
963.15	690	580.582	5805.82	21.7948
993.15	720	607.193	6071.93	21.9183
1023.15	750	629.767	6297.67	22.0717
1053.15	780	668.038	6680.38	22.0664
1083.15	810	706.09	7060.9	22.0612
1113.15	840	743.943	7439.43	22.0561
1143.15	870	781.614	7816.14	22.0509
1173.15	900	819.117	8191.17	22.0458



FLUIDS, package of computer programs for fluid inclusion studies
 Program 2: ISOC, version 01/03
 Product development Ronald J. Bakker

Filename : HPP-2-41a-FIA3

Equation of state : Bakker (1999), Bowers & Helgeson (1983)

Host Mineral : Quartz

Bulk fluid composition:

x(H₂O) = 0.969085

x(Na⁺) = 0.015457

x(Cl⁻) = 0.015457

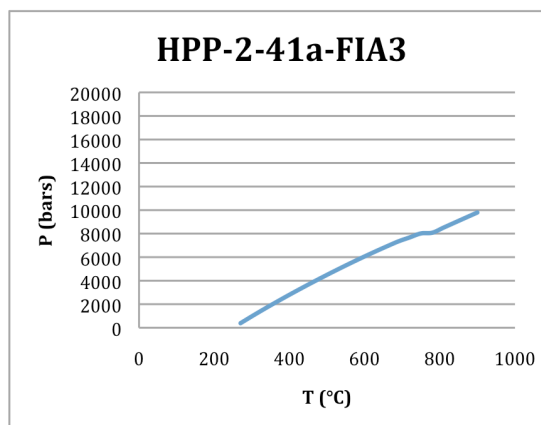
Salinity Aqueous Phase (associated molecules)

	Mass%	Molality
NaCl	4.92143	0.88538

Molar Volume = 20.587968 cc/mol

Density = 0.891881 g/cc

T(K)	T(°C)	P(MPa)	P(bar)	V(cc/mol)
298.15	25	0.1	1	20.588
298.15	25	0.1	1	20.588
298.15	25	0.1	1	20.588
298.15	25	0.1	1	20.588
298.15	25	0.1	1	20.588
298.15	25	0.1	1	20.588
298.15	25	0.1	1	20.588
298.15	25	0.1	1	20.588
298.15	25	0.1	1	20.588
543.15	270	38.6914	386.914	20.7848
573.15	300	97.0199	970.199	20.7768
603.15	330	153.667	1536.67	20.7704
633.15	360	208.829	2088.29	20.7659
663.15	390	262.643	2626.43	20.7636
693.15	420	315.204	3152.04	20.7637
723.15	450	366.574	3665.74	20.7664
753.15	480	416.788	4167.88	20.7719
783.15	510	465.856	4658.56	20.7803
813.15	540	513.771	5137.71	20.792
843.15	570	560.502	5605.02	20.8072
873.15	600	605.994	6059.94	20.8262
903.15	630	650.17	6501.7	20.8495
933.15	660	692.926	6929.26	20.8777
963.15	690	734.13	7341.3	20.9113
993.15	720	767.7	7677	20.9898
1023.15	750	801.532	8015.32	21.0603
1053.15	780	807.7	8077	21.3058
1083.15	810	850.931	8509.31	21.3004
1113.15	840	893.969	8939.69	21.2951
1143.15	870	936.832	9368.32	21.2896
1173.15	900	979.537	9795.37	21.2842



FLUIDS, package of computer programs for fluid inclusion studies
 Program 2: ISOC, version 01/03
 Product development Ronald J. Bakker

Filename : HPP-2-41a-FIA4

Equation of state : Bakker (1999), Bowers & Helgeson (1983)

Host Mineral : Quartz

Bulk fluid composition:

x(H₂O) = 0.928454

x(Na⁺) = 0.035773

x(Cl⁻) = 0.035773

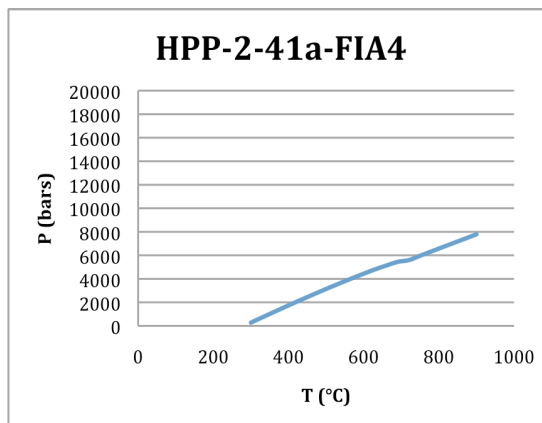
Salinity Aqueous Phase (associated molecules)

	Mass%	Molality
NaCl	11.1138	2.13871

Molar Volume = 21.579424 cc/mol

Density = 0.872022 g/cc

T(K)	T(°C)	P(MPa)	P(bar)	V(cc/mol)
298.15	25	0.1	1	21.5794
298.15	25	0.1	1	21.5794
298.15	25	0.1	1	21.5794
298.15	25	0.1	1	21.5794
298.15	25	0.1	1	21.5794
298.15	25	0.1	1	21.5794
298.15	25	0.1	1	21.5794
298.15	25	0.1	1	21.5794
298.15	25	0.1	1	21.5794
298.15	25	0.1	1	21.5794
298.15	25	0.1	1	21.5794
573.15	300	27.7919	277.919	21.828
603.15	330	72.1621	721.621	21.8293
633.15	360	116.22	1162.2	21.8316
663.15	390	159.81	1598.1	21.8355
693.15	420	202.811	2028.11	21.8416
723.15	450	245.128	2451.28	21.8504
753.15	480	286.682	2866.82	21.8626
783.15	510	327.398	3273.98	21.8784
813.15	540	367.206	3672.06	21.8986
843.15	570	406.034	4060.34	21.9234
873.15	600	443.803	4438.03	21.9535
903.15	630	480.426	4804.26	21.9895
933.15	660	512.976	5129.76	22.0637
963.15	690	544.005	5440.05	22.1453
993.15	720	559.19	5591.9	22.3918
1023.15	750	596.236	5962.36	22.3864
1053.15	780	633.041	6330.41	22.3812
1083.15	810	669.63	6696.3	22.3761
1113.15	840	706.019	7060.19	22.371
1143.15	870	742.226	7422.26	22.3659
1173.15	900	778.264	7782.64	22.3609



FLUIDS, package of computer programs for fluid inclusion studies
 Program 2: ISOC, version 01/03
 Product development Ronald J. Bakker

Filename : HPP-2-47-FIA3

Equation of state : Bakker (1999), Bowers & Helgeson (1983)

Host Mineral : Quartz

Bulk fluid composition:

x(H₂O) = 0.969085

x(Na⁺) = 0.015457

x(Cl⁻) = 0.015457

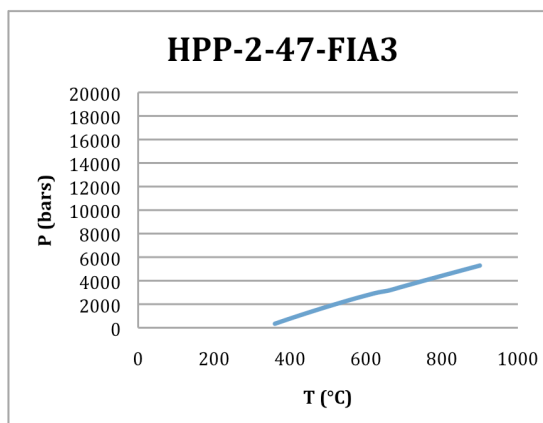
Salinity Aqueous Phase (associated molecules)

	Mass%	Molality
NaCl	4.92143	0.88538

Molar Volume = 24.970649 cc/mol

Density = 0.735344 g/cc

T(K)	T(°C)	P(MPa)	P(bar)	V(cc/mol)
298.15	25	0.1	1	24.9706
298.15	25	0.1	1	24.9706
298.15	25	0.1	1	24.9706
298.15	25	0.1	1	24.9706
298.15	25	0.1	1	24.9706
298.15	25	0.1	1	24.9706
298.15	25	0.1	1	24.9706
298.15	25	0.1	1	24.9706
298.15	25	0.1	1	24.9706
298.15	25	0.1	1	24.9706
298.15	25	0.1	1	24.9706
298.15	25	0.1	1	25.3214
633.15	360	33.8958	338.958	25.3376
663.15	390	66.9551	669.551	25.3517
693.15	420	99.1097	991.097	25.369
723.15	450	130.416	1304.16	25.3902
753.15	480	160.905	1609.05	25.4163
783.15	510	190.589	1905.89	25.448
813.15	540	219.459	2194.59	25.4863
843.15	570	247.494	2474.94	25.5321
873.15	600	273.844	2738.44	25.6103
903.15	630	298.592	2985.92	25.7151
933.15	660	316.512	3165.12	25.9899
963.15	690	343.769	3437.69	25.9837
993.15	720	370.775	3707.75	25.9782
1023.15	750	397.55	3975.5	25.973
1053.15	780	424.115	4241.15	25.9682
1083.15	810	450.489	4504.89	25.9636
1113.15	840	476.686	4766.86	25.9591
1143.15	870	502.72	5027.2	25.9547
1173.15	900	528.604	5286.04	25.9504



FLUIDS, package of computer programs for fluid inclusion studies
 Program 2: ISOC, version 01/03
 Product development Ronald J. Bakker

Filename : HPP-2-62-FIA2

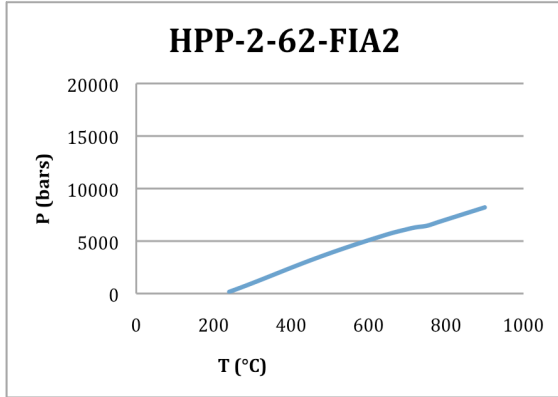
Equation of state : Bakker (1999), Bowers & Helgeson (1983)
 Host Mineral : Quartz

Bulk fluid composition:
 $x(\text{H}_2\text{O}) = 0.846037$
 $x(\text{CO}_2) = 0.059451$
 $x(\text{Na}^+) = 0.047256$
 $x(\text{Cl}^-) = 0.047256$

Salinity Aqueous Phase (associated molecules)

	Mass%	Molality
NaCl	15.3447	3.10047

Molar Volume = 22.399229 cc/mol
 Density = 0.920600 g/cc



T(K)	T(°C)	P(MPa)	P(bar)	V(cc/mol)
298.15	25	0.1	1	22.3992
298.15	25	0.1	1	22.3992
298.15	25	0.1	1	22.3992
298.15	25	0.1	1	22.3992
298.15	25	0.1	1	22.3992
298.15	25	0.1	1	22.3992
298.15	25	0.1	1	22.3992
298.15	25	0.1	1	22.3992
513.15	240	16.0605	160.605	22.5956
543.15	270	56.8541	568.541	22.6
573.15	300	99.251	992.51	22.6031
603.15	330	142.785	1427.85	22.6055
633.15	360	186.908	1869.08	22.6084
663.15	390	230.998	2309.98	22.6124
693.15	420	274.433	2744.33	22.6186
723.15	450	316.719	3167.19	22.6278
753.15	480	357.585	3575.85	22.6404
783.15	510	396.992	3969.92	22.657
813.15	540	435.055	4350.55	22.6778
843.15	570	471.923	4719.23	22.7034
873.15	600	507.69	5076.9	22.7341
903.15	630	542.364	5423.64	22.7705
933.15	660	575.877	5758.77	22.8134
963.15	690	603.891	6038.91	22.9068
993.15	720	629.404	6294.04	23.0177
1023.15	750	644.977	6449.77	23.222
1053.15	780	680.341	6803.41	23.2175
1083.15	810	715.56	7155.6	23.213
1113.15	840	750.644	7506.44	23.2084
1143.15	870	785.602	7856.02	23.2037
1173.15	900	820.444	8204.44	23.1991

FLUIDS, package of computer programs for fluid inclusion studies
 Program 2: ISOC, version 01/03
 Product development Ronald J. Bakker

Filename : HPP-3-01b-FIA1

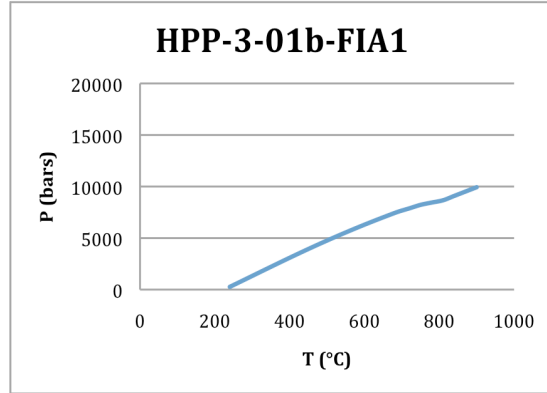
Equation of state : Bakker (1999), Bowers & Helgeson (1983)
 Host Mineral : Quartz

Bulk fluid composition:
 $x(\text{H}_2\text{O}) = 0.903920$
 $x(\text{CO}_2) = 0.027520$
 $x(\text{Na}^+) = 0.034280$
 $x(\text{Cl}^-) = 0.034280$

Salinity Aqueous Phase (associated molecules)

	Mass%	Molality
NaCl	10.9581	2.10506

Molar Volume = 20.777426 cc/mol
 Density = 0.938500 g/cc



T(K)	T(°C)	P(MPa)	P(bar)	V(cc/mol)
298.15	25	0.1	1	20.7774
298.15	25	0.1	1	20.7774
298.15	25	0.1	1	20.7774
298.15	25	0.1	1	20.7774
298.15	25	0.1	1	20.7774
298.15	25	0.1	1	20.7774
298.15	25	0.1	1	20.7774
298.15	25	0.1	1	20.7774
298.15	25	0.1	1	20.7774
513.15	240	26.433	264.33	20.9526
543.15	270	79.3641	793.641	20.9486
573.15	300	132.591	1325.91	20.9444
603.15	330	185.838	1858.38	20.9406
633.15	360	238.844	2388.44	20.9379
663.15	390	291.351	2913.51	20.9367
693.15	420	343.112	3431.12	20.9375
723.15	450	393.91	3939.1	20.9407
753.15	480	443.582	4435.82	20.9465
783.15	510	492.028	4920.28	20.9552
813.15	540	539.204	5392.04	20.9672
843.15	570	585.101	5851.01	20.9826
873.15	600	629.711	6297.11	21.0018
903.15	630	673.004	6730.04	21.0253
933.15	660	714.907	7149.07	21.0536
963.15	690	755.305	7553.05	21.0873
993.15	720	788.203	7882.03	21.1649
1023.15	750	822.132	8221.32	21.2299
1053.15	780	844.636	8446.36	21.3621
1083.15	810	866.554	8665.54	21.4923
1113.15	840	908.988	9089.88	21.4872
1143.15	870	951.276	9512.76	21.4819
1173.15	900	993.431	9934.31	21.4767

FLUIDS, package of computer programs for fluid inclusion studies
 Program 2: ISOC, version 01/03
 Product development Ronald J. Bakker

Filename : HPP-3-01b-FIA2

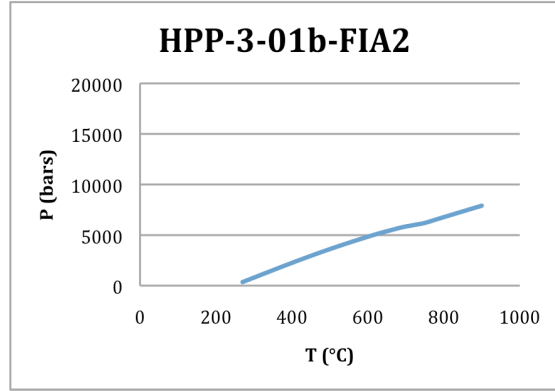
Equation of state : Bakker (1999), Bowers & Helgeson (1983)
 Host Mineral : Quartz

Bulk fluid composition:
 $x(\text{H}_2\text{O}) = 0.885025$
 $x(\text{CO}_2) = 0.052402$
 $x(\text{Na}^+) = 0.031286$
 $x(\text{Cl}^-) = 0.031286$

Salinity Aqueous Phase (associated molecules)

	Mass%	Molality
NaCl	10.2913	1.96227

Molar Volume = 22.726951 cc/mol
 Density = 0.883500 g/cc



T(K)	T(°C)	P(MPa)	P(bar)	V(cc/mol)
298.15	25	0.1	1	22.727
298.15	25	0.1	1	22.727
298.15	25	0.1	1	22.727
298.15	25	0.1	1	22.727
298.15	25	0.1	1	22.727
298.15	25	0.1	1	22.727
298.15	25	0.1	1	22.727
298.15	25	0.1	1	22.727
298.15	25	0.1	1	22.727
298.15	25	0.1	1	22.727
543.15	270	35.0899	350.899	22.947
573.15	300	79.3366	793.366	22.9486
603.15	330	123.48	1234.8	22.9506
633.15	360	167.335	1673.35	22.9535
663.15	390	210.672	2106.72	22.9581
693.15	420	253.24	2532.4	22.9649
723.15	450	294.805	2948.05	22.9748
753.15	480	335.185	3351.85	22.9881
783.15	510	374.27	3742.7	23.0054
813.15	540	412.029	4120.29	23.0273
843.15	570	448.479	4484.79	23.0542
873.15	600	483.656	4836.56	23.0867
903.15	630	517.582	5175.82	23.1253
933.15	660	547.672	5476.72	23.2
963.15	690	576.9	5769	23.2757
993.15	720	598.727	5987.27	23.4251
1023.15	750	620.174	6201.74	23.5694
1053.15	780	654.563	6545.63	23.5649
1083.15	810	688.795	6887.95	23.5604
1113.15	840	722.884	7228.84	23.5558
1143.15	870	756.841	7568.41	23.5512
1173.15	900	790.675	7906.75	23.5466

FLUIDS, package of computer programs for fluid inclusion studies
 Program 2: ISOC, version 01/03
 Product development Ronald J. Bakker

Filename : HPP-3-04a-FIA1

Equation of state : Bakker (1999), Bowers & Helgeson (1983)

Host Mineral : Quartz

Bulk fluid composition:

x(H₂O) = 0.872419

x(CO₂) = 0.030349

x(Na⁺) = 0.048616

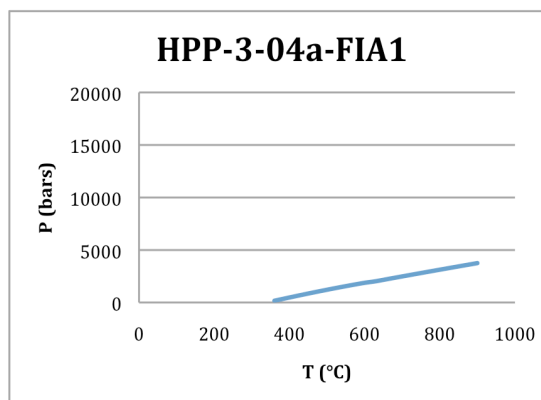
x(Cl⁻) = 0.048616

Salinity Aqueous Phase (associated molecules)

	Mass%	Molality
NaCl	15.3143	3.09322

Molar Volume = 29.184004 cc/mol

Density = 0.681700 g/cc



T(K)	T(°C)	P(MPa)	P(bar)	V(cc/mol)
298.15	25	0.1	1	29.184
298.15	25	0.1	1	29.184
298.15	25	0.1	1	29.184
298.15	25	0.1	1	29.184
298.15	25	0.1	1	29.184
298.15	25	0.1	1	29.184
298.15	25	0.1	1	29.184
298.15	25	0.1	1	29.184
298.15	25	0.1	1	29.184
298.15	25	0.1	1	29.184
298.15	25	0.1	1	29.184
298.15	25	0.1	1	29.184
298.15	25	0.1	1	29.184
633.15	360	16.6966	166.966	29.6324
663.15	390	39.9069	399.069	29.6606
693.15	420	62.835	628.35	29.6923
723.15	450	85.2775	852.775	29.7289
753.15	480	107.115	1071.15	29.7718
783.15	510	128.311	1283.11	29.8224
813.15	540	148.881	1488.81	29.8821
843.15	570	168.628	1686.28	29.9695
873.15	600	187.378	1873.78	30.0952
903.15	630	202.593	2025.93	30.4264
933.15	660	222.312	2223.12	30.4197
963.15	690	241.869	2418.69	30.4138
993.15	720	261.273	2612.73	30.4086
1023.15	750	280.533	2805.33	30.404
1053.15	780	299.656	2996.56	30.3997
1083.15	810	318.651	3186.51	30.3957
1113.15	840	337.524	3375.24	30.3919
1143.15	870	356.284	3562.84	30.3882
1173.15	900	374.935	3749.35	30.3847

FLUIDS, package of computer programs for fluid inclusion studies
 Program 2: ISOC, version 01/03
 Product development Ronald J. Bakker

Filename : HPP-3-04a-FIA2

Equation of state : Bakker (1999), Bowers & Helgeson (1983)
 Host Mineral : Quartz

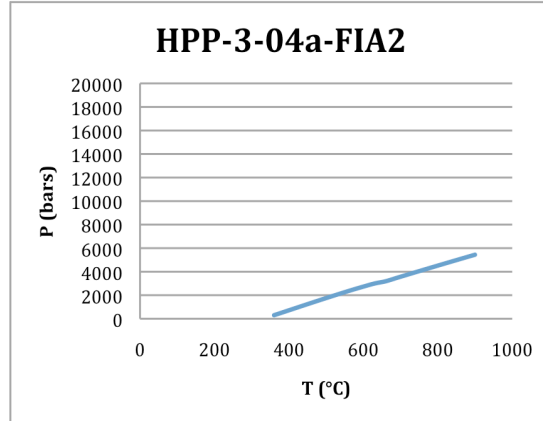
Bulk fluid composition:
 $x(\text{H}_2\text{O}) = 0.868810$
 $x(\text{Na}^+) = 0.065595$
 $x(\text{Cl}^-) = 0.065595$

Salinity Aqueous Phase (associated molecules)

	Mass%	Molality
NaCl	19.6794	4.19089

Molar Volume = 23.741750 cc/mol
 Density = 0.820778 g/cc

T(K)	T(°C)	P(MPa)	P(bar)	V(cc/mol)
273.15	0	206.075	2060.75	23.5985
303.15	30	49.3402	493.402	23.7137
298.15	25	0.1	1	23.7418
298.15	25	0.1	1	23.7418
298.15	25	0.1	1	23.7418
298.15	25	0.1	1	23.7418
298.15	25	0.1	1	23.7418
298.15	25	0.1	1	23.7418
298.15	25	0.1	1	23.7418
298.15	25	0.1	1	23.7418
298.15	25	0.1	1	23.7418
298.15	25	0.1	1	23.7418
298.15	25	0.1	1	24.0755
633.15	360	29.9903	299.903	24.0942
663.15	390	61.2437	612.437	24.1093
693.15	420	92.664	926.64	24.1265
723.15	450	124	1240	24.1468
753.15	480	155.06	1550.6	24.1712
783.15	510	185.696	1856.96	24.2006
813.15	540	215.784	2157.84	24.2359
843.15	570	245.217	2452.17	24.278
873.15	600	273.051	2730.51	24.351
903.15	630	299.356	2993.56	24.4481
933.15	660	318.512	3185.12	24.71
963.15	690	347.441	3474.41	24.7036
993.15	720	376.138	3761.38	24.6978
1023.15	750	404.615	4046.15	24.6924
1053.15	780	432.885	4328.85	24.6874
1083.15	810	460.962	4609.62	24.6825
1113.15	840	488.858	4888.58	24.6779
1143.15	870	516.585	5165.85	24.6733
1173.15	900	544.154	5441.54	24.6688



FLUIDS, package of computer programs for fluid inclusion studies
 Program 2: ISOC, version 01/03
 Product development Ronald J. Bakker

Filename : HPP-3-15-FIA1

Equation of state : Bakker (1999), Bowers & Helgeson (1983)

Host Mineral : Quartz

Bulk fluid composition:

x(H₂O) = 0.956182

x(Na⁺) = 0.021909

x(Cl⁻) = 0.021909

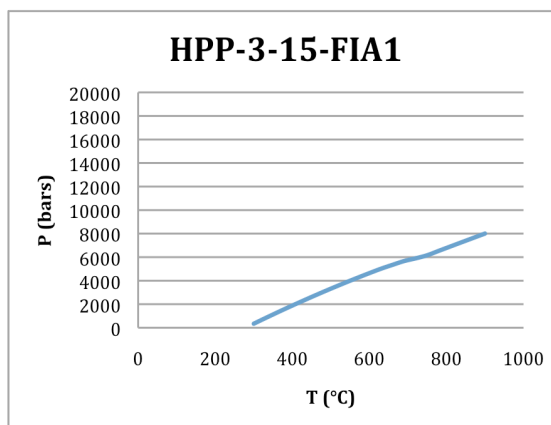
Salinity Aqueous Phase (associated molecules)

	Mass%	Molality
NaCl	6.92109	1.27188

Molar Volume = 21.641849 cc/mol

Density = 0.855137 g/cc

T(K)	T(°C)	P(MPa)	P(bar)	V(cc/mol)
298.15	25	0.1	1	21.6418
298.15	25	0.1	1	21.6418
298.15	25	0.1	1	21.6418
298.15	25	0.1	1	21.6418
298.15	25	0.1	1	21.6418
298.15	25	0.1	1	21.6418
298.15	25	0.1	1	21.6418
298.15	25	0.1	1	21.6418
298.15	25	0.1	1	21.6418
298.15	25	0.1	1	21.6418
573.15	300	34.1823	341.823	21.8862
603.15	330	81.6732	816.732	21.8853
633.15	360	128.128	1281.28	21.8859
663.15	390	173.589	1735.89	21.8885
693.15	420	218.08	2180.8	21.8935
723.15	450	261.608	2616.08	21.9015
753.15	480	304.168	3041.68	21.9129
783.15	510	345.74	3457.4	21.9279
813.15	540	386.294	3862.94	21.9472
843.15	570	425.783	4257.83	21.9711
873.15	600	464.149	4641.49	22.0002
903.15	630	501.318	5013.18	22.035
933.15	660	534.455	5344.55	22.1053
963.15	690	566.528	5665.28	22.1778
993.15	720	589.69	5896.9	22.3332
1023.15	750	616.086	6160.86	22.4453
1053.15	780	653.343	6533.43	22.4401
1083.15	810	690.381	6903.81	22.435
1113.15	840	727.22	7272.2	22.43
1143.15	870	763.879	7638.79	22.4249
1173.15	900	800.371	8003.71	22.4198



FLUIDS, package of computer programs for fluid inclusion studies
 Program 2: ISOC, version 01/03
 Product development Ronald J. Bakker

Filename : HPP-3-15-FIA2

Equation of state : Bakker (1999), Bowers & Helgeson (1983)

Host Mineral : Quartz

Bulk fluid composition:

x(H₂O) = 0.925484

x(Na⁺) = 0.037258

x(Cl⁻) = 0.037258

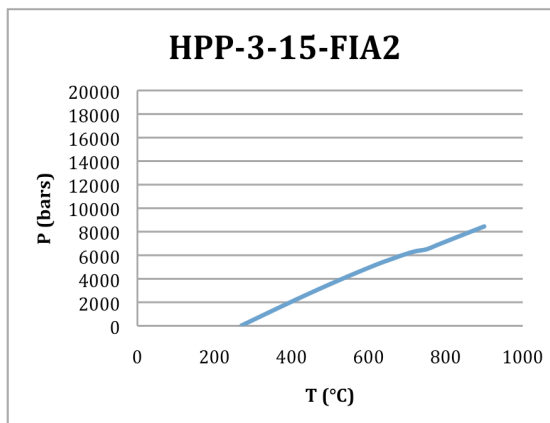
Salinity Aqueous Phase (associated molecules)

	Mass%	Molality
NaCl	11.5548	2.23466

Molar Volume = 21.049479 cc/mol

Density = 0.895559 g/cc

T(K)	T(°C)	P(MPa)	P(bar)	V(cc/mol)
298.15	25	0.1	1	21.0495
298.15	25	0.1	1	21.0495
298.15	25	0.1	1	21.0495
298.15	25	0.1	1	21.0495
298.15	25	0.1	1	21.0495
298.15	25	0.1	1	21.0495
298.15	25	0.1	1	21.0495
298.15	25	0.1	1	21.0495
298.15	25	0.1	1	21.0495
298.15	25	0.1	1	21.0495
543.15	270	2.46475	24.6475	21.2766
573.15	300	49.5108	495.108	21.276
603.15	330	96.5845	965.845	21.2755
633.15	360	143.425	1434.25	21.2759
663.15	390	189.842	1898.42	21.2779
693.15	420	235.691	2356.91	21.282
723.15	450	280.858	2808.58	21.2886
753.15	480	325.251	3252.51	21.2982
783.15	510	368.787	3687.87	21.3113
813.15	540	411.388	4113.88	21.3281
843.15	570	452.978	4529.78	21.3492
873.15	600	493.471	4934.71	21.375
903.15	630	532.775	5327.75	21.4061
933.15	660	568.011	5680.11	21.469
963.15	690	602.85	6028.5	21.5276
993.15	720	632.546	6325.46	21.6251
1023.15	750	650.403	6504.03	21.8211
1053.15	780	689.691	6896.91	21.8158
1083.15	810	728.761	7287.61	21.8106
1113.15	840	767.631	7676.31	21.8054
1143.15	870	806.319	8063.19	21.8002
1173.15	900	844.839	8448.39	21.795



FLUIDS, package of computer programs for fluid inclusion studies
 Program 2: ISOC, version 01/03
 Product development Ronald J. Bakker

Filename : HPP-3-15-FIA3

Equation of state : Bakker (1999), Bowers & Helgeson (1983)

Host Mineral : Quartz

Bulk fluid composition:

x(H₂O) = 0.972387

x(Na⁺) = 0.013807

x(Cl⁻) = 0.013807

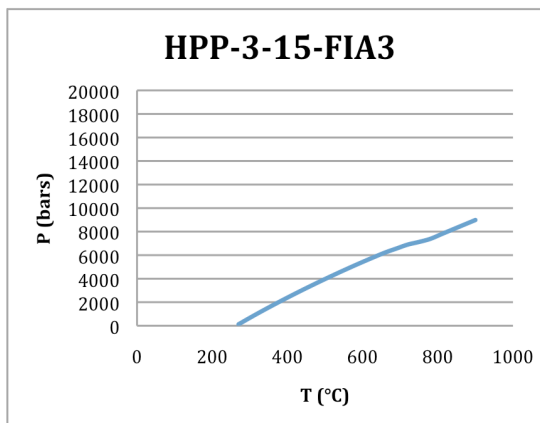
Salinity Aqueous Phase (associated molecules)

	Mass%	Molality
NaCl	4.40477	0.78815

Molar Volume = 21.088927 cc/mol

Density = 0.868939 g/cc

T(K)	T(°C)	P(MPa)	P(bar)	V(cc/mol)
298.15	25	0.1	1	21.0889
298.15	25	0.1	1	21.0889
298.15	25	0.1	1	21.0889
298.15	25	0.1	1	21.0889
298.15	25	0.1	1	21.0889
298.15	25	0.1	1	21.0889
298.15	25	0.1	1	21.0889
298.15	25	0.1	1	21.0889
298.15	25	0.1	1	21.0889
298.15	25	0.1	1	21.0889
543.15	270	12.1307	121.307	21.3095
573.15	300	67.1408	671.408	21.3032
603.15	330	120.395	1203.95	21.2986
633.15	360	172.122	1721.22	21.2959
663.15	390	222.485	2224.85	21.2954
693.15	420	271.593	2715.93	21.2974
723.15	450	319.518	3195.18	21.3022
753.15	480	366.302	3663.02	21.3102
783.15	510	411.959	4119.59	21.3214
813.15	540	456.482	4564.82	21.3363
843.15	570	499.842	4998.42	21.3553
873.15	600	541.989	5419.89	21.3786
903.15	630	582.853	5828.53	21.4069
933.15	660	622.339	6223.39	21.4406
963.15	690	656.2	6562	21.5139
993.15	720	689.656	6896.56	21.583
1023.15	750	712.035	7120.35	21.7325
1053.15	780	738.314	7383.14	21.8433
1083.15	810	778.661	7786.61	21.8381
1113.15	840	818.812	8188.12	21.8329
1143.15	870	858.784	8587.84	21.8276
1173.15	900	898.593	8985.93	21.8223



FLUIDS, package of computer programs for fluid inclusion studies
 Program 2: ISOC, version 01/03
 Product development Ronald J. Bakker

Filename : HPP-3-19-FIA1

Equation of state : Bakker (1999), Bowers & Helgeson (1983)

Host Mineral : Quartz

Bulk fluid composition:

x(H2O) = 0.829929

x(CO2) = 0.070119

x(Na+) = 0.049976

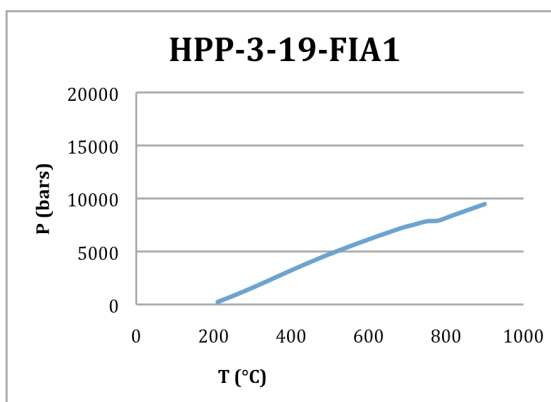
x(Cl-) = 0.049976

Salinity Aqueous Phase (associated molecules)

	Mass%	Molality
NaCl	16.3471	3.34258

Molar Volume = 21.703475 cc/mol

Density = 0.965700 g/cc



T(K)	T(°C)	P(MPa)	P(bar)	V(cc/mol)
298.15	25	0.1	1	21.7035
298.15	25	0.1	1	21.7035
298.15	25	0.1	1	21.7035
298.15	25	0.1	1	21.7035
298.15	25	0.1	1	21.7035
298.15	25	0.1	1	21.7035
298.15	25	0.1	1	21.7035
483.15	210	24.1759	241.759	21.8553
513.15	240	66.5259	665.259	21.8589
543.15	270	111.401	1114.01	21.8604
573.15	300	158.342	1583.42	21.8605
603.15	330	206.818	2068.18	21.8601
633.15	360	256.144	2561.44	21.8599
663.15	390	305.509	3055.09	21.8608
693.15	420	354.101	3541.01	21.8637
723.15	450	401.3	4013	21.8693
753.15	480	446.807	4468.07	21.878
783.15	510	490.645	4906.45	21.8901
813.15	540	533.017	5330.17	21.9058
843.15	570	574.143	5741.43	21.9252
873.15	600	614.144	6141.44	21.9488
903.15	630	653.023	6530.23	21.9771
933.15	660	690.691	6906.91	22.0106
963.15	690	727.005	7270.05	22.0502
993.15	720	756.155	7561.55	22.1383
1023.15	750	784.847	7848.47	22.2238
1053.15	780	791.848	7918.48	22.4647
1083.15	810	830.935	8309.35	22.46
1113.15	840	869.905	8699.05	22.4553
1143.15	870	908.767	9087.67	22.4505
1173.15	900	947.527	9475.27	22.4457

FLUIDS, package of computer programs for fluid inclusion studies
 Program 2: ISOC, version 01/03
 Product development Ronald J. Bakker

Filename : HPP-3-19-FIA2

Equation of state : Bakker (1999), Bowers & Helgeson (1983)

Host Mineral : Quartz

Bulk fluid composition:

x(H₂O) = 0.852861

x(CO₂) = 0.100078

x(Na⁺) = 0.023531

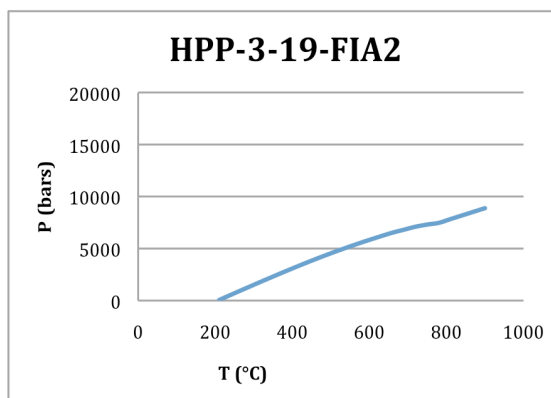
x(Cl⁻) = 0.023531

Salinity Aqueous Phase (associated molecules)

	Mass%	Molality
NaCl	8.21768	1.53149

Molar Volume = 23.078583 cc/mol

Density = 0.916200 g/cc



T(K)	T(°C)	P(MPa)	P(bar)	V(cc/mol)
298.15	25	0.1	1	23.0786
298.15	25	0.1	1	23.0786
298.15	25	0.1	1	23.0786
298.15	25	0.1	1	23.0786
298.15	25	0.1	1	23.0786
298.15	25	0.1	1	23.0786
298.15	25	0.1	1	23.0786
483.15	210	5.04771	50.4771	23.2538
513.15	240	54.4135	544.135	23.2525
543.15	270	103.176	1031.76	23.2513
573.15	300	151.482	1514.82	23.2505
603.15	330	199.347	1993.47	23.2503
633.15	360	246.677	2466.77	23.2514
663.15	390	293.291	2932.91	23.2542
693.15	420	338.958	3389.58	23.2592
723.15	450	383.44	3834.4	23.267
753.15	480	426.536	4265.36	23.278
783.15	510	468.112	4681.12	23.2927
813.15	540	508.108	5081.08	23.3114
843.15	570	546.531	5465.31	23.3346
873.15	600	583.426	5834.26	23.3629
903.15	630	618.839	6188.39	23.3968
933.15	660	652.791	6527.91	23.4371
963.15	690	681.431	6814.31	23.5188
993.15	720	710.108	7101.08	23.593
1023.15	750	730.798	7307.98	23.7313
1053.15	780	747.154	7471.54	23.9014
1083.15	810	782.562	7825.62	23.8973
1113.15	840	817.867	8178.67	23.893
1143.15	870	853.08	8530.8	23.8886
1173.15	900	888.207	8882.07	23.884

FLUIDS, package of computer programs for fluid inclusion studies
 Program 2: ISOC, version 01/03
 Product development Ronald J. Bakker

Filename : HPP-3-19-FIA3

Equation of state : Bakker (1999), Bowers & Helgeson (1983)

Host Mineral : Quartz

Bulk fluid composition:

x(H2O) = 0.837877

x(CO2) = 0.081878

x(Na+) = 0.040123

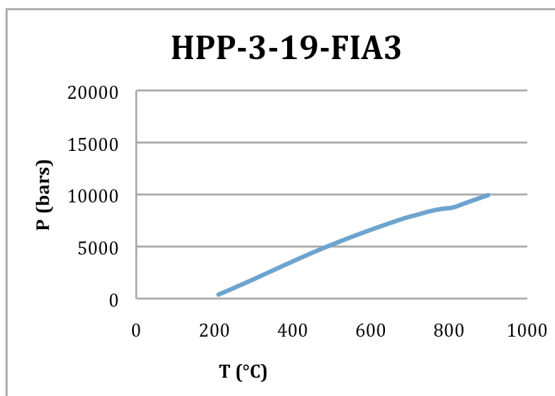
x(Cl-) = 0.040123

Salinity Aqueous Phase (associated molecules)

	Mass%	Molality
NaCl	13.4498	2.6581

Molar Volume = 21.797886 cc/mol

Density = 0.965400 g/cc



T(K)	T(°C)	P(MPa)	P(bar)	V(cc/mol)
298.15	25	0.1	1	21.7979
298.15	25	0.1	1	21.7979
298.15	25	0.1	1	21.7979
298.15	25	0.1	1	21.7979
298.15	25	0.1	1	21.7979
298.15	25	0.1	1	21.7979
298.15	25	0.1	1	21.7979
483.15	210	38.1969	381.969	21.9409
513.15	240	86.145	861.45	21.9408
543.15	270	135.444	1354.44	21.9395
573.15	300	185.887	1858.87	21.9375
603.15	330	237.16	2371.6	21.9355
633.15	360	288.805	2888.05	21.9341
663.15	390	340.238	3402.38	21.934
693.15	420	390.839	3908.39	21.9359
723.15	450	440.076	4400.76	21.9403
753.15	480	487.619	4876.19	21.9476
783.15	510	533.379	5333.79	21.9581
813.15	540	577.46	5774.6	21.972
843.15	570	620.048	6200.48	21.9897
873.15	600	661.304	6613.04	22.0113
903.15	630	701.298	7012.98	22.0374
933.15	660	740	7400	22.0685
963.15	690	777.294	7772.94	22.1054
993.15	720	807.268	8072.68	22.1876
1023.15	750	838.831	8388.31	22.2537
1053.15	780	861.494	8614.94	22.3741
1083.15	810	875.805	8758.05	22.5454
1113.15	840	915.644	9156.44	22.5407
1143.15	870	955.388	9553.88	22.5359
1173.15	900	995.043	9950.43	22.531

FLUIDS, package of computer programs for fluid inclusion studies
 Program 2: ISOC, version 01/03
 Product development Ronald J. Bakker

Filename : HPP-3-23-FIA1

Equation of state : Bakker (1999), Bowers & Helgeson (1983)

Host Mineral : Quartz

Bulk fluid composition:

x(H₂O) = 0.891524

x(CO₂) = 0.036930

x(Na⁺) = 0.035773

x(Cl⁻) = 0.035773

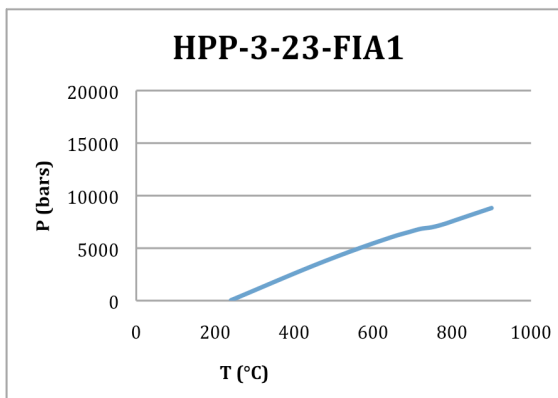
Salinity Aqueous Phase (associated molecules)

	Mass%	Molality
NaCl	11.5211	2.2273

Molar Volume = 21.626799 cc/mol

Density = 0.914500 g/cc

T(K)	T(°C)	P(MPa)	P(bar)	V(cc/mol)
298.15	25	0.1	1	21.6268
298.15	25	0.1	1	21.6268
298.15	25	0.1	1	21.6268
298.15	25	0.1	1	21.6268
298.15	25	0.1	1	21.6268
298.15	25	0.1	1	21.6268
298.15	25	0.1	1	21.6268
298.15	25	0.1	1	21.6268
513.15	240	3.93857	39.3856	21.825
543.15	270	51.3028	513.028	21.8246
573.15	300	99.1093	991.093	21.8237
603.15	330	147.083	1470.83	21.823
633.15	360	194.943	1949.43	21.8232
663.15	390	242.393	2423.93	21.8249
693.15	420	289.138	2891.38	21.8287
723.15	450	334.919	3349.19	21.8351
753.15	480	379.544	3795.44	21.8447
783.15	510	422.908	4229.08	21.8577
813.15	540	464.981	4649.81	21.8745
843.15	570	505.78	5057.8	21.8956
873.15	600	545.324	5453.24	21.9213
903.15	630	583.607	5836.07	21.9522
933.15	660	620.58	6205.8	21.9889
963.15	690	652.151	6521.51	22.0665
993.15	720	683.159	6831.59	22.1418
1023.15	750	699.6	6996	22.3339
1053.15	780	729.569	7295.69	22.4029
1083.15	810	767.831	7678.31	22.398
1113.15	840	805.937	8059.37	22.3932
1143.15	870	843.901	8439.01	22.3882
1173.15	900	881.733	8817.33	22.3833



FLUIDS, package of computer programs for fluid inclusion studies
 Program 2: ISOC, version 01/03
 Product development Ronald J. Bakker

Filename : HPP-3-23-FIA2

Equation of state : Bakker (1999), Bowers & Helgeson (1983)
 Host Mineral : Quartz

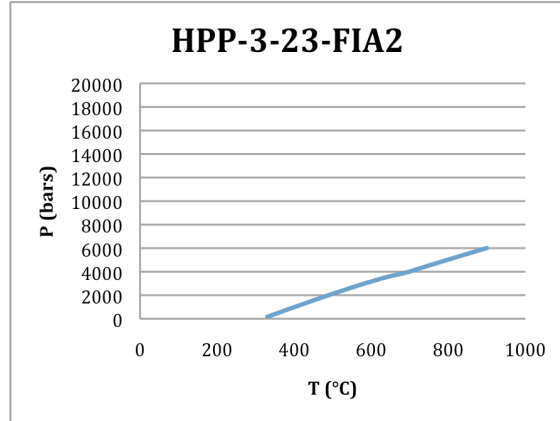
Bulk fluid composition:
 $x(\text{H}_2\text{O}) = 0.919754$
 $x(\text{Na}^+) = 0.040123$
 $x(\text{Cl}^-) = 0.040123$

Salinity Aqueous Phase (associated molecules)

	Mass%	Molality
NaCl	12.401	2.42147

Molar Volume = 23.363862 cc/mol
 Density = 0.809597 g/cc

T(K)	T(°C)	P(MPa)	P(bar)	V(cc/mol)
298.15	25	0.1	1	23.3639
298.15	25	0.1	1	23.3639
298.15	25	0.1	1	23.3639
298.15	25	0.1	1	23.3639
298.15	25	0.1	1	23.3639
298.15	25	0.1	1	23.3639
298.15	25	0.1	1	23.3639
298.15	25	0.1	1	23.3639
298.15	25	0.1	1	23.3639
298.15	25	0.1	1	23.3639
298.15	25	0.1	1	23.3639
298.15	25	0.1	1	23.3639
603.15	330	15.7275	157.275	23.6822
633.15	360	51.3112	513.112	23.6917
663.15	390	86.6119	866.119	23.7028
693.15	420	121.498	1214.98	23.7163
723.15	450	155.865	1558.65	23.7331
753.15	480	189.631	1896.31	23.7539
783.15	510	222.719	2227.19	23.7796
813.15	540	255.061	2550.61	23.8108
843.15	570	286.588	2865.88	23.8483
873.15	600	316.38	3163.8	23.9113
903.15	630	344.978	3449.78	23.9855
933.15	660	369.756	3697.56	24.1228
963.15	690	391.945	3919.45	24.2947
993.15	720	422.483	4224.83	24.289
1023.15	750	452.781	4527.81	24.2837
1053.15	780	482.859	4828.59	24.2787
1083.15	810	512.735	5127.35	24.2738
1113.15	840	542.423	5424.23	24.2691
1143.15	870	571.937	5719.37	24.2644
1173.15	900	601.29	6012.9	24.2599



FLUIDS, package of computer programs for fluid inclusion studies
 Program 2: ISOC, version 01/03
 Product development Ronald J. Bakker

Filename : HPP-3-23-FIA3a

Equation of state : Bakker (1999), Bowers & Helgeson (1983)

Host Mineral : Quartz

Bulk fluid composition:

x(H₂O) = 0.861358

x(CO₂) = 0.067104

x(Na⁺) = 0.035769

x(Cl⁻) = 0.035769

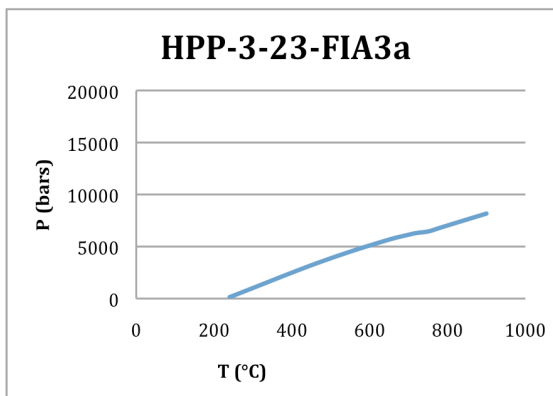
Salinity Aqueous Phase (associated molecules)

	Mass%	Molality
NaCl	11.8757	2.30509

Molar Volume = 22.758146 cc/mol

Density = 0.903500 g/cc

T(K)	T(°C)	P(MPa)	P(bar)	V(cc/mol)
298.15	25	0.1	1	22.7581
298.15	25	0.1	1	22.7581
298.15	25	0.1	1	22.7581
298.15	25	0.1	1	22.7581
298.15	25	0.1	1	22.7581
298.15	25	0.1	1	22.7581
298.15	25	0.1	1	22.7581
298.15	25	0.1	1	22.7581
513.15	240	14.2053	142.053	22.959
543.15	270	57.8129	578.129	22.9614
573.15	300	101.953	1019.53	22.9632
603.15	330	146.408	1464.08	22.9651
633.15	360	190.879	1908.79	22.9677
663.15	390	234.999	2349.99	22.9719
693.15	420	278.37	2783.7	22.9783
723.15	450	320.637	3206.37	22.9875
753.15	480	361.549	3615.49	23.0003
783.15	510	400.993	4009.93	23.0171
813.15	540	438.981	4389.81	23.0383
843.15	570	475.597	4755.97	23.0643
873.15	600	510.934	5109.34	23.0957
903.15	630	545.044	5450.44	23.1331
933.15	660	577.915	5779.15	23.1771
963.15	690	605.299	6052.99	23.2722
993.15	720	630.192	6301.92	23.385
1023.15	750	645.07	6450.7	23.5941
1053.15	780	679.78	6797.8	23.5897
1083.15	810	714.35	7143.5	23.5853
1113.15	840	748.792	7487.92	23.5808
1143.15	870	783.114	7831.14	23.5762
1173.15	900	817.325	8173.25	23.5716



FLUIDS, package of computer programs for fluid inclusion studies
 Program 2: ISOC, version 01/03
 Product development Ronald J. Bakker

Filename : HPP-3-23-FIA3b

Equation of state : Bakker (1999), Bowers & Helgeson (1983)

Host Mineral : Quartz

Bulk fluid composition:

x(H₂O) = 0.877061

x(CO₂) = 0.051393

x(Na⁺) = 0.035773

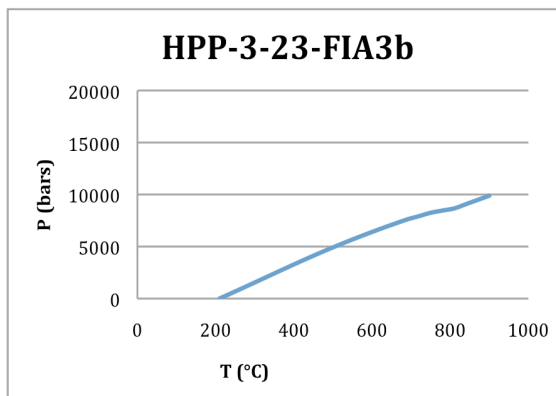
x(Cl⁻) = 0.035773

Salinity Aqueous Phase (associated molecules)

	Mass%	Molality
NaCl	11.6889	2.26403

Molar Volume = 21.270372 cc/mol

Density = 0.947500 g/cc



T(K)	T(°C)	P(MPa)	P(bar)	V(cc/mol)
298.15	25	0.1	1	21.2704
298.15	25	0.1	1	21.2704
298.15	25	0.1	1	21.2704
298.15	25	0.1	1	21.2704
298.15	25	0.1	1	21.2704
298.15	25	0.1	1	21.2704
298.15	25	0.1	1	21.2704
483.15	210	0.75891	7.5891	21.4347
513.15	240	51.2884	512.884	21.4328
543.15	270	102.647	1026.47	21.4299
573.15	300	154.575	1545.75	21.4268
603.15	330	206.796	2067.96	21.4239
633.15	360	258.988	2589.88	21.4218
663.15	390	310.787	3107.87	21.4213
693.15	420	361.817	3618.17	21.4227
723.15	450	411.743	4117.43	21.4265
753.15	480	460.328	4603.28	21.4331
783.15	510	507.456	5074.56	21.4427
813.15	540	553.118	5531.18	21.4557
843.15	570	597.371	5973.71	21.4723
873.15	600	640.277	6402.77	21.4928
903.15	630	681.857	6818.57	21.5178
933.15	660	722.073	7220.73	21.5477
963.15	690	760.819	7608.19	21.5833
993.15	720	792.193	7921.93	21.6635
1023.15	750	824.671	8246.71	21.7307
1053.15	780	846.047	8460.47	21.8655
1083.15	810	866.298	8662.98	22.0023
1113.15	840	907.335	9073.35	21.9974
1143.15	870	948.251	9482.51	21.9924
1173.15	900	989.053	9890.53	21.9873

FLUIDS, package of computer programs for fluid inclusion studies
 Program 2: ISOC, version 01/03
 Product development Ronald J. Bakker

Filename : HPP-3-38-FIA1

Equation of state : Bakker (1999), Bowers & Helgeson (1983)

Host Mineral : Quartz

Bulk fluid composition:

x(H₂O) = 0.962516

x(Na⁺) = 0.018742

x(Cl⁻) = 0.018742

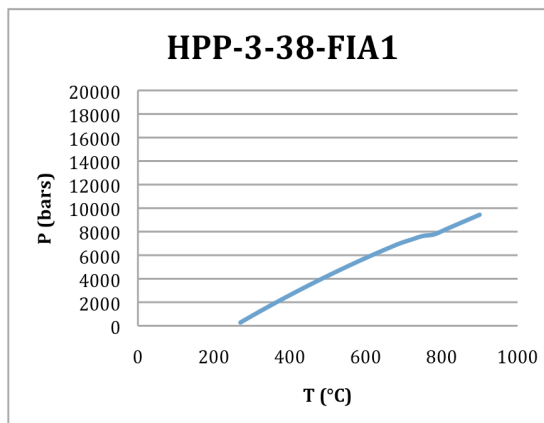
Salinity Aqueous Phase (associated molecules)

	Mass%	Molality
NaCl	5.94339	1.08086

Molar Volume = 20.732019 cc/mol

Density = 0.889238 g/cc

T(K)	T(°C)	P(MPa)	P(bar)	V(cc/mol)
298.15	25	0.1	1	20.732
298.15	25	0.1	1	20.732
298.15	25	0.1	1	20.732
298.15	25	0.1	1	20.732
298.15	25	0.1	1	20.732
298.15	25	0.1	1	20.732
298.15	25	0.1	1	20.732
298.15	25	0.1	1	20.732
298.15	25	0.1	1	20.732
298.15	25	0.1	1	20.732
543.15	270	27.8232	278.232	20.9378
573.15	300	83.7124	837.124	20.9312
603.15	330	138.198	1381.98	20.926
633.15	360	191.404	1914.04	20.9226
663.15	390	243.416	2434.16	20.9213
693.15	420	294.29	2942.9	20.9223
723.15	450	344.059	3440.59	20.9259
753.15	480	392.737	3927.37	20.9324
783.15	510	440.32	4403.2	20.942
813.15	540	486.786	4867.86	20.955
843.15	570	532.097	5320.97	20.9717
873.15	600	576.195	5761.95	20.9925
903.15	630	619	6190	21.0178
933.15	660	660.409	6604.09	21.0482
963.15	690	700.295	7002.95	21.0844
993.15	720	732.351	7323.51	21.1706
1023.15	750	762.85	7628.5	21.2607
1053.15	780	776.522	7765.22	21.4633
1083.15	810	818.598	8185.98	21.458
1113.15	840	860.479	8604.79	21.4526
1143.15	870	902.184	9021.84	21.4473
1173.15	900	943.726	9437.26	21.4419



FLUIDS, package of computer programs for fluid inclusion studies
 Program 2: ISOC, version 01/03
 Product development Ronald J. Bakker

Filename : HPP-4-01-FIA1

Equation of state : Bakker (1999), Bowers & Helgeson (1983)
 Host Mineral : Quartz

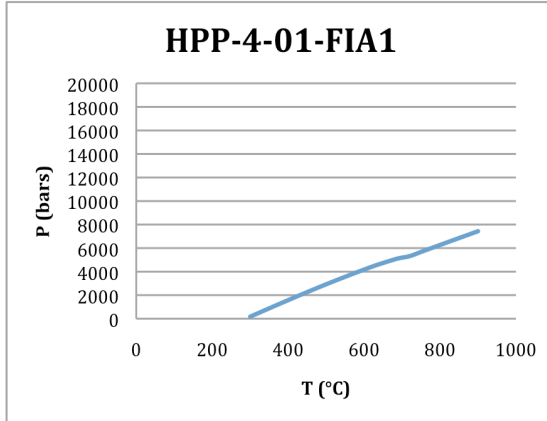
Bulk fluid composition:
 $x(\text{H}_2\text{O}) = 0.922522$
 $x(\text{Na}^+) = 0.038739$
 $x(\text{Cl}^-) = 0.038739$

Salinity Aqueous Phase (associated molecules)

	Mass%	Molality
NaCl	11.9929	2.33093

Molar Volume = 21.827156 cc/mol
 Density = 0.865173 g/cc

T(K)	T(°C)	P(MPa)	P(bar)	V(cc/mol)
298.15	25	0.1	1	21.8272
298.15	25	0.1	1	21.8272
298.15	25	0.1	1	21.8272
298.15	25	0.1	1	21.8272
298.15	25	0.1	1	21.8272
298.15	25	0.1	1	21.8272
298.15	25	0.1	1	21.8272
298.15	25	0.1	1	21.8272
298.15	25	0.1	1	21.8272
298.15	25	0.1	1	21.8272
573.15	300	17.2944	172.944	22.0867
603.15	330	59.6624	596.624	22.0895
633.15	360	101.869	1018.69	22.0932
663.15	390	143.723	1437.23	22.0984
693.15	420	185.078	1850.78	22.1057
723.15	450	225.822	2258.22	22.1159
753.15	480	265.86	2658.6	22.1295
783.15	510	305.11	3051.1	22.1469
813.15	540	343.495	3434.95	22.1688
843.15	570	380.938	3809.38	22.1957
873.15	600	417.359	4173.59	22.2282
903.15	630	452.67	4526.7	22.2669
933.15	660	483.741	4837.41	22.35
963.15	690	512.387	5123.87	22.4523
993.15	720	531.673	5316.73	22.6573
1023.15	750	567.489	5674.89	22.652
1053.15	780	603.067	6030.67	22.6468
1083.15	810	638.429	6384.29	22.6417
1113.15	840	673.594	6735.94	22.6367
1143.15	870	708.576	7085.76	22.6317
1173.15	900	743.39	7433.9	22.6267



FLUIDS, package of computer programs for fluid inclusion studies
 Program 2: ISOC, version 01/03
 Product development Ronald J. Bakker

Filename : HPP-4-01-FIA2

Equation of state : Bakker (1999), Bowers & Helgeson (1983)

Host Mineral : Quartz

Bulk fluid composition:

x(H₂O) = 0.931434

x(Na⁺) = 0.034283

x(Cl⁻) = 0.034283

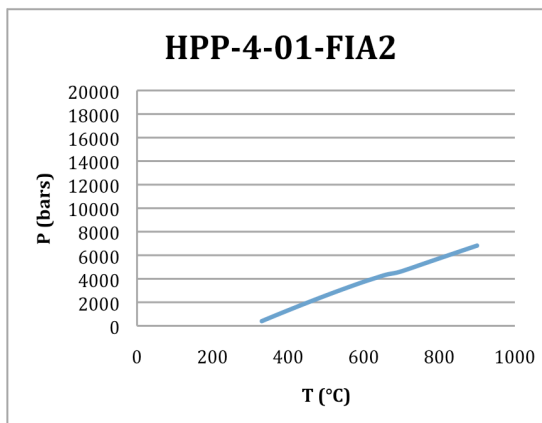
Salinity Aqueous Phase (associated molecules)

	Mass%	Molality
NaCl	10.6699	2.04308

Molar Volume = 22.505912 cc/mol

Density = 0.834639 g/cc

T(K)	T(°C)	P(MPa)	P(bar)	V(cc/mol)
298.15	25	0.1	1	22.5059
298.15	25	0.1	1	22.5059
298.15	25	0.1	1	22.5059
298.15	25	0.1	1	22.5059
298.15	25	0.1	1	22.5059
298.15	25	0.1	1	22.5059
298.15	25	0.1	1	22.5059
298.15	25	0.1	1	22.5059
298.15	25	0.1	1	22.5059
298.15	25	0.1	1	22.5059
298.15	25	0.1	1	22.7818
603.15	330	39.8596	398.596	22.7925
633.15	360	79.7072	797.072	22.7981
663.15	390	119.057	1190.57	22.8053
693.15	420	157.818	1578.18	22.815
723.15	450	195.917	1959.17	22.8278
753.15	480	233.288	2332.88	22.8442
783.15	510	269.87	2698.7	22.8649
813.15	540	305.602	3056.02	22.8906
843.15	570	340.419	3404.19	22.9218
873.15	600	374.251	3742.51	22.9593
903.15	630	405.346	4053.46	23.0298
933.15	660	434.947	4349.47	23.1113
963.15	690	454.188	4541.88	23.3364
993.15	720	484.781	4847.81	23.3769
1023.15	750	518.13	5181.3	23.3716
1053.15	780	551.248	5512.48	23.3665
1083.15	810	584.154	5841.54	23.3616
1113.15	840	616.866	6168.66	23.3567
1143.15	870	649.399	6493.99	23.3518
1173.15	900	681.765	6817.65	23.347



FLUIDS, package of computer programs for fluid inclusion studies
 Program 2: ISOC, version 01/03
 Product development Ronald J. Bakker

Filename : HPP-4-01-FIA3

Equation of state : Bakker (1999), Bowers & Helgeson (1983)
 Host Mineral : Quartz

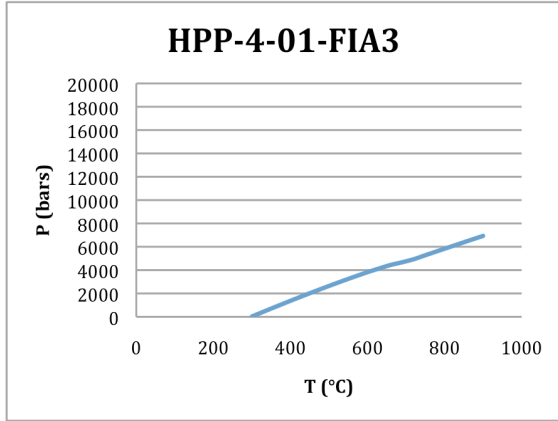
Bulk fluid composition:
 $x(\text{H}_2\text{O}) = 0.931434$
 $x(\text{Na}^+) = 0.034283$
 $x(\text{Cl}^-) = 0.034283$

Salinity Aqueous Phase (associated molecules)

	Mass%	Molality
NaCl	10.6699	2.04308

Molar Volume = 22.383407 cc/mol
 Density = 0.839207 g/cc

T(K)	T(°C)	P(MPa)	P(bar)	V(cc/mol)
298.15	25	0.1	1	22.3834
298.15	25	0.1	1	22.3834
298.15	25	0.1	1	22.3834
298.15	25	0.1	1	22.3834
298.15	25	0.1	1	22.3834
298.15	25	0.1	1	22.3834
298.15	25	0.1	1	22.3834
298.15	25	0.1	1	22.3834
298.15	25	0.1	1	22.3834
298.15	25	0.1	1	22.3834
573.15	300	2.8171	28.171	22.6612
603.15	330	43.5823	435.823	22.6654
633.15	360	83.9673	839.673	22.6705
663.15	390	123.851	1238.51	22.6773
693.15	420	163.141	1631.41	22.6865
723.15	450	201.762	2017.62	22.6987
753.15	480	239.647	2396.47	22.7146
783.15	510	276.736	2767.36	22.7347
813.15	540	312.965	3129.65	22.7596
843.15	570	348.269	3482.69	22.79
873.15	600	382.578	3825.78	22.8265
903.15	630	414.149	4141.49	22.8947
933.15	660	444.358	4443.58	22.9717
963.15	690	467.474	4674.74	23.139
993.15	720	493.81	4938.1	23.2468
1023.15	750	527.613	5276.13	23.2415
1053.15	780	561.182	5611.82	23.2364
1083.15	810	594.539	5945.39	23.2314
1113.15	840	627.701	6277.01	23.2265
1143.15	870	660.683	6606.83	23.2216
1173.15	900	693.499	6934.99	23.2168



FLUIDS, package of computer programs for fluid inclusion studies
 Program 2: ISOC, version 01/03
 Product development Ronald J. Bakker

Filename : HPP-4-02b-FIA1

Equation of state : Bakker (1999), Bowers & Helgeson (1983)
 Host Mineral : Quartz

Bulk fluid composition:

x(H₂O) = 0.975894

x(Na⁺) = 0.012053

x(Cl⁻) = 0.012053

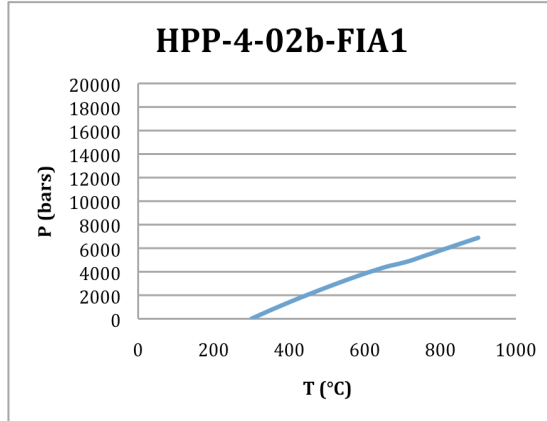
Salinity Aqueous Phase (associated molecules)

	Mass%	Molality
NaCl	3.85354	0.68557

Molar Volume = 22.840247 cc/mol

Density = 0.800589 g/cc

T(K)	T(°C)	P(MPa)	P(bar)	V(cc/mol)
298.15	25	0.1	1	22.8402
298.15	25	0.1	1	22.8402
298.15	25	0.1	1	22.8402
298.15	25	0.1	1	22.8402
298.15	25	0.1	1	22.8402
298.15	25	0.1	1	22.8402
298.15	25	0.1	1	22.8402
298.15	25	0.1	1	22.8402
298.15	25	0.1	1	22.8402
298.15	25	0.1	1	22.8402
573.15	300	0.5673	5.67299	23.1256
603.15	330	44.2358	442.358	23.1274
633.15	360	86.4628	864.628	23.1312
663.15	390	127.426	1274.26	23.1372
693.15	420	167.249	1672.49	23.1462
723.15	450	206.012	2060.12	23.1585
753.15	480	243.759	2437.59	23.1748
783.15	510	280.511	2805.11	23.1955
813.15	540	316.265	3162.65	23.2212
843.15	570	350.996	3509.96	23.2526
873.15	600	384.665	3846.65	23.2904
903.15	630	415.573	4155.73	23.3604
933.15	660	445.094	4450.94	23.4394
963.15	690	467.537	4675.37	23.611
993.15	720	493.196	4931.96	23.7215
1023.15	750	526.271	5262.71	23.7163
1053.15	780	559.111	5591.11	23.7113
1083.15	810	591.737	5917.37	23.7064
1113.15	840	624.17	6241.7	23.7015
1143.15	870	656.425	6564.25	23.6968
1173.15	900	688.518	6885.18	23.692



FLUIDS, package of computer programs for fluid inclusion studies
 Program 2: ISOC, version 01/03
 Product development Ronald J. Bakker

Filename : HPP-4-02b-FIA2

Equation of state : Bakker (1999), Bowers & Helgeson (1983)

Host Mineral : Quartz

Bulk fluid composition:

x(H₂O) = 0.982554

x(Na⁺) = 0.008723

x(Cl⁻) = 0.008723

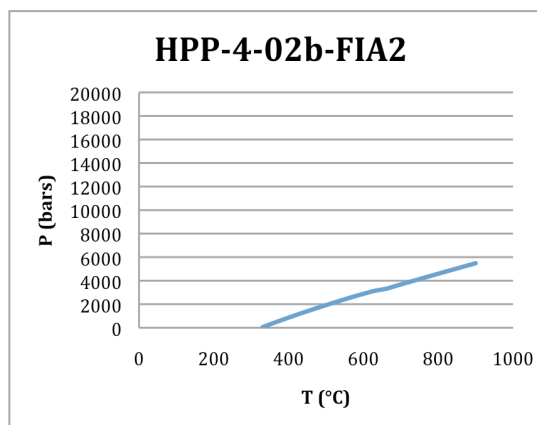
Salinity Aqueous Phase (associated molecules)

	Mass%	Molality
NaCl	2.80041	0.49281

Molar Volume = 24.767380 cc/mol

Density = 0.735280 g/cc

T(K)	T(°C)	P(MPa)	P(bar)	V(cc/mol)
298.15	25	0.1	1	24.7674
298.15	25	0.1	1	24.7674
298.15	25	0.1	1	24.7674
298.15	25	0.1	1	24.7674
298.15	25	0.1	1	24.7674
298.15	25	0.1	1	24.7674
298.15	25	0.1	1	24.7674
298.15	25	0.1	1	24.7674
298.15	25	0.1	1	24.7674
298.15	25	0.1	1	24.7674
298.15	25	0.1	1	24.7674
298.15	25	0.1	1	24.7674
603.15	330	4.98285	49.8285	25.1149
633.15	360	40.578	405.78	25.125
663.15	390	74.9602	749.602	25.1376
693.15	420	108.273	1082.73	25.1536
723.15	450	140.614	1406.14	25.1735
753.15	480	172.043	1720.43	25.1982
783.15	510	202.591	2025.91	25.2284
813.15	540	232.266	2322.66	25.265
843.15	570	261.056	2610.56	25.3089
873.15	600	288.122	2881.22	25.383
903.15	630	313.708	3137.08	25.4777
933.15	660	330.774	3307.74	25.7727
963.15	690	358.725	3587.25	25.7666
993.15	720	386.415	3864.15	25.761
1023.15	750	413.868	4138.68	25.7559
1053.15	780	441.107	4411.07	25.7511
1083.15	810	468.15	4681.5	25.7465
1113.15	840	495.013	4950.13	25.742
1143.15	870	521.713	5217.13	25.7376
1173.15	900	548.26	5482.6	25.7332



FLUIDS, package of computer programs for fluid inclusion studies
 Program 2: ISOC, version 01/03
 Product development Ronald J. Bakker

Filename : HPP-4-06-FIA1

Equation of state : Bakker (1999), Bowers & Helgeson (1983)

Host Mineral : Quartz

Bulk fluid composition:

x(H2O) = 0.871644

x(CO2) = 0.025709

x(Na+) = 0.051323

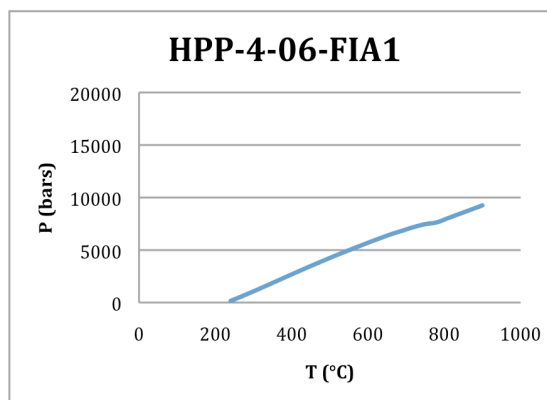
x(Cl-) = 0.051323

Salinity Aqueous Phase (associated molecules)

	Mass%	Molality
NaCl	16.0425	3.2684

Molar Volume = 20.870011 cc/mol

Density = 0.950400 g/cc



T(K)	T(°C)	P(MPa)	P(bar)	V(cc/mol)
298.15	25	0.1	1	20.87
298.15	25	0.1	1	20.87
298.15	25	0.1	1	20.87
298.15	25	0.1	1	20.87
298.15	25	0.1	1	20.87
298.15	25	0.1	1	20.87
298.15	25	0.1	1	20.87
298.15	25	0.1	1	20.87
298.15	25	0.1	1	20.87
513.15	240	15.616	156.16	21.0533
543.15	270	60.101	601.01	21.0549
573.15	300	106.655	1066.55	21.0549
603.15	330	154.559	1545.59	21.0544
633.15	360	203.177	2031.77	21.0541
663.15	390	251.919	2519.19	21.055
693.15	420	300.264	3002.64	21.0577
723.15	450	347.813	3478.13	21.0628
753.15	480	394.331	3943.31	21.0707
783.15	510	439.731	4397.31	21.0818
813.15	540	484.02	4840.2	21.0963
843.15	570	527.221	5272.21	21.1146
873.15	600	569.323	5693.23	21.1371
903.15	630	610.263	6102.63	21.1641
933.15	660	649.933	6499.33	21.1964
963.15	690	684.099	6840.99	21.2658
993.15	720	718.641	7186.41	21.3259
1023.15	750	746.487	7464.87	21.4296
1053.15	780	763.198	7631.98	21.6098
1083.15	810	803.947	8039.47	21.6047
1113.15	840	844.531	8445.31	21.5996
1143.15	870	884.963	8849.63	21.5944
1173.15	900	925.254	9252.54	21.5892

FLUIDS, package of computer programs for fluid inclusion studies
 Program 2: ISOC, version 01/03
 Product development Ronald J. Bakker

Filename : HPP-4-08-FIA1

Equation of state : Bakker (1999), Bowers & Helgeson (1983)

Host Mineral : Quartz

Bulk fluid composition:

x(H₂O) = 0.888943

x(CO₂) = 0.042492

x(Na⁺) = 0.034283

x(Cl⁻) = 0.034283

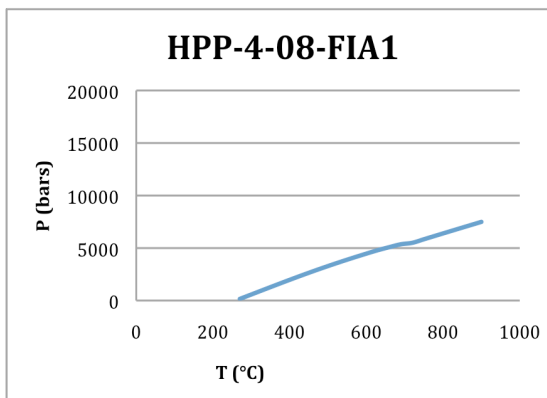
Salinity Aqueous Phase (associated molecules)

	Mass%	Molality
NaCl	11.1232	2.14074

Molar Volume = 22.831890 cc/mol

Density = 0.871100 g/cc

T(K)	T(°C)	P(MPa)	P(bar)	V(cc/mol)
298.15	25	0.1	1	22.8319
298.15	25	0.1	1	22.8319
298.15	25	0.1	1	22.8319
298.15	25	0.1	1	22.8319
298.15	25	0.1	1	22.8319
298.15	25	0.1	1	22.8319
298.15	25	0.1	1	22.8319
298.15	25	0.1	1	22.8319
298.15	25	0.1	1	22.8319
298.15	25	0.1	1	22.8319
543.15	270	15.4231	154.231	23.0681
573.15	300	57.5758	575.758	23.0713
603.15	330	99.7784	997.784	23.0746
633.15	360	141.805	1418.05	23.0788
663.15	390	183.402	1834.02	23.0845
693.15	420	224.312	2243.12	23.0927
723.15	450	264.297	2642.97	23.1038
753.15	480	303.181	3031.81	23.1186
783.15	510	340.865	3408.65	23.1376
813.15	540	377.321	3773.21	23.1613
843.15	570	412.567	4125.67	23.1903
873.15	600	446.63	4466.3	23.2252
903.15	630	479.518	4795.18	23.2666
933.15	660	508.511	5085.11	23.3493
963.15	690	535.798	5357.98	23.4438
993.15	720	549.819	5498.19	23.6944
1023.15	750	583.435	5834.35	23.6897
1053.15	780	616.867	6168.67	23.6851
1083.15	810	650.134	6501.34	23.6805
1113.15	840	683.249	6832.49	23.6759
1143.15	870	716.222	7162.22	23.6713
1173.15	900	749.065	7490.65	23.6667



FLUIDS, package of computer programs for fluid inclusion studies
 Program 2: ISOC, version 01/03
 Product development Ronald J. Bakker

Filename : HPP-4-08-FIA2

Equation of state : Bakker (1999), Bowers & Helgeson (1983)

Host Mineral : Quartz

Bulk fluid composition:

x(H2O) = 0.864334

x(CO2) = 0.079300

x(Na+) = 0.028183

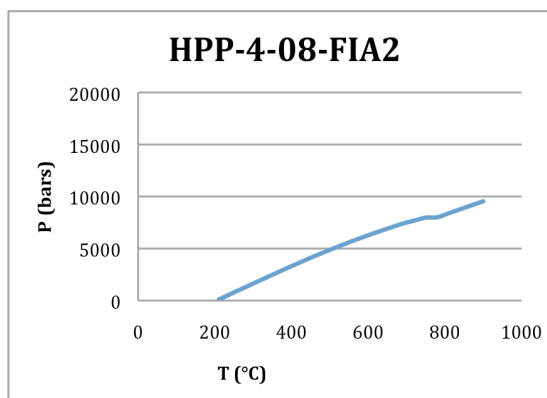
x(Cl-) = 0.028183

Salinity Aqueous Phase (associated molecules)

	Mass%	Molality
NaCl	9.56876	1.80992

Molar Volume = 22.148497 cc/mol

Density = 0.935000 g/cc



T(K)	T(°C)	P(MPa)	P(bar)	V(cc/mol)
298.15	25	0.1	1	22.1485
298.15	25	0.1	1	22.1485
298.15	25	0.1	1	22.1485
298.15	25	0.1	1	22.1485
298.15	25	0.1	1	22.1485
298.15	25	0.1	1	22.1485
298.15	25	0.1	1	22.1485
483.15	210	9.90672	99.0672	22.3133
513.15	240	61.1717	611.717	22.3108
543.15	270	112.318	1123.18	22.308
573.15	300	163.367	1633.67	22.3054
603.15	330	214.241	2142.41	22.3034
633.15	360	264.762	2647.62	22.3024
663.15	390	314.675	3146.75	22.3031
693.15	420	363.683	3636.83	22.3059
723.15	450	411.499	4114.99	22.3112
753.15	480	457.895	4578.95	22.3195
783.15	510	502.736	5027.36	22.331
813.15	540	545.981	5459.81	22.3462
843.15	570	587.667	5876.67	22.3654
873.15	600	627.858	6278.58	22.389
903.15	630	666.607	6666.07	22.4175
933.15	660	703.92	7039.2	22.4515
963.15	690	739.74	7397.4	22.4917
993.15	720	768.378	7683.78	22.5802
1023.15	750	797.023	7970.23	22.6626
1053.15	780	801.039	8010.39	22.9226
1083.15	810	839.575	8395.75	22.9182
1113.15	840	878.001	8780.01	22.9136
1143.15	870	916.325	9163.25	22.9089
1173.15	900	954.555	9545.55	22.9041

FLUIDS, package of computer programs for fluid inclusion studies
 Program 2: ISOC, version 01/03
 Product development Ronald J. Bakker

Filename : HPP-4-08-FIA3

Equation of state : Bakker (1999), Bowers & Helgeson (1983)

Host Mineral : Quartz

Bulk fluid composition:

x(H₂O) = 0.911132

x(Na⁺) = 0.044434

x(Cl⁻) = 0.044434

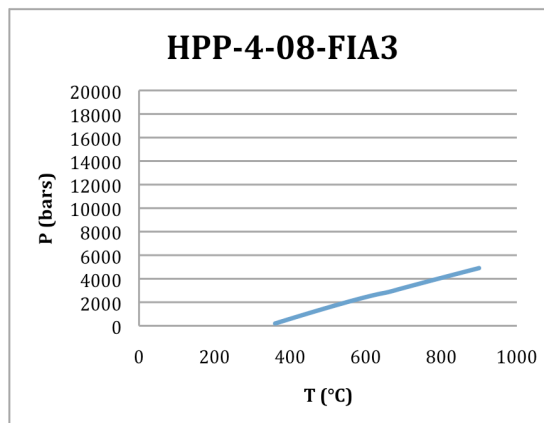
Salinity Aqueous Phase (associated molecules)

	Mass%	Molality
NaCl	13.6635	2.70702

Molar Volume = 25.121286 cc/mol

Density = 0.756809 g/cc

T(K)	T(°C)	P(MPa)	P(bar)	V(cc/mol)
298.15	25	0.1	1	25.1213
298.15	25	0.1	1	25.1213
298.15	25	0.1	1	25.1213
298.15	25	0.1	1	25.1213
298.15	25	0.1	1	25.1213
298.15	25	0.1	1	25.1213
298.15	25	0.1	1	25.1213
298.15	25	0.1	1	25.1213
298.15	25	0.1	1	25.1213
298.15	25	0.1	1	25.1213
298.15	25	0.1	1	25.1213
298.15	25	0.1	1	25.1213
298.15	25	0.1	1	25.1213
633.15	360	19.4354	194.354	25.5046
663.15	390	49.1643	491.643	25.5222
693.15	420	78.6136	786.136	25.5426
723.15	450	107.675	1076.75	25.5666
753.15	480	136.261	1362.61	25.5954
783.15	510	164.299	1642.99	25.63
813.15	540	191.721	1917.21	25.6713
843.15	570	218.463	2184.63	25.7204
873.15	600	243.605	2436.05	25.8085
903.15	630	266.818	2668.18	25.9408
933.15	660	286.713	2867.13	26.1587
963.15	690	312.867	3128.67	26.1523
993.15	720	338.794	3387.94	26.1466
1023.15	750	364.508	3645.08	26.1414
1053.15	780	390.024	3900.24	26.1365
1083.15	810	415.356	4153.56	26.1319
1113.15	840	440.518	4405.18	26.1274
1143.15	870	465.52	4655.2	26.123
1173.15	900	490.373	4903.73	26.1188



FLUIDS, package of computer programs for fluid inclusion studies
 Program 2: ISOC, version 01/03
 Product development Ronald J. Bakker

Filename : HPP-4-10-FIA1

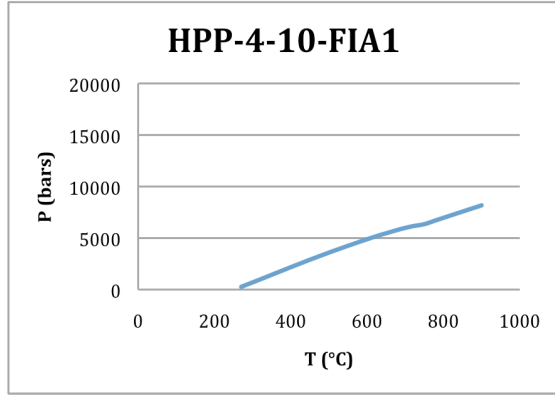
Equation of state : Bakker (1999), Bowers & Helgeson (1983)
 Host Mineral : Quartz

Bulk fluid composition:
 $x(\text{H}_2\text{O}) = 0.879676$
 $x(\text{CO}_2) = 0.028721$
 $x(\text{Na}^+) = 0.045802$
 $x(\text{Cl}^-) = 0.045802$

Salinity Aqueous Phase (associated molecules)

	Mass%	Molality
NaCl	14.4541	2.89012

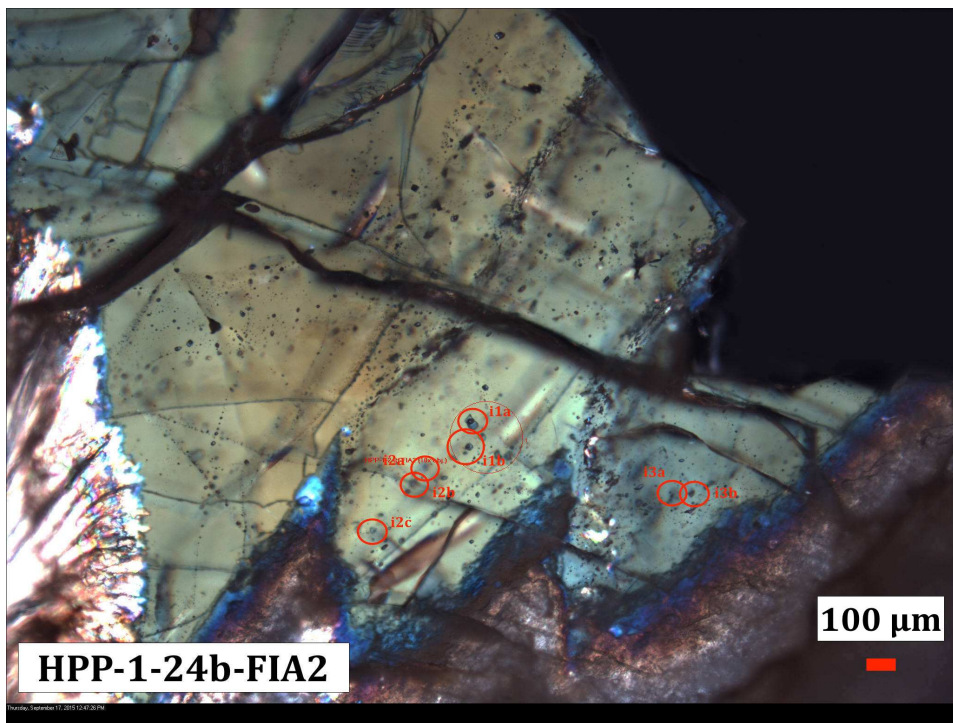
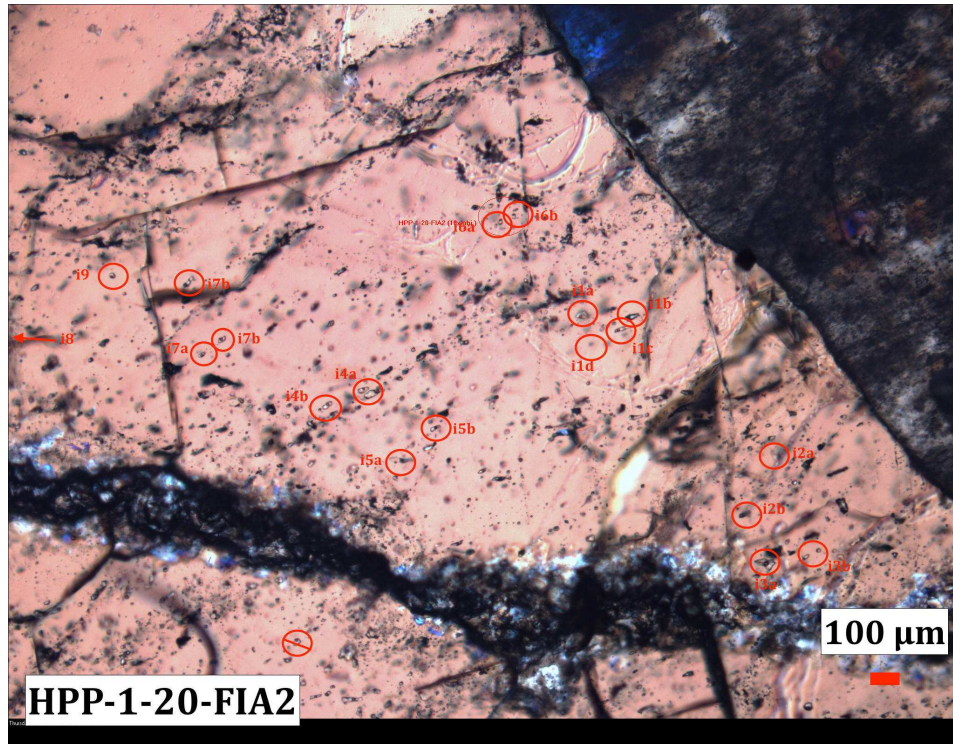
Molar Volume = 21.758432 cc/mol
 Density = 0.909500 g/cc

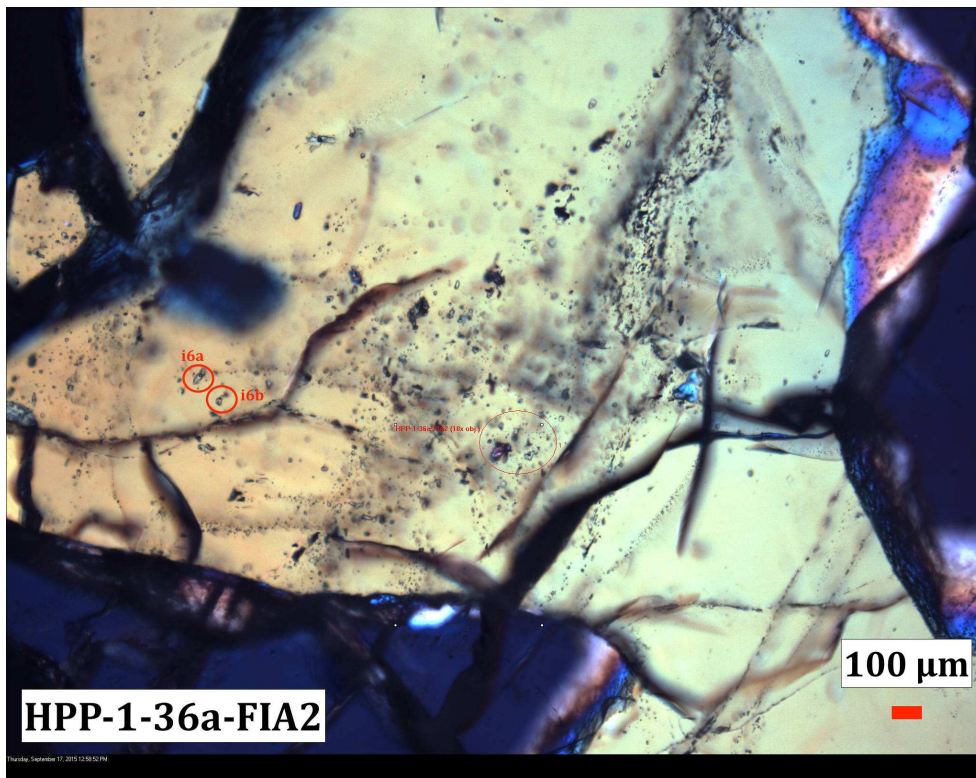
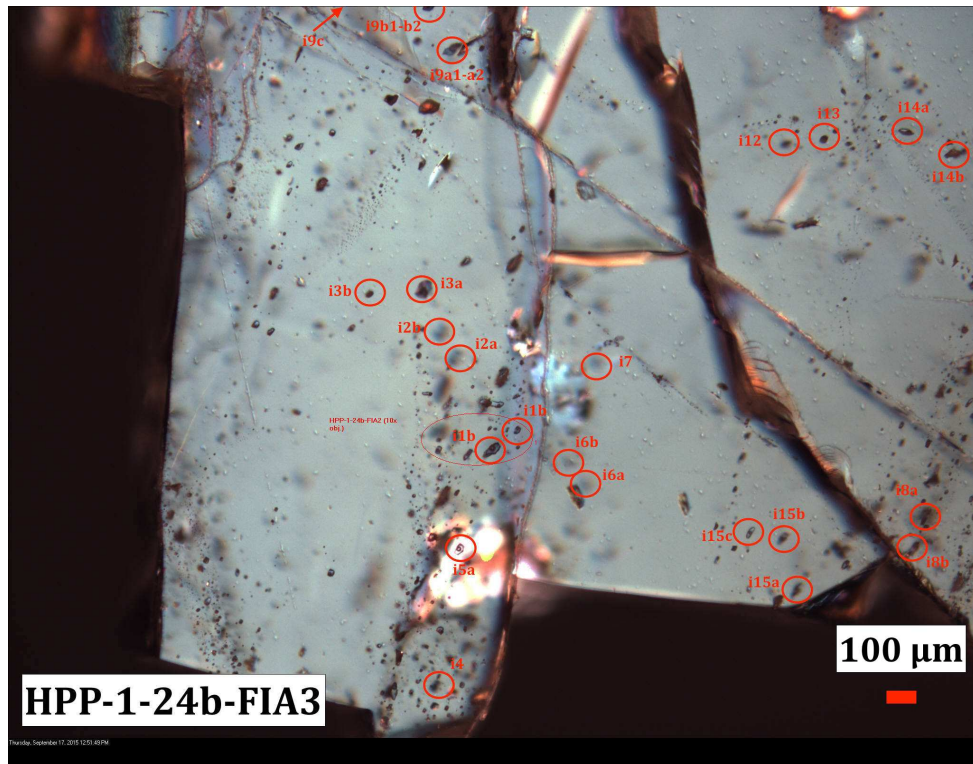


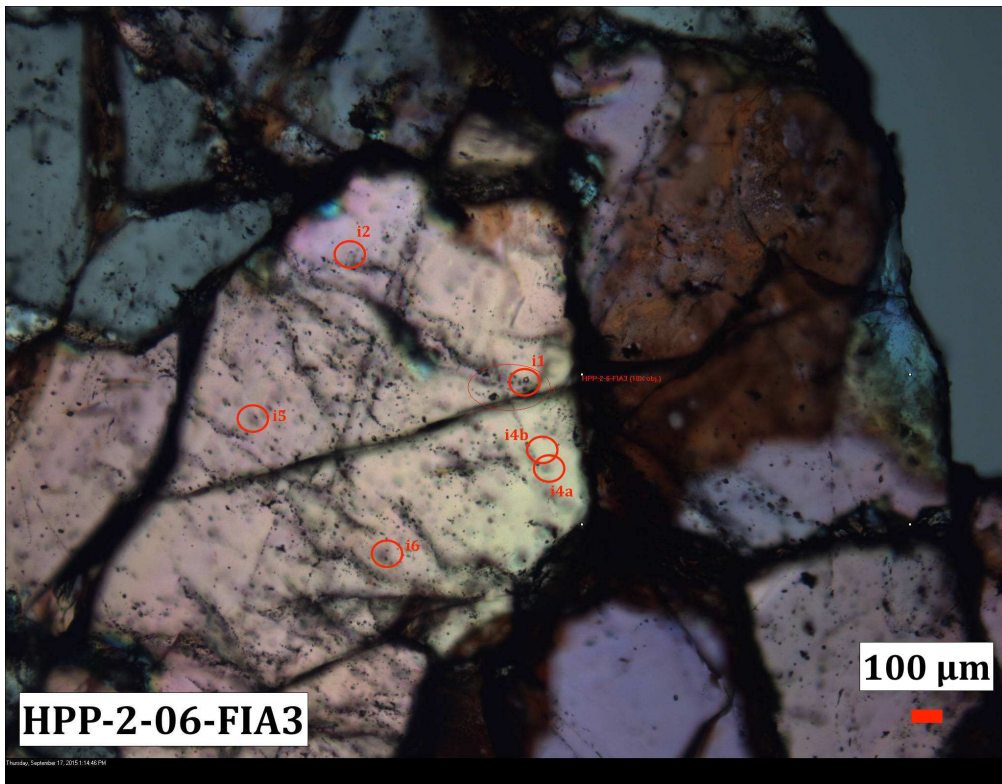
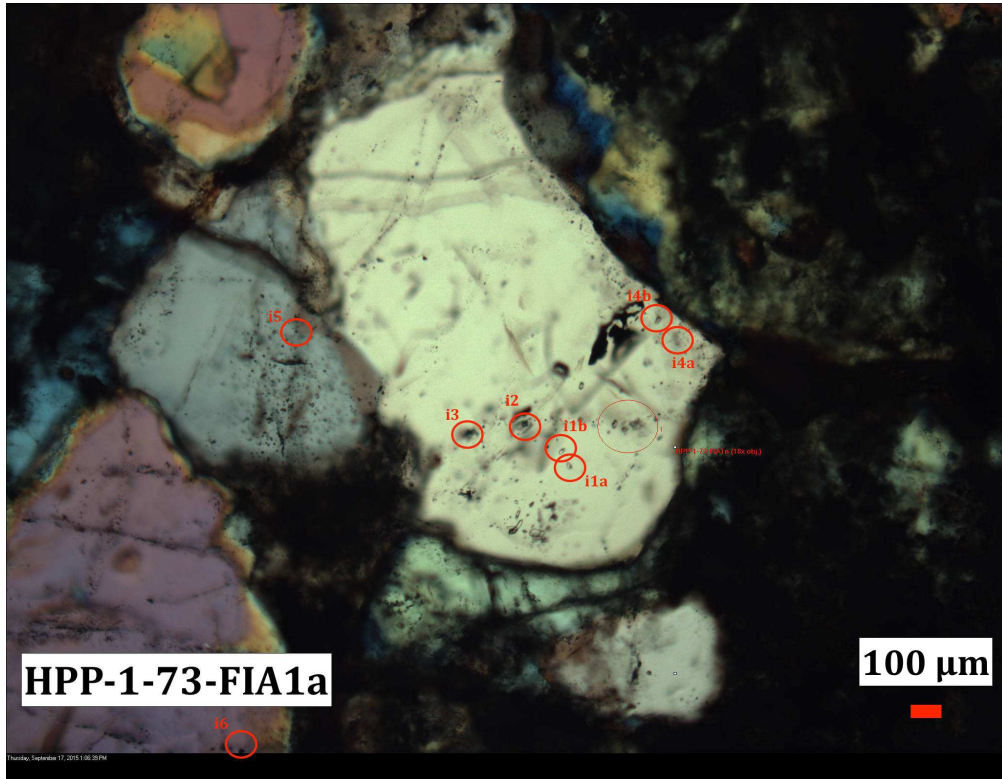
T(K)	T(°C)	P(MPa)	P(bar)	V(cc/mol)
298.15	25	0.1	1	21.7584
298.15	25	0.1	1	21.7584
298.15	25	0.1	1	21.7584
298.15	25	0.1	1	21.7584
298.15	25	0.1	1	21.7584
298.15	25	0.1	1	21.7584
298.15	25	0.1	1	21.7584
298.15	25	0.1	1	21.7584
298.15	25	0.1	1	21.7584
298.15	25	0.1	1	21.7584
543.15	270	26.6428	266.428	21.9753
573.15	300	69.8429	698.429	21.9776
603.15	330	113.889	1138.89	21.9794
633.15	360	158.309	1583.09	21.9818
663.15	390	202.653	2026.53	21.9854
693.15	420	246.51	2465.1	21.991
723.15	450	289.549	2895.49	21.9994
753.15	480	331.556	3315.56	22.011
783.15	510	372.441	3724.41	22.0264
813.15	540	412.199	4121.99	22.0459
843.15	570	450.853	4508.53	22.0699
873.15	600	488.41	4884.1	22.099
903.15	630	524.834	5248.34	22.1337
933.15	660	557.392	5573.92	22.202
963.15	690	589.359	5893.59	22.2684
993.15	720	615.313	6153.13	22.3872
1023.15	750	634.915	6349.15	22.5606
1053.15	780	671.738	6717.38	22.5557
1083.15	810	708.38	7083.8	22.5509
1113.15	840	744.856	7448.56	22.546
1143.15	870	781.179	7811.79	22.5411
1173.15	900	817.36	8173.6	22.5362

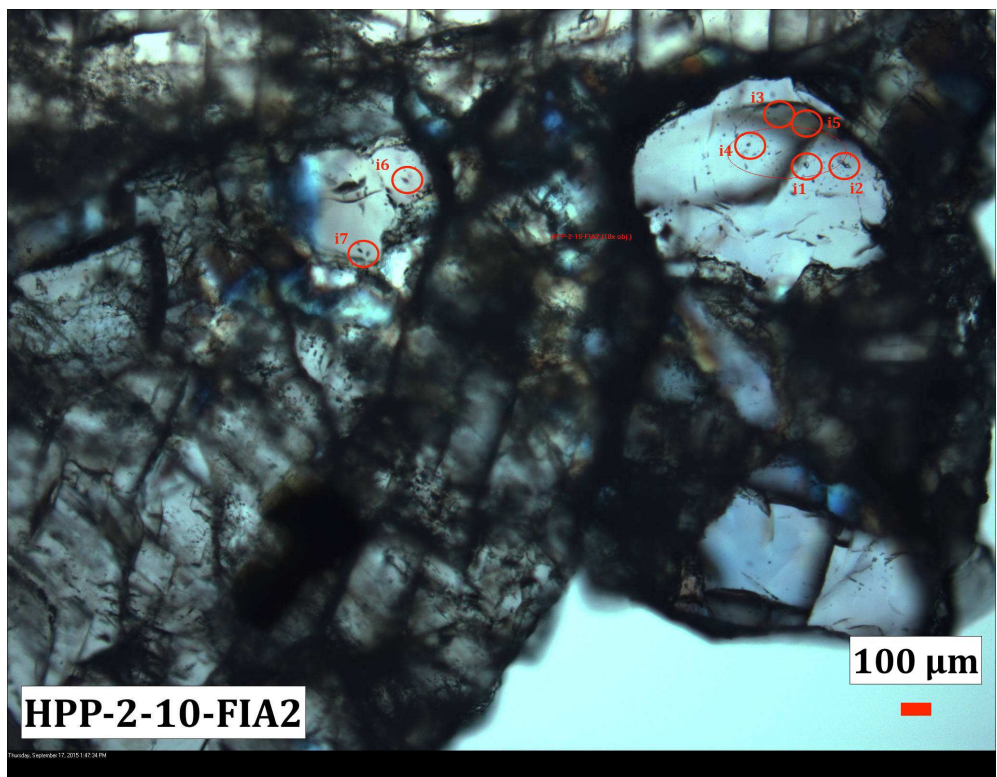
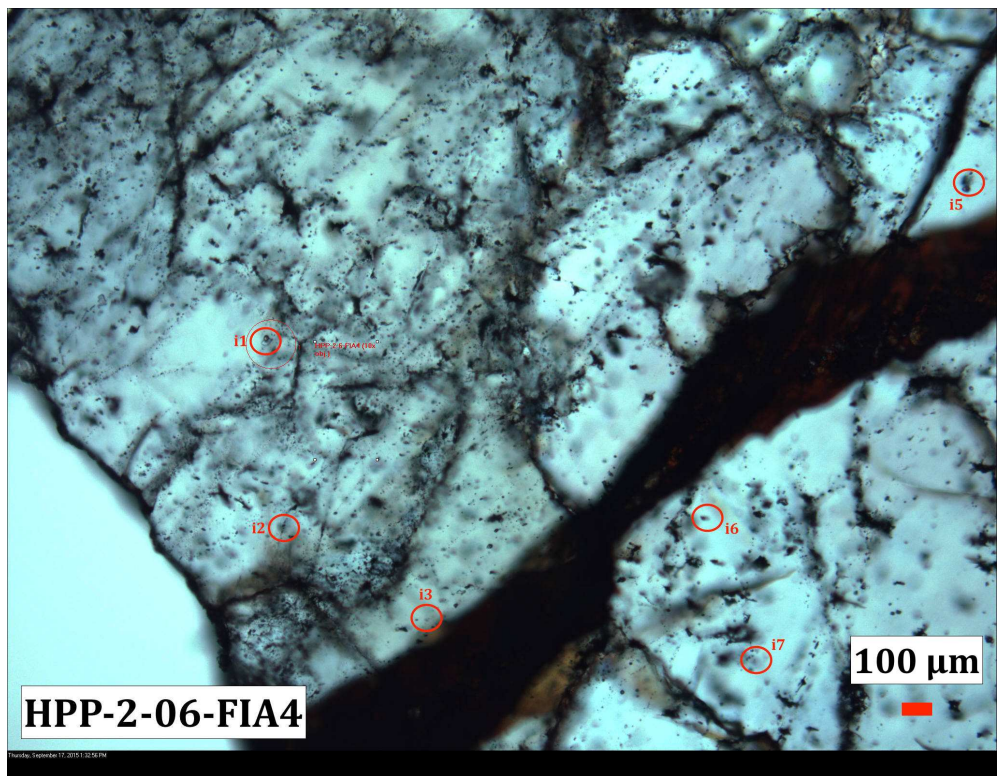
APPENDIX F: LA-ICP-MS DATA

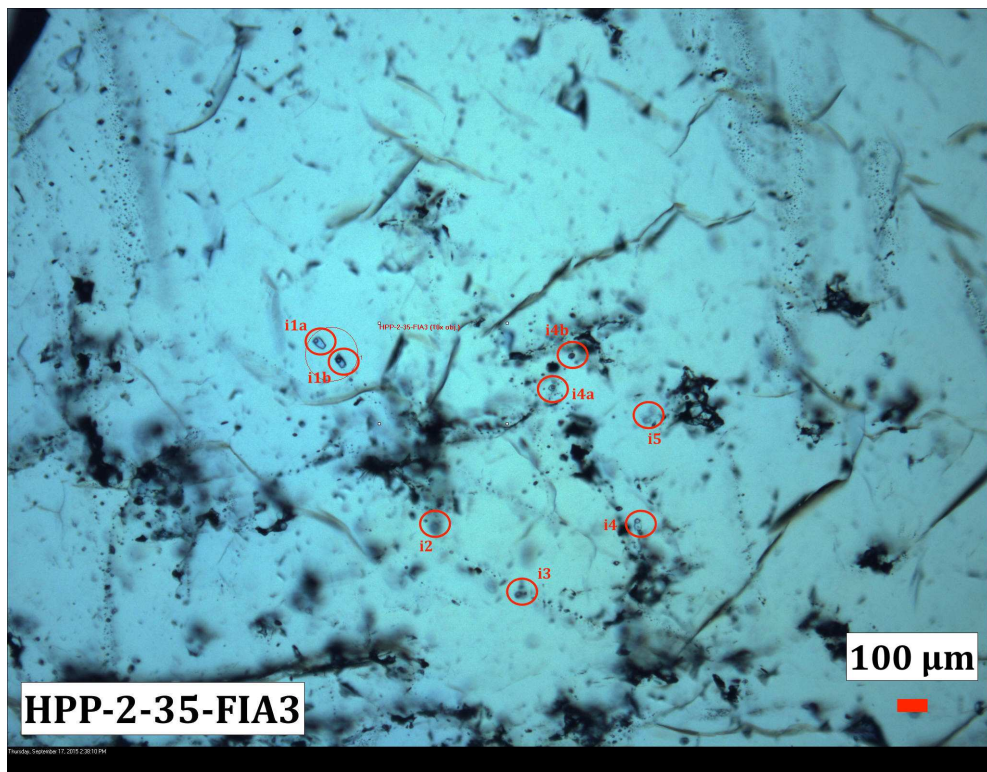
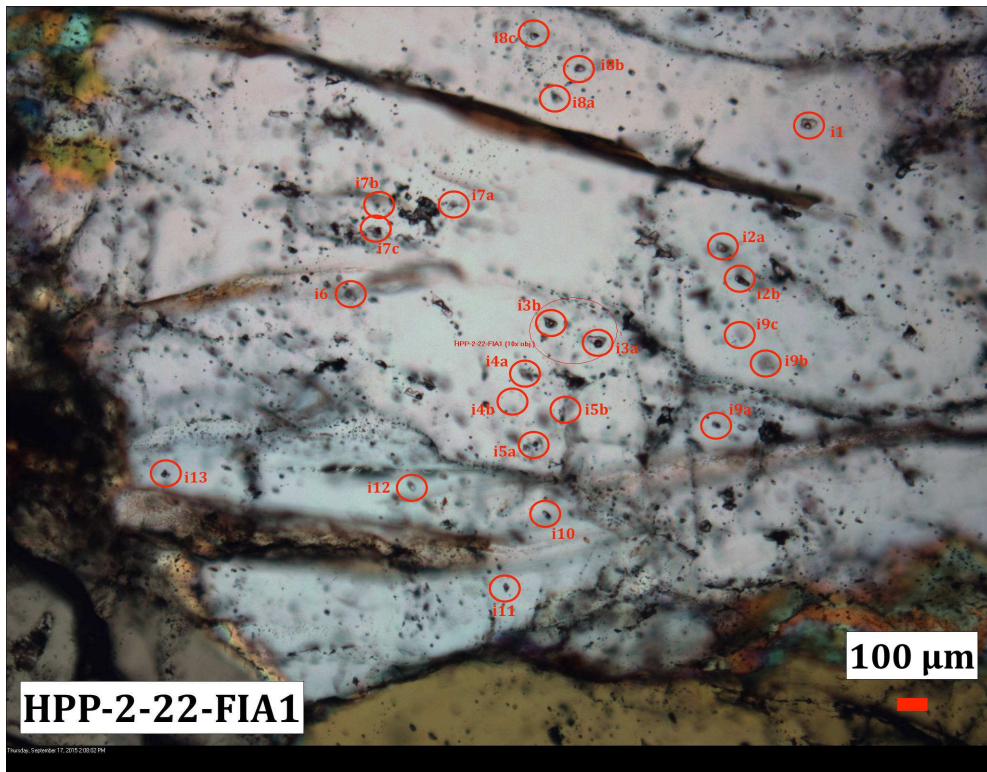
APPENDIX F.1: ANNOTATED LA-ICP-MS FLUID INCLUSION SAMPLE PHOTOMICROGRAPHS

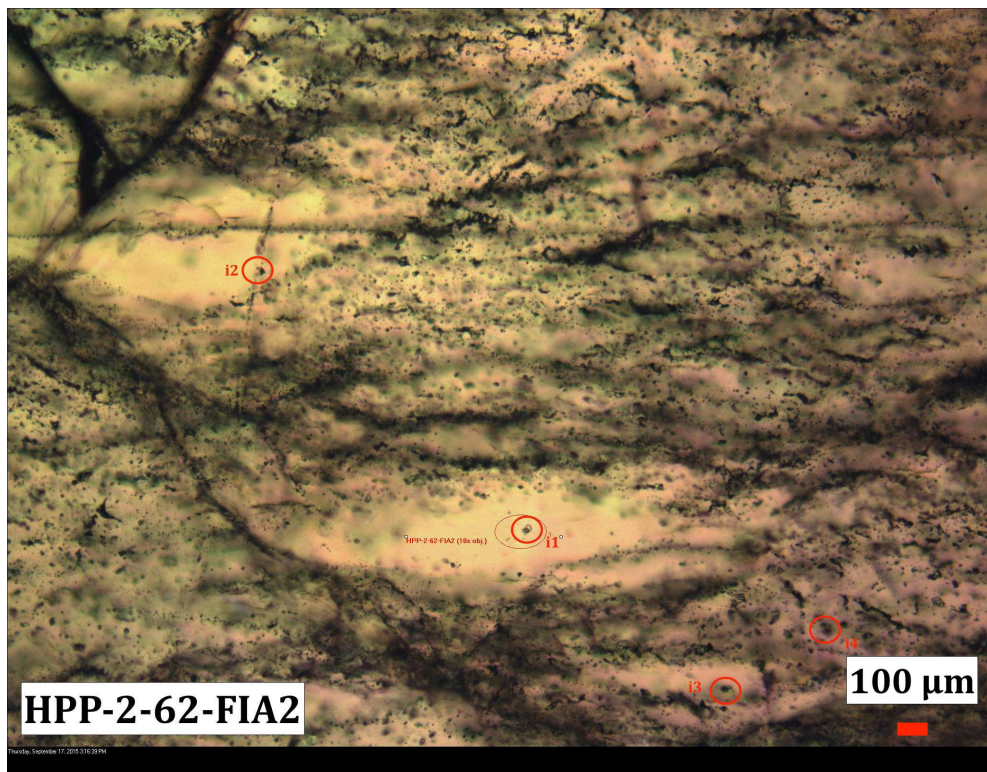
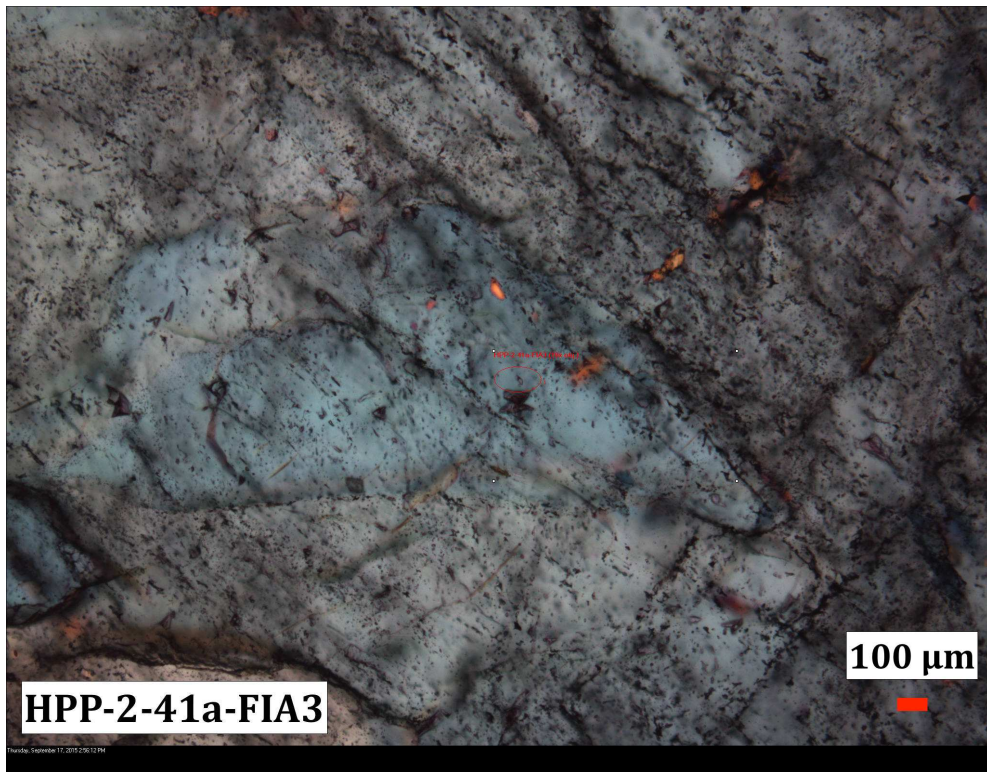


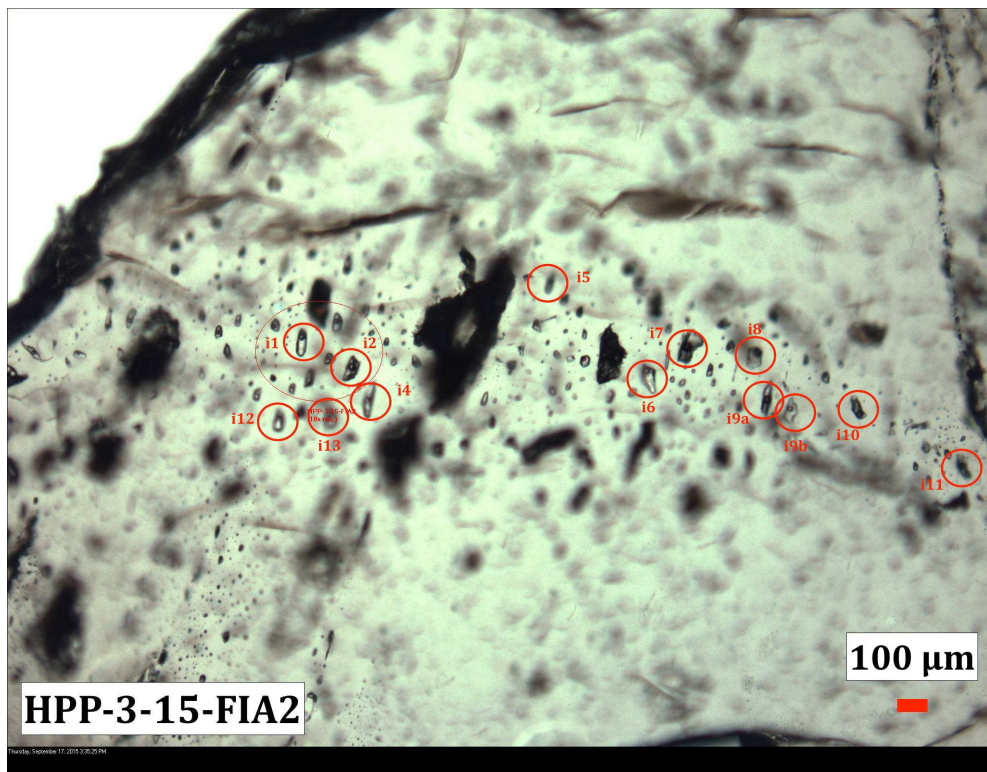
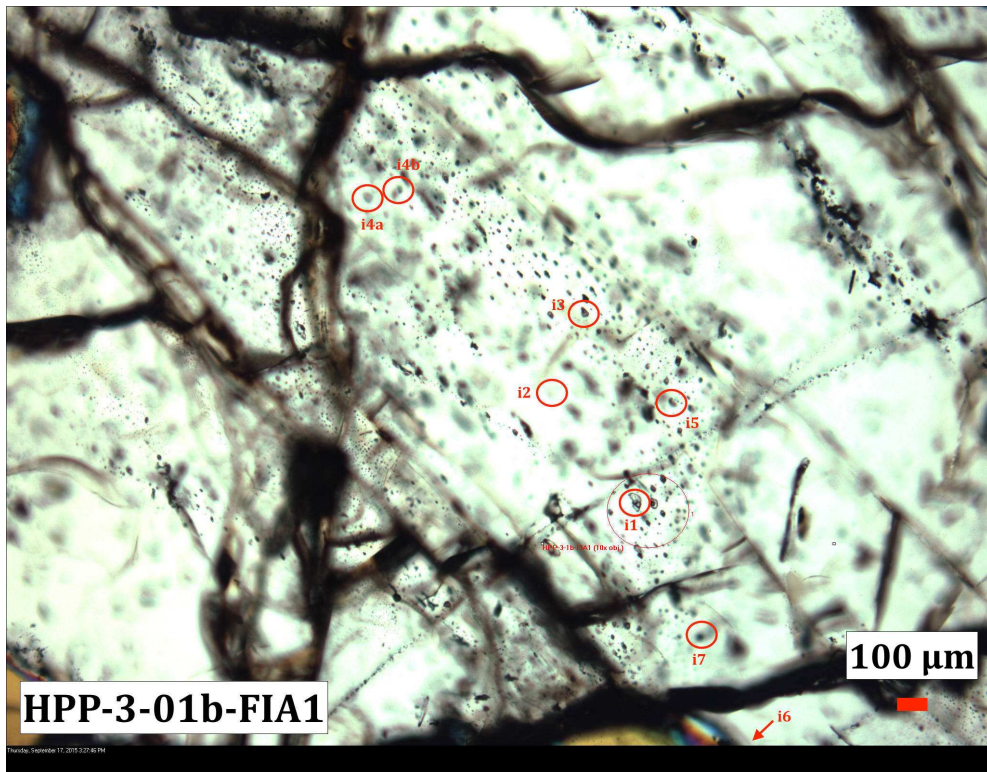


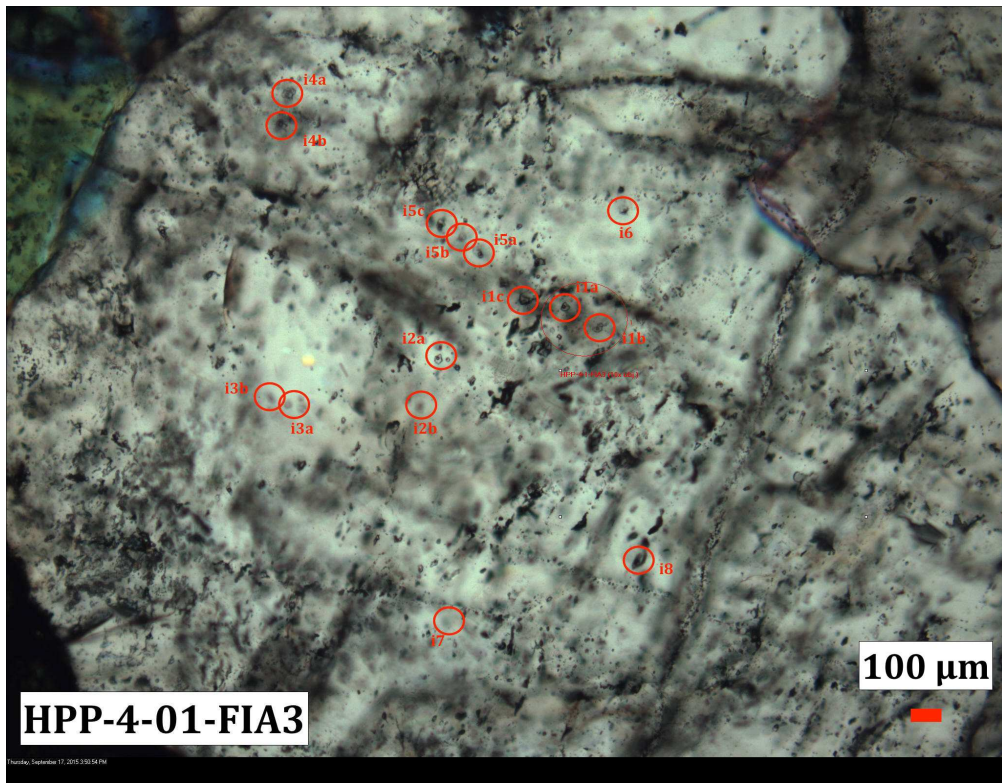
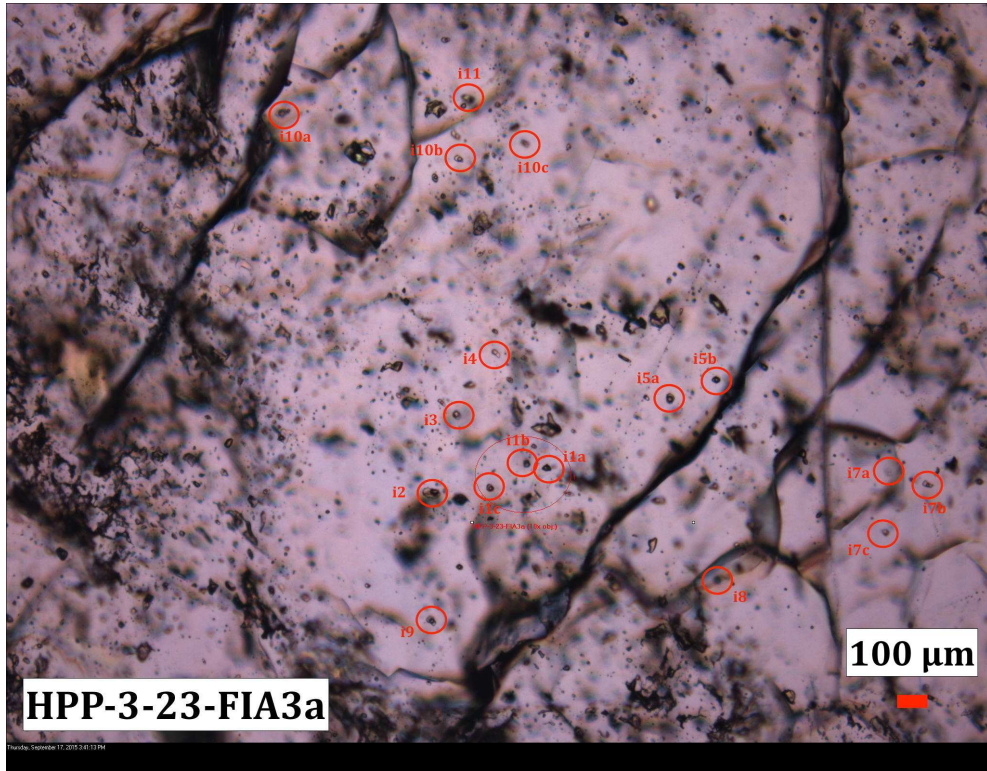


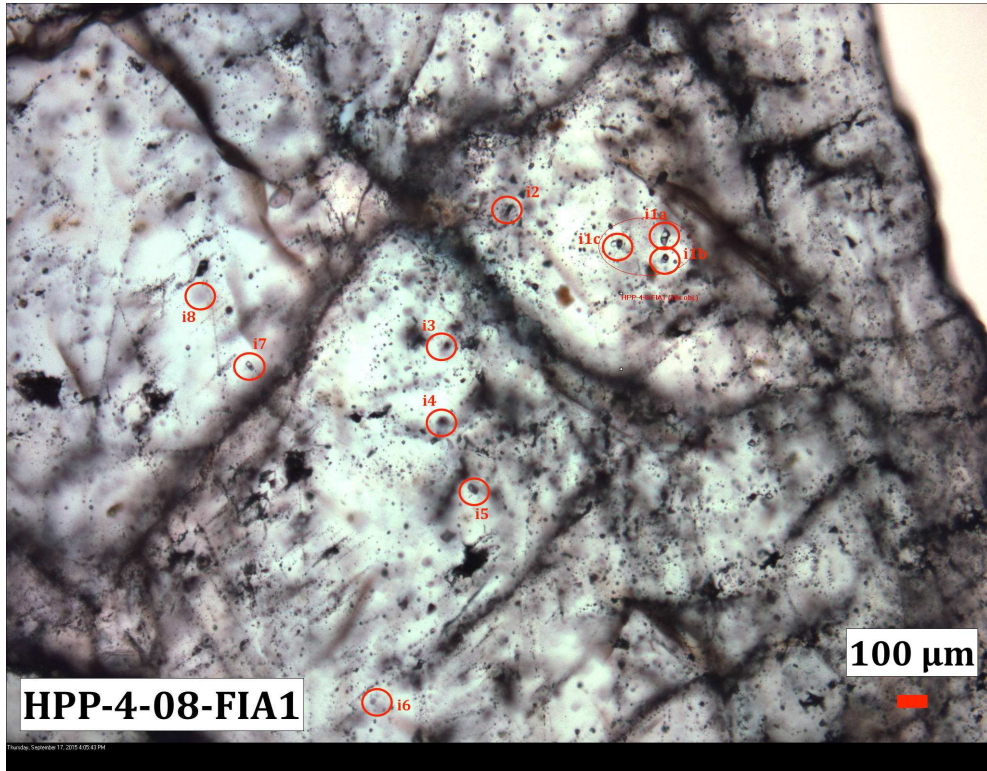












F.2: LA-ICP-MS DATA

F.2.1: RAW LA-ICP-MS DATA FOR SELECT INCLUSIONS

Full ID	Sample ID	Assemblage Number	LA-ICP-MS Run ID	Feature Type	Assemblage Type	Assemblage Interpretation	Na (ppm) (int. standard)	Li (ppm)	Li ±2SE (ppm)
HPP-1-24b-FIA2_i1b	HPP-1-24	FIA2	i1b	Miarolitic Cavity	Type (A)	Primary	12706	740	260
HPP-1-24b-FIA2_i3c	HPP-1-24	FIA2	i3c	Miarolitic Cavity	Type (A)	Primary	12706	310	210
HPP-1-24b-FIA2_i4a	HPP-1-24	FIA2	i4a	Miarolitic Cavity	Type (A)	Primary	12706	700	1300
HPP-2-06-FIA4_i1	HPP-2-06	FIA4	i1	Type (I) Quartz Vein	Type (B)	Primary	7513	570	130
HPP-2-06-FIA4_i2	HPP-2-06	FIA4	i2	Type (I) Quartz Vein	Type (B)	Primary	7513	154	83
HPP-2-10-FIA2_i5	HPP-2-10	FIA2	i5	Aplite	Type (C)	Pseudosecondary	708	21	20
HPP-2-22-FIA1_i13	HPP-2-22	FIA1	i13	Type (I) Quartz Vein	Type (B)	Primary	7513	153	89
HPP-2-22-FIA1_i1b	HPP-2-22	FIA1	i1b	Type (I) Quartz Vein	Type (B)	Primary	7513	198	63
HPP-2-22-FIA1_i6	HPP-2-22	FIA1	i6	Type (I) Quartz Vein	Type (B)	Primary	7513	132	49
HPP-2-35-FIA3_i1a	HPP-2-35	FIA3	i1a	QF Pegmatite	Type (B)	Primary/Pseudosecondary	8812	730	200
HPP-2-35-FIA3_i2	HPP-2-36	FIA3	i2	QF Pegmatite	Type (B)	Primary/Pseudosecondary	8812	305	42
HPP-2-35-FIA3_i4	HPP-2-37	FIA3	i4	QF Pegmatite	Type (B)	Primary/Pseudosecondary	8812	470	320
HPP-2-35-FIA3_i6b	HPP-2-38	FIA3	i6b	QF Pegmatite	Type (B)	Primary/Pseudosecondary	8812	450	110
HPP-2-44-FIA3_i9	HPP-2-44	FIA3	i9	Aplite (Layered QF Pegmatite)	Type (C)	Secondary	12706	1050	390
HPP-2-62-FIA2_i6a	HPP-2-62	FIA2	i6a	QF Pegmatite	Type (B)	Primary	19511	-	-
HPP-3-01b-FIA1_i3	HPP-3-01b	FIA1	i3	MQF Pegmatite	Type (C)	Primary	13965	-	-
HPP-3-01b-FIA1_i5	HPP-3-01b	FIA1	i5	MQF Pegmatite	Type (C)	Primary	13965	198	89
HPP-3-15-FIA2_i1	HPP-3-15	FIA2	i1	QF Pegmatite	Type (A)	Primary	15224	261	89
HPP-3-15-FIA2_i10	HPP-3-15	FIA2	i10	QF Pegmatite	Type (A)	Primary	15224	177	39
HPP-3-15-FIA2_i11	HPP-3-15	FIA2	i11	QF Pegmatite	Type (A)	Primary	15224	136	50
HPP-3-15-FIA2_i12	HPP-3-15	FIA2	i12	QF Pegmatite	Type (A)	Primary	15224	380	390
HPP-3-15-FIA2_i2	HPP-3-15	FIA2	i2	QF Pegmatite	Type (A)	Primary	15224	174	36
HPP-3-15-FIA2_i5	HPP-3-15	FIA2	i5	QF Pegmatite	Type (A)	Primary	15224	190	150
HPP-3-15-FIA2_i7	HPP-3-15	FIA2	i7	QF Pegmatite	Type (A)	Primary	15224	233	89
HPP-3-15-FIA2_i8	HPP-3-15	FIA2	i8	QF Pegmatite	Type (A)	Primary	15224	150	23
HPP-3-15-FIA2_i9a	HPP-3-15	FIA2	i9a	QF Pegmatite	Type (A)	Primary	15224	214	48
HPP-3-15-FIA2_i9b	HPP-3-15	FIA2	i9b	QF Pegmatite	Type (A)	Primary	15224	660	790
HPP-3-23-FIA3a_i5a	HPP-3-23	FIA3a	i5a	Type (III) Quartz Vein	Type (B)	Primary	14594	390	480
HPP-3-23-FIA3a_i5b	HPP-3-23	FIA3a	i5b	Type (III) Quartz Vein	Type (B)	Primary	14594	219	380
HPP-4-01-FIA3_i1a	HPP-4-01	FIA3	i1a	Type (II) (skarn) Quartz Vein	Type (A)	Primary	13965	290	200
HPP-4-01-FIA3_i1c	HPP-4-01	FIA3	i1c	Type (II) (skarn) Quartz Vein	Type (A)	Primary	13965	194	85
HPP-4-01-FIA3_i2a	HPP-4-01	FIA3	i2a	Type (II) (skarn) Quartz Vein	Type (A)	Primary	13965	82	72
HPP-4-01-FIA3_i4b	HPP-4-01	FIA3	i4b	Type (II) (skarn) Quartz Vein	Type (A)	Primary	13965	302	93
HPP-4-01-FIA3_i5a	HPP-4-01	FIA3	i5a	Type (II) (skarn) Quartz Vein	Type (A)	Primary	13965	170	130
HPP-4-01-FIA3_i8	HPP-4-01	FIA3	i8	Type (II) (skarn) Quartz Vein	Type (A)	Primary	13965	250	150
HPP-4-08-FIA1_i1b	HPP-4-08	FIA1	i1b	Type (III) Quartz Vein	Type (B)	Primary	13965	1500	2900
HPP-4-08-FIA1_i4	HPP-4-08	FIA1	i4	Type (III) Quartz Vein	Type (B)	Primary	13965	-	-

Full ID	B (ppm)	B ±2SE (ppm)	Mg (ppm)	Mg ±2SE (ppm)	Al (ppm)	Al ±2SE (ppm)	Si (ppm)	Si ±2SE (ppm)	Cl (ppm)	Cl ±2SE (ppm)	K (ppm)
HPP-1-24b-FIA2_i1b	1240	530	5700	7200	7700	2200	36000000	11000000	-	-	4000
HPP-1-24b-FIA2_i3c	980	840	-	-	1540	620	14000000	7800000	10000	8100	-
HPP-1-24b-FIA2_i4a	2900	1100	-	-	5000	5300	55000000	72000000	-	-	-
HPP-2-06-FIA4_i1	-	-	-	-	280	210	67000000	14000000	5000000	35000000	500
HPP-2-06-FIA4_i2	180	240	-	-	240	270	33300000	9700000	-	-	-
HPP-2-10-FIA2_i5	70	100	3.7	5.6	310	120	9000000	4300000	-	-	29
HPP-2-22-FIA1_i13	230	150	-	-	1310	440	33200000	6400000	3100	5400	-
HPP-2-22-FIA1_i1b	70	100	-	-	270	280	29000000	14000000	-	-	710
HPP-2-22-FIA1_i6	420	150	-	-	236	99	41400000	5500000	-	-	1660
HPP-2-35-FIA3_i1a	120	200	-	-	5100	1700	155000000	33000000	17200	9400	-
HPP-2-35-FIA3_i2	250	350	60	130	1700	1900	80000000	12000000	20000	31000	170
HPP-2-35-FIA3_i4	900	1300	50	130	2600	2200	170000000	12000000	69000	60000	-
HPP-2-35-FIA3_i6b	380	280	-	-	3810	570	99900000	18000000	40000	12000	-
HPP-2-44-FIA3_i9	520	280	29	43	15000	1900	63000000	32000000	-	-	600
HPP-2-62-FIA2_i6a	60000	10000	1300	2600	20000	33000	220000000	390000000	1000	56000	26000
HPP-3-01b-FIA1_i3	60000	11000	-	-	30000	54000	100000000	1.80E+08	70000000	1.30E+07	-
HPP-3-01b-FIA1_i5	-	-	-	-	1660	790	13600000	2.80E+06	-	-	-
HPP-3-15-FIA2_i1	-	-	-	-	1800	1000	47000000	2.90E+06	-	-	1320
HPP-3-15-FIA2_i10	-	-	-	-	700	260	28000000	1.10E+06	-	-	902
HPP-3-15-FIA2_i11	-	-	-	-	2700	4300	52000000	7.70E+06	-	-	2000
HPP-3-15-FIA2_i12	-	-	22	89	80000	14000	160000000	2.90E+07	-	-	2600
HPP-3-15-FIA2_i2	-	-	-	-	500	250	14000000	1.00E+06	4300	5300	940
HPP-3-15-FIA2_i5	-	-	90	170	-	-	-	-	60000000	1.10E+06	-
HPP-3-15-FIA2_i7	-	-	9	8.5	970	380	21000000	1.20E+06	-	-	1170
HPP-3-15-FIA2_i8	70	100	12	12	570	350	22000000	1.40E+06	-	-	1670
HPP-3-15-FIA2_i9a	-	-	220	440	1710	850	39000000	2.00E+06	4700	9100	1160
HPP-3-15-FIA2_i9b	-	-	-	-	11000	17000	30000000	4.90E+07	-	-	80000
HPP-3-23-FIA3a_i5a	350	480	-	-	2280	540	25400000	3.70E+06	-	-	1600
HPP-3-23-FIA3a_i5b	560	380	-	-	1690	380	22700000	3.20E+06	240000	190000	800
HPP-4-01-FIA3_i1a	380	230	-	-	1280	690	77000000	3.70E+06	-	-	1200
HPP-4-01-FIA3_i1c	500	700	-	-	2400	1600	21000000	1.80E+07	-	-	-
HPP-4-01-FIA3_i2a	560	460	60	92	550	230	69000000	4.60E+06	-	-	1300
HPP-4-01-FIA3_i4b	240	250	-	-	5100	1300	22200000	3.80E+06	-	-	2000
HPP-4-01-FIA3_i5a	640	530	-	-	1700	1200	19800000	8.60E+06	-	-	-
HPP-4-01-FIA3_i8	400	300	-	-	1290	770	97000000	6.30E+06	17000	26000	850
HPP-4-08-FIA1_i1b	4300	7400	-	-	300	1400	700000000	1.20E+08	9000000	1.60E+06	35000
HPP-4-08-FIA1_i4	290	470	190	300	550	930	85000000	6.00E+06	46000	87000	1400

Full ID	K ±2SE (ppm)	Ca(43) (ppm)	Ca(43) ±2SE (ppm)	Ca(44) (ppm)	Ca(44) ±2SE (ppm)	Fe(54) (ppm)	Fe(54) ±2SE (ppm)	Fe(57) (ppm)	Fe(57) ±2SE (ppm)	Co (ppm)	Co ±2SE (ppm)
HPP-1-24b-FIA2_i1b	1700	70000	60000	40000	32000	1000	2100	-	-	-	-
HPP-1-24b-FIA2_i3c		-		-		-		1300	2700	27	40
HPP-1-24b-FIA2_i4a		-		-		-		-		-	
HPP-2-06-FIA4_i1	810	-		40000	11000	-		-		-	
HPP-2-06-FIA4_i2		-		-		-		-		-	
HPP-2-10-FIA2_i5	95	-		-		-		-		-	
HPP-2-22-FIA1_i13		-		-		-		-		-	
HPP-2-22-FIA1_i1b	290	-		-		-		-		-	
HPP-2-22-FIA1_i6	750	-		-		-		-		-	
HPP-2-35-FIA3_i1a		-		100000	27000	-		-		-	
HPP-2-35-FIA3_i2	860	-		50000	12000	70000	14000	670	960	-	
HPP-2-35-FIA3_i4		-		17000	64000	-		-		28	66
HPP-2-35-FIA3_i6b		-		-		-		-		-	
HPP-2-44_FIA3_i9	1300	-		600000	140000	2600	6600	800	1100	-	
HPP-2-62-FIA2_i6a	54000	-		-		210000	380000	-		-	
HPP-3-01b-FIA1_i3		-		-		8000000	1.50E+06	80000	14000	-	
HPP-3-01b-FIA1_i5		-		50000	26000	50000	15000	-		-	
HPP-3-15-FIA2_i1	370	17000	19000	-		-		-		-	
HPP-3-15-FIA2_i10	94	-		-		1700	2200	-		-	
HPP-3-15-FIA2_i11	2300	40000	13000	1400	1900	2400	5600	-		-	
HPP-3-15-FIA2_i12	2400	600000	140000	-		-		600	1200	-	
HPP-3-15-FIA2_i2	110	-		70000	10000	-		170	400	1.6	1.8
HPP-3-15-FIA2_i5		-		-		3400	5700	-		12	23
HPP-3-15-FIA2_i7	330	-		1000	1900	100	1100	-		-	
HPP-3-15-FIA2_i8	630	-		6600	7300	500	1700	-		-	
HPP-3-15-FIA2_i9a	180	-		-		370	920	-		-	
HPP-3-15-FIA2_i9b	12000	180000	380000	16000	29000	-		-		-	
HPP-3-23-FIA3a_i5a	1900	-		-		-		1800	1600	-	
HPP-3-23-FIA3a_i5b	1800	-		80000	14000	-		-		-	
HPP-4-01-FIA3_i1a	1300	100000	54000	-		-		-		-	
HPP-4-01-FIA3_i1c		-		-		19000	36000	500	1500	-	
HPP-4-01-FIA3_i2a	630	-		11000	11000	-		-		-	
HPP-4-01-FIA3_i4b	1300	-		-		-		600	1100	-	
HPP-4-01-FIA3_i5a		-		-		11000	30000	-		-	
HPP-4-01-FIA3_i8	910	-		-		-		-		-	
HPP-4-08-FIA1_i1b	66000	-		200000	460000	-		-		-	
HPP-4-08-FIA1_i4	1800	100000	150000	-		-		300	1400	-	

Full ID	Ni (ppm)	Ni ±2SE (ppm)	Cu (ppm)	Cu ±2SE (ppm)	Zn(66) (ppm)	Zn(66) ±2SE (ppm)	Zn(68) (ppm)	Zn(68) ±2SE (ppm)	As (ppm)	As ±2SE (ppm)	Rb (ppm)
HPP-1-24b-FIA2_i1b	-	-	-	-	80000	11000	-	-	170	140	26
HPP-1-24b-FIA2_i3c	120	260	-	-	-	-	1400	1400	70	170	9
HPP-1-24b-FIA2_i4a	-	-	450	940	-	-	3200	6200	-	-	-
HPP-2-06-FIA4_i1	-	-	-	-	-	-	-	-	47	46	6.8
HPP-2-06-FIA4_i2	-	-	44	83	-	-	-	-	-	-	4.6
HPP-2-10-FIA2_i5	7	14	26	23	-	-	60	120	107	48	2.1
HPP-2-22-FIA1_i13	-	-	162	81	-	-	-	-	21	47	12.4
HPP-2-22-FIA1_i1b	-	-	-	-	-	-	-	-	-	-	13
HPP-2-22-FIA1_i6	-	-	-	-	-	-	-	-	-	-	16.9
HPP-2-35-FIA3_i1a	-	-	57	76	470	600	900	1900	-	-	28
HPP-2-35-FIA3_i2	-	-	-	-	310	640	-	-	260	320	80
HPP-2-35-FIA3_i4	-	-	150	250	-	-	-	-	-	-	8
HPP-2-35-FIA3_i6b	-	-	-	-	360	300	840	580	-	-	13.4
HPP-2-44-FIA3_i9	-	-	-	-	-	-	320	410	-	-	-
HPP-2-62-FIA2_i6a	-	-	-	-	80000	18000	-	-	-	-	-
HPP-3-01b-FIA1_i3	80000	17000	-	-	-	-	-	-	-	-	-
HPP-3-01b-FIA1_i5	-	-	70	220	660	720	1700	1900	-	-	20
HPP-3-15-FIA2_i1	20	39	-	-	-	-	-	-	41	32	10.5
HPP-3-15-FIA2_i10	-	-	-	-	-	-	-	-	-	-	13.6
HPP-3-15-FIA2_i11	-	-	50	110	-	-	-	-	80	150	15.6
HPP-3-15-FIA2_i12	80	160	-	-	490	950	-	-	-	-	21
HPP-3-15-FIA2_i2	-	-	-	-	50	120	-	-	-	-	17.8
HPP-3-15-FIA2_i5	-	-	70	140	-	-	-	-	100	190	20.4
HPP-3-15-FIA2_i7	9	11	-	-	-	-	60	54	-	-	13.8
HPP-3-15-FIA2_i8	-	-	-	-	-	-	-	-	-	-	30
HPP-3-15-FIA2_i9a	-	-	-	-	-	-	-	-	-	-	30
HPP-3-15-FIA2_i9b	-	-	-	-	140	220	2000	3800	-	-	61
HPP-3-23-FIA3a_i5a	-	-	410	280	-	-	-	-	110	140	16
HPP-3-23-FIA3a_i5b	-	-	-	-	-	-	1100	1700	-	-	17
HPP-4-01-FIA3_i1a	120	160	-	-	-	-	-	-	-	-	39
HPP-4-01-FIA3_i1c	-	-	-	-	-	-	2100	3100	140	270	16
HPP-4-01-FIA3_i2a	-	-	70	110	320	670	500	1800	60	110	12.1
HPP-4-01-FIA3_i4b	-	-	-	-	-	-	-	-	-	-	26
HPP-4-01-FIA3_i5a	-	-	70	110	-	-	-	-	-	-	5.1
HPP-4-01-FIA3_i8	-	-	-	-	-	-	700	1300	-	-	9
HPP-4-08-FIA1_i1b	-	-	-	-	-	-	50000	11000	-	-	38
HPP-4-08-FIA1_i4	170	250	250	190	-	-	2600	2800	-	-	15

Full ID	Rb ±2SE (ppm)	Sr (ppm)	Sr ±2SE (ppm)	Mo (ppm)	Mo ±2SE (ppm)	Ag (ppm)	Ag ±2SE (ppm)	Sn (ppm)	Sn ±2SE (ppm)	Sb (ppm)	Sb ±2SE (ppm)
HPP-1-24b-FIA2_i1b	22	4.3	5.8	-	-	-	-	200	150	-	-
HPP-1-24b-FIA2_i3c	15	14	13	-	-	-	-	-	-	-	-
HPP-1-24b-FIA2_i4a	-	-	-	-	-	-	-	1000	1300	-	-
HPP-2-06-FIA4_i1	8.2	-	-	-	-	-	-	-	-	-	-
HPP-2-06-FIA4_i2	5.4	1.8	4.2	-	-	-	-	-	-	-	-
HPP-2-10-FIA2_i5	2	3.4	2.8	-	-	-	-	-	-	-	-
HPP-2-22-FIA1_i13	8	1.8	3.9	-	-	-	-	-	-	-	-
HPP-2-22-FIA1_i1b	11	4.9	5.9	-	-	-	-	60	77	2.8	6.5
HPP-2-22-FIA1_i6	6.2	-	-	-	-	-	-	35	40	-	-
HPP-2-35-FIA3_i1a	15	-	-	-	-	-	-	150	140	-	-
HPP-2-35-FIA3_i2	130	-	-	-	-	-	-	80	110	-	-
HPP-2-35-FIA3_i4	16	2.5	6.2	-	-	-	-	190	210	-	-
HPP-2-35-FIA3_i6b	9.7	-	-	-	-	-	-	115	92	-	-
HPP-2-44-FIA3_i9	-	-	-	43	59	-	-	170	160	-	-
HPP-2-62-FIA2_i6a	-	-	-	-	-	-	-	1800	3200	-	-
HPP-3-01b-FIA1_i3	-	-	-	2000	3900	-	-	800	1700	-	-
HPP-3-01b-FIA1_i5	19	-	-	-	-	-	-	-	-	-	-
HPP-3-15-FIA2_i1	9.1	29	15	-	-	-	-	22	33	-	-
HPP-3-15-FIA2_i10	3.6	39	12	-	-	-	-	34	19	-	-
HPP-3-15-FIA2_i11	8.8	22	10	-	-	-	-	70	140	-	-
HPP-3-15-FIA2_i12	11	27	13	-	-	-	-	-	-	-	-
HPP-3-15-FIA2_i2	7.1	29	11	-	-	-	-	16	15	-	-
HPP-3-15-FIA2_i5	9.5	-	-	13	28	6	12	140	290	-	-
HPP-3-15-FIA2_i7	3.1	25.9	4.7	-	-	0.9	1.7	9.2	6.8	-	-
HPP-3-15-FIA2_i8	11	34	12	-	-	-	-	18	21	-	-
HPP-3-15-FIA2_i9a	11	26	11	-	-	-	-	34	17	-	-
HPP-3-15-FIA2_i9b	53	51	44	-	-	-	-	-	-	-	-
HPP-3-23-FIA3a_i5a	18	-	-	-	-	-	-	220	200	-	-
HPP-3-23-FIA3a_i5b	11	-	-	-	-	-	-	153	96	-	-
HPP-4-01-FIA3_i1a	33	12	10	-	-	-	-	-	-	-	-
HPP-4-01-FIA3_i1c	20	20	25	-	-	-	-	180	200	-	-
HPP-4-01-FIA3_i2a	7.9	5.1	6.1	-	-	18	39	-	-	-	-
HPP-4-01-FIA3_i4b	17	13.3	9.5	-	-	-	-	150	110	-	-
HPP-4-01-FIA3_i5a	6.8	22	20	1	19	-	-	160	140	-	-
HPP-4-01-FIA3_i8	11	3.1	3.5	-	-	-	-	160	190	-	-
HPP-4-08-FIA1_i1b	52	-	-	-	-	-	-	600	1300	-	-
HPP-4-08-FIA1_i4	14	-	-	-	-	-	-	-	-	-	-

Full ID	Cs (ppm)	Cs ±2SE (ppm)	Ba (ppm)	Ba ±2SE (ppm)	La (ppm)	La ±2SE (ppm)	W (ppm)	W ±2SE (ppm)	Pb (ppm)	Pb ±2SE (ppm)	Bi (ppm)	Bi ±2SE (ppm)
HPP-1-24b-FIA2_i1b	119	33	-	-	140	250	-	-	-	-	-	-
HPP-1-24b-FIA2_i3c	50	16	-	-	-	-	-	-	-	-	-	-
HPP-1-24b-FIA2_i4a	73	73	-	-	-	-	-	-	-	-	-	-
HPP-2-06-FIA4_i1	10.2	7.1	-	-	-	-	-	-	-	-	-	-
HPP-2-06-FIA4_i2	3.9	4.2	-	-	-	-	-	-	-	-	-	-
HPP-2-10-FIA2_i5	1.11	0.88	-	-	0.15	0.31	-	-	24	14	-	-
HPP-2-22-FIA1_i13	11.5	7.2	-	-	-	-	-	-	28.1	6.5	-	-
HPP-2-22-FIA1_i1b	1.9	2.6	-	-	-	-	-	-	-	-	-	-
HPP-2-22-FIA1_i6	28.8	7.1	-	-	-	-	-	-	-	-	-	-
HPP-2-35-FIA3_i1a	48	20	-	-	-	-	-	-	-	-	8	10
HPP-2-35-FIA3_i2	31	50	-	-	-	-	0.8	1.7	-	-	-	-
HPP-2-35-FIA3_i4	2.2	4.4	-	-	-	-	-	-	-	-	-	-
HPP-2-35-FIA3_i6b	25	13	-	-	-	-	48	32	-	-	-	-
HPP-2-44-FIA3_i9	5.6	4.5	-	-	-	-	-	-	-	-	-	-
HPP-2-62-FIA2_i6a	330	550	-	-	-	-	-	-	-	-	-	-
HPP-3-01b-FIA1_i3	-	-	-	-	-	-	-	-	-	-	-	-
HPP-3-01b-FIA1_i5	18	15	-	-	-	-	-	-	17	22	-	-
HPP-3-15-FIA2_i1	16.3	7.2	-	-	-	-	-	-	1.4	5.6	-	-
HPP-3-15-FIA2_i10	15.8	5.7	-	-	-	-	-	-	-	-	-	-
HPP-3-15-FIA2_i11	43	46	-	-	-	-	-	-	-	-	-	-
HPP-3-15-FIA2_i12	80	110	-	-	-	-	-	-	-	-	-	-
HPP-3-15-FIA2_i2	19.5	8.8	-	-	-	-	-	-	-	-	-	-
HPP-3-15-FIA2_i5	-	-	5	11	0.29	0.61	-	-	4.6	8.6	-	-
HPP-3-15-FIA2_i7	20	5.1	-	-	-	-	-	-	-	-	-	-
HPP-3-15-FIA2_i8	37	15	-	-	-	-	-	-	-	-	-	-
HPP-3-15-FIA2_i9a	22.8	7.9	0.4	1.6	1.6	2.3	-	-	2.7	3.2	-	-
HPP-3-15-FIA2_i9b	60	69	-	-	-	-	-	-	1.5	6.5	-	-
HPP-3-23-FIA3a_i5a	16	11	-	-	5.8	8.1	-	-	61	42	-	-
HPP-3-23-FIA3a_i5b	20	8.9	-	-	-	-	-	-	-	-	-	-
HPP-4-01-FIA3_i1a	11.2	8.3	-	-	-	-	-	-	-	-	-	-
HPP-4-01-FIA3_i1c	131	96	-	-	-	-	41	38	4	12	-	-
HPP-4-01-FIA3_i2a	33	19	-	-	-	-	28	56	-	-	7	15
HPP-4-01-FIA3_i4b	74	17	-	-	-	-	-	-	3	10	-	-
HPP-4-01-FIA3_i5a	66	25	-	-	-	-	-	-	-	-	-	-
HPP-4-01-FIA3_i8	22	13	-	-	-	-	-	-	-	-	-	-
HPP-4-08-FIA1_i1b	380	730	-	-	-	-	-	-	900	1800	-	-
HPP-4-08-FIA1_i4	10.5	7.8	-	-	-	-	-	-	7	12	-	-

F.2.2: RAW LA-ICP-MS DATA FOR HOST QUARTZ OF SELECT INCLUSIONS

Full ID	Sample ID	Assemblage ID	LA-ICP-MS Run ID	Feature Type	Li (ppm)	Li ±2SE (ppm)	B (ppm)	B ±2SE (ppm)	Mg (ppm)	Mg ±2SE (ppm)	Al (ppm)	Al ±2SE (ppm)	Si (ppm)	Si ±2SE (ppm)
HPP-1-24b-FIA2_i1b_SiO2	HPP-1-24	FIA2	i1b	Miarolitic Cavity	12.5	2.8	-	-	-	-	-	-	73.4	7
HPP-1-24b-FIA2_i3c_SiO2	HPP-1-24	FIA2	i3c	Miarolitic Cavity	9.3	2.9	-	-	-	-	-	-	79.2	9.4
HPP-1-24b-FIA2_i4a_SiO2	HPP-1-24	FIA2	i4a	Miarolitic Cavity	6.4	2.5	-	-	26	16	-	-	80	11
HPP-2-06-FIA4_j1_SiO2	HPP-2-06	FIA4	i1	Type (I) Quartz Vein	5.2	1.4	-	-	27	13	-	-	39.5	5.2
HPP-2-06-FIA4_j2_SiO2	HPP-2-06	FIA4	i2	Type (I) Quartz Vein	-	-	-	-	31	18	2.6	1.4	38.9	6.8
HPP-2-10-FIA2_i5_SiO2	HPP-2-10	FIA2	i5	Aplite	-	-	-	-	-	-	9.6	5.8	70	17
HPP-2-22-FIA1_i13_SiO2	HPP-2-22	FIA1	i13	Type (I) Quartz Vein	-	-	-	-	-	-	-	-	231	44
HPP-2-22-FIA1_i1b_SiO2	HPP-2-22	FIA1	i1b	Type (I) Quartz Vein	5.2	2.3	-	-	-	-	-	-	33.8	6.3
HPP-2-22-FIA1_i6_SiO2	HPP-2-22	FIA1	i6	Type (I) Quartz Vein	6	2.1	-	-	-	-	-	-	34.8	5
HPP-2-35-FIA3_i1a_SiO2	HPP-2-35	FIA3	i1a	QF Pegmatite	9.5	4.4	-	-	-	-	-	-	97	23
HPP-2-35-FIA3_i2_SiO2	HPP-2-36	FIA3	i2	QF Pegmatite	6.1	1.9	-	-	-	-	-	-	93	25
HPP-2-35-FIA3_i4_SiO2	HPP-2-37	FIA3	i4	QF Pegmatite	7.3	2.9	-	-	-	-	-	-	50.6	7.8
HPP-2-35-FIA3_i6b_SiO2	HPP-2-38	FIA3	i6b	QF Pegmatite	5.9	2.6	-	-	-	-	-	-	86	15
HPP-2-44-FIA3_i9_SiO2	HPP-2-44	FIA3	i9	Aplite (Layered QF Pegmatite)	8.1	1.8	-	-	-	-	-	-	149	24
HPP-2-62-FIA2_i6a_SiO2	HPP-2-62	FIA2	i6a	QF Pegmatite	4.5	1.4	-	-	-	-	-	-	53.2	6.5
HPP-3-01b-FIA1_i3_SiO2	HPP-3-01b	FIA1	i3	MQF Pegmatite	6.8	2	-	-	-	-	-	-	66	8.2
HPP-3-01b-FIA1_i5_SiO2	HPP-3-01b	FIA1	i5	MQF Pegmatite	7.9	2	8.7	6.7	-	-	-	-	63.3	8.6
HPP-3-15-FIA2_i1_SiO2	HPP-3-15	FIA2	i1	QF Pegmatite	11.3	1.1	-	-	19.1	5.7	-	-	173	12
HPP-3-15-FIA2_i10_SiO2	HPP-3-15	FIA2	i10	QF Pegmatite	11.6	1.3	-	-	-	-	-	-	170	12
HPP-3-15-FIA2_i11_SiO2	HPP-3-15	FIA2	i11	QF Pegmatite	8.8	1.5	-	-	47	13	-	-	187	14
HPP-3-15-FIA2_i12_SiO2	HPP-3-15	FIA2	i12	QF Pegmatite	11.2	1.8	-	-	35	14	-	-	185	13
HPP-3-15-FIA2_i2_SiO2	HPP-3-15	FIA2	i2	QF Pegmatite	11.1	1.7	-	-	16	10	-	-	179	13
HPP-3-15-FIA2_i5_SiO2	HPP-3-15	FIA2	i5	QF Pegmatite	11.8	1.7	-	-	-	-	-	-	138.3	9.8
HPP-3-15-FIA2_i7_SiO2	HPP-3-15	FIA2	i7	QF Pegmatite	10.6	1.3	-	-	13.2	6.7	-	-	185	12
HPP-3-15-FIA2_i8_SiO2	HPP-3-15	FIA2	i8	QF Pegmatite	11.2	1.3	-	-	-	-	-	-	166	10
HPP-3-15-FIA2_i9a_SiO2	HPP-3-15	FIA2	i9a	QF Pegmatite	8.5	1.6	-	-	14.8	7.7	-	-	153	21
HPP-3-15-FIA2_i9b_SiO2	HPP-3-15	FIA2	i9b	QF Pegmatite	9.7	2.1	-	-	17.7	7.7	-	-	152	17
HPP-3-23-FIA3a_i5a_SiO2	HPP-3-23	FIA3a	i5a	Type (III) Quartz Vein	4	1.1	-	-	-	-	-	-	40.7	4.1
HPP-3-23-FIA3a_i5b_SiO2	HPP-3-23	FIA3a	i5b	Type (III) Quartz Vein	4.4	1.3	-	-	-	-	-	-	40.2	4.6
HPP-4-01-FIA3_i1a_SiO2	HPP-4-01	FIA3	i1a	Type (II) (skarn) Quartz Vein	7.3	1.7	-	-	-	-	-	-	66.6	7.4
HPP-4-01-FIA3_i1c_SiO2	HPP-4-01	FIA3	i1c	Type (II) (skarn) Quartz Vein	5.7	2.8	-	-	-	-	-	-	45	11
HPP-4-01-FIA3_i2a_SiO2	HPP-4-01	FIA3	i2a	Type (II) (skarn) Quartz Vein	6.8	1.7	-	-	-	-	-	-	90	11
HPP-4-01-FIA3_i4b_SiO2	HPP-4-01	FIA3	i4b	Type (II) (skarn) Quartz Vein	8.8	2.3	-	-	-	-	-	-	83	11
HPP-4-01-FIA3_i5a_SiO2	HPP-4-01	FIA3	i5a	Type (II) (skarn) Quartz Vein	3.6	1	-	-	-	-	-	-	58	14
HPP-4-01-FIA3_i8_SiO2	HPP-4-01	FIA3	i8	Type (II) (skarn) Quartz Vein	5.8	2.4	-	-	107	29	-	-	64	13
HPP-4-08-FIA1_i1b_SiO2	HPP-4-08	FIA1	i1b	Type (III) Quartz Vein	4.6	1.5	-	-	-	-	-	-	34.3	5.8
HPP-4-08-FIA1_i4_SiO2	HPP-4-08	FIA1	i4	Type (III) Quartz Vein	1.39	0.7	-	-	-	-	-	-	26.2	4

Full ID	Cl (ppm)	Cl ±2SE (ppm)	K (ppm)	K ±2SE (ppm)	Ca(43) (ppm)	Ca(43) ±2SE (ppm)	Ca(44) (ppm)	Ca(44) ±2SE (ppm)	Fe(54) (ppm)	Fe(54) ±2SE (ppm)	Fe(57) (ppm)	Fe(57) ±2SE (ppm)	Co (ppm)	Co ±2SE (ppm)	Ni (ppm)
HPP-1-24b-FIA2_11b_SiO2	-	-	-	-	-	-	-	-	6	39	-	-	0.08	0.18	-
HPP-1-24b-FIA2_13c_SiO2	50	270	30	67	-	-	-	-	9	36	-	-	-	-	-
HPP-1-24b-FIA2_14a_SiO2	-	-	120	130	-	-	-	-	-	-	-	-	-	-	-
HPP-2-06-FIA4_11_SiO2	-	-	7	15	-	-	-	-	23	95	-	-	-	-	-
HPP-2-06-FIA4_12_SiO2	-	-	-	-	-	-	-	-	150	150	54	23	-	-	-
HPP-2-10-FIA2_15_SiO2	-	-	-	-	-	-	-	-	-	-	-	-	-	-	-
HPP-2-22-FIA1_113_SiO2	480	470	-	-	-	-	-	-	130	490	-	-	-	-	-
HPP-2-22-FIA1_11b_SiO2	30	130	18	36	-	-	-	-	32	82	-	-	-	-	-
HPP-2-22-FIA1_16_SiO2	-	-	38	34	-	-	-	-	-	-	-	-	-	-	-
HPP-2-35-FIA3_11a_SiO2	2590	910	-	-	-	-	-	-	-	-	48	46	-	-	-
HPP-2-35-FIA3_12_SiO2	1330	370	-	-	-	-	-	-	-	-	-	-	-	-	-
HPP-2-35-FIA3_14_SiO2	1980	580	-	-	-	-	-	-	-	-	-	-	-	-	-
HPP-2-35-FIA3_16b_SiO2	2390	620	-	-	-	-	-	-	90	430	-	-	-	-	-
HPP-2-44_FIA3_19_SiO2	-	-	38	27	-	-	-	-	70	200	-	-	-	-	-
HPP-2-62-FIA2_16a_SiO2	-	-	-	-	-	-	-	-	-	-	-	-	-	-	-
HPP-3-01b-FIA1_13_SiO2	-	-	-	-	-	-	-	-	20	460	-	-	-	-	-
HPP-3-01b-FIA1_15_SiO2	-	-	-	-	-	-	-	-	-	-	-	-	-	-	-
HPP-3-15-FIA2_11_SiO2	1500	730	40	10	-	-	-	-	-	-	-	-	-	-	-
HPP-3-15-FIA2_110_SiO2	-	-	21	11	-	-	-	-	-	-	-	-	-	-	-
HPP-3-15-FIA2_111_SiO2	-	-	27	16	-	-	-	-	-	-	-	-	-	-	-
HPP-3-15-FIA2_112_SiO2	-	-	20	15	-	-	-	-	-	-	-	-	-	-	-
HPP-3-15-FIA2_12_SiO2	790	820	30	12	-	-	-	-	40	130	-	-	-	-	-
HPP-3-15-FIA2_15_SiO2	700	1600	28	15	-	-	-	-	80	140	-	-	-	-	-
HPP-3-15-FIA2_17_SiO2	360	600	34.9	6.4	-	-	-	-	-	-	-	-	-	-	-
HPP-3-15-FIA2_18_SiO2	90	780	29.1	9.1	-	-	-	-	5	83	-	-	-	-	-
HPP-3-15-FIA2_19a_SiO2	-	-	35	15	-	-	-	-	2	83	-	-	-	-	-
HPP-3-15-FIA2_19b_SiO2	-	-	11	14	-	-	-	-	-	-	-	-	-	-	-
HPP-3-23-FIA3a_15a_SiO2	1200	1500	-	-	-	-	-	-	-	-	-	-	-	-	-
HPP-3-23-FIA3a_15b_SiO2	-	-	-	-	-	-	-	-	70	420	-	-	-	-	-
HPP-4-01-FIA3_11a_SiO2	-	-	10	20	-	-	-	-	10	180	-	-	-	-	-
HPP-4-01-FIA3_11c_SiO2	1500	2800	12	55	-	-	-	-	170	560	-	-	-	-	-
HPP-4-01-FIA3_12a_SiO2	-	-	10	16	-	-	-	-	-	-	-	-	-	-	-
HPP-4-01-FIA3_14b_SiO2	100	1300	9	25	-	-	-	-	30	220	-	-	-	-	-
HPP-4-01-FIA3_15a_SiO2	-	-	-	-	-	-	-	-	-	-	-	-	-	-	-
HPP-4-01-FIA3_18_SiO2	400	2400	29	42	-	-	-	-	40	500	-	-	-	-	-
HPP-4-08-FIA1_11b_SiO2	-	-	-	-	-	-	-	-	310	220	-	-	-	-	-
HPP-4-08-FIA1_14_SiO2	400	1000	-	-	-	-	-	-	-	-	-	-	-	-	-

Full ID	Ni ±2SE (ppm)	Cu (ppm)	Cu ±2SE (ppm)	Zn(66) (ppm)	Zn(66) ±2SE (ppm)	Zn(68) (ppm)	Zn(68) ±2SE (ppm)	As (ppm)	As ±2SE (ppm)	Rb (ppm)	Rb ±2SE (ppm)	Sr (ppm)	Sr ±2SE (ppm)	Mo (ppm)	Mo ±2SE (ppm)
HPP-1-24b-FIA2_i1b_SiO2	-	-	-	20	27	-	-	-	-	-	-	-	-	-	-
HPP-1-24b-FIA2_i3c_SiO2	-	-	-	-	-	-	-	-	-	-	-	-	-	-	-
HPP-1-24b-FIA2_i4a_SiO2	-	-	-	-	-	-	-	-	-	-	-	-	-	-	-
HPP-2-06-FIA4_i1_SiO2	-	-	-	-	-	-	-	-	-	-	-	-	-	-	-
HPP-2-06-FIA4_i2_SiO2	-	-	-	-	-	-	-	-	-	-	-	-	-	-	-
HPP-2-10-FIA2_i5_SiO2	-	-	-	-	-	-	-	78	16	-	-	0.67	0.43	-	-
HPP-2-22-FIA1_i13_SiO2	-	-	-	27	86	-	-	-	-	-	-	-	-	-	-
HPP-2-22-FIA1_i1b_SiO2	-	-	-	-	-	-	-	-	-	-	-	-	-	-	-
HPP-2-22-FIA1_i6_SiO2	-	-	-	-	-	-	-	-	-	-	-	-	-	-	-
HPP-2-35-FIA3_i1a_SiO2	-	-	-	26	66	-	-	-	-	-	-	-	-	-	-
HPP-2-35-FIA3_i2_SiO2	-	-	-	23	23	-	-	-	-	-	-	-	-	-	-
HPP-2-35-FIA3_i4_SiO2	-	-	-	-	-	-	-	-	-	-	-	-	-	-	-
HPP-2-35-FIA3_i6b_SiO2	-	-	-	24	42	-	-	-	-	-	-	-	-	-	-
HPP-2-44_FIA3_i9_SiO2	-	-	-	10	17	-	-	-	-	-	-	-	-	-	-
HPP-2-62-FIA2_i6a_SiO2	-	-	-	-	-	-	-	-	-	-	-	-	-	-	-
HPP-3-01b-FIA1_i3_SiO2	-	-	-	-	-	-	-	-	-	-	-	-	-	-	-
HPP-3-01b-FIA1_i5_SiO2	-	-	-	-	-	-	-	-	-	0.21	0.19	-	-	-	-
HPP-3-15-FIA2_i1_SiO2	-	-	-	-	-	-	-	-	-	0.228	0.077	0.046	0.039	-	-
HPP-3-15-FIA2_i10_SiO2	-	-	-	-	-	-	-	-	-	0.168	0.077	0.049	0.046	-	-
HPP-3-15-FIA2_i11_SiO2	-	-	-	-	-	-	-	-	-	0.41	0.17	0.15	0.11	-	-
HPP-3-15-FIA2_i12_SiO2	-	-	-	-	-	-	-	-	-	0.21	0.14	-	-	-	-
HPP-3-15-FIA2_i2_SiO2	-	-	-	-	-	-	-	-	-	0.17	0.13	0.061	0.067	-	-
HPP-3-15-FIA2_i5_SiO2	-	-	-	-	-	-	-	-	-	-	-	-	-	-	-
HPP-3-15-FIA2_i7_SiO2	-	-	-	7.3	8.9	-	-	-	-	0.24	0.11	-	-	-	-
HPP-3-15-FIA2_i8_SiO2	-	-	-	-	-	-	-	-	-	0.156	0.079	-	-	-	-
HPP-3-15-FIA2_i9a_SiO2	-	-	-	-	-	-	-	-	-	0.18	0.11	0.052	0.058	-	-
HPP-3-15-FIA2_i9b_SiO2	-	-	-	14	16	-	-	-	-	0.22	0.15	0.11	0.14	-	-
HPP-3-23-FIA3a_i5a_SiO2	-	-	-	13	15	-	-	-	-	-	-	-	-	-	-
HPP-3-23-FIA3a_i5b_SiO2	-	-	-	-	-	-	-	-	-	-	-	-	-	-	-
HPP-4-01-FIA3_i1a_SiO2	-	-	-	-	-	-	-	-	-	-	-	-	-	-	-
HPP-4-01-FIA3_i1c_SiO2	-	-	-	-	-	-	-	-	-	-	-	-	-	-	-
HPP-4-01-FIA3_i2a_SiO2	-	-	-	-	-	-	-	-	-	-	-	0.09	0.088	-	-
HPP-4-01-FIA3_i4b_SiO2	-	-	-	-	-	-	-	-	-	-	-	0.15	0.12	-	-
HPP-4-01-FIA3_i5a_SiO2	-	-	-	10	19	-	-	-	-	-	-	-	-	-	-
HPP-4-01-FIA3_i8_SiO2	-	-	-	-	-	-	-	-	-	-	-	-	-	-	-
HPP-4-08-FIA1_i1b_SiO2	-	-	-	-	-	-	-	-	-	-	-	-	-	-	-
HPP-4-08-FIA1_i4_SiO2	-	-	-	-	-	-	-	-	-	-	-	-	-	-	-

Full ID	Sample ID	Feature Type	Chip ID	LA-ICP-MS Run ID	Analytical Notes
HPP-1-20-FIA2_i1b	HPP-1-20	Granite (altered)	FIA2	i1b	b chipped at start
HPP-1-20-FIA2_i1c	HPP-1-20	Granite (altered)	FIA2	i1c	c possible at 135 sec
HPP-1-20-FIA2_i2a	HPP-1-20	Granite (altered)	FIA2	i2a	maybe at 45 sec
HPP-1-20-FIA2_i4a	HPP-1-20	Granite (altered)	FIA2	i4a	maybe at 27 sec; two inclusions next to each other
HPP-1-20-FIA2_i4b	HPP-1-20	Granite (altered)	FIA2	i4b	?
HPP-1-20-FIA2_i5b	HPP-1-20	Granite (altered)	FIA2	i5b	Major crack/chip at first, possible inclusion at 54 sec
HPP-1-20-FIA2_i6a	HPP-1-20	Granite (altered)	FIA2	i6a	Maybe at 37 sec. Chipped at the start.
HPP-1-20-FIA2_i7a	HPP-1-20	Granite (altered)	FIA2	i7a	Pretty chippy, but (a) and maybe (b) @ 47 sec, 50 sec
HPP-1-24b-FIA2_i1b	HPP-1-24b	Miarolitic Cavity	FIA2	i1b	Maybe at 40 sec, more chippy than i1a
HPP-1-24b-FIA2_i2b	HPP-1-24b	Miarolitic Cavity	FIA2	i2b	(a) went right away with chip, (b) may be gone too
HPP-1-24b-FIA2_i3c	HPP-1-24b	Miarolitic Cavity	FIA2	i3c	Na peak at 65 sec
HPP-1-24b-FIA2_i4a	HPP-1-24b	Miarolitic Cavity	FIA2	i4a	Cracked, chipped. Na at starting ablation
HPP-1-24b-FIA2_i2c	HPP-1-24b	Miarolitic Cavity	FIA2	i2c	maybe at 5.5 sec; hit joystick at 90 sec
HPP-1-24b-FIA3_i9b2	HPP-1-24b	Miarolitic Cavity	FIA3	i9b2	Chipping
HPP-1-24b-FIA3_10a	HPP-1-24b	Miarolitic Cavity	FIA3	10a	Catastrophe
HPP-1-24b-FIA3_12a	HPP-1-24b	Miarolitic Cavity	FIA3	12a	Maybe at 55 sec

Full ID	Iolite Notes	Salinity (wt % eq. NaCl)	Elements strongly correlated with Na	Elements possibly correlated with Na
HPP-1-20-FIA2_i1b	Small Na spike on shoulder of initial, larger Na spike at start of ablation (likely a chip).	3.1		
HPP-1-20-FIA2_i1c	Three closely spaced Na spikes (first two more intense than third) approximately 2/3 through ablation. Cs matches with first peak and overlaps some with second peak.	3.1	Cs	
HPP-1-20-FIA2_i2a	Three Na spikes, decreasing with intensity after initial ablation peak. Second Na spike matches with broad, low Zn(68) peak, and overlaps the preceding Fe-K-Mg-Zn(66)-W peak	3.1		La, Zn(68)
HPP-1-20-FIA2_i4a	Two short Na spikes (first more intense) after Cu-Zn(68) peak. No matching precursor peak for second Na peak. Sr-La-Ag(?) peak between Na peaks.	3.1		
HPP-1-20-FIA2_i4b	One small, symmetrical Na spike after initial ablation peak. No other elements associated.	3.1		
HPP-1-20-FIA2_i5b	Isolated Na spike at 35% through ablation. Correlated with very thin B peak. Overlap with Cs peak.	3.1	B	
HPP-1-20-FIA2_i6a	Two Na peaks near beginning of ablation (could be chips). Second peak has some overlap with B.	3.1		B
HPP-1-20-FIA2_i7a	One thin Na-La spike with overlapping W anomaly at tail end	3.1	La	W
HPP-1-24b-FIA2_i1b	Short, but broad Na peak shortly after start of ablation, but not in initial peak. Well correlated with La. Some overlap with other peaks.	3.2	B, La	Mg, Zn(66), Rb
HPP-1-24b-FIA2_i2b	Very broad, faint Na anomaly (symmetrical). Correlates well with group of several Cs peaks.	3.2	Cs	B, Cu
HPP-1-24b-FIA2_i3c	Moderately broad, asymmetrical Na peak (only visible on log scale).	3.2	Cs, B	Li
HPP-1-24b-FIA2_i4a	Small, asymmetrical Na peak (only visible on log scale).	4.2	B, Cs	
HPP-1-24b-FIA2_i2c	One thin Na spike with overlapping La anomaly at start	4.2		La
HPP-1-24b-FIA3_i9b2	Relatively high, thin Na spike approximately 40% through ablation.	4.2	Pb	
HPP-1-24b-FIA3_10a	One, slightly broader Na peak after initial ablation spike (two initial Na peaks). Strongly correlated with La.	4.2	La	W
HPP-1-24b-FIA3_12a	Broad, weak Na anomaly with broad early plateau. Correlated well with a group of multiple Cs peaks.	4.2	Cs	La

Full ID	Sample ID	Feature Type	Chip ID	LA-ICP-MS Run ID	Analytical Notes
HPP-1-24b-FIA3_i15c	HPP-1-24b	Miarolitic Cavity	FIA3	i15c	at 65 sec
HPP-1-36a-FIA2_i3b	HPP-1-36a	Type (IV) Microcrystalline Quartz Vein	FIA2	i3b	Conchoidal fracture
HPP-1-36a-FIA2_i4	HPP-1-36a	Type (IV) Microcrystalline Quartz Vein	FIA2	i4	many inclusions in this run; maybe at 35 sec, 47 sec
HPP-1-73-FIA1a_i1a	HPP-1-73	Type (IV) Microcrystalline Quartz Vein	FIA1a	i1a	Maybe an inclusion at 58s
HPP-1-73-FIA1a_i2	HPP-1-73	Type (IV) Microcrystalline Quartz Vein	FIA1a	i2	catastrophic chipping, maybe at 36 sec
HPP-1-73-FIA1a_i4a	HPP-1-73	Type (IV) Microcrystalline Quartz Vein	FIA1a	i4a	Blew out quickly. Na peak at 52 sec.
HPP-1-73-FIA1a_i4b	HPP-1-73	Type (IV) Microcrystalline Quartz Vein	FIA1a	i4b	Fractured during last run, trying anyway. Maybe at 40 sec. *Possible feldspar contamination.
HPP-1-73-FIA1a_i5	HPP-1-73	Type (IV) Microcrystalline Quartz Vein	FIA1a	i5	Cracked. Possible inclusion at 60 sec.
HPP-1-73-FIA1a_i6	HPP-1-73	Type (IV) Microcrystalline Quartz Vein	FIA1a	i6	Conchoidal fracturing. Big peak at 36 sec.
HPP-1-73-FIA1a_i7	HPP-1-73	Type (IV) Microcrystalline Quartz Vein	FIA1a	i7	Fractured. Possible inclusion at 42 sec.
HPP-2-06-FIA3_i1	HPP-2-06	Type (I) Quartz Vein	FIA3	i1	Under a crack; chipped
HPP-2-06-FIA3_i3	HPP-2-06	Type (I) Quartz Vein	FIA3	i3	Chipped after two pulses, Na peak at ~75 sec from other inclusion?
HPP-2-06-FIA3_i4b	HPP-2-06	Type (I) Quartz Vein	FIA3	i4b	Both (a) and (b) chipped, but possible inclusion ablation at 45 sec and 95 sec.
HPP-2-06-FIA4_i1	HPP-2-06	Type (I) Quartz Vein	FIA4	i1	Initial Na peak, then at 70 sec (high quality Na peak)

Full ID	Iolite Notes	Salinity (wt % eq. NaCl)	Elements strongly correlated with Na	Elements possibly correlated with Na
HPP-1-24b-FIA3_i15c	One small Na spike with preceding K spike	4.2		
HPP-1-36a-FIA2_i3b	Relatively large Na peak approximately 25% through ablation. Matches well with one Cs spike, but there are other Cs spikes without Na	1.7		Cs
HPP-1-36a-FIA2_i4	Three small Na spikes (not including initial peak), with minor La spike with the first. Timing doesn't seem to match with analytical notes.	1.7		La
HPP-1-73-FIA1a_i1a	Short, intense Na spike approximately 50% through short ablation. Strong correlation with intense La peaks. Overlaps with subsequent Ca(44) peaks for this and initial Na peak.	3.7	La	Ca(44)
HPP-1-73-FIA1a_i2	One thin Na spike shortly after initial peak. Directly preceded (slightly overlapped) by Zn(68) spike. Perfectly matching Sn peak. Very small matching W peak. Inconsistent overlapping with La.	3.7	Sn	W
HPP-1-73-FIA1a_i4a	Small, sharp Na spike at 40% through ablation. Some overlap with Li, Fe(57) peaks.	3.7		Li, Fe(57)
HPP-1-73-FIA1a_i4b	Two short Na spikes on either side of a more intense Na anomaly that matches with K spike before steady increase of K (likely due to ablation of fspar). Also large, perfectly matching La spike.	3.7	La, K	
HPP-1-73-FIA1a_i5	Strange double Na peak about 50% through ablation before large Fe-K peak.	3.7	B	Li
HPP-1-73-FIA1a_i6	Single Na spike several seconds after initial Si peak (no Na). Correlates well with Li, B? (very small peak). Large Zn(68) peak before Na spike. Inversely correlated to La counts here.	3.7	Li	B
HPP-1-73-FIA1a_i7	Small Na peak very soon after start of ablation. Strongly correlated with Zn(66).	3.7	Piece of standard.	
HPP-2-06-FIA3_i1	Very small Na spike after initial chipping that correlates poorly with Al (slightly after), and Sn (only slightly above background).	2.9		Al, Sn
HPP-2-06-FIA3_i3	Later Na peak recorded is very small, but broad.	2.9	Cs	B
HPP-2-06-FIA3_i4b	Relatively large, thin Na spike well after initial Si peak. Well correlated with matching Rb spike, (also present at beginning of ablation). Overlap with large W spike and small Sb spike.	2.9	Rb	W, Sb
HPP-2-06-FIA4_i11	High quality, broad Na peak approximately 55% through ablation. Strongly correlated with Li, Cs	1.9	Li, Cs	

Full ID	Sample ID	Feature Type	Chip ID	LA-ICP-MS Run ID	Analytical Notes
HPP-2-06-FIA4_i2	HPP-2-06	Type (I) Quartz Vein	FIA4	i2	Trying 90 um surface cleaning pulses. Chips! At 95 sec (high quality Na peak).
HPP-2-06-FIA4_i5	HPP-2-06	Type (I) Quartz Vein	FIA4	i5	Chipped initially. 45 seconds; 50 seconds for the inclusions.
HPP-2-06-FIA4_i6	HPP-2-06	Type (I) Quartz Vein	FIA4	i6	Chipped, look for inclusion at ~45 sec.
HPP-2-10-FIA2_i5	HPP-2-10	Aplite	FIA2	i5	Chipped, but maybe at 35 sec.
HPP-2-22-FIA1_i1b	HPP-2-22	Type (I) Quartz Vein	FIA1	i1b	Yeah! 120 sec.
HPP-2-22-FIA1_i2a	HPP-2-22	Type (I) Quartz Vein	FIA1	i2a	Chipped
HPP-2-22-FIA1_i2b	HPP-2-22	Type (I) Quartz Vein	FIA1	i2b	Maybe at 37 sec. Definitely at 55 sec.
HPP-2-22-FIA1_i3a	HPP-2-22	Type (I) Quartz Vein	FIA1	i3a	Maybe at ~60 sec.
HPP-2-22-FIA1_i3b	HPP-2-22	Type (I) Quartz Vein	FIA1	i3b	Maybe at ~40 sec.
HPP-2-22-FIA1_i6	HPP-2-22	Type (I) Quartz Vein	FIA1	i6	Long weird peak at 65 sec.
HPP-2-22-FIA1_i7a	HPP-2-22	Type (I) Quartz Vein	FIA1	i7a	Okay at ~100 sec.
HPP-2-22-FIA1_i7b	HPP-2-22	Type (I) Quartz Vein	FIA1	i7b	Chips!
HPP-2-22-FIA1_i7c	HPP-2-22	Type (I) Quartz Vein	FIA1	i7c	Inclusion ablated at 35 sec (maybe at 30 sec). At 90 sec.
HPP-2-22-FIA1_i11	HPP-2-22	Type (I) Quartz Vein	FIA1	i11	Run with i10.
HPP-2-22-FIA1_i12	HPP-2-22	Type (I) Quartz Vein	FIA1	i12	Maybe at 45 sec.
HPP-2-22-FIA1_i13	HPP-2-22	Type (I) Quartz Vein	FIA1	i13	Catastrophe, but maybe an inclusion at 65 sec.

Full ID	Iolite Notes	Salinity (wt % eq. NaCl)	Elements strongly correlated with Na	Elements possibly correlated with Na
HPP-2-06-FIA4_i2	High quality, moderately broad, flat-topped Na peak approximately 75% through ablation.	1.9	Li, Cs, Rb, Sr	Ni
HPP-2-06-FIA4_i5	Several asymmetrical peaks, but one larger, central one. Correlates strongly with K, Li, and Cs.	1.9	K, Li, Cs, Pb	La
HPP-2-06-FIA4_i6	Very broad, but much higher than background, Na peak (only visible on log scale).	1.9	Rb, Li, Cs, Sb	
HPP-2-10-FIA2_i5	Broad, high-quality Na peak with preceding subpeak approximately halfway through ablation.	0.2	Al, Rb, Pb, Sr	B, Cu
HPP-2-22-FIA1_i1b	Beautiful, smooth, broad, and nearly symmetrical Na peak approximately 66% through ablation. Correlates perfectly with Li.	1.9	Li, Rb, B	
HPP-2-22-FIA1_i2a	Spiky, jagged Na peak with no clear apex approx 50% through ablation. Much larger, smoother Na peak at initial ablation spike that is correlated with Li, Cs, B?	1.9		Cs?
HPP-2-22-FIA1_i2b	Short, fairly broad peak with jagged top.	1.9	K, Al, Rb, Sr, Cs	
HPP-2-22-FIA1_i3a	Very broad, flat peak over final 30% of ablation; unclear if it's a single inclusion or two.	1.9	Cs, B, Rb	Li
HPP-2-22-FIA1_i3b	Small, somewhat broad Na peak near the end of ablation.	1.9	B, Li, Cs	
HPP-2-22-FIA1_i6	Very broad, symmetrical Na peak/hill over approx 25% of ablation period starting at ~50% through ablation. Perfectly correlated with Cs	1.9	Cs, Rb, B	
HPP-2-22-FIA1_i7a	Narrow Na peak tapering downward at approximately 25% through ablation.	1.9	Cs, Li	
HPP-2-22-FIA1_i7b	Short, broad Na peak with significant notch at the center.	1.9	Li	Sr
HPP-2-22-FIA1_i7c	Initial Na spike present. Two (1) and (2) short, broader peaks approx 45% and 60% through ablation, one (3) very intense, narrow Na spike at the end of ablation.	1.9	(1) ; (2) Cs; (3) Cs, Li, Rb, Pb	
HPP-2-22-FIA1_i11	Smooth, symmetrical Na peak much higher than background at approximately 70% through ablation. Thin Na spike earlier at approx. 25% through run.	1.9	Li,Rb	
HPP-2-22-FIA1_i12	Short, but relatively broad Na anomaly about double background values and approximately 35% through ablation.	1.9	B	Rb
HPP-2-22-FIA1_i13	Large, nearly symmetrical, smooth Na peak approximately 60% through ablation. Thin spike before at approximately 40% through ablation. Correlates well with several elements, slightly inconsistent with Rb.	1.9	Li, Cs, Pb	Rb, B

Full ID	Sample ID	Feature Type	Chip ID	LA-ICP-MS Run ID	Analytical Notes
HPP-2-35-FIA3_i1a	HPP-2-35	QF Pegmatite	FIA3	i1a	Cracking, but maybe at 50 sec?
HPP-2-35-FIA3_i1b	HPP-2-35	QF Pegmatite	FIA3	i1b	Weird peak; chipping.
HPP-2-35-FIA3_i2	HPP-2-35	QF Pegmatite	FIA3	i2	Chipped right away, but Na peak at 75 sec with no chip that we could see.
HPP-2-35-FIA3_i3	HPP-2-35	QF Pegmatite	FIA3	i3	~45 sec maybe. Definitely strong Na peak at 85 sec but ablation ended. Re-ablated at 120 sec with more Na peak?
HPP-2-35-FIA3_i4	HPP-2-35	QF Pegmatite	FIA3	i4	MINERAL INCLUSION: Na, Al, W? at 50 sec. Na peak at 65 sec.
HPP-2-35-FIA3_i5	HPP-2-35	QF Pegmatite	FIA3	i5	Chipped at start, but no Na peak then. Na peak at ~65 sec and ~80 sec.
HPP-2-35-FIA3_i6a	HPP-2-35	QF Pegmatite	FIA3	i6a	Chipped at first. Na peak at ~42 sec maybe, then Na-Al peak at 50 sec.
HPP-2-35-FIA3_i6b	HPP-2-35	QF Pegmatite	FIA3	i6b	115 sec, 120 sec
HPP-2-41a-FIA3_i2	HPP-2-41a	Type (III) Quartz Vein	FIA3	i2	Chipping!
HPP-2-41a-FIA3_i3a	HPP-2-41a	Type (III) Quartz Vein	FIA3	i3a	Solitary Na peak at 40 sec, but initial ablation very chippy. Same run as i3b.
HPP-2-41a-FIA3_i3b	HPP-2-41a	Type (III) Quartz Vein	FIA3	i3b	Same run as i3a. Maybe 110 and/or 115 sec, but might be chipping. Weird little peaks.
HPP-2-41a-FIA3_i4	HPP-2-41a	Type (III) Quartz Vein	FIA3	i4	Solitary Na peak at 40 sec.
HPP-2-44-FIA3_i3	HPP-2-44	Aplite (Layered QF Pegmatite)	FIA3	i3	Chipping. Al+Na peaks.
HPP-2-44-FIA3_i4	HPP-2-44	Aplite (Layered QF Pegmatite)	FIA3	i4	Chipped. Al peaks.

Full ID	Iolite Notes	Salinity (wt % eq. NaCl)	Elements strongly correlated with Na	Elements possibly correlated with Na
HPP-2-35-FIA3_i1a	Broad, low symmetrical Na peak approximately 50% through ablation.	2.2	Cs, Rb	B
HPP-2-35-FIA3_i1b	Rounded, fairly broad Na peak at start of ablation. May not represent just a fluid inclusion.	2.2	Cs, Rb, Li, B	Sr, Pb, La
HPP-2-35-FIA3_i2	Intense, moderately narrow Na peak much higher than background at ~70% through ablation. Followed by transient Na spike at ~80% through ablation.	2.2	Cs, Rb, B, Li, As	
HPP-2-35-FIA3_i3	Intense, moderately broad Na peak at the very end of ablation. When ablation was reinitiated, the peak continued, demonstrating considerable breadth.	2.2	B, Li, Cs, Rb	Mo
HPP-2-35-FIA3_i4	Two Na peaks, the first (1) (at 30% through ablation) is broader and tapers forward. The second (2) (at 50% through ablation) is narrow and sharp. The first is likely a mineral inclusion due to elemental associations.	2.2	(1) Al, K, Rb, Cs, Cu, Li; (2) B, Rb	(1) W, Te
HPP-2-35-FIA3_i5	One relatively small, pointed but moderately broad Na peak ~60% through ablation.	2.2		
HPP-2-35-FIA3_i6a	Low, very broad Na anomaly with at least three sub-peaks. However, central sub-peak at 30% through ablation is most intense.	2.2	Al, Cs	Rb, Li
HPP-2-35-FIA3_i6b	Has 3 Na peaks, (not counting) initial spike. (1) is broad, pointed, and asymmetrical and occurs at 25% through ablation. (2) is larger, broadest, and slightly asymmetrical and occurs at 50% through ablation. (3) is shorter than (2), broad, and asymmetrical, occurs at the end of ablation, and is a mineral inclusion due to high Al, K.	2.2	(1) B; (2) B, Cs, Rb; (3) Al, K, W, Rb	(1) As; (2) Li; (3) Ni
HPP-2-41a-FIA3_i2	Narrow, intense Na spike ~30% through ablation. May be the product of an ablated chip.	1.6	Pb	Li
HPP-2-41a-FIA3_i3a	Narrow, intense Na spike ~15% through ablation. May be the product of an ablated chip.	1.6		Li, Sr
HPP-2-41a-FIA3_i3b	Three or four strange peaks with variable breadth (some broad, others narrow) throughout ablation. Almost no elemental associations.	1.6		Li
HPP-2-41a-FIA3_i4	Two sharp, narrow, intense Na spikes. First (1) is less intense and slightly broader at 5% through ablation. Second (2) is very intense at 15% through ablation.	1.6	(1) W	(1) Ni; (2) As
HPP-2-44-FIA3_i3	Broad, relatively smooth double Na peak at 35% through ablation.	3.2	Al	Co
HPP-2-44-FIA3_i4	Moderately broad, pointed, then tapering Na peak near start of ablation, but after initial spike.	3.2		Cu, W

Full ID	Sample ID	Feature Type	Chip ID	LA-ICP-MS Run ID	Analytical Notes
HPP-2-44-FIA3_i5	HPP-2-44	Aplite (Layered QF Pegmatite)	FIA3	i5	~45 sec Na peak with matching Al peak
HPP-2-44-FIA3_i7	HPP-2-44	Aplite (Layered QF Pegmatite)	FIA3	i7	Chipping. Al peaks with matching minor Na peaks.
HPP-2-44-FIA3_i9	HPP-2-44	Aplite (Layered QF Pegmatite)	FIA3	i9	Chips at 60 sec. Al-Na peak.
HPP-2-62-FIA2_i1	HPP-2-62	QF Pegmatite	FIA2	i1	Fractured straight off in large chunks.
HPP-2-62-FIA2_i4	HPP-2-62	QF Pegmatite	FIA2	i4	~50 um deep, trying 90 um spot two times to start with, then 32 um. Still got chipping when starting with Na peak. Inclusion Na peak at 90 sec.
HPP-2-62-FIA2_i5a	HPP-2-62	QF Pegmatite	FIA2	i5a	Shooting just with 32 um spot size as it is only ~30 um deep. Chipping to start. Na-Al peak at ~50 sec.
HPP-2-62-FIA2_i5b	HPP-2-62	QF Pegmatite	FIA2	i5b	Next to i5a. Checking to see if included in i5 ablation. Al peak at 40-45 sec. Na peak at 38 sec.
HPP-2-62-FIA2_i6a	HPP-2-62	QF Pegmatite	FIA2	i6a	Chips at start. Maybe at 38 sec; another Na peak at 55 sec.
HPP-2-62-FIA2_i6b	HPP-2-62	QF Pegmatite	FIA2	i6b	Chips start at 105 sec. Maybe Na peak at 115 sec.
HPP-3-1b-FIA1_i1	HPP-3-1b	MQF Pegmatite	FIA1	i1	Some chip. Na peak at 50 sec; Na-Al peak together at 68 sec.
HPP-3-1b-FIA1_i3	HPP-3-1b	MQF Pegmatite	FIA1	i3	Cracks at first, Na +/- Al peak at 65 sec.
HPP-3-1b-FIA1_i4a	HPP-3-1b	MQF Pegmatite	FIA1	i4a	Chips at start. Possibly catastrophic. Ran out of time for b.
HPP-3-1b-FIA1_i5	HPP-3-1b	MQF Pegmatite	FIA1	i5	Chips. Maybe at 60 sec.
HPP-3-15-FIA2_i1	HPP-3-15	QF Pegmatite	FIA2	i1	Minor chipping; Intense Na peak at 85 sec.
HPP-3-15-FIA2_i2	HPP-3-15	QF Pegmatite	FIA2	i2	Minor cracking, then a shadow across sample. But strong Na peak at 55 sec.

Full ID	Iolite Notes	Salinity (wt % eq. NaCl)	Elements strongly correlated with Na	Elements possibly correlated with Na
HPP-2-44-FIA3_i5	Two narrow Na spikes; first (1) is thinner and at 20% through ablation, second (2) is slightly broader; (but still pointed) at 60% through ablation.	3.2	(1)Li, B; (2)Li, B, Cs	
HPP-2-44-FIA3_i7	Very broad Na anomaly with three sub-peaks beginning at approximately 20% through ablation after very intense initial Na spike.	3.2	Al, Li	Cs
HPP-2-44-FIA3_i9	Moderate Na peak with steep beginning and tapered ending approximately 55% through ablation.	3.2	Al, Li, B	
HPP-2-62-FIA2_i1	Short Na peak with large shoulder on left side very near to start of ablation. May be from a chip.	5.0	K, Al	La, B, Cu
HPP-2-62-FIA2_i4	Broad, low, pointed Na peak approximately 60% through ablation.	5.0	Rb, Sr	
HPP-2-62-FIA2_i5a	Very broad, roughly symmetrical Na anomaly approximately 30% through ablation.	5.0	Al, K, Rb, Cs	Pb, Sr
HPP-2-62-FIA2_i5b	Intense, narrow Na spike approximately 15% through ablation.	5.0	Pb	
HPP-2-62-FIA2_i6a	Narrow Na spike shortly after start of ablation, broader but shorter Na peak at approximately 35% through ablation.	5.0	Cs, Li	Pb
HPP-2-62-FIA2_i6b	Relatively short Na spike shortly after initial spike at the start of ablation.	5.0	Cs, Li	
HPP-3-1b-FIA1_i1	Two Na peaks. The first (1) is pointed, but only moderately broad and occurs at 25% through ablation. The second (2) is low, very broad, and mostly symmetrical with no major sub-peaks and occurs at ~60% through ablation.	3.6	(1) La; (2) Al, Cs, Co	(2) Rb, Li
HPP-3-1b-FIA1_i3	Highly asymmetrical Na peak with intense spike at start and gradual, broad, tapering finish. Starts at 50% through ablation.	3.6	Li, B, Rb, Cs, Al	
HPP-3-1b-FIA1_i4a	Intense, fairly broad Na peak with some tapering observed at the start of ablation. May be difficult to distinguish from chips and noise from the start of ablation.	3.6	Li, B, Rb, Cs, Al, La, As, Zn, Sr	Pb
HPP-3-1b-FIA1_i5	Broad, high-quality Na peak (not especially intense) at ~55% through ablation.	3.6	Rb, Cs	Ni
HPP-3-15-FIA2_i1	Very intense, fairly broad Na peak at ~70% through ablation and followed by narrow Na spike (less intense) and low, broad Na anomaly near the end of ablation.	3.9	K, Li, Cs, Rb, Sr	Cu
HPP-3-15-FIA2_i2	Very intense, fairly broad, high-quality Na peak at 55% through ablation.	3.9	K, Li, Cs, Rb, Sr, Co	

Full ID	Sample ID	Feature Type	Chip ID	LA-ICP-MS Run ID	Analytical Notes
HPP-3-15-FIA2_i3	HPP-3-15	QF Pegmatite	FIA2	i3	Initially chips, possibly gone at start of ablation.
HPP-3-15-FIA2_i5	HPP-3-15	QF Pegmatite	FIA2	i5	Minor chips at start. Maybe at 60 sec (very low Na peak) - NO. Good peak at 140 sec.
HPP-3-15-FIA2_i6a	HPP-3-15	QF Pegmatite	FIA2	i6a	Minor chipping to start; Na peak at 55 sec and at 125 sec.
HPP-3-15-FIA2_i6b	HPP-3-15	QF Pegmatite	FIA2	i6b	Na inclusion at 125 sec.
HPP-3-15-FIA2_i7	HPP-3-15	QF Pegmatite	FIA2	i7	Big inclusion. Na peak at 75 sec.
HPP-3-15-FIA2_i8	HPP-3-15	QF Pegmatite	FIA2	i8	Na peak at 105 sec.
HPP-3-15-FIA2_i9a	HPP-3-15	QF Pegmatite	FIA2	i9a	Minor chipping. Na peak at 65 sec.
HPP-3-15-FIA2_i9b	HPP-3-15	QF Pegmatite	FIA2	i9b	Na peak at 50 sec.
HPP-3-15-FIA2_i10	HPP-3-15	QF Pegmatite	FIA2	i10	Little chipping at first, Na peak at 95 sec.
HPP-3-15-FIA2_i11	HPP-3-15	QF Pegmatite	FIA2	i11	(Maybe at 35 sec - NO) Na peak for inclusion is at 105 sec.
HPP-3-15-FIA2_i12	HPP-3-15	QF Pegmatite	FIA2	i12	Na peak at 40 sec.
HPP-3-23-FIA3a_i4	HPP-3-23	Type (III) Quartz Vein	FIA3a	i4	Great ablation, small Na peak at ~70 sec. No other peaks except for Na observed.

Full ID	Iolite Notes	Salinity (wt % eq. NaCl)	Elements strongly correlated with Na	Elements possibly correlated with Na
HPP-3-15-FIA2_i3	Moderately broad, pointed Na peak at 90% through ablation. Relatively low compared to i1 and i2.	3.9	Li, Rb	Cs
HPP-3-15-FIA2_i5	Wide, double-topped Na peak at the end of ablation.	3.9	K, Li, Cs, Rb, Sr	
HPP-3-15-FIA2_i6a	Three Na peaks. First (1) is relatively minor, but still moderately broad and occurs at 45% through ablation. Second (2) is most significant, fairly broad and very intense and occurs at 60% through ablation. Third (3) is broad, flat-topped and occupies the final 25% of the ablation.	3.9	(1) Cs, Rb, Sr; (2) K, Li, Cs, Rb, Sr; (3) Cs, Rb, Sr	
HPP-3-15-FIA2_i6b	Composite Na anomaly. (1) Moderately broad, smooth Na peak followed by (2) broad, flat-topped Na anomaly starting at 40% through ablation and continuing to 85% through ablation.	3.9	(1) K, Cs, Rb; Sr; (2) Cs, Rb, Sr	(1) Li; (2) K, Li
HPP-3-15-FIA2_i7	Very large, intense, smooth, fairly broad Na peak at 55% through ablation.	3.9	K, Al, Li, Cs, Rb, Sr, B	
HPP-3-15-FIA2_i8	Large, intense Na peak at the end of ablation.	3.9	K, Al, Li, Cs, Rb, Sr, B	
HPP-3-15-FIA2_i9a	(1) Intense, wide but pointed Na peak at 35% ablation followed by dip and then (2) a broader, lower Na anomaly peaking at 75% ablation. May be two inclusions or a single inclusion leaking slowly after initial peak.	3.9	(1) K, Li, Cs, Rb, Sr, La; (2) Cs, Rb, Sr	(2) K, Li
HPP-3-15-FIA2_i9b	(1) Intense, wide but pointed Na peak at 35% ablation followed by dip and then (2) a broader, lower Na anomaly peaking at 75% ablation. May be two inclusions or a single inclusion leaking slowly after initial peak.	3.9	(1) K, Li, Cs, Rb, Sr, La; (2) Cs, Rb, Sr	
HPP-3-15-FIA2_i10	Probably two separate inclusions. First (1) is observed as a wide, intense, pointed Na peak with minor shoulder on beginning side. Second (2) is less intense, broader, but truncated by the end of ablation and probably cannot be used.	3.9	(1) K, Li, Cs, Rb, Sr; (2) Cs, Sr	(2) Rb
HPP-3-15-FIA2_i11	Intense Na peak with very minor tapering at finish that occurs at 90% through ablation.	3.9	K, Li, Cs, Rb, Sr, B	
HPP-3-15-FIA2_i12	Large, intense, slightly rounded Na peak at 10% through ablation followed by very broad, low Na anomaly that may be part of the same inclusion.	3.9	K, Li, Cs, Rb, Sr	
HPP-3-23-FIA3a_i4	Low, pyramidal, nearly symmetrical Na anomaly at ~55% ablation.	3.7	Li	K

Full ID	Sample ID	Feature Type	Chip ID	LA-ICP-MS Run ID	Analytical Notes
HPP-3-23-FIA3a_i5a	HPP-3-23	Type (III) Quartz Vein	FIA3a	i5a	Nice ablation. Small Na peak at 90 sec.
HPP-3-23-FIA3a_i5b	HPP-3-23	Type (III) Quartz Vein	FIA3a	i5b	Minor chips at start; right on crack. Otherwise great ablation. Vague peak at 75 sec.
HPP-3-23-FIA3a_i6	HPP-3-23	Type (III) Quartz Vein	FIA3a	i6	Chipping! But Na peak at 65 sec.
HPP-3-23-FIA3a_i7a	HPP-3-23	Type (III) Quartz Vein	FIA3a	i7a	Chipping. Maybe at 59 sec?
HPP-3-23-FIA3a_i7c	HPP-3-23	Type (III) Quartz Vein	FIA3a	i7c	At 155 sec. Na with Al peak.
HPP-3-23-FIA3a_i8	HPP-3-23	Type (III) Quartz Vein	FIA3a	i8	Chipped. Na peak at ~70 sec?
HPP-3-23-FIA3a_i9	HPP-3-23	Type (III) Quartz Vein	FIA3a	i9	Nice ablation, strange broad Na peak 85-115 sec.
HPP-3-23-FIA3a_i11	HPP-3-23	Type (III) Quartz Vein	FIA3a	i11	Chips. Maybe at 85 sec.
HPP-4-01-FIA3_i1a	HPP-4-01	Type (II) (skarn) Quartz Vein	FIA3	i1a	Chip right away. Small Na peak at 55 sec. Large Na peak at 95 sec.
HPP-4-01-FIA3_i1c	HPP-4-01	Type (II) (skarn) Quartz Vein	FIA3	i1c	Really huge chip. First Na peak at 60 sec; the second is at ~80 sec. Did W saturate? Look at counts.
HPP-4-01-FIA3_i2a	HPP-4-01	Type (II) (skarn) Quartz Vein	FIA3	i2a	Huge chip. Na peak at 60 sec? At 75 sec?
HPP-4-01-FIA3_i3a	HPP-4-01	Type (II) (skarn) Quartz Vein	FIA3	i3a	Chips. Bizzare Na peak with Al at 35-50 sec.
HPP-4-01-FIA3_i4b	HPP-4-01	Type (II) (skarn) Quartz Vein	FIA3	i4b	Chips, but maybe Na peak at ~60 sec.

Full ID	Iolite Notes	Salinity (wt % eq. NaCl)	Elements strongly correlated with Na	Elements possibly correlated with Na
HPP-3-23-FIA3a_i5a	Low, broad Na anomaly (not really a peak) at 75% through ablation.	3.7	Cs, Rb, Pb, Cu	Co
HPP-3-23-FIA3a_i5b	Low, broad Na anomaly (not really a peak) at 55% through ablation.	3.7	Cs, Rb	Ni
HPP-3-23-FIA3a_i6	Relatively minor Na peak at approximately 40% through ablation.	3.7		Rb, B, Zn(66)
HPP-3-23-FIA3a_i7a	Jagged, prominent, but poorly defined Na peak with multiple sub-peaks at 25% through ablation.	3.7	Cs, Rb	B
HPP-3-23-FIA3a_i7c	Major, well-defined, moderately broad Na peak at the end of ablation.	3.7		
HPP-3-23-FIA3a_i8	Narrow, intense Na spike at 15% through ablation.	3.7		
HPP-3-23-FIA3a_i9	Narrow, intense Na spike with minor tapering on both sides at 75% ablation.	3.7		B, Li
HPP-3-23-FIA3a_i11	Minor Na peak with small pointed shoulder sub-peaks at approximately 75% through ablation.	3.7		
HPP-4-01-FIA3_i1a	Two Na peaks. The first (1) is at 25% ablation and is moderately thin and minor compared to the second (2), which is wider, smooth, and broad and is at 75% ablation.	3.6	(1) Cs; (2) Li, Cs, B	
HPP-4-01-FIA3_i1c	Two Na peaks. The first (1) is broader, smoother, and tapers slightly as it finishes and occurs at 40% through ablation. The second (2) is very thin and intense and probably doesn't reflect ablation of an inclusion and occurs at 70% through ablation.	3.6	(1) Li, Rb, Cs, B, W; (2)	
HPP-4-01-FIA3_i2a	Four Na peaks. The first (1) is a thin spike with minor tapering at 40% through ablation. The second (2) is the most significant, (broader, smoother and as intense as (1)) at 60% through ablation. The third (3) is next to, but distinct from (2) and has two sub-peaks, and is less intense than the first two. The fourth (4) is less intense, but broad and pointed.	3.6	(2) Rb, Cs; Sr; As, B; (3) K, Rb, Cs, B; (4) Cs, As	(1) Li, Sr; (2) Li
HPP-4-01-FIA3_i3a	Two Na peaks. The first (1) is intense, very broad, and smooth with a rounded top and occurs immediately after the initial Na spike at the start of ablation. The second (2) is much less broad or intense, and is followed by a low, rounded Na anomaly and occurs at 75% through ablation. Al spectra exactly matches Na spectra.	3.6	(1) Al, Cs, Rb, Sr, B; (2) Al, Sr, Ag	
HPP-4-01-FIA3_i4b	Broad, somewhat jagged, pyramidal Na peak (not very intense) at approximately 50% through ablation.	3.6	Cs, Rb, Sr, B	Al, Cu

Full ID	Sample ID	Feature Type	Chip ID	LA-ICP-MS Run ID	Analytical Notes
HPP-4-01-FIA3_i5a	HPP-4-01	Type (II) (skarn) Quartz Vein	FIA3	i5a	Small chip at 45 sec. Weird Al spectra. Na peak at 85 sec. Chipped at 95 sec.
HPP-4-01-FIA3_i5b	HPP-4-01	Type (II) (skarn) Quartz Vein	FIA3	i5b	Focused at 45 sec. Probably not an inclusion there, even with Na peak.
HPP-4-01-FIA3_i6	HPP-4-01	Type (II) (skarn) Quartz Vein	FIA3	i6	Chip. Maybe at 60 sec.
HPP-4-01-FIA3_i7	HPP-4-01	Type (II) (skarn) Quartz Vein	FIA3	i7	Na peak at 55 sec.
HPP-4-01-FIA3_i8	HPP-4-01	Type (II) (skarn) Quartz Vein	FIA3	i8	Cracked at ~35 sec. Na peak at 43 sec.
HPP-4-08-FIA1_i1a	HPP-4-08	Type (III) Quartz Vein	FIA1	i1a	Crack at start. Maybe Na peak at 120 sec.
HPP-4-08-FIA1_i1b	HPP-4-08	Type (III) Quartz Vein	FIA1	i1b	Crack at start. Na peak at 93 sec.
HPP-4-08-FIA1_i2	HPP-4-08	Type (III) Quartz Vein	FIA1	i2	Na peak at 40 sec.
HPP-4-08-FIA1_i4	HPP-4-08	Type (III) Quartz Vein	FIA1	i4	Cracked at start. Na peak at 85 sec.
HPP-4-08-FIA1_i6	HPP-4-08	Type (III) Quartz Vein	FIA1	i6	Wide band of elevated Na at 45 sec (maybe).
HPP-4-08-FIA1_i8	HPP-4-08	Type (III) Quartz Vein	FIA1	i8	Chip at 40 sec. Na peak probably not inclusion.

Full ID	Iolite Notes	Salinity (wt % eq. NaCl)	Elements strongly correlated with Na	Elements possibly correlated with Na
HPP-4-01-FIA3_i5a	Two Na peaks. The first (1) is pointed, moderately broad and occurs at 70% through ablation. The second (2) is thin, less intense, and occurs with Si and K spikes at the end of ablation due to chipping.	3.6	(1) Cs, Sr, Cu; (2) Cs, K, La, Cu	(2) Si, Li, Rb, Sr, Mo, Sb
HPP-4-01-FIA3_i5b	Na peak composed of two subpeaks; the first is broader and lower, the second is thin and more intense. This peak occurs at 15% through ablation.	3.6	Li, Rb, B, Cs, Pb, La, As, Cu, Ni, Co (Probably the result of focusing)	
HPP-4-01-FIA3_i6	Narrow, intense Na spike at 40% through ablation. Peak is negatively correlated with Al.	3.6		K
HPP-4-01-FIA3_i7	Two Na peaks. The first (1) is low, smooth, and rounded, and occurs at 10% ablation. The second (2) is more pronounced, (still smooth but pointed), and occurs at 40% through ablation.	3.6	(1) Cs, Sr, B; (2) Al, Sr	(1) Rb, Li
HPP-4-01-FIA3_i8	Intense, pointed, somewhat broad Na peak at 15% through ablation followed by very broad, low Na anomaly that may be part of the same inclusion.	3.6	Cs, B	Li, Sr
HPP-4-08-FIA1_i1a	Low, relatively minor, pointed Na peak at 30% ablation. Only double background values.	3.6		
HPP-4-08-FIA1_i1b	Two Na peaks. The first (1) is minor, almost flat-topped, and not significantly more intense than background values. This peak occurs at 40% ablation. The second (2) is much more intense, pointed, moderately broad, and tapered slightly as it ends. This peak occurs at 80% ablation.	3.6	(1) ; (2) Cs, Cu, B	(2) Rb
HPP-4-08-FIA1_i2	Single, smooth Na peak (moderately broad and tapered, but not very intense) at 15% ablation.	3.6	Li, Rb, W, Zn(66), Ni	La
HPP-4-08-FIA1_i4	One large, smooth Na peak at the end of ablation.	3.6	Li, Cs, B, K, Cu, Rb	
HPP-4-08-FIA1_i6	Rounded, broad, and low Na peak immediately after initial Na spike at the start of ablation.	3.6	Rb	La, Pb, Li, Cu, B
HPP-4-08-FIA1_i8	Pointed Na peak at ~15% ablation followed by low, broad, vague Na anomaly.	3.6	B, Li, Cs, Rb, Sr	